Trinity College Dublin
Coláiste na Tríonóide, Baile Átha Cliath
The University of Dublin

Development of gene therapies for retinal degenerations

A thesis submitted to the University of Dublin for the degree of Doctor of Philosophy

2022

Ciara Shortall

Supervised by Prof. G Jane Farrar

Declaration

I declare that this thesis has not been submitted as an exercise for a degree at this or any other university and it is entirely my own work, except where otherwise stated.
I agree to deposit this thesis in the University's open access institutional repository or allow the library to do so on my behalf, subject to Irish Copyright Legislation and Trinity College Library conditions of use and acknowledgement.

Signed

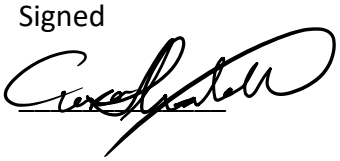

Ciara Shortall

Summary

This thesis explores potential gene therapies for retinal degenerations, both inherited and acquired, using adeno-associated virus (AAV) vectors for gene delivery.

Inherited retinal degenerations (IRDs) are a leading cause of vision loss for people of working age and exhibit extreme genetic heterogeneity, with over 270 known genes implicated. Retinitis pigmentosa (RP) represents the most common IRD, with a prevalence of 1 in 4,000 people. This progressive rod-cone dystrophy can be caused by mutations in any of over 80 different genes. The study presented in the second chapter of this thesis relates to X-linked RP (XLRP) caused by loss-of-function mutations in the *RP2* gene. The effects of two different *RP2* mutations were investigated using patient-derived fibroblasts and, through a collaborative effort, *RP2* null retinal organoids (ROs) were used to model this form of XLRP. A novel early-onset rod degeneration phenotype emerged in *RP2* null ROs, which could be prevented by highly efficient transduction with an AAV2/5-CAG-RP2 gene replacement vector. In addition, a preliminary evaluation of the tolerance of *in vivo* AAV-mediated RP2 overexpression after subretinal vector delivery in wild type mice was undertaken.

The research presented in chapter 3 of the thesis then explores the feasibility of a gene editing-based 'suppression and replacement' therapy for autosomal dominant RP (ADRP) due to rhodopsin (*RHO*) mutations. The ultimate aim of this project is to assess the therapeutic efficacy of insertion of a rhodopsin mini-gene into the *RHO* 5'UTR, which should simultaneously suppress expression of pathogenic alleles and provide a replacement coding sequence. A current obstacle in the development of gene editing therapeutics lies in the inefficiency of precise editing in post-mitotic cells. In this thesis chapter, the efficiency of a homology-independent targeted integration (HITI) strategy for gene insertion upstream of the human *RHO* start codon was explored. A dual AAV CRISPR-Cas9 based platform was developed to mediate insertion of an *EGFP* mini-gene into the *RHO* 5'UTR in photoreceptors of a humanised mouse model of *RHO*-ADRP. Although the experiment described in this thesis requires replication and further validation, initial results are promising, with a relatively high proportion of transduced photoreceptors (up to 43%) apparently expressing integrated EGFP sequences.

Gene therapies targeted towards specific genes hold great promise for monogenic inherited diseases. However, the extreme genetic heterogeneity of IRDs has made development of appropriate treatments challenging, as each gene-specific therapeutic must be assessed and achieve regulatory approval independently. Additionally, there is a significant need to develop effective treatments for age-related multifactorial retinal degenerations, such as glaucoma – the most common cause of irreversible blindness globally. Thus, there is considerable interest in developing gene-independent therapeutics that can modulate common degenerative mechanisms. Mitochondrial dysfunction is emerging as a major underlying factor in multiple types of retinal degeneration, including glaucoma. The study described in the final research chapter in this thesis explores whether increasing mitochondrial electron transport chain (ETC) activity could be beneficial in a glaucomatous context. The yeast Ndi1 gene encodes a single unit NADH dehydrogenase capable of substituting for ETC complex I, a huge multimeric protein. Intravitreal delivery of an AAV2/2-CMV-Ndi1 vector led to a significant increase in NADH oxidation activity in retinal and optic nerve tissue of the DBA/2J glaucomatous mouse model. Retinal ganglion cell body density was significantly preserved in DBA/2J eyes treated with this transkingdom gene therapy, while a trend of increased inner retinal function (assessed via electroretinogram) was also observed.

Overall, the data presented in this body of work support the immense potential of gene therapies for the treatment of rare monogenic retinal degenerations, such as RP2 and rhodopsin-linked RP, and also common multifactorial forms of ocular disease such as glaucoma.

Acknowledgements

Thank you to my brilliant supervisor, Prof. Jane Farrar, for all the guidance and support throughout the years, and for being a seemingly inexhaustible source of great ideas, compassion and chocolate.

Sincere thanks also to:

Our resident post-docs for training me to be a scientist (and putting up with my slightly unconventional working hours). Thanks to Dr Arpad Palfi for help with project planning, tissue sectioning, draft feedback and his enviable ability to always see through the nonsense. Thanks to Dr Naomi Chadderton for being an incredible one-woman vector core, Dr Sophia Millington-Ward for all the ERG work (that not even a pandemic could stop) and to Mr Paul Kenna for kindly doing the many injections I requested.

Matt, Killian, Danny, Adrian, Adlet, Laura (x2) and Iris for being great lab mates and friends over the years.

All on the third floor, for being lovely people to work with/around – particularly my 'room mates': Jeff, Ruth and Paul.

Our brilliant technical staff: Charlie, Brenda, Rachel, Dave, Paul, Philip and David.

My 'minions,' Emily, Laura, Emma, Cristina and Sukanya, for helping with these projects as part of their undergraduate and master's degrees.

Emma, my steadfast friend and favourite insomniac.

Thanks most of all to Fynn and my wonderful family - Mum, Dad, Eoin and Eimhear - for their unwavering love and support throughout this saga.

For my parents, Seamus and Mary.

Funding

The work described in this thesis was funded by grants awarded to Prof. G Jane Farrar by Science Foundation Ireland, Health Research Charities Ireland and Fighting Blindness Ireland.

Publications

Resulting from this work:

- Lane, A., Jovanovic, K., Shortall, C., Ottaviani, D., Brugulat Panes, A., Schwarz, N., Guarascio, R., Hayes, M.J., Palfi, A., Chadderton, N., Farrar, G.J., Hardcastle, A.J., Cheetham, M.E. (2020) Modeling and Rescue of RP2 Retinitis Pigmentosa Using iPSC-Derived Retinal Organoids. Stem Cell Reports, 15, 67-79.
  (Included in Appendix 1)

Related:

- Palfi, A., Yesmambetov, A., Millington-Ward, S., Shortall, C., Humphries, P., Kenna, P.F., Chadderton, N., Farrar, G.J. (2020) AAV-Delivered Tulp1 Supplementation Therapy Targeting Photoreceptors Provides Minimal Benefit in Tulp1−/− Retinas. Frontiers in Neuroscience, 14.
- Maloney, D.M., Chadderton, N., Millington-Ward, S. ,Palfi, A., Shortall, C., O'Byrne, C., Cassidy, L., Keegan, D., Kenna, P., Farrar, G.J. (2020) Optimized OPA1 Isoforms 1 and 7 Provide Therapeutic Benefit in Models of Mitochondrial Dysfunction. *Frontiers in Neuroscience,* 14.

Abbreviations

AAV	Adeno-associated virus
AD	Autosomal dominant
AH	Aqueous humour
AMD	age-related macular degeneration
AR	Autosomal recessive
ARL3	ADP ribosylation factor-like GTPase 3
ATP	Adenosine triphosphate
BSA	Bovine serum albumin
C57	C57BL/6J mouse strain
CAG	A synthetic promoter comprised of the CMV enhancer followed by the promoter, first exon and intron of the chicken β actin gene
Cas	CRISPR-associated protein
CDS	Coding sequence
CI	Complex I of the electron transport chain
CMV	Cytomegalovirus (usually referring to a promoter element)
CRISPR	clustered regularly interspaced short palindromic repeats
crRNA	CRISPR RNA; referring to the variable (targeting) region of a guide RNA
ds	Double-stranded
DSB	Double-stranded break
DsRed	A red fluorescent protein originating from *Discosoma* coral
ECM	Extracellular matrix
EGFP	Enhanced green fluorescent protein
ER	Endoplasmic reticulum
ERG	Electroretinogram
ESC	Embryonic stem cell (hESC = human ESC)
ETC	Electron transport chain
GAP	GTPase activating protein
GCL	Ganglion cell layer
GEF	Guanine nucleotide exchange factor
GFAP	Glial fibrillary acidic protein; a marker of gliosis
GM130	A cis-Golgi matrix protein

GOF	Gain-of-function
gRNA	Guide RNA
HDR	Homology-directed repair
HEK 293	Immortalised human embryonic kidney epithelial cell line
HeLa	Immortalised human cervical epithelial cell line
hGH	Human growth hormone
hGRK1	Human rhodopsin kinase (or G protein-coupled receptor kinase 1)
HITI	Homology-independent targeted integration
hPSC	Human pluripotent stem cell (iPSC or ESC)
HTG	Hypertensive glaucoma
huNdi1	Humanised (via codon optimisation) Ndi1
IBA1	Ionized calcium binding adaptor molecule 1; a microglial marker
ICC	Immunocytochemistry
IgG	Immunoglobulin
IHC	Immunohistochemistry
ILM	Inner limiting membrane
INL	Inner nuclear layer
IOP	Intraocular pressure
IPL	Inner plexiform layer
iPSC	Induced pluripotent stem cell (hiPSC = human iPSC)
IRD	Inherited retinal degeneration
ITR	Inverted terminal repeat
IVT	In vitro transcription
KO	Knockout
LCA	Leber congenital amaurosis
LHON	Leber hereditary optic neuropathy
LOF	Loss-of-function
mo	Months old
MOI	Multiplicity of infection
mtDNA	Mitochondrial DNA
NADH	Nicotinamide adenine dinucleotide (NAD) + hydrogen (H)
Ndi1	A yeast mitochondrial NADH dehydrogenase

NF200	Neurofilament 200 (or neurofilament heavy polypeptide, NEFH)
NFL	Nerve fibre layer
NHEJ	Non-homologous end-joining
NHP	Non-human primate
NMD	Nonsense-mediated decay
NTG	Normotensive glaucoma
OLM	Outer limiting membrane
ON	Optic nerve
ONH	Optic nerve head
ONL	Outer nuclear layer
OPL	Outer plexiform layer
OS	Outer segments
OXPHOS	Oxidative phosphorylation
PACG	Primary angle-closure glaucoma
PBS	Phosphate-buffered saline
PCR	polymerase chain reaction
PhNR	Photopic negative response
POAG	Primary open angle glaucoma
Poly(A)	Polyadenylation signal
PR	Photoreceptor
PTC	Premature termination codon
RFNL	Retinal nerve fibre layer
RGC	Retinal ganglion cell
RHO	Rhodopsin
RNFL	Retinal nerve fibre layer
RO	Retinal organoid
ROS	Reactive oxygen species
RP	retinitis pigmentosa
RP2	Retinitis pigmentosa 2
Rp2h	Retinitis pigmentosa 2 homolog (murine equivalent of *RP2*)
RPC	Retinal progenitor cells
RPE	Retinal pigment epithelium

RT-qPCR	Reverse-transcription quantitative real-time PCR
sc	Self-complementary
SD	Standard deviation
sgRNA	Single guide RNA
SNP	Single nucleotide polymorphism
ss	Single-stranded
TCA cycle	Tricarboxylic acid cycle
TLR	Toll-like receptor
TM	Trabecular meshwork
tracrRNA	Trans-activating CRISPR RNA
UTR	Untranslated region
vg	Vector genomes
WB	Western blot
WT	Wild-type
XL	X-linked

Contents

1 General introduction

1.1 The eye

Famously described by Darwin as an organ of ‘extreme perfection and complication’, the eye (Fig. 1.1) is a highly organised, sophisticated structure tasked with converting visual stimuli into electrical signals. Unfortunately, the more complex a system, the more points of potential failure.

1.1.1 The anterior segment

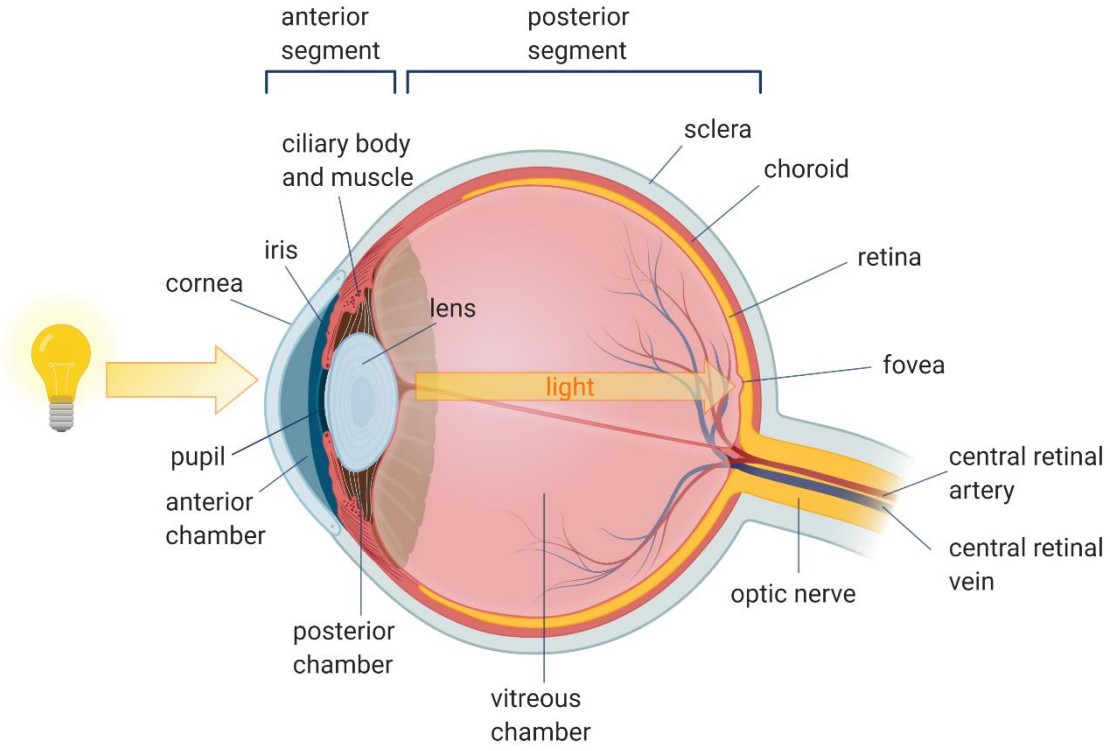

Figure 1.1. Anatomy of the eye.

Light must pass through the cornea, aqueous humour, pupillary aperture of the iris, the lens and vitreous humour before finally reaching the light-sensitive membrane known as the retina. Figure created using BioRender.com.

Light is focused by the refractive power of the transparent cornea and lens. Suspensory ligaments connect the lens, which is naturally elastic, to ciliary muscles that control its curvature, enabling the eye to change focus depending on an object’s relative distance. The iris also regulates its shape, but in response to lighting conditions. This tissue consists of two pigmented layers: a stroma (fibrovascular cells) and underlying epithelial cells. The stroma is connected to sphincter and dilator muscles that allow the iris to control the size of its pupil and, therefore, how much light ultimately reaches the retina (Snell and Lemp,

1998). To compensate for the avascular nature of many anterior segment tissues, the anterior and posterior chambers are filled with a nutrient-filled aqueous humour (AH) that is secreted by the ciliary body. AH also provides structural support, sustaining intraocular pressure. However, this fluid must be cleared at a rate equal to its production. Approximately 90% of aqueous leaves the eye through the trabecular meshwork in the iridocorneal angle, where it drains into Schlemm's canal and a series of collector channels and aqueous veins, and is cleared into the venous system (Fig. 1.2) (Snell and Lemp, 1998). The remaining fluid exits via the 'unconventional' pathway, moving through the ciliary muscle, choroid and sclera (Johnson et al., 2017).

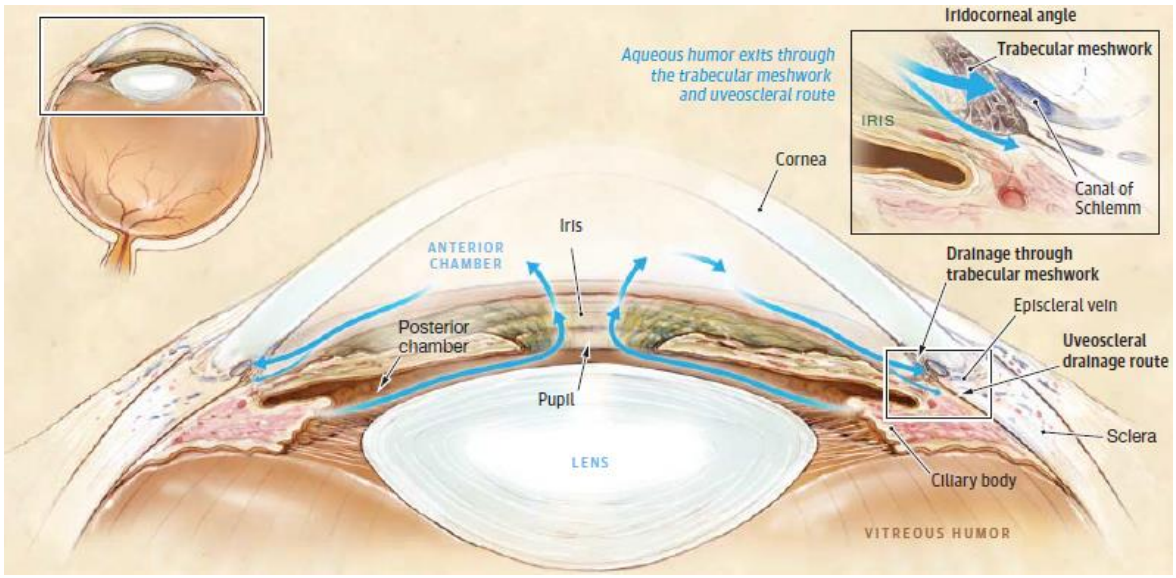

Figure 1.2. Aqueous dynamics in the anterior segment.

Figure reproduced from Weinreb et al., 2014.

1.1.2 The retina

The retina is an outpost of the brain responsible for detecting photons of light and relaying this information to the visual cortex as electrical signals, initiating the formidable task of visual processing. This thin, transparent membrane is comprised of five major neuronal classes: photoreceptors (rods and cones), bipolar cells, horizontal cells, amacrine cells and retinal ganglion cells (RGCs), alongside supportive glial cells (Fig.1.3.A). This laminated structure is separated into three nuclear layers (outer and inner nuclear layers (ONL/INL), and ganglion cell layer (GCL)) and two synaptic layers (outer and inner plexiform layers (OPL/IPL) (Fig.1.3.B). Somewhat counterintuitively, the photon-detecting

photoreceptors (PRs) are located at the back of the retina, so light must first pass through the upper transparent cell layers. Visual information must be passed from PRs to bipolar cells and on to RGCs in the front/inner retina before it can be delivered to the brain.

Phototransduction is initiated in photoreceptors outer segments (POS) (see Fig. 1.C for detailed depiction of photoreceptor structure), which are essentially highly specialised, non-motile cilia. POS contain tightly-packed stacks of opsin - a G-protein coupled receptor (GPCR) bound to the 11-*cis*-retinal chromophore. When exposed to light, 11-*cis*-retinal is changed to all-*trans*-retinal and the resultant change in GPCR conformation initiates a signalling cascade, which ends in photoreceptor hyperpolarisation (Tsin et al., 2018). In this way, light intensity is expressed using graded changes in membrane potential and neurotransmitter release (Bertalmío, 2020).

Photoreceptors have different spectral sensitivities, depending on the type of opsin they possess. Rod photoreceptors, which express rhodopsin, are extremely sensitive (capable of detecting a single photon of light) and are the predominant type of photoreceptor outside of the central retina (macula). Overall, rods outnumber cones in the retina by ~20:1 (Masland, 2012). In the human retina, there are normally 3 different types of cone photoreceptor: S-, M- and L- cones, which contain opsins sensitive to short, medium and long wavelength light, respectively (Hoon et al., 2014). Cones are concentrated in the macula, particularly so in the fovea – a small pit in the centre of the macula where inner retinal cells are displaced so that light shines more directly on its dense population of cones (Snell and Lemp, 1998). Although they are ~100 times less sensitive than rods, cones can respond to light much faster. Rods therefore enable monochromatic sight in low (scotopic) lighting, and peripheral vision. Cones facilitate trichromatic and central vision in brightly-lit (photopic) conditions, in which rods are saturated (Hoon et al., 2014, Bertalmío, 2020). Rods vastly outnumber corresponding RGCs in peripheral regions, and so the signals of many different rod cells converge onto a single ganglion cell. In contrast, each foveal cone is connected to a distinct RGC, which enables a high degree of spatial resolution and visual acuity in this region (Bertalmío, 2020).

Photoreceptor outer segments are surrounded by microvilli of the retinal pigment epithelium (RPE), which facilitates nutrient exchange between PRs and the choroid and is vital for the upkeep of POS. Used (all-*trans*) chromophore is transported from photoreceptor outer segments (POS) to the retinal pigment epithelium (RPE), where it is

reisomerised to the excitable 11-*cis* form and delivered back to the photoreceptors (Strauss, 2005). RPE cells also phagocytose and recycle shed POS, which must be completely replaced roughly every 10 days (Young, 1971). While the constant renewal of POS may prevent against accumulation of components damaged by photooxidative stress (Pearring et al., 2013), the rapid rate of protein turnover means that photoreceptors cells are especially sensitive to perturbations in protein trafficking. Many severe forms of inherited retinal degeneration are thought to be caused by defects in OS trafficking, one of which will be discussed in chapter 2.

The human retina contains approximately 126 million photoreceptors but only ~1 million retinal ganglion cells (RGCs), which transmit visual information to the brain. Signals produced by photoreceptors must therefore be efficiently condensed. Photoreceptors form synapses with bipolar cells (BCs) in the OPL. Photoreceptor hyperpolarisation leads to a reduction in the continuous release of glutamate across the PR-bipolar cell synapse. There are 12 different types of BC, only one of which interacts with rods. The main subdivision of BC types is between ON and OFF cells; ON cells are excited by a reduction in photoreceptor glutamate release, while OFF cells are inhibited. Input from as many as 1500 rod cells can converge onto one BC, which allows amplification of the signal from these highly sensitive cells and reduction of noise, while each cone cell forms connections with 12 different BCs. Cone BCs form synapses with RGCs, while rod BCs connect to amacrine cell intermediates before ganglion cells. Signals propagated along the parallel, vertical paths from PR to RGC are subject to lateral inhibition mediated by horizontal and amacrine cells, which enhances contrast and sharpness of the transmitted visual information (Bertalmío, 2020, Meister and Tessier-Lavigne, 2013).

Approximately 20 distinct types of RGC have been identified, which can relay different aspects of a retinal image (i.e. colour, contrast, spatial and temporal resolution, motion, edge detection). RGCs are the only class of retinal neuron that can fire action potentials and do so in response to the graded glutamate release of bipolar or amacrine cells. These action potentials must be transmitted to the brain for further processing and interpretation. RGC axons therefore traverse the retina in the nerve fibre layer (NFL, or retinal nerve fibre layer (RFNL)) before converging and exiting the eye in the form of the optic nerve, which connects the retina to the brain (Bertalmío, 2020, Meister and Tessier-Lavigne, 2013). The unique cellular architecture and high energy demands of RGCs makes

them extremely vulnerable to metabolic deficiencies – an issue that will be explored in the context of glaucoma in chapter 4.

Retinal neurons are dependent on the support of macroglia (Müller cells and astrocytes) and microglia (Fig.1.3.D).

Müller glia span the full width of the neuroretina; their processes extend vertically from the INL in both directions. Tight-junctions between Müller cells and photoreceptor inner segments form the outer limiting membrane (OLM) barrier between the retina and subretinal space (Reichenbach and Bringmann, 2020), while Müller cell endfeet covered with basal lamina make up the inner limiting membrane (ILM) – a barrier that separates retina from the vitreous body (Snell and Lemp, 1998). Their processes also extend to form supportive sheaths around neurons. Müller glia play an important role in channelling light to photoreceptors. They also provide photoreceptors with metabolic substrates, trophic and antioxidant factors, facilitate exchange of nutrients and metabolic waste products, and control extracellular levels of neurotransmitters, water and ions. Regulation of immune response and inflammation are additional, important components of their repertoire (Reichenbach and Bringmann, 2013, Reichenbach and Bringmann, 2020).

Astrocytes are mainly present in the GCL and NFL, and in the optic nerve. They share functions with the Müller glia, including regulation of ion and neurotransmitter concentrations in the extracellular fluid, and can deliver neurotrophic factors to neurons in times of stress. Microglia - the immune cells of the retina - survey the OPL, IPL and GCL, phagocytosing cellular debris and pathogens. They too can provide trophic factors. While they are capable of antigen presentation, they normally act to suppress inflammation (Reichenbach and Bringmann, 2020).

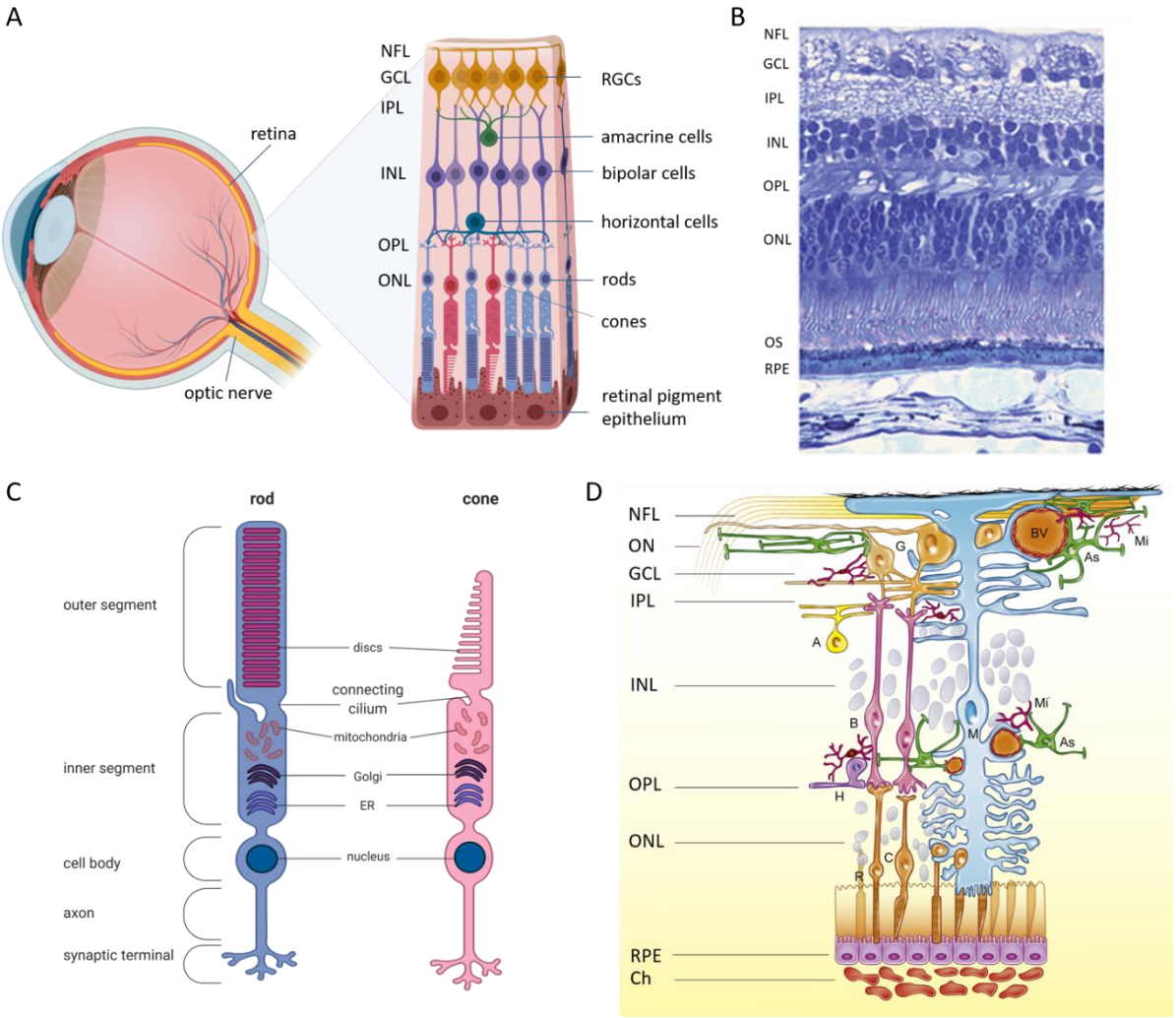

Figure 1.3. The retina.

(A) Schematic of the laminated neuroretina and RPE. ONL = outer nuclear layer; OPL = outer plexiform layer; INL = inner nuclear layer; IPL = inner plexiform layer; GCL = ganglion cell layer; NFL = nerve fibre layer.

(B) Light micrograph of a human retinal cross-section.

(C) Illustration of rod and cone photoreceptor cells. Outer segments contain discs of opsin, formed by in-folding of the plasma membrane (PM). In rods, these discs are ultimately detached from the PM, whereas cones opsin discs remain tied to the PM. Photoreceptor inner segments are mitochondria-rich and contains the protein-making apparatus. Newly synthesised proteins destined for the OS must be trafficked through the connecting cilium. ER = endoplasmic reticulum.

(D) Schematic illustrating retinal neural, glial and vascular cells of the retina. M = Muller cell; Mi = microglial cell; As = astrocyte; BV = blood vessel; ON = optic nerve; Ch = choroid; G = ganglion cell; A = amacrine cell; B = biopolar cell; H = horizontal cell; R = rod; C = cone.

Figures B and D are adapted from Wright et al., 2010 and Vecino et al., 2016, respectively. A and C were created using Biorender.com.

1.2 Blindness

Humans are deeply reliant on sight in our attempts to navigate and appreciate the world. Visual impairment is linked to loss of independence, increased risks of depression and falls, lower rates of employment and workplace productivity, and educational attainment, and higher (non-eye related) medical costs (Marques et al., 2020, Javitt et al., 2007, Galvin et al., 2020). In a US survey, participants consistently ranked blindness as a worse condition than HIV/AIDS, loss of limb, deafness, heart disease or arthritis. Depending on the ethnic group, blindness was also feared more than cancer (Caucasian) or Alzheimer's disease (Asian/Hispanic), or both (African American) (Scott et al., 2016). In 2015, 253 million people were thought to be moderate to severely visually impaired or blind worldwide (Bourne et al., 2017), a figure which is set to increase as the populations of developing nations age. The global economic cost of visual impairment has been estimated as $2954 billion (USD) (Gordois et al., 2012). The leading causes of blindness are cataracts and glaucoma (Flaxman et al., 2017). Glaucoma will be discussed in chapter 4, which explores a potential gene-based therapy for this condition.

When it comes to individuals between 15 to 45 years of age, inherited retinal degenerations (IRDs) are the major cause of sight loss (Cremers et al., 2018). IRDs represent a clinically and genetically diverse group of conditions in which retinal cells progressively die, leading to a state of legal blindness. Over 270 genes have been linked to IRDs[1] and the genetic basis of ~28-50% of cases remain unresolved (Farrar et al., 2017). While there may be other IRD-causing genes yet to be identified, much of remaining caseload may arise from non-coding or structural variants in genes already implicated (Whelan et al., 2020, Farrar et al., 2017). Depending on the genetic insult, IRDs can be juvenile or adult-onset, syndromic or non-syndromic, and primarily affect rods (rod-cone dystrophies), cones (cone-rod dystrophies) or retinal ganglion cells (optic neuropathies). Although individually rare, IRDs have been estimated to collectively affect 1 in 2000 people (Cremers et al., 2018). 1 in 2.3-3.5 people are estimated to be carriers of an autosomal recessive IRD (Hanany et al., 2020). Until recently, IRDs and their consequences had not been as well-studied as other sources of debilitating visual

[1] https://sph.uth.edu/retnet/sum-dis.htm [accessed: 22/11/20]

impairment due to the low prevalence of IRDs individually. Thanks to patient-led efforts[2], the full impact of IRDs is now starting to be understood. In 2019, the economic and well-being costs of IRDs amounted to £42.6 million in the Republic of Ireland (ROI) and £523.3 million in the UK, with the majority of these costs being shouldered by affected individuals, their family and friends, and society. Individuals affected by IRDs were 40-56% less likely to be in paid employment and the majority of those surveyed reported experiencing anxiety (>85%) and depression (>63%) as a result of their condition (Galvin et al., 2020).

1.3 Retinitis pigmentosa

Retinitis pigmentosa (RP) is the most common IRD, with an estimated global prevalence of 1 in 4000 people - ranging from 1 in 750 to 1 in 9000, depending on the population (Verbakel et al., 2018). RP, typically a rod-cone dystrophy, can involve autosomal dominant (AD), autosomal recessive (AR), and X-linked (XL) modes of inheritance - representing 30-40%, 50-60% and 5-15% of cases, respectively (Verbakel et al., 2018). In the early days of IRD genetics (c. the late 1980s/early 1990s), it was therefore suspected that 3 different genes would be implicated in RP – one for each mode of transmission (Prof. G Jane Farrar, personal communication). Fast-forward to 2020 and 89 different genes have been linked to this incredibly heterogeneous disease[3].

In RP, apoptotic rod death is followed by secondary cone degeneration. This is at least partly due to the fact that rods secrete a protein that enhances cone survival by promoting aerobic glycolysis (rod-derived cone viability factor, RdCVF) (Aït-Ali et al., 2015). Thus, while disease course varies across cases, RP generally begins with night blindness (nyctalopia) and delayed dark adaptation, followed by a progressive restriction of the visual field that gives rise to 'tunnel vision'. Macular cones usually function normally until the late stages of disease, with central vision loss apparent by the age of 60 (Takahashi et al., 2018), although it can arise earlier. Age of onset can vary from early childhood to adulthood. XLRP patients tend to present with an earlier age of onset and

[2] https://www.retina-international.org/ird-counts-study-results-released-today-at-euretina19/ [accessed: 21/11/20]
[3] https://sph.uth.edu/retnet/sum-dis.htm#B-diseases [accessed: 21/11/20]. Note: this figure relates to non-syndromic RP.

faster disease progression than ARRP or ADRP, while central vision is generally preserved for longer in ADRP cases (Verbakel et al., 2018).

Clinical hallmarks of RP evident upon fundus examination include blood vessel attenuation (likely due to decreased metabolic demand (Ma et al., 2012)), a pale/'waxy' optic disc , and presence of 'bone spicules' - pigment-containing cells that accumulate around intraretinal blood vessels in regions of degeneration (Fig. 1.4). The origin of these pigmentary deposits, from which the disease gets its name, remains unresolved; they have been proposed to be ectopic RPE cells, or pigment-phagocytosing macrophages or Müller glia (Takahashi et al., 2018). Rod and cone electroretinogram (ERG) responses are also absent and markedly reduced, respectively, from the middle stage of disease (Hamel, 2006).

The genetic heterogeneity of RP is a great obstacle in the path to finding treatments for this condition, as there is no universally applicable therapeutic approach. Currently, the only approved RP treatment is a gene replacement therapy for a recessive subtype caused by biallelic *RPE65* mutations (which will be further discussed in the next section). It is therefore vitally important to develop effective therapeutics for the remaining majority of RP cases in order to address this substantial unmet clinical need.

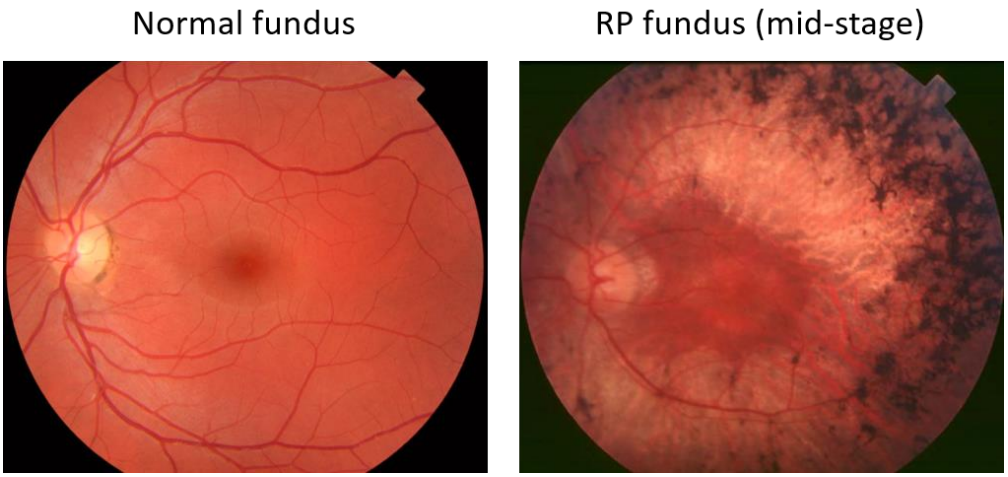

Figure 1.4. Comparison of normal and RP fundus photographs.
The fundus of an individual with mid-stage RP is shown on the right (reproduced from Hamel et al. 2006). Retinal vein attenuation and mid-peripheral bone-spicules are evident. A normal fundus is included for comparison (left) (taken by Mikael Häggström and used with permission).

1.4 Gene therapy

A gene therapy, as defined by the European Medicines Agency (EMA), is a medicine that:

> "contains an active substance which contains or consists of a recombinant nucleic acid used in or administered to human beings with a view to regulating, repairing, replacing, adding or deleting a genetic sequence",
> where "its therapeutic, prophylactic or diagnostic effect relates directly to the recombinant nucleic acid sequence it contains, or to the product of genetic expression of this sequence."[4,5]

The concept of gene therapy has been around for quite some time; in 1966, Edward Tatum suggested the possibility of using viral gene transfer to mediate 'genetic therapy' (Tatum, 1966). Viruses are, of course, highly efficient gene delivery systems, having evolved to circumvent the cell's membrane defence. It would be another 24 years before the first FDA-approved gene therapy clinical trial commenced, in an attempt to treat severe combined immunodeficiency (SCID) caused by loss-of-function mutations in the adenosine deaminase gene (*ADA*). A retrovirus was used for genomic insertion of a wild-type *ADA* allele into patient T cells *ex vivo* and modified cells were then delivered back into the patients' bloodstream. The results were promising, with improved immune function sustained up to 2 years after treatment (Blaese et al., 1995). However, the field of gene therapy soon suffered two significant setbacks. In 1999, Jesse Gelsinger tragically died in a clinical trial testing an adenoviral gene replacement vector for the treatment of ornithine transcarbamylase (OTC) deficiency. The high dose of adenovirus administered triggered a major immune response, which led to multi-organ failure (Wilson, 2009). Another major upset occurred during clinical trials for X-linked SCID, which, like the ADA-SCID trials, employed an *ex vivo* retroviral gene replacement strategy. The initial results of these trials (in the early 2000s) were positive, with improved T cell function noted in most treated patients. However, 5 out of 20 patients subsequently developed T cell leukaemia – one of whom subsequently died. This malignant transformation arose from disrupted regulation of proto-oncogene expression following nearby integration of retroviral long

[4] Note: vaccines against infectious diseases are excluded from this definition.
[5] Directive 2001/83/EC of the European Parliament and of the Council of 6 November 2001 on the Community code relating to medicinal products for human use

terminal repeat (LTR) elements with inherent promoter activity (Williams and Thrasher, 2014).

These tragic events understandably inspired hesitancy, particularly in the Western world, and it would be roughly a decade before public faith in the field of gene therapy was restored. The dangers of insertional mutagenesis and immune response have been largely overcome by employing self-inactivating (SIN) retroviruses, which lack promoter activity due to a partial LTR deletion, for *ex vivo* therapies or by adoption of recombinant adeno-associated virus (rAAV) vectors for *in vivo* applications. rAAV vectors are non-integrating, much less immunogenic than adenovirus and can provide persistent episomal expression. Now, in the 'modern era of gene therapy,' over 2500 gene therapy clinical trials have been registered, tackling a wide variety of inherited and acquired diseases (Anguela and High, 2019).

Over 20 gene therapies have been approved for commercial distribution by various regulatory bodies across the world (reviewed by Ma et al. 2020). In 2017, Luxturna™ (voretigene neparvovec-rzyl), an AAV-based gene replacement therapy for a recessive IRD, made history as the first US Food and Drug Administration (FDA)-approved gene therapy for an inherited disease[6]. EMA approval followed soon after (in 2018) and the FDA formally recognised the 'great promise' of gene therapy, announcing efforts to expedite the development of new gene-based therapeutics (FDA, 2018). Gene therapy's coming-of-age was largely attributed to the safety and efficacy of AAV vectors for *in vivo* gene transfer (FDA, 2019). Another AAV gene replacement therapeutic, Zolgensma, has since received FDA and EMA approval for treatment of spinal muscular atrophy.

1.4.1 AAV

AAV is a small, non-enveloped virus of the *Parvoviridae* family, comprised of an icosahedral protein capsid (25 nm in diameter) and linear single-stranded (ss) genome of 4.7 kb (Grieger and Samulski, 2005, Samulski and Muzyczka, 2014). The economical AAV genome consists of *rep* and *cap* genes that utilise multiple open reading frames and alterative splicing to express proteins needed for replication and capsid production/assembly, respectively. These coding sequences are flanked by two 145bp

[6] Glybera, an AAV-based gene replacement therapy for a rare inherited lipoprotein lipase deficiency, was the first gene therapy to be approved by the EMA in 2012. However, it was not commercially successful and is no longer in production (Senior, 2017).

inverted terminal repeats (ITRs), which form T-shaped hairpin structures that act as both origins for viral genome replication and a signal to stimulate genome packaging into newly synthesised capsids. Wild-type AAV requires proteins of a co-infecting 'helper' virus to replicate and is therefore classed as a *Dependoparvovirus*. Indeed, AAV was first discovered as a contaminant in isolated adenoviral samples (hence its name). Although more than 70% of people are estimated to have been infected with some form of AAV, the virus is not pathogenic to humans (Samulski and Muzyczka, 2014). In its latent phase (in the absence of a helper virus) wild-type AAV integrates into the host genome – predominantly at a site in chromosome 19 known as AAV integration site 1 (AAVS1), which contains Rep binding sites (Balakrishnan and Jayandharan, 2014).

ITR sequences are the only viral *cis* elements needed for rAAV vector production. This means viral coding sequences can be completely removed and substituted with a desired expression cassette – provided the Rep and Cap proteins, along with the required helper viral factors, are supplied *in trans*. Therefore, co-transfection of a producer cell line with three different plasmids containing (i) the transgene cassette with an AAV ITR either side, (ii) *rep* and *cap* genes and (iii) adenoviral helper genes is sufficient to ensure assembly of the rAAV. Recombinant AAV vectors are thus replication-incompetent in the absence of Rep protein and are incapable of site-specific integration into AAVS1. Very low rates of rAAV integration at other genomic sites have been noted in human and NHP tissues after vector administration (Wang et al., 2019a).

AAV particles are capable of transducing both dividing and post-mitotic cells. They can enter a cell through several different endocytic pathways, which are stimulated upon binding of virions to glycosylated primary receptors and proteinaceous secondary co-receptors on the cell surface (Dhungel et al., 2020) (Fig.1.5). There are a variety of naturally occurring AAV serotypes (AAV1, AAV2, AAV3, etc.), which differ in terms of amino acid composition at capsid 'variable regions.' Variable region residues determine what receptors an AAV particle may bind to and hence decide a serotype's cellular tropism. A proportion of internalised particles (~20% in the case of AAV2) escape late endosomes and are imported into the nucleus via nuclear pore complexes (Büning and Srivastava, 2019). After nuclear entry, the viral capsid is uncoated, freeing the AAV genome. Second strand synthesis is then initiated from a self-priming ITR hairpin to enable transcription of the delivered genes. At this point, double-stranded AAV genomes

can be maintained in a circular extrachromosomal DNA (episomes) or integrated into the host cell genome (Fig.1.5).

In rAAV production, ITR sequences from AAV2 are used to flank the desired transgene expression cassette, while the *cap* gene supplied *in trans* is selected from a serotype with affinity for the cell-type of interest. For example, an AAV made with AAV2 ITR sequences and AAV5 capsid proteins would be classified as a pseudotyped AAV2/5 vector. AAV2 was one of the first AAV serotypes identified (in 1965) and is the most thoroughly characterised (Choi et al., 2005). It can efficiently transduce the RPE and has demonstrated an excellent safety profile in the human retina (Maguire et al., 2008, Bainbridge et al., 2008, Hauswirth et al., 2008, Jacobson et al., 2012, Russell et al., 2017, Maguire et al., 2019). AAV2/5 and 2/8 more efficiently transduce photoreceptors (Suracea and Auricchio, 2008), however, and there are several potential therapeutics utilising these serotypes currently under clinical development (reviewed by Buck et al. 2020).

Additionally, next generation AAV vectors modifying the vector's tropism through the targeted mutation of genes encoding the capsid proteins have the potential to greatly improve transduction efficacy. For example, mutating the tyrosine residue at position 733 of a capsid surface protein to phenylalanine has been shown to enable faster and stronger transgene expression – an improvement hypothesized to be facilitated by reduced phosphorylation of tyrosine residues and thus reduced ubiquitination and degradation of the vector by host cell proteasomes (Pang et al., 2011). Transduction efficiency can also be improved through AAV capsid engineering, using rational design, directed evolution or *in silico* design strategies (Wang et al., 2019a). Indeed, these technologies are currently being extensively utilised to generate novel AAV serotypes.

The most notable disadvantages of AAV vectors are its limited cargo size (~4.8 kb) and the fact that full transgene expression is delayed for about 1-2 months while the virion coat is shed and a complement to the ssDNA is synthesized (Wu et al., 2010, Bucher et al., 2020). To circumvent packaging constraints, dual and triple AAV platforms are under development, in which the transgene sequence is split across vectors and, following transduction, can be spliced together at the DNA, mRNA or protein level – though such systems are of course not as efficient as single vector platforms (Tornabene, 2020). Moreover, accurate and robust assembly of the full length transgene using these systems

has yet to be thoroughly explored. In order to reduce the time taken before onset of expression, self-complementary AAV (scAAV) vectors can be utilised, in which the transgene and its inverted complement are included in the cassette and can form a functional template without delay, enabling significantly more efficient transgene expression (Natkunarajah et al., 2008, Greenwald et al., 2020). Of course, a downside to this approach is that the vector's already limited transgene-carrying capacity is halved. scAAV vectors also appear to be more immunogenic, enhancing AAV genome detection by Toll-like receptor (TLR) 9 (Bucher et al., 2020).

(i)

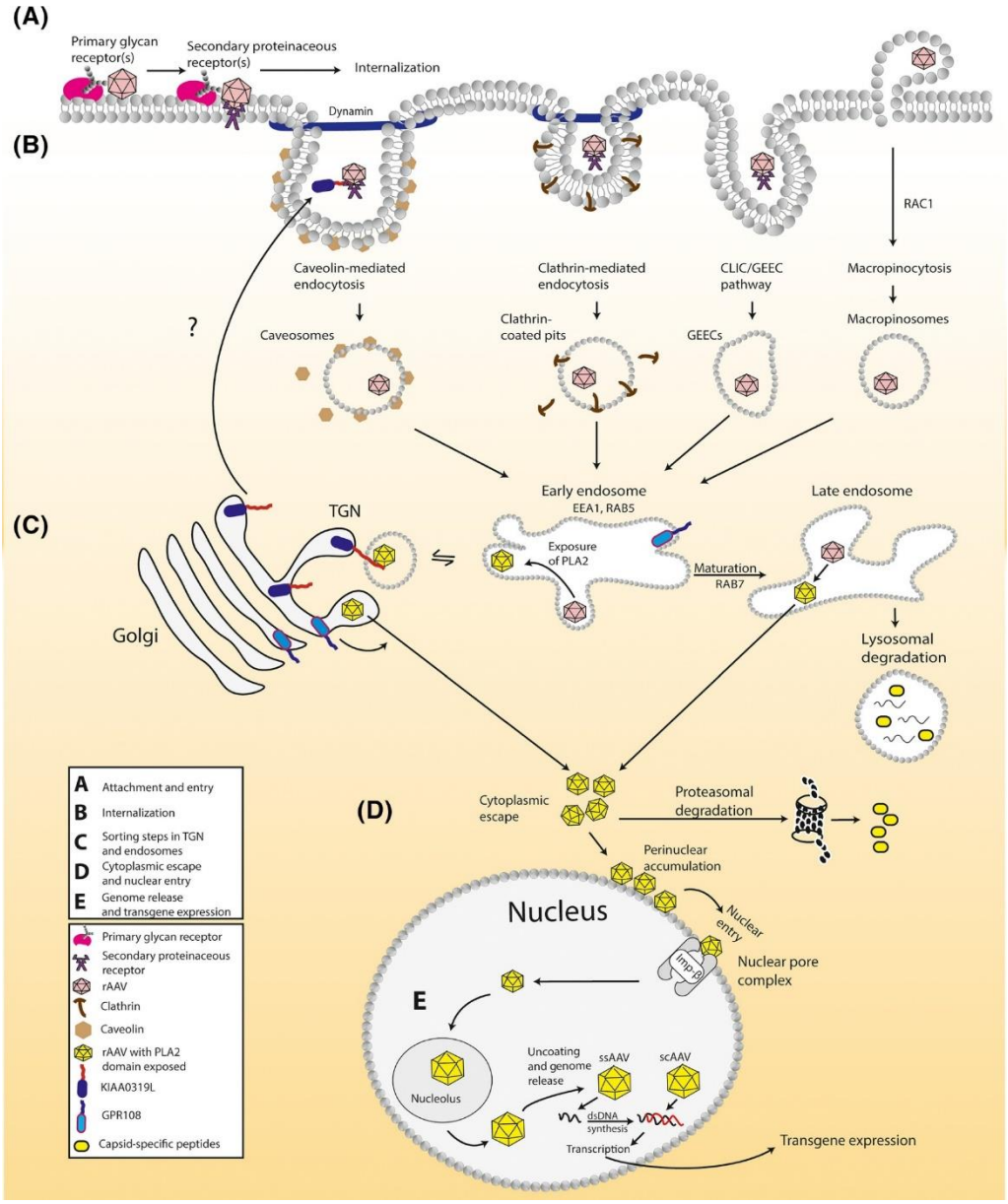
(A)
Primary glycan receptor(s)
Secondary proteinaceous receptor(s)
Internalization
(B)
Dynamin
RAC1
Caveolin-mediated endocytosis
Clathrin-mediated endocytosis
CLIC/GEEC pathway
Macropinocytosis
Caveosomes
Clathrin-coated pits
GEECs
Macropinosomes
?
Early endosome
EEA1, RAB5
Late endosome
(C)
TGN
Golgi
Exposure of PLA2
Maturation
RAB7
Lysosomal degradation
A Attachment and entry
B Internalization
C Sorting steps in TGN and endosomes
D Cytoplasmic escape and nuclear entry
E Genome release and transgene expression
Primary glycan receptor
Secondary proteinaceous receptor
rAAV
Clathrin
Caveolin
rAAV with PLA2 domain exposed
KIAA0319L
GPR108
Capsid-specific peptides
(D)
Cytoplasmic escape
Proteasomal degradation
Perinuclear accumulation
Nucleus
Nuclear entry
Imp-β
Nuclear pore complex
E
Nucleolus
Uncoating and genome release
ssAAV
scAAV
dsDNA synthesis
Transcription
Transgene expression

(ii)

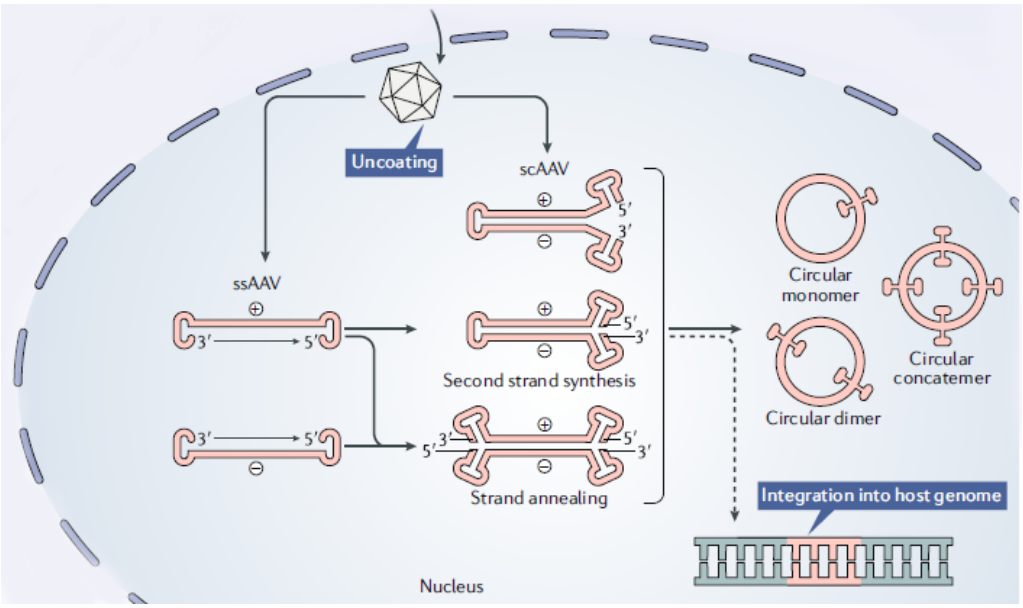
Uncoating
scAAV
ssAAV
Second strand synthesis
Strand annealing
Circular monomer
Circular concatemer
Circular dimer
Integration into host genome
Nucleus

Figure. 1.5. Schematic of AAV transduction.

(i) AAV particles bind to primary and secondary cell surface receptors and are endocytosed. Once internalised, virions are sorted in endosomal and Golgi compartments, and undergo various capsid conformation changes – e.g. exposure of phospholipase A2 (PLA2) domains, which is required for endosomal escape. KIAA0319L and GPR108 are entry factor proteins enriched in the Golgi that appear to be essential in facilitating transduction. Virions make their way into the cytosol and enter the nucleus through nuclear pore complexes or, alternatively, undergo proteasomal degradation. TGN = trans Golgi network; GEEC = glycosylphosphatidyl-achored protein (GPI-AP)-enriched compartment; imp-β = importin β.

(ii) Within the nucleus, AAV particles shed their capsid coats and the released single-stranded genome is converted to dsDNA via second strand synthesis or annealing of sense and antisense strands. Alternatively, scAAV genomes, which are already double-stranded, can bypass the rate-limiting step of second strand synthesis. Double-stranded rAAV genomes are predominantly maintained as episomes (consisting of one or multiple genomes) but a small proportion of AAV genomes may undergo integration into host DNA.

Figures reproduced from (i) Dhungel et al. 2020 and (ii) Wang et al. 2019.

1.4.2 Gene therapies for ocular disease

The retina has proven to be an optimal context in which to test the potential of *in vivo* gene therapy for a number of reasons. The eye is an easily accessible organ, meaning drugs can be administered relatively non-invasively and experimental outcomes can also be monitored using non-invasive imaging techniques. Ideal within-subject experimental controls are readily available in the form of untreated contralateral eyes. Additionally, the small size of the eye and post-mitotic nature of retinal cells means that relatively low dosages are required and transgene-expressing AAV episomes will not be diluted out, as they would be in dividing cells.

Ocular immune privilege is also a major advantage; the intraocular space is naturally anti-inflammatory and immunosuppressive to protect against collateral damage to its important, non-regenerative tissues (Streilein, 2003). The eye's microenvironment is guarded by blood-ocular barriers, which tightly regulate the entry and exit of molecules and cells. The blood-aqueous barrier is sealed by tight junctions (TJs) of non-pigmented epithelial cells of the ciliary body and endothelial cells of the iris vasculature, while the inner and outer blood-retinal barriers are formed by TJs of the endothelial cells of retinal blood vessels and retinal pigment epithelium, respectively (Cunha-Vaz, 1997). Ocular

tissues also produce immunomodulatory factors that suppress inflammation (Streilein, 2003).

Substances can be delivered to the retina through intravitreal or subretinal injection, where the syringe contents are released into the vitreous body or between the photoreceptor and RPE layer, respectively (Fig. 1.6). Intravitreal (IVT) injection is the least invasive administration route of the two, as subretinal (SR) injection necessitates a transient detachment of the neuroretina from the RPE and has been associated with damage to central retinal structure in some patients (Gamlin et al., 2019). Transduction in the subretinal space is also limited to cells that come into direct contact with the bleb of injected fluid. With regard to IVT injection, although AAV can effectively transduce RGCs from intravitreal starting point, it cannot efficiently penetrate the outer retina. In the vitreous, AAV is diluted, exposed to neutralising antibodies and its entry to the retina is further impeded by the ILM. Efforts to overcome these obstacles include directed evolution of serotypes with the ability to pass through the ILM and development of a sub-ILM injection technique (Dalkara et al., 2013; Boye et al., 2016). However, these innovations have not yet succeeded in transducing photoreceptors as efficiently as SR injection. Delivery of AAV to the vitreous also appears to be more immunogenic than delivery to the subretinal space (Li et al., 2008, Seitz et al., 2017). SR injection thus remains the current method of choice for delivering therapies targeting the outer retina.

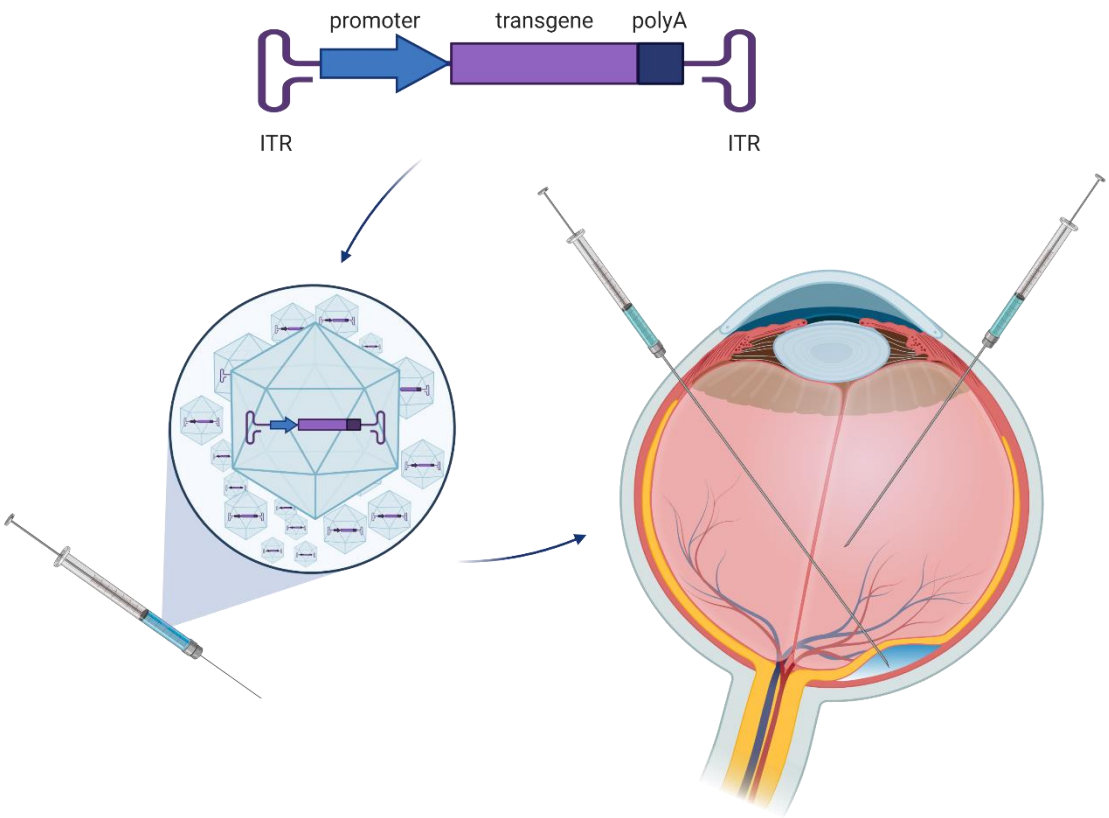

Figure 1.6. Schematic of steps involved in retinal gene therapy.

A rAAV genome is synthesised to include an expression cassette for a therapeutic transgene, flanked by ITR sequences necessary for viral packaging. The recombinant genome is then packaged into an AAV capsid of choice and the resulting viral particles are injected either subretinally or intravitreally, depending on the target cell-type.

Figure created using Biorender.com.

The recent FDA (2017) and EMA (2018) approvals of Luxturna™ (Spark Therapeutics), an AAV-based gene replacement therapy for retinal degeneration due to biallelic *RPE65* mutations (presenting as Leber Congenital Amaurosis or RP), was a landmark achievement for the gene therapy field. Luxturna is an AAV2/2 vector that carries a human *RPE65* coding sequence under the control of the constitutive CAG promoter, which is comprised of the cytomegalovirus (CMV) early enhancer followed by the promoter, first exon and first intron of the chicken β-actin (CBA) gene. When subretinally injected, this vector restores expression of RPE65, a vital enzymatic component of the visual cycle, in RPE cells. Proof-of-concept for a *RPE65* gene replacement strategy was established in pre-clinical studies utilising canine and murine *RPE65*$^{-/-}$ models (Acland et al., 2001, Acland et al., 2005, Bennicelli et al., 2008), with improved visual function

maintained for up to a decade in treated dogs (Cideciyan et al., 2013). After safety assessment in non-human primates, clinical trials of this therapeutic strategy commenced from 2007 in small cohorts of patients aged 8 – 44 years (reviewed by Pierce and Bennett, 2015). The AAV2/2-hRPE65 vectors used demonstrated excellent safety profiles, with no serious adverse events or signs of systemic toxicity observed – indeed, many of the adverse events that were reported could be attributed to the surgical procedure, which was optimised over time. Significant improvements in visual function were evident in many subjects, which were more pronounced in juvenile subjects and could be sustained for at least 3 years (Pierce and Bennett, 2015). Remarkably, increased retinal function led to improved connectivity of the retinal and visual cortex neural networks, suggesting that the brain is sufficiently plastic to adapt to restoration of retinal function in adulthood (Ashtari et al., 2015). Importantly, subsequent vector administration to the contralateral eye in patients is not only tolerated but effective – assuaging fears that an initial treatment might prime a humoral or cell-mediated response against the AAV capsid or transgene product (Bennett et al., 2016). Moreover, a recent NHP study suggests that a second treatment in the same eye may even be tolerated, should it be necessary (Weed et al., 2019). Bilateral administration of a dosage of 1.5E11 viral genomes (vg) was tested in a randomised, controlled phase III clinical trial and again proved safe and effective, leading to improved light sensitivity and navigational capacity (Russell et al., 2017). The visual improvements gained appear to peak 1 month after administration of Luxturna™ and to be stable for at least four years (Maguire et al., 2019).

The success of Luxturna™ has paved the way for other *in vivo* gene therapies to follow. There are currently at least 38 registered clinical trials testing gene therapies for retinal degenerations. These strategies include gene replacement therapies, use of antisense oligonucleotides to correct mRNA splicing or target mutant mRNA for degradation, direct editing of a disease gene sequence, as well as gene-independent nucleic acid-based therapeutics (Buck and Wijnholds, 2020). It is also worth noting the promising pre-clinical progress of a two-component 'suppression and replacement' strategy for (non-haploinsufficient) *RHO*-linked ADRP, in which endogenous alleles are knocked down through RNA interference (RNAi) and a RNAi-resistant replacement copy is supplied (Millington-Ward et al., 2011, Cideciyan et al., 2018).

In this PhD thesis, studies exploring the development of a gene replacement therapy for XLRP (chapter 2 a gene editing-based suppression and replacement strategy for ADRP (chapter 3) and a gene-independent therapy for glaucoma, a multifactorial optic neuropathy (chapter 4) will be presented.

1.5 Gene editing

AAV-mediated gene augmentation is clearly a very promising strategy for treatment of recessive or haploinsufficient forms of disease. However, as noted earlier, not all genes are suitably sized for AAV delivery and others may be retinotoxic when overexpressed. While AAV-mediated gene expression in the retina appears stable for at least 11 years (Cideciyan et al., 2013, Wojno et al., 2013), directly modifying an individual's genome should, in principle, ensure life-time transgene expression at an endogenous level. Moreover, gene replacement may not be feasible or effective in late-stage retinal degeneration. In such cases, as well as those displaying dominant negative or gain-of-function modes of action, it may be preferable to directly edit an individual's genome *in vivo* or to transplant replacement cells that have been genetically corrected *ex vivo*. With the rapid advancement of gene editing technology in recent years, such treatments appear increasingly within reach.

1.5.1 A double-stranded breakthrough

Homologous recombination (HR) has been used to modify mammalian genomes since the 1980s in the form of gene targeting – a discovery that enabled the generation of transgenic mice and earned Mario Capecchi, Oliver Smithies and Martin Evans the 2007 Nobel Prize in Physiology or Medicine. A desired sequence could be incorporated into a cell's genome at a specific location if the exogenous sequence was flanked with long stretches of sequence homologous to the target region (homology arms). The efficiency of gene targeting in mammalian cells (without selection) is quite low (< 1 in 10^6 mouse embryonic stem cells). Importantly, gene targeting efficiency could be increased by 2-3 orders of magnitude if an endonuclease was used to make a double stranded break (DSB) in the target region (Rouet et al., 1994, Elliott et al., 1998). DSBs can be mended with high fidelity by homology directed repair (HDR) or through non-homologous end-joining (NHEJ), which is more error prone and often results in the incorporation of indels. A donor template flanked by homology arms (~0.5-2 kb) can therefore be supplied to direct precise modification of a cleaved locus via homologous recombination (Yamamoto and

Gerbi, 2018). Alternatively, if a knockout is required, induction of a DSB can be sufficient to nullify a gene via frameshift.

Until 2012, the main endonucleases used to induce DSBs for gene editing were zinc finger nucleases (ZFNs) and transcription activator-like effector nucleases (TALENs) (Urnov, 2018). These technologies (ZNFs and TALENs) are undoubtedly powerful and have facilitated development of *ex vivo* treatments, such as transplantation of gene-edited T cells and haematopoietic stem cells (Qasim et al., 2017)(ClinicalTrials.gov identifier: NCT02500849), and the first in-human *in vivo* gene editing trial (NCT03041324)(Sheridan, 2018). However, ZFN and TALEN-mediated gene editing is inherently time-consuming and labour-intensive due to the fact that these endonucleases rely on protein-based recognition of DNA - requiring new proteins to be engineered and validated for each target. This obstacle was overcome with the discovery of the RNA-based CRISPR-Cas editing system – the second Nobel Prize-winning innovation to be featured in this subsection.

1.5.2 CRISPR-Cas gene editing

Clustered regularly interspaced short palindromic repeats (CRISPR) were first noted as an 'unusual nucleotide arrangement with repeated sequences' in the *E. coli* genome in the 1980s (Nakata et al., 1989). The origin of these mysterious motifs and the process they function within would not be elucidated until 2005-2011 (reviewed by Urnov, 2018). We now know that CRISPR elements are part of an adaptive immune system present in many types of bacteria and archaea – a defence system reminiscent of RNA interference (RNAi) in eukaryotic cells. When a bacteriophage genome or plasmid enters a bacterial cell, short fragments of this DNA are incorporated into the bacterial genome as 'spacer' sequences between repeat sequences in CRISPR arrays – a record of infection events. These sequences are transcribed and processed into short CRISPR RNAs (crRNAs), which are comprised of a 5' spacer sequence and 3' repeat sequence. CrRNAs form a complex with CRISPR-associated (Cas) nucleases and, by then hybridising to DNA complementary to the spacer sequence (the proto-spacer motif), target foreign material for destruction. For cleavage of the target (or 'DNA interference') to occur, an additional short (~3bp) motif must be directly adjacent the proto-spacer. This sequence is known as a protospacer adjacent motif (PAM) and allows the cell to distinguish protospacers of invading DNA from spacer sequences in its own CRISPR arrays. There are two different classes of

CRISPR-Cas systems – Class I require multiple Cas proteins for target cleavage, while only one Cas protein is necessary in the simpler Class II platforms. There are three different types within the Class II CRISPR-Cas family (Type II, V and VI) - the most well-known of these being Type II, which utilises the Cas9 nuclease. Type II CRISPR-Cas targeting (illustrated in Fig.1.7) requires a 5'-NGG-3' PAM and a second short RNA that binds to the crRNA - termed the trans-activating crRNA (tracrRNA) (reviewed by Jiang and Doudna, 2017).

The *Streptococcus pyogenes* (Sp) CRISPR-Cas9 system was demonstrated to be reprogrammable in ground-breaking work led by Emmanuelle Charpentier and Jennifer Doudna. The crRNA-tracrRNA duplex was simplified into a single guide RNA (sgRNA) and successfully engineered to direct cleavage at specific genomic regions in bacterial and human cells by replacing the spacer element (Jinek et al., 2012, Jinek et al., 2013). This relatively simple and easily-adaptable RNA-based system could, in principle, be used to create a DSB in any genomic region with a suitably located PAM.

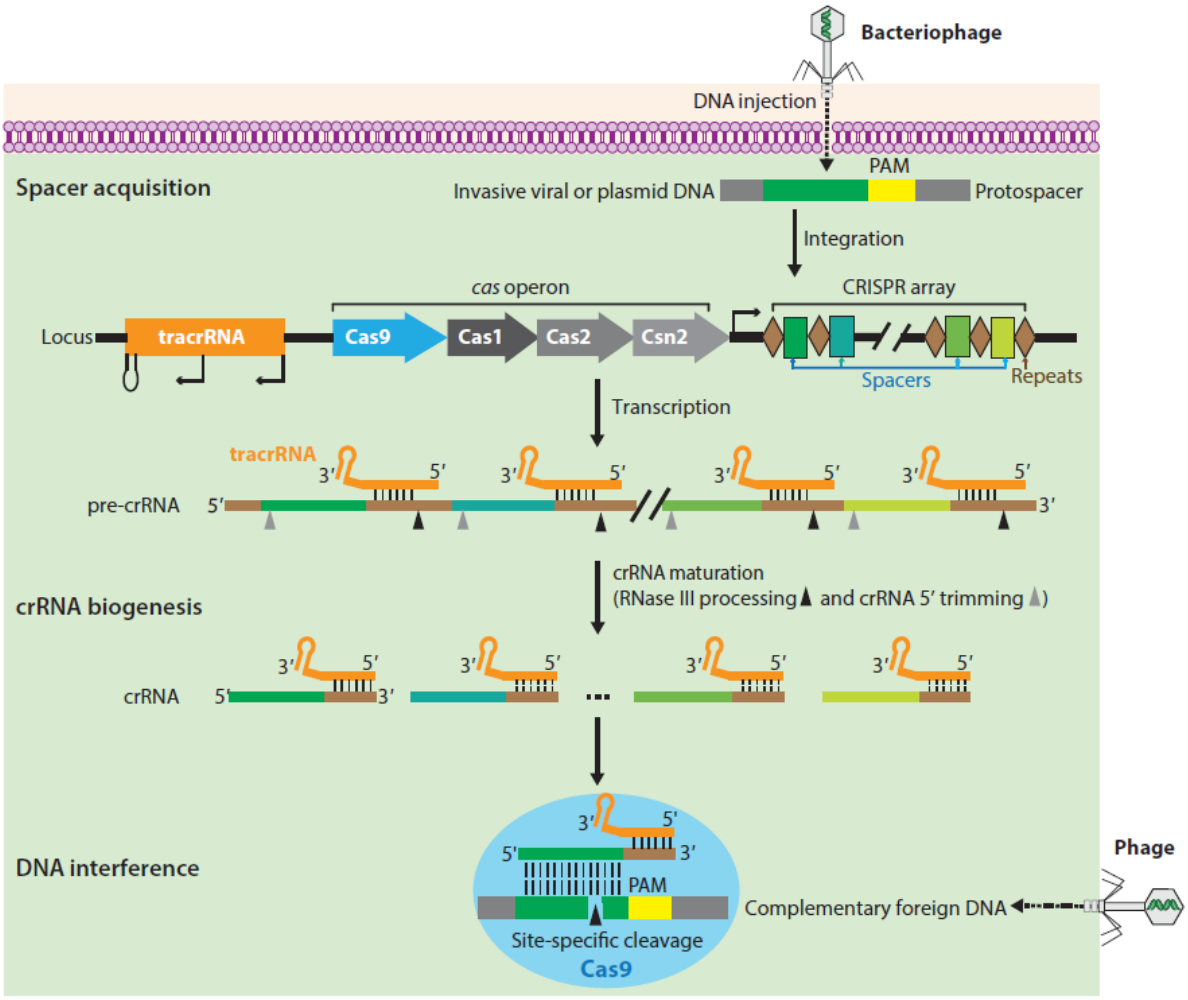

Figure 1.7. Type II CRISPR-Cas system for bacterial adaptive immunity.

CRISPR arrays consist of repeat sequences (brown diamonds) separated by spacer sequences (rectangles). The Cas operon encodes Cas9 nuclease and other proteins involved in the creation of spacer elements (Cas1, Cas2 and Csn2). A tracrRNA gene encodes a noncoding RNA capable of hybridising with the repeat sequence. When a phage injects its genetic material into the bacterial cell, a new spacer is generated based on this foreign DNA derived from the invasive genetic elements is incorporated into the CRISPR array by the acquisition. The CRISPR array is transcribed in full to form a precursor (pre-) crRNA. TracrRNA binds to repeat motifs and enables processing of pre-crRNA by RNase III and other nucleases, producing a mature crRNA of 20 nucleotides. The crRNA–tracrRNA duplex then forms a ribonucleoprotein complex with Cas9 and guides the endonuclease to cleave phage DNA upon re-infection. Figure reproduced from Jiang and Doudna, 2017.

CRISPR-Cas gene editing (Fig. 1.8) is now almost a ubiquitous tool in molecular biology research - facilitating swift generation of cell and animal models, and design of large-scale genetic screening experiments. Since its discovery in 2012, this editing platform has expanded rapidly.

For example, Cas9 proteins from other bacterial species, such as *S. aureus* and *C. jejuni* utilise alternative PAM sites and have more compact coding sequences, and a 'near-PAMless' Cas9 variant was recently engineered (Walton et al., 2020). Nickases, in which one of the two Cas9 catalytic sites is inactivated, can be paired to produce staggered nicks that are repaired with higher fidelity than DSB and minimise off-target effects (Trevino and Zhang, 2014). Cas12a (also known as Cpf1) can also be used to produce staggered DSBs (Safari et al., 2019), while Cas13 can target and degrade RNA (Abudayyeh et al., 2017).

Dead Cas proteins (dCas) are capable of binding but not cutting DNA due to complete catalytic inactivation and can thus be fused to other enzymes to mediate a variety of edits that do not require a DSB or donor DNA template. Dead Cas proteins have been combined with transcriptional activators and repressors to facilitate epigenome editing (Pei et al., 2019), while linkage of dCas or nickases to cytosine or adenosine deaminases (base editors) enables direct editing of DNA or RNA bases (Porto et al., 2020).

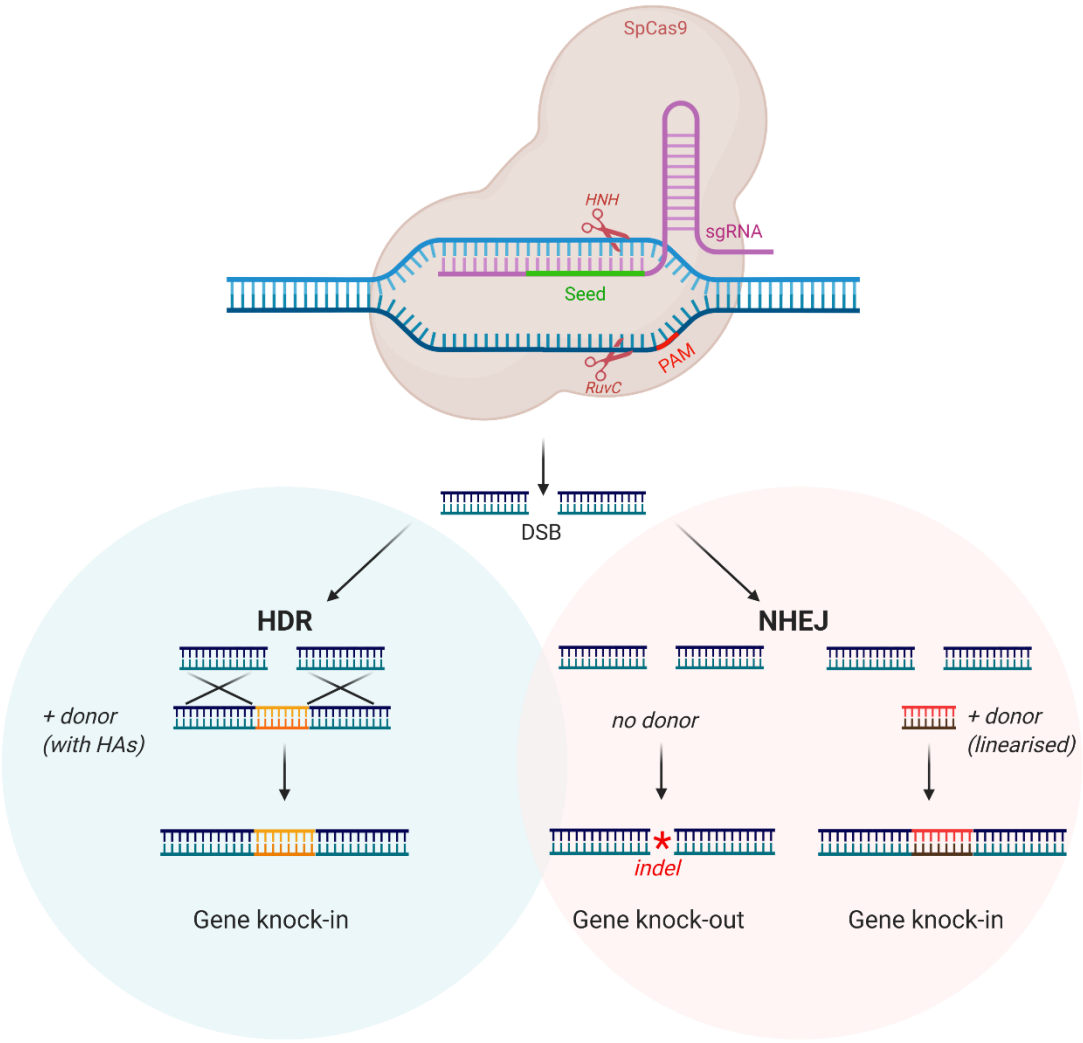

Figure 1.8. CRISPR-Cas9 gene editing.

Target sites of 17-20 nt with a suitably located PAM site can be selected for Cas9 cleavage. After PAM recognition, the 10-12 nt of sgRNA closest to the PAM (the 'seed') binds to the target DNA. If the seed is suitably complementary to the genomic DNA, the remaining (PAM-distal) region of the sgRNA will hybridise to the target. Cas9 then cleaves both strands of DNA using its two catalytic sites (HNH and RuvC), at a position 3 bp upstream of the PAM. Once a double-stranded break is formed, it can be repaired through HDR or NHEJ. A small modification or large gene insertion can be achieved by HDR if a donor DNA template with flanking homology arms (HAs) is supplied alongside the Cas9/gRNA complex. This donor DNA can be double or single stranded, circular or linear in nature. In the absence of a donor template, the DSB ends will be religated through the more error-prone NHEJ process – thus possibly forming frameshift inducing indels. It is also possible to create a gene knock-in using NHEJ, whereby a linear double-stranded donor fragment is ligated into the DSB. However, HDR is thought to be the most precise way of achieving such an edit. Figure created using Biorender.com.

While ‘base editors’ can induce C-T/U or A-G/I transitions, the recently developed ‘prime editing’ system (dubbed ‘search and replace’ as opposed to ‘cut and paste’ editing) allows conversion of a nucleotide to any base, as well as short insertions or deletions. In this platform, a Cas9 nickase is combined with a reverse transcriptase and an extended RNA (prime editing gRNA; pegRNA) that functions as both a guide and an editing template. Part of the pegRNA binds to the nicked DNA strand and acts as a primer for the reverse transcriptase, adding a new sequence. Another gRNA then facilitates nicking of the opposing strand to stimulate resolution of the mismatch. This technology has yielded promising results *in vitro* (Anzalone et al., 2019, Sürün et al., 2020, Schene et al., 2020), and it will be interesting to see if it performs similarly *in vivo*. It is worth noting that although base editing and prime editing hold great therapeutic potential, the Cas9 fusion proteins required are currently beyond the packaging limit of AAV (Wang et al., 2020).

1.5.3 Taking CRISPR-Cas to the clinic

It is clear that gene editing has the potential to facilitate life-changing treatments for individuals afflicted by inherited disease. The main obstacles to translation of CRISPR-Cas editing to *in vivo* therapeutic applications currently lie in its potential to elicit off-target effects, the possible immunogenicity of Cas proteins and low HDR efficiency in post-mitotic cells.

Multiple mismatches between a sgRNA and target site can be tolerated, particularly outside of the 10-12 nt ‘seed’ region proximal to the PAM site (Jiang and Doudna, 2017), and non-canonical PAM sites can also function at lower efficiencies (Cui et al., 2020), leading to potentially deleterious non-specific edits. Many strategies are being explored to minimise off-target effects and maximise their detection (reviewed by Li et al., 2019c). It recently came to light that unintended ‘on-target effects’ can also be an issue; large, complex chromosomal rearrangements (deletions/ inversions/ duplications/ translocations) can apparently occur during repair of a single DSB and go unnoticed by commonly used short-range amplification-based methods of edit detection (Kosicki et al., 2018, Weisheit et al., 2020). It will therefore be important to conduct careful analyses of both target and predicted off-target sites during pre-clinical assessment of potential therapeutics.

Pre-existing antibodies and T cells against Sp and SaCas9 proteins have been detected in people (Simhadri et al., 2018, Charlesworth et al., 2019, Wagner et al., 2019), while non-

human primates have been shown to possess SaCas9 antibodies (Maeder et al., 2019) - not a surprising finding, given these nucleases are sourced from common bacterial species. Recently, systemic administration of AAV-SaCas9 was shown to provoke a cytotoxic T cell response in the liver of mice previously immunised against SaCas9 (Li et al., 2020). It will therefore be important to assess humoral and cell-mediated immune responses when developing Cas9-based therapeutics. Structural alteration of the Cas9 protein or utilisation of Cas9 orthologues in microbial species less likely to infect humans may provide a means of circumventing pre-existing immunity (Wignakumar and Fairchild, 2019). Fortunately, this matter is less of an issue in the immune privileged context of the eye. Thus far, subretinal administration of AAV2/5-hGRK1-SaCas9 vectors has been well-tolerated in NHPs, with only mild immune responses noted. In fact, NHPs with larger T cell responses to SaCas9 actually displayed higher editing efficiencies in two separate studies (reviewed by Quinn et al., 2020).

This year saw commencement of the first ever clinical trial of an *in vivo* CRISPR-Cas therapeutic[7]. Editas Medicine's 'Edit-101' is designed to remove an intronic LCA-causing variant (IVS26) in *CEP290*, thereby preventing inclusion of a cryptic exon and formation of a premature stop codon. The size of the *CEP290* CDS (~7.5kb) precludes a straight-forward gene replacement strategy for this IRD. Edit-101 is comprised of a single AAV2/5 vector that expresses two sgRNAs targeting intronic regions flanking the pathogenic variant, and SaCas9 under the control of the photoreceptor specific hGRK1 promoter. During pre-clinical validation of this strategy, Maeder et al. (2019) verified that both deletion and inversion of the cut fragment could correct the splicing defect *in vitro*. Based on clinical data (Geller et al., 1992, Geller and Sieving, 1993), Maeder et al. estimate that visual acuity can be mostly preserved if approximately 10% of foveal cones are functional. They therefore hypothesise that 'productive editing' (deletion/inversion) efficiencies of 10% or higher would achieve clinical benefit. This theoretical therapeutic threshold was achieved or surpassed in human retinal explants (17%), a humanised mouse model of CEP290 IVS26 (21%) and NHPs (28%) – though the sgRNA sequences had to be modified somewhat for NHP testing due to interspecies differences. No adaptive immune response toward SaCas9 was detected in treated NHPs, and antibodies directed against AAV5 did not appear to reduce editing efficiency. Critically, no off-target effects were detected in

[7] https://www.nature.com/articles/s41587-020-0493-4 [accessed: 06/11/20]

transduced human cells *in vitro* or *ex vivo* (Maeder et al., 2019). It is important to note, however, that mutations must be present at a frequency of at least 0.1% to be detected by the sequencing method used in this study and it is therefore possible that rare off-target mutations are present but escaping detection (Quinn et al., 2020).

The EDIT-101 strategy does not require a precise modification, only needing to disrupt the IVS26 mutation, and so can rely on the error-prone but relatively efficient process of NHEJ. A similar strategy (EDIT-102) is also in development to tackle the most common cause of Usher Syndrome Type II, a truncating frameshift mutation in exon 13 of *USH2A*. Like *CEP290*, the *USH2A* CDS is too large for single AAV vector gene replacement (15.6 kb). Fortunately, skipping of exon 13 renders a functional USH2A protein, and so CRISPR-Cas-mediated deletion or inversion of this exon is a promising strategy[8,9] (Pendse et al., 2020)[10].

Looking ahead, NHEJ-mediated gene knockout would in principal be beneficial in dominant negative or gain-of-function IRDs, where the pathogenic allele could be specifically targeted. This strategy has proven beneficial in two autosomal dominant models of rhodopsin-associated RP (Bakondi et al., 2016, Li et al., 2018). Indeed, Editas Medicines have announced development of CRISPR-Cas therapy targeting *RHO*-linked ADRP, though the details of this strategy have yet to be disclosed[8].

Cases of recessivity or haploinsufficiency are more challenging to address with gene editing technology, as high-fidelity editing would of course be required and HDR is inefficient in post-mitotic cells such as photoreceptors. Efficient, precise modification will also be essential for the development of mutation-independent gene editing strategies – for both recessive and dominantly inherited disorders – which, of course, would be preferable to independently developing a multitude of treatments tailored toward specific mutations. This issue, and a potential strategy to resolve it, will be explored in chapter 3.

[8] https://www.editasmedicine.com/gene-editing-pipeline/ [accessed: 07/11/20]
[9] https://www.editasmedicine.com/wp-content/uploads/2020/05/Mukherjee_ASGCT-2020-USH2A-poster_final.pdf [accessed: 07/11/20]
[10] Pendse et al. 2020 is a pre-print.

1.6 Gene-independent therapeutic strategies

The extreme genetic heterogeneity of IRDs and the widespread prevalence of multifactorial retinal degenerations, such as age-related macular degeneration (AMD) and glaucoma, has inspired exploration of gene-independent therapeutic approaches that modulate common aspects of retinal degeneration. Such strategies include delivery of neurotrophic factors (Daly et al., 2018) or antioxidants (Murakami et al., 2020), and modulation of immune response and cell death pathways (Wang et al., 2019c, Ozaki et al., 2020). Optogenetic and stem cell-derived photoreceptor transplantation technologies (and even a combination of these two strategies) are also making steady progress toward the treatment of end-stage outer retinal degenerations (Berry et al., 2019, Gasparini et al., 2019, Garita-Hernandez et al., 2019).

Bioenergetics is increasingly under focus in the context of retinal disease. Boosting cellular energy production (via stimulation of aerobic glycolysis or the phosphocreatine system) has been shown to increase cone survival and function in murine models of RP (Byrne et al., 2015, Aït-Ali et al., 2015, Narayan et al., 2019). Mitochondrial defects have long been known to cause inherited optic neuropathies such as Leber hereditary optic neuropathy (LHON) and dominant optic atrophy (DOA), in which RGCs selectively die (Newman and Biousse, 2004). There is now also ample evidence to suggest that mitochondrial decline is a major underlying aspect of age-related retinal degenerations, such as AMD and glaucoma, which will be elaborated upon in subsequent sections. Improving mitochondrial function thus represents a promising gene-independent therapeutic approach for a variety of retinal dystrophies.

1.7 Mitochondria

1.7.1 Structure, function and network dynamics

The mitochondrion, famously dubbed 'the powerhouse of the cell', originated at least 1.5 billion years ago when a bacterium capable of oxidative energy production survived engulfment by a eukaryotic progenitor cell (presumably dependent on glycolysis and fermentation) and gradually transitioned from an endosymbiont to a permanent, integrated organelle (Martin and Mentel, 2010). Oxidative phosphorylation enabled organisms to thrive in broader environmental conditions and facilitated an explosion of diverse, complex, multicellular life. Mitochondria are found in almost all eukaryotes (with only one exception found to have completely lost their mitochondria to-date (Karnkowska and Hampl, 2016)).

While the primary role of the mitochondrion is production of ATP via oxidative phosphorylation (OXPHOS), they carry out a variety of other important functions, such as regulation of calcium homeostasis, neurotransmitter production, homeostatic signalling pathways (proliferation, differentiation and stress response) (Nunnari and Suomalainen, 2012) and apoptosis (Bock and Tait, 2020).

Mitochondria, like their bacterial predecessors, are double-membraned. Electron transport chain proteins are located in the inner mitochondrial membrane (IMM). The IMM is highly invaginated, forming cristae, which increases its surface area and ATP production capacity considerably. They also contain multiple copies of their own circular genome, which encodes 13 proteins. Mitochondria carry multiple nucleoids – usually a single circular genome coated with proteins essential for transcription (Boguszewska et al., 2020). Mammalian mitochondrial inheritance is exclusively maternal[11]. The high cellular copy number of mitochondrial DNA (mtDNA) means a mixed population of wild-type and mutant mtDNA (heteroplasmy) is possible, which can lead to variable penetrance of disease.

Mitochondrial mass is regulated through a constant interplay of biogenesis and mitophagy, while the dynamics of the mitochondrial network is controlled by the fission

[11] In 2018, a high-profile apparent case of biparental maternal inheritance in three families was reported (Luo et al., 2018). However, a subsequent study provides compelling evidence that this was likely due to detection of large mitochondrial-derived sequences incorporated into the nuclear genome, which could give the appearance of heteroplasmy (Wei et al., 2020).

and fusion of organelles (Carelli et al., 2015) (Fig. 1.9.A). Mitochondria rapidly split and merge in response to variations in energy level and stressors. Fusion of mitochondria enables complementation to increase functional capacity under times of stress; wild-type organelles can share their RNA and protein with mutant ones, lessening the mutational load. Damaged mitochondrial components could alternatively be isolated through fission for removal by mitophagy and replaced via compensatory mitochondrial biogenesis (Youle and van der Bliek, 2012). These processes are thus vital for mitochondrial quality control. However, they can also lead to clonal expansion of deleterious mtDNA mutations (inherited or somatic) (see Fig. 1.9.B). MtDNA mutations have been observed to undergo clonal expansion in cells from a variety of tissues, including skeletal muscle, hippocampal and midbrain dopaminergic neurons, resulting in focal respiratory chain deficiency (reviewed by Larsson, 2010). In order to induce respiratory chain dysfunction in a cell, it is thought that the proportion of mutated mitochondrial genomes much reach 60-80% - depending on the nature of mutation and cell type in question (reviewed by Craven et al., 2017).

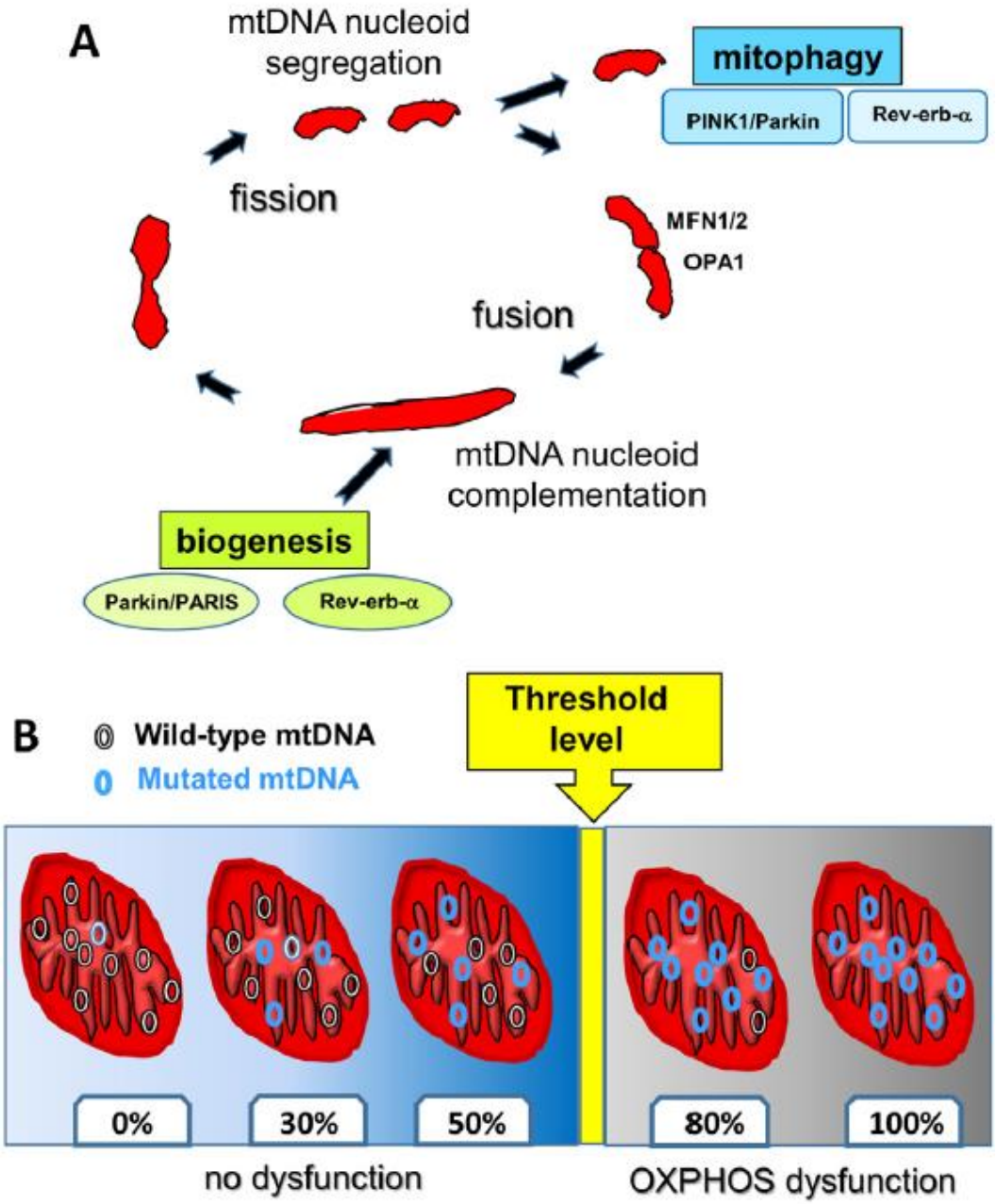

Figure 1.9. Schematic of mitochondrial fission and fusion.

(A) The interplay between mitochondrial biogenesis, fusion, fission and mitophagy are illustrated. Key proteins and pathways involved in these processes are highlighted (e.g. OPA1 and MFN1/2 protein in fusion, and the Parkin/PARIS pathway in biogenesis and mitophagy).

(B) Mutated mtDNA can undergo clonal expansion in mitochondria and, once this mutational load reaches a certain threshold, oxidative phosphorylation becomes dysfunctional.

Figure reproduced from Carelli et al. 2015.

1.7.2 ATP production

Glucose can be converted to ATP, the energetic currency of the cell, by glycolysis in the cytoplasm or via the tricarboxylic acid (TCA) cycle (also known as the Krebs cycle) and oxidative phosphorylation in mitochondria. Glycolysis, which does not require oxygen, produces 2 net molecules of ATP per molecule of glucose. Further aerobic respiration in the mitochondria, however, can generate a ~15 fold higher yield of ATP. In principle, 30 molecules of ATP can be generated during aerobic respiration: 2 from glycolysis, while 2 and 26 can be produced from the TCA cycle and oxidative phosphorylation, respectively.

In addition to ATP, glycolysis generates 2 molecules of pyruvate. In aerobic conditions, acetyl-CoA is produced through oxidation of pyruvate. Acetyl-CoA then enters the TCA cycle in the mitochondrial matrix and is oxidised. Importantly, reduced cofactors with high electron transfer potential, NADH and $FADH_2$, are produced during this process.

During oxidative phosphorylation, electrons are transferred from NADH and $FADH_2$ to oxygen molecules, with the aid of multiple electron carriers, to produce ATP (see Fig. 1.10). The energy released from electron transfer is used to pump protons from the mitochondrial matrix into the intermembrane space. The resulting proton (or electrochemical) gradient is resolved by transfer of protons back from the intermembrane space through Complex V, ATP synthase. Passage of protons through Complex V generates a mechanical force that is used to catalyse conversion of ADP to ATP – a process called chemiosmosis.

NADH donates two electrons to Complex I, NADH:ubiquinone oxidoreductase, which are then transferred to ubiquinone. During this process, four protons are driven through Complex I into the intermembrane space. Complex II, or succinate-Q oxidoreductase, functions as a second entry point to the ETC and is also part of the TCA cycle. Complex II oxidises succinate using FAD as a cofactor, transfers electrons to ubiquinone and is the only ETC protein complex that does not generate a proton-motive force. At Complex III, Q-cytochrome c oxidoreductase, electrons are transferred from ubiquinone to cyctochrome c, and 2 protons are pumped into the intermembrane space. Cytochrome c then carries electrons to Complex IV, cytochrome c oxidase. In this last step of the ETC, electrons are donated to oxygen, the final electron acceptor, to form two molecules of H_2O. The energy released by reduction of oxygen enables transfer of 4 protons across the membrane. Formation of H_2O requires consumption of protons from the matrix, which

further contributes to the establishment of a proton gradient. Complex V, ATPase, then acts as an ion channel to allow transfer of protons back to the matrix. Passage of protons through the membrane-spanning subunit (F_0) of ATPase creates a mechanical force that rotates 'proton-driven motor' subunit (F_1), which binds ADP. As the F_1 motor rotates, its three catalytic sites change conformation and ATP is synthesised and released via a rotational catalysis mechanism (Berg et al., 2002).

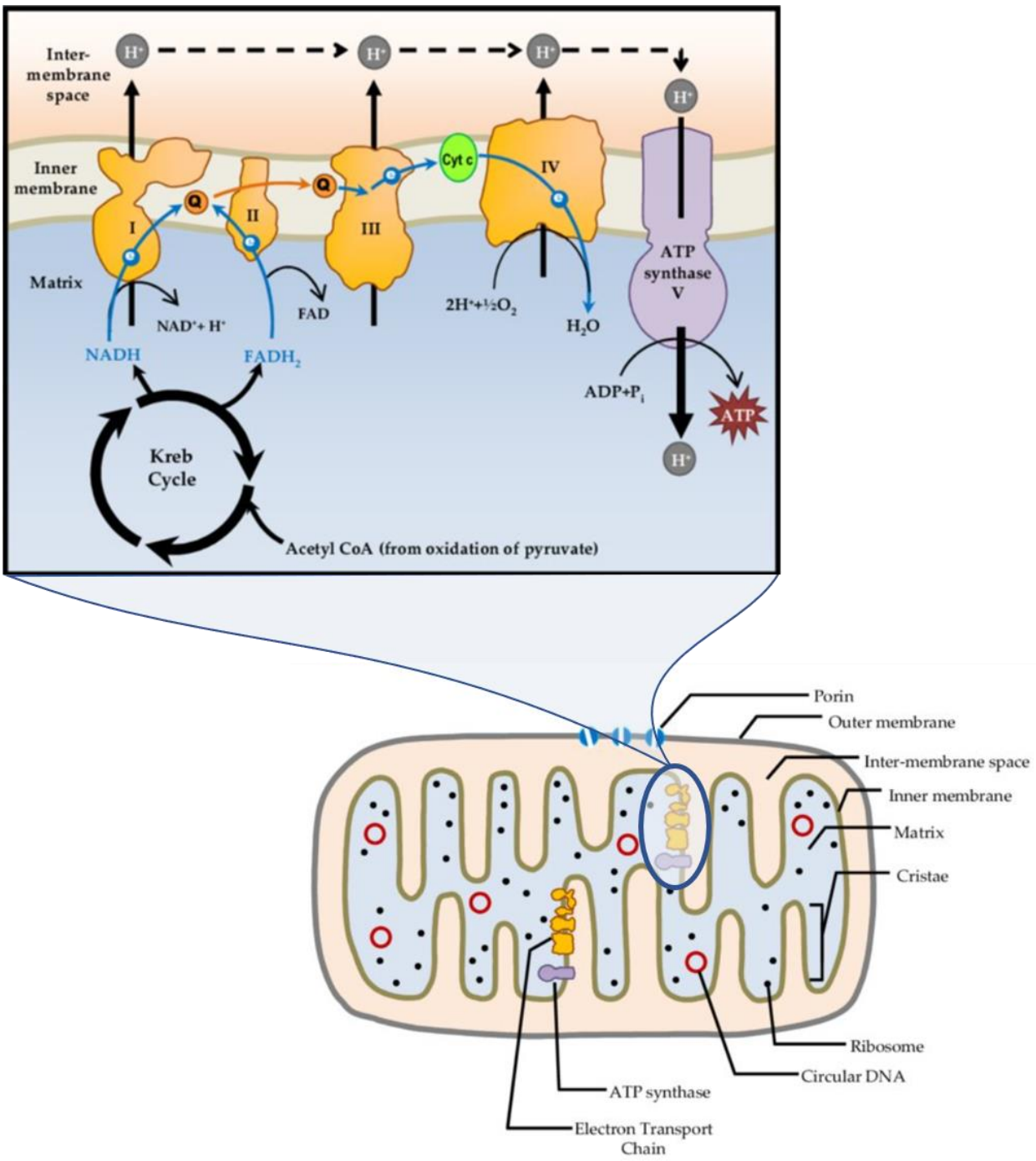

Figure 1.10. Mitochondrial structure and electron transport chain function.

Schematic adapted from Mohamed Yusoff et al., 2015.

1.7.3 Oxidative stress

The electron transport chain is not 100% efficient; some electrons and protons inevitably 'leak' from the system. Escaped electrons can interact with oxygen molecules to generate reactive oxygen species (ROS), including superoxide anion free radicals ($O_2^{\bullet-}$) and hydrogen peroxide (H_2O_2) (Zhao et al., 2019). H_2O_2 can further react with iron or copper molecules to produce hydroxyl free radicals ($^{\bullet}OH$) (Fenton reaction) (Masuda et al., 2017). Mitochondria are the primary producer of ROS in the cell (other sources include pollution, smoking and light-induced oxidative stress). While electron leakage can occur at Complexes I, II and III of the ETC (Fig. 1.11), Complex I is the main source of ROS generation (Zhao et al., 2019).

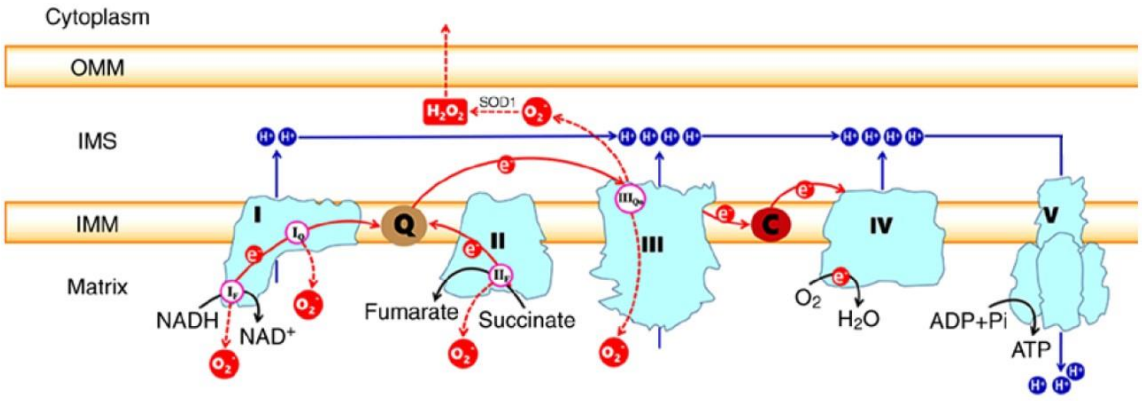

Figure 1.11. Illustration of electron leakage in the electron transport chain.
Superoxide ($O_2^{\bullet-}$) is produced at sites in all of the ETC protein complexes: I_F and I_Q in CI, II_F in CII and $IIIQ_o$ in CIII. $O_2^{\bullet-}$ generated from Complex III can enter the matrix or intermembrane space (IMS). In the IMS, SOD1 can catalyse conversion of $O_2^{\bullet-}$ to hydrogen peroxide, which is capable of diffusing into the cytoplasm. Electron pathways are shown as red arrows, while substrate reactions are depicted in black. Blue arrows illustrate proton pumping. Abbreviations: Q = ubiquinone; C = cytochrome c; OMM = outer mitochondrial membrane; IMS = intermembrane space ; IMM = inner mitochondrial membrane. Figure reproduced from Zhao et al. 2019.

Normally, 0.2-2% of electrons that enter the ETC are redirected toward ROS production. This proportion increases in conditions that impair ETC efficiency, such as hypoxia. The low level of ROS generated under normal physiological conditions is an important element of intracellular signalling pathways - through oxidative modification of redox-sensitive proteins, ROS is involved in the regulation of cell proliferation, autophagy, apoptosis, necrosis, pyroptosis and innate immunity (Zhao et al., 2019). On the other

hand, oxidative stress, when the level of ROS exceeds the antioxidant capacity of the cell, can be extremely damaging to cellular components - causing DNA mutation, lipid peroxidation and protein oxidation. As the main site of ROS production and possessing circular genomes that lack protective histones, mitochondria are especially vulnerable to oxidative damage. Oxidative stress is thought to be involved in the pathogenesis of cancer (Aggarwal et al., 2019), cardiovascular disease (Senoner and Dichtl, 2019) and several age-related neurodegenerative disorders, including Parkinson's disease (Dias et al., 2013, Wei et al., 2018), Alzheimer's disease (Cheignon et al., 2018) and glaucoma (see chapter 4). It has also long been hypothesised to play a central role in the ageing process itself.

1.7.4 Mitochondrial dysfunction in aging

Mitochondrial dysfunction is an established hallmark of aging (Lopez-Otin et al., 2013). Reduced activities of ETC Complexes I, II and IV have been observed in aged rodent, NHP and human tissues (Shigenaga et al., 1994, Ojaimi et al., 1999, Petrosillo et al., 2009, Pollard et al., 2016). In terms of morphology, mitochondria of aged rats were noted to be smaller and more numerous in the heart (Frenzel and Feimann, 1984) or enlarged with a vacuolated matrix and abnormal cristae pattern in the liver (Wilson and Franks, 1975, Brandt et al., 2017).

The biological basis of ageing remains unresolved, with over 300 'theories of ageing' proposed (Vina et al., 2007) but mitochondrial dysfunction is critical to many of these ideas. Cellular damage induced by free radicals was first postulated to drive ageing in the 1950s (Harman, 1956). As the central role of mitochondria in ROS production became recognised, this hypothesis developed into the mitochondrial free radical theory of ageing (MFRTA) (Harman, 1972) (Miquel et al., 1980). The MFRTA posits that because the mitochondrion is the primary site of ROS production it is also the main target of oxidative damage. According to the MFRTA, oxidative damage to mtDNA, protein and lipids impairs mitochondrial function, which in turn increases generation of ROS. A vicious cycle would thus ensue, leading to dysfunction of cells and tissues, and driving the ageing process.

Over the years, this theory was supported by results from several studies. Mitochondrial DNA is reported to contain 10-20 fold more oxidation lesions than nuclear DNA (Cadenas and Davies, 2000). Oxidative damage to mtDNA was shown to accumulate in human and rodent tissues with age (Halliwell and Aruoma, 1991, de la Asuncion et al., 1996, Mecocci et al., 1993). The level of such damage was also found to be inversely related to

mammalian lifespan (Barja and Herrero, 2000). In rodents, it was observed that the sex with the higher longevity produced lower amounts of reactive oxygen species (Borras et al., 2003) (Ali et al., 2006).

Most of the evidence supporting this theory was correlative, however, and multiple lines of evidence contradictory to the MFRTA have since emerged. For instance, the naked-mole-rat (NMR) is the longest living rodent, with a maximum lifespan approximately 10 times longer than that of a mouse. Most unexpectedly, NMR tissues displayed greatly elevated levels of oxidative damage compared to mouse samples, without compensatory upregulation of antioxidant production (Andziak et al., 2006). Studies with transgenic mice have found that altered expression of antioxidant enzymes, and thereby oxidative damage level, has no effect on lifespan (Perez et al., 2009).

Importantly, an increased number of oxidative lesions may not necessarily translate into more mutations. The most commonly used measure of oxidative damage to mtDNA is modification of guanosine to 8-oxo-2'-deoxyguanosine (8-oxo-dG), which can, in principle, bind to adenosine and create G:C to T:A transversions. Improvement in the sensitivity of sequencing methods in the last decade has enabled detection of rare mitochondrial mutations in heteroplasmic samples (Kennedy et al., 2013). It was subsequently confirmed that mtDNA point mutations do indeed accumulate in tissue with age. Transition mutations predominate, however, indicating replication error and/or spontaneous deamination as the source of mutation rather than oxidative stress (Kennedy et al., 2013, Arbeithuber et al., 2020). MtDNA deletions have also been shown to accumulate with age in many tissues, including the retina (Barreau et al., 1996) and brain (Corral-Debrinski et al., 1992). Such deletions mostly occur near regions of homology or secondary structure and are thought to be a result of slippage during replication (reviewed by Kauppila et al., 2017).

It seems that direct oxidation of mtDNA, therefore, may not fuel age-related tissue deterioration. This finding appeared to be at direct odds with the MFRTA. A recent study appeared to provide a means of reconciliation: oxidative stress significantly impairs the proof-reading exonuclease activity of the mtDNA polymerase, Pol γ (Anderson et al., 2020). The catalytic active site of the exonuclease (*exo*) domain appears to be especially susceptible to oxidation, which increases the total negative charge of the area and reduces its affinity for DNA. The error rate of Pol γ increased by up to 20 fold when

exposed to high (but physiological) concentrations of hydrogen peroxide for one hour. Anderson et al. thus proposed a modified MFRTA vicious cycle theory, whereby mtDNA mutation is mediated by oxidative damage to Pol γ and in turn increases ROS production.

This hypothesis can be explored in the context of the mtDNA mutator mouse model, in which the Pol γ *exo* domain is made defective by mutation of a critical catalytic subunit residue (Trifunovic et al., 2004, Kujoth et al., 2005). Homozygous mutator mice undoubtedly underwent accelerated ageing, exhibiting phenotypes such as weight loss, cardiac enlargement, muscle loss, infertility, alopecia, decreased bone density and spinal curvature after ~25 weeks of age. While wild-type C57BL/6 mice have a median lifespan of 126 weeks (Yuan et al., 2009), the corresponding timepoint in mutator mice is just 48 weeks. The mtDNA mutation rate of homozygous mutator mice is 3-11 fold higher than wild-type mice (Trifunovic et al., 2004, Kujoth et al., 2005). Subsequent amino acid substitutions lead to destabilisation of ETC complexes (Edgar et al., 2009) and an extreme reduction in respiratory activity (Trifunovic et al., 2005) and reduction in membrane potential (Hiona et al., 2010). However, this impairment does not appear to significantly increase oxidative damage (Trifunovic et al., 2005). Indeed, there was no difference in ROS level between mutator mice and controls at 2 months of age and by 40 weeks ROS was only elevated in some of the tissue types tested (Logan et al., 2014). The surprisingly low amount of oxidative stress observed, combined with the fact that mutation load in this model increases linearly over time rather than exponentially (Trifunovic et al., 2005), refutes the concept of a vicious cycle of mtDNA mutation and ROS production.

Notably, while there was only a limited elevation of ROS production in mutator mice in the final stages of ageing, there was substantial increase in cleaved caspase-3 levels in tissues before or during phenotype expression (Kujoth et al., 2005). Kojoth et al. therefore proposed that ageing was driven by a process whereby mitochondrial dysfunction caused by mtDNA mutations led to permeabilsation of the mitochondrial outer membrane, release of cytochrome c and activation of the apoptotic intrinsic pathway via caspase-3.

In summary, while there may not be a mitochondrial mutation/oxidative stress positive feedback loop, there is clear evidence that mitochondria are intimately involved in the process of ageing. Increased signs of oxidative stress are present in normally ageing tissues, which may make mtDNA replication by Pol γ more error-prone. Subsequent

accumulation of mtDNA mutations is likely causative of the reduction in ETC function observed over time.

Whether or not the functional decline of mitochondria is causative or a secondary effect of aging remains to be established. Regardless, it is clear that ageing, a major risk factor for many neurodegenerative diseases, is characterised by an increasingly vulnerable bioenergetic state. Additional mitochondrial insults, due to an individual's genetic background or environmental factors, may therefore be sufficient to push cells over a critical threshold of dysfunction – particularly in the case of cell types with high-energy demands or exposed to especially high levels of oxidative stress.

1.7.5 Retinal bioenergetics and disease

The retina has long been recognised as the highest oxygen-consuming organ in the body – in 1956, Otto Weinberg went so far as to liken the oxygen consumption rate of retinal cells as to that of rapidly-dividing cancer cells (Rajala, 2020). However, despite an abundance of available oxygen, ~90% of glucose is converted to lactate rather than used for OXPHOS. This phenomenon, also observed in tumour cells, is known as the Warburg effect or aerobic glycolysis (Haydinger et al., 2020). While RPE and RGCs rely on oxidative phosphorylation, photoreceptors (comprising ~81% of the mouse retina (Jeon et al., 1998)) are dependent on aerobic glycolysis. Glucose is supplied to photoreceptors by the RPE (Hurley et al., 2015). The lactate produced by aerobic glycolysis in photoreceptors is returned to the RPE to fuel OXPHOS - appearing capable of entering the TCA cycle faster than glucose (Kanow et al., 2017). The increased uptake and rapid processing of glucose facilitated by aerobic glycolysis enables redirection of more glycolytic intermediates towards anabolic processes, which is a particular advantage in photoreceptors due to the constant necessity for outer segment renewal in these cells (Rajala, 2020). Reliance on glycolysis may also allow faster ATP production to satisfy the energy requirements of neuronal signalling (Haydinger et al., 2020). Forcing RPE cells to switch from OXPHOS to glycolysis (simulating a state of hypoxia or perhaps mitochondrial dysfunction) results in starvation of photoreceptors (Kanow et al., 2017).

As detailed in the previous section, general mitochondrial function is established to decline with age. Signs of this phenomenon have also been noted in retinal cells, specifically: aged rodent retinas have reduced levels of mtDNA repair enzymes and display increased levels of oxidative DNA damage in photoreceptors and RGCs (Wang et

al., 2010a), while aged human donor retinas also exhibit more mtDNA deletions in foveal cones (Barron et al., 2001). Mitochondrial dysfunction may thus be a major underlying factor in the pathogenesis of complex age-related retinal diseases, such as age-related macular degeneration (AMD), diabetic retinopathy and glaucoma.

Retinal tissue donated from AMD patients exhibit fewer mitochondria than control samples and those mitochondria present display structural defects and accumulation of mtDNA mutations in the RPE – the degree of which correlates with disease severity. RPE cells from AMD patients also produce less ATP, indicating impaired oxidative phosphorylation (reviewed by Eells, 2019). It is hypothesised that in AMD invading macrophages use up much of the glucose that the RPE relies upon, therefore disturbing the delicate energy balance between photoreceptors and RPE cells (Leveillard et al., 2019).

In diabetic retinopathy, chronic hyperglycaemia leads to elevated ROS production and oxidative stress – possibly due to saturation of the electron transport chain (Eells, 2019). In hyperglycaemic retinal endothelial cells, mitochondria display an altered morphology, reduced respiration capacity, accumulation of mtDNA mutations, alongside impaired mitochondrial DNA repair and biogenesis (reviewed by Kowluru and Mishra, 2015, Kowluru, 2017).

There is an especially large amount of evidence implicating mitochondrial dysfunction in the pathogenesis of glaucoma, which leads to selective degeneration of retinal ganglion cells (see chapter 4).

Thus, interventions that can improve mitochondrial function and/or reduce oxidative stress hold great promise for the treatment of age-related retinal disease. In chapter 4, one such potential therapeutic is explored in the context of a murine model of glaucoma.

1.8 Objectives

Retinal degenerations are manifold and multifaceted. Developing effective treatments for these conditions has been challenging and requires a huge collective effort. This thesis describes efforts to address three different types of retinal degeneration using three different potential therapeutic strategies.

In chapter 2, cell and retinal organoid models are used to explore the pathogenesis of *RP2*-associated XLRP and the potential of AAV gene replacement to rescue this form of retinal degeneration.

Chapter 3 explores the potential of a NHEJ-based method for efficient and precise gene editing in photoreceptors. It describes the development a gene editing-mediated mutation-independent 'suppression and replacement' strategy for IRDs due to dominant negative or toxic gain-of-function mutations, and preliminary tests of this platform in a murine model of *RHO*-linked RP.

Finally, in Chapter 4, we move from the outer to the inner retina to explore a potential gene independent therapeutic for glaucoma, using a transkingdom gene therapy to boost RGC mitochondrial function.

2 Development of an AAV gene replacement therapeutic for *RP2*-associated XLRP

2.1 Acknowledgment of contributions

AAV gene replacement study concept: Prof. G Jane Farrar and Dr Arpad Palfi.

Design and manufacture of pAAV-CAG-RP2: Dr Arpad Palfi, with assistance from Áine O'Toole.

AAV production: Dr Naomi Chadderton.

Retinal organoid modelling and rescue study concept: Prof. Michael E Cheetham (University College London), Prof. Alison J Hardcastle (UCL), Prof. G Jane Farrar.

iPSC and retinal organoid experimental work: Dr Amelia Lane (UCL), Dr Katarina Jovanovic (UCL).

Clinical and genetic characterisation of individuals affected by RP:
Mr Paul Kenna (TCD; Royal Victoria Eye and Ear Hospital, Dublin), Mr David Keegan (Mater Hospital, Dublin), Dr Matthew Carrigan, Dr Adrian Dockery.

Processing of R120X-A and C4 skin biopsy samples: Prof. Sanbing Shen (NUI Galway).

Assistance with generation and maintenance of primary fibroblast cultures: Dr Daniel Manraj Maloney.

Subretinal injection: Mr Paul Kenna.

Retinal cryosectioning: Dr Arpad Palfi.

General assistance: Emily Breslin and Cristina Borcea contributed to various parts of this project, as part of their undergraduate thesis work.

RP2del23 mice were kindly provided by Dr Toby Hurd (University of Edinburgh).

2.2 Introduction

2.2.1 X-linked RP

X-linked retinitis pigmentosa (XLRP) comprises 8-16% of total RP cases, affecting between 1 in 15,000-26,000 males (De Silva et al., 2020). Mutations in retinitis pigmentosa GTPase regulator (*RPGR)* account for 70-80% of XLRP cases (Shu et al., 2007), while retinitis pigmentosa 2 *(RP2)* variants are responsible for 7-20% (Schwahn et al., 1998, Mears et al., 1999, Sharon et al., 2003, Hardcastle et al., 1999, Breuer et al., 2002). RPGR and RP2 have also been found to be causative in 15% of reported simplex RP cases (Branham et al., 2012). The Oral-facial-digital 1 gene *(OFD1)* has additionally been implicated in one XLRP pedigree (Webb et al., 2012). In one large IRD cohort, X-linked inheritance was displayed by 4% of genetically unresolved cases (Garafalo et al., 2020).

XLRP is the most severe type of RP, progressing more rapidly than autosomal forms (Jauregui et al., 2019). Of note, all three XLRP-associated genes encode cilia-associated proteins and ciliopathy-related forms of arRP are established to progress faster than non-ciliopathies (Takahashi et al., 2019). Symptoms of nyctalopia and loss of peripheral vision begin in childhood (age of onset from 0 to 14) and at least 20% of XLRP patients are reported to be legally blind by 40 years of age (De Silva et al., 2020). Individuals affected by XLRP additionally exhibit an early-onset macular atrophy that is unusual for RP, where central vision is usually affected last. Onset of macular degeneration is especially early in RP2 patients (De Silva et al., 2020), which may underly the more severe loss of visual acuity reported in these individuals relative to *RPGR*-XLRP patients (Sharon et al., 2003, Kurata et al., 2019, Prokisch et al., 2007). In a cohort of RP2-affected males under the age of 12 (n = 11), the majority of patients exhibited macular atrophy (91%) and high myopia (82%) (Jayasundera et al., 2010). Despite the unusual degree of macular involvement, RP2 is still primarily a rod-cone dystrophy with 90% of patients displaying a clear rod-cone ERG deficit pattern (Jayasundera et al., 2010). RP2 patients also sometimes present with atrophy of the choriocapillaris and RPE – a phenotype reminiscent of choroideremia (Vorster et al., 2004, Jayasundera et al., 2010).

Obligate carriers of X-linked IRDs often exhibit some degree of visual impairment, which has led to some XLRP variants being described as semi-dominant (Banin et al., 2007, Pomares et al., 2009). Over 90% of obligate XLRP carrier females present with an abnormal ERG response (Comander et al., 2015, Kurata et al., 2019). XLRP carrier

phenotypes vary considerably among affected individuals. If disease symptoms are present, they are generally milder than those observed in males. However, carrier females occasionally present with 'male' phenotypes; 2.5% of XLRP obligate 'carriers' were legally blind from as young as 35 years of age in one cohort (Comander et al., 2015). *RP2*-XLRP carriers, specifically, have been noted to exhibit macular atrophy (Jayasundera et al., 2010), 'patchy' peripheral degeneration and a curious tapetal-like reflex (glittering particulates due to increased reflectivity of POS) in fundus images (De Silva et al., 2020). The high degree of variation in XLRP carrier phenotype severity is proposed to be a consequence of a combination of genetic modifiers, environmental factors and skewed X chromosome inactivation (XCI) (Talib et al., 2018). The clinical severity of disease in *RPGR*-XLRP carriers was recently demonstrated to correlate with the level of wild-type XCI, supporting the hypothesis of skewed XCI in severely affected females (Fahim et al., 2020). Presentation of severe disease features can lead to female carriers being erroneously diagnosed with autosomal dominant or simplex RP (Churchill et al., 2013, Birtel et al., 2018); in one cohort 8.5% of families originally designated as having ADRP were found to actually have XLRP (Churchill et al., 2013).

Three different AAV-based gene replacement therapies for RPGR-XLRP have reached Phase I/II clinical trial (Cehajic Kapetanovic et al., 2019). Recent results from dose escalation trials run by NightstaRx (Cehajic-Kapetanovic et al., 2020) and MeiraGTx [12] are promising, with no serious adverse events reported and several patients showing improved visual field or retinal sensitivity 6-12 months post-treatment. Although only tested in male patients so far, such treatments are also being advocated for carrier females presenting with severe 'male' phenotypes (Salvetti et al., 2020).

With regard to treatment for *RP2*-XLRP, an AAV-mediated gene replacement therapy showed promise in a null mouse model (Mookherjee et al., 2015) but, as of yet, there are no reports of follow-up studies in larger mammals or moves toward a clinical trial. Studies using patient-derived in *vitro* models also indicate that translational read-through inducing drugs (TRID) may be a viable option for patients with *RP2* nonsense mutations (Schwarz et al., 2015, Schwarz et al., 2017). However, the majority of individuals affected

[12] https://www.modernretina.com/view/aao-2020-gene-therapy-for-x-linked-retinitis-pigmentosa-achieves-significant-visual-gains-at-1-year Accessed: 20-11-20

by RP2 XLRP (84% of probands described in the literature; see Appendix 2) do not carry a nonsense variant and so would not qualify for such a treatment.

2.2.2 RP2

The RP2 locus was mapped to a 5 cM region in Xp.11.3 via linkage studies (Bhattacharya et al., 1984) and the five-exon *RP2* gene (NM_006915.3) was subsequently identified by positional cloning (Schwahn et al., 1998). The 350 aa RP2 protein is ubiquitously expressed at a low level (estimated to comprise ~0.01% of total protein across a variety of tissues) (Schwahn et al., 1998, Chapple et al., 2000). In human donor retinal tissue, RP2 was found to localise to the plasma membrane of cells in all layers and appeared evenly distributed across the plasma membrane of photoreceptor cells (Grayson et al., 2002). A later study employing a different antibody partially contradicted these results, with RP2 appearing more concentrated in photoreceptor inner segments and synaptic regions and almost absent in the outer segments (Holopainen et al., 2010). Further studies noted RP2 enrichment at the ciliary basal body and centriole, periciliary ridge and Golgi of murine photoreceptors (Evans et al., 2010), and along the ciliary axoneme of hTERT-RPE cells (Schwarz et al., 2017) and renal epithelial cells (Hurd et al., 2010). Single cell transcriptome analysis of adult donor samples confirmed RP2 expression in all neuroretinal cell types except RGCs, with (surprisingly) particularly high expression in microglia (Lukowski et al., 2020, de Silva et al., 2020).

The N-terminal domain of RP2 contains dual acylation sites and a region with 30% sequence homology to tubulin folding co-factor C (TBCC), while the C-terminal domain includes a region with homology to nucleoside diphosphate kinase (NDPK) (Evans et al., 2006). X-ray crystallography revealed that the N-terminal domain (228 aa) forms a β-helix structure, followed by a C-terminal ferredoxin-like α/β domain (Kuhnel et al., 2006).

The function of the NDPK domain in RP2 remains to be elucidated. NDPKs are involved in the production of NTPs and also demonstrate 3’ to 5’ exonuclease activity. RP2 is classed as a pseudokinase protein; a key catalytic residue is altered in the RP2 NDPK domain, resulting in a lack of kinase activity (Yoon et al., 2006). Many pseudokinases are involved in ciliary functioning and intracellular trafficking, with the defective kinase domain acting as a scaffold for the formation of protein complexes or enabling vesicle association (Jacobsen and Murphy, 2017). RP2 notably demonstrates exonuclease activity and appears to translocate to the nucleus to participate in base excision repair under

conditions of oxidative stress (Yoon et al., 2006). A complete C-terminal domain also appears to be essential for maintaining RP2 protein stability (Liu et al., 2017).

Much more is known with regard to the N-terminal domain of RP2. Post-translational acyl modifications (myristoylation at residue G2 and palmitoylation at C3) enable RP2 to travel from intracellular membranes to the cytoplasmic face of the plasma membrane and to the cilium (Chapple et al., 2000, Evans et al., 2010, Hurd et al., 2010). RP2 is trafficked to the cilium by importin β2, which binds to a short sequence motif within the TBCC domain (Hurd et al., 2011)

TBCC, along with other chaperone co-factors, is involved in the assembly of α/β-tubulin heterodimers. Newly formed heterodimers are subsequently released from the chaperone complex when TBCC stimulates the GTPase activity of β-tubulin (Tian and Cowan, 2013). While RP2 is capable of catalysing hydrolysis of β-tubulin-bound GTP, it cannot fulfil the heterodimer-forming role of TBCC (Bartolini et al., 2002). This, and the fact that TBCC does not localise to the plasma membrane, means that RP2 and TBCC are unlikely to have shared functionality (Lyraki et al., 2016). The primary role of the TBCC domain in RP2 appears to be enabling it to bind to a small GTPase, ADP-ribosylation factor like GTPase 3 (ARL3) (Bartolini et al., 2002, Kuhnel et al., 2006) – an interaction that increases the intrinsic GTPase activity of ARL3 by 90,000 fold (Veltel et al., 2008).

At least 108 variants in RP2 have been flagged as possibly pathogenic (see Appendix 2) and, as of yet, no gain-of-function mutations have been identified. 52% of *RP2*-XLRP patients reported in the literature carry mutations exclusively affecting an exon 2 region encoding the TBCC domain (residues 42 to 192), while the most commonly reported *RP2* mutation is p.Arg118His (11% of reported probands). The Arg118 residue is thought to be an 'arginine finger' essential for catalysing GTP hydrolysis. The Arg188His mutation reduces the affinity of RP2 for ARL3 by 800 fold and abolishes its GTPase activating protein (GAP) activity (Kuhnel et al., 2006, Bartolini et al., 2002). When all missense mutations affecting this residue are considered, they account for 15% of probands described in the literature (Appendix 2). Mutation of a conserved amino acid necessary for positioning the Arg188 residue for catalysis (p.Glu138Gly), also dramatically reduces the strength of RP2-ARL3 interaction (Kuhnel et al., 2006).

The second most commonly reported mutation (6% of reported probands; Appendix 2) is a nonsense variant, p.Arg120X, demonstrated to cause nonsense-mediated decay (NMD) of the RP2 transcript (Schwarz et al., 2015). The majority of known missense variants, small in-frame deletions and C-terminal truncation mutations are also predicted to lead to reduced RP2 levels by destabilising the protein and causing proteasome-mediated degradation (Liu et al., 2017).

The ARL3 small GTPase is a microtubule-associated protein that is especially concentrated at the connecting cilium (Grayson et al., 2002), and essential for ciliogenesis and trafficking of lipid-modified proteins to photoreceptor outer segments (Hanke-Gogokhia et al., 2016). While RP2 functions as the GAP of ARL3, ARL13B fulfils the role of its guanosine nucleotide exchange factor (GEF) and is localised in the connecting cilium and outer segment (Gotthardt et al., 2015). Missense mutations in *Arl3* have been linked to RP and Joubert syndrome (Holtan et al., 2019, Alkanderi et al., 2018).

ARL3 coordinates lipidated protein trafficking in conjunction with its effector proteins, phosphodiesterase 6 delta (PDE6δ) and uncoordinated 119 protein (Unc119), that can extract and solubilise membrane-bound proteins. PDE6δ transports prenylated proteins like PDE6 and rhodopsin kinase, while UNC119 binds to myristoylated cargo such as rod transducin α and nephrocystin-3 (NPHP3). Based on the results of a number of studies (Ismail et al., 2011, Wright et al., 2011, Zhang et al., 2011, Schwarz et al., 2012b), a model was proposed whereby PDE6δ and Unc119 capture proteins associated with organelle membranes (i.e. ER, Golgi or vesicles) and carry these cargo proteins to the cilia, where they encounter a pool of GTP-bound ARL3. Binding of ARL3-GTP to PDE6δ/Unc119 allosterically displaces cargo proteins, which can then be transported through the cilium via the intraflagellar transport (IFT) system. RP2 then inactivates ARL3, freeing PDE6δ and Unc119 to collect more cargo. A ciliary gradient of ARL-GTP and -GDP is thought to be maintained by the positioning of RP2 (enriched at the basal body) and ARL13B (exclusively localised to the cilium) (Gotthardt et al., 2015) (Fig. 2.1).

Loss of RP2 is theorised to result in increased levels of activated ARL3 and, consequently, mistrafficking of cilia-targeted proteins. RPE and fibroblast cells with *RP2* null mutations or overexpressing a constitutively active form of ARL3 (ARL3-Q71L) are reported to display fragmented Golgi and dispersal of intraflagellar transport protein 20 (IFT20), which is involved in transport of vesicles from the Golgi to the cilium (Evans et al., 2010,

Schwarz et al., 2015). Transgenic mice overexpressing ARL3-Q71L in rods ($rod^{Arl3\text{-}Q71L}$) also exhibit notably 'dilated' ER and Golgi (Wright et al., 2016), suggesting that a build-up of mistrafficked lipid-modified protein may lead to swelling and fragmentation of these organelles.

ARL3 was recently found to activate STAT3 (signal transducer and activator of transcription 3), which is involved in the regulation of many different processes, including cell proliferation, survival, migration and inflammation (Togi et al., 2016). This raises the possibility that STAT3-dependent pathways may be altered in *RP2*-XLRP. However, although ARL-GTP increases STAT3 activation in HeLa cells (Togi et al., 2016), this result failed to be replicated in a mouse model with constitutively active ARL3 (ARL3-Q71L) (Little, 2019).

RP2 is capable of directly trafficking at least one protein; it binds the β subunit of rod transducin (G protein subunit β1; GNβ1) until competition from ARL3-GTP stimulates its release (Schwarz et al., 2012a). The N-terminal domain of RP2 has also been demonstrated to interact with N-ethylmaleimide sensitive factor (NSF), a protein involved in the fusion of vesicles and membranes (Holopainen et al., 2010), which further supports a role for RP2 in the regulation of intracellular protein trafficking. It has additionally been shown to interact with polycystin 2 protein and is necessary for its correct localisation within the cilium (Hurd et al., 2010). RP2 furthermore appears to regulate the activity of ciliary kinesins and, therefore, perhaps general transport of proteins through the cilia (Schwarz et al., 2017). Recent evidence suggests that RP2 may also play a role in actin remodelling and positive regulation of cell motility via inhibition of osteoclast-stimulating factor 1 (OSTF1) (Lyraki et al., 2018).

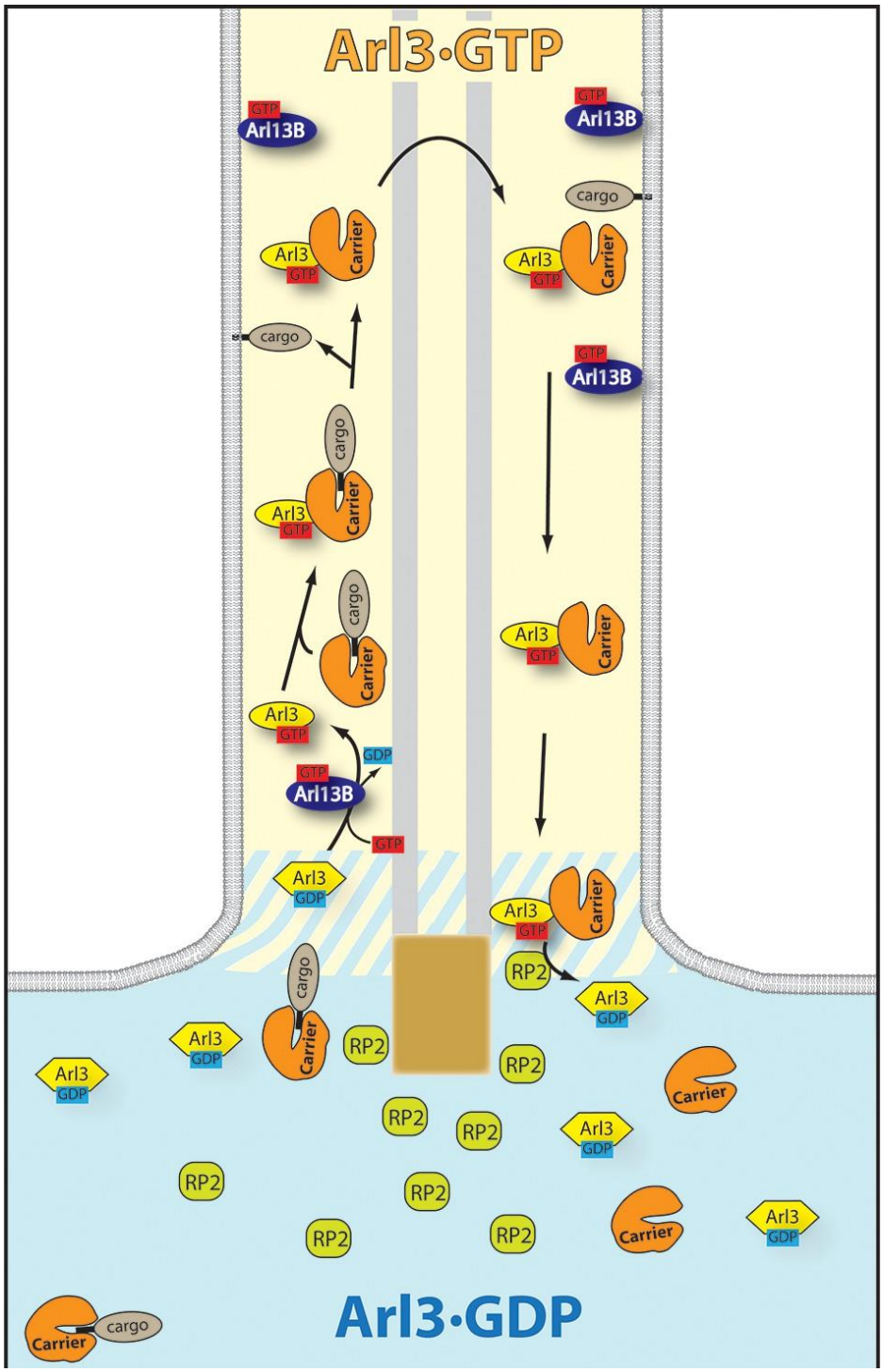

Fig 2.1. ARL3-dependent trafficking of lipid-modified proteins.

Figure reproduced from Gotthardt et al., 2015.

Fig 2.1. ARL3-dependent trafficking of lipid-modified proteins (continued).

A gradient of ARL3-GTP/GDP is established across the connecting cilium and periciliary region, controlled by localisation of its GEF (ARL13B) and GAP (RP2). ARL13B activates ARL3 along the cilia while a pool of RP2 around the basal body deactivates it. PDEδ and Unc119 (carrier proteins) transport lipid-modified proteins to the cilium, where ARL3-GTP stimulates cargo release. As carrier:ARL3 complexes exit the cilium, RP2 deactivates ARL3, releasing the carriers to retrieve more lipidated cargo.

2.2.3 *RP2* and *ARL3* mutant animal models

The human *RP2* and murine *Rp2h* (RP2 homolog) genes encode highly similar proteins, with 88% of amino acids identical and 42% of non-identical residues having similar physico-chemical properties (BLAST[13] alignment). A number of *RP2*-XLRP mouse models have been generated, which are compared in Table 2.1. Interestingly, these mice exhibit conflicting phenotypes.

The first mouse, $Rp2h^{\Delta E2/Y}$, was generated by Cre-Lox-mediated excision of exon 2 (Li et al., 2013, Li et al., 2015), while the $Rp2h^{GT/Y}$ model was later produced by insertion of a gene trap after exon 1 (Zhang et al., 2015a). $Rp2h^{\Delta E2/y}$ mice show rod and cone ERG defects from 1 month, and significant ONL thinning by 5 months (Li et al., 2013, Mookherjee et al., 2015). While the rod ERG deficit stabilised at 4 months of age, cone response continued to deteriorate so that at 18 months of age rod and cone function was reduced by 22% and 67%, respectively (Mookherjee et al., 2015). M-cone opsin, rhodopsin and (prenylated) PDE6 were notably mislocalised or absent (Li et al., 2013, Mookherjee et al., 2015), while cone outer segments and axonemes were elongated (Li et al., 2015). This effect was phenocopied with cone-specific, but not rod-specific, *Rp2h* KO mice (Li et al., 2015). Rod dysfunction was in general much milder than that of cones in $Rp2h^{\Delta E2/Y}$ mice. To further investigate the predominant cone defect, Li et al. (2019d) generated a rod-less S-cone-enriched *Rp2h* null model ($Rp2h^{\Delta E2/Y}$,$NRL^{-/-}$) . These mice also displayed abnormal cone OS lengthening, but S-cone function or opsin localisation was unaffected, suggesting separate roles for RP2 in negative regulation of cone OS length

[13] https://blast.ncbi.nlm.nih.gov/Blast.cgi?PROGRAM=blastp&PAGE_TYPE=BlastSearch&LINK_LOC=blasthome

and trafficking of some opsin proteins. Mookherjee et al. (2015) achieved long term (18 month) rescue of the cone ERG and trafficking defects in Rp2h$^{\Delta E2/Y}$ mice after subretinal injection of scAAV2/8-GRK1-RP2. This treatment did not improve the mild rod dysfunction observed, however, and was actually toxic to rods at a certain dose (1E9 vg/eye).

Zhang et al.'s *Rp2h*$^{GT/Y}$ model also exhibited rod and cone ERG defects from 1 month of age but these responses declined at a similar rate up to 6 months. In contrast to Li et al.'s model, *Rp2h*$^{GT/Y}$ mice did not exhibit ONL thinning or mislocalisation of opsins, while potential cone elongation was not examined. A defect was noted, however, in the trafficking of prenylated proteins GRK1 and PDE6 (Zhang et al., 2015a). GRK1, PDE6 and transducin α levels were also notably mislocalised in *rp2* null zebrafish models (Liu et al., 2015, Liu et al., 2017).

In an attempt to resolve the phenotypic discrepancy between the two RP2 XLRP mouse models, the Hurd group used CRISPR Cas9-mediated editing to generate an additional KO mouse with a frameshift mutation in exon 2, *Rp2h*$^{\Delta 23/Y}$, which does not express detectable RP2 protein (Little, 2019)[14]. They also created a *Rp2h*$^{E135G/Y}$ mouse to mimic a pathogenic missense variant (p.E138G) that reduces the affinity of RP2 for ARL3 to a non-physiologically relevant level (150 fold reduction) (Kuhnel et al., 2006). This should, in principle, enable delineation of ARL3-dependent and -independent effects of RP2 loss. *Rp2h*$^{\Delta 23/Y}$ photoreceptors mistrafficked M/L-cone opsin, rhodopsin and GRK1, displayed ONL thinning from 3 months and both rod and cone ERG defects from 6 months. Cone elongation has not yet been investigated in this model. In contrast, *Rp2h*$^{E135G/Y}$ mice experienced a considerably slower disease progression and had not developed a rod ERG defect by 12 months. The relatively milder phenotype in *Rp2h*$^{E135G/Y}$ mice suggests that RP2 may carry out important ARL3-unreleated functions. As discussed earlier, RP2 may be involved in vesicle trafficking via interaction with NSF and actin remodelling through inhibition of OSTF1. Alternatively, this finding may relate to speculated functions of the NDPK domain: oxidative stress response and facilitation of protein-protein interactions. However, it is also possible that the E135G mutation dramatically reduces but does not completely eliminate RP2-ARL3 interactions, resulting in a milder disease (Little, 2019).

[14] Abigail Little, PhD thesis (2019): 'Functional analysis of RP2 and ARL3 in X-linked retinitis pigmentosa.' https://era.ed.ac.uk/handle/1842/35803. Accessed 03/10/20. Work not yet published.

The phenotypic variation observed across these models is puzzling and, as all were generated on a C57BL/6 background, differences are most likely a consequence of the different methods of transgenesis employed. No RP2 protein was detected in *Rp2h*$^{\Delta E2/Y}$ mice (Li et al., 2013), though Zhang et al. proposed that if some mutant protein (possessing a NDPK domain) was produced it could conceivably act in a dominant-negative manner (Zhang et al., 2015a). Although RP2 protein expression was not detected in *Rp2h*$^{GT/Y}$ mice, the antibody used for immunoblotting was raised against a C-terminal region and therefore would not be sensitive to the truncated gene-trap fusion protein. Such a protein might retain the ability to localise to the plasma membrane and cilium but would lack both the TBCC and NDPK domains. The frameshift and missense mutations in *Rp2h*$^{\Delta 23/Y}$ and *Rp2h*$^{E135G/Y}$ mice were generated more precisely via CRISPR-Cas editing and should, in principle, better mimic the effects of pathogenic mutations found in patients. However, confounding off-target effects are still a very real possibility when employing a CRISPR-Cas editing method.

Further insights into the pathogenesis of XLRP can be gained using *Arl3* mutant models, which are compared in Table 2.2. *Arl3*$^{-/-}$ mice develop a severe systemic ciliopathy and do not live longer than three weeks. In the retina, they lack cone OS and rhodopsin is mislocalised (Schrick et al., 2006). Ciliogenesis is also hindered in a retina-wide Arl3 knockout mouse (Hanke-Gogokhia et al., 2016), while lipid-modified proteins were mistrafficked or degraded with rod-specific overexpression of *Arl3*^{Q71L}, a constitutively active mutant form of Arl3 (Wright et al., 2016). A CRISPR-Cas generated ubiquitous *Arl3*^{Q71L} model also displayed degraded GRK1 and additionally demonstrated dysregulated trafficking of rhodopsin and M cone opsin (Little, 2019). All *Arl3*^{Q71L} mice exhibited photoreceptor degeneration, which supports the hypothesis that elevated ARL3-GTP levels are central to the pathogenesis of *RP2*-XLRP pathogenesis. Interestingly, ARL3-GTP level was substantially higher and disease progression was more rapid in *Arl3*^{Q71L} than *Rp2h* null mice, suggesting there may be additional factors involved in the regulation of ARL3 activation capable of compensating for RP2 loss (Little, 2019). Such mechanisms may be sufficient in other cell-types but inadequate in the face of the exceptionally high rate of protein turnover in photoreceptor cells, leading to a retina-specific disorder.

The fact that OS development was blocked in Arl3 knockout but not *Arl3*^{Q71L} mice implies that Arl3-GTP is required for ciliogenesis, which may explain the elongated cone OS in

Rp2h$^{\Delta E2/Y}$ mice (Li et al., 2015). Cone OS were also noted to appear longer in *Arl3*^{Q71L} mice, though this observation was not quantified (Little, 2019).

In summary, based on the transgenic animal work so far, it is likely that RP2 plays essential roles in the trafficking of lipid-modified proteins important for photoreceptor function, such as rhodopsin kinase, rod transducin subunits and PDE6, to the OS via regulation of ARL3 activity. RP2 and ARL3 appear to be additionally involved in the trafficking of M cone opsin and rhodopsin, and work together to negatively regulate cone OS length. There is evidence to suggest, however, that there are additional roles carried out by RP2 independent of ARL3 that are important for photoreceptor function, possibly involving separate protein trafficking pathways and/or oxidative stress response.

It is important to note that the phenotypes of the *RP2* knockout mouse models described are considerably milder than the human disease. XLRP patients often experience macular atrophy in childhood (Jayasundera et al., 2010), which translates into regions of ONL thinning (visualised via OCT imaging) (Hufnagel et al., 2018)[15] (Fujinami et al., 2020). Rod dysfunction nevertheless remains the prominent disease feature, as assessed by ERG (Jayasundera et al., 2010). In contrast, *Rp2h* null mice exhibit cone-predominant dysfunction (Li et al., 2013, Mookherjee et al., 2015) and the earliest reports of partial ONL thinning occurs when they have reached adulthood (Little, 2019, Li et al., 2013). It is therefore possible that other proteins are capable of partially compensating for loss of RP2 in murine photoreceptors. This represents an obstacle in understanding the pathogenesis of *RP2*-XLRP and assessing potential therapeutics. Hence, one objective of the project outlined in this thesis was to supplement understanding of XLRP with human-derived *in vitro RP2* null models.

[15] Hufnagel et al. 2018 is a conference abstract (not peer-reviewed).

Genotype	*Rp2h*$^{\Delta E2/Y}$	*Rp2h*$^{GT/Y}$	*Rp2h*$^{\Delta 23/Y}$	*Rp2h*$^{E135G/Y}$
Reference(s)	Li et al. 2013 and 2015; Mookherjee et al. 2015	Zhang et al. 2015	Little et al. 2019	Little et al. 2019
Method of generation	Exon 2 excised via Cre-Lox recombination. No protein detected.	Protein truncated after exon 1 via gene trap.	23bp deletion in exon 2 via CRISPR/Cas editing. No protein detected.	Missense mutation in exon 2 via CRISPR/Cas editing. Protein incapable of inactivating ARL3.
Cone ERG defect	1 mo	1 mo	6 mo	9 mo
Rod ERG defect	1 mo (stabilises at 4 mo)	1 mo	6 mo	No
ONL thinning	5 mo	No	3 mo: reduced peripheral ONL thickness. 9 mo: thickness reduced across most of ONL.	6 mo: reduced peripheral ONL thickness. 9 mo: thickness reduced across most of ONL.
Mistrafficking of lipid-modified proteins	6.5 mo: PDE6 OS intensity reduced. Transducin α not mislocalised. GRK1 not tested.	1 mo: GRK1 and PDE6 mislocalised. Transducin α not mislocalised.	3 mo: GRK1 mislocalised. PDE6 and transducin not tested.	3 mo: GRK1 mislocalised. PDE6 and transducin not tested.
Mistrafficking of opsins	1 mo: cone M/L opsin mislocalised. 5 mo: rhodopsin OS intensity reduced.		3 mo: rhodopsin mislocalised 6 mo: cone M/L opsin mislocalised.	9 mo: rhodopsin mislocalised 9 mo: cone M/L opsin mislocalised.
Abnormal cone morphology	Cone OS and axoneme elongated.	Not analysed.	Not analysed	Not analysed

Table 2.1. Mouse models of *RP2*-XLRP. The age that phenotypes are first observed are listed. mo = months old.

Genotype	*Ret.Arl3*$^{-/-}$	*Rod.Arl3*$^{-/-}$	*Rod.Arl3*^{Q71L}	*Arl3*$^{Q71L/+}$	*Arl3*$^{Q71L/Q71L}$
Reference(s)	Hanke-Gogokhia et al. 2016	Hanke-Gogokhia et al. 2016	Wright et al. 2016	Little et al. 2019	Little et al. 2019
Method of generation	Inverted loxP-flanked gene trap inserted in Arl3 intron 1. Retina-specific Cre expression activates gene trap.	Inverted loxP-flanked gene trap inserted in Arl3 intron 1. Rod-specific Cre expression activates gene trap.	Random insertion. Arl3^{Q71L} overexpressed by Rho promoter.	CRISPR-Cas editing	CRISPR-Cas editing
Cone ERG defect	P15	1 mo	No	3 mo	3 mo
Rod ERG defect	P15	1 mo	1 mo	9 mo	3 mo
ONL thinning	P15	P15	2 mo	6-9 mo	1-6 mo
Mistrafficking of lipid-modified proteins	P10: GRK1, PDE6 and transducin α mislocalised.	P15: GRK1, PDE6, transducin α and γ mislocalised.	1 mo: GRK1 level reduced. PDE6 and transducin γ mislocalised.	1 mo: GRK1 level reduced.	1 mo: GRK1 level reduced.
Mistrafficking of opsins	P10: rhodopsin, M/L and S opsin mislocalised	No.	Rhodopsin not analysed.	6 mo: rhodopsin mislocalised. 9 mo: M/L cone opsin mislocalised.	1 mo: rhodopsin mislocalised. 6 mo: M/L cone opsin mislocalised
Abnormal PR OS morphology	Rod and cones had **no** CC or OS in central retina.	No	N/A	Not quantified.	Not quantified.

Table 2.2. Mouse models of *Arl3*-related retinal degeneration. The age that phenotypes are first observed are listed. mo = months old.

2.2.4 *In vitro* models of retinal disease

While the utilisation of transgenic animals been invaluable to biomedical research, inter-species variability remains a major obstacle to drug development, where ~86% of drugs that enter the clinical trial stage ultimately fail to be approved by regulatory authorities (Aasen and Vergara, 2020). Interspecies differences present numerous obstacles to the search for retinal therapeutics. For one, the murine retina does not have a fovea, with cones making up just ~3% of photoreceptors (Carter-Dawson and LaVail, 1979, Jeon et al., 1998). Murine retinas possess only two types of opsin – M- and S-opsin, with cones expressing one or both of these pigments (Nadal-Nicolás et al., 2020). The RPE cells of mice are also larger and can exhibit three fold higher phagocytic capacity than their human counterparts (Volland et al., 2015). Transgenic model phenotypes often do not adequately recapitulate human disease - as is the case with XLRP, choroideremia (Vasireddy et al., 2013) and Usher syndrome (Williams, 2008) to name a few. Additionally, AAV serotype tropisms and promoter activities can vary considerably between species (Stieger et al., 2008) (Vandenberghe and Auricchio, 2012, Watakabe et al., 2015, Juttner et al., 2019, Khabou et al., 2018b). Research using non-human primates (NHPs) is undoubtedly of value but is (rightly) limited due to ethical concerns, in addition to the prohibitive cost of running such experiments. Fortunately, human-derived cell models of disease are increasingly providing a means to bridge the gap between rodents and humans in a pre-clinical setting.

Patient-derived primary dermal fibroblast and peripheral blood lymphocytes have been used to model a number of non-syndromic inherited retinal degenerations (Vasireddy et al., 2013, Schwarz et al., 2015, Moosajee et al., 2016, Liao et al., 2017, Maloney et al., 2020) . This approach is feasible when the implicated gene is broadly expressed in many cell types. However, anything less than a retinal context is obviously suboptimal when studying a retinal disease. Additionally, the amount of available primary cell material is inherently limited, as cells inevitably approach replicative senescence.

The development of induced pluripotent stem cells (iPSCs) (Takahashi and Yamanaka, 2006), a renewable source of regenerative material free from the ethical concerns of embryonic stem cells (ESCs), revolutionised biomedical science and accelerated a paradigm shift toward personalised medicine. IPSCs have enabled development of autologous cell replacement therapies and have also greatly enhanced the power of *in*

vitro disease modelling. A variety of easily accessible cell types (dermal fibroblasts, peripheral blood lymphocytes, hair follicle keratinocytes and renal epithelial cells from urine samples) can now be reprogrammed to pluripotency by transfection with the Yamanaka factors (OCT3/4, SOX2, KLF4 and c-MYC) (Okita et al., 2011, Staerk et al., 2010, Re et al., 2018, Zhou et al., 2012).

Normal embryonic development is orchestrated by delicately balanced gradients of secreted signalling molecules. Neural induction is initiated by fibroblast growth factor (FGF) secretion and repression of Wnt and bone morphogenetic protein (BMP)-signalling. Restriction of Wnt signalling is particularly important for the designation of an 'eye field' of retinal progenitor cells in the anterior neuroectoderm. Under the influence of TGF-ß, FGF and sonic hedgehog (Shh) factors, the eye field splits in two, and grooves termed optic sulci form (Sinn and Wittbrodt, 2013). Around week 3 of development, as the neural tube closes, optic sulci evaginate or 'bud' to form optic vesicles (OV). At this point, OV neuroepithelium can give rise to both RPE and neural retina. Growth factors such as FGF secreted from the overlying lens precursor structure stimulate differentiation of the apical OV neuroepithelium into neuroretinal precursor cells, while posterior neuroepithelial regions are designated to form the RPE. The neural region of the optic vesicle then invaginates, positioning itself closer to the RPE and creating an optic cup structure. At this point, BMP activity is necessary for maintaining neuroretinal fate, while the RPE relies on Wnt signalling (Fuhrmann, 2010, Patel and Sowden, 2019) (Fig. 2.2). Retinoic acid signalling is also involved in the formation of the optic cup structure (Duester, 2009) and needed for continued development and expansion of the eye (Smith et al., 2018). Differentiation of precursor cells in the neuroretinal layer starts with 'early-born' ganglion, horizontal, amacrine and cone photoreceptor cells, while rod photoreceptor, bipolar and Müller glia are 'late-born' and continue maturing after birth (Bassett and Wallace, 2012). Initiation of the retinal progenitor cell (RPC) differentiation process appears to be dependent on FGF (Sinn and Wittbrodt, 2013), while retinoic acid signalling regulates photoreceptor differentiation (Stevens et al., 2011).

Retinal cells can be differentiated from pluripotent stem cells by simulating signalling and environmental cues present during normal embryonic development *in vitro.* PSCs can be pushed toward a retinal progenitor fate by addition of Wnt and Nodal inhibitors to cell suspension and growing adherent cell aggregates on plates coated in ECM components.

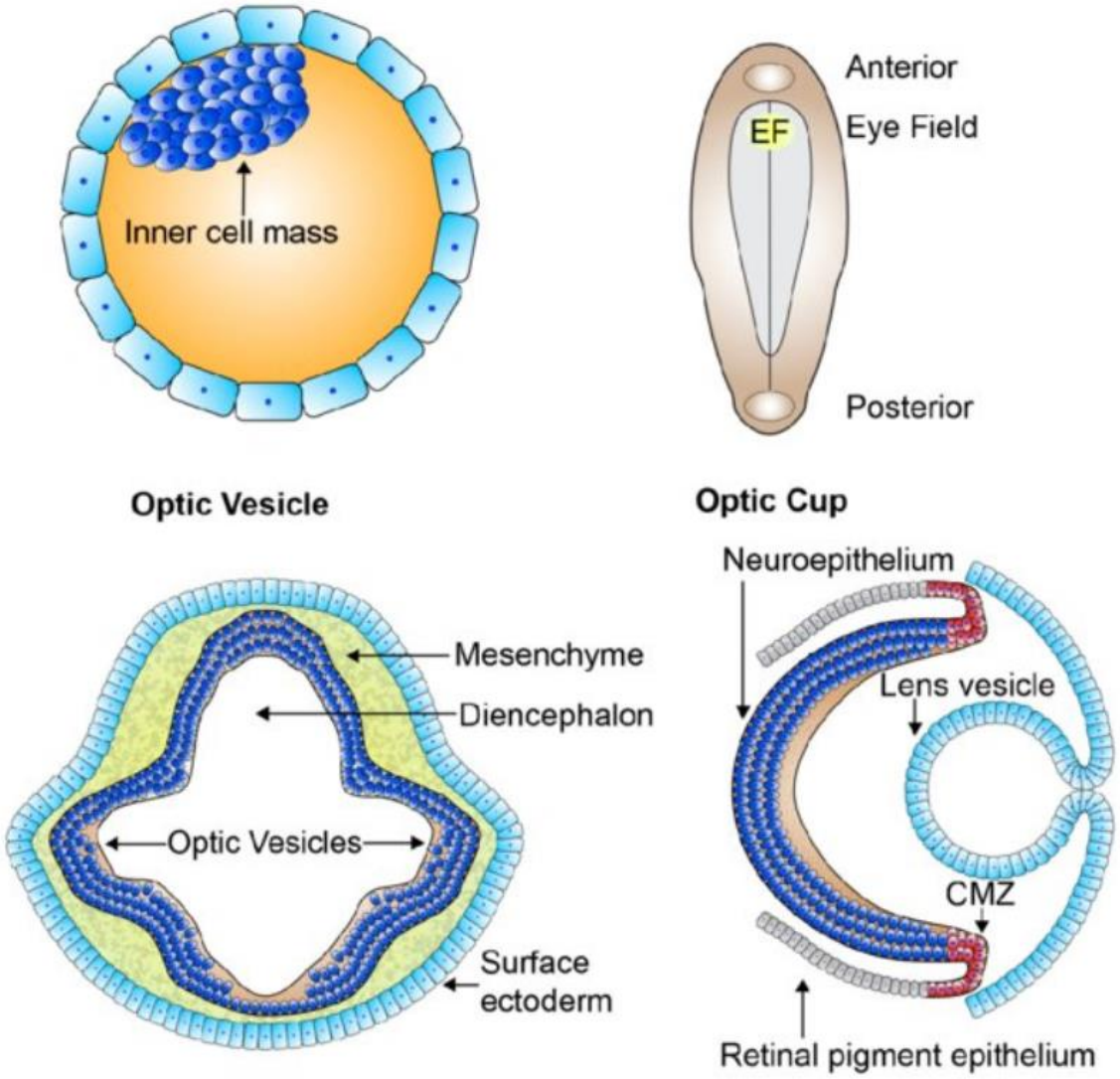

Figure 2.2. Schematic of early retinal development. Pluripotent cells in the inner mass of a blastocyst form a neuroectodermal plate. An eye field is designated in the anterior neural plate and splits in two. From the developing eye fields, optic vesicles evaginate, extending towards the surface ectoderm. Signalling molecules secreted from the lens placode (a thickened region of surface ectoderm) stimulate the distal optic vesicle to invaginate, forming an optic cup structure. The inner layer of optic cup neuroepithelium becomes the neuroretina, while the outer layer forms the RPE and the anterior rims ciliary marginal zones (CMZ) give rise to the iris and ciliary body. The lens placode also invaginates to form a lens vesicle.
Figure reproduced from Quinn and Wijnholds, 2019.

Photoreceptor differentiation can then be induced by addition of retinoic acid and taurine, though only a small percentage of cells subsequently express markers of PR maturity (Osakada et al., 2008, Hirami et al., 2009). PSCs can also be directed to an RPE cell fate by modulation of BMP, Wnt and FGF signalling (Buchholz et al., 2013, Leach et al., 2015) Alternatively, removal of bFGF from PSC culture media stimulates PSCs to spontaneously differentiate into RPE cells (Buchholz et al., 2009, Ferguson et al., 2015). These '2D' culturing protocols, where adherent monolayers are grown on a flat surface, are undoubtedly of value. However, the fact that they lack the complex, heterotypic organisation of a normal retina is an inherent and sizeable disadvantage.

PSCs grown in aggregates, or embryoid bodies, in serum-free suspension cultures naturally progress to a neural fate without the addition of extrinsic signalling molecules (Eiraku et al., 2008). Meyer et al. (2009, 2011) succeeded in generating PSC-derived eye fields and optic vesicles. Aggregates of PSCs were cultured in suspension under serum and bFGF-free conditions, then transferred to neural induction medium (containing N2[16] neuronal supplement) and grown adherently on laminin-coated plates. This induced formation of neural-tube like structures (rosettes), which displayed an eye field expression profile (Pax6 and Rx positive). Neuroepithelial rosettes were then supplemented with B27[17] to promote retinal differentiation and transferred to suspension culture to form 3D neurospheres of retinal precursor cells that resembled optic vesicles.

Yoshiki Sasai's group went further - producing self-organising optic cups from mouse and human ESC cultures in two ground breaking studies (Eiraku et al., 2011, Nakano et al., 2012). hESCs were aggregated in suspension to form floating embryoid bodies in serum-free medium supplemented with (growth factor-reduced) Matrigel[18], a solution rich in basement membrane matrix components, a Wnt inhibitor (to counteract the caudalisation effect of knock-out serum in the media) and ROCK inhibitor (to suppress dissociation-induced apoptosis). In such conditions, embryoid bodies spontaneously formed neuroepithelial vesicles – at which point FBS and a Shh agonist was added to

[16] https://www.thermofisher.com/ie/en/home/technical-resources/media-formulation.166.html. Accessed 20/09/20.
[17] https://www.thermofisher.com/ie/en/home/technical-resources/media-formulation.250.html. Accessed 20/09/20.
[18] https://ecatalog.corning.com/life-sciences/b2c/EUOther/en/Surfaces/Extracellular-Matrices-ECMs/Corning%C2%AE-Matrigel%C2%AE-Matrix/p/corningMatrigelMatrix. Accessed 20/09/20.

promote neuroretinal differentiation, while a Wnt agonist was used to encourage RPE maturation. Remarkably, optic vesicles self-organised into double-walled optic cup-like structures (Nakano et al., 2012). When the neuroretinal regions of these optic cups were isolated and further grown in suspension under high oxygen conditions they matured into retinal organoids (ROs): 3D laminated structures containing all types of RPC-derived neuroretinal cells. The order of neuroretinal cell-type birth in organoids even mirrored that seen *in vivo*. However, photoreceptors did not develop outer segments in this system (Eiraku et al., 2011, Nakano et al., 2012).

Zhong et al. (2014) modified the Sasai protocol substantially – establishing a mixed 2D/3D culture protocol that did not require exogenous signalling factors (i.e. Wnt inhibitor) to induce retinal progenitor cell (RPC) development. The initial aggregates were formed in suspension from clumps of dissociated 2D adherent PSC cultures. Embryoid bodies were directed towards a neuronal cell fate in serum-free N2-supplemented media, then seeded onto Matrigel-coated dishes in B27 media. After four weeks of differentiation, the neuroretinal layers of the developing optic vesicles were isolated and cultured in suspension (normal oxygen conditions) to form spherical retinal organoids. FBS, taurine and retinoic acid was added at this stage to promote neuroretinal cell survival, though it was necessary to reduce retinoic acid concentration at a certain point and switch B27 supplement to N2 in order to encourage photoreceptor maturation. Crucially, these ROs were the first to demonstrate development of rudimentary photoreceptor outer segments (from Week 21 – 28). Some of these photoreceptors were even shown to be light-sensitive via patch clamp recording (Zhong et al., 2014). A later study noted ribbon synapses at the base of RO photoreceptors (D160) and demonstrated PR synaptic functionality via changes in membrane capacitance at D300 (Wahlin et al., 2017).

Most subsequent studies have utilised optic vesicle-derived retinal organoids (ROs) (Fig. 2.3), derived using variations of the Zhong and Nakano protocols, as opposed to invaginated optic cups. ROs often contain small clumps of pigmented RPE but lack an appropriately positioned continuous RPE layer. In contrast, while the positioning of neuroretina against RPE in optic cups is desirable, the neuroretinal structures of Sasai's optic cups appeared less stable and less capable of maturation than those of ROs. However, a more recent study found that addition of insulin growth factor 1 (IGF-1) to otherwise minimal media (B27 supplemented) could produce optic cups with

substantially accelerated photoreceptor maturation that maintain longer-term integrity (Mellough et al., 2015).

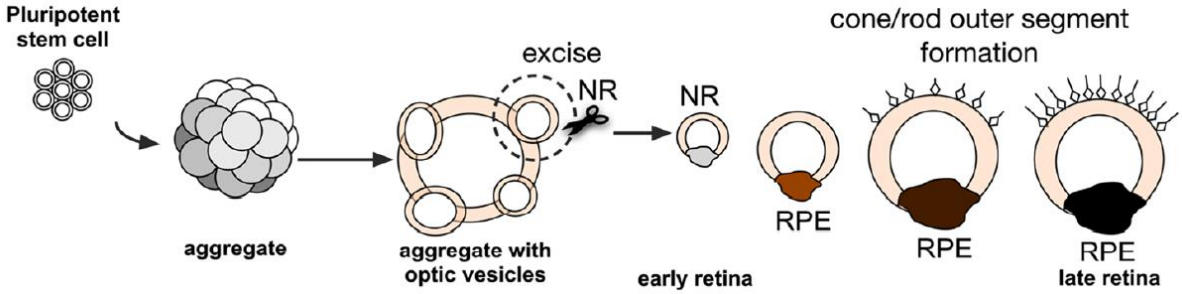

Fig. 2.3. Illustration of the procedure for retinal organoid generation. PSCs are aggregated and grown as embryoid bodies. Optic vesicles form and are isolated, and the neuroepithelial layer differentiates into neural retina (NR). Pigmented regions of ectopic RPE and a brush border of developing photoreceptor outer segments are shown. Figure reproduced from Wahlin et al. 2017.

Retinal organoid production is inherently variable, with ROs differing in terms of size, shape, uniformity, cellular composition, and differentiation efficiency - largely depending on the hPSC line used (Wahlin et al., 2017, Capowski et al., 2019). In an effort to standardise comparison of ROs within and across studies, Capowski et al. developed a light-microscopy-based staging system that fit ROs differentiated from 16 different hiPSC and hESC lines (see Fig 2.4). At Stage 1 (~D30-70), ROs are spherical with a phase-bright outer rim of neuroepithelium. This outer rim consists of an outer layer of retinal progenitor cells above a layer of starburst amacrine cells and RGCs. By Stage 2 (~D70-120), ROs have grown larger, with a phase-dark core and diminished outer-rim brightness. At this point, the RGC layer is degenerating, while the RPC outer layer is differentiating into photoreceptor, horizontal and amacrine cells. At stage 3 (~D120+), photoreceptors express cone and rod-specific markers, with rods outnumbering cones 4:1, and newly born Müller glia facilitate the formation of an outer limiting membrane. A thin phase-bright outer-rim is again evident via light microscopy, and a hair-like 'brush border' of nascent photoreceptor outer segments covers the spheroid. The neuroretinal tissue is now clearly stratified, containing an OPL positive for presynaptic markers and an INL with bipolar cells. The inner layers, however, continue to degenerate. As ROs are not vascularised, a necrotic core grows inside the organoid due to insufficient passive diffusion of nutrients and oxygen. Lack of microglia and astrocytes may also contribute to inner layer disorganisation (Capowski et al., 2019).

Neuroretinal cell types differentiate from RO RPCs in the same order that they would *in vivo*. Importantly, ROs have also been shown to closely replicate the timeline of retinogenesis in the human foetal retina when assessed by single cell RNA-seq (scRNA-seq) (Sridhar et al., 2020, Cowan et al., 2020). By 38 weeks of development (the average length of a pregnancy), RO transcriptomes 'stabilise' – bearing many similarities to that of an adult peripheral retina (Cowan et al., 2020). However, while the expression signature of retinal lineage marker genes does not appear dependent on the differentiation method used, it does vary substantially between PSC lines (Mellough et al., 2019).

Retinal organoids are an invaluable tool in the advancement of precision medicine and have already been used to model a number of IRDs (Phillips et al., 2014, Parfitt et al., 2016, Megaw et al., 2017, Shimada et al., 2017, Schwarz et al., 2017, Deng et al., 2018, Quinn et al., 2019, Huang et al., 2019, Buskin et al., 2018). Some of these studies further succeeded in rescuing deleterious phenotypes using antisense oligonucleotides or CRISPR-Cas editing (Parfitt et al., 2016, Deng et al., 2018, Buskin et al., 2018). Schwarz et al. (2017) modelled RP2 loss with R120X patient-derived ROs and uncovered a potential role for RP2 and Arl3 in the regulation of ciliary kinesin protein activity. The mislocalisation of ciliary tip kinesins observed in *RP2* null organoids at ~D150 could be rescued by treatment with a translational read-through drug (Schwarz et al., 2017).

The potential of retinal organoid technology for modelling diseases and screening potential therapeutics is clearly substantial. A major aim of this project was to further explore potential phenotypes in *RP2* null ROs – employing additional cell lines and longer term analyses – and, additionally, to establish whether an AAV-mediated gene replacement strategy would be efficacious in these models.

A

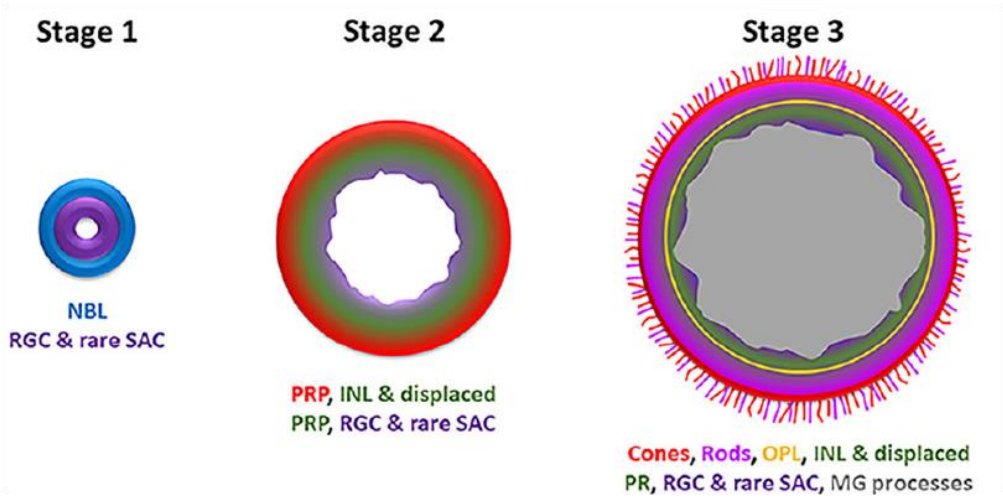

B

Staging retinal organoids

Stage		Morphological features	Molecular markers	Fetal retina epoch
Stage 1	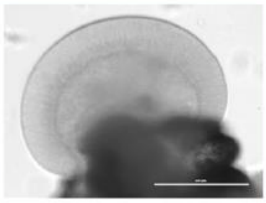	○ Phase-bright neuroepithelium ○ Often columnar organization visible ○ Cup-like shape ○ Rapid growth ○ Several weeks post isolation	○ Retinal progenitors: RAX, VSX2, PAX6 ○ Neurogenesis: ASCL1, NEUROD1, NEUROG1, ATOH1 ○ Ganglion and Starburst amacrine cells: BRN3A/B, SNCG, HuC/D, CHAT, NEFL	○ **First epoch** ○ Mitosis and retinal progenitor genes (*FGF19*, *LIN28B*, *PRTG*, *SFRP2*) ○ Retinal ganglion cell genes (*ATOH7*, *DLX2*, *POU4F2*)
Stage 2	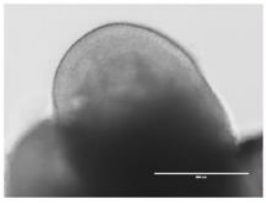	○ Phase dark core develops ○ Grown together tend to merge forming multi-lobular aggregates ○ May remain at this stage	○ Interneurons: ONECUT1/2, TFAP2A/C, CALB2 ○ Photoreceptor precursors: OTX2, CRX, NRL, NR2E3, THRB2, RXRG ○ Synaptogenesis: VAMP2, SNAP25, STX3, SYP, SYT1, CPLX3, PCLO	○ **Second epoch** ○ Horizontal and amacrine cell genes (*PROX1*, *ASCL1*) ○ Synapse genes (*NRXN1/3*, *SCN2A*, *CACNA1C*)
Stage 3	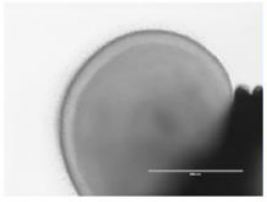	○ Outer lamina clearly defined ○ Brush-like apical protrusions at the rim ○ Center dense and opaque ○ Arise around 15-20 weeks post-isolation	○ Opsins: OPN1SW, OPN1MW, RHO ○ Phototransduction: GNAT1/2, GNGT1/2, SAG, ARR3, CNGB1/3 ○ Outer segment: ROM1, ABCA4, PRPH2, RPGR ○ Müller glia: RLBP1, VIM	○ **Third epoch** ○ Photoreceptor and bipolar cells genes (*OTX2*, *NRL*, *RCVRN*, *TULP1*, *GNAT1/2*, *GRM5/6/7/8*)

Figure 2.4 Stages of retinal organoid development.

(A) A schematic illustrating the cellular composition of retinal organoids across the three stages of development. Figure reproduced from Capowski et al. 2019.

(B) Representative light microscopy images of ROs at the different stages are shown (scale bar = 400 µm). The table on the right outlines key morphological and molecular markers of ROs, alongside corresponding foetal development stage features. Figure reproduced from Kruczek and Swaroop, 2020.

2.2.5 Objectives of chapter 2

The objectives of the project described in this chapter were:

I. Investigate the consequences of RP2 loss using primary fibroblast and retinal organoid models.
II. Evaluate the efficacy of AAV-mediated RP2 replacement in these *in vitro* models of *RP2*-XLRP.
III. Assess the tolerability of AAV-RP2 treatment in the wild-type murine retina.

2.3 Results

2.3.1 Identification of individuals with pathogenic *RP2* variants

A 34 year old male RP proband harbouring a c.358C>T nonsense mutation (p.Arg120X) was identified through the Target 5000 programme. The patient's obligate carrier mother was confirmed to be heterozygous for the c.358C>T mutation by Sanger sequencing (Fig. 2.7.B).

This pathological variant has been found in several cohorts of European, Chinese and North American origin (Hardcastle et al., 1999, Mears et al., 1999, Liu et al., 2001) (Vorster et al., 2004, Neidhardt et al., 2008, Riera et al., 2017). As mentioned previously, a survey of *RP2* pathogenic mutations documented in the literature was undertaken and c.358C>T was found to be the most commonly reported *RP2* nonsense mutation and the second most common mutation overall (Appendix 2). The relatively high incidence of this mutation across multiple populations and the observation of a case of c.358C>T *de novo* germline mosaicism prompted Vorster et al. (2004) to propose that the affected nucleotide may be a mutation hotspot. Fibroblasts derived from a c.358C>T patient were found to have reduced RP2 mRNA expression and a complete lack of RP2 protein (Schwarz et al., 2015). It was therefore concluded that the mutant transcript underwent nonsense-mediated decay (NMD).

The affected individual, 'R120X-A', had been clinically assessed and diagnosed with RP by Dr Paul Kenna. He had suffered from night blindness since childhood and experienced a progressive deterioration of photopic vision from his early teenage years. By 34 years of age, his visual acuity was restricted to perception of light. Fundus imaging of the patient revealed bone spicule deposits, atrophic macular regions and attenuation of blood vessels (Fig. 2.5.B).

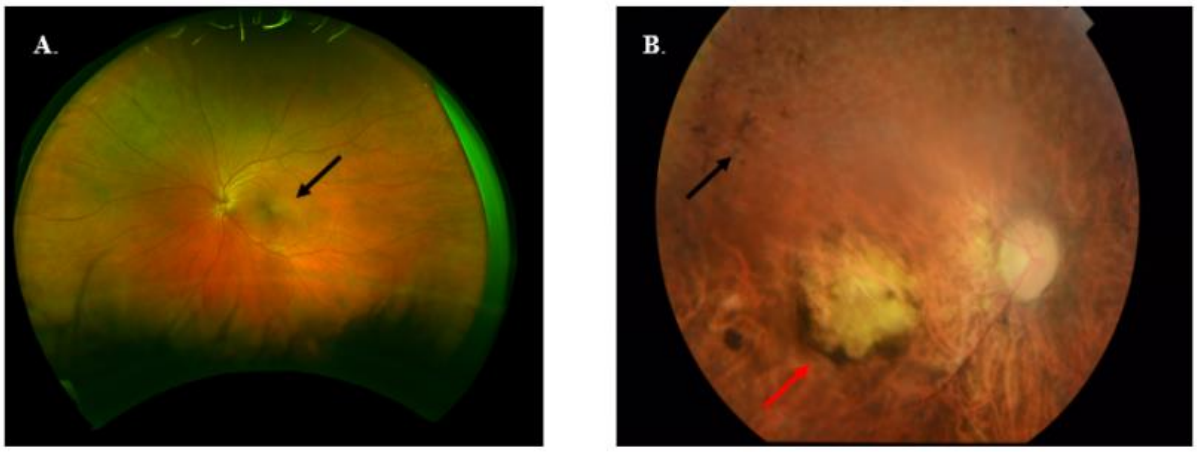

Figure 2.5. Fundus images of the retina of the proband (B) and their unaffected carrier mother (A).

(A) The fundus image of the retina, taken with an Optos wide-field fundus camera, shows a normal optic disc, normal vasculature (note the vasculature appears thin due to the wide-field nature of the image) and absence of the pigment deposits prominent in the fundus images of her son. The proband's mother did show a small area of hyperpigmentation at the central macula (not easily seen in the image, marked with an arrow) which may be a subtle indication of her being a carrier of an X-linked RP gene variant.

(B) Photographs of the central retina of the right and left eyes, taken with a Topcon fundus camera, showed marked pallor of the optic discs, severe attenuation of the retinal vasculatures, bilateral atrophic changes of the macular areas (red arrow) and extensive 'bone spicule' pigment deposits (black arrow), typical of those seen in Retinitis Pigmentosa, in the more peripheral retinal areas in each eye.

This figure and legend were kindly provided by Dr Paul Kenna.

Interestingly, a small area of macular hyperpigmentation was observed in the otherwise normal fundus of the patient's unaffected mother. This was astutely noted as a possible subclinical carrier phenotype at the time of examination by Dr Paul Kenna (Fig. 2.5.A).

An additional 68 year old male RP proband was identified with a novel c.425delA (p.Asp142IlefsTer14) candidate variant (Dockery et al., 2017). At the time of writing, samples from family members were not available for segregation analysis of this variant. The mutation was not reported in the Genome Aggregation Database (gnomAD (a collection of 125,748 exomes and 15,708 genomes (Karczewski et al., 2020)) or the NCBI dsSNP variant database (Sherry et al., 2001).

The c.425delA frameshift mutation would cause a premature stop codon to form in exon 2, at c.463-465 of the normally 1053 bp coding sequence. Hence, nonsense-mediated decay of the transcript would likely occur. As outlined previously, loss of function is the mechanism behind the vast majority of documented RP2 cases. Considering this and the variant's absence in control population collections, c.425delA was classed as 'likely pathogenic' as per guidelines set by the American College of Medical Genetics and Genomics and the Association for Molecular Pathology (Richards et al., 2015).

2.3.2 Characterisation of patient-derived primary fibroblast models of RP2

A collection of patient and control-derived dermal fibroblast cells was established in order to investigate the consequences of *RP2* null mutations (Fig. 2.6.A). Fibroblast cultures were generated from skin biopsies donated by the two affected individuals described and are henceforth referred to as 'R120X-A' and 'N142fs'. Fibroblasts from an additional R120X patient, 'R120X-B', were obtained from the Hardcastle lab (UCL). Characterisation of these cells had previously been carried out by Schwarz et al. (2015), as previously mentioned. Unfortunately, R120X-B cells were several years old at the time of this study and appeared to be approaching senescence. For this reason, they were only included in a few of the experiments that follow.

Several sources of control fibroblasts were obtained for this study, either commercially or produced from volunteered skin biopsies. The age of biopsy donors ranged from new-born ('BJ' fibroblasts derived from a neonatal foreskin sample) to 68 years old.

Primary cell cultures generated in-house were tested for expression of fibroblast surface protein to confirm their fibroblast identity and validate the protocol used (Fig. 2.6.B). Fibroblast genotypes were also verified at regular intervals by Sanger sequencing (Fig. 2.7).

A

Name	Sex	Age	Source
R120X-A	Male	34	Farrar lab, TCD
R120X-B	Male	25-26	Hardcastle lab, UCL
N142fs	Male	68	Farrar lab, TCD
BJ	Male	Neonate	ATCC; CRL-2522
C1	Male	26	Farrar lab, TCD
C2	Male	27	Farrar lab, TCD
C3	Female	32	Farrar lab, TCD
C4	Male	66	Farrar lab, TCD
C5	Female	40	ATCC; PCS-201012

B

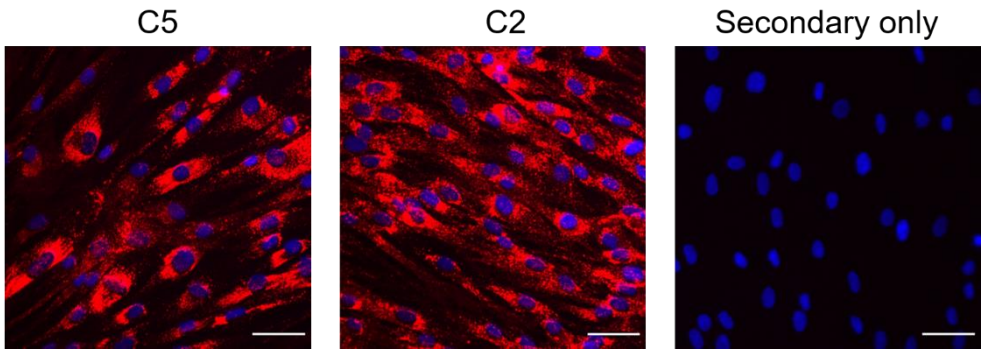

Fig. 2.6. Establishment of a collection of patient and control-derived primary human dermal fibroblast cells.

(A) Information relevant to fibroblast cultures used in this study is presented, including the age and sex of biopsy donors. Patient-derived fibroblasts are named after the *RP2* mutation harboured (p.R120X or N142fs). BJ and C1-C5 fibroblasts were generated from unaffected individuals. Most patient and control cultures were derived by the Farrar lab. Fibroblast obtained from an additional *RP2* p.R120X patient (R120X-B) were provided by the Hardcastle lab (Schwarz et al., 2015). Two control fibroblast cultures were sourced commercially (ATCC).

(B) Anti-fibroblast surface protein antibody (Sigma-Aldrich; F4771) was used to confirm the correct cellular identity of newly derived cultures via ICC. In the representative images shown, cells derived in the Farrar lab, C2, were compared to C5 commercially obtained fibroblasts and found to express fibroblast surface protein similarly. Cells stained with the secondary antibody alone act as a negative control. Scale bar = 50µm.

When assessed by RT-qPCR, expression of the RP2 transcript was depleted in both R120X-A and N142fs fibroblasts (Fig. 2.8.A). Although R120X-B cells were not included in this RNA expression test, they previously exhibited an approximately 80% reduction in RP2 expression relative to BJ control fibroblasts (Schwarz et al., 2015). A similar level of depletion was observed in the current study; the relative amount of RP2 mRNA in R120X-A fibroblasts was 15.96% that of BJ cells (0.16 ± 0.01 vs 1.0 ± 0.17, respectively). Interestingly, RP2 expression across control fibroblasts differed considerably. In light of this variation, it seemed important to compare patient cell RP2 levels to sex- and age-matched control cells where possible. When compared to fibroblasts from unaffected adult males (C1 and C2), RP2 mRNA expression was reduced by 90% in R120X-A ($p = 0.0144$) and 61% in N142fs cells ($p = 0.0611$) ($n = 2$) (Fig. 2.8.B). Cells from C4 (a 66 year old male) would have been a more appropriate control for N142fs fibroblasts, which were derived from a 68 year old donor. Unfortunately, they were unavailable at the time of this test but will be included for comparison in future analyses.

RP2 RNA expression was also compared between fibroblasts from male and female donors. The RT-qPCR primers used were designed to be intron-spanning (to discourage amplification of gDNA) (Schwarz et al., 2015). Additionally, low signal from DNA carryover in samples was assessed using control reactions that did not include reverse transcriptase. Thus, any difference observed between male and female samples was not simply due to difference in genomic *RP2* copy number.

RP2 expression in control fibroblasts was significantly higher in those from female donors ($p = 0.0202$, $n = 2$) (Fig. 2.8.C). This was an interesting observation, as RP2 is reported to be completely silenced during X-inactivation (Carrel and Willard, 2005, Fahim and Daiger, 2016). The limited amount of male and female donors at the time of writing precluded us

from investigating this matter further. However, the results of this test do emphasise the importance of using sex-matched controls where possible.

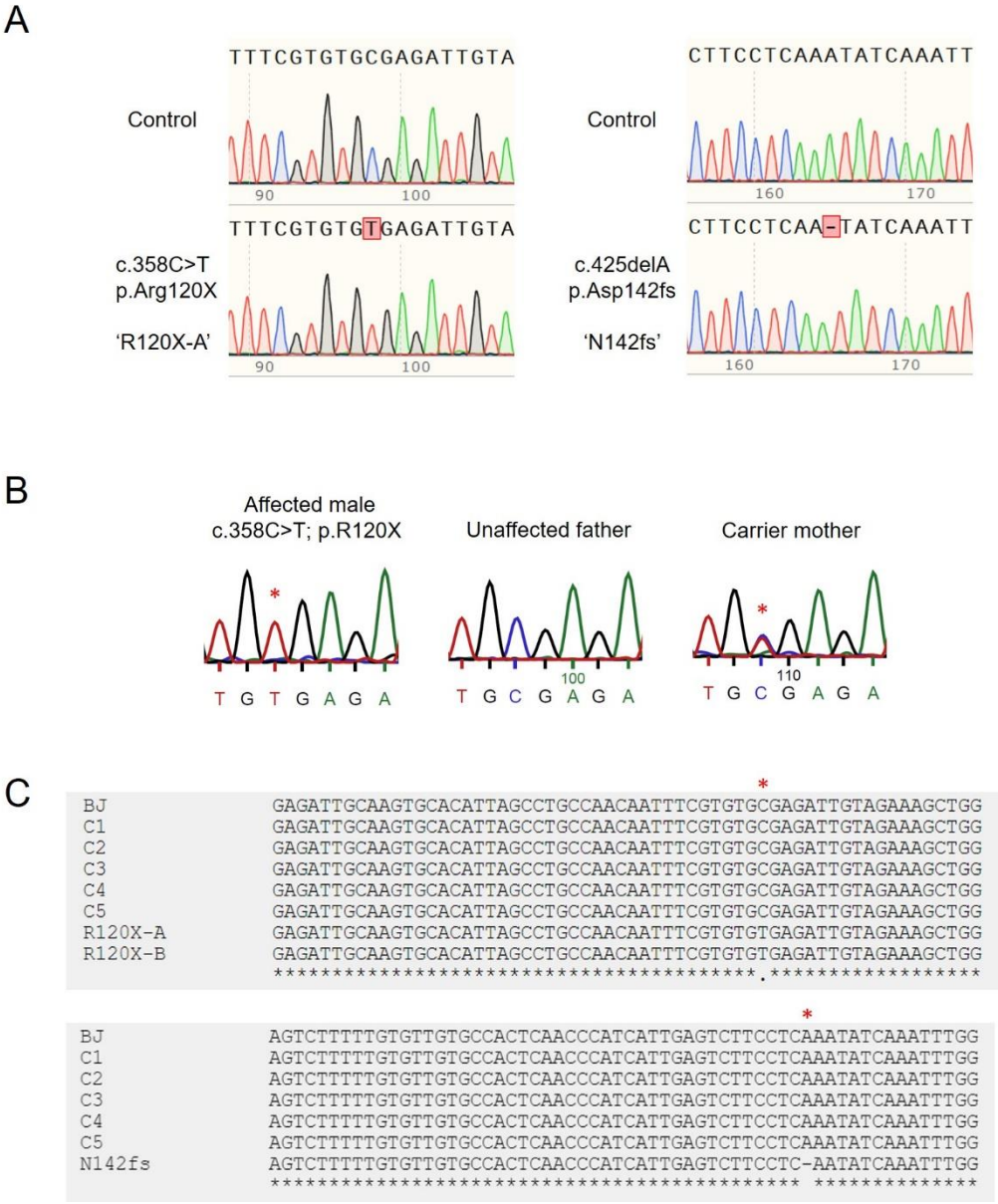

Fig. 2.7. Genotyping of samples from affected and control individuals.

(A) The *RP2* c.358 and c.425 regions were Sanger sequenced in patient and control fibroblasts to confirm their genotype. Sequencing chromatograms are presented.

(B) Sequencing results from the R120X-A pedigree are shown. In R120X-A fibroblasts, the C to T transition is evident (red asterisk). Fibroblasts from the patient's unaffected father (C4) were free of this mutation. A chromatogram from the proband's carrier mother confirms her carrier status, displaying a heterozygous double peak (C/T) at c.358.

Note: In the case of the proband's mother, analysis was carried out on DNA extracted from a peripheral blood sample, rather than fibroblasts.

Fig. 2.7. Genotyping of samples from affected and control individuals (continued).
(C) The relevant *RP2* regions were routinely Sanger sequenced in all control and patient-derived fibroblast populations to confirm their genotype. An alignment of chromatogram data is shown, produced using the MAFFT online tool (Katoh et al., 2019). Red asterisks indicate nucleotides of interest: c.358 (top panel) and c.425 (bottom panel).

RP2 protein expression could not be detected by Western blot in the patient-derived cell cultures studied (Fig. 2.8.D and E). Absence of truncated RP2 protein in R120X-A and N142fs cells was verified using an antibody gifted by the Hardcastle/Cheetham groups (Fig. 2.8.E), which is thought to bind to an epitope within amino acids 8-15 (Chapple et al., 2002). These results suggest that *RP2* c.358C>T and c.425delA mutant transcripts are degraded by NMD in patient-derived fibroblasts.

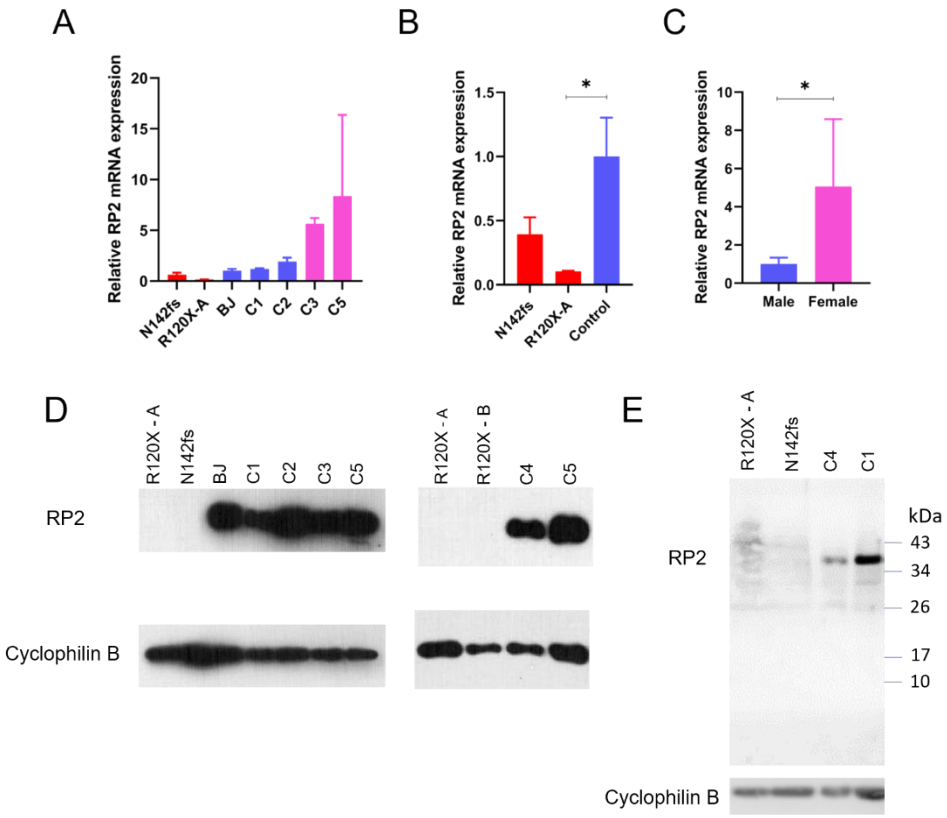

Fig. 2.8. RP2 expression in patient and control fibroblast cells.

(A) RP2 mRNA levels were assessed by RT-qPCR across patient and control cells. Both R120X and N142fs cells produced lower amounts of RP2 than controls. Notably, RP2 expression was highly variable between control lines. For each group, n = 2 culture flasks. RP2 levels were normalised against β-actin expression.

(B) In light of the variation in RP2 expression observed across cells, it was decided to use only adult male control cells for comparison. Hence, the 'control' group in this graph is the average of C1 and C2 values. RP2 expression was reduced in R120X and N142fs cells by 90% ($p = 0.0144$) and 61% ($p = 0.0611$), respectively. A one-way ANOVA was performed to test for significance, followed by Dunnett's multiple comparisons test.

(C) Control fibroblasts from female donors expressed significantly more RP2 mRNA than those from male donors ($p = 0.0202$; Student's t-test).

Values shown are means ± SD.

(D and E) RP2 protein was not detected by Western blot in any of the three types of patient-derived fibroblasts available. Immunoblotting was performed using two different polyclonal RP2 antibodies: Proteintech cat. no.: 14151-1-AP (D) and a second antibody known to be capable of detecting short N' protein fragments (Chapple et al., 2002) (E). Cyclophilin B (19 kDa) was used as a loading control.

2.3.3 AAV-mediated gene replacement restores RP2 expression in null fibroblasts

An AAV vector was designed to deliver a functioning copy of human *RP2* to target cells (Fig. 2.9). As RP2 is ubiquitously expressed at a relatively low level (Chapple et al., 2000) and its importance in the RPE has yet to be defined, it was decided to drive transgene expression with a constitutively active promoter rather than a photoreceptor-specific element. This would also enable testing of the vector in non-retinal patient-derived models, such as fibroblast cell cultures. The CAG promoter was selected for this purpose (Niwa et al., 1991). This synthetic 'promoter' sequence is comprised of the cytomegalovirus (CMV) early enhancer followed by the chicken β-actin (CBA) promoter, first exon and first intron, which contains an additional enhancer element. A rabbit β-globin splice acceptor is also featured. Importantly, as previously outlined, this promoter has been used safely and effectively in human RPE and forms part of an FDA and EMA-approved AAV gene replacement therapeutic (Maguire et al., 2019). There are also seven clinical trials testing AAV-CAG vectors currently registered on clinicaltrials.gov (reviewed by Buck and Wijnholds, 2020).

As the *RP2* coding sequence (CDS) is relatively short (1053 bp), it was possible to also include a 1169 bp region of the 3'UTR to encourage more natural post-transcriptional regulation of the transgene. The endogenous *RP2* poly(A) signal (240 bp) was also combined with a well-characterised minimal poly(A) sequence to ensure efficacious termination of transcription (Levitt et al., 1989).

High titre AAV-CAG-RP2 virus was produced and used to transduce patient and control derived fibroblast cell models (for associated methods and titers see sections 2.5.9 and 2.5.10). Attempts were made to detect RP2 protein in untreated and transduced fibroblast cells by ICC with multiple different antibodies (Proteintech: 14151-1-AP, Sigma Aldrich: HPA000234, and a custom made antibody gifted by the Hardcastle/Cheetham groups (Chapple et al., 2000)). However, in my hands, these antibodies did not emit a clear signal for endogenous or AAV-overexpressed RP2 in fibroblasts (data not shown). Given the above, an AAV-CAG-EGFP reporter vector was generated for use in assessing AAV transduction efficiencies (Fig. 2.9).

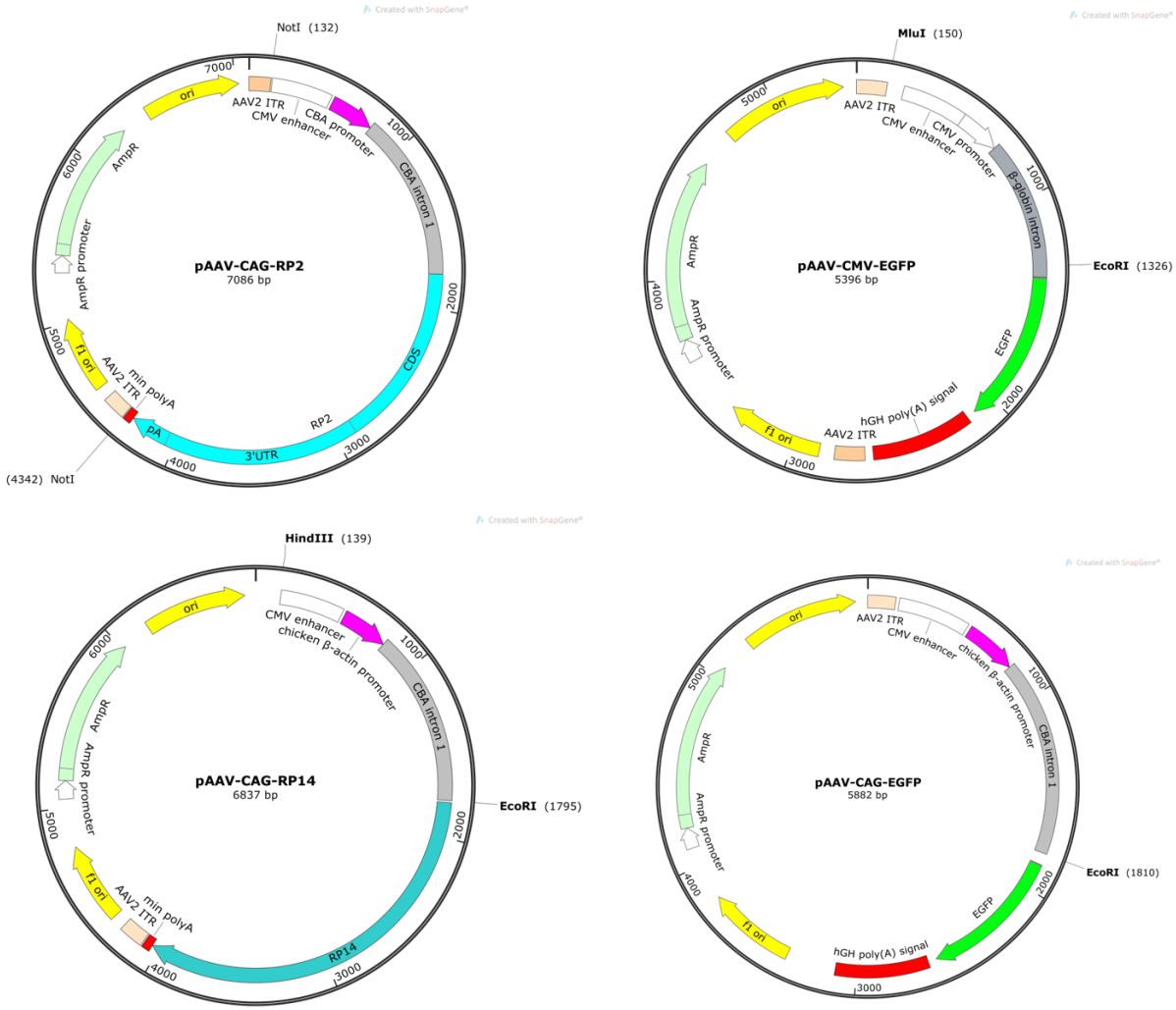

Fig. 2.9. RP2 and EGFP vector design and construction.

A CAG-RP2 fragment was synthesised and cloned into pAAV-MCS using flanking NotI sites. The CAG promoter is made up of the CMV IE enhancer (white), CBA promoter (pink) and CBA intron 1 (grey). The human *RP2* sequence is shown in blue, comprised of the CDS, a 1.2 kb section of the RP2 3'UTR and the endogenous RP2 poly(A) signal. An additional minimal rabbit β-globin poly(A) sequence was attached (red).

To make a matching CAG-EGFP vector, the CMV promoter from pAAV-CMV-EGFP (Palfi et al., 2010) and replaced with the CAG sequence from pAAV-CAG-RP14 (Palfi et al., 2020b). A 'half-blunted, half-sticky' strategy was used; pCMV-EGFP and pCAG-RP14 were cut with MluI and HindIII, respectively, then blunted with Klenow fragment. Both plasmids were then cut with EcoRI and the desired fragments were ligated together.

The CAG-EGFP expression cassette was packaged into three different AAV serotypes commonly used to transduce retinal cells: 2/2, 2/5 and 2/8 (for titers, see section 2.5.10). AAV tropism was then examined in primary dermal fibroblasts, which were transduced using a multiplicity of infection (MOI) of 1E5 vg per cell (see section 2.5.10 for protocol). Three days after AAV transduction, native EGFP fluorescence was quite weak (as evaluated by fluorescence microscopy) and so reporter signal was boosted by probing with an anti-GFP antibody. AAV2/2 significantly outperformed 2/5 and 2/8 vectors, transducing an average of 55.5 ± 1.8% of cells analysed at a MOI of 1E5 vg/cell ($p < 0.05$; n = 2 experiments, 2 wells per experiment) (Fig. 2.10.A and B).

AAV2/2-CAG-EGFP was clearly the more efficient choice of serotype for use in primary fibroblasts. This vector was then tested at a range of lower doses to determine whether a more dilute working dosage of AAV2/2 was feasible. Both control and patient-derived fibroblasts were tested in this experiment and were found to be transduced similarly (Fig. 2.10.C). Results from the two cell types were hence averaged for further analysis. The dose response data resembled a sigmoidal curve – transduction efficiency rose steeply between doses 1E2 to 1E4, then appeared to plateau at 1E5 (Fig. 2.10.D). Based on this result, future working doses between 1E4 to 1E5 vg/cell seemed optimal - transducing 50.8 ± 8.8% and 55.8 ± 2.5% of cells, respectively. The transduction efficiency obtained at 1E5 vg/cell was considerably higher than that of other reports using AAV2/2-CMV-GFP at similar doses (19-34% efficiency) (Vasireddy et al., 2013, Ellis et al., 2013). This may be due differences in AAV production methodologies and AAV batches, the different promoter used and/or the fact that other studies may not have boosted GFP fluorescence using ICC.

Transduction of R120X-A fibroblasts with AAV2/2-CAG-RP2 (1E5 vg/cell) for three days restored RP2 expression. RP2 RNA was overexpressed by 3.7 fold in AAV-treated cells relative to wild-type control samples (n = 2 wells) (Fig. 2.11.A). At the protein level, AAV-mediated RP2 expression exceeded the normal endogenous level by 1.5 fold when assessed by immunoblotting (n = 2 wells) (Fig. 2.11.B and C). Of course, considering the mean observed transduction efficiency is 56% at the dose used, it is likely that RP2 overexpression levels are, in fact, approximately double these estimates in cells that were actually transduced. These experiments served to confirm the functionality of the AAV2/2-CAG-RP2 vector. However, the estimated levels of overexpression are

preliminary, as the sample groups consisted of two wells from the same plate; independent replicate experiments would need to be performed to obtain an accurate estimate.

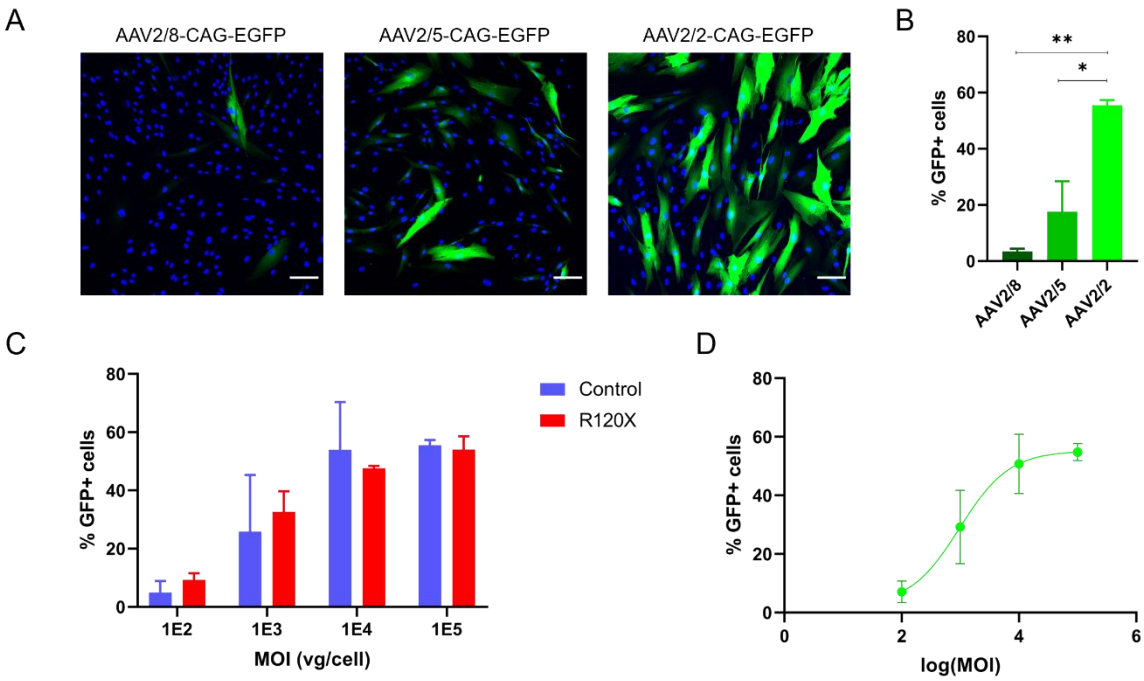

Fig. 2.10. AAV transduction of primary dermal fibroblasts.

(A) The CAG-EGFP expression cassette was packaged in AAV2/2, 2/5 and 2/8 to evaluate the transduction profile of each serotype for primary fibroblasts. Three days post transduction, cells were evaluated for EGFP immunofluorescence and counterstained with DAPI. C5 control cells were used in this test. Scale bar = 100µm.

(B) Transduction efficiency was expressed as the percentage of EGFP-positive cells. AAV2/2-CAG-EGFP transduced an average of 55.5% of cells and was significantly more efficient than 2/5 or 2/8 vectors ($p = 0.0195$ and 0.008, respectively; n = 2 experiments (2 wells per experiment). MOI: 1E5 vg/cell. A one-way ANOVA was performed to test for significance, followed by Tukey's multiple comparisons test. *$p < 0.05$, **$p < 0.01$.

(C) A dose curve test was carried out with AAV2/2-CAG-EGFP in order to determine an appropriate working range of viral concentration. R120X-A and C5 control fibroblasts displayed similar levels of transduction.

(D) Control and R120X cell transduction efficiencies were averaged and plotted against log transformed AAV concentration. The data followed a sigmoidal shape. The curve shown was fitted using non-linear regression, with a 'log (agonist) vs. response – variable slope (four parameters)' model (GraphPad Prism, v.8.4) ($r^2 = 0.8723$).

Values shown are means ± SD. n = 2 experiments, with two wells (an average of 1199 cells) analysed per experimental group.

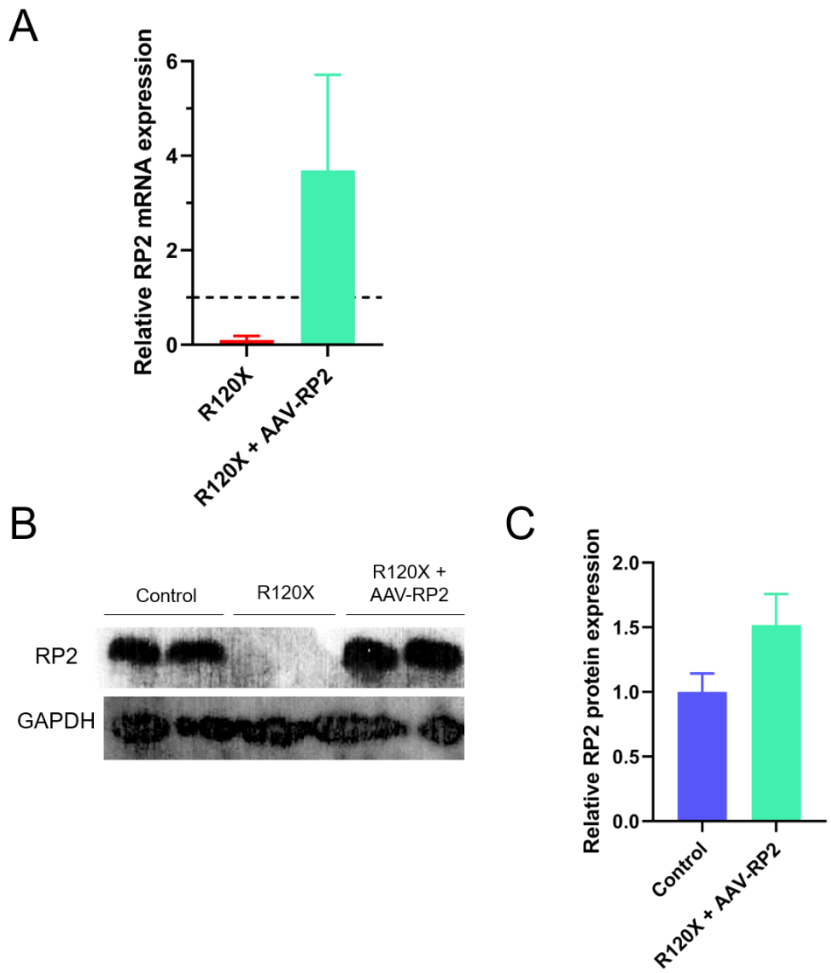

Fig. 2.11. AAV-mediated gene replacement in *RP2* null fibroblasts.

R120X-A fibroblasts were transduced with AAV2/2-CAG-RP2 for three days at a MOI of 1E5 vg/cell and RP2 expression was subsequently assessed via RT-PCR (A) and Western blot (B and C).

(A) RP2 mRNA was found to be expressed at a level approximately 3.69 fold that of control fibroblasts (C1 and C2 cells; indicated by dashed line). Values shown are means ± SD, n = 2 wells.

(B) RP2 protein expression was restored in AAV-transduced patient fibroblasts, as assessed by Western blot.

(C) The level of RP2 protein expression shown in (B) was quantified using densitometry (ImageJ). Transgenic RP2 protein was overexpressed by approximately 1.5 fold in transduced R120X-A cells, relative to C5 control cells (R120X-A + AAV: 1.5 ± 0.2; control: 1.0 ± 0.1). Values shown are means ± SD, n = 2 wells. Note: this is a rough estimation of RP2 overexpression, as the GAPDH signal in some lanes unfortunately overlapped and were therefore suboptimal for performing densitometry, and a replicate experiment has not yet been performed.

2.3.4 Exploration of potential disease-associated phenotypes in *RP2* null fibroblasts

While the ability of AAV2/2-CAG-RP2 to restore RP2 expression was confirmed, it remained to be seen whether gene replacement could provide functional rescue in *RP2* null fibroblasts. Although *RP2* mutations cause a non-syndromic retinal degeneration, there is precedent to speculate that fibroblasts lacking this normally ubiquitous protein might exhibit subtle, sub-pathological phenotypes. Schwarz et al. (2015) observed several such phenotypes in R120X-B fibroblasts, including reduced Golgi cohesion, dispersal of intraflagellar trafficking protein and altered transport of transfected Gβ1 transducin subunit protein. These phenotypes were reversed through plasmid-mediated RP2 expression or treatment with translational read-through drugs. Unfortunately, as previously mentioned, R120X-B cells were unsuitable for repeat morphological tests during the current study.

Golgi apparatus cohesion was assessed in R120X-A, N142fs and control fibroblasts by quantifying the cellular area positive for GM130, a cis-Golgi marker (Fig. 2.12.A and B). In this immunocytochemistry test, a significant increase in GM130 area is suggestive of Golgi fragmentation (Evans et al., 2010, Schwarz et al., 2015). R120X-A Golgi were indeed enlarged compared to those in cells from all control donors. A fold change of roughly 1.4 had previously been noted in the GM130-stained area of R120X-B fibroblasts compared to BJ control cells (Schwarz et al., 2015). Relative to the same (though a later passage) BJ cells, GM130 regions in R120X-A cells were 1.76 fold larger (57.00 ± 8.95 µm vs 101.87 ± 19.05 µm; $p < 0.0001$, n = 9-15 images analysed).

The fact that R120X fibroblasts derived from two different individuals performed similarly in this test was encouraging. GM130-stained areas in R120X-A cells were additionally significantly larger than all other control fibroblasts ($p < 0.05$; n = 6-15 images analysed). However, this effect was not replicated with the N142fs cell model, in which GM130-positive area was actually smaller than cells from three control donors. Given these data, it would seem that the enlarged Golgi morphology witnessed in R120X cells was unlikely due to lack of RP2 protein.

Another concern was that, from even cursory observation, it was obvious that fibroblasts from different donors varied in terms of growth profiles. This difference was especially pronounced when comparing BJ to other fibroblasts at confluent states; BJ fibroblasts were packed much more tightly.

In general, more tightly packed fibroblast monolayers, with a higher cellular density, displayed a more compact cell morphology with less total cellular area. Unfortunately, the overlapping conformation of fibroblasts at higher density makes accurate quantification of cellular area difficult, so cell densities of confluent cultures were compared instead. It became clear that cultures derived from different donors behaved differently in this respect (Fig. 2.12.C). In particular, BJ fibroblast monolayers were significantly denser than all other cells apart from C3. Strikingly, a significant inverse correlation was evident between cell density of fibroblast cultures and mean cis-Golgi area ($r_s = -0.7554$; $p < 0.0001$) (Fig. 2.12.D). The possibility that altered cell density was a primary defect in R120X fibroblasts was considered, as impaired ciliary function could conceivably affect cell migration. Indeed, impaired migration and wound healing has been noted in *RP2* null immortalised RPE cells (Lyraki et al., 2018). However, R120X-A and N142fs cell densities were not significantly lower compared to the majority of controls tested.

Fibroblast culture growth profiles may be influenced by a variety of factors – donor age, health and genetic background, cell passage number, culture conditions and length/conditions of cell stock storage. Biopsy processing protocols may also differ slightly between labs. Primary cells, of course, have finite life spans and grow senescent as they reach the Hayflick limit (40-60 population doublings (PD)). Approaching senescence, fibroblast cultures change from tightly-packed, spindle-shaped cells to slow growing, broad cells with irregular shaped edges that cannot form dense monolayers. Cell characteristics may also change over time as populations are subject to selection pressure in artificial culture conditions. For the experiments described, cells were generally used below passage 10 (P10) (approximately 15 PD). This was feasible for all cultures except BJ and C5, which were used at approximately P15.

In summary, GM130 area and fibroblast monolayer density appear to be interdependent, and it seems likely that Golgi apparatus size is influenced by monolayer density/cellular spread rather than vice versa. Considering the conflicting GM130 area results obtained in R120X-A and N142fs cells and the apparent dependence of cis-Golgi morphology on monolayer density, a relatively variable characteristic in primary cell cultures, this phenotype did not appear to be robust and was therefore not prioritised for further study during this thesis project. However, it should be noted that the results presented are

from a single experimental run; it would be worthwhile to perform independent replicate experiments in the future to enable a confident conclusion to be drawn with regard to this phenotype.

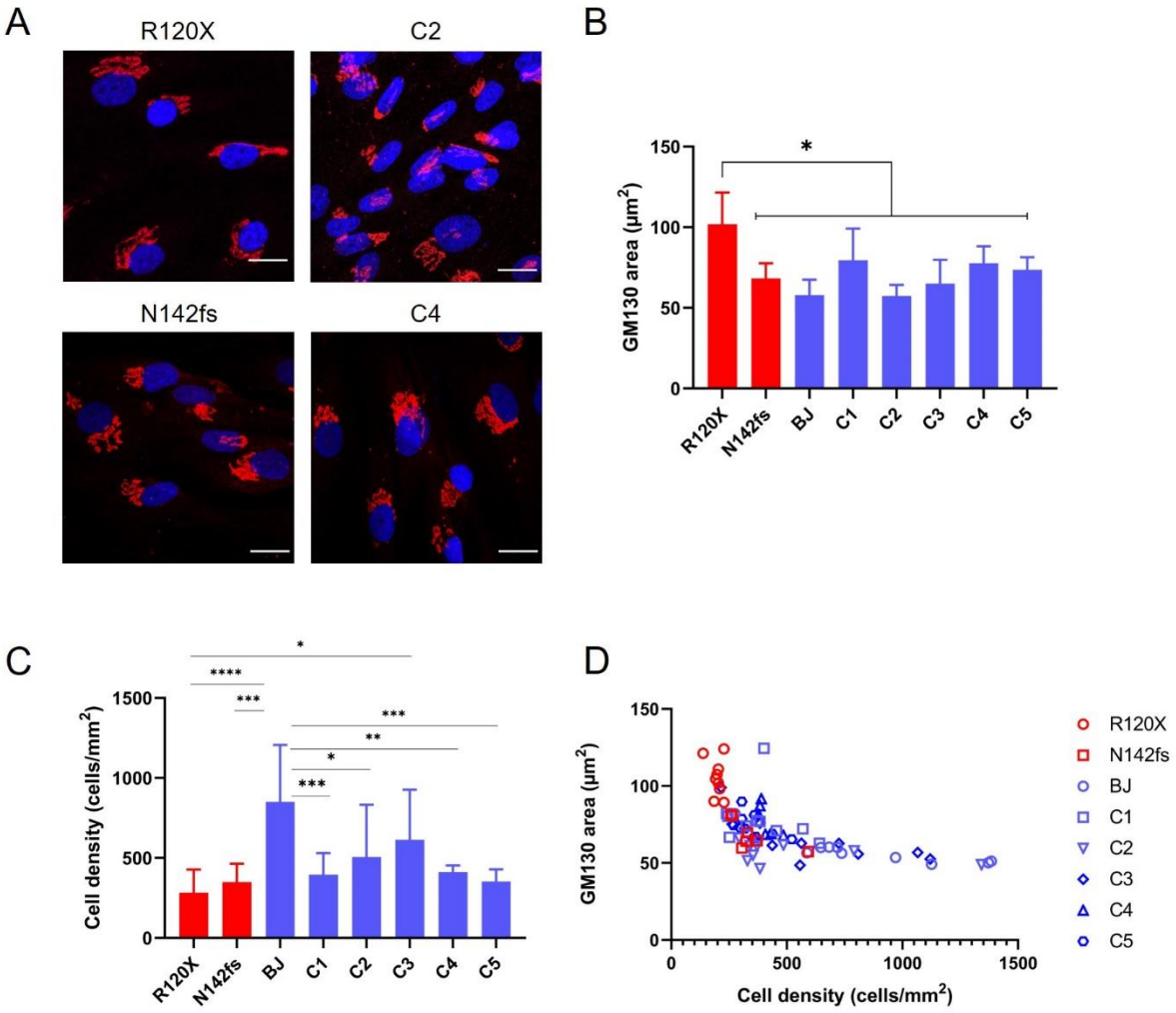

Fig. 2.12. GM130 area and cell density of patient and control fibroblasts.

(A) Representative high magnification ICC images of GM130 localisation (red). This cis-Golgi marker was used to examine Golgi cohesion. Cells were counterstained with DAPI. Scale bar = 20µm. Note: The R120X and C2 cells displayed were imaged using different acquisition settings than those for N142fs and C4 cells.

Fig. 2.12. GM130 area and cell density of patient and control fibroblasts (continued).
(B) GM130 area was quantified using the Fiji auto-threshold tool. R120X-A cells displayed significantly larger GM130-positive regions than all other cells examined. Notably, N142fs mutant fibroblasts did not exhibit an increase in GM130 area compared to controls. Values shown are means ± SD. Statistical significance was determined using a one-way ANOVA and Tukey's post hoc test. The p values for each cell line comparison, from left to right on the graph, were $p < 0.0001$, $p < 0.0001$, $p = 0.031$, $p < 0.0001$, $p < 0.0001$, $p = 0.0159$ and $p < 0.0002$. Measurements were carried out on confocal images obtained with a 20X objective. The number of cells per image ranged from 28 to 231, with an average of 72. Total GM130 area was measured per image and then divided by the number of cells featured to calculate the average area per cell. This was carried out on 6 to 15 images per cell type.
(C) The degree of cell density at confluency was found to vary between cells from different donors. R120X cell layers were significantly less dense than BJ and C3 cells. BJ cells were significantly more tightly packed than all other cell lines except C3 (n = 6-15 images; one-way ANOVA). *$p < 0.05$, **$p < 0.01$, ***$p < 0.001$, ****$p < 0.0001$. Values shown are means ± SD.
(D) A significant inverse correlation was evident between mean GM130 area per cell and cell density. Spearman correlation coefficient (rs) = -0.7554; $p < 0.0001$.

It was decided to explore another quantitative assay more directly related to an established aspect of RP2 function. As RP2 is known to act as a GTPase for ARL3, it was hypothesised that *RP2* null cells would have higher levels of ARL3-GTP. Hence, a means of quantifying activated ARL3 levels in fibroblasts was sought.

Initially, this was attempted with an 'Arl3 activation assay kit' (New East Biosciences, 83001), which utilises an antibody specific to GTP-bound Arl3 to pull down the activated protein. Captured ARL3-GTP is then detected by Western blot, using a non-conformation specific Arl3 antibody. Lysates loaded with GDP or GTPγS, a non-hydrolysable version of GTP, functioned as controls. This method was attempted using control and patient fibroblasts, and wild-type mouse retinal samples (Fig. 2.13). An immunoblot signal was obtained at ~23 kDa. However, if this band was Arl3 protein (predicted MW: 20 kDa), the signal was not specific to the active conformation as it was present in GDP-loaded negative controls. Alternatively, the 23 kDa band was simply background, and this technique was not sensitive enough to detect ARL3-GTP at its level of concentration in the samples tested.

The kit used was relatively expensive (~€40 per reaction) and its use was not referenced in any publications. Additionally, although the protocol outlined was for cell culture lysates, the example data provided was from tests performed on purified ARL3 protein, rather than cell lysate samples. Abcam had recently discontinued a highly similar product (ab173254) because quality tests had raised doubt as to whether it was specifically detecting activated Arl3 protein (personal communication). Given these concerns, an alternative assay was sought.

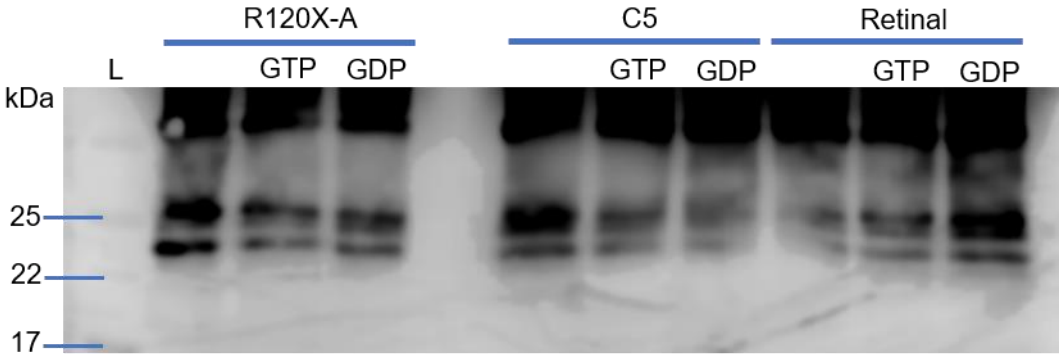

Fig. 2.13. Pull down assay with an Arl3-GTP specific antibody.

The Arl3 activation assay kit was tested on R120X-A and C5 fibroblasts, and wild-type mouse retinal samples. Lysates were incubated with a monoclonal antibody specific to the activated conformation of Arl3, which was then immunoprecipitated on protein A/G agarose beads. Pulled down samples were then immunoblotted with a polyclonal Arl3 antibody. Negative and positive control samples were loaded with GDP or GTPγS before immunoprecipitation. For each of the three sample groups in the blot shown, lysates were loaded followed by GTP and GDP-treated controls. A protein ladder (L) is also faintly visible.

A band of ~23 kDa was present in all samples, including GDP-loaded negative controls. If the band observed was Arl3 protein (predicted MW: 20 kDa), the antibody did not appear specific for activated protein conformation.

An ARL3-GTP pull down assay was described in the literature that utilised GST-tagged ARL2BP, a ciliary protein known to specifically bind to Arl3 in its active conformation, as bait (Togi et al., 2016). In this publication, endogenous Arl3-GTP protein in HEK 293 lysates was bound to ARL2BP-GST and captured on glutathione Sepharose beads, then detected by immunoblotting with an Arl3 antibody.

It was decided to attempt this assay with primary fibroblast lysates, testing both ARL2BP-GST and RP2-GST as bait protein. In preparation for the experiment, plasmids expressing

these recombinant proteins were acquired or synthesised, along with an empty (GST-only) negative control plasmid (Fig. 2.13.A). IPTG-induced production of recombinant protein from pGST and pRP2-GST in *E. coli* cultures was verified – proteins were captured on glutathione Sepharose beads, eluted and analysed by SDS-PAGE (Fig. 2.13.B).

Cloning of pARL2BP was not yet completed at the time of this experiment. However, a commercial sample of purified ARL2BP-GST protein was available (LS Bio, LS-G22232-20) and included for comparison. A band was evident around the predicted molecular weight of ARL2BP-GST (46 kDa). However, there were two additional bands of approximately 25 kDa present at higher concentrations than the desired protein - likely truncated GST proteins. The cloned pARL2BP-GST plasmid will be tested in future with the hope of producing more pure solutions.

Unfortunately, this pulldown strategy had not been tested on fibroblast lysates at the time of writing this thesis due to time constraints and the closure of the Genetics TCD labs for approx. 4 months during 2020 due to Covid-19. It should be noted that Togi et al. (2016) used leukaemia inhibitory factor (LIF) to stimulate activation of Arl3 in HEK 293 cells before lysis and immunoprecipitation. It is very possible that the endogenous level of ARL3-GTP present in control or even *RP2* null fibroblasts may be below the detection threshold of this assay. In fact, Little et al. (2019) recently found that they could not detect endogenous ARL3-GTP in wild-type and $Rp2h^{\Delta 23/Y}$ tissue using a similar pull down assay that was validated using $Arl3^{Q71L}$ mouse samples. Due to the milder phenotype observed in *Rp2h* null mice, it has been hypothesised that mice may have additional GAPs that can partially compensate for RP2 loss (Zhang et al., 2015a). There is therefore a small chance that ARL3-GTP levels may be more easily quantified in patient-derived fibroblasts. However, a large amount of starting material will likely be required per sample, if this test is to be successful. LIF-stimulated cultures will be used as positive controls to confirm functionality of the protocol. Purified Arl3 protein loaded with GTγS and GDP would be desirable additional controls.

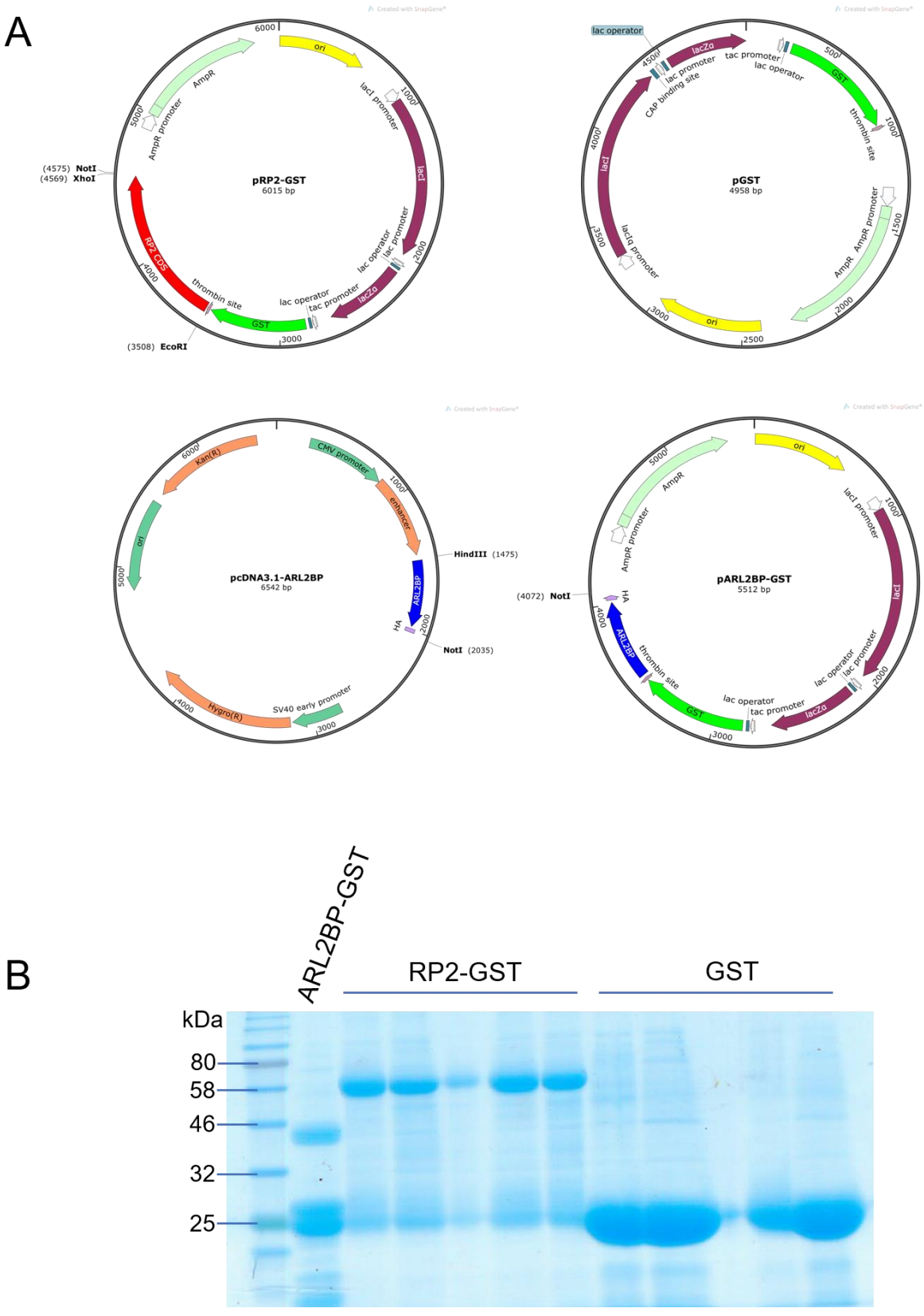

Fig. 2.13. Preparation of GST-tagged RP2 and ARL2BP.

Fig. 2.13. Preparation of GST-tagged RP2 and ARL2BP (continued).

(A) A plasmid expressing GST-tagged RP2 (pRP2-GST) was acquired commercially. (Addgene plasmid # 86072). The RP2 sequence was excised using XhoI and EcoRI sites, which were blunted to allow circularisation of the backbone - generating pGST, a negative control plasmid.

To create an ARL2BP-GST expressing vector, the ARL2BP coding sequence was isolated from pcDNA3.1-ARL2BP (Sino Biological, HG14357-CY) via HindIII and NotI sites. This fragment was used to replace the RP2 CDS in pRP2-GST, which was released by NotI and EcoRI digestion. HindIII and EcoRI cut sites were blunted before ligation of fragments to form pARL2BP-GST.

(B) IPTG-induced expression of GST (26 kDa) and RP2-GST (67 kDa) in *E. coli* cultures was verified. Recombinant proteins were precipitated on glutathione Sepharose beads and SDS-PAGE was performed on eluates. RP2-GST was observed at a slightly lower position than expected. However, my experience, endogenous RP2 has also migrates slightly faster than predicted (data not shown). Some truncated GST protein is also possibly present in RP2-GST lysates. In future, an untransfected control lysate will be included to distinguish background bacterial protein from possible truncated recombinant proteins.

A commercial sample of purified ARL2BP-GST protein was included for comparison. Although an appropriately sized band was obtained, there were two additional bands of approximately 25 kDa present at higher intensities. These were likely truncated GST fragments.

2.3.5 *RP2* null retinal organoid models exhibit a rod degeneration phenotype

While the ubiquitous nature of RP2 expression makes it possible to explore its function using non-retinal cells such as fibroblasts, it would of course be preferable to examine the consequences of RP-associated mutations in a photoreceptor-containing model. As discussed previously, transgenic mouse models published to date do not satisfactorily recapitulate the progression of *RP2*-XLRP in humans. Advances in stem cell technology provided the opportunity to study the pathology of RP2 in an artificial human retinal context - modelling the disease with 3D retinal organoids (ROs).

R120X-A, R120X-B and BJ control fibroblasts were reprogrammed into induced pluripotent cells (iPSC) by nucleofection of plasmids expressing the Yamanaka factors (Okita et al., 2011), as previously described by Schwarz et al. (2015). As outlined in the previous section, experiments with fibroblast models had highlighted the potential for inter-donor variation when working with patient-derived models. Importantly, an additional *RP2* null isogenic model was generated for this RO study. BJ fibroblasts were simultaneously made pluripotent and gene-edited as previously described (Howden et al., 2015). A CRISPR/Cas9 guide RNA targeting RP2 exon 2 was used to induce an 8bp deletion (c.371_378delAAGCTGGA; p.Lys124SerfsTer11), generating RP2 knock-out (RP2 KO) iPSCs (Fig. 2.14.A). Absence of RP2 protein in these cells was confirmed (Fig. 2.14.B) and iPSCs were differentiated into retinal organoids using established protocols (Nakano et al., 2012, Zhong et al., 2014).

By day 180 (D180) of RO differentiation, a laminated neuroretinal structure was visible, with a 'brush border' of rudimentary photoreceptor outer segments (Fig. 2.14.C). Cells in the ONL were immunoreactive for photoreceptor markers: recoverin (rods and cones) and cone arrestin (cones) (Fig. 2.14.D). Immunocytochemistry also confirmed the presence of important photoreceptor structural landmarks in all ROs: TOM-20-reactive mitochondria-rich inner segments, and polyglutamylated tubulin (GT335)-positive connecting cilia (CC) above an F-actin stained outer limiting membrane (OLM) (Fig. 4.14.D). Outer segment development could be inferred from bulging upper CC present from D150 (visualised with ciliary markers Arl13b and GT335) (Lane et al., 2020; Fig S1.C[19]). Electron microscopy revealed the presence of disorganised discs in these ciliary

[19] A copy of Lane et al. 2020 is included in Appendix 1.

protrusions by D180 – further evidence of early photoreceptor outer segment formation (Fig. 2.14.F).

RP2 protein was detected in control RO ONL and INL cells by ICC, displaying characteristic plasma membrane localisation, and absent in *RP2* null ROs (Fig. 2.14.D). When assessed by RT-qPCR, RP2 mRNA expression in mutant ROs was reduced by approximately 70-90% relative to BJ control ROs (n = 3 independent organoids) (Fig. 2.14.E) - a similar depletion to that observed in R120X-A patient-derived fibroblasts relative to BJ fibroblasts (84%).

ONL thickness was measured in ROs from D120-180 to check for potential photoreceptor loss in *RP2* null ROs. At D180, all three *RP2* null organoid models displayed significantly thinner ONLs than control organoids ($p \leq 0.01$; n = 3-10 organoids) (Fig. 2.15.A and B), suggesting an elevated level of photoreceptor cell death during development. A significant rise in TUNEL reactivity in the ONL at D150 indicated a peak of apoptosis at this timepoint ($p \leq 0.05$; n = 5) (Fig. 2.15.C and D). To probe this degenerative phenotype further, RNA-seq was performed on D150 RP2-KO, R120X-A and control ROs. This revealed significant upregulation of genes in the p53 signalling pathway in *RP2* mutant samples, including pro-apoptotic genes such as p53, p21, BAX and PUMA (Lane et al., 2020) - further evidence that loss of RP2 led to heightened cell death in retinal organoids.

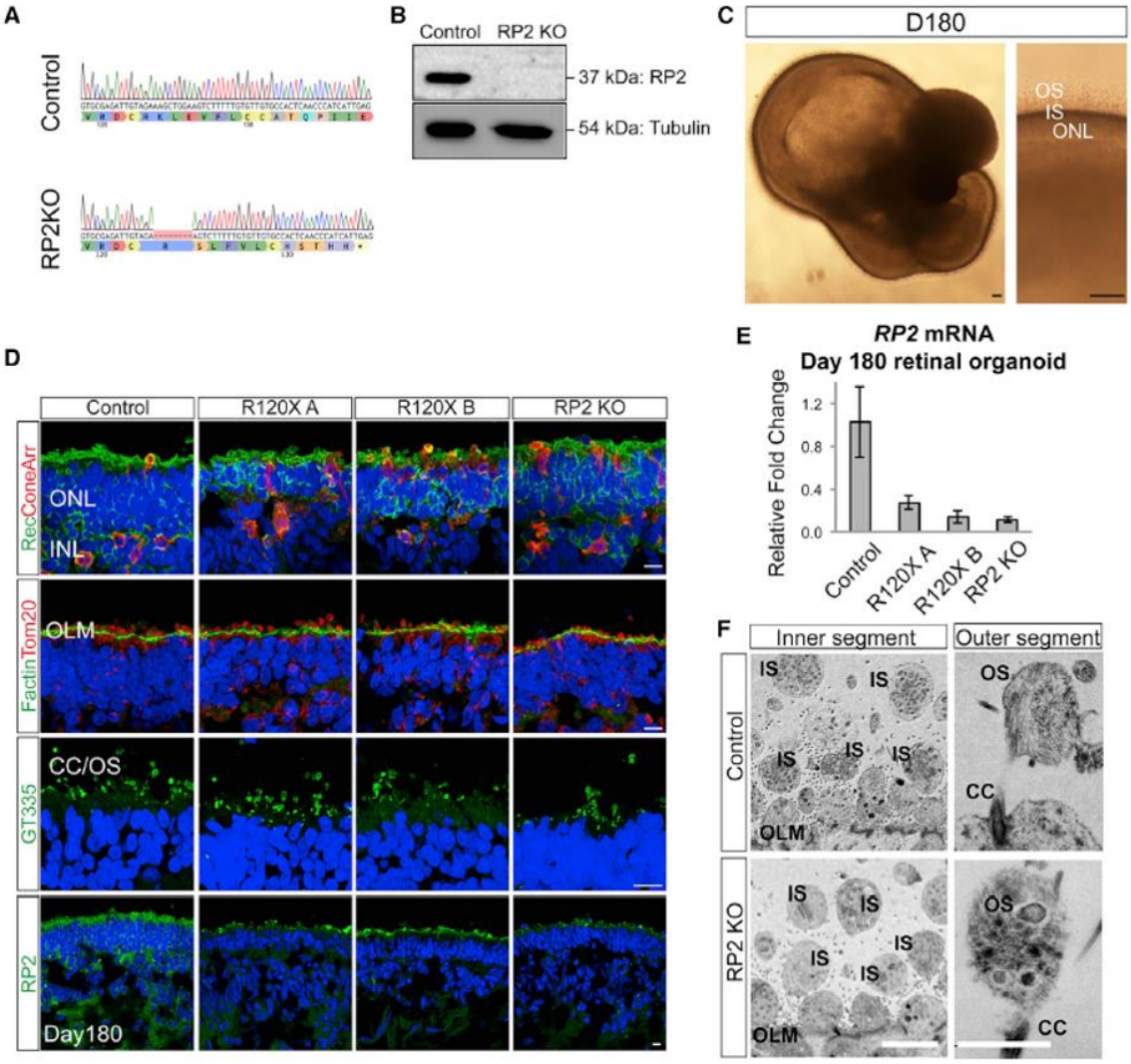

Figure 2.14. Retinal Organoids from R120X, RP2 KO, and Isogenic Control iPSCs.

Figure 2.14. Retinal Organoids from R120X, RP2 KO, and Isogenic Control iPSCs (continued).
(A) Sanger sequence trace of edited RP2 KO iPSCs. CRISPR/Cas9 gene editing was used to create an 8-bp deletion in exon 2 of RP2 by NHEJ.
(B) Western blot and immunocytochemistry (ICC) of control and RP2 KO iPSC. Scale bar = 50 μm.
(C) Retinal organoid morphology at D180, a layer of IS/OS is visible by differential interference contrast above the transparent ONL. Scale bar = 50 μm.
(D) ICC of retinal organoids at D180. Photoreceptors (recoverin and cone arrestin [coneArr]), outer limiting membrane (OLM, F actin), mitochondria (Tom20), and connecting cilia/OS (GT335) expression in the ONL of control and *RP2* null iPSC retinal organoids. RP2 is expressed at the plasma membrane of cells in the ONL and inner nuclear layer (INL) in control organoids and is absent in *RP2* null ROs. Note: there is some background signal in the outermost regions of RP2 *null* ROs stained for RP2. Scale bar = 10 μm.
(E) qPCR of RP2 mRNA in whole retinal organoids at D180 (n = 3 independent organoids). Mean ± standard error of the mean (SEM).
(F) Electron micrographs of control and RP2 KO retinal organoid photoreceptors at D180. Scale bars = 5 μm (left), 1 μm (right). OS: outer segment, IS: inner segment, CC: connecting cilia, OLM: outerlimiting membrane.
Figure and legend adapted from Lane et al. (2020).

The period of cell death observed in *RP2* null ROs (D150 to 180) correlated with a notable increase of rhodopsin and rod transducin (GNAT1) mRNA expression in control organoids. This rise in rod marker expression was less pronounced in *RP2* KO ROs (Fig. 2.16.B). A significant reduction in the number of photoreceptors immunoreactive for rhodopsin was also observed in mutant ROs at D180 (Fig. 2.16. A and C).

In contrast to the depletion of rod cell markers, cone numbers did not appear decreased in *RP2* null ROs. In fact, these models displayed significantly elevated proportions of cone-arrestin positive photoreceptors in the remaining ONL at D180 relative to controls ($p<0.01$; $n = 3$-10) (Lane et al., 2020; Fig. S4.A). Reduction in ONL thickness in organoids lacking RP2 could therefore be attributed to specific degeneration of developing rod photoreceptors. In order to confirm that rod development was not simply delayed, *RP2* KO organoids were cultured until D300, at which point they still exhibited notably fewer rod cells (Fig. 2.16.E).

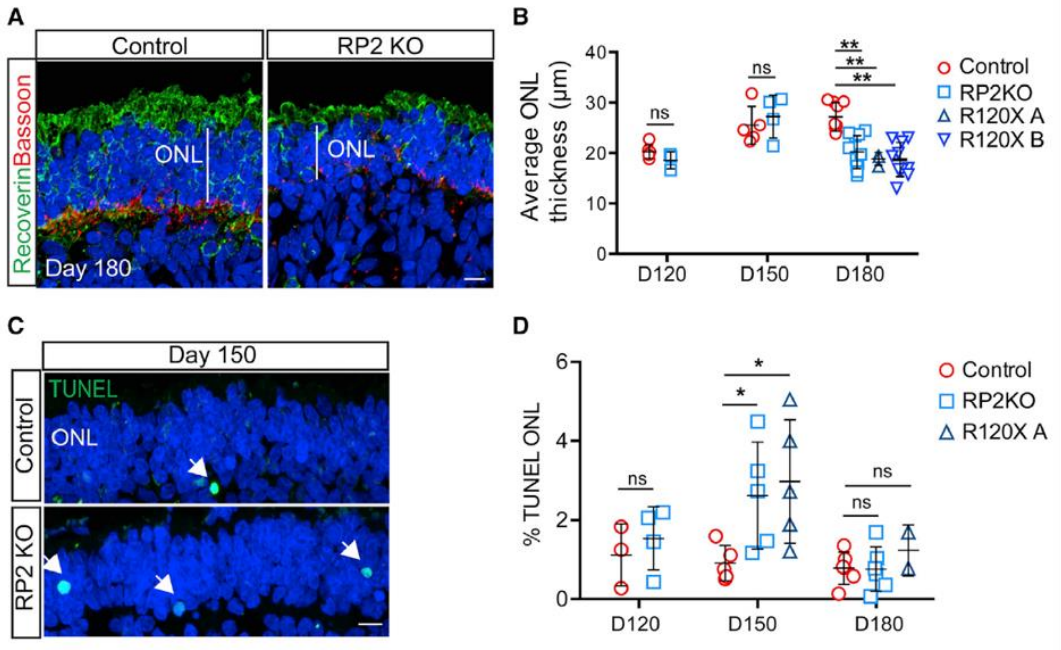

Fig. 2.15. Photoreceptor Cell Death in RP2 KO Organoids.

(A) ICC of control and RP2 KO retinal organoids showing reduced ONL thickness in RP2 KO. Recoverin staining demarcates the ONL terminating in the synaptic layer stained with Bassoon. Scale bar = 10 µm.

(B) Mean ONL thickness per organoid was measured from tilescans of cryosections of a whole organoid at D120, D150 (n = 5 control; n = 4 RP2 KO at both time points), and D180. Significant ONL thinning was recorded at D180 in RP2 KO (n = 9 independent organoids) and R120X lines (n = 3 R120X A organoids, n = 9 R120X B organoids), but not in controls (n = 10 independent organoids; $p \leq 0.01$; mean ± SD).

(C) TUNEL reactive nuclei (arrows) in the ONL of RP2 KO and isogenic control organoids at D150. Scale bar, 10 µm.

(D) Quantification of TUNEL reactivity. RP2 KO organoids had a significantly higher proportion of TUNEL-positive cells at D150 (n = 5 independent organoids $p \leq 0.05$, mean ± SD) but not at D120 (n = 3 control; n = 4 RP2 KO) or D180 (n = 5 control; n = 6 RP2 KO). R120X organoids also had increased TUNEL reactivity at D150 (n = 5 at D150 n = 2 at D180 independent organoids).

Figure and legend reproduced from Lane et al. (2020).

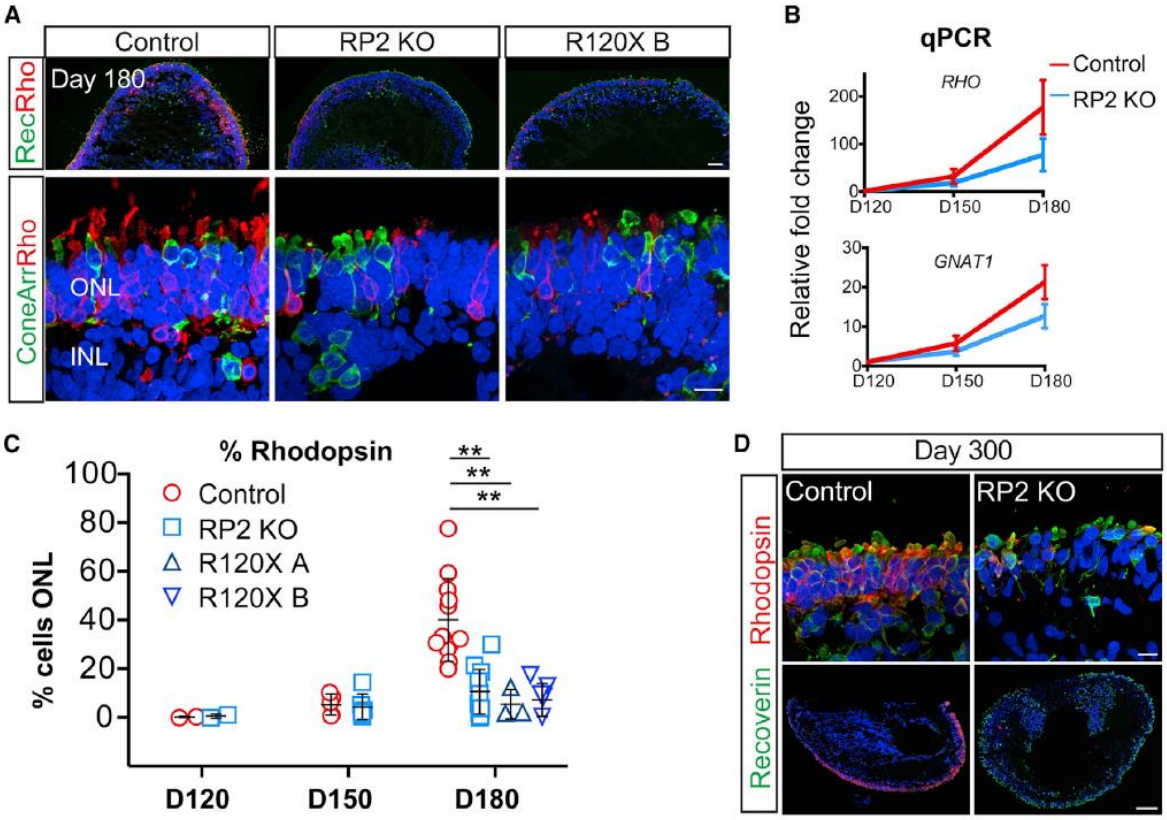

Fig. 2.16. Reduced Number of Rod Cells in RP2 KO and R120X Patient Retinal Organoids

(A) ICC of retinal organoids. Low (upper panel) and high (lower panel) power magnification of recoverin, rhodopsin, and cone arrestin immunoreactivity in the ONL at D180 in control, RP2 KO, and R120X RP2 retinal organoids. Scale bars = 50 µm and 10 µm.

(B) RHO and GNAT1 levels in retinal organoids. qPCR showing relative fold change in mRNA in control and RP2 KO retinal organoids at D120, D150, and D180 (n = 3, 3, 4 independent organoids). Mean ± SEM.

(C) Quantification of rhodopsin-positive cells as a percentage of ONL in control, RP2 KO and R120X patient cell lines from D120 to D180 of differentiation. Each data point represents the mean of 1 independent organoid, counts are from tilescans of whole organoid cross sections (D120 n = 2 control, n = 2 RP2 KO; D150 n = 5 control, n = 6 RP2 KO; D180 n = 12 control, n = 11 RP2 KO, n = 3 R120X A, n = 5 R120X B; **p ≤ 0.01; mean ± SD).

(D) High and low magnification of control and RP2 KO organoids at D300 of differentiation stained with recoverin and rhodopsin. Scale bars = 10 µm (upper panel) and 100 µm (lower panel).

Figure and legend reproduced from Lane et al. (2020).

2.3.6 AAV-RP2 treatment prevents rod degeneration in *RP2* KO retinal organoids

It was sought to rescue the degenerative phenotype witnessed in *RP2* null retinal organoids using AAV-mediated gene replacement. As mentioned previously, three AAV serotypes commonly used in retinal experiments were available in our lab: AAV2/2, 2/5 and 2/8.

AAV2/5 and 2/8 serotypes have been established to outperform 2/2 in murine photoreceptors by our lab (unpublished data) and others (Lebherz et al., 2008). AAV2/8 transduces photoreceptors more efficiently in adult murine (Allocca et al., 2007) (Natkunarajah et al., 2008) and porcine retinas (Mussolino et al., 2011), while AAV2/5 is more efficient than AAV2/8 in neonatal murine photoreceptors (Watanabe et al., 2013). While (to my knowledge) AAV2/5 and 2/8 vectors have not been directly compared in non-human primates (NHPs), both serotypes have proven capable of transducing photoreceptors in this context (Boye et al., 2012, Vandenberghe et al., 2013). AAV2/5, however, performed significantly better than 2/8 in the photoreceptors of human retinal explants (Wiley et al., 2018).

Attempts were made to transduce retinal organoids with both AAV2/5 and AAV2/8 vectors generated for this study. At the commencement of this project, there were no published reports of hPCS-derived retinal organoid transduction with AAV. One transduction study carried out with mouse ESC-derived organoids had utilised 1E10 vg AAV2/8YF-Rho-GFP per organoid (Santos-Ferreira et al., 2016).

Using our AAV2/5 and AAV2/8-EGFP vectors, the Cheetham group determined that a dosage of 1E11 vg per hiPSC-derived RO was more efficient than 1E10 vg (data not shown). Relatively large doses of virus seem to be required to achieve effective transduction in these cultures - likely due, at least in part, to the dilution of AAV in the media. For comparison, 1E11 vg per RO is approximately one hundred times more AAV2/5 than would typically be used in murine intraocular injections by the Farrar lab. Testing AAV treatments at concentrations higher than 1E11 vg per RO was impractical due to AAV production constraints. The number of experimental repeats feasible was also limited.

RP2 KO organoids were treated with AAV2/5-CAG-RP2 (1E11 vg) from D140 to D180. The timeframe for transduction was chosen as a balance between the temporal constraints of

photoreceptor maturation and degeneration. ROs would need to be treated before the onset of rod death to maximise potential benefit. On the other hand, it was important to allow RO photoreceptors to mature for as long as possible before transduction. Recent data from (Gonzalez-Cordero et al., 2018) had demonstrated that RO rods could be transduced at week 17 (~D119) but not at week 13 (D91). The difference was proposed to depend on development of outer segments, initiated during week 16 of differentiation. The presence of outer segments thus appears to be especially important for mediating AAV entry in rods (Petit et al., 2017). At D140, *RP2* KO organoids were confirmed to have brush borders comprised of inner and outer segments.

RP2 immunoreactivity was assessed in treated *RP2* KO organoid cryosections to estimate AAV transduction efficacy (Fig. 2.17.A-D). 90 ± 7% of ONL cells expressed the transgene – an unprecedented level of AAV transduction efficiency in retinal organoids (see Discussion (2.4.2)). Both rod and cone photoreceptors showed uptake of the virus (Fig. 2.17.F). In contrast, only 3± 0.4% % of inner retinal cells were RP2-positive (n = 3).

The AAV transgene expression pattern seen in ROs resembled expression profiles observed after subretinal AAV injection in mice, where transgene expression in the neuroretina, for the most part, does not extend beyond the photoreceptor layer, (for an example, see Fig. 2.19.) This confinement of AAV-mediated transgene expression is proposed to be at least in part a consequence of the OLM acting as a barrier to AAV diffusion from the subretinal space (Petit et al., 2017). In ROs, the presence of an intact OLM was confirmed, as evidenced by a characteristic dense layer of actin filaments (Fig. 2.14). Although this barrier is semi-permeable, AAV diameter (25 nm) exceeds the estimated pore size (~6 nm) (Omri et al., 2010) and virions should thus be prevented from penetrating inner retinal layers. However, it is interesting to note that AAV2/5 also displayed a high degree of photoreceptor specificity relative to other serotypes when used to transduce human retinal explants (Wiley et al., 2018).

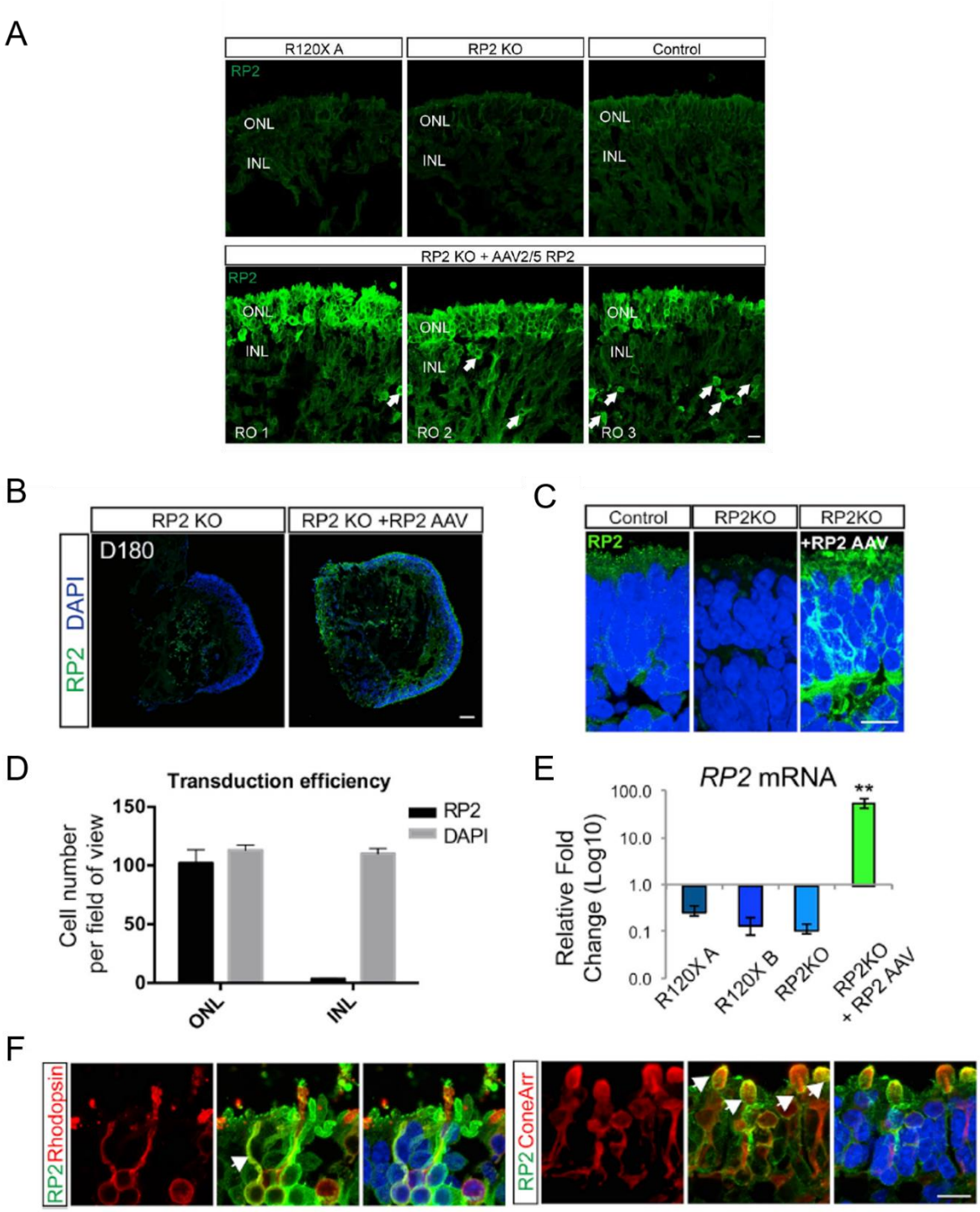

Fig. 2.17. AAV2/5-CAG-RP2 transduction of RP2 KO retinal organoids.

(A) Top row: ICC for RP2 in untreated D180 RP2 R120X A and RP2 KO and control ROs. Bottom row: RP2 immunostaining after six weeks of AAV2/5-CAG-RP2 transduction in 3 different organoids (RO1, RO2 and RO3). Transgene expression is largely confined to the ONL. The few strongly positive cells for RP2 outside of the ONL are indicated with arrows. Scale bar = 10 µm.

(B) RP2 expression in whole retinal organoid sections. Transgene expression was visible across the vast majority of the ONL in AAV-treated RP2 KO ROs. Scale bar = 50 µm.

Fig. 2.17. AAV2/5-CAG-RP2 transduction of RP2 KO retinal organoids (continued).

(C) High-power magnification of RP2 immunoreactivity in photoreceptors. Scale bar = 10 µm.

(D) Cells with RP2 immunoreactivity in the ONL and INL were scored against DAPI (mean = 90% ± 7% ONL versus 3% ± 0.4% INL, n = 3 independent organoids; mean ± SD).

(E) qPCR of RP2 mRNA transcript levels in AAV-transduced RP2 KO organoids relative to endogenous expression in control organoids (n = 3 independent organoids; mean = 55-fold ±7.7 SEM).

(F) ICC co-staining RP2 with cone arrestin or rhodopsin showing AAV-driven RP2 expression in both rod and cone photoreceptors. Scale bar = 10 µm.

Figure and legend adapted from Lane et al. (2020).

RP2 mRNA expression in AAV-treated ROs was assessed by RT-qPCR and found to be 55 ± 7.7 fold higher than the endogenous level of expression in control organoids (n = 3) (Fig. 2.17.E). Mean ONL thickness was significantly increased in organoids that received AAV-RP2 ($p = 0.016$, n = 4-6) – an almost complete rescue of this phenotype (Fig. 2.18.A and B). Rhodopsin mRNA expression notably increased in organoids that received AAV-RP2 (Fig. 2.18.E). The balance between rod and cone numbers in treated ROs was also somewhat corrected; the proportion of rhodopsin-expressing photoreceptors was roughly doubled in AAV-RP2 transduced samples (n = 5-6) (Fig. 2.18.D), while the number of cone-arrestin positive cells was reduced to a level close to that of control ROs (n = 5-6) ((Lane et al., 2020); supplementary fig.5.D).

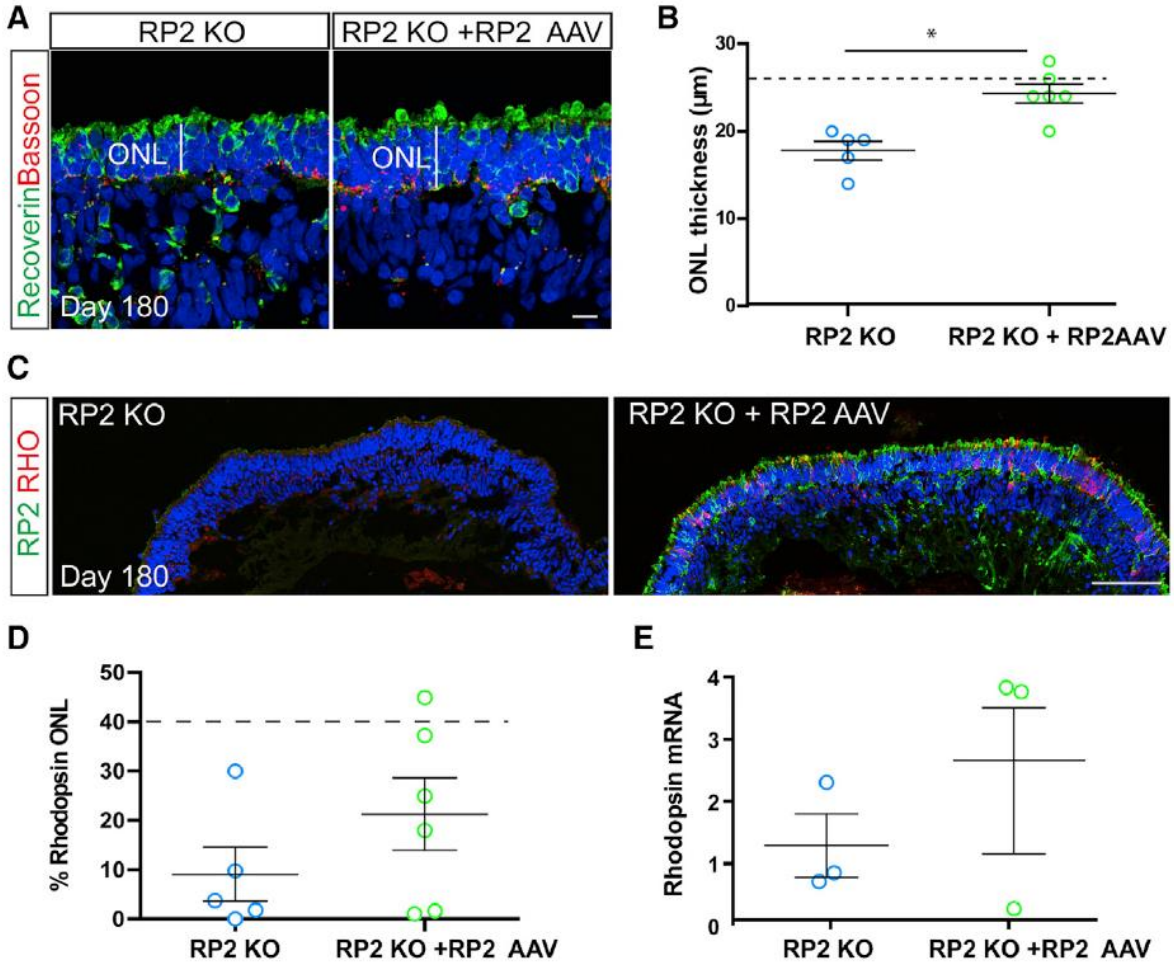

Fig. 2.18. Figure 5. AAV2/5-Driven RP2 Overexpression Rescues Photoreceptor Survival

(A) ICC of retinal organoid ONL with recoverin (green) and Bassoon (red) in RP2 KO control and AAV RP2-treated retinal organoids showing improved ONL thickness in the AAV-treated group. Scale bar = 10 µm.

(B) Quantification of ONL thickness in control and AAV transduced retinal organoids (n = 5 RP2-KO, 6 RP2 KO + AAV independent organoids, *p = 0.016, mean ± SEM). Dotted line represents mean thickness in isogenic control parent cell line.

(C) ICC showing RP2 (green) and rhodopsin (red) expression after transduction. Scale bar = 50 µm.

(D) Quantification of ICC to assess rhodopsin positive cells in control and RP2 AAV-transduced RP2 KO retinal organoids. Dotted line represents average control values (n = 5 RP2 KO, n = 6 RP2 KO + RP2 AAV independent organoids, p = 0.23; mean ± SEM).

(E) qPCR for RHO mRNA levels in control and RP2 AAV-treated RP2 KO retinal organoids (n = 3 independent organoids). Mean ± SEM.

Figure and legend reproduced from Lane et al. (2020).

2.3.7 AAV-mediated RP2 overexpression in the wild-type murine retina

While the results of AAV-CAG-RP2 treatment in retinal orgnaoid models of RP were very promising, it is important to acknowledge and address some of the limitations of the technology. For example, retinal organoids do not produce a correctly localised, continuous layer of RPE, are not vascularised and lack astrocytes (reviewed in (Capowski et al., 2019)). Importantly, it is currently not possible to simulate the complexities of retinal immune response using these *in vitro* models.

It is therefore vitally important to assess tolerance of AAV-mediated gene delivery and transgene overexpression *in vivo*. With this in mind, the AAV2/2, 2/5 and 2/8-CAG-RP2 vectors generated for the study and previously evaluated in cells and ROs were further evaluated in the murine retina. Given differing transduction profiles between cell types and between species (as observed in this study and other studies), an additional evaluation of AAV serotypes was undertaken in wild type mice. AAV-CAG-RP2 vectors were subretinally injected into wild type mice. When titre-matched at doses of 3E8 vg, AAV2/8-CAG-RP2 dramatically outperformed the other vectors – producing 8-21 fold more RP2 mRNA than the other serotypes two weeks after subretinal injection (Fig. 2.19.A).

It is important to note that the AAV dosage used in this *in vivo* serotype comparison study was relatively low for the 2/5 serotype. For example, efficient photoreceptor transduction has previously been observed two weeks after subretinal injection of 1.5E9 vg AAV2/5-CMV vectors (Palfi et al., 2012) – a dose five times higher than the one employed in this study. Interestingly, AAV2/8 appears to have a relatively rapid time course of transgene expression due to particularly fast second strand synthesis (Davidoff et al., 2005).

Having confirmed that AAV2/8 was the most efficient serotype choice for murine photoreceptor transduction, we sought to examine the effects of different doses of AAV2/8-CAG-RP2. A 2X dilution curve (ranging from 3.9E7 to 6.1E8 vg) was tested in wild-type mice and RP2 transgene expression was assessed uisng IHC. A dilute amount of AAV2/8-Rho-EGFP ‘tracker virus’ (Rho-EGFP construct described by Palfi et al. 2010) was added to AAV-RP2 solutions before ocular injection, to allow for easy identification of transduced retinal areas for cryosectioning and staining. The dosages of both vectors used are listed in Table 2.3. The 1.7kb murine rhodopsin promoter used is highly efficient, enabling minimisation of the overall viral load.

RP2 was overexpressed in all AAV-treated retinas, with areas of overexpression confined to the ONL (Fig. 2.19.B). Transduction efficiencies were estimated by quantifying the area of RP2 overexpression in whole retinal sections and normalising against the corresponding DAPI-positive area. Transduced areas were easily defined, displaying a very high intensity of RP2 immunoreactivity relative to untransduced areas. In addition, as evident in Fig. 2.20.A, EGFP-positive and RP2-positive regions were closely aligned. AAV dosages of 3.9E7 and 3E8 vg transduced 21.5 ± 13% and 39.6 ± 12.9% of total retinal area, respectively (n = 3 retinas). When only the photoreceptor layer was considered, the percentage of ONL area transduced was 36 ± 16.9% and 64.9 ± 6.9% for the 3.9E7 and 3E8 vg doses, respectively (Fig. 2.19.C)[20]. RP2 immunoreactivity in the ONL clearly intensified with increasing AAV concentration (Fig. 2.19.D). Even at the lower doses, RP2 was overexpressed relative to the endogenous level in 'no AAV' control retinas. It should be noted that while the antibody used is highly effective in detecting overexpressed RP2, it is not yet certain whether the signal produced in untransduced retinas accurately represents the degree of endogenous RP2 expression. This will be verified in future by assessing background signal in retinas of RP2 KO mice.

[20] It should be noted that these are rough estimates of transduction efficiency based on image analyses (see Fig. 2.19.C and section 2.5.20 for protocol details). More accurate measurements of transduction efficiency could be obtained in the future using FACS.

RP2 vg	EGFP vg
6.0E+08	1.2E+07
3.0E+08	2.4E+06
1.5E+08	1.2E+06
7.8E+07	7.9E+05
3.8E+07	7.9E+05

Table 2.3. AAV2/8-CAG-RP2 dosage curve.

AAV2/8-CAG-RP2 dosages are shown, expressed in viral genomes, along with the amount of co-injected AAV2/8-Rho-EGFP tracker vector.

RP2 transgene mRNA overexpression was quantified via RT-PCR, using primers targeting a region homologous to human and murine sequences (Fig. 2.19.E-G). Again, as seen previously in fibroblast AAV dose response tests (see Fig. 2.10), the dose response data appeared to fit a sigmoidal curve when plotted. Transduction of retinal cells after subretinal injection of virus therefore appear to reach a point of saturation at a certain dosage of AAV.

RP2 overexpression peaked with a 51.7 fold increase at 3E8 vg relative to the endogenous level, while the lowest AAV dose elicited a 1.36 fold excess of RP2 mRNA. It is important to note that mRNA levels were quantified using whole retinal samples. Considering that only 36-65% of the ONL was transduced and that photoreceptors make up 81% of the mouse neuroretinal population (calculated from data presented by Jeon et al., 1998), it is likely that the level of RP2 overexpression in actual transduced cells was much higher – at a rough estimate, approximately 5 and 98 fold higher than endogenous expression at the lower and higher ends of the dose curve, respectively. In future, transduced areas could be isolated from retinas co-injected with AAV-RP2 and AAV-EGFP via FACs before RNA extraction to enable more accurate quantitation of overexpression levels.

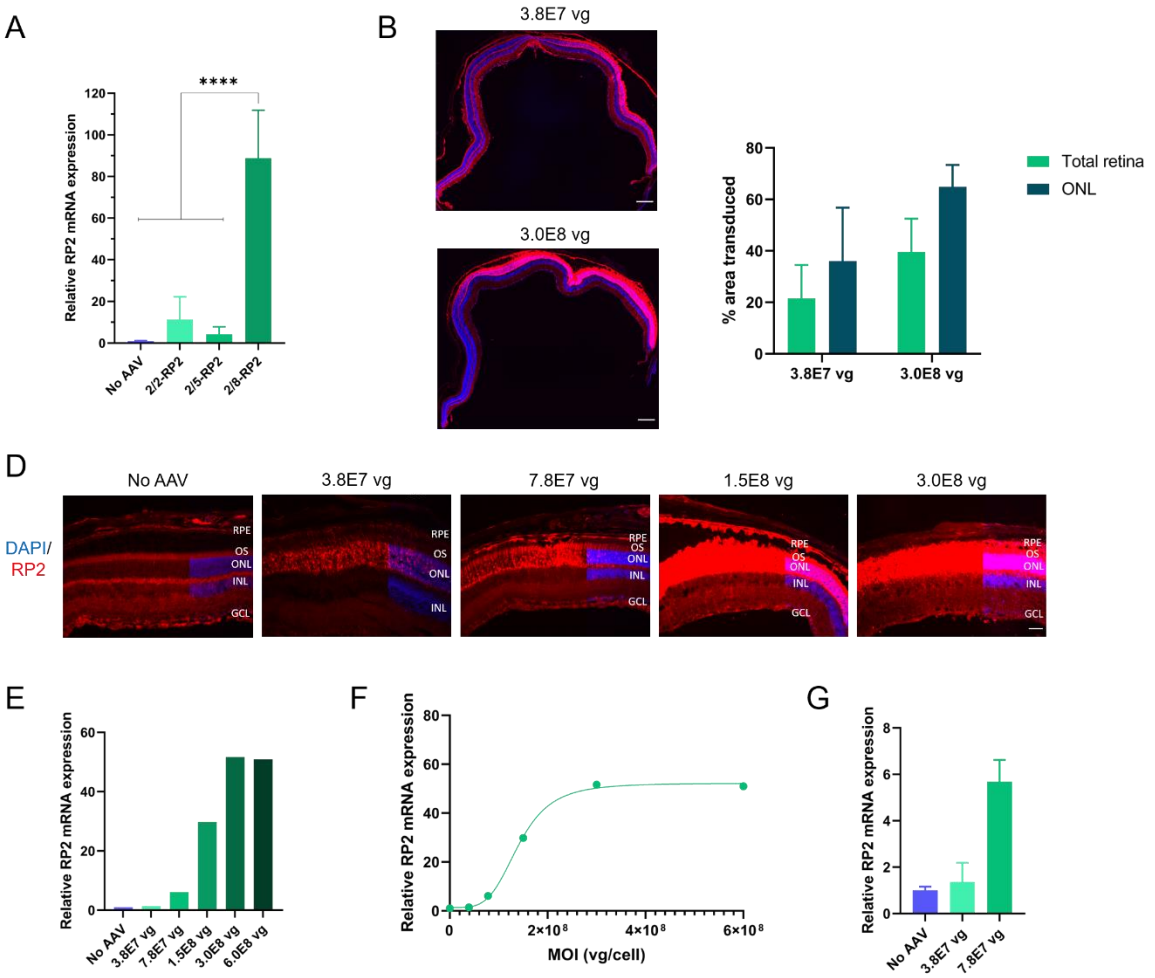

Fig. 2.19. AAV-mediated RP2 overexpression in wild-type murine retinas.

(A) AAV2/2, 2/5 and 2/8 tropisms were evaluated in a retinal context. AAV-CAG-RP2 virions were subretinally injected (3E8 vg) and RP2 expression was quantified via RT-qPCR in whole retinal samples two weeks later. AAV2/8-CAG-RP2 was the only virus to express significantly more RP2 than 'no AAV' control retinas. It also dramatically outperformed 2/5 and 2/2, expressing at a level 8 – 21 times higher than that of the other vectors. Values shown are means ± SD; $p < 0.0001$. The n values were as follows: No AAV and AAV2/2-RP2 = 4, AAV2/5-RP2 = 7, AAV2/8-RP2 = 3 retinas.

(B) An AAV2/8-CAG-RP2 dose curve was tested in wild-type retinas. Representative IHC images of whole retinal sections from two dose groups are shown. RP2 expression is shown in red. Tissue was counterstained with DAPI (blue). Scale bar = 200µm.

Fig. 2.19. AAV-mediated RP2 overexpression in wild-type murine retinas (continued).
(C) Transduction efficiencies were calculated by quantifying areas highly immunoreactive for RP2 in whole retinal cryosections. The Fiji 'Threshold' tool was used to highlight regions of RP2 overexpression before area measurement. Values were normalised against DAPI-positive area. For total retinal meaurements, RPE was removed from images before analysis using the 'Freehand selections' and 'Fill' tools. To calculate the proportion of ONL area transduced, all other retinal layers were removed and areas positive for RP2-overexpression and DAPI were quantified as before. n = 3 retinas (one whole retinal section analysed per retina).
(D) RP2 expression was analysed via IHC on retinal sections from four dosage groups. All AAV-treated retinas exhibited more intense RP2 staining than uninjected 'no AAV' retinas. Transgenic RP2 expression appeared confined to photoreceptors and RPE cells and increased with AAV dosage. Scale bar = 50µm. At least one (but mostly two) retinal sections from 3 different injected eyes were examined.
(E) RP2 mRNA expression in AAV-injected retinas was quantified relative to the endogenous level in uninjected control retinas. RNA from three different retinas per group were pooled for RT-PCR analysis. RP2 expression grew dramatically with increasing AAV concentration, peaking at the 3E8 vg dose. The amount of RP2 detected in retinas treated with this dose was 51.7 times greater than the endogenous level.
(F) The data from (E) followed a sigmoidal shape. A curve was fitted using the '[Agonist] vs. response -- Variable slope (four parameters)' model in GraphPad Prism (r^2 = 0.998).
(G) Retinal samples from the two lowest dose groups were analysed separately to more accurately quantify RP2 overexpression. The mean RP2 RNA levels detected in this test were extremely similar to data from pooled samples observed in (E). RP2 was overexpressed by 1.36 and 5.69 fold at the 3.8E7 and 7.8E7 vg doses, respectively ('no AAV': 1.00 ± 0.13; '3.8E7 vg': 1.36 ± 0.68; '7.8E7 vg': 5.69 ± 0.76). Values shown are means ± SD, n = 3 retinas.
Note: Two different AAV2/8-CAG-RP2 preparations were used in (A) and (B-G).

In addition to evaluation of transgene expression, EGFP-positive sections from wild type retinas in the AAV-RP2 dose curve experiment were further evaluated for indications of potential toxicity. Obvious signs of a negative effect associated with the AAV2/8-CAG-RP2 gene therapy delivered subretinally to wild type mice such as ONL thinning or disorganisation were not present – average ONL thickness across retinal cryosections did not vary significantly between uninjected and AAV-injected groups (Fig. 2.20.A).

A preliminary evaluation of markers of macroglia and microglia activation (GFAP and IBA1, respectively), and IgG production (Fig. 2.20.C and D) was also undertaken using AAV2/8-CAG-RP2 dose curve retinal samples. Image thresholding and integrated density measurement (facilitated by Fiji) were used to estimate relative protein abundance in these samples (see section 2.5.20.3 for method details).

During gliosis, GFAP, an intermediate filament protein, undergoes upregulated expression in activated astrocytes and is additionally expressed in Müller glia cells (Reichenbach and Bringmann, 2020). With regard to the AAV2/8-CAG-RP2 experiment, GFAP expression was restricted to astrocytes in uninjected retinas and 'AAV-EGFP only' negative control retinas. However, in retinas that received both the high and lower dose AAV-RP2 vectors, GFAP-positive Müller glia processes extending throughout the retinal layers were evident. Areas of Müller cell gliosis closely aligned with transduced regions (Fig. 2.20.C). When compared to an uninjected retina, the amount of retinal GFAP in AAV-CAG-RP2 3.9E7 vg and 3.8E8 vg groups was 4.9 and 3.3 fold higher, respectively (n = 2 for RP2-injected retinas, n = 1 for control retinas; 2-3 sections analysed per retina) (Fig. 2.20.D). Although these increases were not significant in this pilot study, this was most likely due to the extremely limited sample sizes available.

In contrast, GFAP expression in the single Rho-EGFP control retinal sample available was only 1.4 fold higher than the uninjected retinal sample (Fig. 2.20.D). Unfortunately, there were no more RP2/EGFP-positive sections of injected eyes available for analysis after this point. The ability to increase numbers was restricted by the introduction of significantly reduced colony sizes in the animal facilities in TCD during the first Covid-19 lockdown. EGFP-negative regions of injected retinas were nonetheless tested for expression of two other markers of immune response.

Ionized calcium-binding adaptor protein-1 (IBA1) is a microglial-specific protein that is increased upon cell activation. Although expression of this marker varied between experimental groups, a clear trend was not evident (n = 1-2) (Fig. 2.20.C and D). There was significantly more immunoglobulin (IgG) present in AAV-RP2 treated retinas relative to Rho-EGFP and uninjected controls, however ($p < 0.01$, n = 1-2) (Fig. 2.20.C and D).

The GFAP, IBA1 and IgG data presented here are from very preliminary tests conducted with extremely limited sample sizes, and using a semi-quantitative method (IHC). However, it does appear that subretinal injection of AAV2/8-CAG-RP2 induced an altered immunological profile, even at the lowest dose of AAV tested (albeit the lowest dose may still represent a 5X over expression of RP2). As both the time-frame of overexpression (two weeks) and sample group sizes in these tests were clearly sub-optimal, preparations are underway for a repeat experiment (outlined in Table 2.4). A 5X dilution curve of three AAV doses has been chosen, based on the results of initial expression tests (Fig. 2.19), and an additional PBS-injected negative control group has been added. Of note, transgene expression from AAV2/8 vectors has been noted to plateau at seven weeks post-administration (Natkunarajah et al., 2008). Retinas will be assessed three months after subretinal injection, at which point the vector will have been expressing fully for roughly one month. Retinal detachment is known to activate Müller glia (Bringmann et al., 2009). Although the transient retinal detachment induced by subretinal injection normally resolves within 24 hours in mice (Wert et al., 2012), it is possible that gliosis persists for some time after. Analysing tissues three months post-injection and including PBS-injected control eyes should allow delineation of immune response to the vector from reaction to the surgical procedure itself. In principle, immune response(s) may be due to over-expression of the transgene, to the AAV vector and/or to impurities in the particular batch of AAV vector. Therefore, to explore these options, an additional batch of virus has been generated and is being used in the proposed study.

Fig. 2.20. Assessment of AAV-CAG-RP2 tolerance in the murine retina (overleaf).

(A) Average ONL thickness did not vary significantly between uninjected (n = 3) and AAV-CAG-RP2 injected eyes (n = 3 per AAV dosage). ONL length was quantified across DAPI-stained retinal cryosections using the line tool in Fiji. 8-12 measurement were taken per retina and averaged. In the case of injected eyes, only transduced parts of the retina (RP2/EGFP positive) were measured. For each retina, 2-4 sections were examined. One-way ANOVA and Tukey's post hoc tests were applied to test for significance (uninjected vs RP2 3.9E7 vg: $p = 0.1049$, uninjected vs RP2 3.8E8 vg: $p = 0.9394$).

(B) Subretinal injections contained AAV2/8-CAG-RP2 and a tracker virus (AAV2/8-Rho-EGFP) to enable easy identification of transduced retinal regions for use in IHC analysis. Regions of EGFP (green) and RP2 (red) overexpression were consistently closely aligned.

(C) Expression of immune response markers was examined in AAV-RP2 treated retinas. Retinas that received only AAV2/8-Rho-EGFP and uninjected retinas ('no AAV') were included as negative controls. Representative IHC images are shown. GFAP expression (red, top row) was upregulated in retinal regions where RP2 was overexpressed. GFAP-positive Müller glial processes extended from the GCL to the ONL in EGFP-expressing areas of retinas that received AAV-RP2. This was not observed in negative control retinas, where only astrocytes in the GCL were GFAP-positive.

RP2/EGFP-negative retinal regions of injected eyes were additionally tested for IBA1 and IgG production. No obvious difference was seen in IBA1 across experimental groups. IgG immunoreactivity, however, appeared more abundant in retinas that received AAV-RP2.

Two retinas (one whole retinal section each) were examined per experimental group for GFAP and IgG staining, while IBA1 staining was performed on one retinal section per group. DAPI area (blue) was cropped to allow better visualisation of signal in red and green channels. Scale bars = 200µm.

(D) The amount of GFAP, IBA1 and IgG protein in IHC samples described in (C) was quantified by calculating the integrated density values (mean pixel intensity x area; Fiji) of immunoreactive regions and normalising against the DAPI-positive area of retinal sections. In the case of GFAP, only transduced (EGFP-positive) regions were analysed in injected samples. The number of retinas analysed per group were as follows: **GFAP -** uninjected (1), Rho-GFP only (1), CAG-RP2 3.9E7 vg (2), CAG-RP2 3E8 vg (2). 2-3 sections were examined per retina. **IBA1 -** uninjected (1), Rho-GFP only (2), CAG-RP2 3.9E7 vg (1), CAG-RP2 3E8 vg (1). 1 section was examined per retina. **IgG –** uninjected (1), Rho-GFP only (1), CAG-RP2 3.9E7 vg (2), CAG-RP2 3E8 vg (2). 1-2 sections were examined per retina. One-way ANOVA and Tukey's multiple comparisons tests were performed to test for significance. ** $p < 0.01$.

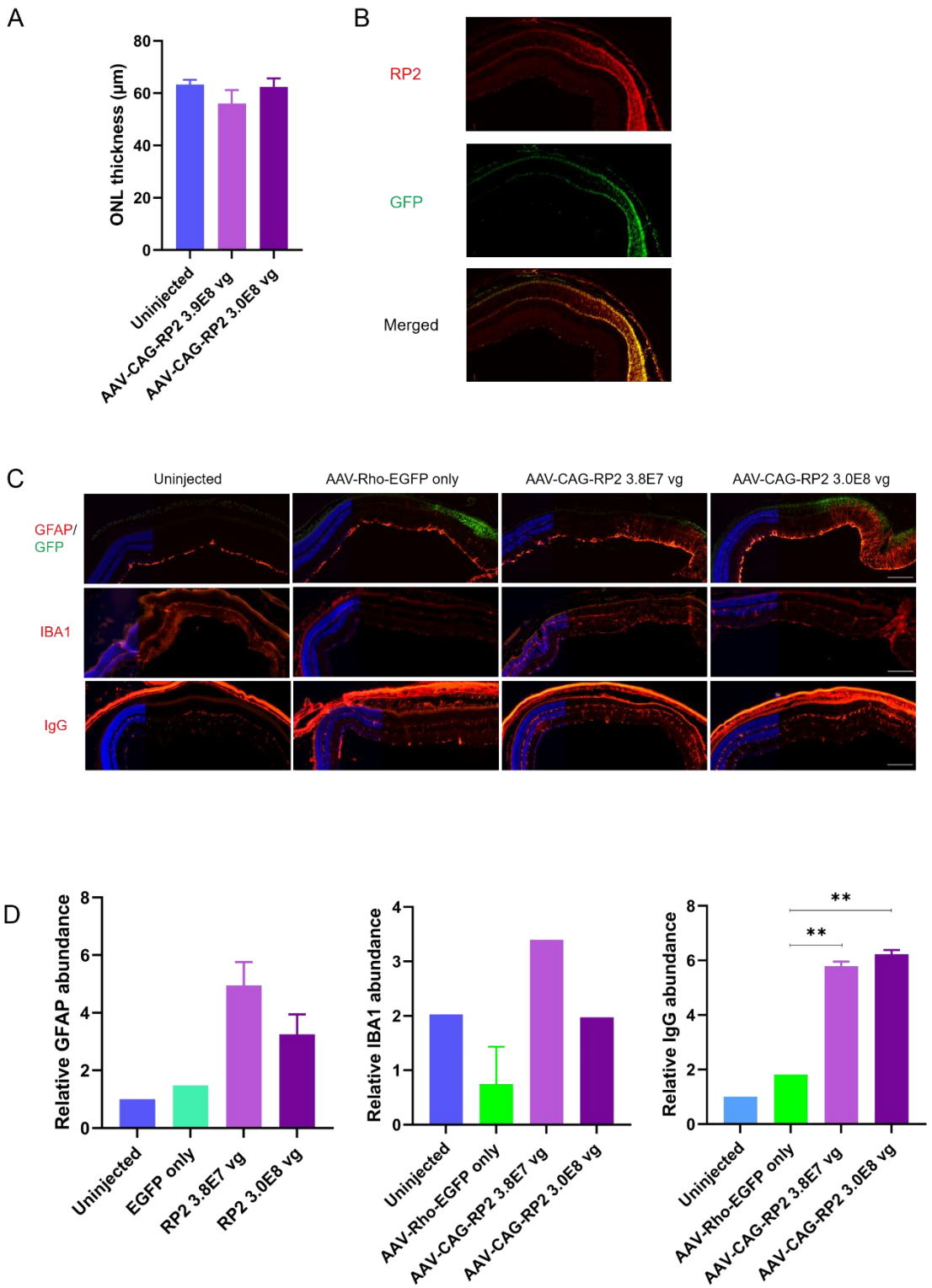

Fig. 2.20. Assessment of AAV-CAG-RP2 tolerance in the murine retina.

Group	AAV-CAG-RP2 (vg)	AAV-RHO-EGFP (vg)	RP2:EGFP	No. retinas for IHC	No. retinas for RNA
Dose 1	1E8	7.9E5	121:1	4	4
Dose 2	2E7	7.9E5	24:1	4	4
Dose 3	4E6	7.9E5	5:1	4	4
EGFP only	-	7.9E5	-	4	4
PBS only	-	-	-	4	4

Table 2.4. Long term RP2 overexpression experiment design.

A new AAV2/8 preparation was used in this experiment and was established to be roughly twice as potent as the preparation used in the original dose curve. AAV-RP2 concentrations were therefore adjusted accordingly. AAV-Rho-EGFP concentration was kept at a minimal level.

Of course, it would be preferable to test the efficacy and safety profile of the AAV-RP2 vector in a *Rp2h* null mouse model. Fortunately, to this end, the *Rp2h*$^{\Delta 23/Y}$ knock out mouse was recently made available to us by Dr Toby Hurd (University of Edinburgh). This model features a CRISPR Cas9-induced 23 bp deletion in *Rp2h* exon 2 (c.410_432delCCACAAACATCAAGTTTGGCTGT, p.Ser137PhefsTer7) (Fig. 2.21). The mutant transcript presumably undergoes NMD, as no RP2 protein is detected (Little, 2019). As outlined previously in Table 2.1, affected Rp2h$^{\Delta 23/Y}$ mice display significantly reduced rod and cone ERG amplitudes from 6 months of age and reduced ONL thinning starting from 3 months. A Rp2h$^{\Delta 23/Y}$ colony is currently being established by our lab and will be further characterised. The results of the AAV-RP2 tests in wild-type mice as outlined above will enable an optimal dosage range to be chosen for future work with the *Rp2h* null model. Examining the effects of AAV-mediated RP2 replacement in *Rp2h*$^{\Delta 23/Y}$ mice will complement the AAV-RP2 rescue that has been observed using *in vitro* models as part of this study.

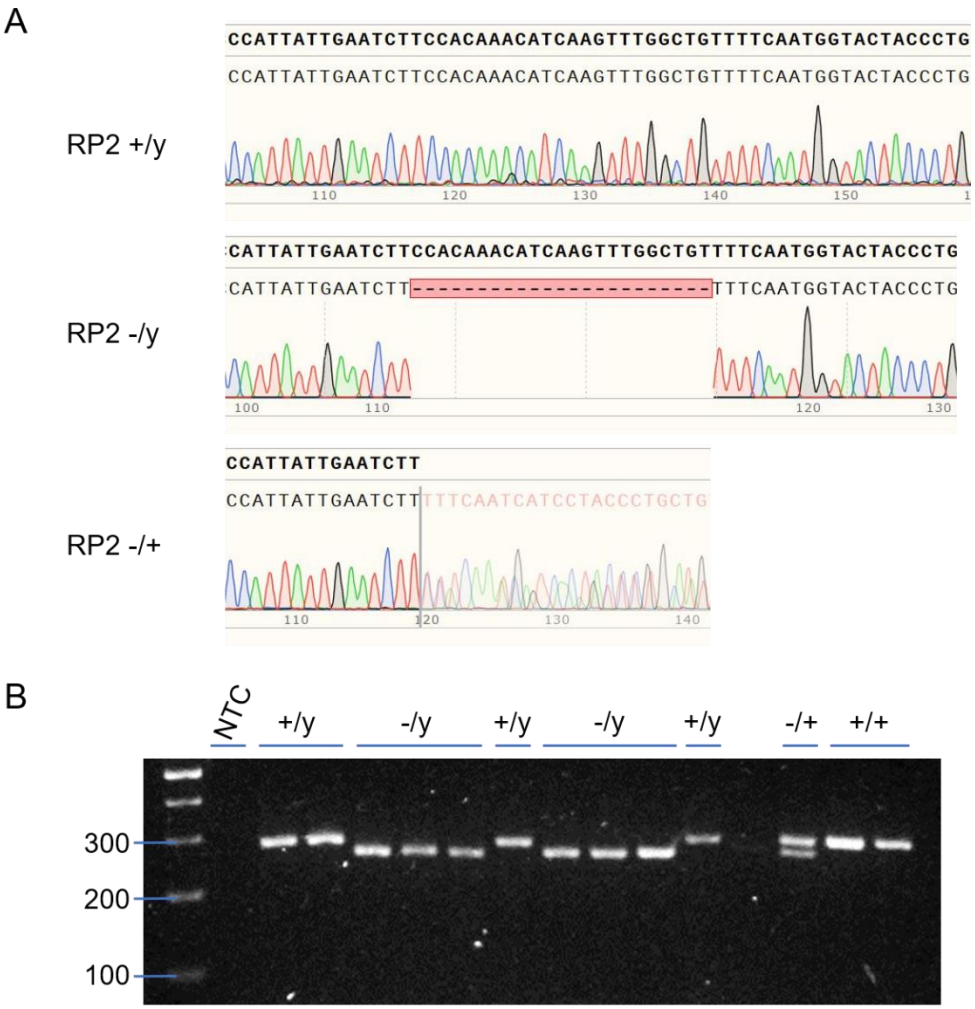

Figure 2.21. *Rp2h*$^{\Delta 23/Y}$ mouse genotyping.

(A) Sanger sequencing chromatograms from wild-type male, *Rp2h* null male and carrier female littermates are shown, aligned to a reference *Rp2h* sequence (MGI:1277953). A 23 bp deletion is evident in -/y males. Double peaks stop heterozygous female sequence reads aligning to the reference from the deletion site onwards.

(B) A region of *Rp2h* exon 2 surrounding the 23bp deletion site was amplified from DNA isolated from ear clip tissue samples. A WT allele produces a 284 bp amplicon, while a mutant allele yields a 261 bp fragment. PCR products were separated on 3% agarose gels. In the example gel shown, multiple different genotypes are visible: WT males (+/y), hemizygous null males (-/y), WT females (+/+) and carrier females (-/+).

2.4 Discussion

2.4.1 Patient-derived fibroblasts as personalised models of disease

Patient-derived fibroblast cultures offer a means of means of examining the effects of pathogenic mutations in the context of a patient's particular genetic background and, moreover, of testing the efficacy of potential therapeutics in this setting.

In this study, RP2 mRNA expression was downregulated in R120X and N142fs patient fibroblasts and RP2 protein could not be detected (Fig. 2.8). It is not surprising that both variants appear to cause nonsense-mediated decay of RP2 mRNA, considering their locations. NMD is initiated when exon-exon junction complexes (EJCs) bound to mRNA fail to be cleared by the ribosome due to the presence of an upstream premature stop codon. Nonsense mutations therefore typically need to occur more than ~55bp before the last EJC for NMD to be triggered (Nagy and Maquat, 1998). Conversely, when PTCs are located within the first exon, translation can sometimes be reinitiated at a downstream start codon (Neu-Yilik et al., 2011, Moey et al., 2016). As the Arg120X and Asp142fsIleTer14 variants are located relatively centrally in the second exon of the RP2 transcript, NMD would be predicted to occur.

The fact that RP2 expression in N142fs fibroblasts was almost 4 fold higher than in R120X cells suggests the N142fs mutant transcript could be more stable than the former, which could be due to the PTC locations (differing by 106bp). However, NMD efficiency is thought to vary between individuals, possible due to differential expression of proteins critical to the NMD pathway (Nguyen et al., 2014). Importantly, individuals with nonsense mutations that had higher levels of baseline mRNA were shown to respond better to translational read-through drugs (Linde et al., 2007b).

This study confirmed the pathogenicity of a novel candidate variant, *RP2* c.425delA. The differences in RP2 transcript level between R120X and N142fs cells were also interesting. In the future, similar studies assessing the degree of NMD efficiency in personalised cell models could be beneficial in predicting the efficacy of translational read-through therapies for patients with *RP2* nonsense mutations like p.Arg120X. However, in light of the fact that NMD efficiency has also been shown to differ across cell types (Linde et al., 2007a), such studies may be best carried out using patient-derived retinal organoids.

As part of this study high titre AAV vectors were generated either carrying a reporter gene or the therapeutic RP2 gene of interest. AAV2/2-CAG-RP2 treatment was successful in restoring RP2 expression in patient-derived fibroblasts as evaluated at RNA and proteins levels (Fig. 2.11). Unfortunately, robust morphological or biochemical phenotypes were not established in *RP2* null cells, despite attempting multiple assays, and so functional rescue-mediated by AAV-CAG-RP2 treatment could not be assessed in these cell models. However, an efficient strategy for AAV treatment of primary dermal fibroblasts was validated, which proved useful for subsequent studies testing the efficacy of gene replacement in IRD patient-derived fibroblast models for dominant optic atrophy (Maloney et al., 2020).

2.4.2 Modelling and rescue of RP2 loss in retinal organoids

As discussed earlier, mouse models of *RP2*-XLRP do not faithfully recapitulate the early-onset, rapidly progressing nature of the human disease – particularly in terms of rod-related functional defects. Mookherjee et al. (2015) noted that alternative animal models may therefore be required to assess capacity of therapeutics to protect rod photoreceptors. Examining the consequences of RP2 loss with hPSC-derived retinal organoids uncovered an early-onset rod degenerative phenotype not previously documented in mouse models. Of note, photoreceptor degeneration and upregulation of a p53 pathway gene were also observed in *RPGR* null ROs in a similar time frame (Deng et al., 2018). Mouse models of *RPGR*-XLRP had also failed to adequately represent the severity of the human disease, exhibiting late-onset degeneration (Hong et al., 2000) and displayed conflicting phenotypes depending on the background strain used (Brunner et al., 2010).

Significant signs of photoreceptor degeneration were evident in *RP2* null ROs at a stage that corresponds to a 6 month old foetus (Fig. 2.15 and 2.16). Interestingly, photoreceptor OS development was also impaired in zebrafish *rp2* knockdown models – though cones were more severely affected than rods (Patil et al., 2011). A developmental defect would have implications for a potential window for therapeutic intervention – if degeneration starts during retinal development, could treatment during childhood or later be effective in stopping or reversing disease progression? It was recently shown that AAV-mediated replacement of *Tulp1*, a gene active during early post-natal development in multiple retinal cell types, provided only minimal benefit in a null mouse model -

despite the fact that treatment was administered before the onset of degeneration (Palfi et al., 2020a, Palfi et al., 2020b).

However, it is important to note that evidence of photoreceptor developmental defects has not been observed in *RP2*-XLRP patients. It is quite possible that the early rod degeneration observed is an organoid-specific phenotype, as ROs are subjected to artificial stresses that may exacerbate or accelerate an underlying defect. In particular, ROs do not possess a continuous layer of RPE to support photoreceptors, which are regularly subjected to shear forces during media changes. They also lack important cell types such as microglia and astrocytes. A major effort is underway to increase the physiological fidelity, reproducibility and scalability of RO models - promoted by the National Eye Institute (NEI) (Wright et al., 2020). In one such innovation, the 'retina-on-a-chip', ROs are coated in hyaluronic acid gel (to mimic the interphotoreceptor matrix) and placed on a layer of iPSC-derived RPE cells in a microfluidic chamber. Media is perfused through the chamber to enable better nutrient exchange while avoiding shear forces (Achberger et al., 2019). PSC-derived microglia have also recently been incorporated into RO structures (Chichagova et al., 2020)[21]. Other proposals include the addition of a choroid to aid with nutrient exchange, and astrocytes to enhance RGC maturation and facilitate the formation of an ILM (Wright et al., 2020, Capowski et al., 2019). Co-culturing of retinal and fore-brain structures may even enable the formation of a connecting optic nerve (Capowski et al., 2019). The use of nanotechnology to direct the release of growth factors and cytokines to specific cell types may also enable ROs to reach a higher level of complexity (Wright et al., 2020). Improving the ability of ROs to faithfully recapitulate foetal retinal development in a reproducible manner will allow more confident interpretation of disease phenotypes observed in this context.

Treatment of *RP2* null ROs with AAV2/5-CAG-RP2 appeared effective in preventing rod degeneration, as assessed by ONL thickness preservation (Fig. 2.18). Of note, to the best of my knowledge, this was the first study to rescue photoreceptor loss in a retinal organoid model (without pre-differentiation gene editing of the PSC line). In future, it would be interesting to analyse photoreceptor function in *RP2* null ROs using measures of light sensitivity. Other groups have achieved this using electrophysiological read-outs

[21] Chichagova et al. 2020 was a conference abstract and not peer-reviewed.

(Zhong et al., 2014, Wahlin et al., 2017, Hallam et al., 2018) and calcium imaging (Achberger et al., 2019). This is not currently a robust means of assessing functional deficit or rescue, however, as ROs only exhibit light sensitivity approximately 15-37% of the time (Wright et al., 2020).

The level of RO transduction achieved in this study was unprecedented (90% of the ONL). Other studies assessing the potency of AAV2/5 vectors in ROs reported efficiencies of 4-7.5% (Gonzalez-Cordero et al., 2018, Quinn et al., 2019). Several serotypes have been tested in this context and, with the exception of AAV2/2-7m8 (Garita-Hernandez et al., 2020), the transduction capacities were generally quite low (≤ 21%). Studies to-date that have quantified AAV transduction efficiency in ROs were compared in an effort to ascertain why our study achieved a higher level of RO transduction than others (Table 2.5). The timing of transduction is likely a major factor in determining the success of an experiment such as this, as development of rod outer segments (~D120) appears key for facilitating AAV uptake (Gonzalez-Cordero et al., 2018). The length of transduction before analysis is also important, as transgene expression does not begin immediately. AAV2/5-CBA-GFP vector has been shown to express in the neuroretina from 7 days post-injection, with the level of expression steadily increasing for at least another 21 days (Kong et al., 2010). In our study, AAV2/5-CAG-RP2 was administered at a time when developing photoreceptor outer segments were evident and allowed to express for 40 days – a substantially longer transduction period than other comparable studies. Additionally, RP2 transgene expression was detected using a sensitive polyclonal antibody rather than the native GFP fluorescence used by other studies.

The fact that AAV-mediated gene replacement was capable of rescuing rod degeneration in *RP2* null ROs is promising and, along with evidence that *RP2* augmentation preserves cone function in a null mouse model (Mookherjee et al., 2015), indicates that this strategy may be a viable option for treatment of XLRP in the future. To get to the point of human clinical trial(s) for RP2-linked XLRP, of course, will require more thorough optimisation of vector design and AAV dosage, together with toxicology and biodistribution studies in non-human primates. In concert with this, careful evaluation of clinical trial design, including the optimal outcome measures, will be required.

Study	AAV vector	Transduction efficiency	Transduction method	Method of transgene detection	AAV production method	Organoid differentiation protocol
Gonzalez-Cordero et al., 2018	**Serotype:** 2/2, 2/5, 2/8, 2/8T, 2/9, ShH10. **Construct:** CAG-GFP.	(2/2) 19%, (2/5) 4%, (2/8) 4%, (2/8T) 5.5%, (2/9) 4%, (ShH10) 21%. Positive cells mainly in ONL. ShH10 additionally transduced Müller glia.	**Titer:** 1.2E11vg/ organoid. **Period:** D119-133 (14 days). **Details:** not specified.	Flow cytometry, detecting native GFP fluorescence.	Purification: Sepharose column. Titering: qPCR against SV40 pA signal.	hESC-derived. Method adapted from Zhong et al., 2014.
Quinn et al., 2019	**Serotype:** 2/5, 2/9, ShH10. **Construct:** CMV-EGFP-WPRE.	(2/5) ~7.5%, (2/9) 0%, (ShH10) ~7.3%. Positive cells were mainly Müller glia, with occasional positive PRs.	**Titer:** 5E9vg/ organoid. **Period:** D220-234 (14 days). **Details:** AAV (<10ul) added to 2 ROs in 96-well plate with 50ul media. Another 50ul media added 24 hr later, then media changed.	Fluorescence microscopy, detecting native GFP fluorescence.	Purification: Iodixanol density gradient. Titering: qPCR. Target region not specified.	hiPSC-derived. Adapted method from Zhong et al., 2014.
Garita-Hernandez et al., 2020	**Serotype:** 2/2, 2/8, 2/9, 2/2-7m8. **Construct:** CAG-EGFP.	(2/2) 1.6%, (2/8) 6.8%, (2/9) 2.5%, (2/2-7m8) 64.4%.	**Titer:** 5E10vg/ organoid. **Period:** D44-70 (26 days). **Details:** 10-12 organoids transduced together in well	Flow cytometry, detecting native GFP fluorescence.	Purification: $CsCl_2$ density gradient. Titering: qPCR. Target region not specified.	hiPSC-derived. Protocol from Reichman et al., 2014 and 2017. D42-49: Notch inhibitor added to increase RPC production. Protocol produces cone-enriched organoids.

			of 6-well plate. Media changed 72 hr later.			
Lane et al., 2020	**Serotype:** 2/5. **Construct:** CAG-RP2.	90% ONL (rods and cones), <1% INL	**Titer:** 1E11vg / organoid. **Period:** D140-180 (40 days). **Details:** ROs incubated with 21 µl AAV and 54 µl media in a well of a 96-well plate for 8 hours before topping up media to 200 µl. 50/50 media changes then carried out every 2 days.	IHC.	Purification: $CsCl_2$ density gradient. Titering: qPCR. Primers against central transgene.	hiPSC-derived. Protocol adapted from Zhong et al., 2014.

Table 2.5. AAV transduction efficiency in retinal organoids.

Studies that have quantified AAV transduction efficiencies in ROs are summarised and compared. Note: there are a number of other published studies that have reported successful, but not quantified, AAV transduction of ROs using AAV2/9, 2/2m8, 2/2 and PhP.eB serotypes (Welby et al., 2017, Khabou et al., 2018b, Tornabene et al., 2019, Cowan et al., 2020)

2.4.3 Evaluation of vector tolerance and choosing an optimal construct

AAV-mediated RP2 overexpression in photoreceptors of *RP2* KO ROs was not obviously toxic, as ONL thickness improved compared to untreated ROs. However, as discussed in the previous subsection, a retinal organoid is not an optimal model in which to assess the safety profile of a therapeutic. We therefore sought to examine *in vivo* RP2 overexpression in a murine retinal context.

Various AAV serotypes were tested in wild type mice to ascertain the optimal serotype for expression of the *RP2* replacement gene. AAV2/2, 2/5 and 2/8 vectors were subretinally injected in wild type mice and AAV2/8 was found to provide the highest levels of transgene expression post injection, in line with prior studies (Allocca et al., 2007, Natkunarajah et al., 2008). Using various AAV2/8-CAG-RP2 doses from 3.8E7 vg to 6.0E8 vg, overexpression of RP2 was achieved in wild-type murine photoreceptors. The cellular levels of overexpression achieved within this dosage curve were roughly estimated to range from 5 to 98 fold higher than endogenous RP2 expression and will be more precisely quantified in future tests.

Gene augmentation therapies have the potential to elicit toxic effects through transgene overexpression (phenotoxicity), the vector used for delivery and/or the mode of administration. For example, overexpression of wild-type rhodopsin (murine or human) has been noted to cause photoreceptor degeneration in transgenic mice (Olsson et al., 1992, Sung et al., 1994, Li et al., 1996, Tan et al., 2001).[22] In the case of RP2, it is possible that transgene overexpression could lead to reduced activation of ARL3, perhaps even phenocopying an ARL13B-deficient background like that linked to Joubert Syndrome (Dilan et al., 2019). Treatment with an AAV-RP2 vector at a dose of 1E9 vg/eye was reported to elicit photoreceptor toxicity in a *Rp2h* null mouse model, though it was not determined whether the vector or transgene overexpression was the cause of this reaction (Mookherjee et al., 2015).

In the preliminary retinotoxicity assessment described in this chapter, it is notable that ONL thinning was not observed in eyes subretinally injected with AAV2/8-CAG-RP2 (Fig. 2.20.A). However, albeit a rather preliminary study requiring further animal numbers in

[22] Note: AAV-mediated rhodopsin overexpression (by 58%) appeared well-tolerated (Mao et al., 2011) but transgenic overexpression (as little as 23%) was toxic in mice (Tan et al., 2001), indicating that abnormally high rhodopsin levels may be problematic in developing rods specifically (Cideciyan et al., 2018).

the future, Müller glia were found to be activated in AAV2/8-CAG-RP2 transduced retinas - the area of Müller glia activation being closely aligned with the region of AAV transduction (Fig.2.20.C). This reactive gliosis could be initiated by cytokines or growth factors released by damaged photoreceptors or RPE. This could also potentially be a result of direct AAV detection by toll-like receptors expressed by Müller glia (Xiong et al., 2019).

Gliosis is an injury response that attempts to protect neuronal tissue from further damage. Once activated, Müller glia can promote neuronal survival by release of neurotrophic factors and antioxidants, and uptake of (neurotoxic) excess glutamate. However, prolonged gliosis can be more harmful than helpful – particularly in a diseased retina. Müller glia release pro-inflammatory cytokines and chemokines that attract monocytes/macrophages, which in turn can damage photoreceptors by release of ROS and harmful cytokines. High levels of nitric oxide production by Müller glia can also cause oxidative damage to proteins, while the formation of glial scars can hinder retinal repair or remodelling (reviewed by Bringmann et al., 2009). As mentioned earlier, gliosis is known to occur after retinal detachment (Bringmann et al., 2009). For this reason, it will be especially important to include a PBS-injected negative control group in future experiments (as discussed in section 2.3.7). Likewise, it is important to carefully evaluate the purity profile of the AAV-CAG-RP2 and AAV-EGFP vector batches to clarify whether differences in immune response(s) are a function of overexpression of the transgene or due to potential differences in batch purity.

IBA1 upregulation was not detected in the non-transduced regions of injected eyes tested. However, the sample sizes for this test were particularly limited (often n = 1 section from 1 eye). Xiong et al. (2019) notably observed IBA1 upregulation in retinas transduced with 3E9 vg of an AAV2/8-CMV-EGFP vector. It is therefore possible that microglial activation may have been observed in the experiment described in this chapter if additional sections with transduced retinal regions had been available for analysis. Strikingly, mouse IgG levels were significantly increased even in non-transduced areas of AAV-injected eyes, indicating a humoral immune response. The extremely limited number of AAV2/8-Rho-EGFP injected control retinal sections looked similar to uninjected eyes in terms of GFAP, IBA1 and IgG levels.

The upregulation of GFAP and IgG observed in AAV-RP2 injected eyes may have been due overexpression of the therapeutic gene and or to the viral load (4E7 – 3E8 vg AAV-CAG-RP2 plus 1E6 vg AAV-Rho-EGFP), as discussed. However, this response could equally have been elicited by immunogenicity of the viral capsid or contaminants in the research-grade viral preparations used in this study as also eluded to. No definitive conclusions can be made from the preliminary results presented, given the small samples numbers used. However, these early results clearly highlight that a more extensive study will be important (as has been planned and detailed previously).

RPE health was not analysed during this study but could be assessed in future tests using RPE flatmounts (as described by Xiong et al. 2019). It may also be prudent to perform functional tests, given Mookherjee et al.'s (2015) observation of a dose-dependent rod ERG deficit when using an AAV-RP2 vector.

In future experiments, additional negative controls will be necessary. Contralateral control eyes will need to be treated with an equal dosage of a non-RP2 vector. It is not uncommon for groups to inject control eyes with an equivalent amount of AAV-GFP for this purpose. However, recent work suggests that GFP expression exerts retinotoxicity even at doses as low as 5E9 vg per eye. This experimental set up could therefore create a confounding bias, whereby the therapeutic-injected eye would show improvement relative to toxic effects of GFP in negative control eyes (Khabou et al., 2018a). Another strategy is to inject empty AAV capsids into control eyes. However, the capsid is not the only immunogenic element of an AAV particle – the AAV genome can be recognised by TLR9, while dsRNA produced as a consequence of 3'ITR promoter activity could activate TLR3 (Xiong et al., 2019, Shao et al., 2018). Ideally, therefore, this experiment would be repeated using a non-coding AAV2/8-CAG vector in contralateral control eyes to ascertain whether the gliosis and IgG infiltration observed are a result AAV capsid/genome immunogenicity and/or RP2 overexpression. It would also be prudent to test multiple preparations of the chosen vectors as rAAV purity and potency can vary between batches.

A constitutively active promoter was chosen to drive RP2 expression in this study because RP2 is normally ubiquitously expressed and it remains to be confirmed whether its loss directly affects function of cells outside the neuroretina. RP2 patient iPSC-derived RPE cells were reported to display increased Golgi area and dispersal of IFT20 protein (Schwarz et al., 2015). Immortalised RPE cells (hTERT-RPE) exhibited dispersal of kinesin

proteins from the ciliary tip after RP2 knockdown (siRNA) (Schwarz et al., 2017), while RP2 KO hTERT-RPE cells had migration and wound-healing defects (Lyraki et al., 2018). Regarding other ciliopathies, it is notable that Joubert Syndrome patient iPSC-derived RPE cells did not mature fully and a similar defect was shown to precede photoreceptor degeneration in a mouse model of Bardet-Biedel Syndrome. Immature iPSC-RPE cells exhibited defective phagocytosis and a reduced responsiveness to changes in extracellular potassium levels (May-Simera et al., 2018).

As previously discussed, the clinical presentation of RP2 is quite variable. Interestingly, some RP2 patients have been reported to exhibit a depigmentation of the choroid and RPE characteristic of choroideremia (Jayasundera et al., 2010) – an IRD in which atrophy of the RPE is followed by degeneration of the choroid and neuroretina. Horner et al. (2019) recently reported that a severely affected individual with a novel null *RP2* variant had no independent RPE involvement and therefore proposed that photoreceptor-specific expression of a gene replacement therapeutic should be sufficient. Although some RPE loss was evident in the macula, it was concluded that, since RPE degeneration was not as extensive or severe as the photoreceptor loss observed, *RP2*-XLRP does not involve a primary RPE defect (Horner et al., 2019). However, this analysis was based on a single patient and concerns a disease that exhibits notable phenotypic variation between individuals.

Considering the ubiquitous nature of endogenous RP2 expression and the uncertainty as to its importance in the RPE, a constitutively active promoter would seem prudent. However, cell type-specific promoters offer an added layer of safety, protecting against transgene expression in undesired cells/tissues. Indeed, most of the registered clinical trials of AAV therapeutics for RP utilise photoreceptor or RPE-specific promoters (reviewed in (Buck and Wijnholds, 2020)).

Interestingly, recent studies also suggest that expression from photoreceptor-specific promoters may be inherently less immunogenic than constitutive or RPE-specific promoters. Xiong et al. (2019) observed signs of retinotoxicity (RPE disorganisation/ enlargement/ loss, microglial infiltration of ONL and Müller glia activation) after subretinally delivering AAVs expressing EGFP under the control of constitutive or RPE-specific promoters at a dose of 8E8 vg per eye. Of note, CMV and CAG promoters were particularly damaging to photoreceptors, causing ONL thinning and opsin loss – possibly

due to the viral sequences present in both promoters. The degree of retinotoxicity induced strongly correlated with AAV dosage and these deleterious effects were independent of AAV serotype or production method used (Xiong et al., 2019). Strikingly, constructs employing photoreceptor-specific promoters appear to be significantly better tolerated than vectors with constitutive or RPE-specific promoters (Xiong et al., 2019, Khabou et al., 2018a) . This has led Xiong et al. to propose that the RPE is 'a primary sensor of toxic vectors,' noting that toll-like receptors capable of detecting AAV are expressed in these cells. Microglia and Müller glia also likely play a role in this immune response, as both were activated after subretinal injection of 'toxic' AAV vectors (Xiong et al., 2019, Khabou et al., 2018a).

The nature of the immunogenic trigger hypothesised to be detected by RPE cells remains to be confirmed. Toxicity was linked to promoter activity profile but non-coding control vectors, in which the GFP CDS was reversed (Khabou et al., 2018a) or absent (Xiong et al., 2019), induced similar or equivalent levels of damage to GFP-expressing constructs. RNA transcription from AAV genomes, whether coding or not, therefore appears to stimulate an immune response. Xiong et al. propose that, as ITR sequences demonstrate some promoter activity (Haberman et al., 2000), an antisense transcript could be synthesised from the 3'ITR and hybridise with the sense strand. The resulting double-stranded RNA would be immunogenic, inducing production of interferons and pro-inflammatory cytokines, and apoptosis (Schlee and Hartmann, 2016). Inflammatory cytokines were indeed found to be upregulated in retinas that received AAV-CMV but not AAV-Rho vectors (Xiong et al., 2019).

The apparent immunogenicity of AAV-CAG vectors is quite surprising, as Luxturna™ (AAV2/2-CAG-RPE65) is well-tolerated in patients at a dose of 1.5E11 per eye (Russell et al., 2017, Maguire et al., 2019). NHP data moreover suggests that readministration of the vector to the same (ipsilateral) eye is safe (Weed et al., 2019). However, in the case of IRDs with primary photoreceptor defects, treatment efficacy could potentially be improved if higher doses were tolerated. This could possibly be achieved using photoreceptor-specific promoters.

The human rhodopsin kinase (hGRK1) promoter is active in both rods and cones and relatively short (294 bp), which makes it attractive when designing AAV vectors targeted towards photoreceptors. As a testament to the appeal of this promoter, six registered

clinical trials are testing AAV-hGRK1p vectors (clinicaltrials.gov identifiers: NCT03920007, NCT03328130, NCT03316560, NCT03252847, NCT03116113, NCT03872479).

The hGRK1 element may therefore be both a safer and more efficient choice of promoter for an AAV-RP2 therapeutic, in the event that RP2 expression is not required in the RPE. Mookherjee et al. (2015) obtained partial rescue of the degenerative phenotype in a *Rp2h* null mouse model using a scAAV2/8-GRK1-RP2 vector; cone function was significantly preserved but the milder rod phenotype was not improved. In fact, this vector was significantly toxic to rods at a certain dosage. Considering an AAV2/8-GRK1-GFP virus was well-tolerated at a similar dose (Xiong et al., 2019), it could be argued that the deleterious effects observed by Mookherjee et al. are unlikely to have arisen from detection of the viral capsid. However, the time frame of the two studies were very different and caution should be taken in general when comparing AAV titers, as methods of quantifying AAV can be quite variable (Ayuso et al., 2014, Lock et al., 2010). It is possible that retinotoxicity stemmed from immunogenicity of the double-stranded scAAV genome, AAV batch impurities and/or non-physiological levels of RP2 expression. Unfortunately, the level of RP2 overexpression was not quantified in this study (Mookherjee et al., 2015).

A ssAAV2/8-GRK1-RP2 vector was synthesised as part of this project and will be tested in parallel to the AAV2/8-CAG-RP2 vector in order to establish whether a hGRK1 vector would be better tolerated. If, after performing carefully controlled experiments with our vectors, it was found that the CAG element did indeed have a deleterious effect, it would be worthwhile to explore ways of ameliorating its immunogenicity. There is evidence to suggest that insertion of a reversed poly(A) signal between the transgene cassette and 3'ITR would block 3'ITR promoter activity (Shao et al., 2018). It therefore would be interesting to test whether this strategy could reduce retinotoxicity in vectors with constitutive promoters.

An additional strategy that could be used to increase vector safety profile is codon optimisation of the transgene to increase expression efficiency and thereby minimise the required viral load. Alternatively, if RP2 overexpression is an issue, the *RP2* promoter could be characterised and used to drive transgene expression to better match the endogenous level. Codon optimisation or use of the endogenous promoter has previously been utilised in the design of a number of *RPE65* and *RPGR* gene replacement

therapeutics (clinicaltrials.gov; identifiers: NCT00643747, NCT01496040, NCT02781480, NCT03116113, NCT03316560).

It will ultimately be important to assess the safety profile of AAV-RP2 vectors in a *Rp2h* null animal model. A degenerating retina may be especially susceptible to damage related to vector immunogenicity and/or transgene overexpression. The 'diseased microenvironment,' in combination with the transient injury of retinal detachment, has been proposed to prime a local immune response toward viral vectors (Casey et al., 2020, Bucher et al., 2020). Introduction of a new protein (as would be the case with RP2 replacement in a null background) may itself induce a transgene-specific adaptive immune response (Bucher et al., 2020). Promoter activity may also be altered in a diseased retinal context, where the composition of available transcription factors is possibly changed - though this is more of an issue when using 'native' promoter elements than viral derived sequences (Buck and Wijnholds, 2020). Vector tolerability will therefore additionally be assessed in *Rp2h*$^{\Delta 23/Y}$ mice. Ultimately, once a lead AAV-RP2 gene therapy is optimised, toxicology and biodistribution studies would be required using GLP (good laboratory practise)-grade vector (with minimal impurities) in NHPs prior to progression to human clinical trial.

2.4.4 Assessment of AAV-RP2 efficacy *in vivo*

Rp2h$^{\Delta 23/Y}$ mice exhibit Müller glia activation in the peripheral retina from 1 month, peripheral ONL thinning from 3 months (followed by near universal ONL thinning at 9-12 months), mislocalisation of opsins and GRK1 from 3-6 months, and rod and cone ERG defects at 6 months of age (Little, 2019). It is planned that these phenotypes will be assessed in AAV-RP2-treated and contralateral control eyes (receiving PBS or a very low dose of EGFP tracker virus) for evidence of functional rescue, using doses informed by the studies detailed in this thesis chapter and the additional vector tolerance experiments that are planned. In addition, optokinetic behavioural tests will be used to assess visual function over time in this model, with and without treatment. Considering the previously discussed observations of Schwarz et al. (2015) and Wright et al. (2016), assessment of Golgi and ER area and localisation of IFT proteins in photoreceptors would be of interest. It would also be valuable to directly interrogate RPE health in this model.

Comparing the effects of AAV-CAG-RP2 and AAV-hGRK1-RP2 vectors in the Rp2h$^{\Delta 23/Y}$ mice may help to determine whether RP2 loss results in a primary RPE defect. However, this

experiment would only be appropriately controlled to enable accurate interpretation if the CAG-RP2 and hGRK1-RP2 vectors were found to be similarly tolerated. In addition, the dosage of CAG-RP2 and hGRK1-RP2 vectors may also need to be adjusted based on expression level data to account for differences in promoter strength.

2.4.5 Conclusions

The work described in this chapter of the thesis demonstrates the value and power of cell models of disease and human-derived retinal organoids to model IRDs and assess the efficacy of potential therapeutics. Importantly, the results of this study have strengthened the case for pursuing an AAV-mediated gene replacement therapy for *RP*-associated XLRP. However, the study also highlights the importance of examining the *in vivo* tolerance of would-be treatments in parallel to establishing proof of concept *in vitro*. The results furthermore underscore the importance of optimising therapeutic designs, including the serotype of vector, dosage of virus and promoter sequence. As discussed, it is planned that further work will be carried out in animal models to determine an optimal vector design and dosage for AAV-mediated *RP2* gene augmentation.

2.5 Materials and methods

2.5.1 Agarose gel electrophoresis

Gels were made at concentrations of 1-3% agarose in TAE buffer, depending on the resolution required. Ethidium bromide (EtBr) was added to gel mixtures at a final concentration of 0.5 µg/ml. Samples were loaded in gels with a bromophenol blue and xylene cyanol FF dye mixture (ThermoFisher Scientific, R0611), alongside an appropriate DNA ladder standard (ThermoFisher Scientific, SM0323 or SM1333). Gels were electrophoresed at 100-150V and imaged using a UV transilluminator.

2.5.2 Culture of primary dermal fibroblast cells from skin biopsies

3mm diameter skin biopsies were taken from the inner forearm of participants by medical professionals, using sterile biopsy punches (Integra Miltex; 12-460-406).

Biopsies, consisting of dermis and some subdermal fat, were immediately transferred to ice cold, sterile transportation media (see Table 2.6) and transported to the lab for processing within an hour.

All subsequent steps were performed in a laminar flow hood with sterile solutions and equipment. PBS (Thermo Scientific; 14190094) supplemented with 1% pen-strep was used to wash biopsies, after which they were transferred to fibroblast media (see Table 2.6) pre-warmed to 37°C. Using a scalpel blade, each biopsy was cut to produce 4-6 pieces of roughly equal size. Each biopsy piece was placed in a well of a Nunc 4 well plate containing ~500µl fibroblast culture media. Before transfer of the tissue, a single short score was made in the centre of the well using a scalpel blade, to encourage adherence of the biopsy. It was important not to make the score the full length of the well or to make multiple cuts, as this would limit fibroblast outgrowth. Additionally, plates and media were pre-equilibrated in an incubator for 30 minutes before use (37°C, 5% CO_2).

After a biopsy piece was placed in a well, the level of media was reduced until the topmost part of the biopsy was exposed. This was to prevent biopsies from floating above the plate surface, particularly if there was a lot of fat included in the tissue.

Empty spaces in plates were filled with PBS to prevent evaporation of the minimal amount of fibroblast media biopsy wells. Plates were then placed in an incubator (37°C, 5% CO_2) and checked daily. The media was half-changed every 2-3 days, to minimise disturbance of biopsies before they had fully adhered to the plate surface. This also ensured that any secreted growth or adherence factors would not be completely

removed.

With viable biopsy pieces, keratinocytes could often be seen growing around the tissue from approximately 3 days of culturing. Keratinocytes did not persist in culture for long, as the media formulation used was optimal for fibroblast growth. It generally took about 7 days of culturing before fibroblast outgrowth was observed. At this point, biopsies were tightly adhered to the plate surface and media volume could be increased to fully cover the tissue.

When fibroblast outgrowth extended to the edges of the culture well (3-4 weeks post-plating), cells were subcultured. Cells were split at a ratio of 1:3 or lower. Passaging generally proceeded as follows:

Passage (P)	Culture vessel	Surface area (cm^2)
0	4 well plate	1.9
1	12 well plate	3.5
2	6 well plate	9.6
3	T25 flask	25
4	T75 flask (or 3 x T75 flasks)	75

Fibroblasts were passaged when they had reached 80-90% confluency. During passaging, media was removed, fibroblasts were rinsed with PBS (Thermo Scientific, 14190094) and a minimal amount of TrypLE Express (Thermo Scientific, 12605010) was applied to stimulate detachment of cells. Culture vessels were then incubated at 37°C until the majority of cells changed from a spindle-like morphology to a rounded shape. The culture vessel was then tapped gently until cells began to float freely. An excess of full (serum-containing) media was then applied to stop TrypLE activity. In early passages, where vessel volume was limited, cells were pelleted by centrifugation at 100 x g for 5 mins and resuspended in fresh media to remove TrypLE, and then split at the appropriate ratio. In later passages (~P3+), the enzyme was simply diluted in media at a final ratio of ~1:30. Frozen cell stocks were made from P4 or 5 onwards, when cells had reached ~80% confluency. After detachment of cells with TrypLE, cells were diluted in media (1:10) and pelleted by centrifugation as normal. Fibroblasts were suspended in freezing media (Table 2.6) in cryovials and placed in a Mr Frosty at -80°C. A T75 flask typically yielded ~ 2 x 10^6 cells, which were resuspended in 1ml freezing media. The next day, cell stocks were moved to permanent storage at -80°C.

Transportation media		
Component	Source	Concentration
DMEM	Thermo Scientific; 61965	99%
Penicillin-streptomycin (10,000 U/mL)	Thermo Scientific; 15140122	1%
Complete fibroblast media		
Component	Source	Concentration
DMEM (high glucose, + Glutamax)	Thermo Scientific; 61965	76% for P0, 86 - 88% thereafter
FBS	Sigma Aldrich; F7524	20% for P0, 10% thereafter
MEM non-essential amino acids (100X)	Thermo Scientific; 11140050	1%
Sodium pyruvate (100mM)	Thermo Scientific; 11360039	1%
Penicillin-streptomycin (10,000 U/mL)	Thermo Scientific; 15140122	1% until ~P6, 0% thereafter
Amphotericin B (250 µg/mL)	Sigma Aldrich; A2942	1% until ~P6, 0% thereafter
Freezing media		
Component	Source	Concentration
DMSO	Sigma-Aldrich; D2650	10%
FBS	Sigma Aldrich; F7524	90%

Table 2.6. Fibroblast culture media formulations. Note: after ~P6, fibroblasts were cultured in antibiotic and fungicide-free media.

2.5.3 Fibroblast culture genotyping

Fibroblasts (~ 5 x 10^5) were pelleted as described in section 2.5.2, then washed in PBS and pelleted again. Supernatant was removed and cell pellets were frozen at -20°C.
Genomic DNA was isolated using the Thermo Scientific Genomic DNA Purification Kit. A 250 bp region of RP2 exon 2 encompassing both the c.358 and c.425 mutation sites was amplified using Q5 High-Fidelity DNA Polymerase (NEB; M0491L). Primer sequences and annealing temperatures are given in section 2.5.23. No template control (NTC) reactions were always included and specific amplification was verified by agarose gel electrophoresis. Amplified products were purified using GeneJet PCR Purification Kit (Thermo Fisher Scientific) and Sanger sequenced by Eurofins Genomics.

2.5.4 RT-qPCR

RNA was extracted from fibroblast cultures or snap-frozen whole retinas using the Qiagen RNeasy Mini Kit with minor modification of the given protocol. The on-column DNase digestion step was extended from 15 minutes at RT to 3 hours at 37°C to minimise genomic and AAV DNA contamination. Due to the relatively low RNA content of fibroblast cells, best results were obtained using confluent T75 flasks (~ 2 x 10^6 cells) for RNA isolation. In the case of AAV-transduced samples, 2-3 wells of a 6 well plate were used per sample, in order to better conserve viral stocks.
One-step real-time quantitative reverse transcription PCR (RT-qPCR) reactions were set up using QuantiTect SYBR Green RT-PCR Kit (Qiagen) and run on an Applied Biosystem StepOnePlus machine. The standard curve method for relative quantification was applied, using 5X serial dilutions. Three technical replicates were analysed for each sample. Fibroblast samples to be quantified were run at 1/10 - 1/50 dilutions (depending on whether 6 well plates or T75 flasks were used) against a standard curve made of serially diluted control fibroblast RNA. Retinal RNA samples were run as 1/20 dilutions against a standard curve made from high dose AAV-RP2-injected sample RNA. No template control wells were included. Additional control reactions were run without reverse transcriptase in order to assess the level of DNA carryover in RNA samples. This was particularly important when analysing transduced samples, where a low but notable amount of viral DNA was often detectable even after three hours of DNase digestion.

Thermocycling conditions for RT-qPCR were as follows:

Step	Temp (°C)	Duration	
Reverse transcription	50	20 min	
Activation of polymerase	95	15 min	Cycle repeated 39 times
Cycle denaturation	95	15 sec	
Cycle annealing/ extension	60	1 min	

When performing qPCR on AAV DNA, the initial 50°C thermocycling step was omitted. A final melt curve stage was added, and dissociation peaks were analysed to confirm the absence of primer dimers or contamination in negative controls.

Relative gene expression values were calculated using StepOne Software v.2.3 and the relevant methods outlined in the Applied Biosystems 'Guide to Performing Relative Quantitation of Gene Expression Using Real-Time Quantitative PCR.'
Target gene expression levels were normalised against β-actin expression.

2.5.5 Immunoblotting

2.5.5.1 Cell lysis

Fibroblast cultures (2 -3 wells of a 6 well plate per sample; ~$2.5x10^5$ cells per well) were rinsed with ice-cold PBS and the lysed with 250 µl radioimmunoprecipitation assay (RIPA) buffer (150 mM NaCl, 1% NP40, 0.1% sodium deoxycholate, 0.1% SDS, 50mM Tris pH 7.0) on ice. RIPA buffer was supplemented with a protease inhibitor cocktail (Sigma-Aldrich; 11836153001) just before use. After 10 minutes lysis, a cell scraper was used to ensure no cells remained adherent, then lysates were pipetted up and down multiple times, transferred to Eppendorf tubes. Lysates were kept on ice for a further 10 minutes and vortexed regularly. Debris was then pelleted by centrifugation at 10,000 x g for 15 minutes at 4°C, after which supernatant was collected, aliquoted and stored at -80°C.

2.5.5.2 *SDS-PAGE*

Protein samples were quantified using the Qubit Protein Assay Kit (Thermo Scientific; Q33212). For each sample, 20 µg protein was prepared with Pierce Lane Marking

Reducing Sample Buffer (Thermo Scientific; 39000) and boiled at 99°C for 5 minutes. Polyacrylamide gels were made up as outlined in the tables below:

12% polyacrylamide resolving gel	
Reagent	**Concentration in gel (%)**
dH_20	32.5
30% acrylamide/bis-acrylamide	40
1.5M Tris pH 8.8	25
10% SDS	1
10% APS	1
TEMED	0.1

4% polyacrylamide stacking gel	
Reagent	**Concentration in gel (%)**
dH_20	60
30% acrylamide/bis-acrylamide	13.4
1.5M Tris pH 6.8	25
10% SDS	1
10% APS	1
TEMED	0.1

Gels were placed in an electrophoresis unit filled with PAGE running buffer (25 mM Tris, 19.2 mM Glycine, 0.1% SDS). Samples were loaded alongside a protein standard ladder (NEB; P7712) and separated by electrophoresis at constant voltage (120V) for approx. 2.5 hours. Protein was then electro-transferred onto a methanol activated PVDF membrane at 12V for 2 hours in semi-dry conditions. Transfer buffer consisted of of 25 mM Tris, 19.2 mM glycine, 0.1% SDS and 20% methanol.

2.5.5.3 Western blot

All incubation steps that follow were performed on a rocker. Membranes were washed in 1X TBS-Tween (25 mM Tris, 150 mM NaCl, 2mM KCl, pH 7.4, supplemented with 0.1% Tween detergent) (3 x 10 minutes), then incubated in blocking solution (5% skimmed milk in 1X TBS-T) for 1 hour at RT. Primary antibodies were diluted in blocking solution and applied to membranes overnight, shaking at 4°C. For well characterised loading control primary antibodies such as Cyclophilin B, this incubation step could be shortened to 2 hours at RT. After 3 TBS-T washes, membranes were incubated in HRP-conjugated secondary antibody solutions for 2 hours at RT then washed again.

Pierce ECL blotting substrate (Thermo Scientific; 32106) was used to initiate chemiluminescence on immunoblots, which was imaged using X-ray film.

Antibodies used for immunoblotting are detailed in section 2.5.18.

2.5.5.4 Re-probing blots

Membranes were incubated in Restore Western Blot Stripping Buffer (ThermoFisher Scientific, 21059) for 12 minutes, rocking at RT. After 3 TBS-T washes, blots were blocked and re-probed with new antibodies as before.

2.5.5.5 Densitometry

Band intensity was quantified using densitometry with ImageJ software, employing a commonly used method (Janes, 2015).

2.5.6 Immunocytochemistry

Fibroblasts were seeded in 8 well chamber slides (Miltenyi Biotec; 130-098-272) at a density of 10,000 cells per well. When ~90% confluent (~2 days later), fibroblasts were rinsed with PBS and then serum starved in FBS-free media for 24 hours to induced ciliation of cells. It was important not to serum starve fibroblasts for more than one day, as they became noticeably unhealthy after this point – seeming to retract and loose adherence.

After serum starvation, fibroblasts were rinsed with chilled PBS, fixed in 4% paraformaldehyde (PFA) for 10 minutes and then washed with PBS (3 x 10 mins). Ciliation of fibroblasts after 24 hours in 0% FBS media was confirmed by staining with a cilia marker, ARL13b.

Cells were permeabilised in 0.01% triton for 10 minutes, washed in PBS and blocked for 1 hour at RT. Blocking solution was made up of 10% donkey serum and 3% bovine serum

albumin in PBS and was used for dilution of antibodies in subsequent steps. Fibroblasts were incubated in primary antibody solution overnight at 4°C, then washed in PBS (3 x 10 minutes) and incubated in secondary antibody solution for 1 hour at RT. Cells were washed twice, then stained with DAPI (2 µg/ml) for 2 minutes and washed three times. At this point the detachable wells were removed and a coverslip was applied to the slide with Hydromount (National Diagnostics).

2.5.7 Cloning

2.5.7.1 Restriction digestion and end modification

Restriction enzymes were sourced from NEB and used as per the manufacturer's instructions. Klenow fragment (NEB; M0210S) was sometimes used to blunt cut overhangs and was heat inactivated at 75°C for 20 minutes after use. Cut fragments were gel purified (GeneJet Gel Extraction Kit; Thermo Scientific, K0691) before ligation.

2.5.7.2 Ligation

Ligation was performed using Roche T4 DNA ligase (Sigma-Aldrich; 10481220001). Reactions were set up with cut vector to insert molar ratios of 1:1, 1:3, 1:5 and 1:10, where each reaction contained at least 50 ng backbone vector. Additionally, reactions missing insert DNA or ligase were used as negative controls – enabling assessment of the level of backbone recircularisation and uncut plasmid carryover.

Purified vector and insert DNA concentrations were estimated by agarose gel electrophoresis, in comparison to fragments of known concentration (Thermo Scientific; SM0321 and SM1331). Molar ratios were calculated using the formula:

Amount insert to add (ng) = (desired insert/vector molar ratio) x (mass of vector (ng)) x (insert length (bp)/vector length (bp))

Ligations were incubated at 16°C overnight before transformation into competent *E. coli* cells.

2.5.7.3 Generation of competent E. coli cell stocks

The procedure was carried out using aseptic technique. Reagent solutions were sterilised by autoclaving. *E. coli* XL-1 Blue cells were streaked on selective Luria broth (LB) agar plates (25 µg/ml tetracycline) overnight at 37°C. A single colony was picked and used to inoculate a 5ml selective LB culture overnight at 37°C in an orbital incubator, shaking at 220 rpm. The next day, the starter culture was transferred to 500ml selective LB media

and grown for a further ~3 hours until they reached late exponential growth phase, indicated by an OD_{600} of 0.6-0.7. Cells were then pelleted in 20ml batches by spinning at 3000 rpm for 10 minutes. Each pellet was washed with 20ml chilled 100mM $MgCl_2$, pelleted again, then resuspended in 10ml chilled 100mM $CaCl_2$ and incubated on ice for 20 minutes. Cells were pelleted a final time and then resuspended in 1ml chilled 100 mM $CaCl_2$. Glycerol was added to a final concentration of 15%. Cell suspensions were snap frozen in liquid nitrogen immediately after the addition of cryoprotectant. Batches of competent cells were tested by transformation with serial dilutions of plasmid DNA. When transformed with 10 ng plasmid, competent cells prepared using this procedure should yield at least 100 colonies per plate.

2.5.7.4 Transformation

Approximately 10 ng plasmid, or half of a ligation reaction, was transferred to Eppendorf tubes and made up to 100µl with chilled 100 mM $CaCl_2$. 200 µl competent *E. coli* cells were then added and tubes were incubated on ice for 30 minutes. Cell suspensions were heat shocked in a 42°C for 2 mins, then immediately placed back on ice for 10 minutes. Cells were transferred to 2.7ml pre-warmed LB and grown at 37°C for 90 minutes in an orbital shaker. At this point, the culture was antibiotic-free to allow adequate time for expression of antibiotic-resistance genes in successfully transformed bacterial cells. After incubation, 100 µl of liquid culture was plated onto selective LB agar plates (100µg/ml ampicillin or 50µg/ml kanamycin). Plates were incubated at 37°C for ~16 hours and checked for transformed colonies the next day.

2.5.7.5 Selection of correct clones

Colonies resulting from transformation of ligation reactions were mini prepped (GeneJET Plasmid Mini Prep Kit; Thermo Scientific, K0502) and screened for correct clones using diagnostic restriction digests. Expression cassettes of successful constructs were Sanger sequenced fully (Eurofins Genomics).

2.5.8 Construct sequence information

All constructs for packaging into AAV particles were cloned into the pAAV-MCS backbone (accession no. AF396260.1), which contains AAV2 ITR sequences.

Constructs also contained the following key sequences:

pAAV-CAG-RP2

- CMV IE enhancer (661-1024 bp from GenBank: X03922)
- CBA proximal promoter/intron 1 (251-1542 bp of GenBank: X00182; 1538-39 bp AG were changed to CA)
- Human RP2 CDS (190-1270 bp of RefSeq: NM_006915.2)
- RP2 3'UTR fragment (1271-2440 bp of RefSeq: NM_006915.2) and RP2 poly(A) (50341-50580 bp of RefSeq: NG_009107.1)
- minimal rabbit B-globin poly(A) (Levitt et al., 1989)

pAAV-CAG-EGFP

- CMV IE enhancer (661-1024 bp from GenBank: X03922)
- CBA proximal promoter/intron 1 (251-1542 bp of GenBank: X00182; 1538-39 bp AG were changed to CA)
- EGFP (GenBank: U55761)
- hGH polyadenylation signal (from pAAV-MCS)

2.5.9 AAV production

Endotoxin-free mega preps of pAAV-CAG-EGFP, pAAV-CAG-RP2, pHelper (Agilent Technologies) and rep/cap plasmids (pAAV2/2, pAAV2/5 (Hildinger et al., 2001) and pAAV2/8 (Penn Vector)) were produced using the EndoFree Plasmid Mega Kit (Qiagen). The total quantities of plasmid required per AAV preparation were: 1.25 mg AAV genome plasmid, 1.25 mg rep/cap plasmid and 2.5 mg pHelper.

AAV preparations were produced by Naomi Chadderton using a helper virus-free triple transfection method in HEK293 cells (ATCC; CRL-1573). AAV was purified from HEK 293 cell lysates by precipitation with polyethylene glycol and caesium gradient centrifugation. Chosen fractions underwent dialysis against PBS with 0.001% Pluronic F68.

2.5.10 AAV titering

Viral genome (vg) titers were determined by qPCR using primers targeting the transgene of interest (*RP2* or *EGFP*) or the shared CMV enhancer element. Although commercially validated ITR primers are available that could be used to titer any AAV sample, it was decided against using this quantification method because it could include AAV particles in which the plasmid backbone was incorporated instead of the expression cassette.

AAV samples were diluted 1/15 and treated with DNase (Promega; M6101) to digest any residual plasmid DNA or HEK 293 cell genomic DNA. Samples were then incubated with Proteinase K (Thermo Scientific; 25530) to degrade capsid protein, facilitating access to the viral genome for amplification.

The standard curve method was used for absolute quantitation of viral genome copy numbers, using 10X serial dilutions of a plasmid containing the targeted region.
Plasmid copy number was calculated using the equation:
Single-stranded copy number in 1g DNA =
(2 x Avogadro's number)/(molecular weight of plasmid)
As an average base pair is 650 Daltons, plasmid molecular weight is calculated by multiplying length (bp) by 650.
The result of the above equation is multiplied by 1E9 to convert to copy number/ng, and then multiplied by plasmid concentration as ng/µl (determined using a NanoDrop). The final result is the number of single-stranded plasmid copies per µl of plasmid solution.
Alternatively, an online copy number calculator was used:
http://cels.uri.edu/gsc/cndna.html

AAV preparations were titered as follows:

AAV prep	**Titer (vg/ml) RP2/EGFP primers**	**Titer (vg/ml) CMV primers**
AAV2/2-CAG-RP2	4E10	2E10
AAV2/5-CAG-RP2	2.7E12	1.9E12
AAV2/8-CAG-RP2 P1	1E12	4E11
AAV2/8-CAG-RP2 P2	1.5E12	6.7E11
AAV2/2-CAG-EGFP	2.2E11	4.1E10
AAV2/5-CAG-EGFP	1.7E12	3.6E11
AAV2/8-CAG-EGFP	8.9E11	9.8E10
AAV2/8-Rho-EGFP	2.4E12	N/A

CMV primers, targeting the CMV enhancer region, gave consistently lower values than primers targeting transgenes, reporting an average of 4 fold lower viral genomes. This is likely due to the CMV enhancer element's close proximity to the left ITR, which forms a hairpin structure. When tested on an AAV bicistronic construct that contained a CMV enhancer element in a more central position (not shown), the titer values obtained using CMV and transgene (EGFP) primer sets were almost identical.

It was therefore decided to use the titer values obtained using RP2 and EGFP primers when calculating AAV dosage in subsequent experiments.

2.5.11 AAV transduction of primary fibroblasts

Fibroblasts were seeded as outlined in 8 well chamber slides ($1x10^4$ cells per well) or 6 well plates ($5x10^4$ cells per well) in normal media. The next day, media was replaced with a minimal amount of reduced serum media (2% FBS) – 100-150µl per well of an 8 well chamber slide or 1ml per well of a 6 well plate. FBS content was reduced in order to minimise possible interaction of serum proteins with AAV particles. AAV was added to the well and mixed with the media by gently pipetting. Cells were incubated with AAV overnight. Empty neighbouring wells were filled with PBS in order to reduce evaporation of culture media.

The next day, the media level was topped up to the normal recommended volume (~3 times the minimal level used for transduction), to a final concentration of 10% FBS.

The next day, when cells were ~90% confluent, wells were rinsed with PBS and fibroblasts were serum starved in serum-free media for 24 hours.

2.5.12 ARL3 activation assay

Specific immunoprecipitation and quantification of activated Arl3 was attempted with fibroblast cultures (confluent, ciliated T75 flasks) and murine retinal samples using the Arl3 Activation Assay Kit (NewEast Biosciences; 83001). The kit protocol for adherent cell culture samples was followed. Retinal samples were lysed in 250 kit lysis buffer using a tissue homogeniser and then processed in the same way as cell culture lysates thereafter. For both C5 and R120X-A cells, protein was extracted from three T75 flasks, then pooled together, quantified using the Qubit, and split into 3 different tubes with 2mg total protein. Protein extracted from 2 wild-type 129 mice was also pooled and then split into 3 tubes with 0.5 mg protein. With each set of three, one sample was to be assessed for

endogenous Arl3-GTP and the other tubes functioned as positive and negative controls. Positive controls underwent *in vitro* loading with GTPγS, while negative controls were loaded with GDP, as per kit instructions.

2.5.13 Purification of recombinant GST-tagged proteins

The GST pull down protocol used was based on that described by Jing (2012). GST plasmids (based on pGEX; GE Healthcare) were transformed into E. coli XLI-blue cells. Single colonies were used to inoculate 2ml starter cultures in 2x YT selective media (100 µg/ml ampicillin), which were incubated at 37°C overnight in an orbital shaker. The next morning, starter cultures were used to inoculate 400ml selective cultures at a 1:100 dilution. These were shaken at 37°C for roughly 3 hours, then IPTG was added at a final concentration of 1mM to induce GST-tagged protein expression and cultures were agitated at 30°C for 1 hour. Bacterial cells were pelleted by centrifugation (7700 x g for 10 minutes), resuspended in 20 ml chilled PBS supplemented with protease inhibitor (Sigma-Aldrich; 11836153001) (PBS-PI) and placed on ice. For bacterial lysis, 200µl lysozyme (10 mg/ml) was added, and cell suspensions were subjected to 3 freeze thaws and then sonicated until the solution turned semi-transparent. Debris was removed from lysates by centrifugation at 8000 x g for 10 minutes.

Glutathione Sepharose 4B beads (Thermo Scientific, 11594935) were shaken into a homogenous slurry. 1ml beads were transferred to a 15 ml falcon tube and pelleted at 500 x g for 5 minutes. The ethanol storage solution was then decanted and beads were washed in 10 ml PBS to remove any residual ethanol, span down again and resuspended in 1 ml PBS-PI to make a 50% bead slurry.

400 µl of 50% bead slurry was added to each 20 ml batch of cell lysate and incubated on a roller for 1 hour at RT. Beads were then sedimented by centrifugation and washed with 2 ml PBS-PI three times, each time sedimented by centrifugation. A final wash was performed with RIPA buffer (supplemented with protease inhibitors). The GST-bound 'bait beads' were then resuspended in 1 ml RIPA and kept on ice.

At this point, the purified proteins were analysed using SDS-PAGE. 20 µl GST-beads were boiled with 20 µl 2X reducing sample buffer for 10 mins, then electrophoresed as outlined in section 2.5.5.2. Gels were then stained with PageBlue (Thermo Scientific; 24620) to visualise separated proteins.

2.5.14 Animals

129 S2/SvHsd (Harlan UK Ltd), C57BL/6J (Jackson Laboratory) and *Rp2h*$^{\Delta 23/y}$ (Dr Toby Hurd, University of Edinburgh) mice were maintained under specific pathogen-free (SPF) housing conditions. Procedures were performed in accordance with the European Communities Regulations 2002 and 2005 (Cruelty to Animals Act) and the ARVO 'Statement for the Use of Animals in Ophthalmic and Vision Research.'

2.5.15 Subretinal injection

Subretinal injections of AAV in mice were performed by Dr Paul Kenna, using a protocol previously described by Palfi et al. (2010).

2.5.16 Tissue processing

Mice were sacrificed by CO_2 inhalation.

2.5.16.1 Samples for histology:

Eyes were enucleated using McPherson forceps and fixed in 4% PFA at 4°C overnight. Tissue was then washed in PBS and dissected using a Vannas scissors and forceps under a stereomicroscope. Eyes were cut along the corneal limbus for removal of the cornea and lens. Eye cups were washed in PBS (3 x 10 minutes) and then cryoprotected in increasingly concentrated solutions of sucrose in PBS: 10% and 20% for 20 mins at RT, and 30% sucrose overnight at 4°C. An equal volume of optimal cutting temperature compound (OCT) was added to samples for 15 mins at RT. Samples were transferred to plastic moulds filled with OCT, embedded by freezing with liquid nitrogen and stored at -20°C. OCT sample blocks were sectioned in 12 µm slices using a Leica CM1900-1-1 cryostat. Sections were applied to room temperature slides, dried at room temperature for 1 hour and then stored at -20°C.

2.5.16.2 Samples for RNA extraction:

Eyes were dissected *in situ* immediately after sacrifice. The back of the eye was held with forceps, while a straight scalpel blade was used to cut across the eye in one movement and remove the lens. The retina was then gently pushed out of the eyecup with the forceps and snap frozen on dry ice.

2.5.17 Immunohistochemistry

Sections were removed from freezer storage and dried for 30 mins at RT. A PAP pen was used to draw hydrophobic rings around sections on slides. Sections were hydrated in PBS

for 15 mins in Coplin jars. Slides were dried around the outside of the PAP ring using tissue to remove excess liquid, 120 µl blocking solution was applied and sections were incubated in a humidified chamber for one hour at RT. The blocking solution consisted of 5% donkey serum and 0.3% Triton X-100 diluted in PBS. After incubation, blocking solution was removed. Sections were then incubated in 120ul primary antibody diluted in blocking solution at 4°C overnight. The next day, sections were washed in PBS (3 X 10 mins) and then incubated with secondary antibody diluted in blocking solution for two hours at RT. Sections were washed (2 x 10 mins), stained with DAPI (1µg/ml) for 10 mins and washed again (3 x 10 mins). Coverslips were applied using Hydromount (National Diagnostics) or Aqua Poly/Mount (Polysciences Inc.) aqueous mounting solutions.

2.5.18 Antibodies

Primary antibodies

Antibody	**Source**	**Working dilution**
Rabbit anti-fibroblast surface protein	Sigma-Aldrich; F4771	ICC: 1/100
Rabbit anti-RP2	Proteintech, 14151-1AP	ICC/IHC: 1/100; IB: 1/500
Rabbit anti-Cyclophilin B	Sigma-Aldrich; SAB4200201	IB: 1/1000
Chicken anti-GFP	Abcam; ab13970	ICC: 1/1000
Mouse anti-GM130	BD Biosciences; 610822	ICC: 1/100
Mouse anti-Arl3-GTP	NewEast Biosciences; 26925	IP: 1/100
Mouse anti-Arl3	NewEast Biosciences; 26070	IB: 1/1000
Goat anti-GFAP	Abcam; ab53554	IHC: 1/200
IBA1	Wako Chemicals USA; 019-19741	IHC: 1/100

Secondary antibodies

Antibody	**Source**	**Working dilution**

Donkey anti-rabbit Cy3	Jackson ImmunoResearch; 711-165-152	ICC/IHC: 1/400
Donkey anti-chick Alexa Fluor 488	Jackson ImmunoResearch; 703-545-155	ICC/IHC: 1/400
Donkey anti-mouse Cy3	Jackson ImmunoResearch; 715-165-150	ICC/IHC: 1/400
Donkey anti-goat Cy3	Jackson ImmunoResearch; 705-165-147	ICC/IHC: 1/400
Donkey anti-rabbit HRP	Jackson ImmunoResearch; 711-035-152	IB: 1/10,000
Goat anti-mouse HRP	Jackson ImmunoResearch; 115-035-003	IB: 1/10,000

2.5.19 Microscopy

Fibroblasts were imaged using confocal microscopy (Zeiss, LSM 710).). Images were acquired at multiple focal distances to ensure the entire sample was captured in focus. These Z-stacks were then merged into a 2D image using the 'maximum intensity projection' function in Fiji. The projected image consists of the highest value for each pixel found across all Z slices.

Retinal sections were imaged using an Olympus IX83 inverted motorised epifluorescent microscope with a motorised stage and cellSens software. The enhanced focus imaging (EFI) tool was used, which works similarly to Z stacking, capturing multiple images along the z-axis and combining them into one in-focus image. Frame stitching was used to create composites of whole retinal sections.

2.5.20 Image analysis

2.5.20.1 GM130 area measurement

GM130 immunoreactivity was assessed in fibroblast images taken using a 20X objective. Cells on the edge of the field of view, in which the stained area was incomplete, were removed from the image. GM130-positive area was isolated using the 'Auto-Threshold' function and measured using the 'Analyse Particles' tool in Fiji. The number of cells per image ranged from 28 to 231, with an average of 72. Total GM130 area was measured per image, then divided by the number of cells featured in that image to calculate the

average GM130 area per cell. This was repeated on 6 to 15 images per cell type. Cell numbers per image were determined using the Fiji Cell Counter plug-in.

2.5.20.2 Measurement of ONL thickness

ONL length was measured at 8-12 points across each DAPI-stained whole retinal cryosection using the straight line tool in Fiji and values then were averaged. For injected eye samples, only transduced retinal regions (RP2/EGFP positive) were considered.

2.5.20.3 Quantification of protein expression in IHC samples

Fluorescence intensity across each retinal section was quantified as integrated density (pixel intensity x area) using Fiji. This value was then normalised against the DAPI-positive area of the section, which was calculated using the 'Threshold' and 'Measure' functions of Fiji. In the case of GFAP measurement, only transduced retinal areas (EGFP-positive) were analysed (non-transduced areas were blocked out using the 'Fill' tool before measurement).

When assessing samples stained for IBA1 and IgG, all non-neuroretinal areas were manually blocked out to eliminate non-specific background signal. The photoreceptor outer segment layer was additionally removed before quantification of IBA1/IgG immunoreactivity for the same reason.

2.5.21 RP2del23 mouse genotyping

DNA was isolated from ear clip tissue using the DNeasy Blood and Tissue Kit (Qiagen; 69504). A 284bp region of *Rp2* exon 2 flanking the 23 bp deletion site was amplified using OneTaq polymerase (NEB; M0482S). Primers are listed in the next section. PCR products were separated on 3% agarose gels. Amplicons from founder mice were Sanger sequenced (Eurofins Genomics) to confirm their mutation status.

2.5.22 Primers

qPCR primers		
Target	**Forward (5' to 3')**	**Reverse (5' to 3')**
RP2 (human)	AAGCAGTACAGCTGGGATCA	TCTTGAATGAGAAACTGTTGTCC
RP2 (human and mouse)	ACTGGAGCCTTCTTCCTCA	AAGCCAATAGAAGCATTGTTCC

CMV enhancer	TTACGGTAAACTGCCCACTTG	CGTGAGTCAAACCGCTATCC
β-actin	AGAGCAAGAGAGGCATCC	TCATTGTAGAAGGTGTGGTGC

Genotyping primers			
Target	**Forward (5' to 3')**	**Reverse (5' to 3')**	**Annealing temp (°C)**
RP2 (human)	CACTCTGCTACAGTTAC CATTGA	TGAACTGGAAAGCTAAT TCAGG	63 (with Q5 polymerase)
Rp2h (mouse)	GGGACCAGTGAAAGGC AGTGTC	GGCTCCAGTTGAGCTCTC CTGAC	59 (with OneTaq polymerase)

Note: forward genotyping primers were also used in Sanger sequencing reactions.

2.5.23 Statistics

GraphPad Prism 8 was used to perform statistical tests and for graph production. For each statistical test the significance threshold was set at 0.05. Normality of data distribution was assessed using the Shapiro-Wilk test, which determined whether parametric or non-parametric tests of significance were used subsequently. Data in this chapter were generally normally distributed, and all samples analysed were independent. Hence, the unpaired Student's t-test was used when comparing means of two groups and a one-way ANOVA was performed when analysing means of three or more groups.

Following ANOVA, post hoc analysis was performed using Tukey's test to compare the means of all groups to the mean of every other group. Alternatively, Dunnett's test was used to compare the means of all groups against the mean of one control group.

When GM130 area or cell densities from all groups were compiled into one large data set, the data followed a non-normal distribution. Spearman's rank-order correlation test was

used to investigate possible a correlation between the GM130 area and cell density in this nonparametric data.

3 A ‘HITI’ strategy for gene correction in rhodopsin-linked ADRP

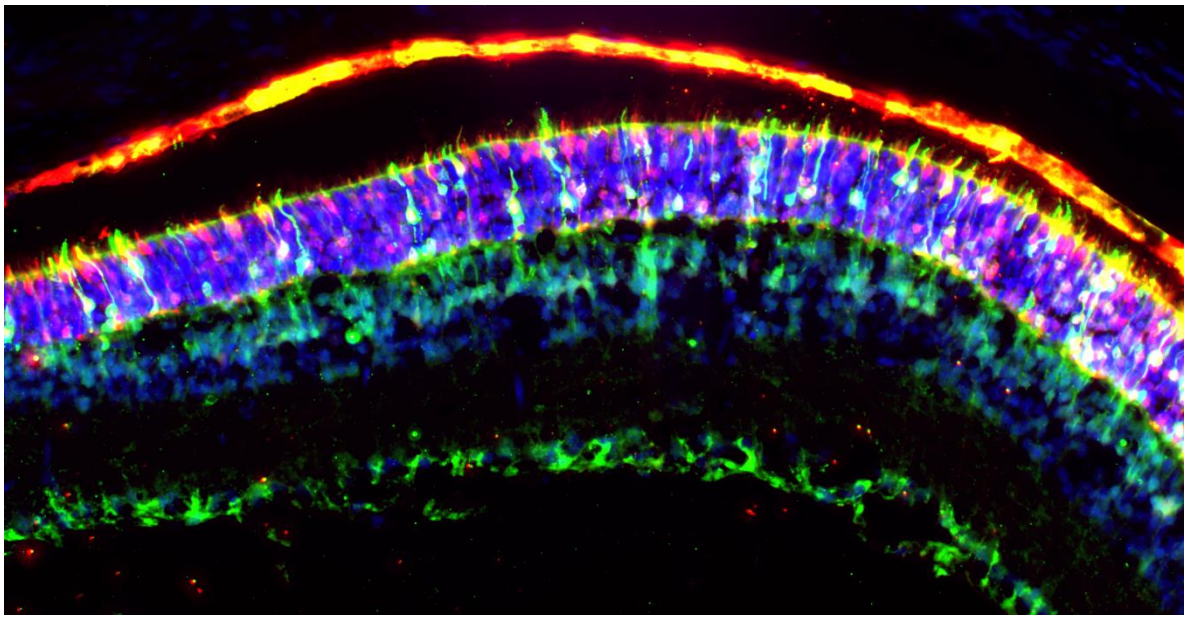

3.1 Acknowledgment of contributions

Study concept: Prof. G Jane Farrar and Dr Arpad Palfi.

RHO 5’UTR sequencing and guide RNA selection: Dr Arpad Palfi.

Manufacture of pAAV-SV40-Cas9, pAAV-hGRK1-Cas9, pAAV-hGRK1-EGFP and pRHO5UTR plasmids: Dr Arpad Palfi.

AAV production: Dr Naomi Chadderton.

Subretinal injection: Mr Paul Kenna.

Retinal cryosectioning: Dr Arpad Palfi.

General assistance: Laura Whelan, Emma Quinn, Cristina Borcea and Sukanja Rajan as part of their undergraduate/Masters thesis work.

3.2 Introduction

3.2.1 Gene editing in post-mitotic cells

As discussed in Section 1.5, gene editing holds great promise for treating inherited retinal degenerations but achieving high-fidelity modifications with sufficient efficiency in retinal cells remains a significant obstacle.

The method by which DSBs are repaired is highly dependent on cell cycle phase. Briefly, in G1 (Gap 1) cells either prepare for DNA replication or enter G0 (resting phase; quiescence). If a cell decides to divide, it enters the S (DNA synthesis) phase, then G2 (Gap 2) and mitosis (M). Homologous recombination (HR) between sister chromatids is vital for maintenance of genomic integrity during cell division, repairing DSBs formed during replication or induced by mutagens. However, recombination between homologous chromosomes in non-dividing cells could be deleterious. HDR is therefore suppressed in G1/G0 cell cycle phases, largely limited to the late S and G2 phases in dividing cells when sister chromatids are available to act as templates. In contrast, NHEJ is predominant in the G1 phase but active to some degree during most stages of the cell cycle – except during mitosis (M), when both HR and NHEJ are suppressed to protect against aberrant chromosome segregation (Zhao et al., 2017). NHEJ is also faster and more active than HDR even in dividing cells, repairing ~75% of DSBs (Mao et al., 2008).

3.2.1.1 HDR

There is a high degree of interest in exploring methods to increase the rate of HDR in post-mitotic cells. For example, one strategy seeks to improve HDR efficiency by physically linking donor DNA and Cas9 protein, thereby increasing template availability at the target site (Devkota, 2018). Many studies have explored inhibition/downregulation of NHEJ enzymes (Liu et al., 2019) or stimulation of key HR pathway components (Song et al., 2016, Devkota, 2018). However, it should be borne in mind that DNA repair processes are essential for maintaining genomic stability and that general, prolonged alteration of repair pathway dynamics could therefore have deleterious effects. Excitingly, delivery of *E. coli* recombinase A (RecA) protein, which facilitates DNA strand exchange (homologous to the eukaryotic Rad51 protein), alongside standard CRISPR-Cas components increased HDR activity in photoreceptors and enabled correction of a point mutation in the rd1 model of ADRP in electroporated cells (Cai et al., 2019). As RecA is linked to the sgRNA, it should be predominantly localised to the target site. Efficiency of this method may be

improved further by converting this strategy into an AAV platform (likely a dual AAV system, as the RecA CDS is 1062 bp). However, it should be noted that mice were treated at P0-P3 in this study. It is thought that photoreceptor proliferation peaks in this timeframe and continues at lower levels until P10 (Vagni et al., 2019). It will therefore be important to assess the ability of the Cas9-RecA system to enhance HDR in adult post-mitotic photoreceptors.

It has long been known that use of AAV vectors can enhance the efficiency of homologous recombination. Russell and Hirata determined that gene targeting efficiency could be increased by 2-3 orders of magnitude if the exogenous sequence was delivered by AAV rather than plasmid or other viral vectors – reaching an efficiency of 1% in some cell types (Russell and Hirata, 1998, Hirata et al., 2002). Addition of an endonuclease-induced DSB was found to increase AAV-mediated gene targeting by >100 fold (Porteus et al., 2003) – though this strategy was found to be similarly efficient to that of a plasmid and endonuclease combination. Of note, single-stranded donors make for better HDR templates than dsDNA (Richardson et al., 2018). The ability of AAV to boost HR has therefore been hypothesised to stem from its high transduction efficiency, combined with the linear, single-stranded nature and long term stability of its genome (Alexander and Russell, 2015). It has also been proposed that DNA damage responses potentially elicited by AAV ITR sequences may upregulate the HR pathway (Hirsch, 2015).

Nishiyama et al. (2017) achieved a relatively high rate of *in vivo* HDR-mediated gene knock-in (~15%) in cortical neurons using a dual AAV system to supply the Cas9, sgRNA and donor template components over 2-3 weeks. Hu et al. (2020) attempted to rescue photoreceptor degeneration in a *Rpgr*$^{-/y}$;*Cas9*$^{+/WT}$ mouse using a HDR strategy, with subretinal injection of separate AAVs encoding an sgRNA and a donor template. Very interestingly, they observed no gene correction 1 month post-injection (PI) but an average of 85% editing efficiency in treated areas at 6 months, which translated to significant preservation of ONL thickness up to 12 months PI. This level of HDR-mediated editing is unprecedented in post-mitotic cells. It is somewhat puzzling that efficiencies of up to 96% were observed in retinal samples, as transduction is normally restricted to photoreceptors and RPE after subretinal injection and the murine neuroretina is comprised of ~81% photoreceptors (Jeon et al., 1998). However, it is possible that RPE was included with the neuroretinal samples harvested and led to inflation of the

efficiency values. It will be important for these results to be replicated in scenarios where Cas9 is delivered exogenously and where other loci are targeted. Even so, this is an important observation that raises the exciting possibility that previous *in vivo* HDR tests in post-mitotic cells may simply have been evaluating editing efficiency too early to see the desired effects.

3.2.1.2 NHEJ and HITI

As mentioned in section 1.5.3, NHEJ-induced specific knock-out of pathogenic alleles has demonstrated benefit in non-haploinsufficient models of dominant RP (Bakondi et al., 2016, Li et al., 2018).

Other researchers have embraced NHEJ as a means of achieving knock-in of transgenes by ligation of cut genomic and donor DNA ends (reviewed by Yamamoto and Gerbi, 2018). Although NHEJ is traditionally thought of as an error-prone and somewhat unreliable process, this idea is being increasingly challenged. DSBs induced by ionising radiation, for example, require processing of incompatible DNA ends before end-joining, and so mutagenesis may be predominantly due to end-processing rather than ligation. The rate of error-free NHEJ repair of compatible ends has been noted to be as high as 75%. This is likely an underestimate as, in the absence of a donor template, a correctly repaired DSB would be continually recut by the Cas9/sgRNA complex until an indel disrupts the target site – making detection of mutations inherently more likely (reviewed by Bétermier et al., 2014).

In the ObLiGaRe (obligate ligation-gated recombination) system, heterodimeric ZFNs are utilised to cleave genomic and donor DNA with compatible overhangs that can be readily ligated (Maresca et al., 2013). A surprisingly high level of precision was observed using this method of gene knock-in, with 75-100% of integration junctions indel-free (Maresca et al., 2013, Yamamoto et al., 2015, Yamamoto and Gerbi, 2018).

Suzuki et al. (2016), developed a similar system based around CRISPR-Cas induced blunt DSBs. Homology-independent targeted integration (HITI) enables preferential integration of a transgene in the desired direction through strategic orientation of sgRNA target sites flanking the donor sequence (Fig. 3.1). When tested *in vitro*, HITI gene knock-in was approximately 10 fold more efficient than HDR, with only 2.1% of HITI integrations in the

wrong orientation. In addition, the majority of knock-in events (~75-90%) were free of indels at the ligated junctions (Suzuki et al., 2016, Yamamoto and Gerbi, 2018).

In vivo efficiency of HITI-based gene knock-in was demonstrated to be 10.6% in cortical neurons two weeks after stereotaxic injection of a dual AAV vector platform. This strategy was then adapted to rescue retinal degeneration in the RCS rat model of *MERTK*-associated ARRP (Fig. 3.2). Although editing efficiency was not quantified in retinal cells, Mertk mRNA expression was restored to 4.5% of the WT level in eyes subretinally injected with AAV-HITI vectors. This translated to significant increases in ONL thickness and outer retinal ERG responses. In comparison, eyes treated with AAVs to mediate HDR-based gene correction of the deletion did not vary significantly from untreated controls. Interestingly, the end-joining precision rate (% indel-free sites) was 96% at the 3' junction but 32% at the 5' junction in treated retinas (Suzuki et al., 2016). It is possible that precision of integration varies depending on the locus targeted, cell type context and delivery system used. However, 100% fidelity may not be necessary when knocking a sequence into a non-coding region, as long as care is taken to avoid disruption of key regulatory and splicing motifs. As previously mentioned, a gene editing therapeutic capable of inducing deletions, inversions and indels in an intronic region is currently in clinical trial (Maeder et al., 2019).

HITI-based knock-in thus appears to be a promising strategy for correction of IRD-causing variants. Indeed, subsequent studies exploring HITI-mediated editing of other RP-related genes are beginning to yield results (Llado Santaeularia et al., 2019)[23](Chou et al., 2020).

A summary of studies to-date that have used gene-editing strategies to edit IRD-related genes *in vivo* is provided in Table 3.1. Several other studies have used CRISPR-Cas to examine the effects of IRD allele correction/nullification in cells stably transfected with a pathogenic allele (Panagiotopoulos et al., 2020) or patient-derived fibroblasts (Fuster-García et al., 2017), iPSCs (Burnight et al., 2017)(Huang et al., 2019, Bohrer et al., 2019, Sanjurjo-Soriano et al., 2020), iPSC-RPE (Sinha et al., 2020) and retinal organoids (Deng et al., 2018).[24]

[23] Llado Santaeularia et al. 2020 is a conference abstract (not peer-reviewed).
[24] Note: in this paper, CRISPR-Cas was used to correct a mutation in an iPSC line before differentiation to retinal organoids.

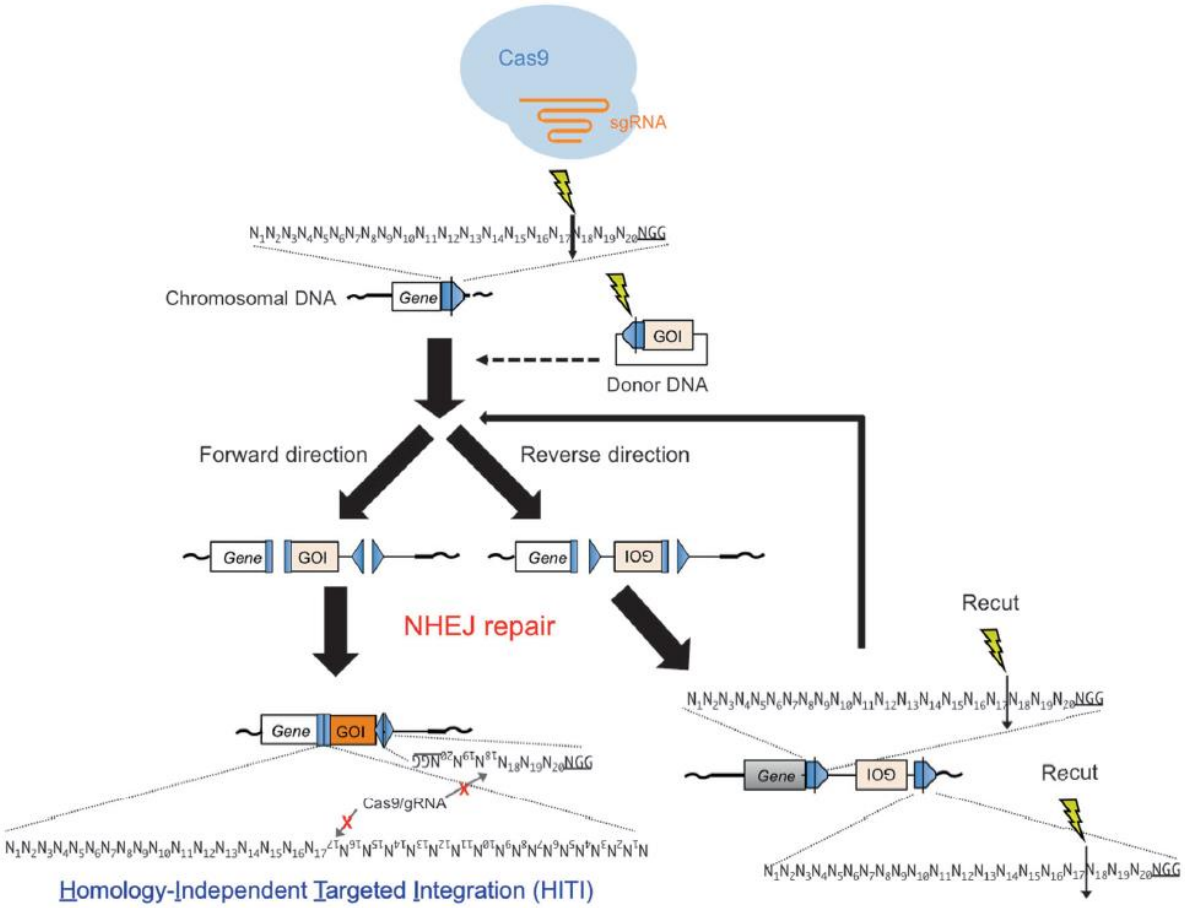

Figure 3.1. Schematic of HITI-based gene knock-in using a plasmid donor sequence.
SgRNA target sites are depicted as blue pentagons, which are split into rectangles and triangles by a black line representing the cut site (3 bp upstream of the PAM). The sgRNA target site in genomic DNA is included in reverse orientation in the donor plasmid. A SpCas9/sgRNA complex cuts the chromosomal and plasmid target sequences. The linearised donor sequence is inserted into the genomic DSB via NHEJ ligation. If the donor is integrated in the wrong orientation, the sgRNA target sites are reformed and recut so that the sequence can be continually freed until it is inserted in the desired direction or an indel disrupts a target site. GOI = gene of interest.
Figure reproduced from Suzuki and Izpisua Belmonte, 2018.

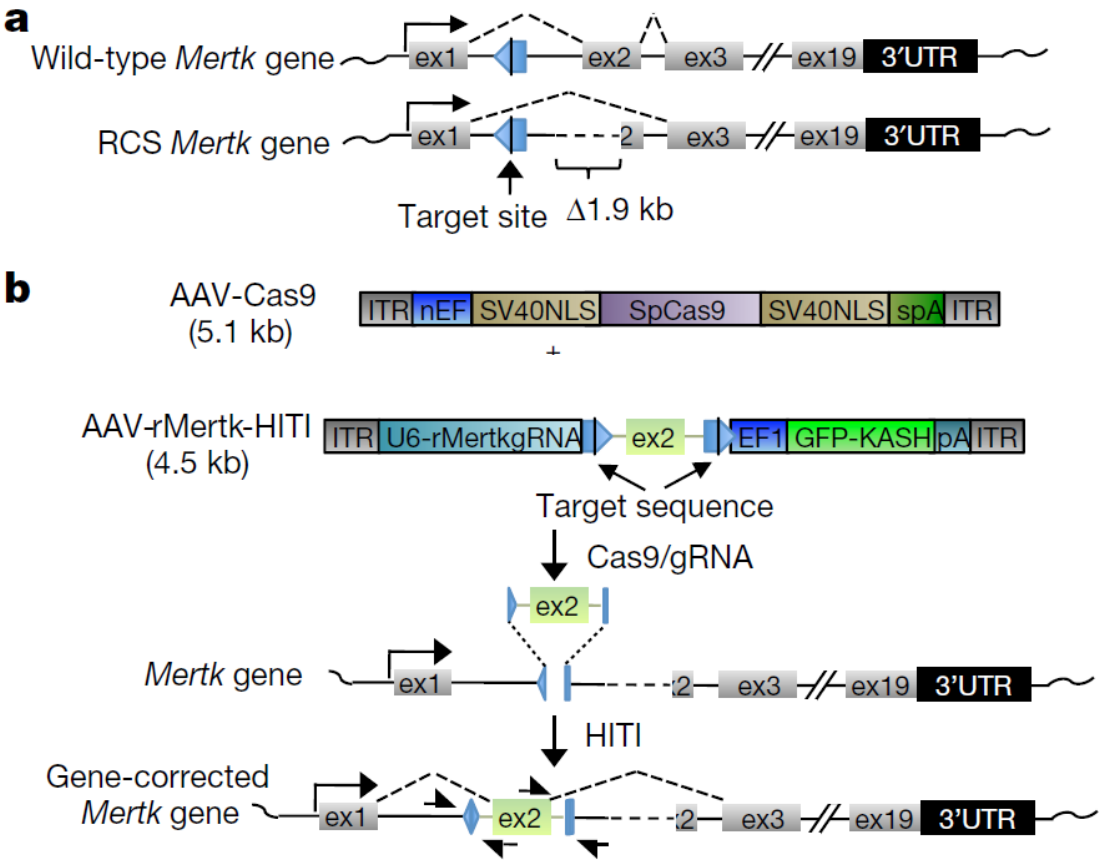

Figure 3.2. Schematic of HITI-based gene correction using a dual AAV platform.

(a) Wild-type and mutated alleles of the *Mertk* gene are shown. In the RCS rat model of RP, exon 2 is skipped due to a 1.9 kb deletion that includes part of exon 2 and its splice acceptor site. The selected sgRNA target site in intron 1 is depicted as a blue pentagon, which is split by a black line representing the cut site.

(b) A SpCas9 expressing vector (AAV-Cas9) is combined with AAV-rMertk-HITI, which contains a sgRNA expression cassette, a sgRNA target site-flanked exon 2 replacement sequence (including appropriate splice sites) and a GFP reporter expression cassette. After cleavage of the genomic and AAV target sites, the donor exon 2 is inserted into intron 1, restoring correct splicing of Mertk.

GFP is fused to the KASH nuclear transmembrane domain that leads to outer nuclear membrane localisation. Black half arrows represent primers used to amplify the edited genomic region.

Figure reproduced from Suzuki et al. 2016, with slight modification.

Study	Gene	Model	Strategy	Editing results
Bakondi et al., 2016	*Rho*	S334ter-3 rat.	Specific knock-out of S334ter allele. SpCas9 + sgRNA in plasmid.	Editing efficiency: ~35% in transfected area. Increased PR no. and OKR in treated eyes.
Latella et al., 2016	*RHO*	Humanised P23H mouse.	Specific knock-out of P23H allele. SpCas9 + 2 sgRNA in plasmid.	Editing efficiency: ~18% in transfected area.
Li et al., 2018	*Rho*	P23H mouse.	Specific knock-out of P23H allele. SpCas9-VQR + sgRNA in plasmid.	Editing efficiency: 45% in transfected area. Increased ONL thickness.
Tsai et al., 2018	*Rho*	P23H and D190N mice.	Ablation of both WT and mutant m*Rho*, combined with supply of WT h*RHO*. SpCas9 + 2 sgRNA + h*RHO* expression cassette. Dual AAV2/8 system.	Editing efficiency: not quantified.
Giannelli et al., 2018	*Rho*	P23H mice.	Specific knock-out of P23H allele. SpCas9-VQR + sgRNA. Plasmid electroporation (subretinal) or dual AAV9.PHP.B injection (intravitreal).	Editing efficiency: **Plasmid electroporation:** 77-88% in transfected area. Increased ONL, longer OS. **AAV transduction:** 50% in highly transduced regions; 3% overall.
Ruan et al., 2017	*Cep290*	WT mice.	Deletion of intronic region corresponding to IVS26 mutation. SpCas9 + 2 sgRNA in dual AAV2/5 system.	Editing efficiency: ~20% of retina. (4 wk PI).
Maeder et al., 2019	*CEP290*	Humanised CEP290 IVS26 mice, WT NHPs.	Deletion or inversion of IVS26 intronic region. SaCas9 + 2 sgRNA in single AAV2/5.	Editing efficiency: >10% of retina in mouse model. Up to 30% in NHPs with sgRNAs targeting region corresponding to human mutation. (6 wk PI).

(Burnight et al., 2017)	*RHO*	Humanised P23H pig.	Allele-specific knock-out of RHO P23H. SaCas9 + sgRNA in single AAV2/5.	Editing efficiency: ~2% of retina overall. (3 wk PI).
(Cai et al., 2019)	*Pde6b*	rd1 mouse.	HDR correction. SpCas9 or SpCas9/RecA + sgRNA in plasmid + ssODN.	Editing efficiency: not quantified. **SpCas9:** no PDE6B expression detected. **SpCas9/RecA:** Restored PDE6B protein to 2% WT level. Increased photoreceptor survival and improved ERG response relative to Cas9 treated eyes.
(Vagni et al., 2019)	*Pde6b*	rd10 mouse.	HDR correction. SpCas9 in plasmid + ssODN.	Editing efficiency: 0.2% of retina. Improved OKR and ERG response. (3 mth PT).
(Suzuki et al., 2016)	*Mertk*	RCS rat.	HITI to knock-in corrected exon. SpCas9 + sgRNA + donor in dual AAV2/8 system.	% not quantified. MERTK mRNA restored to 4.5% WT level. ONL thickness and ERG responses improved. (4-5 wk PT)
(Jo et al., 2019)	*Rpe65*	rd12 mouse.	HDR correction. SpCas9. Dual AAV2/2 system.	~1% HDR and 1.6% NHEJ in-frame deletion of PTC in RPE cells. Improved ERG response. (7 mth PT)
(Suh et al., 2020)	*Rpe65*	rd12 mouse.	Base editing. Adenine base editor + sgRNA in lentivirus.	Editing efficiency: 16% of RPE cells. Improved OKR, VEP and ERG response. (5 wk PT).
(Chou et al., 2020)	*RS1*	WT mice.	HITI knock-in of RS1-GFP into Rosa26 safe harbour. Cas9 + sgRNA + donor in 2 plasmids delivered via nanoparticles (intravitreal).	Editing efficiency: not quantified.
(Nishiguchi et al., 2020)	*Gnat1*	$Gnat1^{IRD2/IRD2}$; $Pde6^{ccpfl1/cpfl1}$ mouse.	Deletion of mutated intronic region and replacement via HITI or MMEJ. SaCas9 + 2 sgRNAs + donor in dual AAV2/8 system.	Editing efficiency: **HITI:** 4.5% of rods. **MMEJ:** 11.1% of rods. Improved OKR, VEP and ERG response. (1 mth PT).

(Hu et al., 2020)	*Rpgr*	Rpgr $^{-/y}$; SpCas9$^{+/WT}$ mouse.	HDR correction SgRNA and donor supplied via dual AAV2/8 system.	Editing efficiency: 1 mth PT: 0% 6 mth PT: 85%. Increased ONL thickness in treated area.

Table 3.1. In vivo CRISPR-Cas9 editing of IRD-related genes.

Strategies to correct IRD-causing alleles via somatic gene editing published to-date are summarised. Plasmid vectors were electroporated and AAV vectors were administered subretinally unless otherwise specified. Depending on the paper, gene editing efficiencies are expressed as a proportion of transfected/transduced cells, as a percentage of the total number of a particular cell-type, or as a proportion of a whole retinal sample. PT = post treatment; MMEJ = microhomology-mediated end joining (will be discussed in section 3.4.4); ssODN = single-stranded donor oligonucleotide; SpCas9-VQR = modified Cas9 protein with altered PAM; SpCas9/RecA = co-delivery of Cas9 and Recombinase A; VEP = visual evoked potential.

3.2.2 Suppression and replacement in rhodopsin-linked RP

HDR, base editing and prime editing may prove to be feasible approaches for correction of pathogenic point mutations or mutation hotspots in IRD genes. However, each targeted treatment would need to be independently validated. A mutation-independent strategy would circumvent this issue, maximising the patient population that could benefit from a single treatment.

One way of achieving this would be to knock-in a replacement 'mini-gene' (CDS and poly(A) signal) into the 5'UTR of a pathogenic allele, before the endogenous start codon. This should, in principle, effectively hijack the gene's promoter to drive expression of a wild-type CDS and prevent transcription of the mutant allele. This one-step suppression and replacement strategy would be applicable to all mutations downstream of the start codon in a given gene, both dominant and recessive. In the case of genes too large for AAV-delivery of a full mini-gene, a partial mini-gene or 'super-exon' (including a 5' splice acceptor site) could be inserted into an intronic region, as previously proposed to correct Cystic Fibrosis-causing *CFTR* alleles (Harrison et al., 2018). As discussed, HDR is not as efficient as NHEJ in post-mitotic cells, and this efficiency would likely further decrease with increasing template length (Li et al., 2014). The requirement for long homology arms (~0.5-2kb) to achieve knock-in of a transgene (Yamamoto and Gerbi, 2018), may also challenge the cargo capacity of AAV. In contrast, HITI could provide a relatively straightforward and efficient means of enacting a suppression and replacement strategy.

We decided to explore a 5'UTR mini-gene insertion strategy in the context of rhodopsin-associated RP. Rhodopsin was the first gene to be linked to autosomal dominant RP (McWilliam et al., 1989, Farrar et al., 1990, Dryja et al., 1990) and since then at least 195 different pathogenic mutations have been identified in this gene[25]. Combined, these variants account for 20-30% of ADRP cases and are also more rarely linked to ARRP or AD congenital stationary night blindness. Rhodopsin is a 348aa G-protein coupled receptor (GPCR) with a photon-absorbing chromophore (11-cis-retinal) that plays an essential role in the process of phototransduction (outlined in section 1.1.3). Dominant rhodopsin mutations act in a dominant negative or toxic gain of function manner. These mutations can result in protein misfolding or alterations in protein trafficking, stability, ability to

[25] http://www.hgmd.cf.ac.uk/ac/gene.php?gene=RHO [accessed: 11/11/20]

dimerise or activate transducin, or give rise to a constitutively active protein. With several possible avenues of dysfunction, it is not surprising that clinical severity can vary substantially depending on the variant implicated (Athanasiou et al., 2018).

A variety of animal *RHO*-ADRP models have been generated (reviewed by Hafezi et al., 2000, Rossmiller et al., 2012). Our group maintains a colony of the humanised *RHO* P347S mouse (Li et al., 1996), which models one of the more clinically severe forms of ADRP. C-terminus mutations such as P347S are thought to impede trafficking of rhodopsin to the OS. The resulting accumulation of mutant protein in inner segment compartments may compromise OS renewal and saturate the cell's degradation pathways (Athanasiou et al., 2018). In *RHO* P347 mice, mutant rhodopsin protein is mainly localised in the OS. However, outer segments are shortened and an abnormal accumulation of rhodopsin-containing vesicles is evident around the IS/OS junction. Photoreceptor degeneration is quite rapid in this model; at 1 month of age an ERG deficit is evident and just 4-5 lines of photoreceptor nuclei remain, compared to ~12 rows of nuclei in control mice. By 4 months of age, the ONL is reduced to 1-2 lines of cells (Li et al., 1996).

The mutation-independent strategy of genetic suppression and replacement was originally envisioned to comprise a suppression effector, such as antisense RNA or a ribozyme, targeted to both alleles of a gene (pathogenic and wild-type) in combination with a replacement DNA sequence immune to suppression (Farrar et al., 2006, Millington-Ward et al., 1997). This approach was tested in the *RHO* P347S mouse model by subretinally injecting two AAV vectors expressing (i) a short hairpin RNA (shRNA) targeting *RHO* and (ii) a *RHO* replacement cDNA made suppression-resistant by introduction of silent mutations at wobble bases. ONL thickness, photoreceptor structure and ERG response were improved in treated retinas for a period of at least 5 months (Millington-Ward et al., 2011). This therapeutic strategy, termed RhoNova, was later acquired by Spark Therapeutics[26].

A subsequent study demonstrated rescue of a *RHO* T47R canine model using a single AAV suppression-replacement system (Cideciyan et al., 2018). A two-part suppression-replacement strategy is complicated by the need to achieve a sufficient level of RNAi knockdown without expressing the replacement gene to a toxic level. Overexpression of

[26] https://sparktx.com/press_releases/spark-therapeutics-announces-acquisition-of-genable-technologies/

wild-type rhodopsin has indeed been shown to be retinotoxic in some cases (Olsson et al., 1992). Considering this, it is possible that a dual AAV shRNA/cDNA platform would be advantageous, as it would allow more scope for fine-tuning the expression levels of these components. Alternatively, a HITI one-step suppression-replacement approach would circumvent this issue – enabling an endogenous level of transgene expression with simultaneous repression of the pathogenic allele.

3.2.3 Objectives of chapter 3

This chapter explores the feasibility of using HITI gene editing to insert a mini-gene into the 5'UTR of the human rhodopsin gene. Here, the efficiency of EGFP knock-in (Fig. 3.3) was evaluated, with a view to ultimately inserting a rhodopsin replacement mini-gene at this locus. At this early stage of the project, the goals were to:

I. Select appropriate Cas9/sgRNA target sites within the RHO 5'UTR.
II. Construct a dual AAV platform for delivery of all components necessary for EGFP knock-in at a chosen target site.
III. Assess the *in vivo* efficiency of this gene editing system in photoreceptors of the humanised *RHO* P347S murine model.

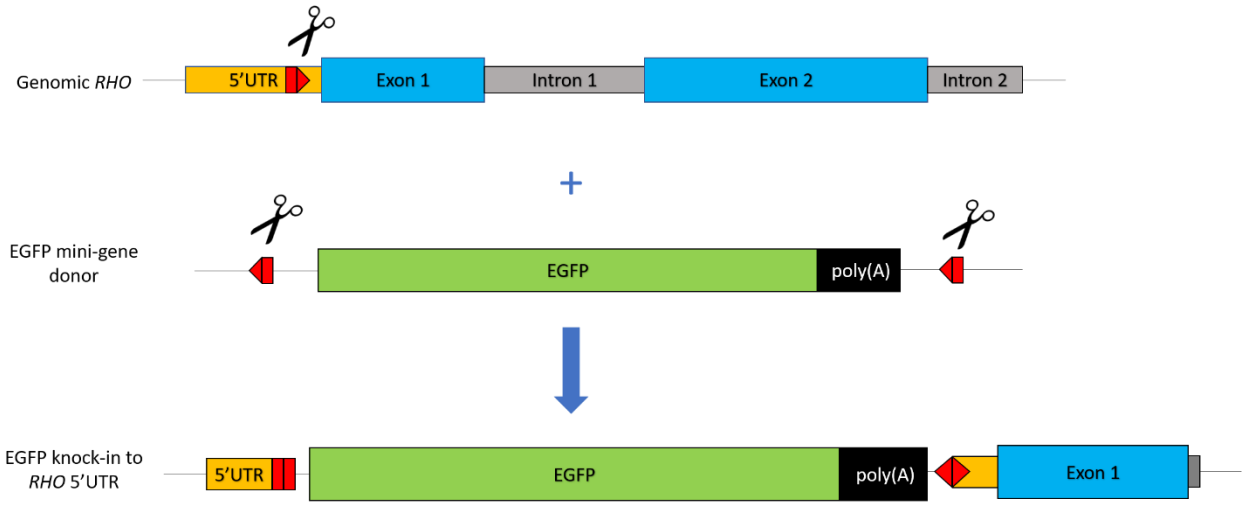

Figure 3.3. Schematic of a HITI strategy for EGFP knock-in to the *RHO* 5'UTR.

A SpCas9/sgRNA target (red pentagon) is selected in the 5'UTR of the human rhodopsin sequence. An EGFP mini-gene HITI donor sequence is synthesised with flanking target sites in the reverse orientation to that of the genomic site, and supplied via AAV. Cas9 and sgRNA, expressed by a separate AAV, form a complex (depicted as scissors) and cut each of the target sites. Cut sites are depicted as black lines through the pentagons. The EGFP minigene is then integrated into the DSB in the *RHO* 5'UTR via NHEJ. As in Fig. 3.1, the integration junctions should be cleaved until the mini-gene is inserted in the correct direction or an indel abolishes a target site.

3.3 Results

3.3.1 Guide RNA design

To implement the gene-editing strategy illustrated in Fig. 3.3, it was necessary to establish a panel of guide RNAs[27] capable of targeting the *RHO* 5'UTR region. Before screening potential gRNA sites, it was prudent to first test for sequence variation across the various models to be utilised in this study. Genetic drift is always a concern when working with isolated animal colonies and frequently passaged cell lines. It was therefore important to check for variation in the mouse colonies and cell lines in use by our lab. A 1.4kb region upstream of the rhodopsin start codon was sequenced in P347S mice and HEK 293 cells, and results were compared to a reference human sequence (RefSeqGene: NG_009115.1; NM_000539). Very little variation was observed between the three sequences – none of which occurred in the 5'UTR region (a sequence alignment is shown in Appendix 3).

Additionally, it was important to examine polymorphism in this region across human populations to ensure a broad utility for any potential future therapeutic arising from the study. Variants with allele frequencies of 0.01 or greater are typically classed as polymorphisms (Genomes Project et al., 2010). By examining the Genome Aggregation Database (gnomAD) v3 dataset (Karczewski et al., 2020), it was determined that two single nucleotide polymorphisms (SNPs) were present in the 5'UTR region of interest: c.-51G>A/T (RefSNP: rs2269736) and c.-26A>G (rs7984) variants with allele frequencies of 0.0817 and 0.3806, respectively. Both polymorphisms were classified as benign in the ClinVar database (NCBI).

A panel of 10 guide RNA target sites in, or close to, the rhodopsin 5'UTR were chosen (Fig. 3.4). Target sites selected were 18 or 20nt long, with a SpCas9 PAM site (5'-NGG-3') directly adjacent to the 3'end. While a length of 20nt is typical for the targeting region of a gRNA (henceforth termed crRNA), there is evidence to suggest that shortening the crRNA to 17-19nt can increase specificity without compromising on-target efficiency (Fu et al., 2014). This finding is somewhat counterintuitive, as one would expect longer sequences to have fewer potential off-target sites. Indeed, predicted off-target sites for 18nt guides were considerably more numerous than those of 20nt sequences (Table 3.2). However, it is proposed that the reduced DNA-binding energies of shorter RNA sequences

[27] Note: all guide RNAs (gRNAs) referred to in this section are single guide RNAs (sgRNAs)

leads to preferential binding to fully complementary sites. Guide on-target efficiency could also be estimated for this panel, as large libraries of sgRNAs have been screened in order to develop algorithms to predict gRNA efficiency based on sequence features (Doench et al., 2016).

Additionally, potential downstream issues were flagged for certain gRNAs. For example, the target site of gRNA9 includes the TATA box of the rhodopsin promoter. Binding of a gRNA9/Cas9 complex might therefore be impaired by the presence of transcription factors or, conversely, obstruct transcription. Several of the gRNA target sites selected also include one of the SNPs identified. This would be especially disruptive where a SNP falls within the seed region of the site, as in gRNAs 1 and 24. In the case of gRNA 26, a SNP changes the PAM from AGG to CGG, which could actually increase targeting efficiency as CGG sites appear optimal (Doench et al., 2014).

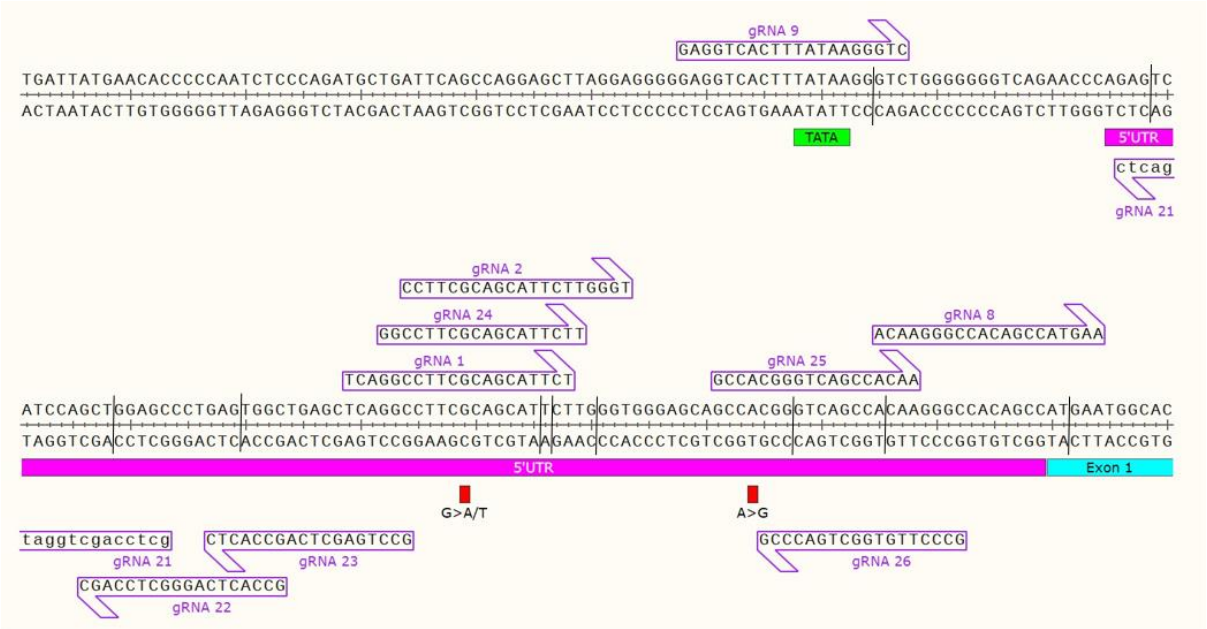

Figure 3.3. Schematic of selected *RHO* gRNA target sites.

Relevant components of the human rhodopsin gene are shown: TATA box of the core promoter sequence (green), 5'UTR (purple), start of exon 1 (blue) and high frequency variants (red). Guide RNA sequences are shown above sense or below antisense DNA, depending on which strand they target. Double-stranded breaks that would result from gRNA/Cas9 targeting are shown as black lines through the genomic sequence.

gRNA name	Target region	Length (nt)	No. potential off target sites per no. mismatches (1, 2, 3, 4)	Predicted efficiency (%)	Potential issues
R1	5'UTR	20	Human: (0, 0, 5, 104) Mouse: (0, 0, 3, 93)	24.24	SNP in central target site
R2	5'UTR	20	Human: (0, 1, 3, 75) Mouse: (0, 0, 6, 83)	50.97	SNP in PAM-distal target site
R8	5'UTR/ Exon 1	20	Human: (0, 1, 9, 197) Mouse: (0, 1, 12, 147)	50.01	Cuts within start codon
R9	Upstream of 5'UTR	20	Human: (0, 1, 8, 115) Mouse: (1, 2, 7, 73)	32.1	Binds to TATA box
R21	5'UTR	18	Human: (1, 10, 154, 1455) Mouse: (1, 16, 129, 1393)	41.33	
R22	5'UTR	18	Human: (0, 25, 225, 2238) Mouse: (1, 13, 181, 1523)	44.41	
R23	5'UTR	18	Human: (1, 25, 250, 2334) Mouse: (0, 17, 201, 2079)	40.67	
R24	5'UTR	18	Human: (0, 3, 65, 1166) Mouse: (0, 3, 52, 735)	33.55	SNP in central target site
R25	5'UTR	18	Human: (0, 6, 81, 863) Mouse: (0, 5, 57, 632)	61.3	SNP in PAM-distal target site
R26	5'UTR	18	Human: (0, 5, 100, 1027) Mouse: (0, 3, 67, 620)	56.8	SNP in 1st nt of PAM

Table 3.3. Rhodopsin guide RNA panel.

Factors for consideration of gRNA suitability are presented. Off-target sites were predicted using the Cas-OFFinder tool (Bae et al., 2014). They are listed in terms of number of predicted sites per number of mismatches. For example, (0, 0, 5, 104) signifies 0 off-target sites with 1 or 2 mismatches, 5 off-target sites with 3 mismatches and 104 off-target sites with 4 mismatches etc. Off target screening was completed using GRCh38/hg38 and mm10 genome assemblies. On-target efficiency scores were calculated using CHOPCHOP (Labun et al., 2019). Note: the algorithm used to calculate targeting efficiency was developed using data from 20 nt target sequences. As efficiency is apparently not reduced when crRNAs are shortened to 18 nt (Fu et al., 2014), on-target efficiency scores were calculated for 20nt crRNA sequences in all cases.

3.3.2 Assessment of efficiencies of *RHO* 5'UTR sgRNA target sites

Once the target site designs had been finalised, gRNAs were synthesised by *in vitro* transcription (IVT), complexed with SpCas9 and transfected into HEK 293 cells. Targeting efficiency could then be determined using an enzyme mismatch cleavage (EMC) assay. In this method, potentially edited sites are amplified, denatured and slowly reannealed to encourage formation of heteroduplexes at indel sites where NHEJ has occurred. Heteroduplex regions can be cleaved by T7 endonuclease I (T7EI) or CELII nuclease and the products are then separated on agarose gels. The proportion of edited amplicon can be estimated by comparing intensity of cleaved fragments to uncut 'parental bands', as described by Guschin et al. (2010).

EMC assays thus provide a faster, more economical means of assessing gene modification rates in sample cell populations when compared to analysis of Sanger sequencing data with algorithms such as TIDE (Brinkman et al., 2014) or ICE (Hsiau et al., 2018). The ability of CELII (also known as Surveyor Nuclease) to recognise and cleave single base pair substitutions is well-established. However, it is outperformed by the T7EI bacterial resolvase when it comes to detecting heteroduplex bulges formed at indel sites >2bp. In addition, the 5'exonuclease activity of CELII generates a higher level of non-specific background as a result of degraded DNA fragments (Vouillot et al., 2015).

It was therefore decided to proceed with a T7EI EMC assay for assessment of editing efficiency with the selected *RHO* gRNA panel. The test was initially performed with gRNAs R1, 2, 8 and 9. A positive control gRNA known to successfully target the *HPRT* housekeeping gene was also included and confirmed that the gRNA synthesis and transfection protocols were successful. A commercial indel-containing DNA template functioned as an additional positive control during the T7EI cleavage tests. The *RHO* gRNA target sites of interest, however, did not appear to contain indels (Fig. 3.5.A and B).

This result was not entirely unexpected. Rhodopsin is, afterall, a rod-specific protein and its heterochromatic state in HEK 293 cells may render it inaccessible to gRNA/Cas9 ribonucleoproteins. Chromatin state has been demonstrated to influence Cas9 binding in several studies. Binding of gRNA/dCas9 at off-target sites was observed to be highly correlated with chromatin accessibility (Wu et al., 2014). Targeting of transcriptional activator proteins to silenced genes to induce chromatin remodelling has been shown to improve Cas9 activity (Daer et al., 2017, Daer et al., 2020), as has fusion of chromatin-

modulating peptides to the Cas9 protein (Ding et al., 2019). In contrast to results obtained with *RHO* gRNAs, gRNA/Cas9 RNPs targeting the ubiquitously expressed *RP2* gene produced clear cleaved bands when the T7EI assay was performed (Fig. 3.5.C).

To circumvent the issue of chromatin state, a modified gRNA efficacy test was devised whereby a plasmid containing the *RHO* section of interest was transfected into cells before the gRNA/Cas9 complexes. This exogenous copy of the target region should be more readily accessible for editing. While euchromatin-associated DNA would of course be preferable to a naked plasmid substrate, this test would at least provide a platform to compare activity of the selected gRNAs in a cellular context. Development of this assay was also faster than the alternative strategy considered, whereby the *RHO* target region would be stably integrated into a safe harbour site such as AAVS1.

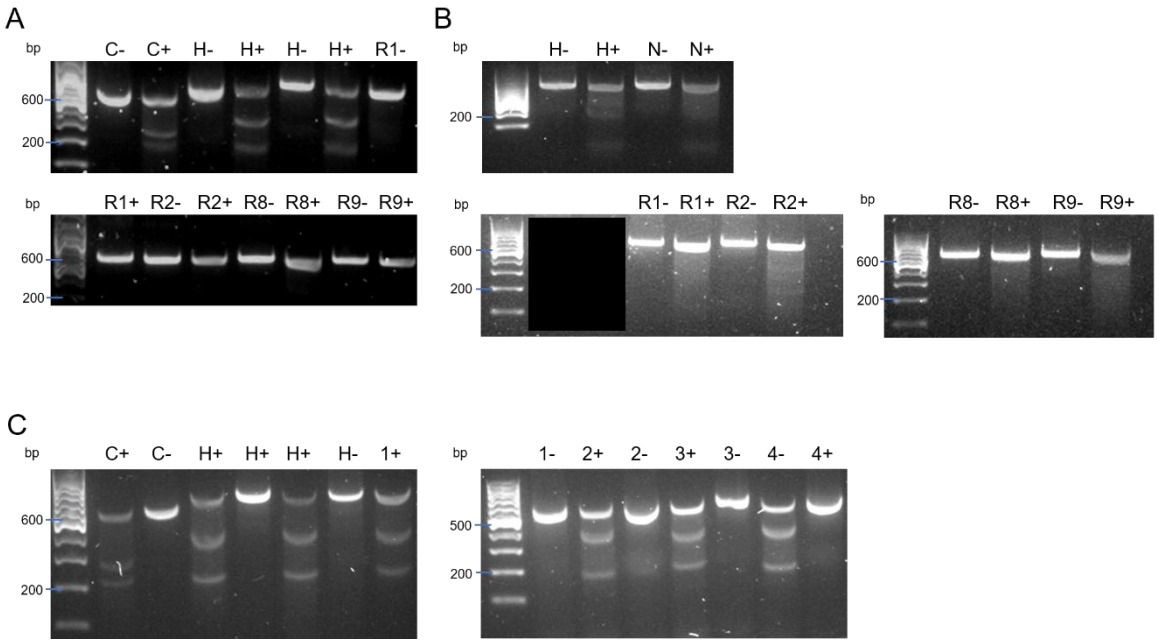

Figure 3.5. T7EI mismatch cleavage tests to assess gRNA editing efficacy.

CRISPR/Cas9 target sites in *RHO* (A and B) and *RP2* (C) were examined for signs of successful gene-editing using the T7EI indel detection assay. HEK 293 cells that had been transfected with gRNA/Cas9 RNPs were lysed, and the relevant genomic regions were amplified. Heteroduplexes were formed and incubated with T7EI, and the resultant DNA fragments were separated on 2% agarose gels. A gRNA known to successfully target the HPRT gene (H) functioned as a positive control. For each sample, reactions were set up with (+) and without (-) the T7EI enzyme. Amplicons of a commercial heteroduplex template (C) functioned as an additional positive control for the cleavage assay.

(A) 'Parental' amplicon bands are visible in all lanes. Additional cleaved bands are evident in positive control C+ and H+ samples. Samples that had been transfected with gRNAs targeting rod-specific RHO (R1, 2, 8, 9) did not produce T7EI-cleaved bands.

(B) The test in (A) was repeated, this time with the addition of a 'no gRNA' (N) transfection control. Cleaved bands are again visible in the H+ control, though less clear in this run. Very faint cleaved bands can also be seen in the R2+ sample. Some non-specific T7EI cleavage is evident in the gRNA negative control (N+) and most (+) reactions. Note: two lanes in the second gel in (B) have been blacked out as they contained samples irrelevant to this test.

(C) The protocol was carried out with gRNAs targeting the ubiquitously expressed *RP2* gene (1-4) for comparison. All gRNACas9-transfected samples yielded clear, specific cleavage bands of expected size.

A 610bp segment of the *RHO* sequence encompassing all target sites was amplified and cloned into pcDNA3.1+ (Fig. 3.6). Short GFP sequences were inserted either side of the plasmid *RHO* copy to enable its specific amplification and distinction from the endogenous sequence during indel detection tests. A GFP-flanked *HPRT* plasmid was also constructed in parallel. This positive control was essential in validating the modified assay, as it was initially uncertain whether DSB formation would cause plasmid DNA to undergo NHEJ or simply degrade in a cellular context. If indels were successfully detected in the *HPRT* plasmid, induced by an established functional gRNA, then results relating to the *RHO* plasmid could be confidently interpreted.

The plasmid-based target efficiency assay functioned well, as demonstrated by cleavage of DNA amplified from exogenous *HPRT*. Indels were also detected in the majority of *RHO* target sites (Fig. 3.7). Densitometry was used to quantify cleaved band intensity relative to parental bands and gene editing efficiency was estimated following the method outlined by Guschin et al. (2010). gRNAs R1 and 2 performed better in the plasmid mismatch cleavage assay than in the original test, while samples treated with R8 and R9 RNPs still displayed no signs of editing. The second batch of *RHO* gRNAs (R21-26) yielded better results still, with all except R26 producing higher editing efficiencies than the *HPRT* positive control.

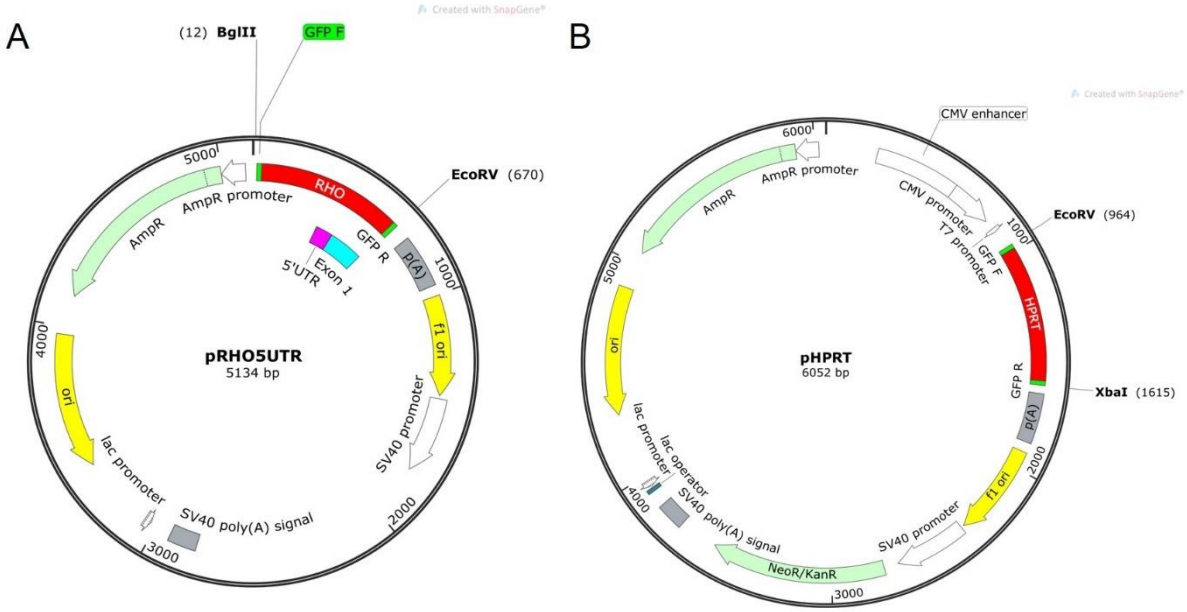

Figure 3.6. Plasmids used in gRNA editing efficiency tests.

Regions containing the (A) *HPRT* and (B) *RHO* target sites to be assessed are shown in red, flanked by short GFP sequences (green). Restriction sites used in the cloning of these constructs are highlighted – BglII and EcoRV in (A), EcoRV and XbaI in (B).

To synthesise these constructs, *RHO* and *HPRT* fragments were amplified from HEK 293 DNA using primers that consisted of a 20bp hybridisation region, 20bp GFP primer sequence and an appropriate restriction site. These restriction sites were used to clone the PCR products into a pcDNA3.1+ backbone. The GFP primer sites (GFP F and R) could then be used for specific amplification of exogenous target regions.

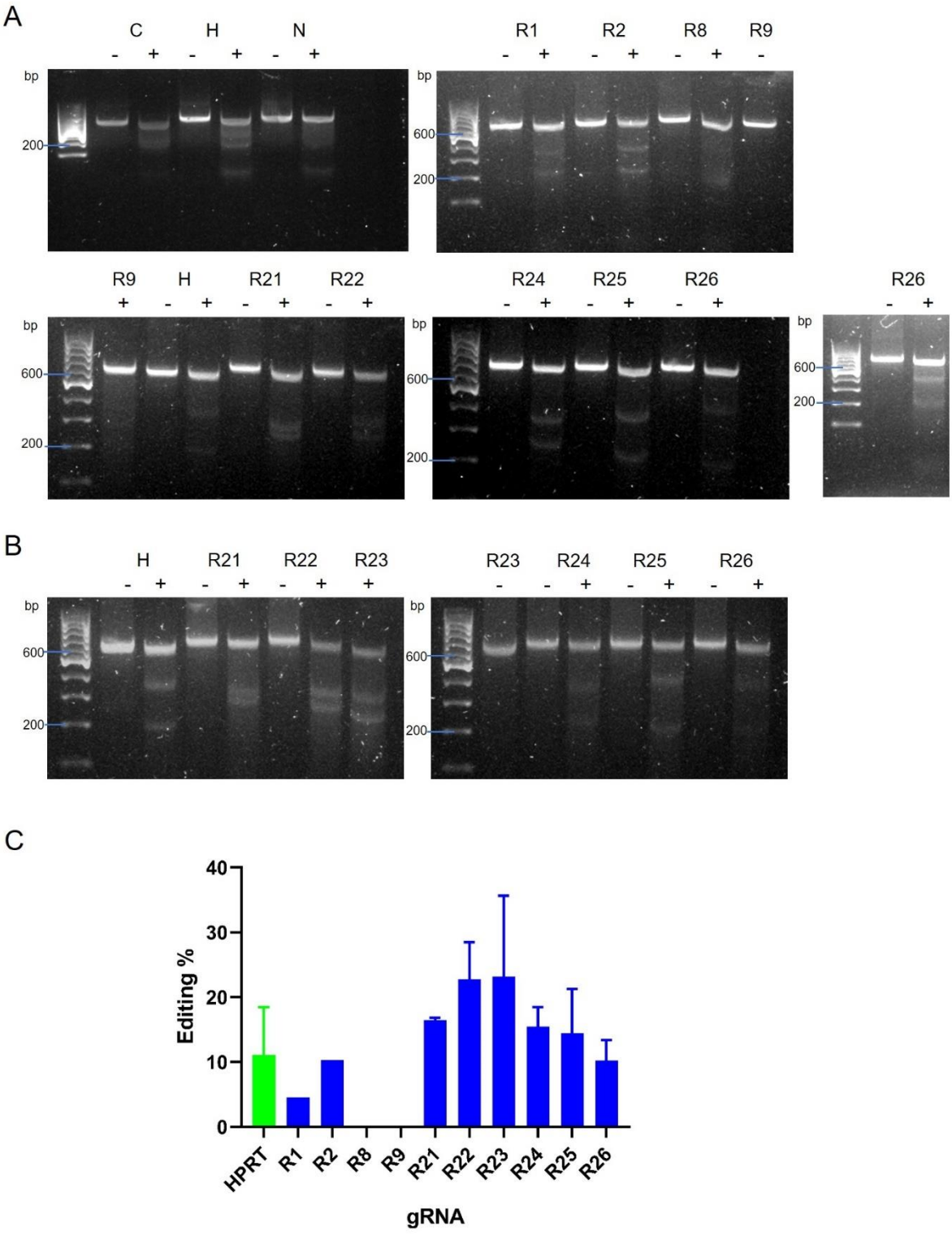
A
C H N
R1 R2 R8 R9
R9 H R21 R22
R24 R25 R26
R26
bp
600
200
B
H R21 R22 R23
R23 R24 R25 R26
C
Editing %
40
30
20
10
0
HPRT R1 R2 R8 R9 R21 R22 R23 R24 R25 R26
gRNA

Figure 3.7. A plasmid-based mismatch detection assay to assess *RHO* gRNA editing efficacy.
pHPRT or pRHO5UTR plasmids were transfected into HEK 293 cells alongside gRNA/Cas9 RNPs. After amplification with GFP primers, gene editing at target sites in the exogenous sequences was assessed via T7EI mismatch cleavage.
T7EI reactions on samples treated with gRNAs targeting HPRT (H), RHO (R1, 2, 8, 9, 21-26) or no gRNA (N) were analysed on 2% agarose gels. An indel-containing template functioned as an additional cleavage positive control (C). Each sample was given a reaction with T7EI (+) and an enzyme-free negative control reaction (-).
(A) Clear cleavage bands are evident in all *RHO* gRNA samples except R8 and 9.
(B) The results of R21-26 were replicated.
(C) Gene editing efficiencies at the various target sites were estimated using the widely used method described by Guschin et al. (2010). Densitometry was performed using Fiji. R1-9: n = 1; R21-26: n = 2, HPRT: n = 3. Values shown for R21-26 and HPRT are means ± SD.

Two *RHO* gRNAs were chosen to proceed with to the next stage of this study. R22 and 23 both had relatively high editing efficiencies (22.76% and 23.14%, respectively; n = 2). However, R22 was chosen because of its lower level of standard deviation. R21 was then ruled out because of its close proximity to R22. Finally, R25 was selected over R24 because, while both sites were affected by SNPs (Fig. 3.3), the variant was positioned more distally to the PAM site in R25 and might therefore be better tolerated (Zheng et al., 2017). It was additionally confirmed that gR22 and gR25 were human-specific and would not be predicted to induce DSBs at corresponding murine sequences due to sequence deviation (Fig. 3.8).

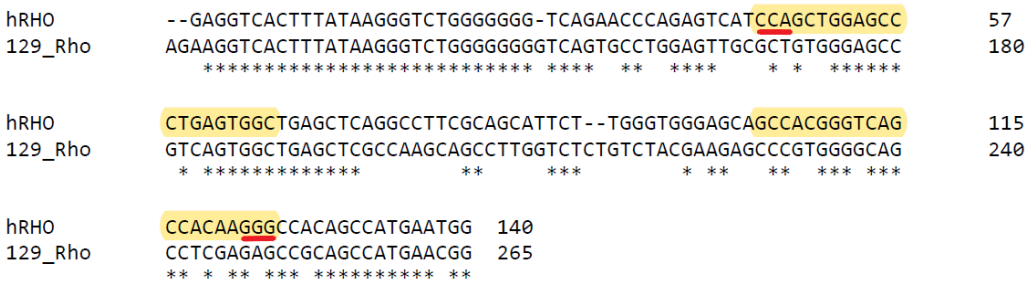

Figure 3.8. Alignment of human and murine Rhodopsin 5'UTR sequences.

The relevant *RHO* region (hRHO) was aligned with the equivalent 129S1/SvImJ sequence (129_Rho). R22 and R25 sites are highlighted in yellow and PAM sites are underlined in red. Multiple mismatches are evident in each target site. Importantly, neither region in the murine sequence has a canonical SpCas9 PAM site.

RHO: RefSeqGene NG_009115.1

Rho: MGP_129S1SvImJ_G0031159

3.3.3 Construction of HITI vectors

As outlined in the introduction, an AAV-delivered HITI gene-editing strategy would require two vectors – a Cas9-expressing AAV, alongside another 'HITI' vector containing a gRNA expression cassette and donor sequence for integration. The aim of this initial study was to determine the *in vivo* gene-editing efficiency of this strategy when targeting *RHO* 5'UTR regions. Hence, an *EGFP* reporter gene integration sequence was chosen, while a separate *DsRed* expression cassette was included to function as a transduction control.

Separate AAV-HITI plasmids were constructed to express the R22 and R25 gRNAs. A negative control plasmid was also synthesised, in which the crRNA sequence of R25 was reversed. This non-targeting gRNA is referred to as gR25X. Sequences of the final gRNA panel and relevant information are outlined in Table 3.4. To make these vectors, a 'HITI insert' was synthesised over the course of four PCR reactions (Fig. 3.9) and then cloned into a DsRed-expressing AAV plasmid (Fig. 3.10.A).

The DsRed plasmid backbone chosen was a modified version of the pAAV-CMV-DsRedExpress2 plasmid previously described by Palfi et al. (2012). A spacer sequence was inserted before the CMV promoter to provide adequate distance between the DsRed expression cassette and the inserted U6-gRNA and EGFP elements - to enable adequate expression of all elements of the construct. An innocuous 206 bp region of the human ubiquitin C (*UBC*) 5'UTR was selected as the spacer element, having previously been used for this purpose in other constructs synthesised by the Farrar lab.

Resulting pAAV-HITI candidate clones were screened with a restriction enzyme digest test (Fig. 3.10.B) and the inserted regions in chosen clones were fully Sanger sequenced. AAV-HITI plasmids were confirmed to express gRNAs when transfected into HeLa cells and evaluated by RT-qPCR (Fig. 3.10.C). AAV constructs were then packaged into AAV2/8 virions using the method described in section 2.5.9. The functionality of viral preparations were confirmed *in vitro*, by verifying DsRed protein expression in transduced cells (Fig. 3.10. D).

gRNA	crRNA sequence (5’ to 3’)	Genomic target site	AAV target site	No. predicted off-targets
gR22	GCCACTCAGGG CTCCAGC	CCAGCTGGAGCCC TGAGTGGC	GCCACTCAGGGCT CCAGCTGG	Human: (0, 25, 225, 2238) Mouse: (1, 13, 181, 1523)
gR25	GCCACGGGTCA GCCACAA	GCCACGGGTCAG CCACAAGGG	CCCTTGTGGCTGA CCCGTGGC	Human: (0, 6, 81, 863) Mouse: (0, 5, 57, 632)
gR25X	TTGTGGCTGACC CGTGGC	N/A	CCGTTGTGGCTGA CCCGTGGC	Human: (0, 3, 79, 900) Mouse: (0, 5, 54, 727)

Table 3.4. gRNAs selected for use in this study and their target sites.

crRNAs and their genomic target sites are shown. PAM sites are highlighted in red. As illustrated in Fig 3.3, to facilitate integration of an insert in the correct orientation, target sites in the AAV construct must be designed in the opposite direction to their genomic counterpart. Predicted off-target sites for each gRNA are summarised. None of these sites were located in the human or murine rhodopsin genes. Note: gR25X cannot cleave the *RHO* 5’UTR or the synthetic target sites in its AAV vector.

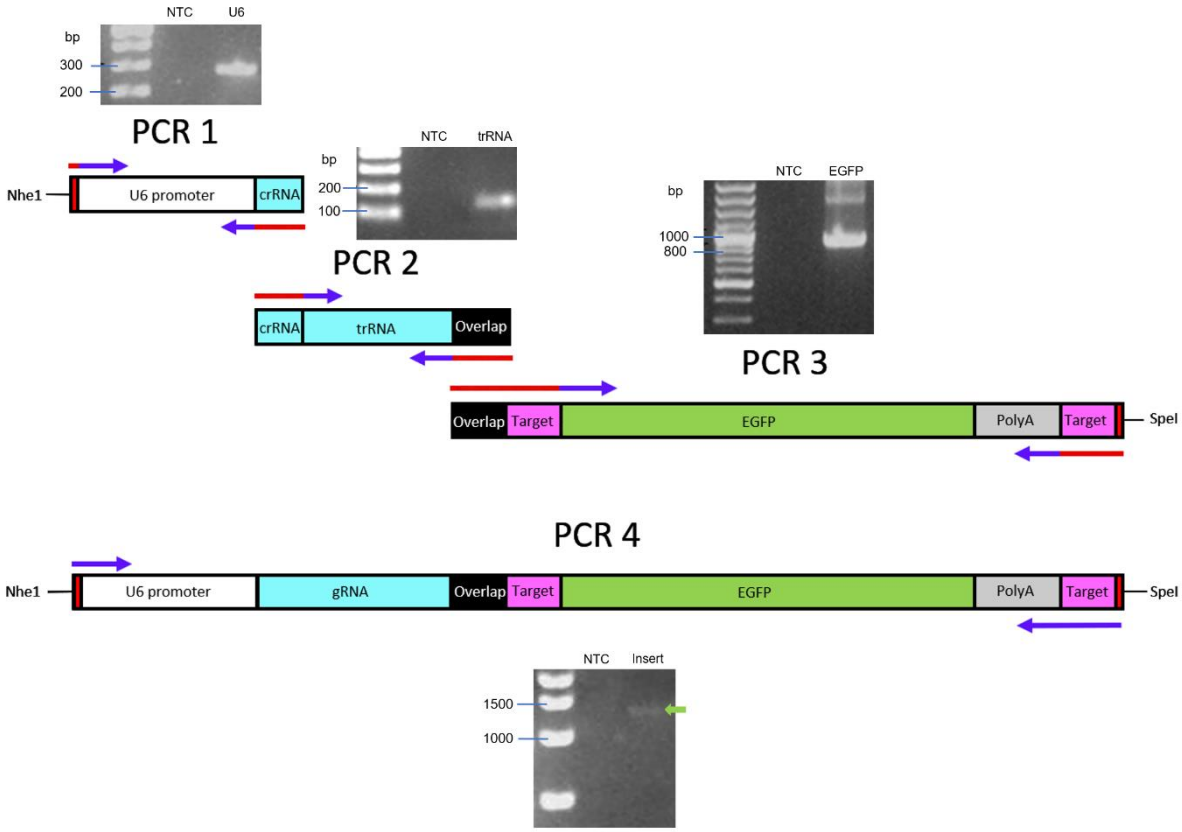

Figure 3.9. Synthesis of the HITI insert.

A strategy for construction of a cloneable insert including the necessary components for HITI gene editing is illustrated. Four different PCR reactions were required to achieve this.

Primers are shown as arrows, in which blue regions anneal to templates and red sections represent new sequences added during the PCR reaction.

In PCR 1, the U6 promoter sequence (white) was amplified from PX552 (Addgene). A 5' NheI restriction site (red) and 3' crRNA sequence (blue) were added during this reaction via non-annealing primer ends.

Next, a tracrRNA scaffold sequence (blue) was amplified from the same plasmid template, with a 5' crRNA sequence added. An arbitrary 'overlap' sequence (black) was also added onto the 3' end of this amplicon to ensure a region of homology would be shared with the product of PCR 3.

For the third PCR, an EGFP CDS (green) and minimal poly(A) sequence (grey) was amplified from pSV40-EGFP (Fig. 3.11). gRNA target sites (purple) were added to flank either side of the EGFP mini-gene, in addition to a 5' 'overlap' sequence and 3' SpeI restriction site (red).

The crRNA and 'overlap' homologous regions enabled joining of the three PCR products and amplification of the full insert sequence in the fourth and final PCR reaction.

Representative gels show PCR products obtained at each of the stages, alongside no-template control (NTC) reactions. For PCRs 1-4, the desired amplicon lengths were 277, 148, 900 and 1305, respectively. Correct PCR products were gel purified before subsequent cloning steps.

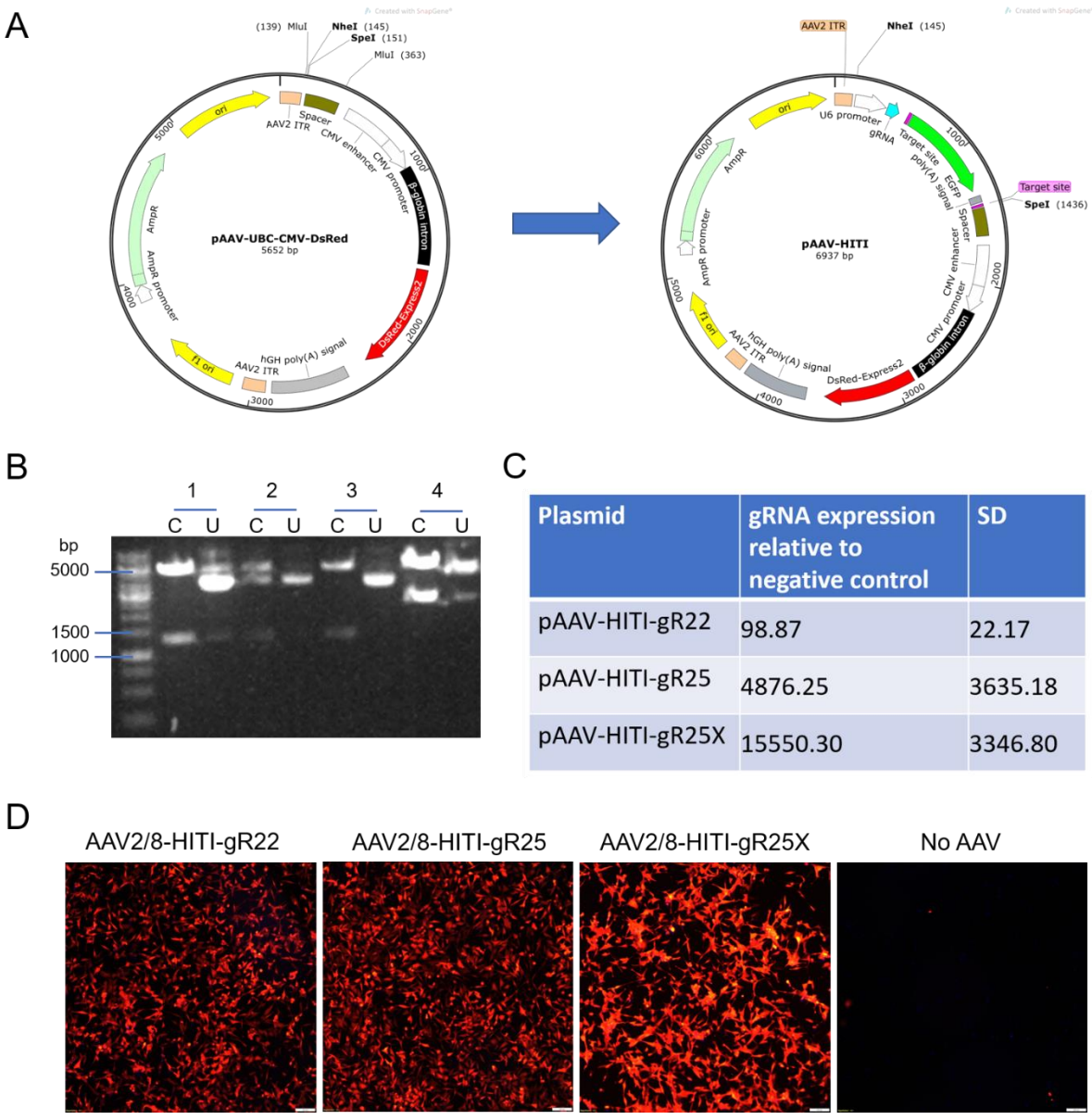

Figure 3.10. Cloning and validation of HITI vectors (cont.)

Figure 3.10. Cloning and validation of HITI vectors (continued).

A) Plasmid maps are shown to illustrate the HITI vector cloning process. During amplification of a *UBC* spacer/linker sequence, MluI sites were also added at each end to enable cloning into a pAAV-DsRed backbone, forming a pAAV-UBC-CMV-DsRed intermediate construct. NheI and SpeI sites were also added to the 5'spacer during amplification to facilitate future addition of HITI inserts (Fig. 3.9), creating pAAV-HITI vectors.

B) Possible pAAV-HITI clones were screened with a NheI/SpeI digest test as these restriction sites would only reform in plasmids in which a HITI insert was incorporated in the correct orientation. Tests of 4 clones are shown – each cut plasmid (C) is run alongside an uncut (U) control. Cut bands of 1291 and 5646 bp indicate that plasmids 1 and 3 are correct constructs.

(C) The capacity of pAAV-HITI constructs to express gRNAs was confirmed by RT-qPCR after transfection into HeLa cells. Cells transfected with pAAV-UBC-CMV-DsRed functioned as a negative control. Expression levels of gRNAs from HITI plasmids are shown relative to negative control samples. All three HITI constructs expressed gRNA in the range of 10^6 to 10^7 copies/µl RNA - levels that were substantially above background. gRNA expression levels across the three constructs cannot be reliably compared, however, as different primers were required for each. The fact that expression levels are relative to extremely low background levels (well below standard curve concentrations) also means that quantitation will not by highly accurate. Nonetheless, the data serves to illustrate that the gRNA expression cassette are functional.

(D) The functionality of AAV2/8-HITI-gR22, R25 and R25X vectors was confirmed by detection of DsRed expression in transduced HeLa cells via fluorescence microscopy. MOI: ~10^5 vg/cell. Scale bar = 100 µm.

The final AAV-HITI constructs easily fit within AAV cargo capacity, at 4.3 kb. Designing appropriately sized AAV-Cas9 vectors was more challenging, as SpCas9 has a relatively large CDS (4.1kb). Choice of regulatory elements was therefore limited. Three different promoters were assessed as part of this study: simian virus 40 (SV40), human cytomegalovirus (CMV) and human rhodopsin kinase (hGRK1) (Table 5.3).

In order to evaluate promoter activity, a series of Cas9 and EGFP-expressing constructs were synthesised (Fig. 3.11)[28].

Promoter	Activity	Length (bp)	Final AAV-Cas9 genome length (bp)
SV40 early promoter	Constitutive	245	4827
CMV	Constitutive	508	5076
hGRK1	Photoreceptor-specific	294	4869

Table 3.5. Potential promoters for driving expression of Cas9.
Length and activity profiles are compared for the different promoter sequences under consideration.

[28] Corresponding Cas9 and EGFP plasmids were made as similar as was feasible but sometimes differed in terms of the intron and poly(A) signal sequences featured.

Figure 3.11. Cas9 and EGFP-expressing vectors.

Figure 3.11. Cas9 and EGFP-expressing vectors (continued).

Plasmids in which SV40 (pink), CMV (white) and rhodopsin kinase (blue) promoters expressed Cas9 (purple) or EGFP (green) were constructed for this study. Introns are shown in grey; poly(A) signals are red. All expression cassettes are flanked by AAV2 ITR sequences (beige). hGH poly(A) = human growth hormone poly(A).

To create the SpCas9-expressing plasmids illustrated, the desired promoter sequence was amplified with flanking 5'XbaI or HindII and 3'AgeI sites, and then cloned into into PX551 (addgene) in place of the original MeCP2 promoter.

The pAAV-CMV-EGFP construct shown was previously synthesised by the Farrar lab (Palfi et al., 2010). The CMV sequence in this plasmid could be swapped for the hGRK1 promoter, which had been amplified with 5'MluI and 3'SacI sites.

To make pAAV-SV40-EGFP, a 'half-blunted-half-sticky' cloning strategy was used. The EGFP CDS was excised from pAAV-CMV-EGFP via BglII and AgeI sites, while Cas9 was cut out of pAAV-SV40-Cas9 via EcoRI and AgeI sites. Cut BglII and EcoRI sites were blunted with Klenow fragment before digestion with AgeI. EGFP was then ligated into the pAAV-SV40 backbone.

CMV- and SV40-EGFP plasmids were transfected into HeLa cells to compare promoter strength. The SV40 promoter proved inefficient *in vitro*, expressing in only 5.88 ± 3.88% of transfected cells (Fig. 3.12.A and B; n = 2 wells). In contrast, the transfection efficiency of pCMV-EGFP was 35.92 ± 18.21%. When Cas9-expressing vectors were compared, the CMV promoter produced 14 times more Cas9 mRNA in transfected HeLa cells than its SV40 counterpart (Fig. 3.13.A). The SV40 element was, therefore, not an optimal choice for this project and was not pursued further. Although the CMV promoter has been demonstrated to function well in retinal cells, by our lab (Palfi et al., 2012), a CMV-SpCas9 construct would be >5kb and may therefore exceed the AAV packaging limit (~4.8 kb, (Wu et al., 2010)).

It was therefore decided to proceed with the rhodopsin kinase promoter – a relatively small regulatory element with photoreceptor-specific activity. Subretinal injection of AAV2/8-hGRK1-EGFP at a dose of 9E8 vg led to almost pan-retinal photoreceptor transduction in the sections analysed (Fig 12.C; n = 2 retinas, 1 cryosection per retina).

Cas9 mRNA expression was confirmed in retinas of mice subretinally injected with 1.5E8 and 1.5E9 vg AAV2/8-hGRK1-Cas9 (Fig. 3.13.B). Surprisingly, higher expression was

observed in samples that received the lower dose. Although this difference was not significant ($p = 0.678$; $n = 5$ retinas), it may be an indicator of possible toxicity at the higher level of Cas9 overexpression. This was taken into consideration when selecting subsequent AAV2/8-hGRK1-Cas9 doses (Table 3.6).

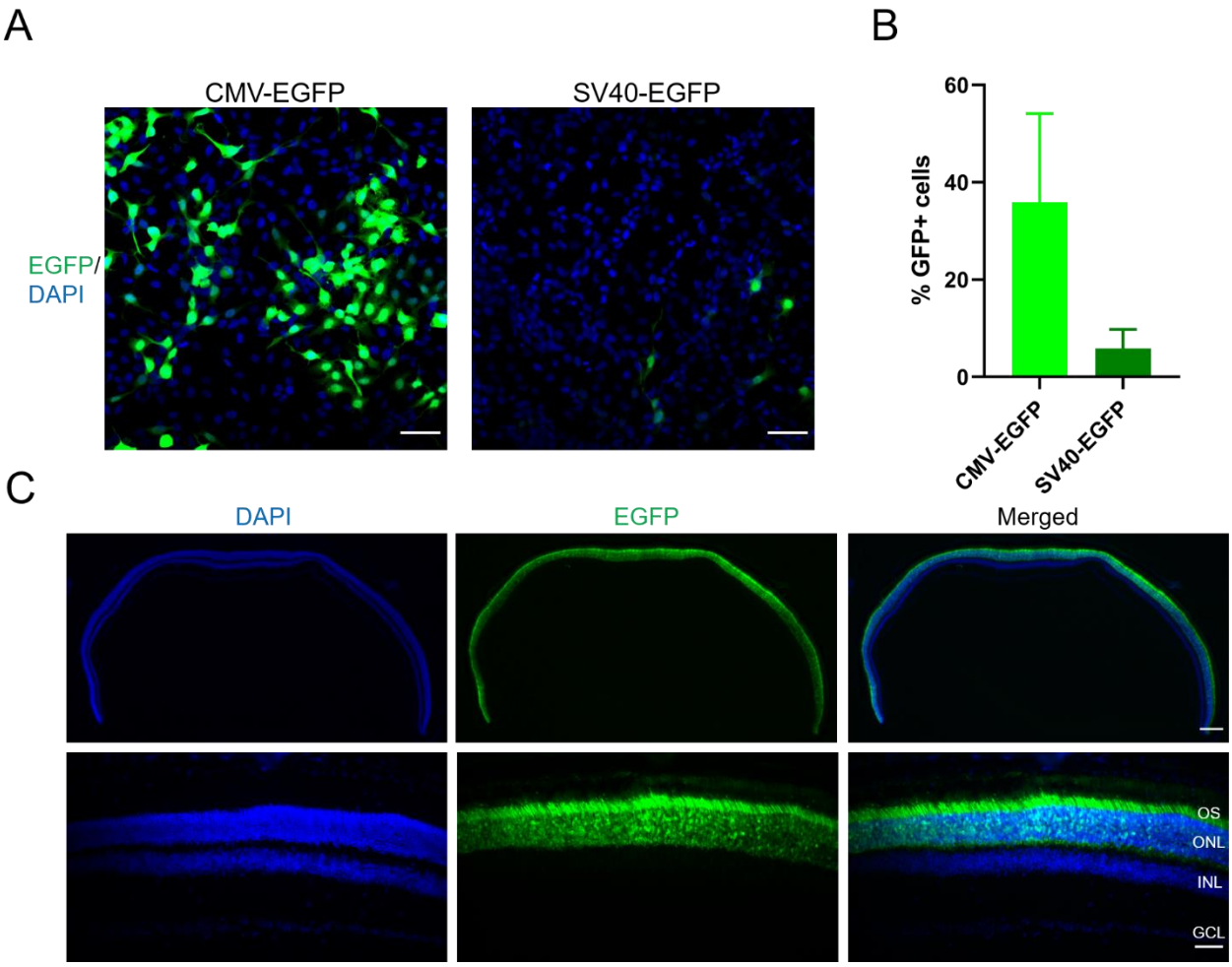

Figure 3.12. Evaluation of promoter activity in EGFP vectors.

A) ICC images show EGFP expression in HeLa cells transfected with pAAV-CMV-EGFP and pAAV-SV40-EGFP. Cells are counterstained with DAPI. Scale bar = 50 µm.

B) Transfection efficiencies were calculated by expressing GFP-positive cells as a percentage of the total number of DAPI-stained cells. 35.92% of cells transfected with the CMV-EGFP plasmid expressed GFP, compared to just 5.98% of SV40-GFP transfected cells. Values shown are mean ± SD, n = 2 wells. For each well, transfection efficiency was calculated in 8-10 fields of view - an average of 307 cells per image.

C) Native EGFP fluorescence was assessed in WT murine photoreceptor cells 2 weeks after subretinal injection of 9E8 vg AAV2/8-hGRK1-EGFP. Representative retinal sections are shown at low (top panels) and high (bottom panels) magnification. Native EGFP fluorescence was evident across the entire length of the photoreceptor layer. Top scale bar = 200 µm; bottom scale bar = 50 µm.

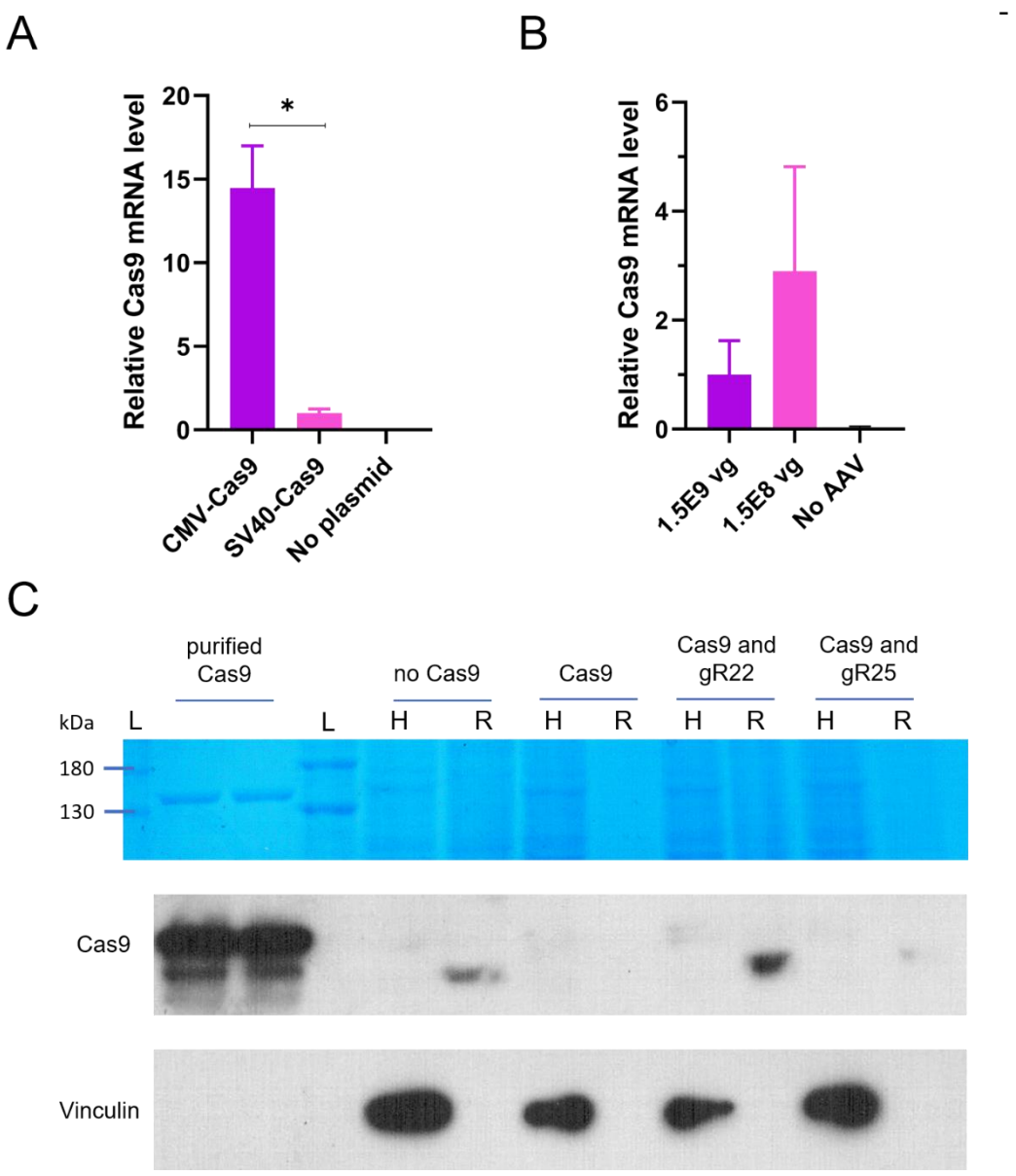

Figure 3.13. Assessment of Cas9-expression in CMV, SV40 and hGRK1-Cas9 vectors.

A) HeLa cells were transfected with pAAV-CMV-Cas9 or pAAV-SV40-Cas9 for 48 hours, after which Cas9 mRNA expression was quantified via RT-qPCR. CMV-driven Cas9 produced 14.48 times more RNA than SV40-Cas9 (14.48 ± 2.52 vs 1.00 ± 0.25) ($p = 0.0172$; unpaired Student's t-test). Values shown are means ± SD, n = 2 wells.

B) AAV2/8-hGRK1-Cas9 expression was assessed in WT murine photoreceptors two weeks post-subretinal injection. Two different doses were tested. Both produced a level of Cas9 mRNA well above background. Values shown are means ± SD; n = 5 retinas per AAV dose and 3 'no AAV' control retinas.

Figure 3.13. Assessment of Cas9-expressing vectors (continued).

C) Attempts were made to detect Cas9 protein in pAAV-CMV-Cas9 transfected HeLa (H) and AAV2/8-hGRK1-Cas9 transduced retinal (R) lysates by SDS-PAGE protein staining (top panel; PAGE Blue stain) and Western blot (middle panel). Purified Cas9 protein (NEB) functioned as a positive control, verifying that the SDS-PAGE/Western blot conditions were suitable and the Cas9 antibody was functional. Samples co-transfected/transduced with gRNA-expressing HITI vectors were included as additional controls to ensure that lack of Cas9 was not simply due to protein instability in the absence of a gRNA. For example, 'Cas9 and gR22' HeLa samples were transfected with equal amounts of pAAV-CMV-Cas9 and pAAV-HITI-gR22 plasmid. The 160 kDa Cas9 protein was not visible in pAAV-CMV-Cas9-transfected cell lysates or AAV2/8-hGRK1-Cas9 transduced retinal samples.

Vinculin protein (124 kDa) was tested for use as a loading control (bottom panel) but the antibody utilised did not appear sensitive to murine protein.

HeLa cells transfected with pAAV-CMV-Cas9 and retinas transduced with AAV2/8-GRK1-Cas9 (1.5E9 vg) were tested for Cas9 protein expression by ICC and IHC using multiple antibodies against Cas9 and its HA tag. These attempts were unsuccessful (data not shown). The experiment was then repeated for sample protein extraction and immunoblotting. It was reasoned that Cas9 protein may be more accessible to antibody probing using this method, as was the case with RP2 protein detection in section 2.3.2. However, Cas9 immunoreactivity failed to be detected in samples that received either CMV- or hGRK1-Cas9 constructs using this method (Fig. 3.13. C). A commercial Cas9 protein sample was used to confirm that antibodies were functional and Cas9 constructs were fully Sanger sequenced to ensure there were no mutations preventing translation. Researchers have previously noted that SaCas9 could not be detected by immunoblotting of retinal lysates after subretinal injection of AAV-Cas9 alone, despite the fact that Cas9 immunoreactivity was evident in samples that had received both Cas9 and gRNA-expressing vectors (McCullough et al., 2019). This observation led McCullough et al. to propose that Cas9 protein may be unstable in the absence of a partner gRNA, at least in a photoreceptor context. However, this phenomenon was not the cause of detection problems in the current study, as Cas9 protein was not detectable in control samples that received both Cas9 and gRNA-expressing vectors either.

In retrospect, it seems likely that the failure to detect Cas9 protein expression in this experiment was likely due to insufficient lysis of the nuclear membrane during lysate preparation, as samples were not sonicated. Indeed, sonication may be particularly important for releasing DNA-binding proteins. These experiments will therefore be repeated with a modified lysis protocol, based on methods previously described (McCullough et al., 2019, Li et al., 2019a).

3.3.4 HITI-mediated gene editing *in vivo*

All three HITI constructs (gR22, gR25 and gR25X) were packaged into AAV2/8 vectors. In an initial dosage test, AAV-HITI-gR25 was combined with AAV-hGRK1-Cas9 for subretinal injection at two different concentrations (Table 3.6). Each dose contained a HITI:Cas9 vector ratio of approximately 4:1.

Dose	AAV2/8-HITI-gR25 (vg)	AAV2/8-hGRK1-Cas9 (vg)
1	6.2E+08	1.4E+08
2	2.1E+08	4.8E+07

Table 3.6. AAV HITI and Cas9 dosages tested.

AAV doses are expressed in terms of viral genomes injected per eye, as determined by qPCR using primers targeting a central region of the expression cassette.

As outlined in section 3.2.2, it was planned to test the dual vector AAV-HITI strategy in a humanised model of ADRP harbouring a *RHO* P347S allele (Li et al., 1996). Homozygous P347 mice exhibit severe, early-onset photoreceptor degeneration. Thus, mice were bred to have one P347S allele to allow a larger window of intervention and to simulate a heterozygous genotype in ADRP. This model has been used on both *rho+/+* and *rho+/-* backgrounds to test a suppression and replacement therapeutic strategy (Chadderton et al., 2009, Millington-Ward et al., 2011). For the current study, it was decided to use a heterozygous null murine *rho* background, as this would more closely replicate a state of natural diploidy. Hence, P347S homozygotes were crossed with *rho-/-* mice (Humphries et al., 1997) to produce progeny with one transgenic P347S allele and one null *rho* copy. *RHO347+/-Rho+/-* mice are henceforth referred to as P347S mice.

In the proposed gene-editing strategy, integration of the EGFP minigene should render the P347S allele non-functional. The remaining wild-type *rho* allele may, in principle, be

sufficient to ‘rescue’ photoreceptor function. This was essentially the case in a previous study by the Farrar lab, when specific RNAi suppression of the human P347S allele on a *rho+/+* background provided functional benefit (Chadderton et al., 2009).

In P347S mice, approximately two third of photoreceptors are reported to be lost by P20-30 (Li et al., 1996). Mice were therefore subretinally injected as neonates (P4-5) and assessed two weeks later in initial tests. Transduction efficiency was assessed by analysing the proportion of the outer nuclear layer that was DsRed-positive in retinal sections. Transduction efficiencies obtained using AAV Dose 1 and Dose 2 differed significantly (41.5 ± 5.3% and 4.3 ± 3.5%, respectively; $p = 0.0005$, $n = 3$ retinas) (Fig. 3.14.A and B).

It was not possible to quantify EGFP-expressing cells based on native fluorescence due to overlapping emission spectra of the chosen reporters, which led to a high level of DsRed bleed-through into the EGFP channel (data not shown). Even without this issue, detection of native fluorescence may still have been challenging, as edited cells would be expressing EGFP from a single genomic copy, as opposed to expression from many episomal AAV or plasmid copies. An anti-GFP antibody was therefore used in combination with a Cy5-conjugated secondary antibody to probe for edited cells. DsRed fluorescence was confirmed not to interfere with Cy5 signal detection; unstained DsRed-positive sections did not emit fluorescence when subjected to Cy5 fluorophore imaging conditions (data not shown). The rate of successful gene integration was estimated by expressing the amount of EGFP positive ONL as a proportion of the transduced (DsRed-positive) ONL area. This editing efficiency was consistent across the AAV Dose 1 and Dose 2 groups (23.1 ± 12.4% and 22.2 ± 10.8%, respectively).

Interestingly, EGFP expression was sometimes detected outside of the ONL in retinas that received the higher AAV dose, despite the use of established photoreceptor-specific promoters. Signal detected in RPE cells may be due simply to phagocytosis of EGFP-containing photoreceptor outer segments. There were, however, instances of DsRed and EGFP-positive cells in the inner retinal layers (Fig. 3.14. C and D). Transgenic expression usually does not extend past the ONL following subretinal injection in WT mice, even when constitutive promoters are employed, such as that used to drive DsRed expression (for example, see Fig. 2.19). This restricted expression profile is proposed to be a consequence of the outer limiting membrane acting as a barrier to AAV diffusion to inner

layers (Petit et al., 2017). However, AAV2/8 has been noted to sometimes transduce inner retinal cells when expressed at relatively high doses, such as that utilised in this study (Dr Arpad Palfi, personal communication). Photoreceptor degeneration may additionally have aided AAV penetration of the inner layers. Indeed, regions of inner retinal DsRed expression tended to occur in or adjacent to sections of the retina displaying degenerative signs, such as photoreceptor rosettes (Fig. 3.14.C).

The fact that some DsRed-positive inner retinal cells also appeared to express EGFP was more puzzling. Afterall, expression of both Cas9 and any integrated EGFP copies would be driven by photoreceptor-specific promoters. It is possible that the promoters used may have altered activity in a degenerating retina than in a healthy one (Buck and Wijnholds, 2020). It is more likely, however, that the seemingly edited inner retinal cells are in fact simply Müller glia that have phagocytosed degenerating photoreceptors (Sakami et al., 2019, Nomura-Komoike et al., 2020, Palfi et al., 2020a). To test this hypothesis, colocalisation of EGFP expression and Müller glia markers, such as CRALBP, will need to be assessed in further experiments.

It was decided to proceed with the higher AAV dose in subsequent tests because transduction efficiencies from the lower were suboptimal. All three AAV-HITI vectors were individually combined with AAV-hGRK1-Cas9 and subretinally injected as before. ‘gR25 only’ and ‘no AAV’ groups were included as additional negative controls. In this test, gR22 performed better than gR25, with gene-editing efficiencies of 43 ± 23.5% and 15.5 ± 14.4%, respectively (n = 4 retinas). The non-targeting gRNA negative control group, ‘gR25X and Cas9’ yielded no EGFP-positive photoreceptors. However, ONL EGFP expression was detected in the other negative control group, ‘gR25 only’ retinas. These positive cells were not rare events, making up 27.6 ± 17.6% of the transduced (DsRed positive) area. The simplest explanation for this finding is, of course, human error. Following the principle of Occam’s razor, it seems most likely that some AAV-Cas9 was added to the ‘g25 only’ solution for injection by mistake. These experiments will be repeated to verify this assumption.

The data presented represent a preliminary evaluation of an interesting mutation-independent HITI-based therapeutic approach for rhodopsin-linked ADRP, an ocular

disorder for which at least 195 disease causing RHO[29] mutations have been identified thus far. Clearly while very interesting and with significant potential, additional work is required to further validate this approach.

[29] http://www.hgmd.cf.ac.uk/ac/gene.php?gene=RHO

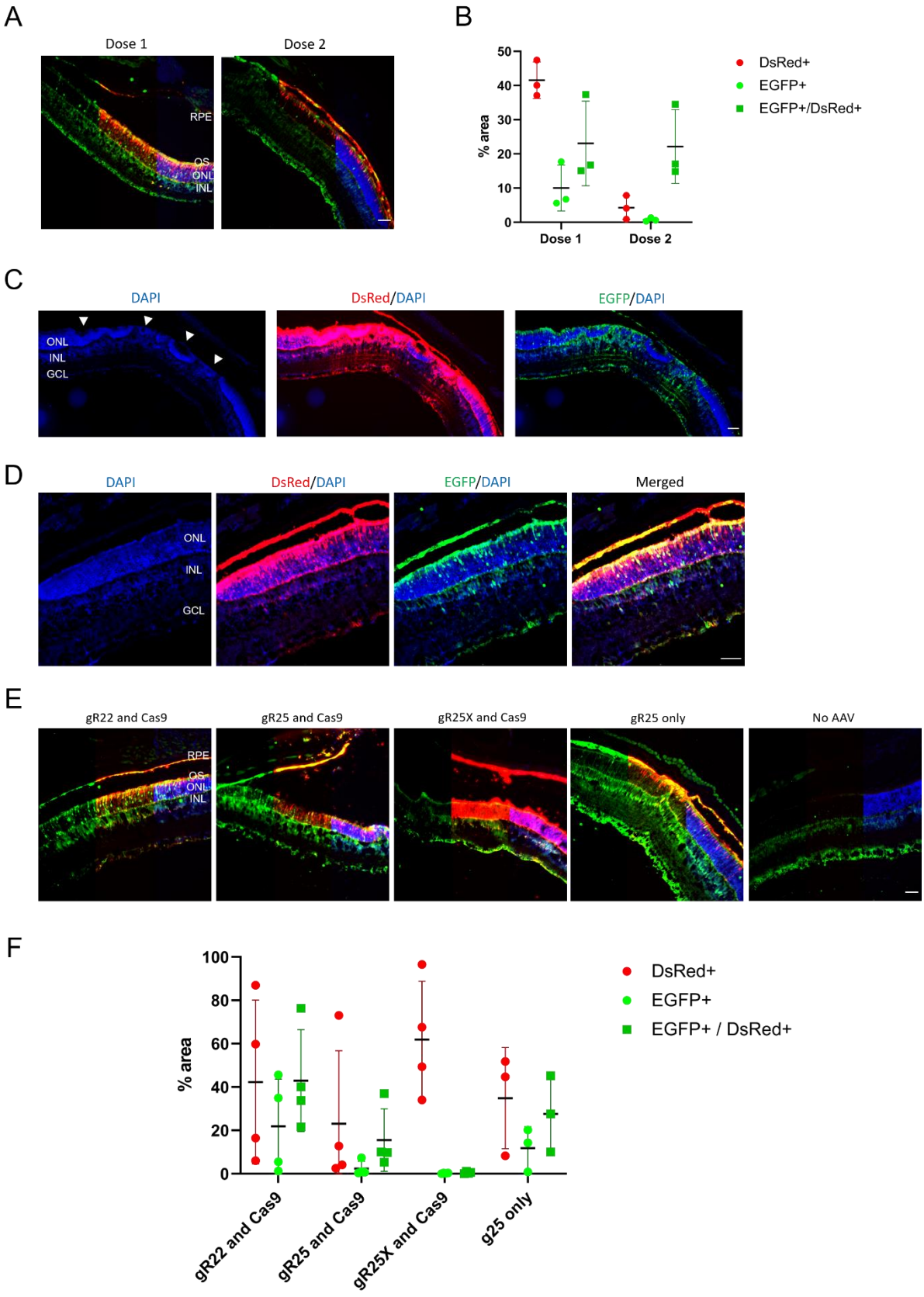

Figure 3.14. HITI editing efficiency in murine photoreceptors.

Figure 3.14. HITI editing efficiency in murine photoreceptors (cont.)

(A) P347S mice were subretinally injected with AAV2/8-HITI-gR25 and AAV2/8-hGRK1-Cas9 at ~P5. Dose 1 retinas received 6.20E+08 vg AAV-HITI and 1.44E+08 vg AAV-Cas9, while Dose 2 retinas were given a solution 3 times less concentrated. Representative IHC retinal sections are shown. Scale bar = 50 μm.

(B) The DsRed-positive area of the ONL was determined in order to estimate transduction efficiency. Gene editing efficiencies were then calculated by expressing EGFP-positive area as a percentage of the DsRed-expressing area (EGFP+/DsRed+). AAV Dose 1 transduced approximately 10 times more of the ONL area than the lower dose tested ($p = 0.0005$; unpaired Student's t-test). The average apparent gene editing rates were essentially the same at both doses (22.2-23.1%). Values shown are means ± SD, n = 3 retinas. For each retina, one whole retinal section was analysed.

(C) Some samples in the Dose 1 group exhibited DsRed expression in inner retinal layers. This tended to occur in, or in close proximity to, regions with photoreceptor rosettes (highlighted with white arrowheads). EGFP-positive cells were also occasionally observed in the inner retina. Scale bar = 50 μm

(D) A higher magnification image of a retinal region with inner retinal layer DsRed and EGFP-positive cells. Scale bar = 50 μm.

(E) The experiment was repeated with all three gRNA-Cas9 vector combinations at Dose 1. A group of retinas receiving AAV2/8-HITI-gR25 without the Cas9 vector functioned as an additional negative control. EGFP positive cells were evident in retinas from all groups that received AAV except 'gR25X and Cas9.' Representative IHC retinal sections are shown. Scale bar = 50 μm.

(F) EGFP and DsRed positive areas of retinal sections were quantified. Gene editing efficiency in 'gR25 and Cas9' retinas was lower than that observed in the previous experiment (15.54% vs 23.06%). 'gRNA R22 and Cas9' was a better performing combination at 42.96%. 'gR25X and Cas9' control retinas displayed a negligible amount of EGFP positive cells – likely due to some background autofluorescence/ nonspecific-antibody binding. 27.63% of transduced photoreceptors in the 'gR25 only' negative control group were EGFP-positive. Values shown are means ± SD, n = 4 retinas.

3.4 Discussion

3.4.1 High efficiency HITI in murine photoreceptors

In the preliminary test of HITI-mediated gene knock-in described in this chapter, 16-43% of transduced ONL cells appeared to have successfully integrated an *EGFP* mini-gene into the *RHO* 5'UTR locus. This experiment will need to be repeated due to observation of apparently edited cells in one out of two of the negative control groups. However, this was most likely simply due to a mix up in preparing reagents.

An alternative explanation would be that EGFP expression in the gR25 HITI vector was 'leaky' due to transcriptional readthrough from the U6 promoter – an interpretation that would cast general doubt upon the authenticity of the gene editing events observed in other experimental groups. This scenario seems very unlikely, however, as the non-targeting gR25X vector, which contains the same EGFP coding sequence, did not yield EGFP positive cells. All HITI vectors were confirmed to contain a transcription termination signal at the end of the gRNA sequence (TTTTTTT) and, even if readthrough did occur, a ribosomal entry site would be needed for translation of EGFP protein. Moreover, if the EGFP positive cells observed were simply a result of readthrough from the U6 promoter, one would expect to see a continuum of EGFP signal intensity that correlated with the strength of DsRed expression. This was not the case; most of the transduced ONL regions, including cells with relatively high levels of DsRed expression, were not EGFP-positive.

When repeating this experiment, it would be informative to include an additional 'gR22 only' negative control group for comparison. *In vitro* tests could also be conducted relatively quickly to investigate the possibility of vector leakiness; HeLa cells could be tested for EGFP expression (via ICC) after transduction with HITI vectors in the absence of Cas9.

In this preliminary study, which needs further validation, the gene knock-in efficiencies in this chapter seem notably higher than that observed by Suzuki et al. when editing the *Tubb3* locus in murine cortical neurons (10.6%). This is not necessarily surprising, as gene editing efficiency is known to vary across target sites and cell types (Shui et al., 2016). Due to the extremely dense packing of the ONL, editing efficiencies were calculated by comparing EGFP and DsRed positive retinal area rather than counting individual cells. It would therefore be informative to quantify EGFP and DsRed positive cells using flow

cytometry and to compare the resulting editing efficiencies to those calculated from histology samples. In future, retinal sections will also be counterstained with a Müller glia marker in order to explore if the occasional inner retinal EGFP positive cells observed are simply due to glial phagocytosis of photoreceptor debris.

In summary, while this test will be repeated in order to more thoroughly analyse the authenticity, efficiency and specificity of editing, the results obtained so far appear promising.

3.4.2 Evaluation of potential phenotypic rescue

The aim of the short term (two week) experiment described was solely to assess *in vivo* gene integration efficiency at the *RHO* 5'UTR sites selected. Given that this strategy appears feasible, albeit further repetition and validation of the approach is required, a longer term study will be carried out to ascertain whether HITI-mediated suppression of the P347S allele alone can provide benefit in this mouse model of ADRP. Insertion of the *EGFP* mini-gene should essentially knock-out the single pathogenic human rhodopsin gene. As these mice are bred on a $rho^{+/-}$ background, the remaining murine wild-type copy should in principle be sufficient to maintain normal function when unimpeded by the dominant allele. In the next experiment, mice will therefore be injected with HITI vectors at ~P3-5 and photoreceptor function and survival will be evaluated one month later via ERG and histology analysis. It will be important to bear in mind the potential for DsRed-induced toxicity when interpreting these results, as the reporter protein is expressed quite highly in transduced retinas. Hence, additional comparisons will be made between mice injected with negative control AAVs and PBS-injected controls.

Of course, the ultimate aim of this project is to assess the potential benefit of a *RHO* mini-gene insertion. Work will soon begin on constructing appropriate AAVs to facilitate this. The *RHO* CDS is 1047 bp and so will fit comfortably within the AAV-HITI vector. A HA/His/FLAG tag could be added onto the rhodopsin protein. The DsRed expression cassette would be removed from this vector to allow dosage optimisation without fear of toxicity due to overexpression of the reporter protein.

3.4.3 Assessment of editing fidelity and specificity

When repeating the EGFP knock-in experiment, EGFP positive cells could be isolated using FACS, and the target regions amplified and Sanger sequenced to examine end-joining

precision at the 5' and 3' integration junctions. Targeted deep sequencing could also be utilised to assess edits at the top predicted off-target sites in whole retinal samples. Recent studies have reported frequent integration of AAV genomes (full and partial) into Cas9/gRNA target sites (Hanlon et al., 2019, Maeder et al., 2019, Nishiguchi et al., 2020). It will therefore also be important to assess the frequency of such insertions in future experiments.

Of course, there is limited value to examining on/off-target effects of this treatment in a mouse. If this therapeutic strategy demonstrates substantial benefit in the P347S model, it will be important to assess editing specificity more thoroughly in the photoreceptors of human-derived retinal organoids or donor retinal explants. Indeed, it may in general be prudent to use personalised retinal cell models to screen for off-target effects, in addition to non-human primate studies, before administration of a gene editing therapeutic to a patient. The importance of screening in the cell type of interest was recently highlighted when Sinha et al. (2020) observed Cas9/gRNA off-target activity in patient derived iPSC-RPE but not in undifferentiated cells. In addition to screening predicted off-target sites, it would be important to employ an unbiased means of detecting non-specific activity, such as GUIDE-seq (Tsai et al., 2015), during pre-clinical assessment of a therapeutic. Considering reports of large deletions at Cas9 target sites (Kosicki et al., 2018), it may also be prudent to perform long-read sequencing at the target locus.

3.4.4 Future directions

The field of gene editing is evolving rapidly, and the CRISPR-Cas toolbox is under constant improvement. The editing strategy described in this chapter could therefore look quite different in a few years' time.

For example, several iterations of Cas9 nuclease have been engineered for greater specificity (Chen et al., 2017, Lee et al., 2018, Tan et al., 2019). In addition, Cas proteins smaller than SpCas9 (CDS: 4.1 kb) are being continually identified. These include SaCas9 (3.2 kb) (Ran et al., 2015), CjCas9 (3 kb) (Kim et al., 2017) and Casφ (~2.1-2.4 kb) (Pausch et al., 2020). The latter of these was, fascinatingly, isolated from a huge bacteriophage that uses a hypercompact CRISPR-Cas system to eliminate DNA of competing phage and plasmids in bacterial host cells. These discoveries enable design of single AAV systems for gene knock-out and small correction strategies. It is therefore possible that a single vector HITI suppression and replacement strategy may be feasible for genes such as rhodopsin at

some point in the future. Utilisation of Cas proteins from more obscure microbes may also enable circumvention of pre-existing immunity.

Transient activity of Cas protein may ultimately be preferable to long term AAV-mediated expression, in order to minimise potential off-target activity and immunogenicity. For this reason, inducible or self-deleting AAV-Cas9 vectors are being explored (de Solis et al., 2016, Ruan et al., 2017, Li et al., 2019a), as well as non-AAV based delivery of Cas9/gRNA RNPs (Givens et al., 2018, Chen et al., 2019b). However, with regard to HDR editing, efficiency appears to be enhanced when a donor template is carried in an AAV (Nishiyama et al., 2017) and expression of CRISPR-Cas components over several months may be necessary (Hu et al., 2020).

It is worth mentioning that 'NHEJ' has thus far been used to refer to the canonical NHEJ pathway (c-NHEJ) in this thesis. There is an alternative NHEJ pathway (alt-NHEJ) that is active to a lesser degree in cells and more error-prone, which can take the form of microhomology-mediated end-joining (MMEJ). In MMEJ, short (2-20bp) complementary regions surrounding a DSB anneal and are ligated, and sequences that fall between the homologous regions are deleted (Seol et al., 2018). Nishiguchi et al. (2020) recently exploited this process to rescue an IRD mouse model by excising and replacing a mutated intronic region of *Gnat1*. Integration of the ~240 bp replacement sequence was more than twice as efficient in retinal cells using MMEJ (11%) than with a corresponding HITI donor (5%). It would be interesting to compare MMEJ and HITI efficiency in the context of the rhodopsin suppression and replacement strategy outlined.

If the gene editing strategy explored in this chapter proves successful, a logical next step would be to investigate similar strategies for other IRDs with toxic gain-of-function modes, as well as the possibility of partial mini-gene insertion for IRDs in which the causative gene is too large to deliver with an AAV vector.

3.4.5 Conclusions

This pilot study provides an initial proof-of-concept for efficient NHEJ mediated gene knock-in at *RHO* 5'UTR sites in post-mitotic photoreceptor cells. The results, while requiring further validation, support the feasibility of a HITI based suppression and replacement strategy for ADRP. Further work will assess the potential of such an approach to rescue retinal degeneration in the P347S murine model, as well as

determining editing precision and specificity. If successful in the context of *RHO*-linked RP, this strategy will be explored for other forms of IRD, and could, in principle, be applicable to any inherited disease affecting post-mitotic cells.

3.5 Materials and methods

3.5.1 In vitro transcription of guide RNAs

Guide RNAs were synthesised using the Invitrogen GeneArt Precision gRNA Synthesis Kit (Thermo Scientific, A29377).

DNA templates for in vitro transcription of gRNAs, including the T7 RNA polymerase promoter, were synthesised using an assembly PCR method (Fig. 3.15).

The target primers used are listed in section 3.5.19. Following *in vitro* transcription and purification, gRNA size, quantity and integrity was assessed using RNA ScreenTape analysis on the TapeStation automatic electrophoresis platform.

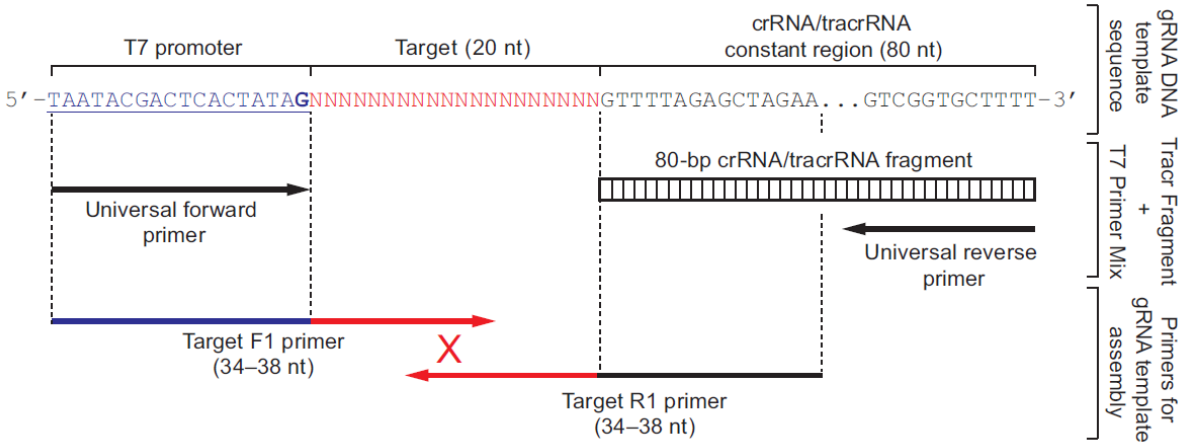

Figure 3.15. Schematic of PCR assembly of a DNA template for IVT of gRNAs.

Overlapping primers (Target F1 and R1) encompass the T7 promoter (blue), target crRNA region (red) and part of the tracrRNA (black). The two primers anneal at the overlapping region and are extended to form a double-stranded DNA fragment. The 3' end of the target primer product can anneal to the 80 bp tracrRNA fragment, which is extended to form a complete gRNA DNA template. The Target F1 and R2 oligonucleotides and tracrRNA fragment therefore act as both primers and templates during this reaction. Additional 'universal' forward and reverse primers are used to amplify the full-length template.

A 5'G is required at the start of transcripts for high-yield IVT reactions. For this reason, the universal forward primer is designed to add a G (bold) at the start of all transcripts.

Figure reproduced from the GeneArt Precision gRNA Synthesis Kit manual.

3.5.2 Cloning

Restriction enzymes were sourced from NEB and used according to the manufacturer's instructions.

When constructing pAAV-HITI plasmids, the pAAV-UBC-CMV-DsRed vector backbone was cut with enzymes that produced compatible cohesive ends. The backbone was therefore dephosphorylated with calf intestinal phosphatase (NEB, M0290) before ligation to prevent recircularisation

Ligations, transformations and mini preps production were carried out as described in section 2.5.7.

3.5.3 Tissue culture

HEK 293 (ATCC, CRL-1573) and HeLa (ATCC, CCL-2) cells were grown at 37°C in 5% CO_2. Cells were maintained in high glucose DMEM with Glutamax (ThermoFisher Scientific; 61965), supplemented with 10% FBS (Sigma Aldrich; F7524) and 1% sodium pyruvate (ThermoFisher Scientific; 11360039).

All subculture and plasmid/AAV treatment steps were performed aseptically in a laminar flow cabinet.

Cells were regularly subcultured at a split ratio of 1:10 or 1:20, once they had reached ~70% confluency. During this procedure, cells were rinsed with PBS and a minimal amount of Trypsin-EDTA (ThermoFisher Scientific, 25200056) was applied. Cells were incubated at 37°C for approximately 2 minutes, until their morphology became rounded and cells began to detach. The culture vessel was tapped gently and an excess (at least 5x) of normal media was used to wash the surface, dislodging any remaining cells. The cell suspension was made homogenous by pipetting and the appropriate volume was transferred to a new culture vessel.

Frozen cell stocks were made following the protocol described in section 2.5.2.

3.5.4 Assessment of gRNA targeting efficiency

3.5.4.1 Transfection of gRNA/Cas9 complexes

HEK 293 cells were seeded in 24 well plates at a density of $1x10^5$ cells per well. The next day, cells were transfected with gRNAs complexed with SpCas9 protein (GeneArt Platinum Cas9 Nuclease; Thermo Scientific, B25640) using GeneArt CRISPRMAX Transfection Reagent (Thermo Scientific, CMAX00001).

Two days later, cells were rinsed with PBS and lysed with DNA extraction buffer (10mM Tris-HCL pH 8, 1mM EDTA, 0.5% SDS, 100mM NaCl, 0.5% proteinase K) at 50°C for 1 hour. Proteinase K was then heat inactivated at 95°C for 10 minutes.

3.5.4.2 T7E1 mismatch cleavage assay (for genomic target sites)

Target regions were amplified using Q5 DNA polymerase (NEB, M0491L). Amplicons were designed so that cleavage at an edited site would result in two fragments easily distinguished by gel electrophoresis. Primers, annealing temperatures and cleaved fragment sizes are listed in section 3.5.19. Amplified products were purified using GeneJet PCR Purification Kit (ThermoFisher Scientific, K0701) and quantified using a NanoDrop spectrophotometer (Thermo Scientific). Purified amplicons were denatured, slowly hybridised and incubated with T7 endonuclease I (NEB, M0302L), following the protocol supplied by NEB[30]. Each sample was made in duplicate – one tube without T7EI enzyme acting as a negative control for assessment of the background level of nonspecific cleavage. In addition, a commercial hybrid DNA amplicon was synthesised using the GeneArt Genomic Cleavage Detection Kit (ThermoFisher Scientific, A24372) and acted as a positive control for the cleavage reaction. Reactions were stopped by addition of EDTA (to a final concentration of 17mM), separated by electrophoresis on 1% agarose gels and visualised using a UV transilluminator. Cleaved DNA fragments were often quite faint. For this reason, agarose gels were made with SYBR Gold (Thermo Scientific, S11494) – a dye established to be at least tenfold more sensitive than ethidium bromide[31].

3.5.4.3 Modified gRNA efficiency assay: mismatch cleavage in exogenous target DNA

In this iteration of the assay, to gRNA/Cas9 complex activity was assessed on plasmid-contained target sites in a cellular context. *RHO* or *HPRT* regions of interest in these plasmids were flanked by short EGFP sequences to allow specific amplification of exogenous gene sequences.

HEK 293 cells were seeded as before (section 3.5.4.1). The next morning, cells were transfected with pRHO5UTR or pHPRT using Lipofectamine 3000 (ThermoFisher Scientific, L3000015). Four hours later, cells were transfected with gRNA/Cas9 complexes, as in section 3.5.4.1.

[30] https://international.neb.com/protocols/2014/08/11/determining-genome-targeting-efficiency-using-t7-endonuclease-i ; accessed: 04/08/20

[31] https://www.thermofisher.com/order/catalog/product/S11494#/S11494 ; accessed: 04/08/20

Two days after transfection, cells were lysed as before and plasmid target regions were amplified using GFP primers. The T7EI mismatch detection assay was then carried out as normal.

3.5.4.4 Calculation of editing efficiency

Following separation of T7EI reaction products, gene editing efficiencies were determined based on the method described by Guschin et al. (2010). Densitometry was performed on cleaved fragments and uncut parental bands using ImageJ, as outlined in section 2.5.5.5. The following equation was used to calculate gene editing efficiency.

$$\% \text{ gene editing} = 100 \times (1 - (1 - \text{fraction cleaved})^{1/2})$$

$$\text{where fraction cleaved} = \frac{\text{sum of cleavage product peaks}}{\text{sum of cleavage product and parent peaks}}$$

3.5.5 Plasmid transfection of HeLa cells

3.5.5.1 Cells for ICC

HeLa cells were seeded overnight on 8 well chamber slides at a density of $5x10^4$ cells per well. The next day, each well was transfected with 250 ng plasmid using Lipofectamine 2000 (ThermoFisher Scientific, 11668019), following the manufacturer's protocol. 48 hours later, cells were rinsed with ice-cold PBS and fixed in 4% PFA for 10 minutes. Cells then underwent three PBS washes. Cells were stained with DAPI (2 µg/ml) for 2 minutes and washed a further three times. The detachable wells were removed and coverslips were applied using Hydromount medium. Transfection efficiencies were evaluated using native EGFP fluorescence.

3.5.5.2 Cells for RNA or protein extraction

HeLa cells were seeded in 6 wells plates at a density of $5x10^5$ cells per well. The next day they were transfected with 1400 ng plasmid using Lipofectamine 2000. Two days later, cells were rinsed with chilled PBS. Cells for RNA extraction were lysed with 350µl RLT buffer from the Rneasy mini kit (Qiagen, 74104), transferred to Eppendorf tubes and snap frozen on dry ice until RNA extraction. Cells for protein extraction were lysed with 300µl RIPA buffer (supplemented with protease inhibitors) and processed as previously described (section 2.5.5).

3.5.6 Transduction of HeLa cells with AAV2/8-HITI

HeLa cells were seeded as described in section 3.5.1. The next day, media was replaced with 150µl reduced serum media (2% FBS) and AAV-HITI vectors were added to wells at a MOI of ~$1x10^5$. After 24 hours, the media was topped up to 300µl (10% FBS). Two days after addition of AAV, cells were live imaged using an epifluorescent microscope and native DsRed fluorescence was assessed.

3.5.7 Construct sequence information

All constructs were cloned into a backbone containing flanking AAV2 ITR sequences.

Constructs contained the following key sequences:

pAAV-CMV-EGFP

- CMV promoter from pAAV-MCS
- β-globin intron from pAAV-MCS
- EGFP (GenBank: U55761)
- hGH polyadenylation signal from pAAV-MCS

pSV40-EGFP

- SV40 promoter (2881 to 3125 bp of GenBank: MT233536.1)
- EGFP (GenBank: U55761)
- Minimal polyadenylation signal from PX551 (Addgene)

pAAV-hGRK1-EGFP

- hGRK1 promoter (1793 to 2087bp of GenBank: AY327580.1)
- EGFP (GenBank: U55761)
- hGH polyadenylation signal from pAAV-MCS

pAAV-CMV-Cas9

- CMV promoter from pAAV-MCS
- SpCas9 and minimal polyadenylation signal from PX551 (Addgene)

pAAV-SV40-Cas9

- SV40 promoter (2881 to 3125 bp of GenBank: MT233536.1)
- SpCas9 and minimal polyadenylation signal from PX551 (Addgene)

pAAV-hGRK1-Cas9

- hGRK1 promoter (1793 to 2087bp of GenBank: AY327580.1)
- SpCas9 and minimal polyadenylation signal from PX551 (Addgene)

pAAV-HITI constructs

- U6 promoter from PX552 (Addgene)
- crRNA of choice
- gRNA scaffold/tracrRNA sequence from PX552 (Addgene)
- EGFP (accession no. U55761) and minimal poly adenylation signal from
- CMV promoter from pAAV-MCS, flanked by gRNA target sites of choice
- DsRed Express 2 (accession no. FJ226077) and hGH polyadenylation signal from pAAV-MCS

3.5.8 AAV production

Endotoxin-free mega preps of pAAV-CMV-NDI1, pAAV2/2 and pHelper (Agilent Technologies) plasmids were produced using EndoFree Plasmid Mega Kit (Qiagen). AAV preparations were produced by Naomi Chadderton, as described in section 2.5.9.

3.5.9 AAV titering

Viral genome (vg) titers were determined by qPCR, as outlined in section 2.5.10, using primers targeting the CMV enhancer region or Cas9 coding sequence. As the CMV enhancer is located centrally in AAV-HITI constructs, the region could be amplified efficiently without the interference from ITR secondary structure.

The titers for each AAV vector were as follows:

AAV prep	Titer (vg/ml)
AAV2/8-HITI-gR22	3.4E12
AAV2/8-HITI-gR25	3.1E12
AAV2/8-HITI-gR25X	2.3E12
AAV2/8-hGRK1-Cas9	3.6E11

3.5.10 Animals

RHO P347S (Li et al., 1996) and *rho*$^{-/-}$ mice (Humphries et al., 1997) were bred on a 129 S2/SvHsd (Harlan, Huntington, UK) background and were maintained under SPF conditions, as previously described (section 2.5.14).

3.5.11 Subretinal Injection

Subretinal injections in neonatal mice were performed by Dr Paul Kenna. Pups were subretinally injected with 1ul AAV solution at P4-P5, as previously described (Millington-Ward et al., 2011).

3.5.12 Tissue processing

Mice were sacrificed by CO_2 inhalation. Retinal samples for histology and RT-qPCR were processed as outlined in section 2.5.16. Retinal samples for protein extraction and immunoblotting were dissected *in situ*, snap frozen on dry ice and stored at -80C.

3.5.13 RT-qPCR

RNA extractions were performed on samples as described in section 2.5.4. Samples were run in triplicate at a 1/50 dilution. Relative gene expression levels were quantified as outlined in section 2.5.4.

3.5.14 Immunohistochemistry

Retinal sections were stained as described in section 2.5.17. Antibodies are listed in section 3.5.18.

3.5.15 Immunoblotting

Sample preparation, SDS-PAGE and immunoblotting were carried out as described previously in section 2.5.5, with minor modifications. As SpCas9 is a relatively large protein (160kDa), protein lysates were separated on 8% polyacrylamide gels, rather than 12%.

Two identical gels were run; one was stained with PAGE blue (Thermo Scientific, 24620), while the other was electro-transferred to a PVDF membrane for immunoblotting.

3.5.16 Microscopy and image analysis

ICC and IHC samples were imaged using an Olympus IX83 inverted motorised epifluorescent microscope and cellSens software, as described in section 2.5.19.

Transduction and editing efficiency calculations were carried out on stitched images of whole retinal sections. One section was evaluated for each of the 3-4 retinas per experimental group.

Counting individual photoreceptors was impractical due to the extremely high density of cells in the ONL. Instead, the area of DAPI-, DsRed- and EGFP-positive regions in the ONL were analysed using Fiji. The ONL was isolated by blacking out all other regions in the image, including photoreceptor outer segments. An example is shown in Fig. 3.16. This was done using the 'Freehand selection' and 'Fill' options, with the aid of a drawing tablet. Areas of interest were highlighted using the 'Threshold' tool and then quantified using the 'Measure' function.

For each image, transduction efficiency was calculated by expressing the DsRed-positive area as a percentage of total ONL area (indicated by DAPI staining). Editing efficiency was estimated by normalising EGFP-positive area against DsRed-positive area.

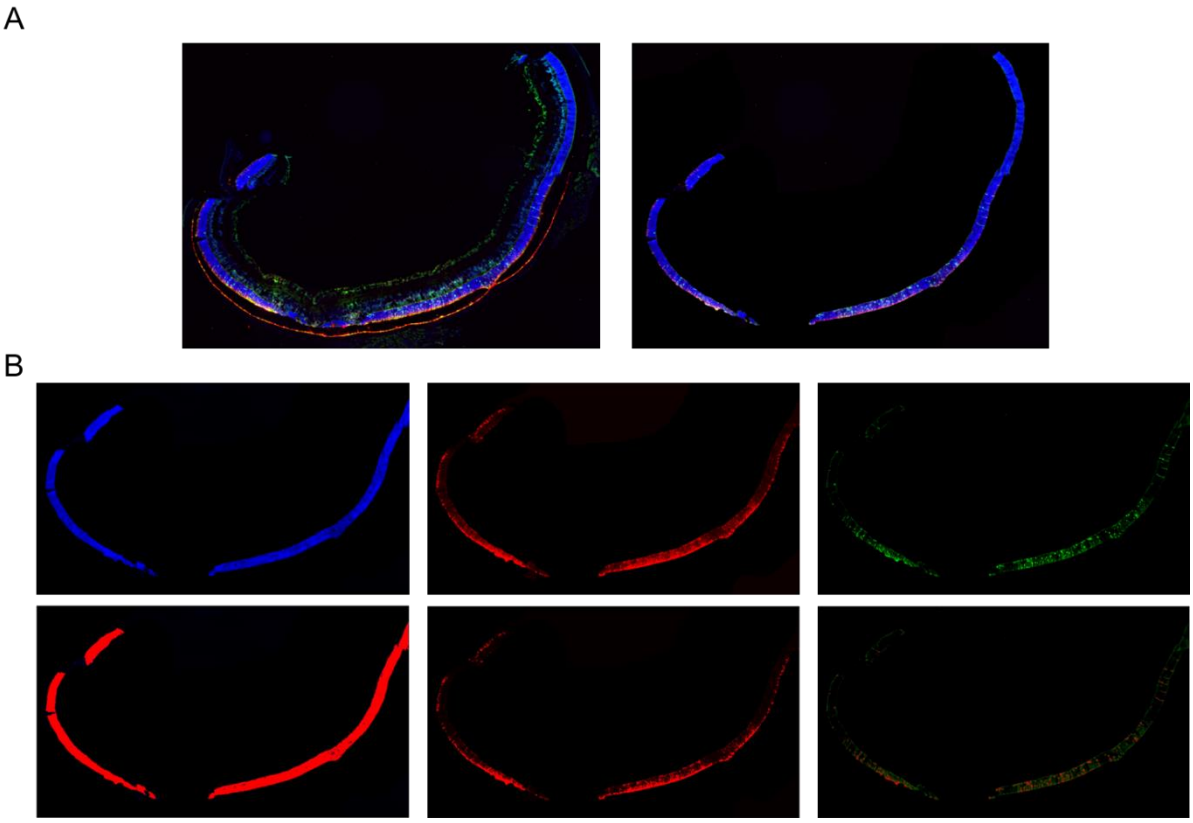

Fig. 3.16. Image processing for gene editing efficiency calculation.

(A) A retinal section image is shown before (left) and after (right) blocking out all areas except the outer nuclear layer.

(B) Top panels: the ONL image was separated into blue (DAPI), red (DsRed) and green (EGFP) colour channels.

Bottom panels: Regions of fluorescence were highlighted in red using the 'Threshold' tool and the area covered was subsequently quantified.

3.5.17 Statistics

Statistics were performed as previously described in section 2.5.23. Data collected in this chapter generally followed a normal distribution. Unpaired Student's t-tests were used to compare group means.

3.5.18 Antibodies

Primary antibodies		
Antibody	**Source**	**Working dilution**
Chicken anti-GFP	Abcam; ab13970	ICC/IHC: 1/1000
Mouse anti-Cas9	Merck Millipore; MAC133	WB: 1/1000
Mouse anti-Vinculin	Proteintech; 66305-1-Ig	WB: 1/5000

Secondary antibodies		
Antibody	**Source**	**Working dilution**
Donkey anti-chicken Alexa Fluor 488	Jackson ImmunoResearch; 703-545-155	ICC/IHC: 1/400
Goat anti-mouse HRP	Jackson ImmunoResearch; 115-035-003	WB: 1/10,000

ICC: immunocytochemistry; IHC: immunohistochemistry; WB: western blot.

3.5.19 Primers

All primers were synthesised by Sigma Aldrich.

3.5.19.1 Primers for PCR assembly of gRNA IVT templates

gRNA	Target sequence	Forward primer (5' to 3')	Reverse primer (5' to 3')
R1	TCAGGCCTTCGCAGCATTCT	TAATACGACTCACTATA**G**TCAGGCCTTCGCAGCA	TTCTAGCTCTAAAACAGAATGCTGCGAAGGCCTG
R2	CCTTCGCAGCATTCTTGGGT	TAATACGACTCACTATA**G**CCTTCGCAGCATTCTT	TTCTAGCTCTAAAACACCCAAGAATGCTGCGAAG
R8	ACAAGGGCCACAGCCATGAA	TAATACGACTCACTATA**G**ACAAGGGCCACAGCCA	TTCTAGCTCTAAAACTTCATGGCTGTGGCCCTTG
R9	GAGGTCACTTTATAAGGGTC	TAATACGACTCACTATA**G**GAGGTCACTTTATAAG	TTCTAGCTCTAAAACGACCCTTATAAAGTGACCT
R21	GCTCCAGCTGGATGACTC	TAATACGACTCACTATA**G**CTCCAGCTGGATGAC	TTCTAGCTCTAAAACGCTGGAGCCCTGACTGGC
R22	GCCACTCAGGGCTCCAGC	TAATACGACTCACTATA**G**CCACTCAGGGCTCCA	TTCTAGCTCTAAAACGCTGGAGCCCTGAGTGGC
R23	GCCTGAGCTCAGCCACTC	TAATACGACTCACTATA**G**CCTGAGCTCAGCCAC	TTCTAGCTCTAAAACGAGTGGCTGAGCTCAGGC
R24	GGCCTTCGCAGCATTCTT	TAATACGACTCACTATA**G**GCCTTCGCAGCATTC	TTCTAGCTCTAAAACAAGAATGCTGCGAAGGCC
R25	GCCACGGGTCAGCCACAA	TAATACGACTCACTATA**G**CCACGGGTCAGCCAC	TTCTAGCTCTAAAACTTGTGGCTGACCCGTGG
R26	GCCCTTGTGGCTGACCCG	TAATACGACTCACTATA**G**CCCTTGTGGCTGACC	TTCTAGCTCTAAAACCGGGTCAGCCACAAGGGC

Forward primer regions annealing to the T7 promoter are shown in blue, while reverse primer sections binding to the tracrRNA fragment are in black. Overlapping target sequences are in red. The T7 promoter element sequence included added a 5'G to the start of each transcript. Hence, the first nucleotide of target sites that naturally began with a 5'G was removed when designing forward primer sequences. Additionally, IVT primers for assembly of HPRT gRNA expression templates were provided in the kit.

3.5.19.2 Amplification of targeted regions for T7EI mismatch detection assay

For analysis of endogenous target regions					
Target	**Forward (5' to 3')**	**Reverse (5' to 3')**	**Annealing temp. (°C)**	**Product size**	**Cleaved fragment sizes (bp)**
Hybrid DNA positive control	Supplied by GeneArt Genomic Cleavage Detection Kit	Supplied by GeneArt Genomic Cleavage Detection Kit	55	516	291 and 225
HPRT	CTTGTTTATGGCCTCCATAG	GATGATGAACCAGGTTATGACC	61	607	386 and 221
RHO, gRNA1	CCAGAGGACATAGCACAGAGGC	ACGGTGACGTAGAGCGTGA	70	602	370 and 232
RHO, gRNA2	CCAGAGGACATAGCACAGAGGC	TGGACGGTGACGTAGAGCGT	70	605	375 and 230
RHO, gRNA8	CCAGAGGACATAGCACAGAGGC	TGGACGGTGACGTAGAGCGT	70	605	416 and 189
RHO, gRNA9	TGTCAGAGGAGTGTGGGGACTG	TACTCGAAGGGGCTGCGTACCA	72	609	417 and 192

HPRT and *RHO* regions of interest were amplified to test for the presence of Cas9-induced indels.

'Parental' amplicon sizes and predicted fragments generated from T7EI cleavage are listed.

For analysis of plasmid-contained target regions					
Target	**Forward (5' to 3')**	**Reverse (5' to 3')**	**Annealing temp. (°C)**	**Product size**	**Cleaved fragment sizes (bp)**
HPRT	GGTGAACTTCAAGATCCGCC	CTTGTACAGCTCGTCCATGC	67	647	406 and 241
RHO, gRNA1	GGTGAACTTCAAGATCCGCC	CTTGTACAGCTCGTCCATGC	67	650	395 and 255
RHO, gRNA2	GGTGAACTTCAAGATCCGCC	CTTGTACAGCTCGTCCATGC	67	650	400 and 250
RHO, gRNA8	GGTGAACTTCAAGATCCGCC	CTTGTACAGCTCGTCCATGC	67	650	441 and 209
RHO, gRNA9	GGTGAACTTCAAGATCCGCC	CTTGTACAGCTCGTCCATGC	67	650	324 and 326
RHO, gRNA21	GGTGAACTTCAAGATCCGCC	CTTGTACAGCTCGTCCATGC	67	650	348 and 302
RHO, gRNA22	GGTGAACTTCAAGATCCGCC	CTTGTACAGCTCGTCCATGC	67	650	358 and 292
RHO, gRNA23	GGTGAACTTCAAGATCCGCC	CTTGTACAGCTCGTCCATGC	67	650	369 and 281
RHO, gRNA24	GGTGAACTTCAAGATCCGCC	CTTGTACAGCTCGTCCATGC	67	650	396 and 254
RHO, gRNA25	GGTGAACTTCAAGATCCGCC	CTTGTACAGCTCGTCCATGC	67	650	425 and 225
RHO, gRNA26	GGTGAACTTCAAGATCCGCC	CTTGTACAGCTCGTCCATGC	67	650	327 and 233

Plasmids were designed to contain short GFP sequences flanking HPRT or RHO regions. GFP primers were therefore used to amplify target regions for T7EI indel detection analysis. Successful Cas9 targeting would induce indels at different sites, depending on the gRNA used. Predicted fragment sizes generated from T7EI cleavage at indel heteroduplex sites are listed.

3.5.19.3 Cloning

PCR primers for cloning of pAAV-CMV-Cas9					
Target	Forward Primer (5'-3')	Reverse Primer (5'-3')	Annealing Temp. (°C)	Product size (bp)	Elements added via primer
CMV promoter	GCAGTCTAGACGTTACAT AACTTACGGTAAATGGC	TAGCACCGGTAGCTCTGC TTATATAGACCTCCCA	64	528	Restriction sites (XbaI and AgeI)

PCR primers for cloning of pAAV-UBC-CMV-DsRed					
Target	Forward Primer (5'-3')	Reverse Primer (5'-3')	Annealing Temp. (°C)	Product size (bp)	Elements added via primer
UBC spacer	GCAGACGCGTGCTAGCACTAGTGTTCCC GAGTCTTGAATGGA	TAGCACGCGTGACGACAAACCGAG TTCTCC	65	238	Restriction sites (MluI, NheI, SpeI)

Primers used in PCR cloning reactions are listed. Non-annealing portions of oligonucleotides (for the addition of new sequence elements) are highlighted in red.

PCR primers for cloning of pAAV-HITI constructs					
Product	**Forward Primer (5'-3')**	**Reverse Primer (5'-3')**	**Annealing Temp. (°C)**	**Product size (bp)**	**Elements added via primer**
U6 promoter fragment for pAAV-HITI-gR22	GCAGGCTAGCGAGGGCCTATTTCCCATGATT	GCTGGAGCCCTGAGTGGCGGTGTTTCGTCCTTTCCACAAG	65	279	Forward: Restriction site and Reverse: gRNA 22 crRNA sequence
U6 promoter fragment for pAAV-HITI-gR25	GCAGGCTAGCGAGGGCCTATTTCCCATGATT	TTGTGGCTGACCCGTGGCGGTGTTTCGTCCTTTCCACAAG	65	279	Forward: Restriction site and Reverse: gRNA 25 crRNA sequence
U6 promoter fragment for pAAV-HITI-gR25X	GCAGGCTAGCGAGGGCCTATTTCCCATGATT	GCCACGGGTCAGCCACAAGGTGTTTCGTCCTTTCCACAAG			Forward: Restriction site and Reverse: gRNA 25X crRNA sequence
gRNA fragment for pAAV-HITI-gR22	GCCACTCAGGGCTCCAGCGTTTTAGAGCTAGAAATAGCAAGTT	GTACACTGGCCAGCGCCTAAAACCCACTTGCACTC	61	148	Forward: gRNA 22 crRNA sequence Reverse: overlap region
gRNA fragment for pAAV-HITI-gR25	GCCACGGGTCAGCCACAAGTTTTAGAGCTAGAAATAGCAAGTT	GTACACTGGCCAGCGCCTAAAACCCACTTGCACTC	61	148	Forward: gRNA 25 crRNA sequence Reverse: overlap region
gRNA fragment for pAAV-HITI-gR25X	TTGTGGCTGACCCGTGGCGTTTTAGAGCTAGAAATAGCAAGTT	GTACACTGGCCAGCGCCTAAAACCCACTTGCACTC			Forward: gRNA 25X crRNA sequence Reverse: overlap region
EGFP for pAAV-HITI-gR22	CGCTGGCCAGTGTACGCCACTCAGGGCTCCAGCTGGCGCCACCATGGTGAGCAAGG	TAGCACTAGTCCAGCTGGAGCCCTGAGTGGCGTTCCTGCGGCCGCACAC	60	900	Forward: overlap, gRNA 22 target site (crRNA plus PAM site) Reverse: gRNA 22 target site, SpeI cut site
EGFP for pAAV-HITI-gR25	CGCTGGCCAGTGTACCCCTTGTGGCTGACCCGTGGCCGCCACCATGGTGAGCAAGG	TAGCACTAGTGCCACGGGTCAGCCACAAGGGGTTCCTGCGGCCGCACAC	60	900	Forward: overlap, gRNA 25 target site Reverse: gRNA 25 target site, SpeI cut site

EGFP for pAAV-HITI-gR25X	CGCTGGCCAGTGTACCCGTTGTGGC TGACCCGTGGCCGCCACCATGGT GAGCAAGG	TAGCACTAGTGCCACGGGTCAGCC ACAACGGGTTCCTGCGGCCGCACA C			Forward: overlap, gRNA 25X target site Reverse: gRNA 25X target site, SpeI cut site
Full insert for pAAV-HITI-gR22: U6, gRNA and EGFP	GCAGGCTAGCGAGGGCCTATTTCCCAT GATT	TAGCACTAGTCCAGCTGGAGCCCT GAGTGGCGTTCCTGCGGCCGCACA C	60	1305	N/A
Full insert for pAAV-HITI-gR25: U6, gRNA and EGFP	GCAGGCTAGCGAGGGCCTATTTCCCAT GATT	TAGCACTAGTCCAGCTGGAGCCCT GAGTGGCGTTCCTGCGGCCGCACA C	60	1305	N/A
Full insert for pAAV-HITI-gR25: U6, gRNA and EGFP	GCAGGCTAGCGAGGGCCTATTTCCCAT GATT	TAGCACTAGTGCCACGGGTCAGCC ACAACGGGTTCCTGCGGCCGCACA C	60	1305	N/A

Non-annealing portions of oligonucleotides are highlighted in red.

3.5.19.4 qPCR

qPCR Primers		
Target	**Forward (5’ to 3’)**	**Reverse (5’ to 3’)**
SpCas9	CCTGTTCGACGACAAAGTGA	GAAGTTTCTGTTGGCGAAGC
CMV enhancer	TTACGGTAAACTGCCCACTTG	CGTGAGTCAAACCGCTATCC
gR22	AGGGCTCCAGCGTTTTAGAG	CGGTGCCACTTTTTCAAGTT
gR25	CGGGTCAGCCACAAGTTTTA	CGGTGCCACTTTTTCAAGTT
gR25X	GACCCGTGGCGTTTTAGAG	CGGTGCCACTTTTTCAAGTT
β-actin	AGAGCAAGAGAGGCATCC	TCATTGTAGAAGGTGTGGTGC
EGFP	GGTGAACTTCAAGATCCGCC	CTTGTACAGCTCGTCCATGC

4 Exploration of a transkingdom gene therapy for glaucoma

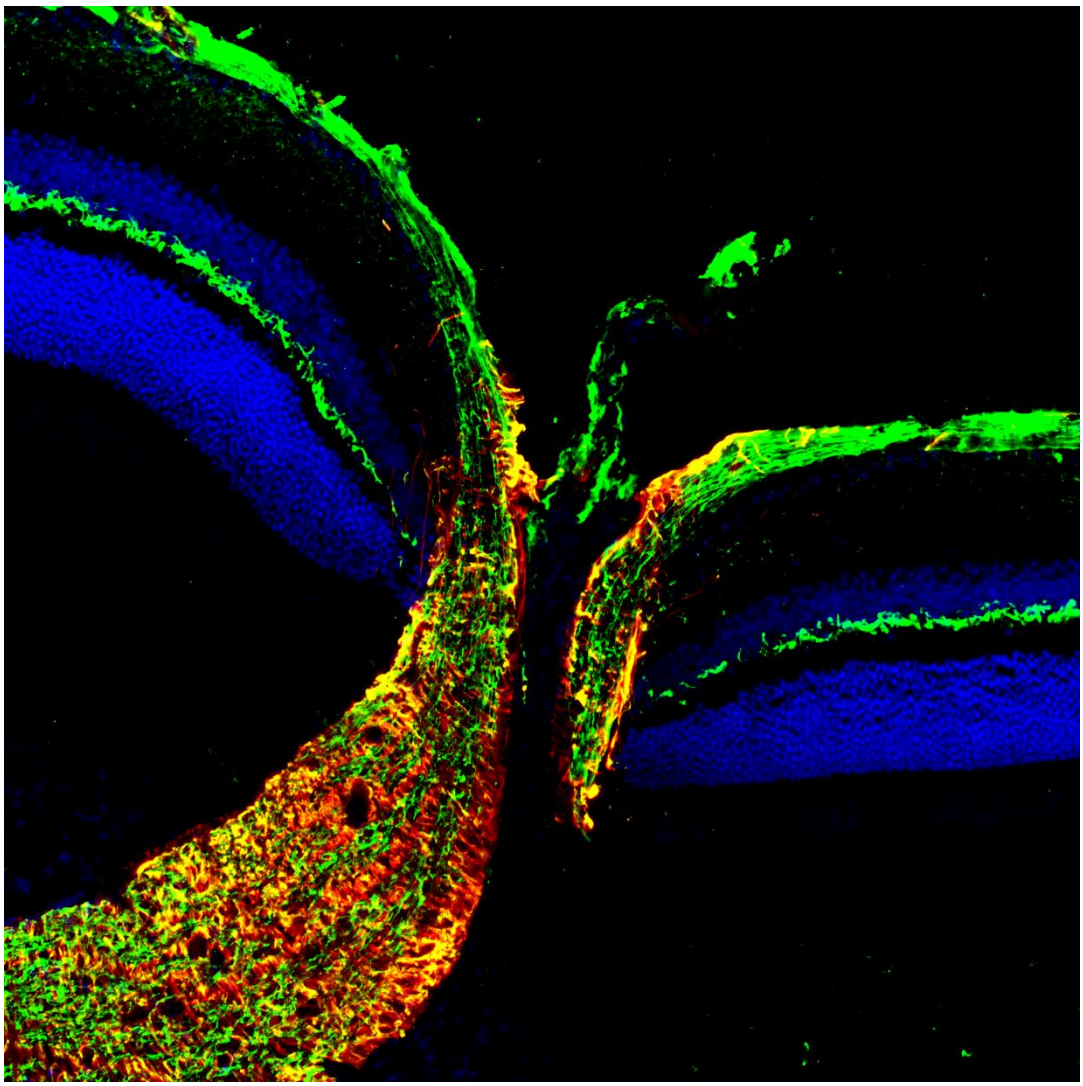

4.1 Acknowledgment of Contributions

Study concept: Prof. G Jane Farrar.

AAV production: Dr Naomi Chadderton.

Intravitreal injections: Mr Paul Kenna.

Electroretinograms: Dr Sophia Millington-Ward.

Retinal cryosectioning and retinal wholemount assistance: Dr Arpad Palfi.

IOP measurement assistance: Dr Jeffrey O'Callaghan.

Flow cytometry assistance: Dr Daniel Manraj Maloney and Dr Sophia Millington-Ward.

4.2 Introduction

4.2.1 Glaucoma

4.2.1.1 Prevalence

Glaucoma is a neurodegenerative disease in which retinal ganglion cells are progressively lost. Globally, this optic neuropathy is the second most common cause of blindness (after cataracts) and is the leading form of irreversible blindness (Kingman, 2004). In 2013, there were an estimated 64.3 million cases of glaucoma worldwide. As populations age, this figure is predicted to rise to 76 million people in 2020 and 111.8 million by 2040 – largely due to substantial increases in life expectancy in Africa and Asia (Tham et al., 2014). 13.9% of individuals with glaucoma are estimated to be bilaterally blind (Quigley and Broman, 2006).

4.2.1.2 Disease presentation

Glaucoma typically manifests during or after middle age and progresses slowly. In developed nations it is estimated that about half of people with glaucoma are unaware they are affected, while this figure can rise to 97% in developing countries (Kingman, 2004, Budenz et al., 2013).

Glaucoma can be considered an umbrella term for a variety of multifactorial optic neuropathies. In each of these conditions, RGC axons degenerate, causing a thinning of the neuroretinal rim and 'excavation' of the optic nerve head (ONH; the site at which RGC axons exit the eye). The optic cup consequently becomes enlarged relative to the optic disc – a phenomenon sometimes referred to as optic disc cupping or excavation (Casson et al., 2012) (Fig 4.1). Peripheral vision is initially affected but visual field loss may not be noticed for some time, as the brain can compensate by 'filling-in' information (Janssen et

al., 2013). Without successful intervention, the disease can progress to a state of complete blindness (Casson et al., 2012).

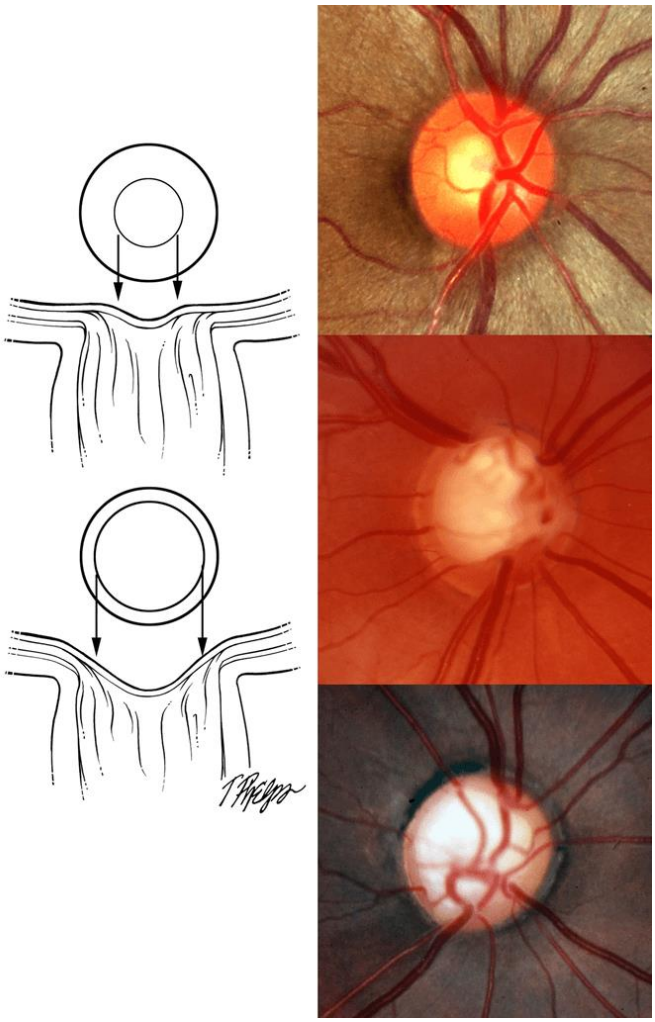

Fig. 4.1. Optic nerve cupping.
Left: A normal optic nerve head is shown above and a glaucomatous ONH with a thinned nerve fibre layer below. In the circles shown, the outer ring represents the optic disc area (corresponding to fibres of the ONH), while the inner ring depicts the cup area (a groove free of fibres in the centre of the ONH). Right: fundus images show retinas with a normal optic cup:disc ratio (top), abnormally enlarged cup (middle) and a severely glaucomatous retina with a large cup:disc ratio (bottom).
Figure reproduced from https://www.hopkinsmedicine.org/wilmer/services/glaucoma/book/ch06s03.html [accessed: 02/09/20].

4.2.1.3 Types of glaucoma

Glaucoma is classed as 'open-angle' or 'angle closure' based on the size of the iridocorneal angle. In angle closure forms of the disease, the angle between the iris and cornea is narrowed, blocking aqueous humour (AH) outflow. In contrast, in open-angle glaucoma the iridocorneal angle is normal but AH drainage is impeded due to downstream trabecular meshwork abnormalities. Blockage of AH drainage, whether through constriction of the iridocorneal angle or increased resistance in the TM, leads to an elevation of intraocular pressure (IOP). Glaucoma is further categorised into primary or secondary forms, based on whether its development is dependent on another underlying condition. It is important to note that glaucoma can develop in the absence of increased

IOP. Primary open-angle glaucoma (POAG) is thus divided into ocular hypertension glaucoma (HTG) and normal-tension glaucoma (NTG) (Saccà et al., 2014).

POAG accounts for 74-86% of primary glaucoma cases (Quigley and Broman, 2006, Tham et al., 2014). Although primary angle closure glaucoma (PACG) is less prevalent globally, the number of blind POAG and PACG patients is thought to be roughly equal because of the severity of PACG progression (Quigley and Broman, 2006). Secondary forms of glaucoma are estimated to occur ~ 9% as often as primary glaucomas (Quigley, 1996) and can arise from trauma or a variety of conditions, including lens abnormalities (phacomorphic or phacolytic glaucoma), inflammation (uveitic glaucoma), diabetes mellitus (neovascular glaucoma), long-term steroid use (corticosteroid-induced glaucoma), pseudoexfoliation syndrome and pigment dispersion syndrome (Krishnadas and Ramakrishnan, 2001).

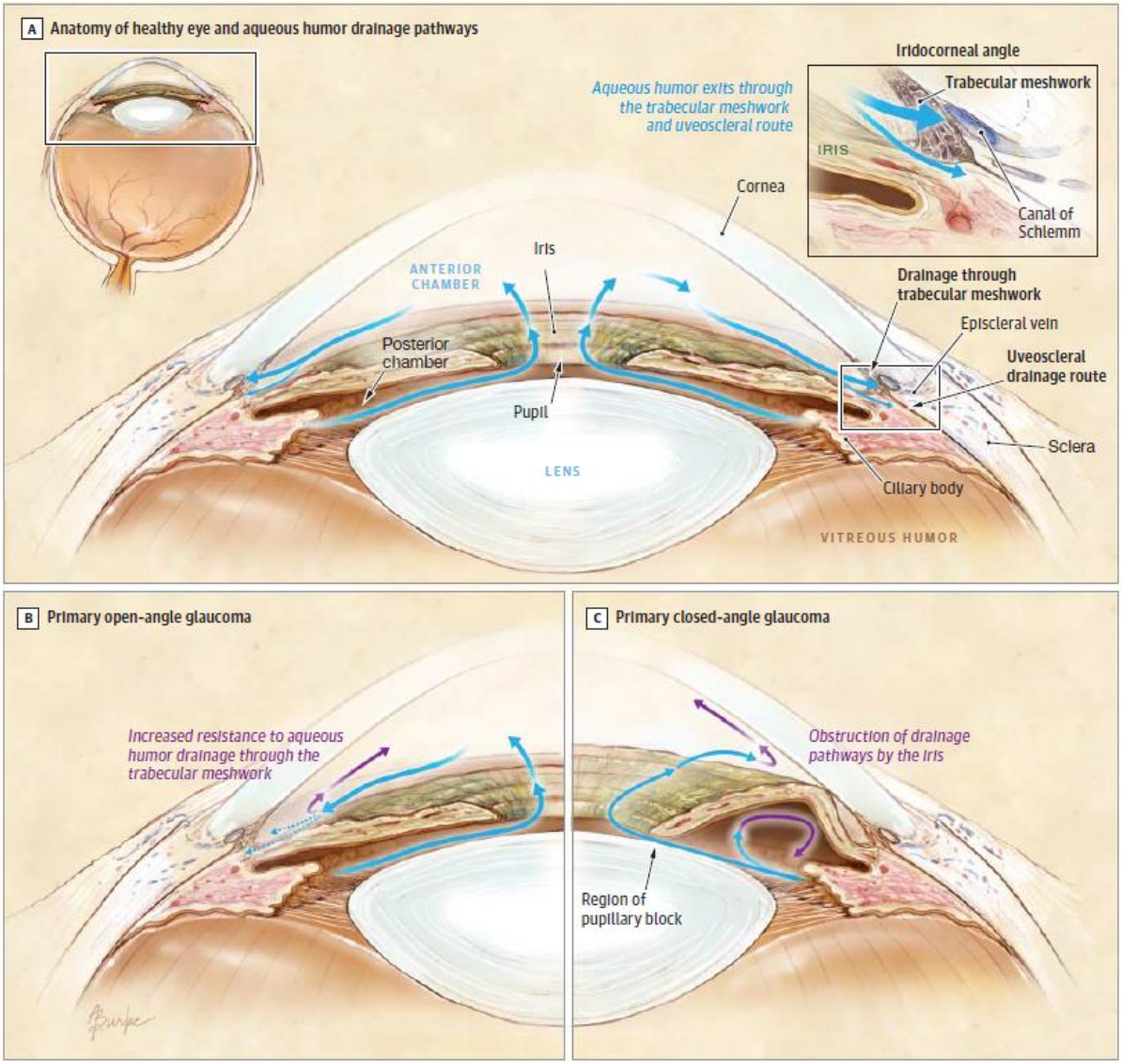

Figure 4.2. Aqueous fluid drainage and its blockage in open- and closed-angle glaucoma. Figure reproduced from Weinreb et al., 2014.

4.2.1.4 Risk factors

4.2.1.4.1 IOP

IOP varies depending on age, sex and ethnicity (Leske et al., 1997) (Hashemi et al., 2005), and also fluctuates diurnally (David et al., 1992). Normal IOP ranges from 10-21 mmHg, whereas individuals with an IOP greater than 21 mmHg are classed as having ocular hypertension (OHT) and considered at risk of developing glaucoma (Wang et al., 2018). As IOP is the only modifiable risk factor for this disease, treatment for glaucoma has thus far relied upon IOP-reducing measures - eye drops containing compounds that lower aqueous humour (AH) production from the ciliary body and/or increase AH drainage. Such treatments include prostaglandins (PGAs), β-blockers, alpha adrenergic agonists,

carbonic anhydrase inhibitors and Rho kinase inhibitors (reviewed by Lusthaus and Goldberg, 2019). These topical treatments are associated with side effects, which range from minor, reversible cosmetic changes in the case of PGAs to bronchoconstriction and systemic hypotension induced by β-blockers. The main obstacle to successful treatment with topical medication is lack of compliance. It has been estimated that, on average, patients only apply half of the eye drops they are prescribed (Quigley, 2019). In cases unresponsive to topical treatment, surgical intervention, such as trabeculotomy or insertion of drainage enhancement devices, may be necessary (Lusthaus and Goldberg, 2019).

However, not all individuals with chronically high IOP develop glaucoma (Lascaratos et al., 2015). Conversely, as mentioned previously, glaucoma can manifest in individuals with normal IOP levels (≤ 21 mmHg; NTG). NTG affects approximately one third of Caucasian patients and is more prevalent still in Asian populations, underlying up to 92% of Japanese POAG cases (Iwase et al., 2004). There must, therefore, be additional factors determining an individual's susceptibility to glaucoma.

4.2.1.4.2 Age

As with many other neurodegenerative disorders, risk of glaucoma increases with age (Suzuki et al., 2006, European Glaucoma Prevention Study et al., 2007, Friedman et al., 2006, Leske et al., 2007), with symptoms typically developing during or after middle age (>40 years). With each decade, the risk of POAG is estimated to increase by 1.4 – 2.3 fold (Rudnicka et al., 2006, Song et al., 2017, Friedman et al., 2006).

4.2.1.4.3 Sex

Interestingly, women are significantly more at risk of angle-closure glaucoma across all populations studied, which is likely a result of a decreased anterior chamber depth (ACD) relative to that of males (reviewed by Amerasinghe and Aung, 2008, Vajaranant et al., 2010). In contrast, women have a reduced likelihood of developing POAG than men and this risk appears to be lower still in women with longer reproductive periods. Estrogen is notably established to have neuroprotective properties and may also be involved in the regulation of IOP and ocular blood flow dynamics (reviewed by Zetterberg, 2016, Nuzzi et al., 2019). It is therefore possible that female levels of estrogen can offer a certain amount of protection to RGCs in some glaucomatous contexts but not others. It is worth noting that the clinical presentation of POAG and PACG can be quite different. PACG

progression is more dependent on IOP (Gazzard et al., 2003), with patients tending to exhibit 'sharp spikes' of IOP (Yousefi et al., 2018), while (as previously mentioned) POAG often occurs at normal IOP levels. PACG patients are three times more likely to progress to a stage of severe visual impairment in both eyes (Sun et al., 2017).

4.2.1.4.4 Ethnicity

People of African descent are disproportionately affected by POAG (Rudnicka et al., 2006, Tham et al., 2014, Friedman et al., 2006) – particularly West Africans (Budenz et al., 2013) – and are also reported to experience an earlier-onset, more severe form of disease (Salowe et al., 2015). In contrast, Asian ethnicity is a higher risk factor for PACG; 80% of individuals affected by PACG are living in Asia (Tham et al., 2014, Song et al., 2017, Quigley and Broman, 2006).

4.2.1.4.5 Heredity

A positive family history of glaucoma greatly increases an individual's chance of developing the disease (Tielsch et al., 1994, Wolfs et al., 1998, Wang et al., 2010b). In particular, siblings of POAG patients are estimated to be 4-15 times more likely to develop glaucoma (Tielsch et al., 1994, Wolfs et al., 1998). The heritability of POAG is estimated to be 70-93% (Sears et al., 2019), while PACG is over 60% heritable in Chinese populations (Wang et al., 2019b).

POAG and PACG are complex inherited traits; the vast majority of cases do not present with a distinct, Mendelian pattern of inheritance. Approximately 5% of POAG cases are autosomal dominant, arising from pathogenic variants in myocilin *(MYOC)*, optineurin *(OPTN)* or tank binding kinase 1 (*TANK1*) (Sears et al., 2019). The remaining 95% of POAG cases not yet linked to a genetic insult suggest that much of the heredity in POAG may be polygenic and/or under environmental influence (Abu-Amero et al., 2015). Genome-wide association studies (GWAS) have identified many additional loci associated with increased risk of POAG, PACG or endophenotypes of these diseases (i.e. IOP, retinal nerve fibre layer thickness or ACD) (reviewed by Liu and Allingham, 2017, Youngblood et al., 2019, Wang et al., 2019b). It has been demonstrated that individuals with a greater 'dose' or cumulative load of risk alleles have a greater risk of developing POAG (MacGregor et al., 2018) or having an earlier onset of disease (Fan et al., 2019). A polygenic risk score was recently developed than can predict these risks and identify patients in need of more

intensive treatment (Craig et al., 2020). Genetic screening may thus be incorporated into practices for the detection and management of glaucoma in the not-too-distant future.

4.2.2 Mitochondrial dysfunction in glaucoma

4.2.2.1 Systemic mitochondrial dysfunction in glaucoma

Mitochondrial involvement in the pathogenesis of glaucoma was first suspected due to the disease's similarity to mitochondriopathies such as Leber hereditary optic neuropathy (LHON) and dominant optic atrophy (DOA), in which RGCs are also preferentially lost. Interestingly, a maternal family history of POAG is reported more frequently than a paternal lineage (Shin et al., 1977, Nemesure et al., 1996), leading to further speculation of a mitochondrial influence.

Of the three genes linked to Mendelian glaucoma, all three have links to mitochondria. The products of *OPTN* and *TANK1* are both involved in mitophagy. Knockdown of *TANK1* causes an accumulation of aberrant mitochondria (Moore and Holzbaur, 2016), while expression of a pathogenic *OPTN* allele leads to elevated mitochondrial degradation and oxidative stress in RGCs (Shim et al., 2016). MYOC has also been established to associate with mitochondria in the TM (Sakai et al., 2007). Overexpression of a POAG-associated MYOC allele resulted in a decrease in ATP production, higher levels of ROS, disrupted calcium homeostasis and increased cell death in primary TM cells (He et al., 2009). SNPs in *OPA1*, a nuclear gene encoding a protein essential for mitochondrial fusion, and *ND2*, a mtDNA encoded Complex I subunit, have been also associated with increased risk of normal tension glaucoma (NTG) development (Yu-Wai-Man et al., 2010, Jeoung et al., 2014). OPA1 expression was further demonstrated to be downregulated in POAG patient peripheral blood leukocytes (Bosley et al., 2011). Thioredoxin reductase 2 (*TXNRD2*), part of the mitochondrial thioredoxin antioxidant system, was identified as a risk factor for POAG in a large GWAS study (Bailey et al., 2016). Other genes with mitochondrial roles (ME3, VPS13C, GCAT, PTCD2) have also been linked to IOP via GWAS (Choquet et al., 2020).

Some African mitochondrial haplotypes have been associated with increased risk of POAG in African American (Collins et al., 2016; L1c2 and L2 haplotypes) and Saudi Arabian cohorts (Abu-Amero et al., 2011; L macro haplogroup). The haplotypes in question are carried by a quarter of African-Americans (Collins et al., 2016), which may offer some

explanation as to why this population is approximately four times more at risk of developing POAG than Caucasians (Tielsch et al., 1991). As mentioned previously, African-American individuals moreover tend to manifest an earlier-onset, more severe and faster progressing form of the disease (Salowe et al., 2015). The Eurasian N1 haplotype appears to confer a protection from POAG in Saudi Arabian individuals (Abu-Amero et al., 2011). Severity of POAG presentation also seems to differ between the implicated African mitochondrial haplotypes - L1c2 being associated with a more severe form of POAG than L1b (Cui et al., 2019). Notably, variants in the L1c2 haplotype include three missense mutations in the cytochrome oxidase c subunit gene (*CO1*), which encodes a key component of the ETC Complex IV. Although the inherited mtDNA haplotype variants in question may alone have only mild effects on mitochondrial function, they are proposed to push the mutational load of mitochondria over a threshold where energy production is insufficient in cells with especially high energy demands, such as RGCs (Collins et al., 2016).

It is interesting that men have an increased risk of developing POAG compared to females across all ethnicities (Khachatryan et al., 2019, Kapetanakis et al., 2016). This pattern has been noted as reminiscent of the incomplete penetrance of LHON (Collins et al., 2018), which is approximately four times more likely to manifest in males than females (Yu-Wai-Man et al., 2002). The sexual dimorphism in LHON is thought to be a consequence of a 'sex-specific selective sieve.' Natural selection can only act upon mtDNA within females and so maternal transmission allows for the accumulation of mtDNA mutations that may be deleterious to males while being neutral or even beneficial to females (Frank and Hurst, 1996, Milot et al., 2017) – an effect termed 'Mother's curse' by evolutionary biologists.

As discussed in section 1.7, mitochondrial DNA is inherently more unstable than the nuclear genome and accumulates mutations at a relatively high rate. As only 3% of the mitochondrial genome is comprised of non-coding DNA (in contrast to 93% of the nuclear genome) (Chial and Craig, 2008), mutations are more likely to be deleterious in this context. Several studies have investigated the possibility that mitochondrial DNA may mutate at an accelerated rate in glaucoma patients by sequencing peripheral blood leukocyte samples. The majority (60%) of POAG patients in a Saudi Arabian cohort were found to have non-synonymous mtDNA mutations – most of which were transversions,

indicating an elevated level of oxidative stress (Abu-Amero et al., 2006). In a study of Indian and Irish POAG patients, half of the cohort contained somatic mtDNA mutations (Sundaresan et al., 2015). 36% of identified mutations were located in genes encoding Complex I subunits. Of the patients who harboured a mtDNA mutation, 31% carried a variant in the *ND5* CI subunit gene specifically. This corroborated the results of a larger Indian study, in which non-synonymous mutations of mtDNA in POAG patients were most often found in *ND5* (24% of cases) (Banerjee et al., 2013). MtDNA mutations have also been noted in blood samples of primary congenital glaucoma, primary angle closure glaucoma, and pseudoexfoliation glaucoma patients, though at lower frequencies (~10-23% of patients) (Sundaresan et al., 2015).

The predominance of mtDNA mutations affecting Complex I is not surprising, as NADH:ubiquinone oxidoreductase dysfunction is the most frequently cited ETC defect in mitochondriopathies (Rodenburg, 2016). Complex I is the largest of the ETC protein complexes with subunits encoded by 45 different genes, mutations in 26 of which have been linked to metabolic disorders (Rodenburg, 2016). (For comparison, the other ETC complexes are comprised of 4-11 subunits.) Additionally, mutations in the genes encoding the assembly factors required for the joining of Complex I subunits, have also been established as pathogenic (Nouws et al., 2012). In the OXPHOS system, Complex I also possesses the largest number of subunits encoded by mtDNA (7); 38% of the mitochondrial genome codes for Complex I subunits - including *ND5,* the largest mitochondrial gene (1811bp).

POAG patient-derived lymphocytes and lymphoblasts have been demonstrated to exhibit significant deficits in mitochondrial respiratory activity (Abu-Amero et al., 2006, Lee et al., 2012), Complex-I enzymatic activity (Van Bergen et al., 2015) and Complex I-driven ATP-synthesis (Lee et al., 2012, Van Bergen et al., 2015). Van Bergen et al. additionally observed reduced Complex II-driven ATP synthesis and impaired growth of POAG lymphocytes when forced to rely on OXPHOS. The abnormal bioenergetic profile of POAG patient lymphocytes was suggested to be a consequence of fragmentation of the mitochondrial network or increased accumulation of mtDNA mutations (Yu-Wai-Man, 2012).

Depletion of antioxidants, including glutathione, has also been observed in POAG patient blood samples (Gherghel et al., 2005, Sorkhabi et al., 2011). Additionally, the plasma

citrate levels of glaucoma patients were noted to be abnormally low. As citrate is produced in the mitochondria for use in the TCA cycle and has antioxidant properties, its depletion is likely indicative of reduced mitochondrial function and/or increased reliance on citrate as an antioxidant (Fraenkl et al., 2011).

Very interestingly, increased systemic mitochondrial efficiency has been linked to reduced susceptibility to POAG. Lascaratos et al. (2015) characterised mitochondrial function in glaucoma 'resistant' individuals, manifesting no glaucomatous features despite having chronically high IOP (ocular hypertension; OHT), and especially susceptible people (NTG patients). Lymphocytes from resistant individuals displayed increased Complex I, II and IV-driven ATP production, increased hyperpolarised mitochondrial membrane potential, more mtDNA and increased tolerance to cytosolic calcium overload compared to both susceptible and unaffected control groups. Despite increased mitochondrial function, samples from the resistant cohort displayed lower levels of oxidative damage than NTG specimens. This suggests an above-average level of mitochondrial efficiency in individuals with high IOP who do not develop glaucomatous optic neuropathy (Lascaratos et al., 2015). Further work suggests that mitochondrial function is also more compromised in normotension compared to hypertension POAG cases (Petriti et al., 2020)[32].

Taken as a whole, the evidence strongly suggests that perturbation of systemic mitochondrial function, in particular Complex I activity, increases susceptibility to POAG.

4.2.2.2 Oxidative stress in the trabecular meshwork

The trabecular meshwork is established as the tissue most susceptible to oxidative damage in the anterior chamber. It appears incapable of mounting the antioxidant responses activated in light-sensing tissues such as the cornea and iris (Izzotti et al., 2009). POAG patient TM cells have been shown to undergo increased DNA oxidation relative to controls. Significantly, the level of oxidative damage in patient cells was proportional to IOP level and restriction of visual field (Sacca et al., 2005). TM cells from POAG patients were shown to have a five-fold increased incidence of a large (4977 bp) mtDNA deletion associated with oxidative damage, which coincided with a similarly sized depletion in mitochondrial number (Izzotti et al., 2010). This elevation of oxidative damage to TM cell mtDNA appears to be restricted to POAG and pseudoexfoliative forms

[32] Petriti et al. 2020 is a conference abstract (not peer-reviewed).

of glaucoma (Izzotti et al., 2011). The 4977bp mtDNA deletion is found to commonly accumulate with age and in mitochondrial disorders (Meissner et al., 2008, Zhang et al., 2015b). This lesion deletes almost one third of the mitochondrial genome, including most of the OXPHOS system (4 Complex I, 1 Complex IV and 2 Complex V subunits as well as all tRNA genes) (Yusoff et al., 2019).

A null mutation in glutathione S-transferase 1 (*GSTM1*), which plays a key role in antioxidant defence, was associated with an increased level of mtDNA damage in POAG patient TM cells (Izzotti et al., 2010). Homozygous *GSTM1* null patients were later found to be significantly more likely to be experience a more severe form of POAG - unresponsive to topical medical treatment and requiring filtration surgery (Saccà et al., 2019). POAG patient-derived TM cells have also displayed impaired mitochondrial function, indicated by decreased membrane potential and ATP production, and higher amounts of ROS (He et al., 2008). Notably, POAG TM cells were more sensitive to Complex I inhibition than controls but tolerated Complex II and III inhibition.

In addition to oxidative stress likely generated via mitochondrial dysfunction, TM cells are constantly exposed to UV-generated ROS from the aqueous humour, cornea and lens epithelium (Stamer and Clark, 2017). Aqueous humour samples of POAG patients also indicated elevated oxidative stress in anterior chamber tissues – antioxidant molecules were depleted, accompanied by an apparent compensatory increase in antioxidant enzyme activity (Ferreira et al., 2004, Sorkhabi et al., 2011).

Oxidative stress has been demonstrated to alter TM cell characteristics *in vitro*. When TM cultures were subjected to hydrogen peroxide, cells exhibited reduced adhesion to ECM components as well as cytoskeletal rearrangement (Zhou et al., 1999). Cell-matrix adhesion is vital for maintaining TM structural integrity and its compromise may lead to cell loss and collapse of the TM (Zhou et al., 1999). Saccá et al. hypothesised that oxidative stress may also contribute to the trabecular thickening and fusion observed in POAG and elderly individuals (Sacca et al., 2007). Thus, oxidative damage to the TM structure may increase AH outflow resistance, leading to elevation of IOP. Mutation of mtDNA or antioxidant genes, such as *GSTM1*, could increase vulnerability to this pathology.

4.2.2.3 RGC mitochondrial dysfunction and degeneration

CNS axons are generally highly dependent on oxidative phosphorylation, with ~70% of ATP generated required for maintenance of membrane resting potential (Osborne et al., 2016, Inman and Harun-Or-Rashid, 2017). To maintain visual perception, RGCs are estimated to use 4.7 x 10^8 ATP molecules per second/per cell (Casson et al., 2019). RGCs are particularly vulnerable to perturbed bioenergetics because of their unique structure. To allow light to pass through to photoreceptors, the portion of RGC axons that traverse the NFL are transparent and, therefore, unmyelinated. Mitochondria are concentrated in unmyelinated axonal regions to enable propagation of action potentials, compensating for the lack of saltatory conduction (Fig. 4.3). As a result, RGCs are thought to be the most mitochondria-rich neurons in the entire CNS (Osborne and del Olmo-Aguado, 2013).

While glaucoma subtypes vary in terms of several parameters, degeneration of RGCs is a feature common to all glaucoma cases. Glaucoma is clinically recognised by thinning of the neuroretinal rim and excavation of the optic disc, as RGC axons degenerate, and deformation of the lamina cribrosa (a structurally supportive mesh of collagen and elastin fibres filling the scleral opening that RGC axons pass through) (Casson et al., 2012, Tan et al., 2018). While RGC density is estimated to decline by approximately 0.4% per year normally, the rate of RGC loss is increased by 10 fold in glaucoma patients (Cordeiro et al., 2011). RGC death in glaucoma is thought, for the most part, to be mediated by apoptosis (Davis et al., 2016), though the initial axonal degeneration appears caspase-independent and to occur via Wallerian degeneration (Inman and Harun-Or-Rashid, 2017).

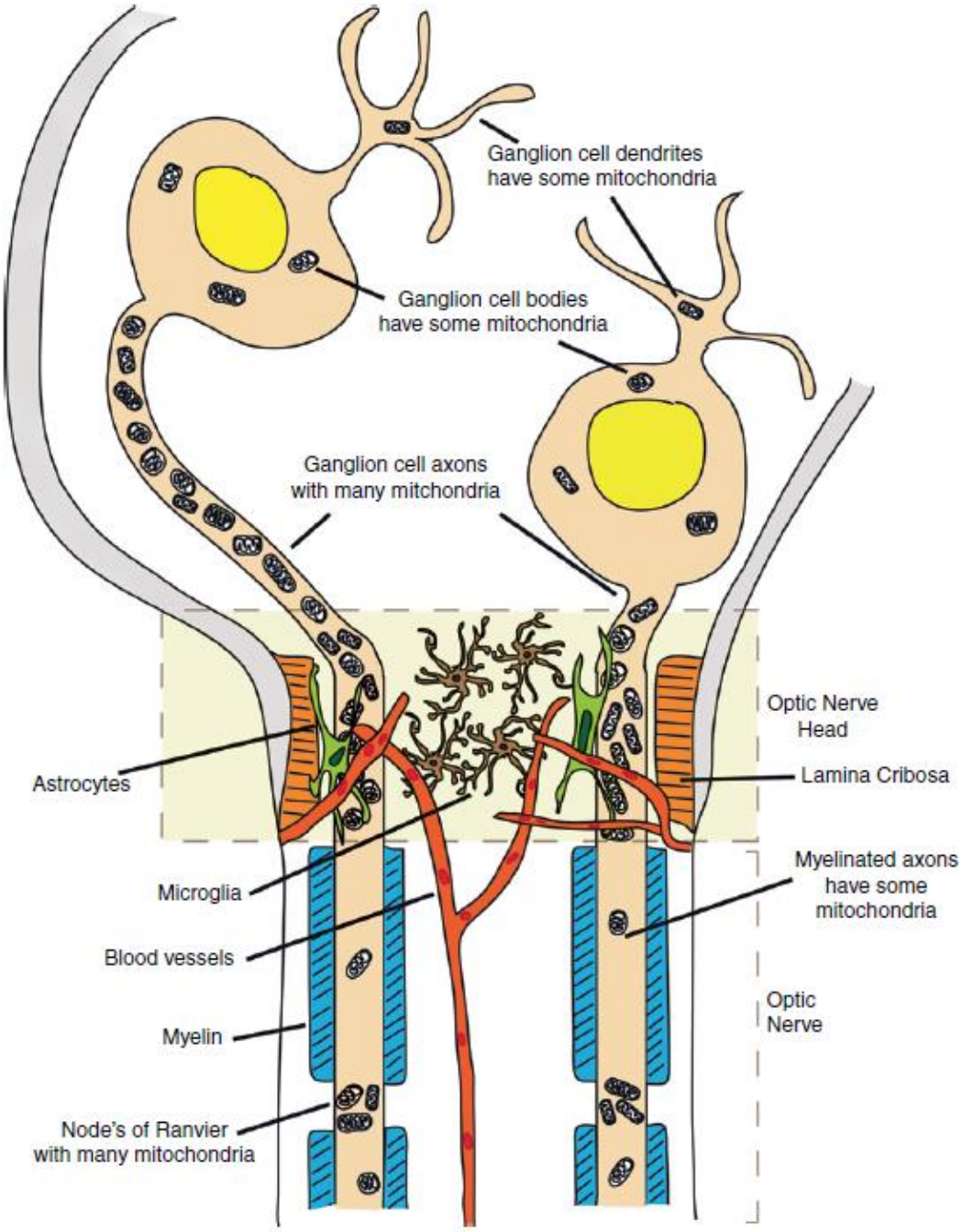

Fig 4.3. Mitochondrial distribution in RGCs.

Mitochondria are enriched in unmyelinated axonal regions (in the retinal globe and ONH). Along the myelinated optic nerve, mitochondria are sparsely distributed - apart from in the nodes of Ranvier (small gaps between myelin sheaths important for propagation of action potentials). The length of unmyelinated axon varies depending on a ganglion cell's position relative to the ONH. Hence, the number of mitochondria per RGC likely varies across the retina. Figure reproduced from Osborne and del Olmo-Aguado, 2013.

Although it is widely accepted that glaucomatous neurodegeneration is initiated by injury to the optic nerve head, the nature of this primary injury has yet to conclusively resolved. The 'mechanical theory' posits that elevated IOP causes nerve fibre bundles to be compressed at the lamina cribrosa, the 'weak spot' of the corneoscleral layer (Downs and Girkin, 2017), resulting in blockage of axoplasmic transport. The subsequent reduced supply of neurotrophic factors would lead to RGC degeneration. However, this model alone does not satisfactorily account for the occurrence of normal-tension glaucoma (Davis et al. 2016).

It is also hypothesised that intracranial pressure (ICP) plays a part in glaucomatous progression, as cerebrospinal fluid fills the subarachnoid space of the optic nerve sheath and the pressure profile there is thought to be similar to ICP. An increased translaminar pressure gradient (the difference between anterior-directed IOP and posterior-directed ICP) would exert mechanical stress on the LC and ONH. Low ICP has been noted in NTG than HTG patients and, conversely, was higher in non-glaucomatous OHT individuals than POAG patients. A surgical intervention that decreases ICP has also been found to significantly increase risk of NTG development (Baneke et al., 2020). It may therefore be the case that a combination of low ICP and normal IOP has a deleterious effect similar to normal ICP and elevated IOP, and that a higher ICP could be protective against raised IOP by maintaining a pressure gradient homeostasis.

The 'ischemic theory' proposes that altered blood flow dynamics cause damage to the ONH, either alone or as a result of mechanical stress caused by elevated IOP or an altered IOP/ICP balance. Altered haemodynamics is recognised as a major risk factor for glaucoma; systemic hypertension or hypotension, reduced ocular blood flow and ocular perfusion pressure have all been associated with POAG progression (Grzybowski et al., 2020, Davis et al., 2016, Kim and Choi, 2019). Linking this concept to mitochondrial dysfunction, Osborne et al. hypothesise that prolonged or repetitive ischemia (and, therefore, hypoxia and nutrient deprivation) impairs ATP production and induces a state of oxidative stress. This would weaken RGCs, making them more susceptible to other relatively minor insults – effectively driving them to a prematurely aged state (Osborne et al., 2016). In this model (Fig. 4.4), glial cells of the ONH are activated by ischemia and release trophic factors, such as glutamate, tumour necrosis factor α (TNFα) and nitric

oxide, in an attempt to prevent further damage. However, prolonged, unregulated release of these factors may cause RGC death via excitotoxicity (Osborne et al., 2016).

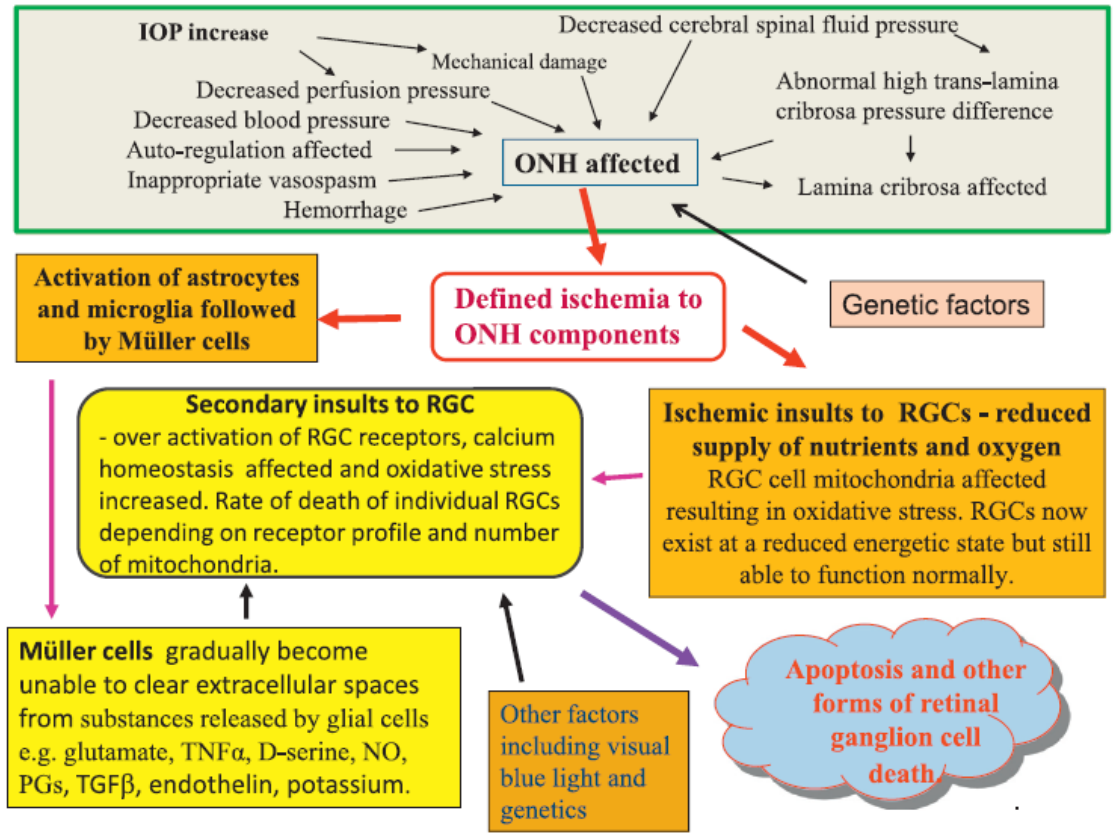

Fig. 4.4. Flow chart illustrating a model of glaucomatous progression after ischemic injury. TNFα = tumor necrosis factor α; NO = nitric oxide; PG =prostaglandins; TGFβ = transforming growth factor β. Figure reproduced from Osborne et al. 2016.

4.2.3 The DBA/2J mouse - a model of secondary angle-closure glaucoma

Many experimental models for glaucoma have been described, the DBA/2J mouse model being by far the most commonly used and well-characterised. “Dilute-brown non-agouti” (DBA) mice are the oldest inbred lab strain (established in 1929-30), with different colonies bred at a variety of institutions over the years. A recessive tyrosinase related protein 1 allele with two missense mutations (*Tyrp1*$^{R326H;C110Y}$ or *‘Typr1*^{b}*’)* causes iris stromal atrophy (Scholz et al., 2008), while an additional nonsense mutation in the glycoprotein NMB gene *(Gpnmb)* arose spontaneously in the 1980s and leads to iris pigment dispersion (IPD) (Anderson et al., 2002, Libby et al., 2005a, John et al., 1998, Schlamp et al., 2006). Tyrp1 and Gpnmb proteins are associated with melanosomes,

which are responsible for incapacitating the cytotoxic by-products of melanin production. Hence, it is thought that mutation of these genes leads to iris cell death by impairing melanosomal sequestration of toxic intermediates (John, 2005). Both *Gpnmb*^{R150X} and *Typr1*^{b} mutant alleles are necessary for initiation of a glaucomatous phenotype; DBA/2J with wild-type *Gpnmb* (DBA/2J-Gpnmb+) manifest a mild iris disease that does not progress to increased IOP or RGC degeneration (Howell et al., 2007b). C57BL/6J (C57) mice, which lack 'Typr1^{b}' and Gpnmb^{R150X} mutations, have traditionally been used as controls for comparison to DBA/2J mice, though they disparate strains. However, DBA/2J-Gpnmb+ mice may now function as an ideal experimental control strain in experiments, if logistically feasible.

Iris atrophy and pigment dispersion is evident at 5-6 months of age in DBA/2J mice. This leads to a build-up of pigment-filled macrophages in the iridocorneal angle and formation of anterior synechiae (regions where the iris adheres to the TM and possibly also the cornea), with corneal endothelial cells growing along the synechiae and reaching the iris (John et al., 1998). These factors lead to closure of the iridocorneal angle and blockage of aqueous drainage, which results in IOP elevation by 8-9 months of age. Evidence of ischemia has been noted in this model from 4 months of age (Chandra et al., 2016, Schuettauf et al., 2004), while reactive gliosis of astrocyte and Müller glia is obvious at ~8 months old (Cwerman-Thibault et al., 2017). Substantial deficits in anterograde and retrograde axonal transport are observed from 9-10 and 13 months, respectively (Dengler-Crish et al., 2014). At 11 months old, thinning of the RNFL and optic cup excavation is noted and most DBA/2J mice exhibit a severe reduction in optic nerve axon number (Libby et al., 2005a). RGC somata show a peak in TUNEL reactivity in the same time-frame (Libby et al., 2005b) and are reported to be significantly reduced in number from 9-18 months (Buckingham et al., 2008, Dengler-Crish et al., 2014, Cwerman-Thibault et al., 2017). Interestingly, the speed of RGC loss can apparently vary between colonies housed at different institutions, possibly due to environmental influences and/or genetic drift (Libby et al., 2005b).

The secondary angle-closure glaucoma that develops in DBA/2J mice shares similarities with human secondary glaucomas arising from pigmentary dispersion and iridocorneal endothelial syndromes (John et al., 1998). The natural, age-dependent IOP elevation and

progressive RGC degeneration exhibited by this strain makes it an invaluable model for studying the mechanisms underlying glaucomatous neurodegeneration.

Analyses of DBA/2J mice have supported the idea that mitochondrial dysfunction plays a central part in the pathogenesis of glaucoma. Mitochondria in RGC axons and dendrites of aged (~9 months+) DBA/2J mice have been described as smaller and more numerous, suggesting a skew towards fission, and possess disrupted/reduced cristae, indicating reduced oxidative capacity (Ju et al., 2008, Coughlin et al., 2015, Kim et al., 2015, Williams et al., 2017). Elevated hydrostatic pressure has been shown to induce similar effects (mitochondrial fission, cristae depletion and ATP level reduction) in cultured cells (Ju et al., 2007)[33]. Of note, overexpression of OPA1, a mitochondrial fusion protein, or inhibition of DRP1, a fission-promoting protein, significantly increased RGC survival in the DBA/2J and/or laser-induced glaucoma mouse models (Ju et al., 2010, Kim et al., 2015, Hu et al., 2018). Williams et al. conducted RNA-seq analysis on RGCs isolated from 9 month old highly-glaucomatous DBA/2J mice (assessed by axon loss) and found significant enrichment of differentially expressed genes in mitochondrial dysfunction and oxidative phosphorylation pathways (relative to pre-glaucomatous DBA/2J and age-matched DBA/2J-Gpnmb+ controls). Mitochondrial fission genes were notably among those differentially expressed (Williams et al., 2017).

Autophagy is upregulated in aged DBA/2J mice. However, in spite of this, dysfunctional mitochondria do not appear to be recycled efficiently (Coughlin et al., 2015). This is possibly a compensatory reaction to a decline in the level of PGC-1α, a key mitochondrial biosynthetic protein (Inman and Harun-Or-Rashid, 2017). Low-functioning mitochondria therefore accumulate, which would be expected to impede ATP production and increase generation of ROS (Inman and Harun-Or-Rashid, 2017).

There are indeed clear signs of oxidative stress in DBA/2J retinas; elevated levels of lipid peroxidation have been observed from 3 months of age, while genes involved in antioxidant response were upregulated from 7 months (Inman et al., 2013, Kim et al., 2015). Treatment with a dietary antioxidant, α -lipoic acid, was effective in decreasing oxidative stress and protected against RGC loss (Inman et al., 2013).

[33] Note: this study was performed on a transformed rat RGC line ('RGC-5'), which was later revealed to be, in actuality, a mouse photoreceptor cell line (611W) (Krishnamoorthy et al., 2013).

Bioenergetic deficits have also been noted in the DBA/2J model preceding the onset of RGC degeneration. Optic nerves of 6 and 10 month old DBA/2J mice displayed a striking reduction in compound action potential amplitude, the extent of this deficit being inversely proportional to IOP level (Baltan et al., 2010). ATP levels were significantly lower in optic nerves of 6 month old mice with high IOP and by 10 months of age all DBA/2J mice showed a similar deficit, regardless of IOP measurement (Baltan et al., 2010). Cwerman-Thibault et al. (2017) noted electron transport chain defects in ageing DBA/2J mice relative to pre-glaucomatous controls. Optic nerve Complex I, III and IV activity was significantly reduced from 5 months, while combined Complex II+III activity was similarly impaired from 8 months of age. A deficit in Complex I activity was also apparent in whole retinal samples from 5 months of age. Retinal Complex II+III, III and IV activity, though not assessed at 5 months, was significantly decreased at 10 months (Cwerman-Thibault et al., 2017). These deficits could be rescued by overexpression of neuroglobin, a mitochondrial protein with neuroprotective properties found to be decreased in aged DBA/2J mice (Cwerman-Thibault et al., 2017).

A disadvantage of assaying retinal and optic nerve samples for mitochondrial function is that it is difficult to ascertain how much RGCs contribute to the readout. RGCs comprise <1% of retinal cells but, as discussed earlier, their axonal regions in the RNFL are unusually mitochondria-rich and heavily dependent on OXPHOS. In contrast, while photoreceptors comprise ~81% of the murine retina (Jeon et al., 1998), possess mitochondria-rich inner segments and boast the highest oxygen consumption rate of any human cell type (Eells, 2019), they are thought to rely primarily on aerobic glycolysis for ATP production (Kanow et al., 2017). In the optic nerve, although myelinated RGC axons take up the majority of space (~57%) they have a relatively low mitochondrial density and so ~72% of optic nerve mitochondrial content is attributed to astrocytes (Perge et al., 2009).

This issue can be circumvented somewhat by treating optic nerve samples with a glial-specific TCA cycle inhibitor (fluorocitrate). In the absence of glial inhibition, ATP production and maximal respiration decreased with age in optic nerves of both DBA/2J and control (DBA/2J-Gpnmb+) mice. Interestingly, the oxygen consumption rate of DBA/2J samples was not significantly altered upon inhibition of ATPase, indicating that the optic nerve population was more reliant on glycolysis.

However, when astrocyte and oligodendrocyte OXPHOS was inhibited, axonal mitochondria of 10 month old DBA/2J mice had a lower maximal respiration rate but generated significantly more ATP than controls. Increased ATP production was unexpected, given the previously discussed morphological abnormalities observed in DBA/2J axonal mitochondria. To explain this result, Jassim et al. propose that highly efficient mitochondria may be selected for in the stressed DBA/2J optic nerve and possibly compensate for the accumulation of dysfunctional organelles (Jassim et al., 2019). This would seem to fit with the RNA-seq data of Williams et al., where OXPHOS genes related to all ETC complexes were upregulated in the RGCs of 9 month old DBA/2J mice.

A further metabolic abnormality was apparent upon ATPase inhibition: the ability of aged DBA/2J axons to switch to glycolysis was significantly impaired. The authors therefore concluded that DBA/2J RGC axons are overly reliant on oxidative phosphorylation and that their upregulation of OXPHOS activity ultimately cannot compensate for an inability to switch to glycolysis when necessary (i.e. hypoxia).

Jassim et al. interpret their results as a consequence of both ETC defects and reduced substrate availability. In axons and glia of the optic nerve, uptake of circulating glucose is mediated by glucose transporter proteins (GLUT1 in glia and GLUT3 in axons). Glia are thought to primarily rely on glycolysis, while RGC axons are dependent on mitochondrially-produced ATP. Glial cells provide further metabolic support to axons by supplying them with additional substrates to fuel OXPHOS; lactate, pyruvate and ketone bodies are transferred via monocarboxylate transporters (MCTs) (Inman and Harun-Or-Rashid, 2017).

At 6 months of age, increased levels of the low cellular ATP sensor pAMPK indicate an energetic crisis in DBA/2J optic nerves. Activated AMPK attempts to restore energy homeostasis in a multitude of ways that discourage ATP consumption and promote ATP production. However, this intervention appears ultimately unsuccessful, as evidenced by sustained AMPK activation, low lactate levels and decreased creatine kinase activity (Harun-Or-Rashid et al., 2018). GLUT1 and MCT2 are notably downregulated in aged DBA/2J mice (see Fig. 4.5). In the case of MCT2, this is likely in response to the low levels of lactate available for transport (Harun-Or-Rashid et al., 2018). Jassim et al. propose that downregulation of glucose and monocarboxylate transporters in the DBA/2J optic nerve

may underly the reduction in maximal respiration rate, which is highly dependent on substrate availability, while the impaired upregulation of glycolysis possibly stems from an insufficient glucose supply (Harun-Or-Rashid et al., 2018). Interestingly, treatment of DBA/2J mice with a ketogenic diet, which forces RGC axons and astrocytes to completely rely on mitochondrially-produced ATP, provided significant protection to RGC axons and somata. An increased level of ketone bodies led to an upregulation of MCTs, increased mitochondrial biogenesis and ETC activity (Harun-Or-Rashid et al., 2018).

Altered NAD levels provide yet more evidence of mitochondrial dysfunction in this model. Total NAD level declined with age in both DBA/2J and control mice (Williams et al., 2017), while the NAD+/NADH ratio was significantly lower in 10 month old DBA/2J relative to age-matched Gpnmb+ mice (Harun-Or-Rashid et al., 2018). Remarkably, treatment with dietary vitamin B3, an NAD+ precursor, could prevent axon degeneration in up to 93% of DBA/2J eyes (Williams et al., 2017). Importantly, POAG patients were recently found to be deficient in plasma NAD relative to controls, further supporting the therapeutic promise of vitamin B3 supplementation (Kouassi Nzoughet et al., 2019).

Clearly, much remains to be elucidated with regard to the pathogenesis of glaucoma. However, there is now an overwhelming amount of evidence to suggest that mitochondrial dysfunction is a prominent feature in the progression of this disease – much of it gained from utilisation of the DBA/2J model. It is possible that metabolic vulnerability stems from a combination of ETC defects and reduced substrate availability. This damage may be initiated by elevated IOP and/or oxygen and nutrient deprivation due to ischemia. Individuals with an accumulation of mitochondrial mutations or lower-than-average mitochondrial efficiency are likely especially susceptible to such stressors.

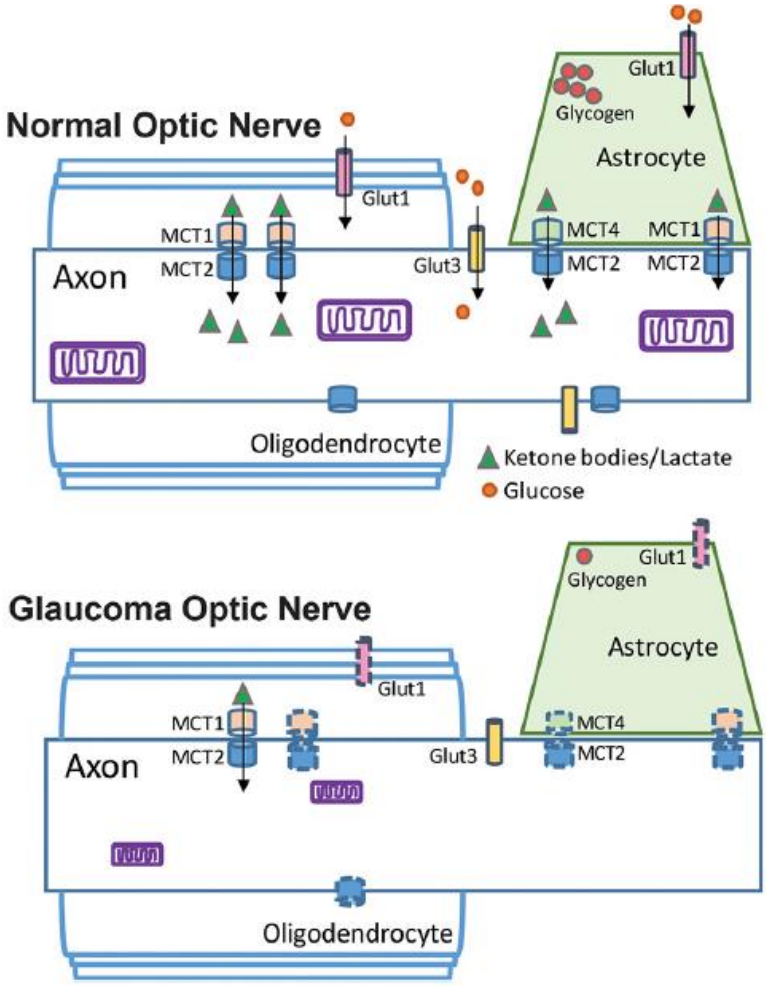

Figure 4.5. Substrate transport in the optic nerve from glial cells to RGC axons.

Glucose enters astrocytes and oligodendrocytes from circulation via GLUT1 and 3 channels. Lactate and ketone bodies are transported from glial cells to axons via MCT proteins. In a glaucomatous optic nerve, glucose is less abundant and GLUT1 and MCT proteins are downregulated. Mitochondria are smaller and less numerous in glaucomatous axons. Figure reproduced from Inman and Harun-Or-Rashid, 2017.

4.2.4 Ndi1 – a single-unit alternative NADH-ubiquinone reductase

As outlined earlier, Complex I is a huge multimeric protein complex, with 38% of the mitochondrial genome dedicated to production of CI subunits alone. Unsurprisingly, Isolated Complex I deficiency is the most commonly observed cause of mitochondrial disorders (such as LHON and Leigh's syndrome) (Sharma et al., 2009). Complex I defects have also been linked to the pathology of multifactorial diseases such as Parkinson's disease (Chen et al., 2019a, Holper et al., 2019), Alzheimer's disease (Adav et al., 2019, Holper et al., 2019), and glaucoma (Lee et al., 2012, Van Bergen et al., 2015, Banerjee et al., 2013, Sundaresan et al., 2015). Restoration or boosting of Complex I activity may therefore by beneficial in both inherited mitochondriopathies and age-related neurodegenerative disease contexts. The size of the NADH:ubiquinone oxidoreductase complex, however, means it is not feasible to employ a straightforward AAV-mediated gene replacement strategy for this purpose.

Fortunately, this issue can be circumvented by taking inspiration from some of our (very) distant eukaryotic cousins. Plant and fungal cells possess two proteins capable of NADH oxidation (without proton pumping): Nde1 in the mitochondrial intermembrane space (external NADH dehydrogenase), and Ndi1, in the mitochondrial matrix (inner NADH dehydrogenase) (Iwata et al., 2012). *Saccharomyces cerevisiae* Ndi1 is a nuclear encoded 513 amino acid protein that acts as a dimer and contains an endogenous mitochondrial localisation signal. Unlike Complex I, Ndi1 is insensitive to rotenone inhibition (Seo et al., 1998, Cui et al., 2012, Iwata et al., 2012). Excitingly, this single unit Complex I substitute protein could be incorporated into the respiratory chain of bacterial and mammalian cells (Kitajima-Ihara and Yagi, 1998, Seo et al., 1998) (see Fig. 4.6) and proved capable of compensating for genetic or rotenone-induced Complex I dysfunction *in vitro* (Seo et al., 2000, Bai et al., 2001). Using Ndi1 to bypass defective Complex I additionally reduced ROS production and vulnerability to ROS-mediated apoptosis in a cell line model of LHON (Park et al., 2007). It is important to note that Complex I NADH oxidation also functions to replenish NAD+ levels required for running of the TCA cycle, which produces metabolites important in biosynthetic and signalling pathways (Martínez-Reyes and Chandel, 2020). Ndi1 thus has multiple modes of potential benefit: (i) restoring electron transfer from NADH to ubiquinone and thus increasing ATP synthesis, (ii) minimising ROS production

from malfunctioning Complex I, (iii) desensitising cells to further ROS-mediated damage to Complex I and (iv) increasing TCA cycle activity.

AAV-mediated Ndi1 expression in the substantia niagra or superior colliculus (where RGC axons terminate) can protect neurons in chemically-induced rodent models of Parkinson's disease and LHON, respectively (Seo et al., 2006, Marella et al., 2010). However, in the case of optic neuropathies, intravitreal injections are obviously preferable to invasive brain surgery. With this in mind, the Farrar lab has demonstrated that intravitreal injection of AAV2/2-CMV-Ndi1 can significantly preserve RGC and visual function in a rotenone-induced mouse model of LHON (Chadderton et al., 2013). A similar approach (intravitreal injection of scAAV-CAG-Ndi1) protected visual function in an experimental autoimmune encephalomyelitis (EAE) animal model of multiple sclerosis (Talla et al., 2013, Talla et al., 2020).

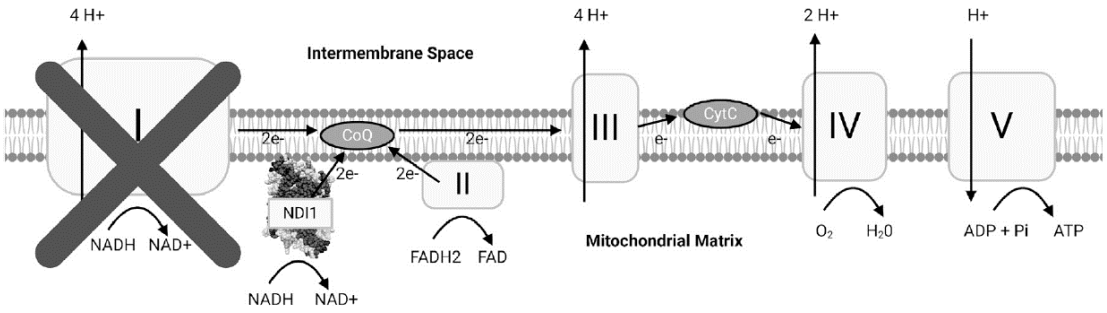

Figure 4.6. Schematic of Ndi1 incorporation into a mammalian ETC chain with Complex I dysfunction. Figure reproduced from McElroy et al. 2020.

4.2.5 Objectives of chapter 4

The aims of the research described in this chapter were to:

I. Characterise a DBA/2J mouse colony, verifying the presence of glaucomatous phenotypes documented by other research groups – particularly in terms of ETC Complex I activity and general health of RGCs.
II. Evaluate the therapeutic potential of AAV-mediated Ndi1 expression in DBA/2J retinal ganglion cells.

4.3 Results

4.3.1 Pigment dispersion and IOP elevation in aged DBA/2J mice

Inbred colonies of lab mice can be subject to genetic drift and deviate phenotypically from a source population over time. With the DBA/2J strain specifically, populations with the same genetic background but bred at different facilities have shown considerable phenotypic variation, suggesting that environmental factors may influence disease progression (Libby et al., 2005a, Turner et al., 2017). It was therefore important to characterise our DBA/2J colony before attempting to rescue phenotypes with potential therapeutics. As part of this endeavour, mice were first tested for the major hallmarks of this model of glaucoma: iris pigment dispersal and elevated intraocular pressure.

As expected, aged DBA/2J mice displayed striking pigment abnormalities when compared to age-matched C57BL/6J (C57) control mice (Fig. 4.7). The pigment of the iris was drastically redistributed, with some areas displaying large aggregates of debris and other completely pigment-free. A similar pattern was evident in the retinal pigment epithelium of these mice.

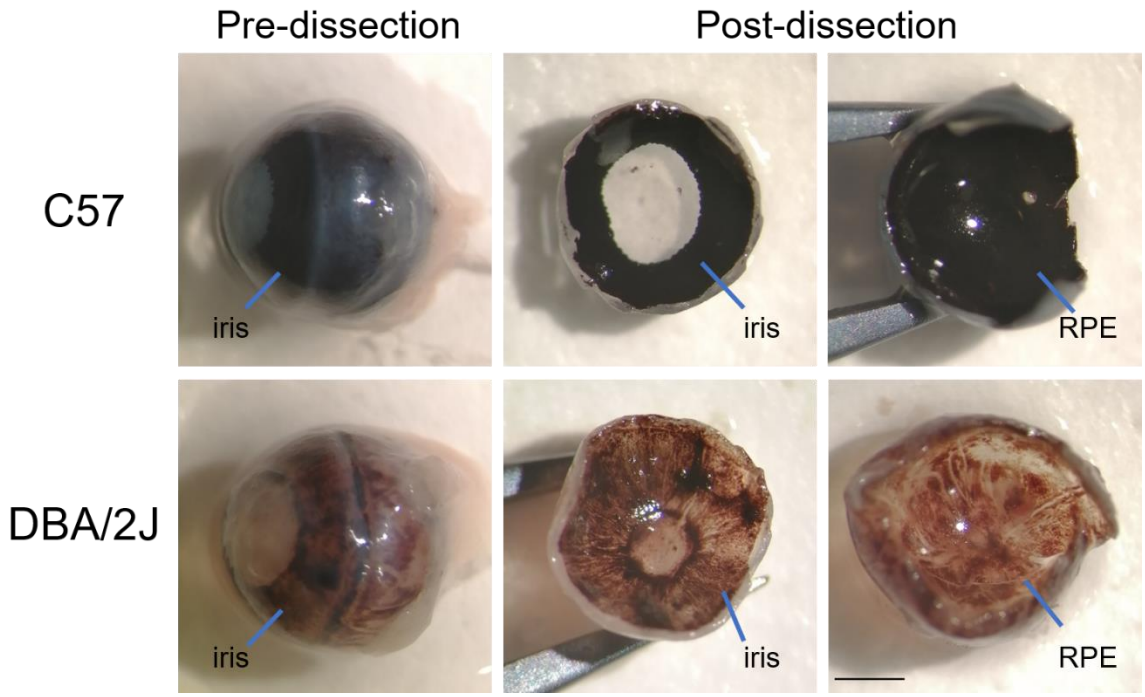

Fig 4.7. Pigment abnormalities in DBA/2J eyes.

Fixed eyes were dissected and imaged under a stereomicroscope. Dispersal of pigment in the iris and RPE of 13 month old DBA/2J mice was evident when compared to age-matched C57 control mice. Scale bar = 1mm.

Intraocular pressure was recorded in DBA/2J mice at three timepoints (Fig. 4.8). Median IOP rose significantly from 2 months of age (11.71 ± 1.29 mmHg) to 10-11 months (16.33 ± 2.95 mmHg) ($p < 0.0001$). This was followed by a relatively abrupt drop to 7.25 ± 0.33 mmHg at 13 months of age. IOP decrease in later life is thought to be a consequence of severe ciliary body atrophy (Libby et al., 2005a). For comparison, Cwerman-Thibault et al. (2017) reported mean IOP values of ~13 mmHg and ~19-22 mmHg in 9-11 month old C57 and DBA/2J mice, respectively, while the mean IOP of 10-11 month old mice in the TCD DBA/2J colony was 18.62 ± 4.826.

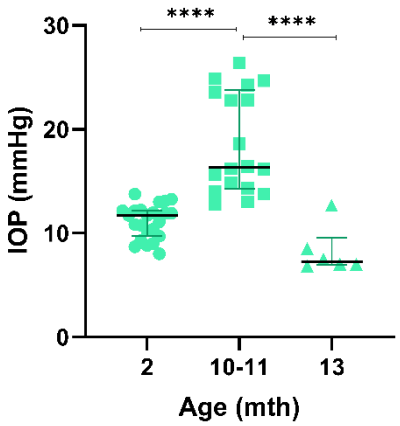

Fig 4.8. DBA/2J IOP measurements over time.

Non-invasive IOP measurements were performed on DBA/2J mice of 2, 10-11 and 13 months of age (n = 23, 18 and 6 eyes, respectively). Readings are represented in millimetres of mercury (mm Hg). Medians and interquartile ranges are shown. The median value for 10-11 month old mice (16.33 ± 2.95 mmHg) was found to be significantly different from both 2 month old (11.71 ± 1.29 mmHg) and 13 month old mice (7.25 ± 0.33 mmHg). For statistical analysis, the Kruskal-Wallis test was performed and followed by Dunn's multiple comparisons post hoc test.

**** $p < 0.0001$

4.3.2 Neurodegeneration in aged DBA/2J optic nerves and retinae

Aged DBA/2J mice were examined for signs of axonal degeneration by performing immunohistochemical analysis on optic nerve cross-sections. Neurofilament 200 (NF200), also known as neurofilament heavy polypeptide (NEFH), is an essential cytoskeletal component in neurons and a commonly used axonal marker. Quantification of NF200-positive regions in optic nerve sections can therefore be used to estimate axon numbers (Cwerman-Thibault et al., 2017). This method of quantitation is not as accurate as paraphenylenediamine (PPD) staining of myelin sheaths in thin resin-embedded tissue sections, which enables counting of individual axons (Anderson et al., 2005). Nevertheless, NF200-staining allows relative comparisons of axonal abundance to be made. A limited number of samples were available for this test (ranging from one to four optic nerves per group) relative to the large cohorts normally used in studies with DBA/2J mice. However, 13 month old DBA/2J mice displayed a notable decrease in axon number compared to their age and gender-matched C57 controls. This was particularly evident in the female cohort, where NF200-positive regions were 0.32 fold fewer in aged DBA/2J mice (aged C57 females: 1.00 ± 0.16, aged DBA/2J females: 0.32 ± 0.28; $p = 0.0155$; $n = 4$) (Fig. 4.9.B).

Glial fibrillary acidic protein (GFAP), a type-III intermediate filament protein, is an established marker of gliosis and has been used to detect activation of astrocytes and Müller glia after optic nerve injury (Chen and Weber, 2002) and in aged DBA/2J mice (Cwerman-Thibault et al., 2017). Elevated expression of GFAP is commonly used as a proxy for neuronal damage. In parallel to the decrease in NF200 expression observed, GFAP expression significantly increased in optic nerves of 13 month old DBA/2J mice compared to age- and gender-matched C57 controls; fold changes were 3.40 for female DBA/2J mice (aged C57: 1.00 ± 0.67, aged DBA/2J: 3.40 ± 0.48; $p = 0.017$, $n = 2$-3) and 2.03 for males (aged C57: 1.91 ± 0.54, aged DBA/2J: 3.88 ± 0.39; $p = 0.001$, $n = 4$) (Fig. 4.9.C).

Similar analyses were applied to optic nerve head sections and no significant differences in overall NF200 or GFAP expression levels were observed in this region (Fig. 4.10.B and C). However, examination of the rest of the retina (non-ONH regions), revealed a striking upregulation of GFAP expression in female 13 month old DBA/2J mice (9.64 ± 3.44 fold; $p = 0.0246$; $n = 4$; Fig. 4.10.D). GFAP-positive regions in these retinas extended from the

ganglion cell layer outward, often as far as the ONL. Müller glia were therefore clearly activated in DBA/2J retinas.

Retinal ganglion cell soma degeneration was evaluated by determining RGC density in retinal wholemount samples. RGC loss does not occur evenly throughout the retina in DBA/2J mice. Instead, a 'fan-shaped' pattern of degeneration is often observed with wedges of RGC loss, narrow at the optic disc and widening toward the periphery (Jakobs et al., 2005) (Schlamp et al., 2006). Such a shape makes sense when one considers that RGC axons converge into axon bundles, which are damaged as they pass through the lamina cribrosa. This pattern is noted to be reminiscent of arcuate scotomas in human glaucoma cases (Howell et al., 2007a). In light of the sectorial nature of degeneration, it was decided that analysis of retinal wholemounts would enable more accurate quantification of RGC numbers than retinal section counts.

As approximately 59% of the murine GCL is thought to be made up of displaced amacrine cells (Jeon et al., 1998), simply staining nuclei (e.g. with DAPI) is not an accurate method for estimating RGC numbers. Using RBPMS (RNA blinding protein with multiple splicing) as a marker allows specific labelling of the entire RGC population (Rodriguez et al., 2014). However, automated cell counting of RBPMS-labelled RGCs is not ideal as cell bodies are often in direct contact with each other, making separation of the detected objects difficult or impossible (Dr Arpad Palfi, personal communication). It was therefore decided to use BRN3A, a POU-domain transcription factor present in approximately 92-96% of rodent RGC somas (Nadal-Nicolás et al., 2012) and widely used for the purpose of RGC labelling (Fig. 4.11.A).

A dramatic decrease in RGC soma density was evident from 7 to 12-13 month of age in DBA/2J mice (3067.16 ± 266.15 to 889.85 ± 835.79 RGCs/mm^2). In contrast, C57 RGC numbers declined relatively modestly with age (3033.33 ± 146.76 RGCs/mm^2 at 2-3 months old vs 2637.68 ± 367.82 RGCs/mm^2 at 12-13 months of age) (Fig. 4.11.B). When DBA/2J data was separated by sex, it was apparent that female mice experienced a faster rate of RGC degeneration than males (Fig. 4.11.C). At 12-13 months of age, mean RGC density was 462.43 ± 332.42 RGCs/mm^2 in females compare to 1507.01 ± 860.81 RGCs/mm^2 in males (n = 7).

To assess statistical significance, a three-way ANOVA was performed on data from 2-3 and 12-13 month old mice of both strains and both sexes. 12-13 month old female DBA/2J mice (462.43 ± 332.42 RGCs/mm^2) had significantly fewer RGCs than sex- and age-matched C57 (2697.16 ± 437.79 RGCs/mm^2) and young DBA/2J controls (3041.23 ± 395.24 RGCs/mm^2), with respective fold changes of 0.17 and 0.15 ($p < 0.0001$; n = 3-7) (Fig.4.11.D). Mean RGC density in aged DBA/2J females (462.43 ± 332.42 RGCs/mm^2) was also significantly lower than that of their male DBA/2J counterparts (1507.01 ± 860.81 RGCs/mm^2) ($p = 0.0124$; n = 7). RGC densities of 12-13 month old male DBA/2Js were significantly reduced in comparison to their 2 month old pre-glaucomatous strain controls (3166.20 ± 250.66 RGCs/mm^2) ($p = 0.0001$; n = 5-7) but not from aged C57 males (2610.28 ± 275.08) ($p = 0.067$). However, it should be noted that the sample group sizes used in this test were suboptimal considering the noted high level of variance documented in this model (Libby et al., 2005a).

Considering these results, it was decided that the efficacy of a therapeutic intervention would be best tested at approximately 12 months of age in DBA/2J females, at which point an estimated 15 ± 11% of RGCs would remain in untreated mice (based on measurements of n = 7). Due to the slower rate of disease progression in males, 48 ± 27% RGCs were predicted to persist at this timepoint (n = 7). It was therefore planned to assess treated males at a later age (15-16 months old) when baseline RGC loss might be more severe.

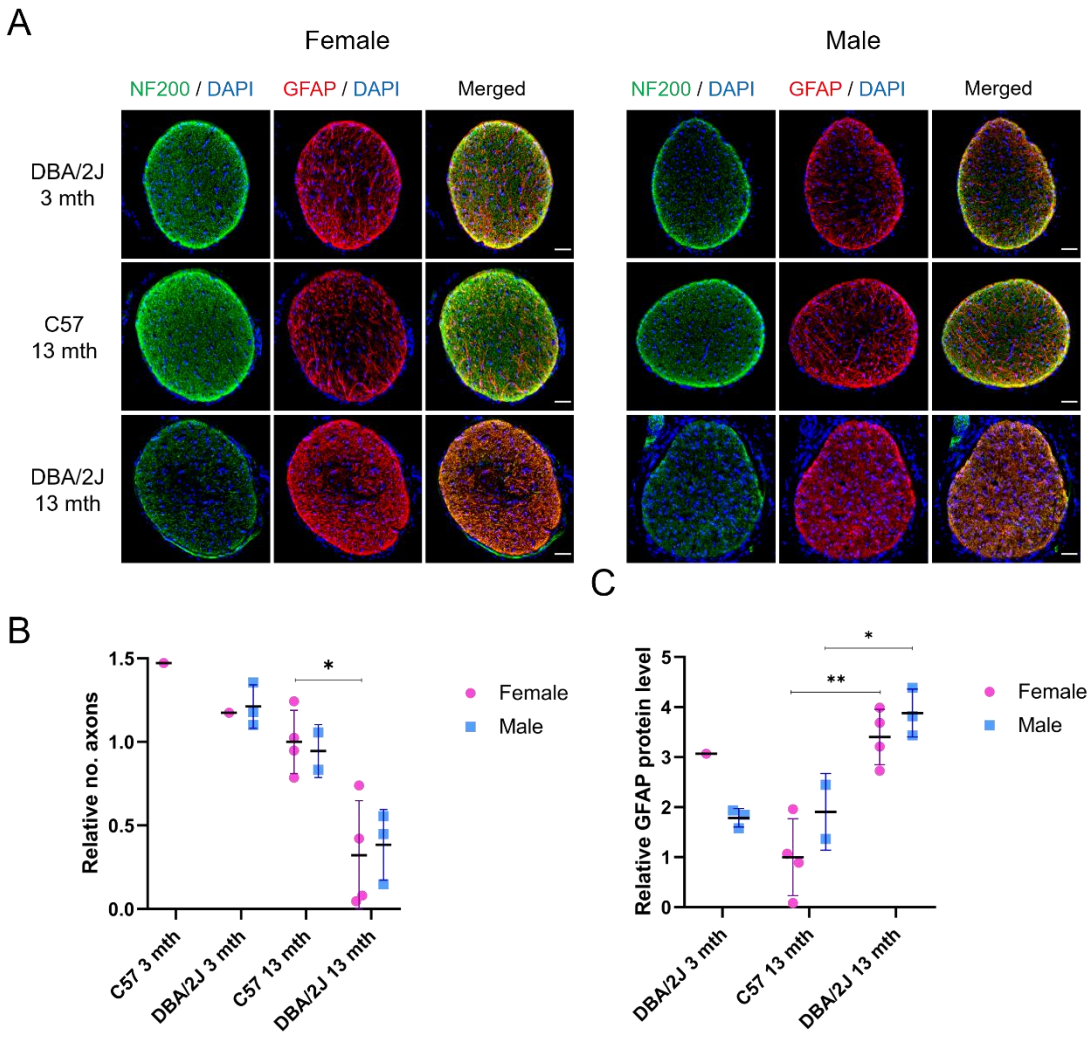

Fig 4.9. Altered NF200 and GFAP expression in aged DBA/2J optic nerve sections.

(A) Representative IHC images of optic nerve sections from DBA/2J and C57 mice of 3 and 13 months of age. Sections were stained for NF200 (green) and GFAP (red) and DAPI (blue) was used to label nuclei. Scale bar = 50µm.

(B) Axon numbers were estimated by quantifying the numbers of NF200 positive areas per section using the 'Count and Measure' module in cellSens software. Values were normalised against section area. 13 month old DBA/2J females were found to have significantly fewer axons than their age and gender-matched C57 controls ($p = 0.0155$, $n = 4$ per group).

(C) GFAP levels were quantified using the Fiji 'Threshold' and 'Measure' tools. GFAP integrated density values were normalised against section area. DBA/2J mice had significantly higher levels of GFAP than their age and gender-matched C57 controls in cohorts of both males ($p = 0.017$, $n = 2$-3) and females ($p = 0.001$, $n = 4$).

Values shown in (B) and (C) are means ± SD. For statistical analysis, a two-way ANOVA was performed to compare DBA/2J 13 month old and C57 13 month old mice in terms of strain and gender. (Insufficient numbers of 3 month old samples were available to analyse the effect of age in a three way ANOVA.)

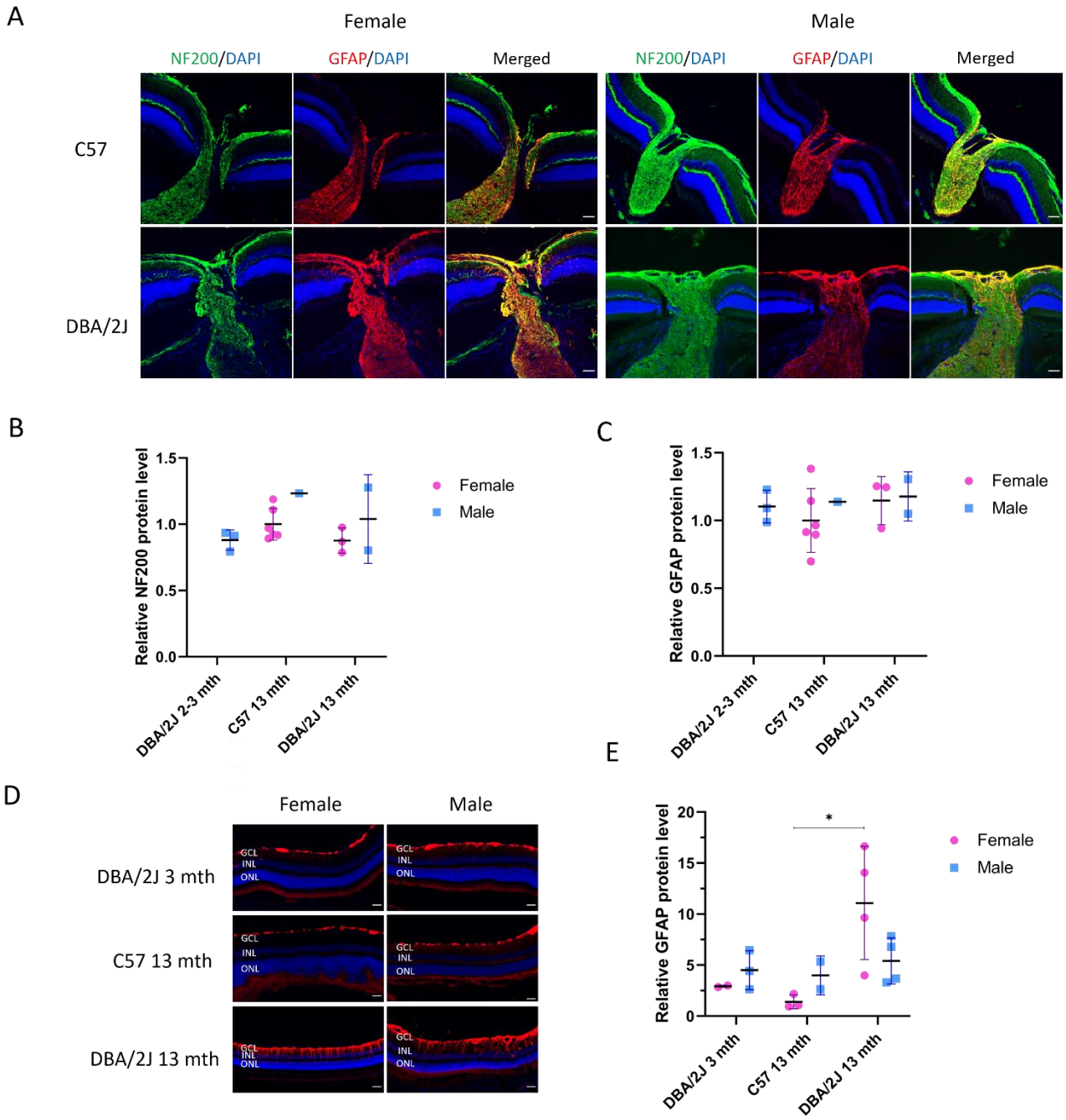

Fig 4.10. NF200 and GFAP expression in retinal and optic nerve head sections.

(A) Retinal sections that included the optic nerve head were selected and stained for NF200 (green) and GFAP (red). Nuclei were counterstained with DAPI (blue). The images shown are from 13 month old DBA/2J and C57 samples. Scale bar = 50µm.

Relative NF200 (B) and GFAP (C) proteins levels were estimated in ONH regions by determining the mean gray values of pixels in the regions of interest using Fiji. n = 2-5 retinas (1 section per retina).

(D) Non-ONH regions of the retina were also stained for GFAP (red). Scale bar = 50µm.

(E) GFAP levels across whole retinal section images (acquired via stitching) were quantified using integrated density values and normalised to the corresponding DAPI area. For this analysis, sections that did not include the ONH were chosen. Values shown are means ± SD. p = 0.0246 (two-way ANOVA and Tukey's multiple comparisons post-hoc test).

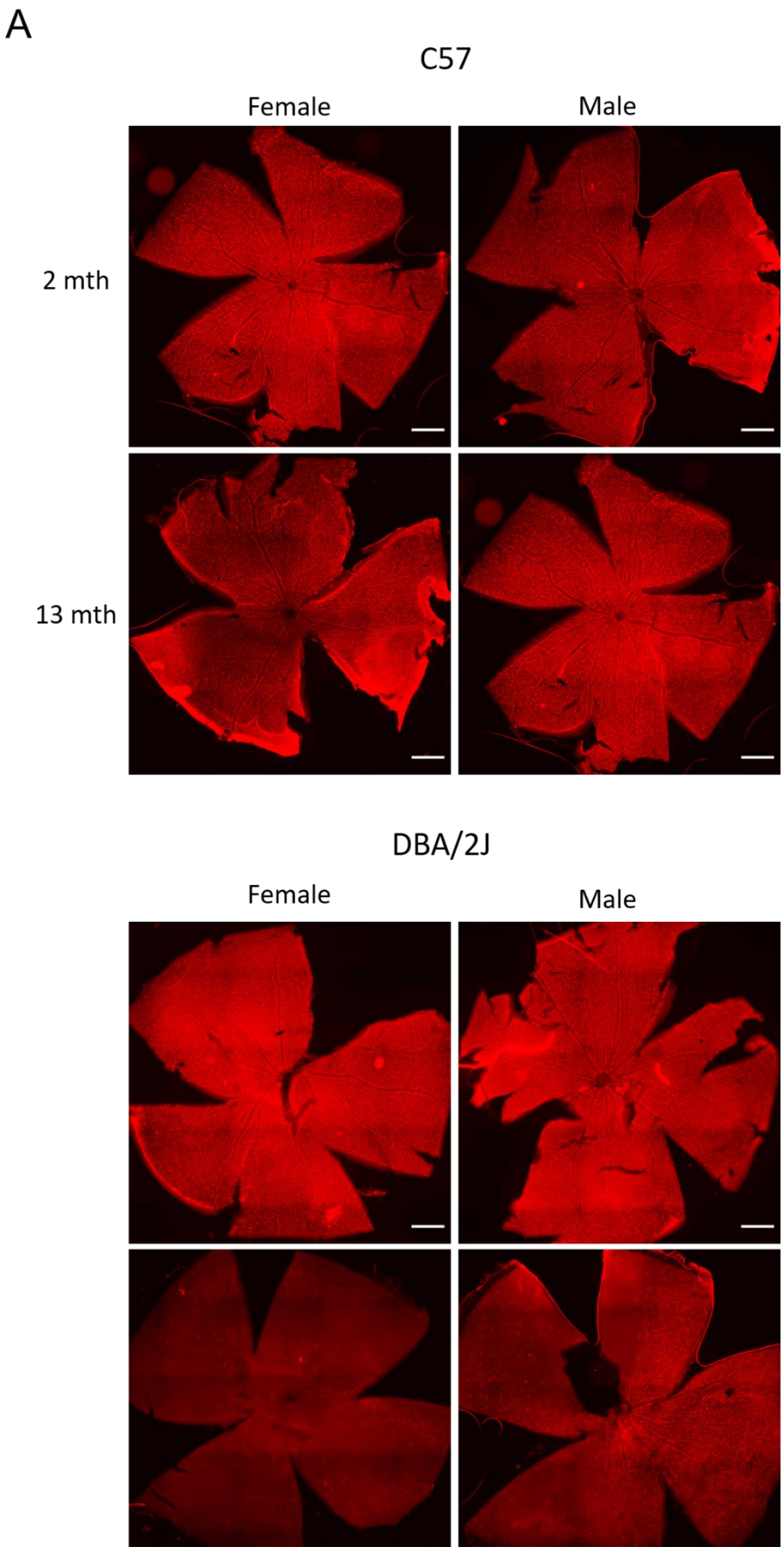

Fig 4.11. Reduced RGC density in aged DBA/2J retinal wholemounts.

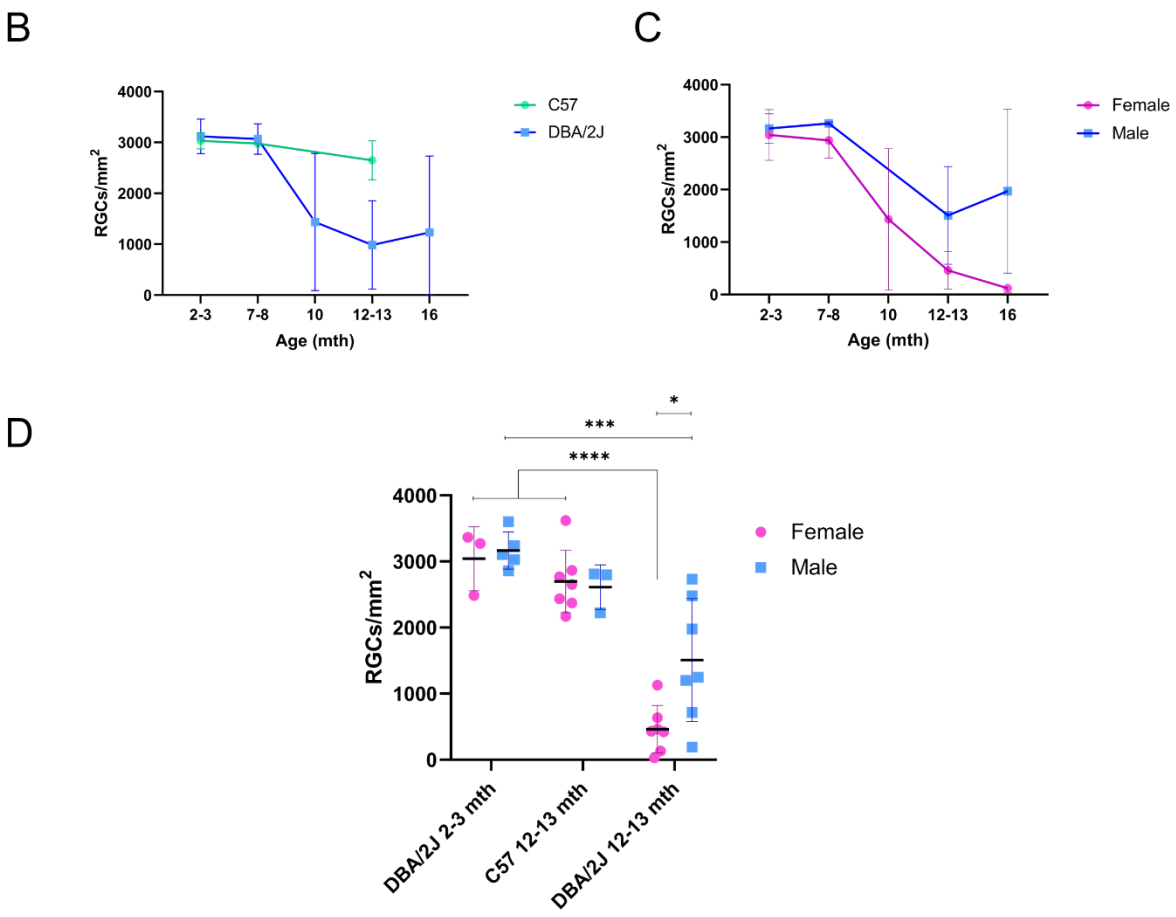

Fig 4.11. Fig 4.11. Reduced RGC density in aged DBA/2J retinal wholemounts (continued).

(A) Retinal wholemounts from C57 and DBA/2J of 2 and 13 months old were stained for BRN3A-positive ganglion cell soma (red). Images shown were acquired in multiple frames (16) that were stitched together using cellSens. Scale bar = 500µm. Fan-shaped areas of RGC loss are evident in the representative wholemount from a 13 month old male DBA/2J mouse. BRN3A labelling was very sparse in the female DBA/2J 13 month old sample shown, signifying more severe RGC degeneration.

(B) The densities of BRN3A-positive 'objects' (cells) in stained wholemounts were calculated using the Count and Measure module in cellSens software and expressed as the number of RGCs per mm^2. RGC density in DBA/2J mice decreased substantially from 10 months of age. In contrast, C57 RGC number was reduced only slightly over time. Sample groups sizes were as follows:
DBA/2J 2 months old (mo) (8 retinas), 7-8 mo (5), 10 mo (4), 12-13 mo (14), 16 mo (5);
C57 2 mo (8), 7-8 mo (1), 12-13 mo (12).

(C) DBA/2J RGC data from (B) was segregated by sex, revealing that female mice experienced a faster, more severe disease progression than males. Sample group sizes:
Female 2 mo (3 retinas), 7-8 mo (3), 10 mo (4), 12-13 mo (7), 16 mo (2);
Male 2 mo (5), 7-8 mo (2), 12-13 mo (7), 16 mo (3).

Fig 4.11. Reduced RGC density in aged DBA/2J retinal wholemounts (continued).
(D) RGC count data from 2-3 and 12-13 month old DBA/2J and C57 mice were collated, segregated by sex and compared. 12-13 month old DBA/2J mice had significantly fewer RGCs relative to gender-matched 2-3 month old DBA/2J controls ($p < 0.0001$ for females; $p = 0.0001$ for males). Aged DBA/2J female RGC numbers were additionally significantly lower than both aged C57 mice ($p < 0.0001$) and DBA/2J males of the same age ($p = 0.0124$). For statistical analysis, a three way ANOVA was performed, followed with Tukey's multiple comparisons test.
Values shown in (B - D) are means ± SD.

4.3.3 Upregulation of oxidative stress markers in glaucomatous DBA/2J mice

Markers of oxidative stress have previously been demonstrated to be upregulated in the DBA/2J model. These include expression of genes linked to oxidative stress response, such as ceruloplasmin *(Cp)*, Heme oxygenase-1 *(Ho-1)* and an inducible form of nitric oxide synthase *(Nos 2)* (Inman et al., 2013).

Ceruloplasmin, a ferroxidase that coverts ferrous (Fe^{2+}) to ferric iron (Fe^{3+}), is suggested to function as an antioxidant by limiting the amount of free radical-producing ferrous iron (Chen et al., 2003). Heme oxygenase-1 is an oxidative stress-induced enzyme that facilitates cleavage of heme, leading to the production of bilirubin, a potent antioxidant. Induction of Ho-1 expression has been demonstrated to have a protective effect in neurons subjected to oxidative stress (Le et al., 1999, Chen et al., 2000). Nos 2 is highly expressed by glial cells during reactive gliosis, which itself can be initiated by oxidative stress, and the subsequent increase in nitrous oxide free radicals (•NO) production can induce nitrosative stress in the surrounding neurons (Moreno et al., 2009, Hass and Barnstable, 2016).

Inman et al. (2013) profiled retinal expression of these genes in DBA/2J and C57 mice from 3 to 10 months of age. For the purposes of this study, it was decided to characterise 12 month old mice in terms of these oxidative stress markers, when significant RGC loss is evident.

RT-qPCR analysis was performed on whole retinal samples from 12-13 month old DBA/2J and C57 mice. Expression of all three oxidative stress markers tested was increased in aged DBA/2J retinas (Fig. 4.12.A). In the case of *Cp* and *Nos2*, these elevations were significant (fold changes of 1.53 and 3.28, respectively; $p < 0.05$). Nos2 is upregulated as

an inflammatory response during reactive gliosis and its expression pattern would thus be expected to mirror that of GFAP. The increased Nos2 expression observed at 12-13 months in this experiment coincides with GFAP upregulation (Fig. 4.10.D and E). Considering these data, it is evident that mechanisms both contributing to and in response to oxidative stress were active in the retinas of 12-13 month old DBA/2J mice.

Oxidative stress status was also evaluated in dissociated retinal cells of 11-12 month old mice using a flow cytometry based assay that utilises 2'-7'-dichlorodihydrofluorescein diacetate (DCFDA), a dye that fluoresces upon oxidation by ROS. DCFDA intensity was not increased in aged DBA/2J retinas relative to pre-glaucomatous DBA/2J and age-matched C57 samples (Fig. 4.12.B). ROS is highly reactive with a short half-life and so is difficult to measure directly (Griendling et al., 2016). It may be that the window for ROS detection had passed by the point of DCFDA analysis – the damage having already been done, as evidenced by a significant decline in RGC soma numbers. To my knowledge, this DCFDA assay has not been performed on DBA/2J retinal samples before.

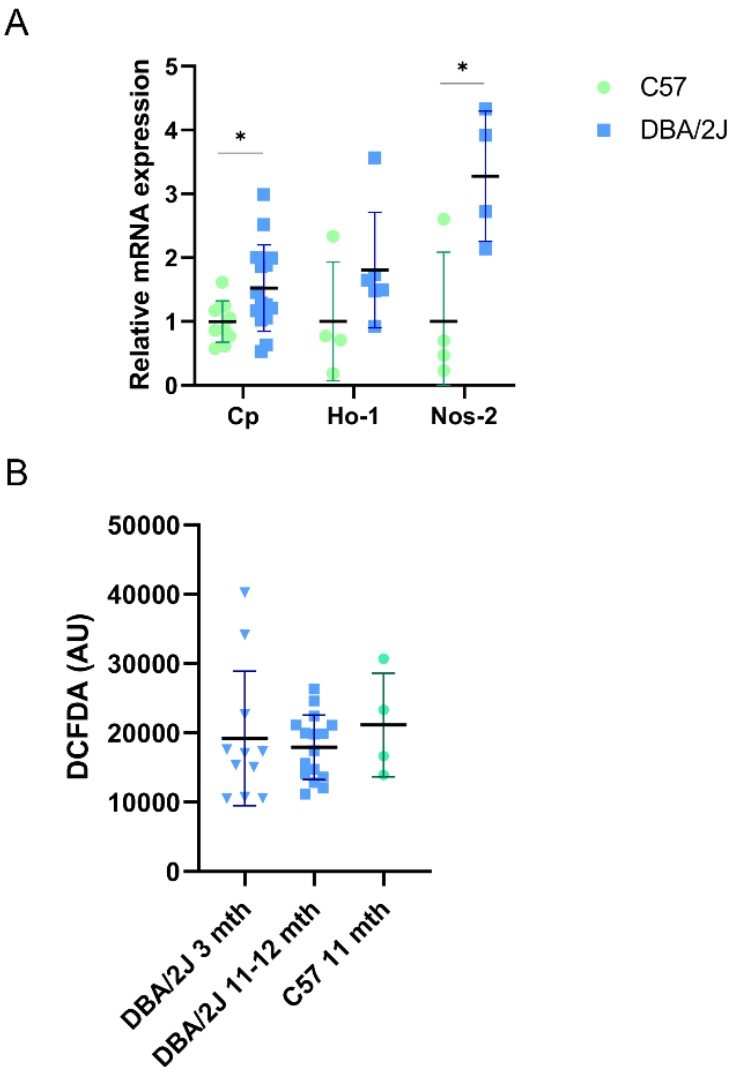

Fig 4.12. Assessment of oxidative stress markers in DBA/2J retinas.

(A) RT-qPCR was performed on 12-13 month old C57 and DBA/2J retinal samples. Expression of oxidative stress markers Cp, Ho-1 and Nos2 were increased in DBA/2J retinas. Cp and Nos2 elevations reached statistical significance ($p = 0.0329$ and $p = 0.0222$, respectively; unpaired Student t test). Target gene expression levels were normalised against β-actin expression. Relative expression levels (C57 vs DBA/2J):

Cp: 1.00 ± 0.31 vs 1.52 ± 0.66

Ho-1: 1.00 ± 0.80 vs 1.81 ± 0.83

Nos2: 1.00 ± 0.94 vs 3.28 ± 0.88

(B) DCFDA intensity (expressed as arbitrary units (AU)), used as a proxy for ROS level, did not differ significantly between DBA/2J 3 month old, DBA/2J 11-12 month old and C57 11 month old mice.

Unlike the histology data presented in the previous section, whole retinal samples were not segregated by sex during data analyses for these experiments. Ganglion cells are vastly outnumbered in the retina and GCL neurons make up approximately 1.3% of the retinal neuron population in mice (calculated from data presented by Jeon et al., 1998). As approximately 50% of neurons in this layer are assumed to be actual retinal ganglion cells (Schlamp et al., 2013), the proportion of the retina comprised of RGCs is likely to be closer to 0.65%. Sample groups were therefore made as large as possible when analysing marker levels in whole retinal samples, to enable detection of potentially subtle differences arising from GCL perturbation. Male and female cohorts were thus analysed together.

4.3.4 Complex I activity in DBA/2J and C57 mice

Deficiencies in multiple complexes of the mitochondrial electron transport chain have been noted in aged DBA/2J mice relative to young, pre-glaucomatous controls (Cwerman-Thibault et al., 2017). Cwerman-Thibault et al. recorded a drop of approximately 50% in retinal Complex I activity from 2 to 10 month old mice. In optic nerves, the deficit reached 60% by 10-12 months of age. Notably, this study did not profile Complex I function in aging C57 or DBA/2J-Gpnmb+ controls. As discussed in Section 1.7.4, mitochondrial function is established to naturally decline with age. It therefore seems prudent to include age-matched controls in such experiments.

In order to assess Complex I activity in our DBA/2J colony, NADH oxidation was measured in retinas of DBA/2J and C57 mice from 3 to 10-11 months of age (Fig. 4.13.A), and in optic nerves from 2-3 to 12-13 months (Fig. 4.13.B and C). The DBA/2J retinal NADH oxidation rate did not decrease over time – indeed, there was a non-significant increase from 3 to 10-11 months ($p = 0.8402$; $n = 6$-9). However, activity in C57 samples was consistently higher than that of age-matched DBA/2Js. At 10-11 months old (the timepoint with the largest available sample sizes), the DBA/2J NADH oxidation rate (22.19 ± 7.43 nmol NADH/min/mg) was 0.66 fold lower than the C57 rate (33.62 ± 19.24 nmol NADH/min/mg) ($n = 9$-11). The fact that such a trend is evident in whole retinal samples, of which retinal ganglion cells comprise a tiny minority, may indicate that other retinal cells may suffer from a bioenergetic deficit in DBA/2J mice from an early age.

In DBA/2J optic nerves, the NADH oxidation rate decreased by 41% from 2 month (28.94 ± 16.17 nmol NADH/min/mg) to 12-13 months of age (17.04 ± 5.95 nmol NADH/min/mg).

This reduction was not significant, however, and a similar trend was evident in C57 optic nerves over time, falling from 23.26 ± 7.59 to 16.97 ± 4.03 nmol NADH/min/mg. The mean oxidation rate of 12-13 month optic nerves was essentially identical in both strains. The data suggest that the declining trend observed in DBA/2J optic nerve Complex I activity is most likely a natural consequence of aging.

It should be noted that the protocol used to assay samples in this study differed to that of Cwerman-Thibault et al. (2017) in some respects. Firstly, Cwerman-Thibault et al. were able to obtain sufficient material from a single optic nerve to run the assay in triplicate. In contrast, in my hands, it was necessary to pool four nerves together to elicit an adequate signal. In addition, I decided to omit BSA from the published homogenisation buffer recipe as its inclusion would have impeded accurate quantitation of sample protein content for normalisation.

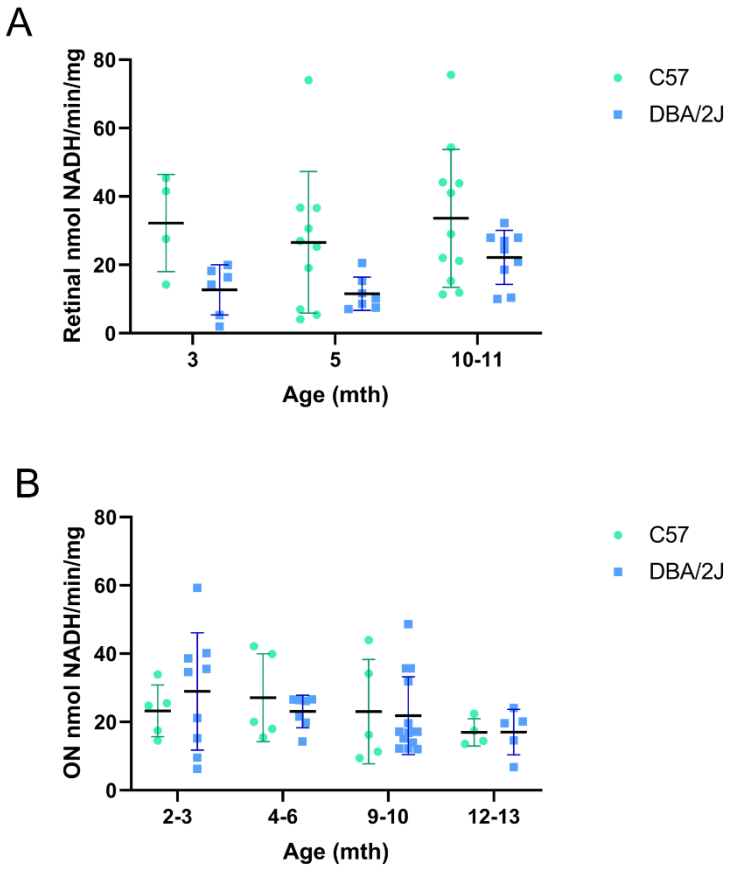

Fig 4.13. Evaluation of Complex I function in DBA/2J retinal and optic nerve samples

(A) To assess Complex I activity, the rate of NADH oxidation was measured in retinal samples from C57 and DBA/2J mice at various ages. Complex I activity in DBA/2J retinas was consistently lower than that of C57 samples. Oxidation rates are expressed as nmol NADH oxidised per minute per mg of total protein analysed. Values shown are means ± SD. Number of retinas per group were as follows:

C57 3 months old (mo) (4), 5 mo (7), 10-11 mo (11);

DBA/2J 3 mo (6), 5 mo (7), 10-11 mo (9).

(B) NADH oxidation rate was also examined in optic nerve samples. Due to the relatively small amount of assayable material present in a single nerve, four optic nerves were pooled together per reaction. Each point shown on the graph thus represents a pooled sample of four nerves. Although average Complex I activity in DBA/2J mice appeared to decrease over time, the differences observed were not significant and a similar trend was evident across age-matched C57 mice. Values shown are means ± SD. Number of optic nerve pools per group were as follows:

C57 2-3 months old (mo) (5), 4-6 mo (5), 9-10 mo (5), 12-13 mo (4);

DBA/2J 2-3 mo (9), 4-6 mo (7), 9-10 mo (14), 12-13 mo (5).

4.3.5 Altered retinal function in DBA/2J mice

Retinal cells elicit electrical responses when stimulated by light. These reactions can be quantified by recording the difference in electrical potential between an electrode placed on the cornea and reference electrodes. Electrical responses differ depending on the type of cell they originate from. Photoreceptor hyperpolarisation produces negative 'a-waves', while inner bipolar and Müller cells generate positive 'b-waves.' In well-lit conditions, retinal ganglion cells emit a negative potential after the b-wave, termed a photopic negative response (PhNR).

In the standard electroretinography protocol used, mice are dark adapted overnight, after which a dim white flash is used to measure the scotopic rod-driven response of ON-bipolar cells. Next, a bright white light is used to obtain a mixed (but rod-dominated) rod and cone-driven response from both photoreceptors and bipolar cells – referred to as a maximal response. Mice are then light-adapted, after which a single-flash cone response (SFC) is obtained. In this readout, the a-wave represents cone photoreceptor and cone OFF-bipolar cell activity, while the b-wave arises from ON- and OFF-bipolar cells. A 10Hz flicker response (10 stimuli per second; too fast for rods to respond) is used to further assess macular cone-driven activity. A single bright flash is again used to generate PhNRs. However, in this case a narrow-band stimuli is recommended to enhance signal (rather than a broadband flash of white light) (Frishman et al., 2018). An orange filter is therefore used to filter the white light of the single flash stimulus used in this test.

PhNRs in aged (11-12 month old) DBA/2J mice were compared to that of C57 controls (Fig. 4.14.A). PhNR amplitude in aged male DBA/2J mice (4.81 ± 2.38 µV) were essentially the same as that of C57 controls (4.75 ± 2.54 µV) (n = 7-8 eyes). (Note: only female age-appropriate C57s were available at the time of this test.) The response again did not decrease in 11-12 month female DBA/2J mice but, in fact, notably increased compared to age-matched C57 mice (10.26 ± 6.44 µV vs 4.75 ± 2.54 µV) ($p = 0.0602$; n = 6-8). The mean PhNR amplitude of DBA/2J females was also significantly larger than that of males ($p = 0.0494$; n = 5-7) – a counterintuitive finding, given that 12-13 month old females have significantly fewer RGCs than their male counterparts.

Given the nature of the disease under study, evaluation of retinal ganglion cell function was the main concern of this test. However, it was decided to additionally assess electrical responses from the more outer retinal neurons in this model. Of note, severe pigment dispersal was evident in the RPE of this colony (Fig. 4.7), which could lead to photoreceptor dysfunction.

The time taken for maximal response a-wave negative potentials to occur (a-wave latency) was notably longer in 9-11 month old DBA/2J mice relative to C57s – particularly for females (Fig. 4.14.B). This suggests a possible defect in rod photoreceptor function as these mice age. DBA/2J a-wave latencies tended to be longer than those of C57 mice in SFC and flicker responses. SFC a-wave amplitudes were also consistently lower in DBA/2J mice (Fig. 4.14.D). Whether this trend suggests early-onset cone dysfunction in DBA/2J mice or is simply an innocuous strain difference in electrophysiology is debatable. Afterall, significant ERG response differences have been noted even between wild-type mouse strains and even between substrains (Reynolds et al., 2008a, Reynolds et al., 2008b). Additionally, it is important to note that none of the a-wave differences outlined above reached significance.

Rod b-wave latencies were significantly longer in DBA/2J aged females compared to both aged C57 and young DBA/2J controls (Fig. 4.14.C). In the maximal, SFC and flicker responses, a trend emerged where DBA/2J mice (young and old) had notably, often significantly, longer latencies than their aged-matched C57 controls. B-wave latencies were significantly longer in DBA/2J females than in males under all ERG conditions. In a non-significant trend, SFC and flicker b-wave amplitudes were smaller in aged DBA/2J females relative to controls (Fig. 4.14.E).

Based on these results, it would seem that RGCs are not the only type of retinal cell affected in this model of disease. Rod-driven bipolar cells are certainly experiencing some level of dysfunction in aged DBA/2J females, as evidenced by significant increases in scotopic b-wave latency relative to both age-matched C57 and young DBA/2J controls.

Cone-driven bipolar cells are also very likely perturbed. Photopic b-wave latencies were consistently, and often significantly, increased in DBA/2J mice relative to their age-matched controls. The b-wave latency of aged DBA/2J females was also significantly longer than that of their male counterparts under all conditions. These aged females

would possibly also have been significantly different to their young DBA/2J controls, had the sample size of the latter group not been so small (n = 2 eyes). It therefore seems likely that both rod and cone-driven bipolar cell function is perturbed in 9-11 month old DBA/2J females.

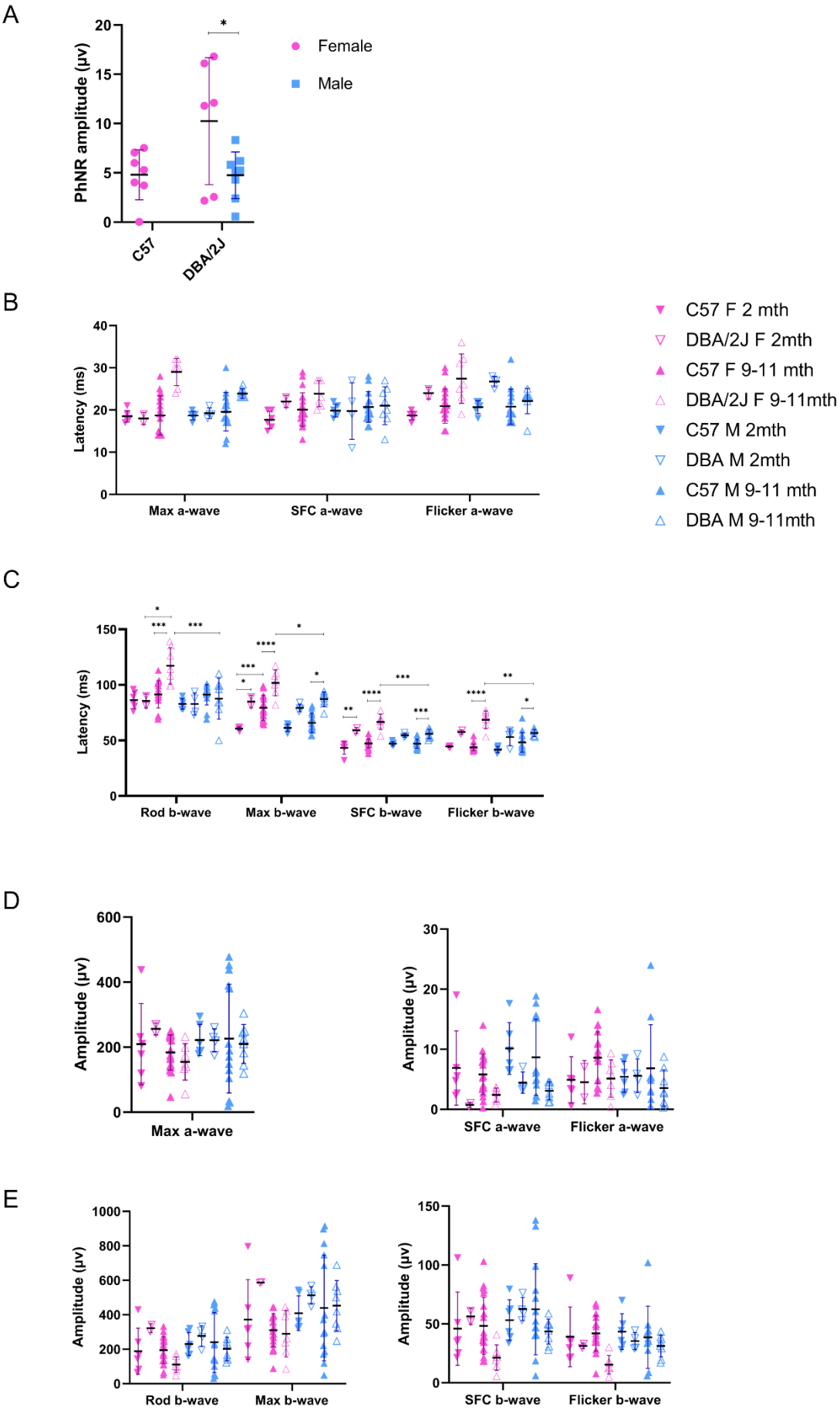

Fig 4.14. ERG deficits in DBA/2J mice.

Fig 4.14. ERG deficits in DBA/2J and C57 mice (continued).

(A) PhNR amplitudes were compared in 11-12 month old C57 and DBA/2J mice. DBA/2J responses were not depleted in comparison to C57 females – in fact in DBA/2J females the mean PhNR was higher than that of C57s. A DBA/2J gender divide was again observed, the female response being significantly higher than the male ($p = 0.0443$; unpaired t test). The number of eyes tested per group were as follows: C57 female (7), DBA/2J female (6), DBA/2J male (8).

(B) Latencies of a-waves from maximal ('max'), SFC and flicker responses are shown. Aged (9-11 month old) DBA/2J mice had notably longer max a-wave latencies than controls, but these differences were non-significant. DBA/2J females also appeared to have prolonged SFC and flicker a-wave latencies compared to their C57 counterparts, though these increases were not significant.

(C) Latencies of b-waves from rod, max, SFC and flicker responses are shown. Rod b-wave latencies were significantly longer in DBA/2J aged females compared to both aged C57 and young DBA/2J controls. In the maximal, SFC and flicker responses, DBA/2J mice had longer latencies than aged-matched C57 controls. b-wave latencies were significantly longer in DBA/2J females than in males under all ERG conditions.

(D) a-wave amplitudes generated under max, SFC and flicker ERG conditions are shown. SFC a-wave amplitudes were notably, but non-significantly, lower in DBA/2J mice compared to their C57 counterparts across all ages and genders.

(E) b-wave amplitudes from all ERG conditions are shown. A non-significant trend emerged, where aged female DBA/2J b-wave amplitudes were lower than aged C57 and young DBA/2J controls in SFC and flicker conditions. Although young female DBA/2J amplitudes were notably high in the rod and max responses, this difference did not reach significance and the sample size for this group was particularly small (n = 2 eyes).

Values shown in in all figures are means ± SD. Three-way ANOVAs were carried out on data shown in (B-E), followed by Tukey's multiple comparisons test. *$p < 0.05$, **$p < 0.01$, ***$p < 0.001$, ****$p < 0.0001$.

The sample group sizes in (B-E) were as follows:

C57 female 2 months old (mo) (6), 9-11 mo (21); C57 male 2 mo (6), 9-11 mo (14);

DBA/2J female 2 mo (2), 9-11 mo (7); DBA/2J male 2 mo (4), 9-11 mo (8).

4.3.6 Assessment of AAV-Ndi1 potency

To deliver Ndi1 cDNA to retinal ganglion cells, an AAV2/2 vector was generated in which the Ndi1 transgene expression was driven by the constitutively active CMV promoter (Fig. 4.15.A). This strategy has previously been employed by the Farrar lab to rescue a rotenone-induced model of LHON (Chadderton et al., 2013). Since then, the *Ndi1* cDNA sequence has been codon optimised for expression in human cells - termed humanised or 'huNdi1'. The huNdi1 construct was shown to express much more highly than the original yeast sequence in HEK 293 cultures (Carrigan, 2014)[34]. It has also been demonstrated to protect human neuroblastoma cells from the effects of phenformin, a Complex I inhibitor (Geoghegan et al., 2017).

Vector potency can vary between rAAVs as a consequence of normal batch-to-batch variability. In order to choose an optimal dose of AAV2/2 Ndi1 to use in this study, newly-made preparations of huNdi1 were tested against a benchmark AAV, 'huNdi1- P1.' The P1 batch of vector had successfully been used in the aforementioned LHON model - generating a beneficial level of long term transgene expression in RGCs (Dr Naomi Chadderton, manuscript in preparation).

To assess potency, AAVs were intravitreally injected in wild-type C57 mice at equivalent doses (~1.6E8 vg/eye). Retinal Ndi1 expression was then quantified via RT-qPCR two weeks post-injection (Fig. 4.15.B). The newer huNdi1 preps both expressed at a higher level than the original P1 batch – an average increase of 125%. It was decided to use huNdi1- P2.1 in the further studies planned, as its expression level more closely matched that of P1 and was less variable than P2.2. Although P1 was injected neat for the two week AAV potency test, it had been used at a 1:2 dilution in the previously mentioned long term study. As P2.1 appeared to express approximately twice as highly as P1 in this test, it was decided to perform future tests with a 1:4 dilution of P2.1.

To assess the therapeutic potential of Ndi1 in the DBA/2J model, pre-glaucomatous mice were intravitreally injected at 2 months of age and evaluated after 10 months of treatment. There were two different treatment groups:
(i) AAV2/2-CMV-huNdi1 in one eye and PBS in the contralateral control eye.

[34]PhD thesis; http://hdl.handle.net/2262/79515

(ii) A 1:1 mix of AAV2/2-CMV-huNdi1 and AAV2/2-CAG-EGFP in one eye, with AAV2/2-CAG-EGFP only in the control eye.

EGFP virus was included in the latter group to enable assessment of transduction efficiency, as a reliable antibody for Ndi1 protein is not yet available (despite the team engaging a contract research organisation to generate an antibody).

Each vector was injected at a dose of 4.1E7 vg per eye. Ideally, the EGFP vector used would have included a CMV promoter to match the Ndi1 vector. However, a CAG-EGFP virus was chosen because its long term potency had been previously characterised. In our lab's experience, CMV and CAG promoter activity do not differ substantially in RGCs (personal communication, Dr Naomi Chadderton) - though another group has found AAV-CMV vectors to provide higher levels of expression in this context (Cao et al., 2019).

Evaluation of transgene expression was undertaken mid-way through the study. Five months after injection of 4.1E7 vg, the mean retinal Ndi1 RNA level was approximately 1.54 fold higher (non-significant) than it had been after two weeks using four times the dose of vector (Fig. 4.15.C). Detection of native EGFP fluorescence was additionally used to verify effective transduction in retinal wholemounts and optic nerve sections (Fig.4.15.D and E).

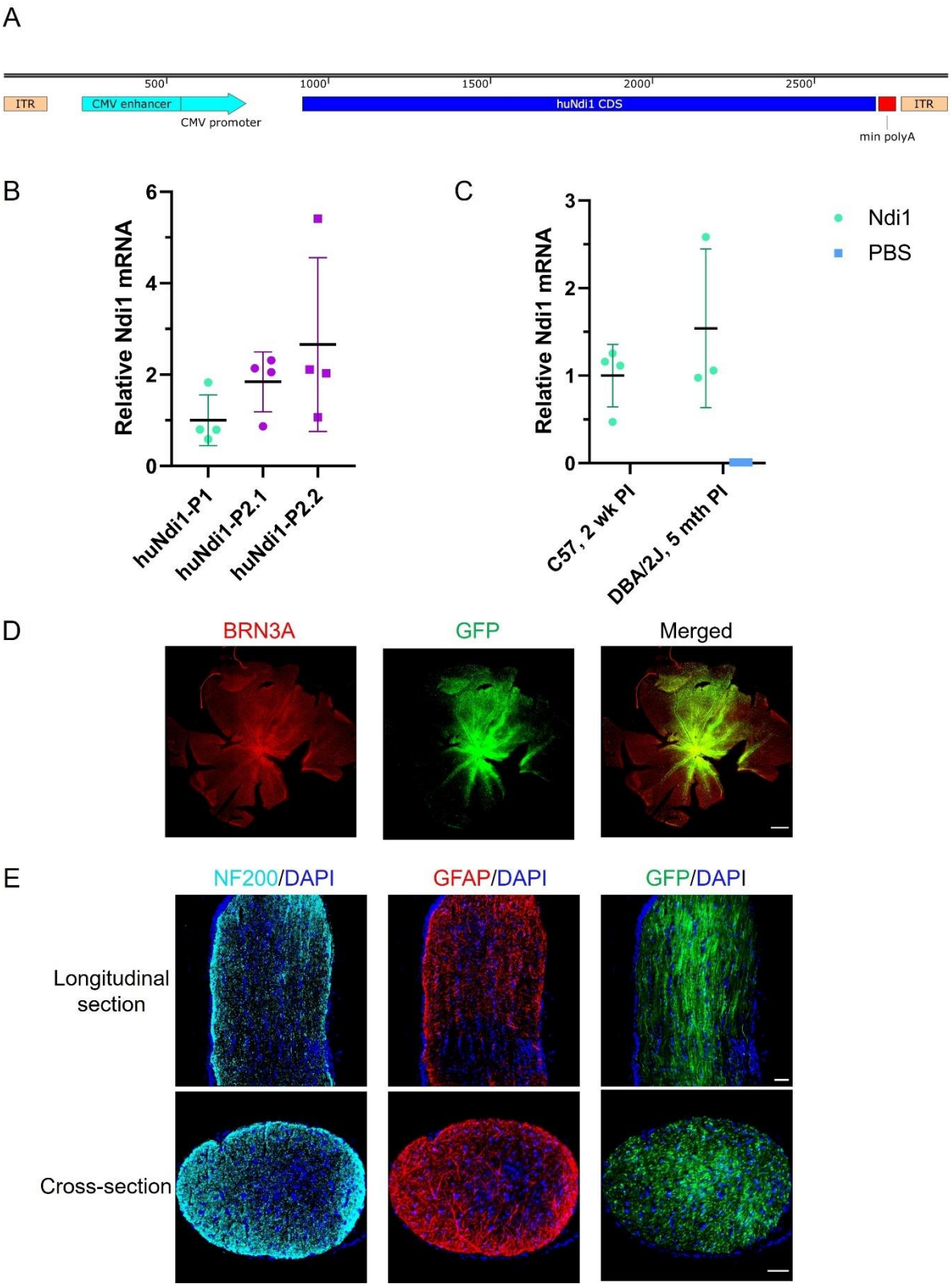

Fig 4.15. AAV preparation potency and intravitreal-injection efficacy.

(A) A schematic of the AAV-CMV-huNdi1 expression cassette is shown.

Fig 4.9. AAV preparation potency and intravitreal-injection efficacy.

(B) RT-qPCR was used to compare various preparations of AAV-CMV-Ndi1 in terms of *in vivo* expression potency. Retinal Ndi1 mRNA levels in wild-type mice were assessed two weeks after intravitreal injection. Values shown are means ± SD, n = 3-4 retinas.

(C) DBA/2J mice were intravitreally injected with AAV2/2-CMV-huNdi1 P2.1 (4.1E7 vg) at two months of age. Ndi1 mRNA levels were assessed five months post-injection (PI) via RT-qPCR. These data were compared to the Ndi1 expression level obtained with the same viral prep in (B), when it had been injected at a dose of 1.6E8 vg/eye for two weeks. PBS-injected DBA/2J retinas were used as negative controls. Values shown are means ± SD, n = 3-4 retinas.

(D) To further assess injection and dosage efficacy, some DBA/2J mice received a 1:1 mix of AAV2/2-CMV-huNdi1 and AAV2/2-CAG-EGFP. Native EGFP fluorescence was evident in retinal wholemounts five months post-injection. Samples were immunostained for BRN3A. Scale bar = 500µm.

(E) Optic nerves of injected eyes were also successfully transduced and transgene expression detected at five months post administration of virus (n = 4). The representative sections shown were counterstained for axon and astrocyte markers (NF200 and GFAP, respectively). Scale bar = 50µm.

4.3.7 Increased NADH oxidation in Ndi1-treated retinas and optic nerves

NADH oxidation was examined in treated tissues in order to confirm functionality of AAV-delivered Ndi1 protein. The overall rate of NADH oxidation was significantly increased in both Ndi1-treated retinal (35.51 ± 5.64 nmol NADH/min/mg) and optic nerve (39.62 ± 16.50 nmol NADH/min/mg) samples relative to PBS-injected controls (retina: 28.11 ± 5.50; ON: 14.81 ± 5.13 nmol NADH/min/mg) ($p < 0.05$; n = 8-9 retinas or n = 4 pooled ON samples) (Fig. 4.16.A and B).

The NADH oxidation rate obtained by this method can be separated so that oxidation arising from endogenous Complex I can be compared to that of the Ndi1 protein. This is achieved by utilising inhibitors specific to each protein (see Section 4.6.13 for protocol details). As shown in Fig. 4.16.C and D, some degree of background 'Ndi1' activity was evident in all untreated samples. In both retinal and optic nerve contexts, the level of Ndi1 activity in AAV-Ndi1 treated tissues was significantly above background oxidation in control samples ($p < 0.05$). Clearly, AAV-delivered Ndi1 was functioning as planned – increasing the NADH oxidation capacity of targeted cells.

NADH oxidation was increased substantially in Ndi1-treated tissues compared not only to contralateral control eyes, but also to wild-type and pre-glaucomatous controls. Overall

retinal and ON NADH oxidation rates were 1.35 and 2.15 fold higher than endogenous levels in pre-glaucomatous DBA/2J mice, respectively. This elevation was significant in retinal samples ($p<0.01$) and possibly also would have been in optic nerves had sample sizes not been so limited (Fig. 4.16.A and B).

It is difficult to accurately quantify increased activity in transduced RGCs. As already discussed, although RGCs possess unusually mitochondria-rich axons, they comprise a minority (<1%) of the total retinal cell population assessed. In contrast, the majority of optic nerve tissue examined appeared to be transduced (n = 4) (Fig. 4.15.E). It is however worth re-emphasising that, despite taking up ~57% of the optic nerve space, RGC axons comprise less than 28% of its mitochondrial content (Perge et al., 2009). Hence, while NADH oxidation increases were measured as approximately 35% and 115% in Ndi1-treated retinal and ON samples, respectively, relative to pre-glaucomatous controls, the actual degree of increased activity in RGC cells is likely much higher.

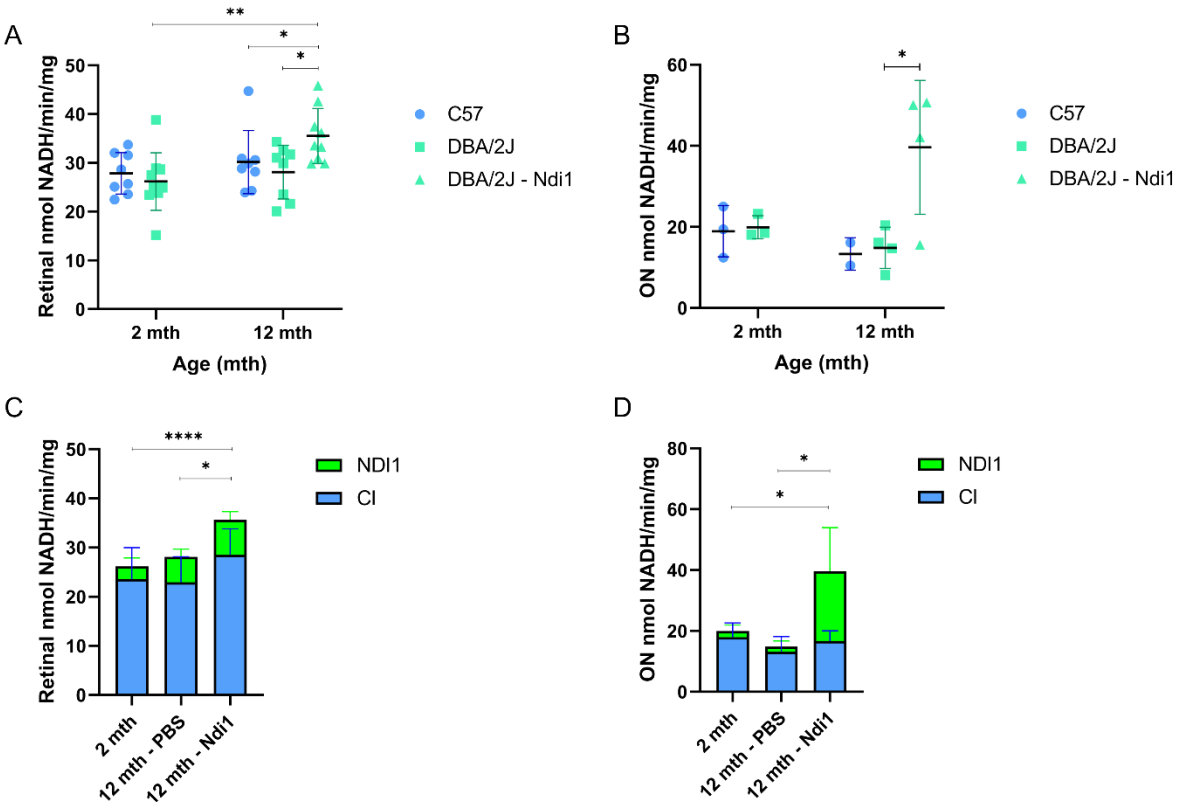

Fig 4.16. Increased NADH oxidation in AAV-Ndi1-treated DBA/2J retinal and optic nerve samples.

NADH oxidation was assessed in retinas of 12 month old DBA/2J mice that had been intravitreally injected with AAV2/2-CMV-huNdi1 10 months previously. For each mouse, a contralateral PBS-injected eye provided a negative control. Uninjected C57 and DBA/2J mice of 2 and 12 months of age were also included in this test for comparison.

(A) Ndi1-treated retinas had a significantly higher rate of NADH oxidation than contralateral PBS-injected, aged C57 and young DBA/2J control retinas ($p = 0.0372$, 0.0474 and 0.0035, respectively).

(B) NADH oxidation was further assessed in pooled optic nerve samples (4 nerves per pool) and found to reduce modestly with age in both strain of mice, replicating the trend in Fig. 4.13.B. Ndi1 treatment significantly increased this activity in 12 month old DBA/2J optic nerves compared to PBS-only control retinas ($p = 0.0289$).

For (A) and (B), a one-way ANOVA was used, followed by Tukey's multiple comparisons test.

Fig 4.16. Increased NADH oxidation in AAV-Ndi1-treated DBA/2J retinal and optic nerve samples (continued).

(C and D) Overall NADH oxidation data was separated into activity attributed to endogenous Complex I and transgenic Ndi1 for DBA/2J retinal (C) and ON (D) samples. Ndi1 activity in AAV-Ndi1-injected tissue was significantly above background levels when compared to PBS-injected and uninjected controls. In (C), $p = 0.0424$ (vs PBS) and $p < 0.0001$ (vs 2 month old DBA/2J). In (D), $p = 0.0181$ and $p = 0.0273$. For statistical analysis, one-way ANOVA and Dunnett's multiple comparisons test were used.
Values shown are means ± SD.

4.3.8 Rescue of RGC soma loss in AAV-Ndi1 treated DBA/2J eyes

EGFP native fluorescence was assessed in Ndi1/EGFP-treated and contralateral EGFP-only retinas 9-10 months post-injection (at 11-12 months of age). EGFP positive RGC somata and axons were evident in retinal wholemounts immunostained for BRN3A (Fig. 4.17.A). The average proportion of GCL area transduced was 31.8 ± 8%. However, retinas from eyes co-injected with AAV-Ndi1 displayed a significantly higher uptake of EGFP (43.22 ± 14.37% vs 20.36 ± 15.4%; $p = 0.0036$; $n = 8$) (Fig. 4.17.B). One might expect a lower level of EGFP expression in cells where its vector is in competition with another. The fact that more EGFP was detected in co-transduced eyes may suggest that Ndi1 expression was beneficial. It is possible that Ndi1-treated cells were healthier and so expressed more of the marker protein. Indeed, retinas that received both Ndi1 and EGFP had higher median RGC densities than their EGFP-only contralateral controls (Fig. 4.17.D).

The area of GCL transduced by AAV was calculated by quantifying the proportion of EGFP-positive area in wholemounts, using the Fiji 'Threshold' and 'Measure' features. This is not a perfect method for quantification of transduced area. For example, amplifying the EGFP signal with immunocytochemistry would likely have yielded a higher efficiency result. Additionally, area determination is sensitive to the image thresholding parameters selected, which in this case were chosen conservatively to minimise the contribution of background fluorescence. Nonetheless, this analysis gives a useful, but likely underestimated, approximation of the proportion of retina transduced. These data will be reanalysed in the near future to generate a more accurate RGC transduction efficiency estimate; individual cells will be counted and those positive for both EGFP and BRN3A will be expressed as a proportion of the total BRN3A-positive cell population.

RGC numbers were determined by counting BRN3A-positive somata. As DBA/2J mice display a high degree of phenotypic variability, sample sizes are recommended to include ideally 40-60 eyes per experimental group (Libby et al., 2005a). The various different treatment cohorts (male and female, GFP and PBS-based vehicles) were therefore combined for analysis, in order to maximise the statistical power of the study. The resulting Ndi1-treated and control groups consisted of 37 paired eyes. The median RGC density in treated retinas was 3.19 fold higher than contralateral GFP/PBS eyes (1942.21 ± 805.41 vs 609.70 ± 451.65 RGCs/mm^2; p = 0.0490, n = 37 pairs of eyes, Wilcoxon matched-pairs signed rank test). Relative to median RGC density in 12-13 month old C57 mice (2618.88 ± 187.85 RGCs/mm^2; n = 12), RGC survival in untreated aged DBA/2J mice was 23.28% in this experiment. With AAV-Ndi1 treatment, 74.16% of RGC somata were preserved[35] in DBA/2J retinas.

The RGC density data was additionally broken down into sub-cohort comparisons so that potential effects of gender and/or EGFP expression on treatment response could be examined (Fig. 4.17.D and E). Median RGC density increases were evident in all Ndi1-treated groups relative to controls – though these increases were not significant. When paired eyes were matched, 59% of Ndi1-treated retinas had higher RGC numbers than their contralateral control. Male retinas had notably higher densities of RGCs than females (as expected) and these densities were higher still when treated with Ndi1. It is notable that the median RGC density of female EGFP-only control eyes was not lower than that of PBS-only retinas. This may indicate that long-term expression of the EGFP transgene was not retinotoxic. However, this cannot yet be definitively concluded because of the small number of female PBS-only control eyes available to analyse (n = 5) and inherently large variance of this model.

As mentioned previously, considering the slower progression of RGC loss evident in males (Fig. 4.11.C), it had been proposed to analyse treated male DBA/2J mice at a later timepoint – approximately 15-16 months of age. Unfortunately, due to work restrictions enforced to combat the COVID-19 pandemic, it was necessary to sacrifice the majority of

[35] While C57BL/6 is distinct from the DBA/2J strain and therefore not an ideal control, aged DBA/2J-Gpnmb+ mice (isogenic DBA/2J controls) have been shown to exhibit very similar RGC densities to their C57 counterparts when assessed by retrograde labelling (Dengler-Crish et al., 2014). We can therefore compare Ndi1-treated DBA/2J retinas with C57 mice to make an informed estimate as to the level of RGC preservation in the former.

males earlier than anticipated. While the overall median RGC density was increased in Ndi1-injected males, benefit was much more pronounced in the limited number of 15 month old mice available (Fig. 4.17.F).

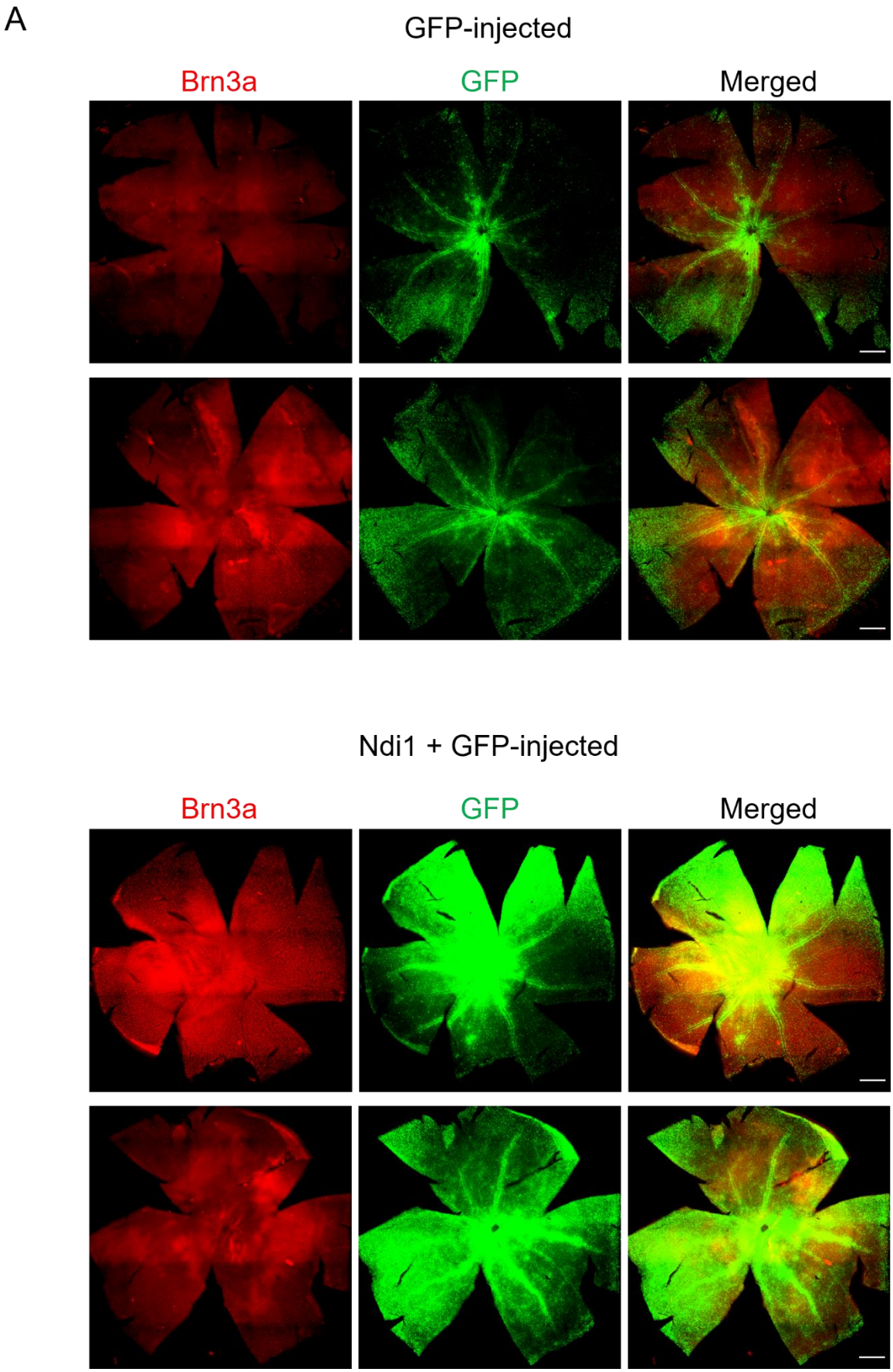

Fig 4.17. AAV-Ndi1 successfully transduced the GCL and increased RGC density in treated DBA/2J mice.

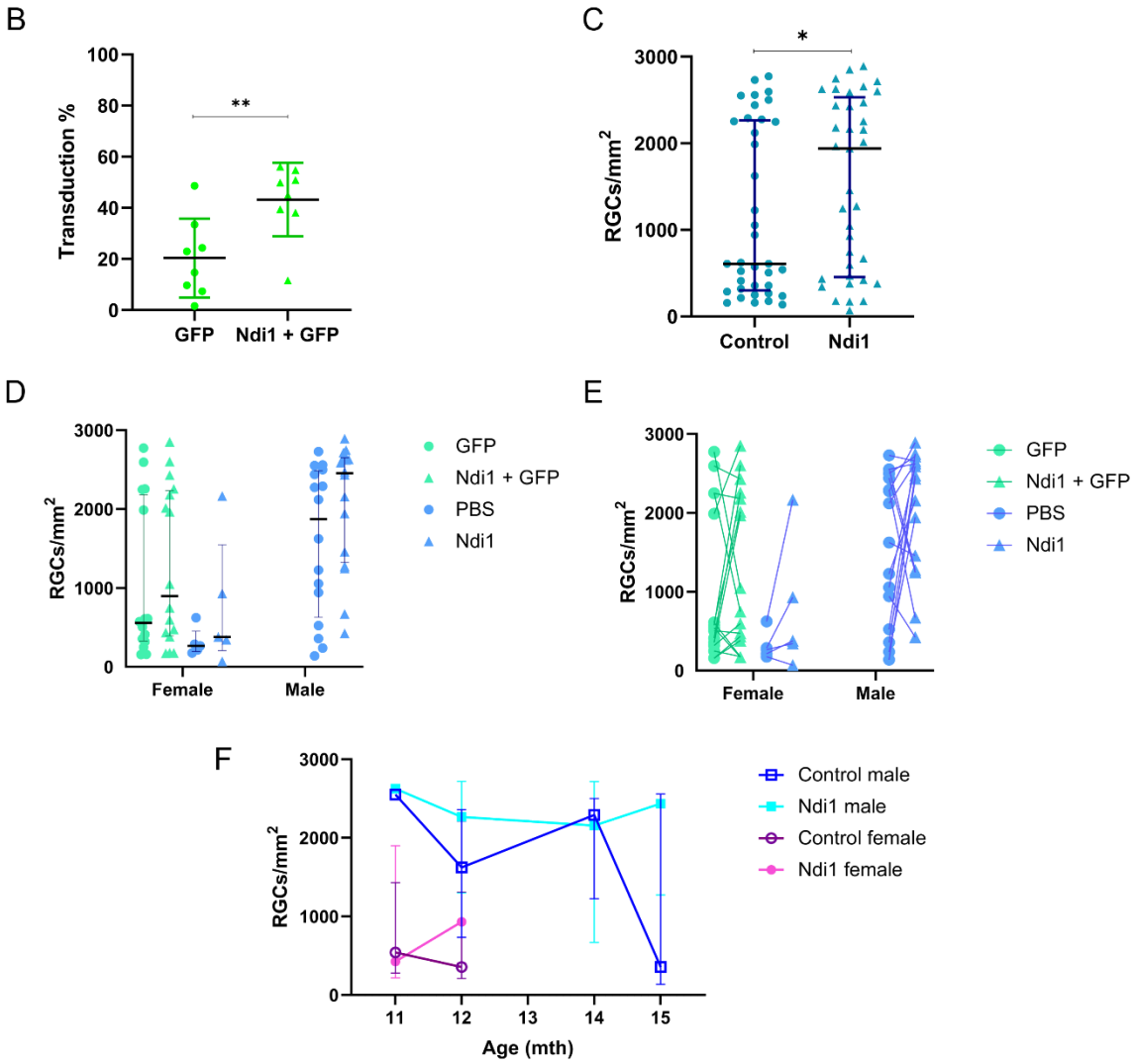

Fig 4.17. AAV-Ndi1 successfully transduced the GCL and increased RGC density in treated DBA/2J mice (continued).

(A) Retinal wholemounts of mice intravitreally injected with AAV-Ndi1 and AAV-EGFP are shown. Samples were stained for BRN3A (red). EGFP-positive RGC somata and axons are visible. Images shown were acquired in multiple frames (16) and stitched using cellSens. Scale bar = 500µm.

(B) Transduction efficiency was estimated by calculating the percentage of EGFP-positive wholemount area, using the 'threshold' and 'measure' functions of Fiji. Eyes that were co-injected with AAV-Ndi1 displayed a significantly larger area of transduction ($p = 0.0036$, $n = 8$; paired t test). Values shown are means ± SD.

Fig 4.17. AAV-Ndi1 successfully transduced the GCL and increased RGC density in treated DBA/2J mice.

(C) BRN3A-positive ganglion cells were quantified in stitched images of retinal wholemounts using the 'Count and Measure' module in cellSens. In this graph, the results of both cohorts were combined so that 'control' refers to mice injected with PBS or AAV-EGFP and 'Ndi1' refers to mice that received AAV-Ndi1, either alone or in combination with AAV-EGFP. The median density of RGCs was significantly higher in Ndi1-treated retinas ($p = 0.0490$, $n = 37$; Wilcoxon matched-pairs signed rank test). Medians and interquartile ranges are shown.

(D) The RGC count data was broken down into sub-cohort comparisons so that the effects of gender and inclusion of GFP could be examined. Non-significant increases in median RGC density were apparent across all cohorts: female GFP/Ndi1, $p = 0.4639$, $n = 16$; female PBS/Ndi1: $p = 0.1875$, $n = 5$; male PBS/Ndi1: $p = 0.1928$, $n = 16$. Male retinas displayed higher densities of RGCs than females but still exhibited a further increase when treated with Ndi1. Medians and interquartile ranges are shown.

(E) Data points from control and treated eyes in (D) are joined to enable visualisation of matching pairs. Medians and interquartile ranges are shown.

(F) RGC count data was replotted against the age of mice at the time of tissue harvesting. Retinas of Ndi1-treated mice displayed increased median RGC density at 12 months of age in females, and at 12 and 15 months of age in males. Female group sizes: 11 months old (mo) (8-9), 12 mo (13). Male group sizes: 11 mo (1), 12 mo (9), 14 mo (3), 15 mo (3). Values shown are medians with interquartile ranges.

4.3.9 A trend of improved photopic negative response in Ndi1-treated mice

To evaluate the potential benefit of Ndi1 on retinal ganglion cell function, the photopic negative response was analysed in 10-11 month old injected DBA/2J mice of both sexes. Overall, median PhNR amplitude in Ndi1-treated eyes was 1.9 fold higher than in contralateral control eyes ($p = 0.1120$, $n = 25$; 3.96 ± 2.16 µV vs 2.08 ± 1.932 µV) (Fig. 4.18.A).

Again, control and Ndi1-treated groups were broken down into subgroups (based on gender and the nature of the control treatment (PBS/GFP)) to explore if a more pronounced effect could be observed in subcohorts (Fig. 4.18.B and C). Median PhNR amplitude in female eyes injected with Ndi1 and GFP was significantly increased by 1.9 fold relative to GFP-only contralateral eyes ($p = 0.0059$, $n = 10$; 4.35 ± 1.36 µV vs 2.3 ± 1.5 µV). Ndi1-treated male eyes demonstrated a nonsignificant rise of 1.5 fold compared to

controls ($p > 0.9999$, n = 11; 1.63 ± 1.63 µV vs 2.44 ± 2.44 µV). In contrast, in the limited number of PBS/Ndi1-injected females, median PhNR in Ndi1-treated eyes was 0.75 fold lower than controls ($p = 0.6250$, n = 4; 3.73 ± 1.985 µV vs 2.805 ± 1.21 µV).

As previously demonstrated in Fig. 4.14.A, female PhNRs were again generally higher (in both PBS and EGFP injected groups) than male responses. The difference was less pronounced on this occasion (Fig. 4.18B), however, and did not reach significance. This is possibly due to the fact that the mice analysed in Fig.4.14.A were slightly older (11-12 months old). ERG amplitudes in general were also notably lower in the later experiment (non-PhNR data not shown) than those recorded in Fig. 4.14.B. It is possible that the ERG electrodes had corroded somewhat in the 8 months between the two tests, leading to generally lower amplitudes in the later experiment.

It is worth noting that varying degrees of corneal abnormalities have been reported in DBA/2J mice from as early as 6 weeks of age, sometimes in combination with neovascularisation (Libby et al., 2005a, John et al., 1998, Turner et al., 2017). Some researchers have also reported that tropicamide was not effective in inducing pupil dilation in these mice from 18 weeks of age (Turner et al., 2017). Such factors may impede stimulation of the retina by light during ERG recording.

In the TCD colony, early corneal clouding and vascularisation were noted to develop during the 12th month of age (assessed by Dr Paul Kenna; data not shown). In the time-frame of ERG analysis (10-11 months of age), obvious pupil dilation defects were not observed. Additionally, PhNR readings were only used if an initial cone-driven response was present in the reading. In the experiment described, data from pre-glaucomatous control mice were unavailable for comparison. However, in future tests, we may implement a policy similar to Cwerman-Thibault et al. (2017), whereby electrophysiological readings in 12 month old mice were discarded if they fell under 25% of the pre-glaucomatous average and severe corneal abnormalities were present.

Intravitreally injected AAV 2/2 virus would not be expected to efficiently transduce outer retinal cells (Cao et al., 2019). Nonetheless, for completeness, all outer retina-derived ERG components outlined in Fig. 4.14.C-F were analysed in Ndi1-treated and control mice. As anticipated, intravitreal delivery of AAV2/2-CMV-Ndi1 did not appear to affect photoreceptor or bipolar cells (data not shown).

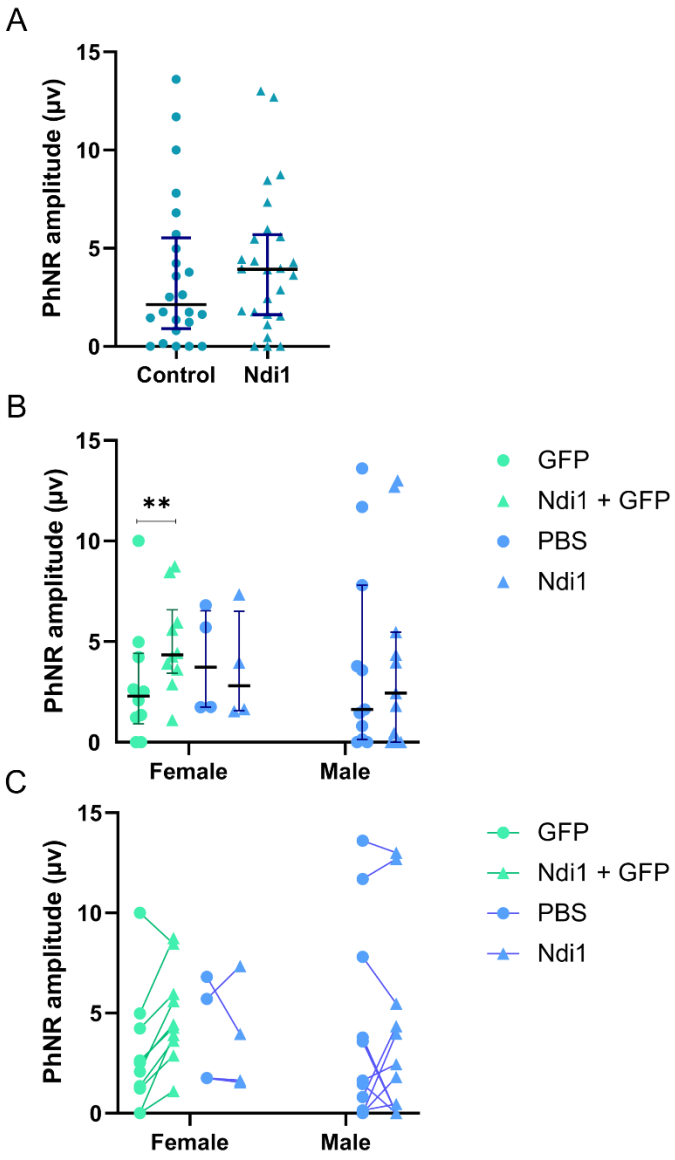

Fig 4.18. Photopic negative response readings in treated 10-11 month old DBA/2J mice.

(A) PhNR was assessed in AAV-Ndi1-treated and control eyes 8-9 months post-intravitreal injection. Ndi1-treated eyes displayed a higher median PhNR amplitude than contralateral control eyes ($p = 0.1120$; $n = 25$ paired eyes). A Wilcoxon matched-pairs signed rank test was used to test for significance.

(B) PhNR data presented in (A) was reformatted and separated into subcohorts for further inspection. GFP-injected females displayed a significant increase in Ndi1-treated eyes ($p = 0.0059$, $n = 10$). The difference between control and Ndi1-injected eyes was not significant in males ($p > 0.9999$, $n = 11$) or in the limited amount of PBS/Ndi1-injected females ($p = 0.6250$, $n = 4$). The female PBS/Ndi1 group was the only cohort not to show some level of increase in Ndi1-injected eyes. Medians and interquartile ranges are shown in (A) and (B). $^{**}p < 0.01$.

(C) A paired plot of the data presented in (B). Matched points illustrate the relationship between samples originating from the same mouse.

4.4 Discussion

4.4.1 Characterisation of a DBA/2J colony

4.4.1.1 Iris disease and IOP elevation

The phenotypic profile of the DBA/2J colony examined as part of the work presented in this chapter generally fit with that previously reported in the literature. Mice clearly developed a serious iris disease with age and, although IOP had only been measured at three timepoints at the time of writing, the IOP profile was similar to those reported previously (Libby et al., 2005a, Cwerman-Thibault et al., 2017) – with a significant peak at 10-11 months of age. In the future, IOP will be more thoroughly characterised in this colony, with monthly measurements taken and compared between sexes. Stratification of mice in accordance with the severity of their IOP profile (i.e. high, medium and low) could aid in the interpretation of other phenotypic readouts and potentially mitigate some of the inherently large variation associated with this model.

4.4.1.2 Neurodegeneration

At 13 months of age, DBA/2J mice displayed signs of neurodegeneration in retinal and optic nerve samples. Optic nerves were clearly gliotic, as evidenced by upregulation of GFAP by astrocytes. GFAP upregulation (indicating Müller glia and astrocyte activation) was also significantly increased in the retinas of female but not male DBA/2J mice. To my knowledge, the extent of gliosis had not been compared between sexes prior to this study. Though the sample size was small for this test (n = 2-4 ONs), the results indicate a possible gender-dependent phenotypic variation that will be important to consider in future experiments.

RGC axon and soma degeneration was also apparent at 13 months. Optic nerve neurofilament content and retinal RGC soma density was significantly reduced in 13 month old DBA/2J females compared to age-matched C57 controls. Reductions were also seen in male samples, which would likely have been significant with a larger sample size (n = 2-4 ONs and 3-7 retinas currently).

It should be noted that reports of the onset of RGC cell body degeneration vary a lot in the literature (outlined in Table 4.1). This is likely dependent on the method of detection used and perhaps, to a lesser extent, the type of control strain and specific colonies analysed.

RGC loss is reported much earlier by studies using BRN3A immunostaining and retrograde labelling than when staining for NeuN, a neuronal DNA-binding protein. Hence, reductions in RGC number observed from 9-13 months using Fluorogold labelling reflect impaired axonal retrograde transport (Buckingham et al., 2008, Dengler-Crish et al., 2014). Additionally, expression of RGC-specific genes (Brn3b, Nfl, Hsp90, Sncg) has been shown to decrease with age in DBA/2J mice (Soto et al., 2008, Buckingham et al., 2008). Reduction in BRN3A and RBPMS positivity is therefore likely due to a general downregulation of RGC-specific genes, representing severe RGC dysfunction rather than actual absence of cells.

Study	Method	Onset of RGC soma loss (month)	Controls
Zhong et al. 2007	Retrograde labelling using Fluorogold; retinal wholemounts	12	Age-matched C57
Buckingham et al. 2008	NeuN staining; retinal wholemounts	18	2-4 mo DBA/2J
Buckingham et al. 2008	Retrograde labelling using Fluorogold; retinal wholemounts	13	3 mo DBA/2J
Dengler-Crish et al. 2014	Retrograde labelling using Fluorogold; retinal wholemounts	9-10	3 mo DBA/2J and 9-12 mo DBA/2J-Gpnmb+
Cwerman-Thibault et al. 2017	BRN3A staining; retinal sections	10	2 mo DBA/2J
Jassim et al. 2020	RBPMS staining; retinal wholemounts	6	Age-matched DBA/2J-Gpnmb+
This study	BRN3A staining; retinal wholemounts	12-13 (earlier time-points not sufficiently studied)	Age-matched C57 and 3 mo DBA/2J

Table 4.1. Onset of significant RGC soma loss reported in the literature. mo = months old.

It is interesting to note that loss of BRN3A-positive RGCs was significantly more pronounced in female DBA/2J mice than males in this study (Fig 4.11). Other researchers have noted more rapidly progressing axon degeneration in female optic nerves (Libby et al., 2005a). It is therefore not surprising that RGC density follows this trend, though it is still important to document and define this gender divide. Zhong et al. also observed reduced RGC densities in females compared to males at 4 and 10 months of age using retrograde labelling, though these differences were not significant (Zhong et al., 2007).

A gender bias is apparent from the very start of DBA/2J disease progression; iris abnormalities and IOP elevation are also noted earlier in female mice (John et al., 1998, Libby et al., 2005a). As mentioned previously (Section 4.2.1.4.3), women are more likely to develop angle-closure glaucoma due to reduced axial length and anterior chamber depth (ACD) relative to males. To my knowledge, it has yet to be confirmed if anterior chamber depth differs between young male and female DBA/2J mice. In females, IOP

begins to rise earlier than males and remains at an above-average level for longer (Libby et al., 2005a). It is therefore possible that a smaller ACD and, consequently, a more severe IOP profile gives rise to the more rapid progression of RGC degeneration in female DBA/2J mice.

4.4.1.3 Electrophysiology

The photonegative response of aged DBA/2J mice was examined in order to assess RGC function. PhNR amplitude was not reduced in 11-12 month old DBA/2J mice relative to age-matched C57 controls. It would be informative to repeat this test with greater sample sizes and, in light of the fact that ERG responses can vary between strains, including pre-glaucomatous DBA/2J controls. Aged DBA/2J females had a significantly higher amplitude than males in the initial characterisation experiment (Section 4.4.5). When the data from PBS-injected 10-11 month DBA/2J mice in Section 4.3.9 is added, however, the difference between PhNRs of male and female DBA/2J mice is still evident but not significant ($p = 0.10$). Grillo et al. reported no significant PhNR reduction in aged DBA/2J mice compared to young controls, though they did not examine male and female response separately (Grillo et al., 2018). The apparent relative increase in female PhNR amplitude was surprising, given the established more rapid progression of RGC degeneration in females. Interestingly, Smith et al. also observed an unexpected rise in PhNR amplitude in an ON transection model of RGC death relative to controls (Smith et al., 2014). In this case, PhNR amplitude increase was proposed to be due to a more rapidly decaying b-wave.

There have been conflicting reports as to whether outer retinal functional deficits are present in the DBA/2J model. Saleh et al. reported negligible changes in light-adapted flash ERG response (Saleh et al., 2007). However, subsequent studies observed clear abnormalities in outer retinal function, which is in agreement with the ERG data presented in this chapter (Table 4.2)

Study	Cohort	Rod a wave	Rod b wave	Mixed a wave	Mixed b wave	Cone a wave	Cone b wave	Flicker response
Harazny et al. 2009	2-10 mo D2 and C57.			Lower amplitude and longer latency from 6 mo D2 vs C57.	Lower amplitude and longer latency from 6 mo DBA vs C57.	N/A	N/A	Lower amplitudes from 6 mo D2 vs C57 at 12 Hz or 2-3 mo at 30 Hz.
Heiduschka et al. 2010	24 ´mo D2 and C57.	Lower amplitude.	Lower amplitude.	Lower amplitude.	Lower amplitude.	N/A	N/A	N/A
Grilla et al. 2018.	11 mo D2 vs 4 mo.	Lower amplitude.	Longer latency, lower amplitude.	Longer latency, lower amplitude.		Longer latency, lower amplitude.	Longer latency.	Longer latency (30 Hz).
This study	2-11 mo D2 and C57.		Longer latencies in 9-11 mo female D2 than males, age-matched C57 and young D2.	Longer latency (ns) in 9-11 mo D2, esp. females. Amplitude lower in D2 mice at all ages (ns).	Longer latency in 9-11 mo D2 females than males.	Trend of lower amplitudes and longer latencies in D2 (vs C57) across all ages.	Trend of longer latencies in D2 (vs C57) across all ages.	Trend of longer latencies in D2 vs C57 across all ages. Amplitude reduced in 9-11 mo female D2 compared to C57 and young D2 (ns) and 9-11 mo D2 males. (10 Hz flicker)

Table 4.2. Comparison of ERG results with data from the literature.

Abbreviations: D2 = DBA/2J; mo = months old; ns = non-significant. Note: Harazny et al. averaged scotopic responses over light intensities ranging from 0.0003 to 3 cd.s/m^2.

It is clear that RGCs are not the only type of retinal cell affected in DBA/2J mice. Rod and cone photoreceptors and bipolar cells also appear to be experiencing some level of dysfunction. In support of this, photoreceptor loss, OPL thinning, loss of horizontal and bipolar cell processes and abnormal rod ribbon synapses have been noted in DBA/2J mice from 2-3 months of age (Fernández-Sánchez et al., 2014, Fuchs et al., 2012). To my knowledge, the work carried out in this chapter is the first time that male and female outer retinal dysfunction has been compared in the DBA/2J model. The data suggests that photoreceptor and bipolar dysfunction follow the general trend of a more rapidly progressing disease in females.

The early onset of ONL/OPL morphological changes indicates that outer retinal defects are at least partially IOP-independent. A somewhat overlooked aspect of the DBA/2J phenotype is depigmentation of the RPE (shown in Fig. 4.1) - likely an additional effect of mutations in *Tyrp1* and/or *Gpnmb*, which are known to be expressed in the developing RPE (Loftus et al., 2009). Gpnmb, specifically, is hypothesised to be involved in disposal of photoreceptor outer segment debris in the RPE (Li et al., 2010). Melanin is proposed to protect the RPE and choroid from light-induced damage by filtering light and scavenging free radicals (Gresh et al., 2003). The pigmented iris also protects the retina from excessive light exposure and so its progressive destruction in DBA/2J mice may lead to elevated levels of metabolic stress in photoreceptors over time (Fuchs et al., 2012). It is quite striking that ocular pigmentation has been shown to positively correlate with rod cell number (Donatien and Jeffery, 2002), with albino Balb/c mice exhibiting substantial photoreceptor loss and ERG deficits (Gresh et al., 2003). Given that outer retinal dysfunction appears IOP-independent, it is interesting that female DBA/2J mice appear more severely affected than males. John et al. (1998) noted that iris defects occurred earlier in females than in males and so it would be interesting to verify whether this is the case with RPE pigment abnormalities also.

It is, of course, important to thoroughly characterise all aspects of retinal function in the DBA/2J model and to clearly define glaucomatous from non-glaucomatous phenotypes. Doing so will help to protect against confounding factors in future experiments seeking to elucidate and treat the pathogenesis of glaucoma.

4.4.1.4 Oxidative stress and mitochondrial dysfunction

Three markers of oxidative stress (*Cp, Nos2* and *Ho-1*) were evaluated during this study and found to be more highly expressed in 11-12 month old DBA/2J retinas relative to age-matched C57 controls (Fig. 4.12). This is in keeping with the data presented by Inman et al. (2013), who noted significantly increased lipid peroxidation from 3 months of age and upregulation of *Cp, Nos-2* and *Ho-1* from 7-10 months.

When ETC Complex I function was assessed, there was a trend towards reduced activity in DBA/2J retinal samples compared to age-matched controls. However, activity did not decline over time in DBA/2J or C57 retinas (Fig 4.13). This suggests a possible inherent Complex I defect in DBA/2J retinal cells. As discussed in Section 4.2.3, it is difficult to estimate how much of such a deficit could be attributed to RGC mitochondrial function specifically. Considering the ERG results, it is possible that the CI assay data reflect some degree of photoreceptor and bipolar cell mitochondrial dysfunction also. The retinal data shown here contradict results presented by Cwerman-Thibault et al. (2017), who found that Complex I activity was significantly reduced in DBA/2J retinas from 5 months of age relative to 2 month old pre-glaucomatous mice. This is possibly a result of the differing protocols used (outlined in Section 4.4.4) and the smaller DBA/2J sample groups available in the current study (n = 6-9 retinas in this study compared to n = 10-26 used by Cwerman-Thibault et al.).

In contrast to the retinal results, the rate of NADH oxidation in optic nerve samples declined similarly with age in DBA/2J and C57 mice, though the modest differences observed were nonsignificant. This may be indicative of a natural, slight deterioration in the function of optic nerve mitochondria over time.

As discussed in Section 4.2.3, ATP production has previously been examined in DBA/2J optic nerves. Baltan et al. (2010), using a luciferase-based ATP synthesis assay, noted that mice with high IOP displayed significantly lower ON ATP production than low-IOP mice at 6 months of age. By 10 months, both high and low IOP mice exhibited low ATP synthesis. However, the level of ATP was not compared to wild-type or pre-glaucomatous controls. Using Seahorse analysis of respiration, Jassim et al. (2019) also found that ATP production declined over time in DBA/2J optic nerves but was lowest, and only significantly lower than DBA/2J-Gpnmb+ controls, at 6 months of age. DBA/2J RGC axons in isolation actually appeared to produce more ATP but were less capable of switching to glycolysis than age-

matched controls. Given this increased (though still insufficient) level of OXPHOS, it would follow that ETC activity is also increased in DBA/2J RGC axons. In support of this, ETC genes were shown to be upregulated in glaucomatous DBA/2J mice (Williams et al., 2017). Any net decrease in whole optic nerve OXPHOS would therefore presumably be due to reduced activity in glial cell mitochondria. However, given the variability associated with both the DBA/2J model and Seahorse analysis, the results of the Jassim et al. study should be replicated before speculating on this matter too much further.

As part of this project, preliminary tests comparing ATP synthesis[36] in 2 and 12 month old C57 and DBA/2J optic nerves were carried out and no significant differences were detected (not shown). It would be useful to repeat this test at 10 months, as ATP diffusion in the optic nerve is proposed to be affected by IOP (Band et al., 2009). IOP is reported to fall back to normal levels after a peak at 10-11 months, due to atrophy of the ciliary body (Libby et al., 2005a, Cwerman-Thibault et al., 2017). Although IOP was not measured at 12 month old mice in our DBA/2J colony, it was no longer elevated at 13 months of age - in keeping with the trend reported by others (Libby et al., 2005a, Cwerman-Thibault et al., 2017). It would therefore be valuable to more thoroughly characterise the IOP profile of mice in our colony and to quantify ATP levels at various timepoints. Our team also recently gained access to a Seahorse Analyser and so may attempt to replicate the protocol utilised by Jassim et al.

4.4.2 Assessment of the therapeutic potential of Ndi1 in a glaucomatous context

The characterisation of the DBA/2J phenotype in the colony in Trinity was an important prerequisite to the exploration of a candidate gene therapy in this mouse model of glaucoma, highlighting the optimal timeframe and outcome measures for the investigation. As part of the study in this thesis, the utility of Ndi1, in essence a single gene substitute for mammalian Complex I function, was explored in DBA/2J mice. Of note, intravitreal injection of AAV2/2-CMV-Ndi1 led to a substantial, long-term increase of NADH oxidation in aged DBA/2J retinas and optic nerves (Fig 4.16). It would be interesting to examine the level of ATP production in treated tissues in the future, as the degree of ATP synthesis will not necessarily match the rate of NADH oxidation –

[36] Optic nerve samples were snap frozen and ATP was extracted using the method described by Yang et al. 2002. ATP levels were quantified using the (luciferase-based) ATP Determination Kit (ThermoFisher Scientific, A22066) and values were normalised against total protein content (quantified via Bradford assay).

particularly because the Ndi1 protein is non-proton pumping. Importantly, Ndi1 delivery has previously been shown to increase ATP production *in vitro* (Park et al., 2007, Maloney, 2020).

In addition to the observation of increased NADH oxidation, a significant (~3 fold) increase in RGC survival was observed in aged DBA/2J mice – resulting in preservation of approximately 74% of RGC cell bodies (Fig 4.17). An overall non-significant trend of increased inner retinal function, as assessed by PhNR, was also apparent (Fig. 4.18). As the sample size for this test (n = 25) was suboptimal, it would be worth repeating with increased numbers. The fact that a female subcohort (Ndi1/EGFP-injected; n = 10) was the only one to display a significant increase in inner retinal function is an interesting result – especially given the general gender bias in disease presentation of DBA/2J mice. It would be prudent to replicate this finding with an adequately sized group of Ndi1/PBS-injected females to confirm that the apparent benefit of Ndi1 was not simply due to mitigation of possible GFP-induced oxidative stress (Ansari et al., 2016). However, in this regard it is encouraging that (i) median RGC density in EGFP-treated retinas was not lower than that of PBS-injected eyes after long-term transgene expression (Fig. 4.17.D) and (ii) Ndi1+EGFP-injected eyes displayed increased PhNR (Fig.4.18.B) despite having a significantly greater level of EGFP expression than their contralateral controls (Fig.4.17.B). It is also possible that RGCs received a lower net dose of AAV-Ndi1 in eyes co-injected with AAV-Ndi1 and AAV-EGFP (at a 1:1 ratio) compared to those of PBS/Ndi1 injected eyes due to competition between the two vectors. This possible lower dose could have been more effective. Therefore, while the observation of significantly increased inner retinal function in Ndi1/EGFP-injected eyes relative to EGFP-injected controls seems promising, this experiment clearly must be repeated.

As part of the future work, it is planned to investigate whether Ndi1 treatment was protective to RGC axons and interrogate whether benefit is achieved through increased ATP production and/or reduction of oxidative stress. Due to time constraints, there are currently a large number of Ndi1-treated and control retinal and optic nerve samples in freezer storage awaiting analysis. This will include tests already described in the chapter: assessment of axon counts via NF200 staining of ON sections and expression levels of GFAP, Nos2, Cp and Ho-1 in retinal samples via RT-qPCR. Additional assays are planned to further probe the levels of oxidative stress and mitochondrial function in these samples.

Assessment of DNA oxidation, protein nitration and lipid peroxidation can be achieved by histological staining for 8-OHdG, 3-NT (3-nitrotyrosine), 4-HNE (4-hydroxynonenal), respectively. These markers were previously demonstrated to be upregulated in 12 month old DBA/2J retinas (Inman et al., 2013) and in optic nerve samples of a rat ON transection model (O'Hare Doig et al., 2014). ETC function can furthermore be assessed by staining for succinate dehydrogenase (SDH; Complex II) and cytochrome c oxidase (COX; Complex IV) activity in ON sections (Harun-Or-Rashid et al., 2020).

It is encouraging that the long-term, considerable increase in NADH oxidation activity achieved by this AAV-delivered transkingdom gene therapy was not overtly toxic to retinas (as assessed by RGC density). Tolerance of this treatment will be examined more closely in future by analysing markers of gliosis and immune response in transduced tissues (GFAP, IBA1, IgG).

The data presented in this chapter suggest that intravitreal delivery of AAV-Ndi1 to pre-glaucomatous DBA/2J mice has a protective effect on RGCs. However, a successful therapeutic for use in humans would need to be effective when delivered after the detection of elevated IOP. It will therefore be important to establish in future experiments whether the Ndi1 vector can elicit similar benefit when administered to DBA/2J mice after elevation of IOP but before the onset of neurodegeneration – perhaps around the 8 month timeframe, when raised IOP is reported in both males and females (Libby et al., 2005a).

In the tests described, an equal amount of GFP tracker AAV was co-injected in many eyes in order to infer and assess the transduction efficiency of intravitreally injected AAV-Ndi1. Now that it has been established that much of the GCL (an estimated 43%) is transduced with the current AAV dose, future experiments may be conducted using PBS or non-coding AAV vectors in contralateral control eyes. Of course, it is very possible that a higher transduction efficiency would lead to increased benefit, and a higher-dose strategy could be explored. Optimising target cell transduction will be an ongoing objective of this project. Of note, a more recent iteration of the optimised Ndi1 coding sequence incorporates an I82V amino acid substitution, ‘huI82V’. Predictive modelling of MHC presentation suggests this variant is likely to be less immunogenic than the original

(Farrar et al., 2019)[37]. In a rotenone-induced model of LHON, huNdi1-I82V was able to provide equivalent benefit at a dose one-sixth lower than the original Ndi1 (Hanlon, 2017)[38]. HuNdiI82V may therefore be both a more tolerated and efficient therapeutic, and it would be valuable to assess its potential in a glaucomatous context. Additionally, it may ultimately be preferable to express Ndi1 using an RGC-specific promoter to minimise the possibility of off-target expression. To this end, the Farrar lab has characterised a small promoter element (199bp) based on the human *NEFH* gene, which drives preferential expression in RGCs and is ideal for use in AAV vectors (Millington-Ward et al., 2020). Future work will therefore test refined AAV-Ndi1 construct iterations.

Intriguingly, a recent paper suggests that intravitreal injection of an rAAV may result in transgene transfer to the contralateral untreated eye (Yu-Wai-Man et al., 2020). This has important implications for experimental design when assessing RGC-targeted gene therapies. In the current project, it will therefore be important to test for Ndi1 DNA and RNA in retinae and optic nerves of contralateral control eyes.

4.4.3 Future directions

4.4.3.1 Expansion of the assays used

As previously mentioned, it will be important to confirm that there is a significant increase in ATP production in Ndi1-treated retinas and optic nerves. Hence, in future experiments the ATP content of Ndi1-treated and control tissues will be quantified using a luciferase-based ATP determination kit and potentially also using Seahorse analysis.

There is also a possibility that Ndi1 expression may lead to increased TCA cycle activity and exert benefit through this mechanism. This could possibly be achieved by quantifying levels of TCA intermediate metabolites (Rathod et al., 2020).

Looking toward future experiments, there are a number of additional means of assessing therapeutic efficacy under consideration. As axoplasmic transport is powered by ATP (Calkins, 2012), it would also be of value to test if the RGC anterograde transport deficit in DBA/2J mice could be rescued by AAV-Ndi1 treatment (Dengler-Crish et al., 2014)[39]. An

[37] Patent no: US10220102B2
[38] PhD thesis; http://hdl.handle.net/2262/82725
[39] In this assay, fluorescently-labelled cholera toxin B subunit is intravitreally injected. The compound is actively taken up by RGC soma and transported to the superior colliculus (SC) of the brain. RGC anterograde transport efficiency can be determined by assessing SC fluorescence 48 hours after injection.

AAV vector expressing DsRed protein with a mitochondrial localisation signal was also constructed as part of this project, with a view to assessing mitochondrial morphology and network dynamics in DBA/2J RGCs before and after treatment. Kim et al. (2015) observed reduced mitochondrial area in RGC dendrites and axons using this strategy. Electron microscopy is also an option, of course, to examine mitochondrial morphology in detail.

It would also be useful to explore other means of assessing retinal function. Our group routinely uses a behavioural optokinetic response (OKR) test to assess visual function. However, a researcher in our lab previously attempted to perform this test on DBA/2J mice and failed to detect a response. In the literature, there are conflicting reports as to whether the DBA/2J mice elicit a detectable OKR (Puk et al., 2008, Barabas et al., 2011, Yang et al., 2018). Inner retina-dependent flash ERG components other than PhNR have previously been shown to be altered with age in the DBA/2J strain, including scotopic threshold response (STR) and oscillatory potentials (OP) (Perez de Lara et al., 2014, Perez de Lara et al., 2015, Grillo et al., 2018, Heiduschka et al., 2010, Wang and Dong, 2016). STR is argued to be a more accurate and sensitive measure of RGC function than PhNR or OP (Smith et al., 2014), and the negative STR has been shown to positively correlate with RGC loss in the DBA/2J model (Grillo et al., 2018). STR analysis will therefore be explored in the future. However, PhNR, STR and OP ERG elements are also influenced by non-RGC inner retinal cells such as amacrine cells. Pattern electroretinogram (PERG), an ERG response to a contrast-reversing pattern (e.g. checkerboard), is thought to be the most specific way of assessing RGC function in mouse models at present (Porciatti, 2015). A substantial deficit in PERG response has been noted in DBA/2J mice by 6 months of age (Howell et al., 2007a, Domenici et al., 2014). This technique also does not require pupil dilation in mice (Porciatti, 2015), which is a considerable bonus with regard to the DBA/2J strain. Unfortunately, our ERG platform is not currently set up to perform PERG analysis. However, this may be an avenue worth pursuing in the future. Measurement of visual evoked potential (VEP), an electrical signal recorded from the visual cortex in response to a flash stimulus, is also an option – albeit a much more invasive one. VEP responses are reported to be significantly reduced in DBA/2J mice from 7 months of age (Domenici et al., 2014).

4.4.3.2 Alternative experimental models

The DBA/2J model has many advantages: it is extremely well-characterised and its age-related, chronic disease progression recapitulates several aspects of human glaucoma. However, DBA/2J mice are a complex and often challenging strain to work with. As mentioned previously, calcification, curvature and neovascularisation of the cornea can lead to inaccurate IOP measurement and, combined with poor pupil dilation, may impede ERG recording (Turner et al., 2017). The degree of RGC degeneration also varies substantially between mice and even between eyes of the same mouse (Libby et al., 2005a). Natural attrition rates of 16-22% have been reported due to non-ocular conditions such as pericarditic calcification and thoracic cavity malformations (Turner et al., 2017, Cwerman-Thibault et al., 2017). These factors mean that very large sample sizes are required to detect effects in long term experiments, which is not always economically feasible and certainly not preferable in terms of use of experimental animals. The DBA/2J phenotypic profile has been shown to vary considerably between colonies bred at different institutions (Turner et al., 2017), which can hinder inter-study comparisons and experimental planning. As illustrated in this results chapter, outer retinal degeneration presents an additional layer of complication in the DBA/2J model.

Many other transgenic and experimentally-induced models of glaucoma have been developed – each with its own advantages and disadvantages (reviewed by Fernandes et al., 2015, Ishikawa et al., 2015, Evangelho et al., 2019). The ocular genetics team at TCD currently has access to the *Tg-MYOC*^{Y437H} model of glaucoma, which carries a human pathogenic myocilin allele. Myocilin mutations are implicated in ~4% of POAG cases (Kwon et al., 2009). However, abnormal accumulation of myocilin is noted in 70-90% glaucoma patients (Stothert et al., 2016). In *Tg-MYOC*^{Y437H} mice, secretion of myocilin is inhibited and the mutant protein accumulates in the endoplasmic reticulum (ER) of TM. ER stress leads to TM atrophy and elevation of IOP. A significant reduction in RGC soma and axon density is observed from 3-5 months of age in these mice (Zode et al., 2011). To date (and to my knowledge), mitochondrial function in RGCs of the *Tg-MYOC*^{Y437H} model has not been characterised. It would therefore be valuable to work toward this by employing some of the assays previously described in this chapter.

Work is currently being undertaken to assess the potential of AAV-Ndi1 treatment to protect RGCs in *Tg-MYOC*^{Y437H} mice via intravitreal injection. Experiments planned to be

carried out with this model will have shorter time-frames and likely require considerably smaller sample sizes than those with DBA/2J mice. *Tg-MYOC*^{Y437H} mice should additionally be more amenable to electrophysiological assessment of retinal function.

It is also planned to test the effects of intracameral injection of AAV-Ndi1 in these mice. As discussed in Section 4.2.2.2, there is evidence to suggest that oxidative stress in TM cells is a major factor in the initiation of glaucoma. With respect to myocilin-linked disease specifically, overexpression of the Y437H allele in HEK 293 cells led to increased ROS production and made cells more vulnerable to oxidative stress-induced apoptosis (Joe and Tomarev, 2010). Expression of another pathogenic myocilin allele in primary TM cultures led to decreased mitochondrial membrane potential, increased ROS levels, lower ATP production and a higher degree of cell death (He et al., 2009). ER stress and oxidative stress are thought to be intimately linked; ROS is produced as a by-product of the unfolded protein response and protein folding is in turn impaired by excess ROS (Chong et al., 2017). Ndi1 expression may therefore be protective in this context, by lessening the overall ROS load. However, due to an apparent lack of second strand synthesis capacity in TM cells, a self-complementary AAV vector may need to be generated to test this hypothesis (Buie et al., 2010).

As illustrated in this results chapter, carrying out long term experiments with age-dependent genetic disease models is a considerable undertaking. It is therefore worth investigating the use of alternative, experimentally-induced glaucomatous models. 'Artificial' means of inducing IOP elevation *in vivo* include laser-induced damage to the TM, injection of microbeads, hyaluronic acid or high-pressure saline into the AC, and subjection of episcleral (aqueous-collecting) veins to cauterisation or injection of hypertonic saline (Ishikawa et al., 2015, Evangelho et al., 2019). Retinal explants are also commonly subjected to hydrostatic pressure for *ex vivo* modelling of glaucoma (Vroemen et al., 2019). Alternatively, the optic nerve can be directly injured by transection, crushing, or intravitreal injection of excitotoxic compounds – though direct, acute injuries may not be ideal for simulating this complex, chronic disease (Kimura et al., 2020).

We are in the process of obtaining primary glaucomatous cells from patient and control donors via our collaborators Prof. Colm O'Brien (Mater Hospital, Dublin) to further explore the therapeutic potential of modulating mitochondrial dysfunction using *in vitro* patient derived cell models. Of note, retinal organoid-grown RGCs are also beginning to

offer insights into the pathogenesis of glaucoma (VanderWall et al., 2020). While ROs lack optic nerve, this disadvantage may be overcome in the future by co-culturing of retinal and cerebral organoids (Capowski et al., 2019). It is possible that engineered ECM scaffolds (Brennan et al., 2019) could even one day be incorporated to simulate a lamina cribrosa. Combining organoid technology with induction of hydrostatic pressure could create a valuable platform for screening therapeutics in the future.

There is considerable interest in developing combinatorial therapeutic strategies for glaucoma due to its complex disease etiology. Strategies that both lower IOP and directly protect RGCs may be appropriate for the majority of glaucoma cases. Conscious of the fact that current IOP-lower drugs are suboptimal - due to side-effects or unresponsiveness - the Humphries lab has developed a number of potential alternative IOP-lowering therapeutics. Supplying aqueous humour with matrix metalloproteinase protein (MMP3) led to remodelling of the TM ECM, which effectively reduced outflow resistance and lowered IOP in wild-type mice (O'Callaghan et al., 2017). Knockdown of tight junction components in Schlemm's canal endothelial cells also increased aqueous outflow and lowered IOP in a model of steroid-induced secondary glaucoma (Cassidy et al., 2020). It is possible that a combination of intravitreal injection of AAV-Ndi1 with topical or intracameral administration of an IOP-lowering agent may act synergistically. As mentioned in section 4.2.3, dietary vitamin B3 supplementation appears to be a highly promising avenue (Williams et al., 2017) and it will be very interesting to see how this treatment fares in clinical trial. It is again possible that this treatment may have optimal effects as part of a multipronged approach. There are a plethora of potential therapeutics in pre-clinical and clinical development targeting different aspects of glaucoma and it seems likely that a combinatorial strategy using multiple drugs will ultimately prove successful.

4.4.4 Conclusions

This study characterised glaucomatous progression in a colony of DBA/2J mice, establishing that the female bias in disease severity extends to RGC soma density, gliosis and outer retinal function. Importantly, a transkingdom gene-based therapy (Ndi1) targeted towards modulating mitochondrial function was found to substantially boost RGC NADH oxidation capacity and preserve RGC density when administered to pre-glaucomatous DBA/2J mice. There is also tentative evidence to suggest that this

treatment may have improved inner retinal function in aged female DBA/2J mice.This study is, to my knowledge, the first demonstration that direct modulation of mitochondrial ETC activity can improve glaucomatous phenotypes, and it strengthens the hypothesis that underlying mitochondrial dysfunction is a major aspect of this disease. It further highlights that targeting mitochondrial dysfunction represents an interesting therapeutic avenue for glaucoma. Further work will interrogate whether the beneficial effects of Ndi1 expression arise from an increase in ATP production, reduction of oxidative stress and/or a boost in TCA cycle activity. The efficacy of AAV-Ndi1 treatment when administered after onset of IOP elevation will also be investigated. This potential therapeutic will additionally be explored in the context of other glaucomatous models and in other relevant tissues vulnerable to mitochondrial dysfunction.

4.5 Materials and Methods

4.5.1 Animals

DBA/2J and C57BL/6J mice (Jackson Laboratory) were maintained under SPF conditions, as previously described (section 2.5.14).

4.5.2 IOP measurement

Non-invasive intraocular pressure measurements were performed using a rebound tonometry protocol optimised by Dr Jeffrey O'Callaghan (O'Callaghan, 2018)[40].

As IOP in mice has been shown to differ substantially between day and night, following a circadian rhythm (Sugimoto et al., 2006, Maeda et al., 2006), all measurements in this study were made during daylight hours. Mice were anaesthetised in an isoflurane chamber, then transferred to a head holder connected to the isoflurane vaporiser and scavenger to ensure they would remain unconscious throughout the procedure. A tonometer (Tonolab, Icare) was used to measure IOP in alternating eyes at one minute intervals from 3 to 8 minutes post-anaesthetisation. Cohorts were split so that an even number of mice underwent initial readings of left or right eyes. IOP readings are notoriously variable. Hence, the tonometer averages five separate readings for each recorded measurement. Three of these measurements were taken for each timepoint, meaning fifteen readings in total were performed during each minute. Data processing was performed using a MATLAB pipeline created by Dr O'Callaghan. IOP data is generally non-parametric, due in part to the fact that the minimum reading possible with the Tonolab is 6mmHg, which can lead to skewed distributions. Non-normal distribution of data was confirmed using a Shapiro-Wilks test. A Hampel filter was used to remove outliers further than 4 median absolute deviations. IOP is known to decay with time under general anaesthesia (Jia et al., 2000). For this reason, median IOPs were calculated for each timepoint and a final median value per eye was obtained for 5 minutes post-anaesthetic by interpolation.

4.5.3 Tissue processing

Mice were sacrificed by cervical dislocation.

[40] http://hdl.handle.net/2262/84993

4.5.3.1 Samples for histology

Eyes, with approximately 4 mm of attached optic nerve, were enucleated using McPherson forceps and fixed in 4% formaldehyde at 4°C overnight, then washed in PBS. Tissue was dissected using a Vannas scissors and forceps under a stereomicroscope. Optic nerves were cut at the base of the eye and separated. Eyes were then cut along the corneal limbus for removal of the cornea and lens.

At this point, samples intended for retinal wholemount histology were further dissected. Sclera and RPE were peeled away from the fixed retina using scissors and forceps. The isolated retinas were then washed thoroughly in PBS and stored at 4°C.

Eye cups and optic nerves to be sectioned were washed in PBS and then cryoprotected in increasingly concentrated solutions of sucrose in PBS: 10% and 20% for 20 mins at RT, and 30% sucrose overnight at 4°C. An equal volume of optimal cutting temperature compound (OCT) was added to samples for 15 mins at RT. Samples were transferred to plastic moulds filled with OCT, embedded by freezing with liquid nitrogen and stored at -20°C. OCT sample blocks were sectioned using a Leica CM1900-1-1 cryostat. Sections were applied to room temperature slides, dried at room temperature for 1 hour and then stored at -20°C.

4.5.3.2 Samples NADH oxidation experiments

Eyes and attached optic nerves were enucleated and immediately placed in ice cold PBS. Optic nerves were separated under a stereomicroscope, rinsed in PBS and snap frozen on dry ice. Eyes were cut along the corneal limbus, corneas and lenses were removed and retinas were peeled away from the sclera and RPE. Isolated retinas were rinsed in PBS and snap frozen. Work was carried out quickly, on tissues from one mouse at a time, to ensure optimal preservation of RNA integrity and enzymatic activity.

4.5.3.3 Samples for RNA extraction

For eyes used in RT-qPCR experiments described in Fig. 4.15, the optic nerves were needed for NADH oxidation tests and so retinal samples were processed as outlined in the section directly above. If the optic nerves were not needed for analysis (e.g. Fig. 4.12), retinas were isolated *in situ*, as outlined in section 2.5.16.

4.5.4 Immunohistochemistry

4.5.4.1 Retinal and optic nerve sections:

Cryosections were stained as described in section 2.5.17.

4.5.4.2 Retinal wholemounts:

Retinas were blocked in a 96 well plate overnight at 4°C. The blocking solution was made up of 5% donkey serum, 0.03% Triton X-100 and 0.1% sodium azide. The next day, block was removed and samples were incubated in primary antibody diluted in blocking solution for 3 days at 4°C. Retinas were washed in PBS (3 x 30 mins) and then incubated in secondary antibody solution overnight at 4°C. Samples were washed again (3 x 30 mins) and transferred to glass slides and covered with PBS. 3-4 incisions were made under a stereomicroscope to allow tissue to lay flat on slides, then excess liquid was removed and coverslips were applied using Hydromount.

4.5.5 Antibodies

Primary antibodies		
Antibody	**Source**	**Working dilution**
Goat anti-BRN3A	Santa Cruz; sc-31984 (discontinued)	1:200
Rabbit anti-BRN3A	Sysy; 411 003	1:4000
Goat anti-GFAP	Abcam; ab53554	1:200
Rabbit anti-NF200	Sigma; N4142	1:200

Secondary antibodies			
Antibody	**Conjugate**	**Source**	**Working dilution**
Donkey anti-goat IgG	Cy3	Jackson ImmunoResearch; 705-165-147	1:400
Donkey anti-rabbit IgG	Cy3	Jackson ImmunoResearch; 711-165-152	1:400
Donkey anti-rabbit IgG	Alexa Fluor-488	Jackson ImmunoResearch; 711-545-152	1:400

4.5.6 Microscopy and image analysis

IHC samples were imaged using an Olympus IX83 inverted motorised epifluorescent microscope and cellSens software. Images were taken using a 10X objective lens and stitched together to create composites of entire sections or wholemounts.

4.5.6.1 Measurement of fluorescence area and intensity

The Fiji threshold tool was used to measure fluorescent signal area and intensity across sections. For whole retinal sections, GFAP fluorescence integrated density values (mean gray value multiplied by area) were normalised against DAPI area. In optic nerve sections, the area of the entire cross section was used for normalisation. When analysing optic nerve head regions, GFAP and NF200 abundance was estimated using mean gray values.

4.5.6.2 Axon counting

An edge detection filter (Laplace 2) was applied to images of NF200 immunoreactivity on optic nerve sections using Olympus cellSen software. Axon numbers were then estimated using the thresholding, segmentation and object counting tools to count NF200-positive spots.

4.5.6.3 RGC counting

2D deconvolution was applied to stitched images of retinal wholemounts stained for BRN3A. The cellSens thresholding, segmentation and object counting tool were then used to count BRN3A-positive regions (RGC somata).

4.5.7 RT-qPCR

RNA was extracted as described in section 2.5.4.

One-step RT-qPCR reactions were set up using QuantiTect SYBR Green RT-PCR Kit (Qiagen) and run on an Applied Biosystem StepOnePlus machine. For Ndi1 expression tests, the standard curve method for relative quantification was applied, using 5X dilutions of retinal RNA known to contain a relatively high amount of transgenic Ndi1 transcript. Samples to be quantified were run at a 1/50 dilution in triplicate. In experiments assessing oxidative stress markers, samples were run in duplicate at a 1/10 dilution and expression was quantified using the ΔCT method.

Target gene expression levels were normalised against β-actin expression.

4.5.8 DCFDA flow cytometry assay

Retinas were isolated from mouse eyes as described in section 4.5.3.1. Once dissected free, retinas were placed in ice cold HBSS (14175, Thermo Fisher Scientific). Samples were trypsinised a 1mg/ml trypsin in HBSS solution for 5 minutes at 37°C. DNase I (10µl of 10mg/ml stock; Sigma, D5025) was then added, samples were mixed by gentle pipetting and retinas were incubated at 37°C for a further 15 minutes. Trypsin inhibitor solution was added to a final concentration of 2 mg/ml and samples were gently inverted. Samples were centrifuged at 600 x g for 5 minutes and supernatant was removed without disturbance of the pellet. Cells were resuspended in HBSS supplemented with DNase I (1ml HBSS and 10µl DNase I per sample). Trypsin inhibitor solution was added to a final concentration of 2 mg/ml and samples were gently inverted. Cell suspensions were incubated with 2µl CellROX Green Reagent (C10444, Thermo Fisher Scientific) (DCFDA) for 2.5 hours at 37°C and were gently inverted at regular intervals during this period. Cells were strained through 0.5 µM filters (CellTrics). 1µl DRAQ5 (BD Biosciences, 564902) was added to suspensions to stain live cells and samples were analysed using a BD Accuri C6 flow cytometer (BD Biosciences). Cells were gated for high DRAQ5 fluorescence and 20,000 events were counted in this gate.

4.5.9 Construct sequence information

AAV-CAG-EGFP construct details are given in section 2.5.8. AAV-CMV-huNdi1 sequences are included in Appendix 4.

4.5.10 AAV production

Endotoxin-free mega preps of pAAV-CMV-NDI1, pAAV2/2 and pHelper plasmids were produced, and AAV preparations were generated by Naomi Chadderton as described in section 2.5.9.

4.5.11 AAV titering

Viral genome (vg) titers were determined by qPCR. The standard curve method was used for absolute quantitation of AAV samples (see section 2.5.10). AAV2/2-CMV-NDI1 and AAV2/2-CAG-EGFP were titered using CMV enhancer primers at 1.3E10 vg/ml and 4.1E10 vg/ml, respectively. Using primers targeting the central transgene (NDI1 or EGFP), these titers of 5.39E10 and 2.22E11 vg/ml were obtained. As discussed in section 2.5.10, the CMV primers tend to underestimate titers and so it was decided to proceed with the Ndi1/EGFP titers for dosing experiments.

4.5.12 qPCR primers

Target	Forward (5' to 3')	Reverse (5' to 3')
Ndi1	CACCAGTTGGGACAGTAGAC	CCTCATAGTAGGTAACGTTC
Cp	TTCAACGGGCTGATGACAAAGTGC	GGCTTGGCCATGAAAGAAAGCTGA
Nos-2	TCATTGTACTCTGAGGGCTGACACA	GCCTTCAACACCAAGGTTGTCTGCA
Ho-1	GGTCCTGAAGAAGATTGCACA	CTTGCACCAGGCTAGCAG
β-actin	AGAGCAAGAGAGGCATCC	TCATTGTAGAAGGTGTGGTGC
CMV enhancer	TTACGGTAAACTGCCCACTTG	CGTGAGTCAAACCGCTATCC

Primers were synthesised by Sigma Aldrich and used as 10 µM solutions.

Cp, Nos-2 and Ho-1 primer sequences are those used by Inman et al. (2013).

4.5.13 NADH oxidation assay

A spectrophotometry assay was used to measure NADH oxidation rates in retinal and optic nerve samples, based on two previously described protocols (Spinazzi et al., 2012, Cwerman-Thibault et al., 2017). This assay had been expanded by Dr Daniel Manraj Maloney to facilitate measurement of Ndi1-specific NADH oxidation activity, and validated in cell culture samples (Maloney, 2020)[41].

[41] http://hdl.handle.net/2262/91379

The principle of the assay is as follows:
Reduced NAD (NADH), unlike oxidised NAD, can absorb light at 340 nM. The rate of NADH oxidation can therefore by quantified by measuring reduction in absorbance at this wavelength over time. NADH and ubiquinone are added to solutions containing lysed mitochondria. NADH oxidation is stimulated by mitochondrial Complex I or transgenic Ndi1 protein and the rate at which NADH absorbance decreases is recorded. The proportion of overall NADH oxidation activity contributed by Ndi1 protein can be determined by adding a Complex I inhibitor, rotenone, to the reaction. The level of background non-specific oxidation is then established by adding flavone to inhibit Ndi1 activity. Throughout the reaction, potassium cyanide inhibits Complex IV function to prevent oxidation of ubiquinone. Note: in initial characterisation experiments that did not include Ndi1-treated samples, flavone was not added to reactions; background NADH oxidation was determined using the signal generated with rotenone inhibition.
To prepare tissue samples for the assay, snap frozen retinas and optic nerves were homogenised in 200 µl ice cold sucrose tissue homogenisation buffer (20mM Tris, 250 mM sucrose, 40mM KCl, 2 mM EGTA, pH 7.5), using a chilled glass 0.1ml homogeniser. One retina was sufficient per assay reaction. However, due to the low amount of material in optic nerves (and low mitochondrial density in the myelinated nerve), it was necessary to pool four optic nerves per sample. After approx. 20 pestle grinding rotations, solutions were transferred to chilled Eppendorf tubes using 1ml syringes and 18G needles. Samples were span at 1000 x g for 8 mins to pellet debris. Supernatants were then transferred to new tubes, snap frozen in liquid nitrogen and stored at -80 °C until analysis.
On the day of the assay, samples were subjected to three liquid nitrogen freeze thaws for mitochondrial lysis. Initially, for experiments shown in Fig. 4.12, samples were run in duplicate (using 50-70 µl per reaction). However, it was later decided to use 130 µl sample per reaction, without technical replicates, to generate maximal, more robust signals. This also enabled all samples for comparison to be run in a single session, using the same reagent solutions and hence minimising variability. Reactions were set up in 1ml Kartell cuvettes as follows:
- 664 µl dH_20
- 130 µl sample
-100 µl potassium phosphate buffer (0.5M; pH 7.5 freshly made)
- 60 µl BSA (50mg/ml, fatty acid-free)

- 30 µl KCN (10 mM, freshly made)
- 10 µl NADH (10 mM, freshly made)

Baseline absorbance of the solution was measured at 340 nM for 30 seconds. 6 µl of ubiquinone (10 mM) was then added to start the oxidation reaction and the decrease in absorbance was measured for 120 seconds. 10 µl (1 mM) of rotenone was added and the trace was recorded for a further 120 seconds. This step was then repeated with 10 µl flavone (5 mM). The solution was mixed well by inversion between each addition and measurement.

Throughout the assay, all samples were kept on ice except for dH_20, potassium phosphate and BSA. Absorbance was measured at RT using a Shimadzu UV-mini 1240 spectrophotometer.

Measurements were recorded and analysed using UVProbe software. Rates of absorbance change (ΔAbs) were determined by measuring the slope of linear trace sections for each reaction condition.

CI + Ndi1 activity: ΔAbs of trace after ubiquinone was added.

Ndi1 activity: ΔAbs of trace after addition of rotenone.

Background activity: ΔAbs of trace after flavone inhibition.

Background activity was subtracted from the 'CI + Ndi1' and 'Ndi1' rates. 'CI' activity was calculated by subtracting 'Ndi1' from 'CI + Ndi1' ΔAbs.

For each sample, NADH oxidation rates were normalised against total protein content. Protein concentrations were determined using the Pierce Coomassie (Bradford) Protein Assay Kit (Thermo Scientific).

Final activity values were expressed as nmol NADH oxidised per minute, per mg of total protein. This was calculated using the equation:

(nmol min − 1 mg − 1) = (Δ Absorbance/min × 1,000)/[(extinction coefficient × volume of sample used in ml) × (sample protein concentration in mg/ml),

where the extinction coefficient of NADH is 6.2 mM/cm.

4.5.14 Intravitreal injection

Intravitreal injections of AAV in mice were performed by Dr Paul Kenna using a protocol previously described (Chadderton et al., 2013).

4.5.15 Electroretinography

Electroretinograms were performed by Dr Sophia Millington-Ward, using a protocol previously described by Chadderton et al. (2009) and based on guidelines outlined by the ISCEV (McCulloch et al., 2015, Frishman et al., 2018).

Dark-adapted rod-only response:

Stimulus: a dim white flash of 0.01 cd.s/m^2 (candelas per meter squared per second; constant luminance).

Dark-adapted combined rod–cone response:

Stimulus: a bright white 3.0 cd.s/m^2 flash.

At this point the mouse was light adapted for 10 mins (with background illumination of 30 candelas/m^2).

4.5.15.1 Light-adapted single-flash cone response:

Stimulus: 3.0 cd.s/m^2 flash.

4.5.15.2 Light-adapted 10 Hz flicker response:

Stimulus: flickering white light with a luminance of 3.0 cd.s/m^2, presented at a rate of 10 flashes per second.

4.5.15.3 Light-adapted photopic negative response (PhNR)

A 3.0 cd.s/m^2 flash passed through an orange filter was used as stimulus. The PhNR, first negative wave following the b-wave, was calculated as the amplitude between the trough of the PhNR wave and baseline. In the case of there being no initial cone-driven response, readings were disregarded. If there was no negative PhNR potential, then the PhNR was called as 0 µv. If both eyes failed to show a successful PhNR deflection, the results of that mouse were omitted.

Note: PhNR readings were sometimes measured without carrying out other ERG tests. In these instances, mice did not need to be dark-adapted beforehand.

4.5.16 Statistics

GraphPad Prism 8 was used to perform statistical tests and for graphing results. For each statistical test the significance threshold was set at 0.05. Normality of data distribution was assessed using the Shapiro-Wilk test, which determined whether parametric or non-

parametric tests of significance were used subsequently. Tests used in this chapter are summarised in the table below.

	Independent samples (unrelated eyes)		Paired samples (contralateral eyes)	
	Parametric	**Non-parametric**	**Parametric**	**Non-parametric**
2 groups	Unpaired Student's t-test		Paired Student's t-test	Wilcoxon matched-pairs signed rank test
3 or more groups		Kruskal-Wallis test		
3 or more groups, considering the effects of strain and gender	Two-way ANOVA			
3 or more groups, considering the effects of strain, gender and age	Three-way ANOVA			

Following ANOVA, post hoc analysis was performed using Tukey's test to compare the means of all groups to the mean of every other group. Alternatively, Dunnett's test was used to compare the means of all groups against the mean of one control group. When using the Kruskal-Wallis test, Dunn's multiple comparison test was subsequently used to compare the mean rank of each group with the mean rank of every other group.

Spearman's rank-order correlation test was used to investigate possible correlations between variables in non-parametric data.

In the main text, parametric data is described in the format of mean ± SD, whereas median ± median absolute deviation (MAD) is used to summarise nonparametric data.

5 Concluding remarks

5.1 Key findings of this thesis and their implications

The purpose of the research presented in this thesis was to explore the potential of three different gene therapy strategies for the treatment of retinal degenerations – two gene-specific approaches targeted toward monogenic inherited diseases and one gene-independent treatment in the context of a multifactorial age-related disease.

The first of these approaches was a gene replacement strategy for X-linked retinitis pigmentosa caused by mutations in *RP2* (chapter 2). Due to differences in disease presentation between patients and murine knockout models, and inconsistencies among the published mouse models themselves, it was decided to explore the use of human-derived cell models. RP2 patient-derived primary fibroblasts displayed reduced mRNA and a lack of detectable protein expression, supporting the pathogenicity of both a well-known nonsense mutation (p.Arg120X) and a novel frameshift variant (p.Asn142fs). After testing multiple AAV serotypes and dosages, it was determined that use of an AAV2/2 vector at a dose of 1E5 vg/cell would be optimal for transduction of primary fibroblast cell models. We designed a gene replacement construct in which the human *RP2* CDS is expressed by the CAG promoter. Transduction of patient fibroblasts with AAV2/2-CAG-RP2 restored RP2 mRNA and protein expression, confirming the functionality of this construct. Patient-derived and gene-edited retinal organoid models of *RP2* XLRP, developed by Mike Cheetham and Alison Hardcastle's groups in UCL, enabled the effects of *RP2* loss to be studied in a human retinal context. *RP2* null ROs exhibited increased rod death during a period of photoreceptor maturation - signified by a rise in ONL apoptosis that was followed by a decrease in ONL thickness and rhodopsin expression relative to control organoids. This early-onset rod degeneration phenotype was not previously observed in animal models, which had presented with relatively mild, cone-dominated phenotypic profiles. Treatment of *RP2* null ROs with an AAV2/5-CAG-RP2 gene replacement vector effectively rescued rod degeneration, as evidenced by preservation of ONL thickness and increased rhodopsin expression. To my knowledge, this was the first study to provide evidence of *in situ* rescue of photoreceptor loss in a retinal organoid model. Moreover, it demonstrated an unprecedented level of RO photoreceptor transduction efficiency (90%). The work described in chapter 2 thus illustrates the power of retinal organoid technology to model IRDs and assess the efficacy of AAV-based gene

therapies. Importantly, it strengthens the case for development of a gene replacement therapeutic for treatment of *RP2*-associated XLRP. An important part of such development will be assessment of vector tolerance and dosage optimisation in *RP2* null animal models as well as NHPs. An AAV2/8 RP2 vector was confirmed to be more potent than 2/2 or 2/5 vectors over a two week period following subretinal injection. Preliminary results obtained as part of this project suggested a potential immune response toward subretinally injected AAV2/8-CAG-RP2 in wild-type mice when there was significant over expression of the therapeutic transgene. Future work will investigate tolerance of AAV-RP2 vectors more thoroughly in wild-type and *Rp2h* knockout mice to determine an optimal vector design and dosage - albeit such studies ultimately would require GLP grade vector and evaluation in NHPs.

While gene replacement holds great promise for the treatment of recessive diseases, such a strategy may be inappropriate in cases of dominant negative or, particularly, toxic gain-of-function mutations. The Farrar lab has pioneered the development of suppression and replacement strategies for dominantly inherited diseases, having particular success in the context of *RHO*-associated ADRP. In chapter 3, I attempted to build upon this progress by exploring gene editing-based suppression and replacement of the rhodopsin gene. The ultimate goal of this project is to insert a *RHO* mini-gene into the genomic *RHO* 5'UTR using a 'homology-independent targeted integration' approach.

To assess the feasibility of this strategy, I first screened several *RHO* 5'UTR gRNA target sites for Cas9 cleavage efficiency *in vitro* and selected two sites for *in vivo* testing. I then constructed a dual AAV platform that would, in principle, mediate cleavage at a genomic gRNA target site and insertion of an EGFP reporter mini-gene into this double-stranded break. Preliminary results using the humanised *RHO* P347S murine mouse model indicate that relatively high efficiencies of successful integration into the *RHO* 5'UTR can be achieved using this method; mean editing efficiencies of between 16% to 43% were obtained. However, as discussed in chapter 3, this test requires replication and further validation, due in part to anomalous results from one of the negative control groups. Much remains to be done with regard to this project. The editing efficiency estimations should be confirmed using a more accurate FACS-based method, and the precision and specificity of editing examined by sequencing on- and off-target sites. The potential for knockout of the pathogenic *RHO* P347S allele alone (via EGFP integration) to provide

benefit will also be evaluated in longer term experiments. Of course, the ultimate goal of this research project is to test *RHO* suppression and replacement. A new HITI vector, containing a *RHO* mini-gene rather than reporter gene sequences, will therefore be generated and its capacity to rescue photoreceptor degeneration in the *RHO* P347 model will be assessed.

Although this project is very much at an early stage, the results obtained so far are encouraging and, if they withstand replication, will add strong support to the feasibility of HITI-based gene editing in neuronal cells. Importantly, while we are now exploring this mutation-independent strategy in the context of *RHO*-associated ADRP, it would in principle be applicable to any non-haploinsufficient forms of dominant disease affecting post-mitotic cells. If successful, such a strategy might even be desirable in relation to some recessive or haploinsufficient forms of IRD in which genes require a precise level of transgene expression and/or are too large to be delivered in a single AAV vector. As discussed previously, the latter scenario could be addressed by adapting the HITI strategy for integration of partial mini-genes into intronic sites.

Due to the heterogeneity of IRDs and the prevalence of multifactorial forms of blindness, it is important to investigate shared pathogenic aspects of retinal disease and methods to modulate common disease mechanisms. Altered bioenergetics is steadily emerging as an underlying factor in many forms of retinal disease. In particular, there is a wealth of evidence linking mitochondrial dysfunction to the pathogenesis of glaucoma. The study presented in chapter 4 explored whether boosting the activity of a key electron transport chain complex using a transkingdom gene therapy could protect retinal ganglion cells in a murine model of glaucoma. AAV-mediated delivery of a codon optimised yeast NADH dehydrogenase sequence (huNdi1) substantially increased NADH oxidation in retinas and optic nerves, and significantly increased survival of RGC somata in DBA/2J glaucomatous mice. An inner retina-derived electrophysiological response was also significantly increased in female eyes that received AAV-Ndi1 in one eye and an AAV-EGFP reporter vector in both eyes. Further work will be conducted to replicate these findings (in the absence of a reporter vector), to confirm whether RGC axons are preserved in addition to their somata and to explore potentially more robust means of measuring RGC function. The mechanism of Ndi1-derived benefit also requires elucidation; it may be due to one or

a combination of factors, including increased mitochondrial ATP production, alleviation of oxidative stress and increased TCA cycle activity.

The data presented in chapter 4 support the idea of underlying mitochondrial dysfunction in glaucoma and the therapeutic potential of neuroprotective strategies that can boost mitochondrial function. This study also highlights the promise of transkingdom gene therapies employing parsimonious coding sequences. As discussed earlier, mitochondrial defects have been observed in AMD and diabetic retinopathy (section 1.7.5). Mitochondrial dysfunction also appears widely implicated in neurodegenerative disease, including Parkinson's disease (Chen et al., 2019a, Holper et al., 2019), Alzheimer's disease (Adav et al., 2019, Holper et al., 2019) and amyotrophic lateral sclerosis (Newman et al., 2020). Strategies that can increase ETC activity may thus have quite a broad utility.

5.2 Future directions for the field

This thesis has explored potential gene-specific therapeutics for monogenic IRDs and a gene-independent approach for treatment of a multifactorial optic neuropathy. It is worth noting again that gene-independent therapeutics targeting common degenerative pathways have the potential to benefit inherited retinal disease, in addition to complex cases lacking an obvious genetic target. Identifying a neuroprotective agent applicable to multiple different types of IRD would aid substantially in meeting the challenge presented by this extremely heterogeneous group of conditions. However, broad applicability may come at the expense of potency; it remains to be seen whether an IRD treatment could be sufficiently effective without addressing the causal genetic defect - though the use of RdCVF to preserve cones in RP has yielded quite promising pre-clinical results and is moving to clinical trial (Byrne et al., 2015)[42]. It is plausible that combinatorial strategies will ultimately emerge as optimal and that use of a neuroprotective agent in combination with a gene-specific therapeutic would significantly enhance treatment efficacy for some forms of IRD. Indeed, while Luxturna™ can significantly improve visual function, it has been questioned whether such a treatment is alone sufficient to halt degeneration (Cideciyan et al., 2013). It could take an estimated 5-10 years to answer this question, due to the slow, natural rate of visual deterioration (Pierce and Bennett, 2015). It is therefore

[42] https://sparingvision.com/en/spvn06 [accessed 20/11/20]

imperative to continue to investigate both gene-specific and gene-independent therapeutic approaches for IRDs.

In parallel, it is important to explore ways in which gene editing technology could aid in addressing the unmet clinical need presented by retinal degenerations. An efficient and specific method of gene editing in post-mitotic cells must be established in order to realise the immense therapeutic potential of this technology. As discussed in section 1.5, base editing and prime editing strategies hold great promise as mutation-specific therapeutics – particularly in the case of genes too large for AAV-mediated replacement. However, most of these tools do not fit within a single AAV vector at present. RNA base editors are particularly attractive as their effects would, in principle, be reversible if expression of editing components was regulated by an inducible promoter (Fry et al., 2020). It will be very interesting to examine the efficiency and specificity of such a system in a retinal context. However, mutation-independent therapeutics would ultimately be preferable. It is therefore important to continue to investigate means of improving methods of large-scale DNA editing *in vivo*, such as HITI. As discussed in previous chapters, minimisation of deleterious off/on-target effects and immune response toward bacterial Cas proteins will also be important points of focus for the field as gene editing therapies progress toward the clinic. It is also interesting to note that precise editing of mtDNA, which was heretofore not possible due to difficulty importing nucleic acids into mitochondria and the propensity of mtDNA to degrade when cut, now appears feasible. Excitingly, a 'CRISPR-free' mitochondrial base editor that does not require cutting of the DNA template and employs protein-based guides was recently developed (Mok et al., 2020).

Our understanding of the pathogenic mechanisms involved in retinal degenerations is rapidly increasing thanks to advances in genetics (via whole genome and exome sequencing (Carss et al., 2017, Ratnapriya et al., 2020) and GWAS (Han et al., 2020, Fritsche et al., 2016, Youngblood et al., 2019)), transcriptomics (Kim et al., 2018, Lukowski et al., 2019a, Voigt et al., 2019), proteomics (Velez et al., 2018, Meyer et al., 2019, Mirzaei et al., 2020)) and metabolomics (Leruez et al., 2018, Hou et al., 2020, Acar et al., 2020). Such progress will inevitably increase the number of therapeutic targets for both monogenic IRDs and multifactorial ocular disorders. Understanding wild type and pathogenic epigenetic profiles in retinal disease (Farinelli et al., 2014, Zheng et al., 2018,

Corso-Díaz et al., 2018, Porter et al., 2019) will also likely offer opportunities for targeted and subtle therapeutic manipulation of epigenetic states using CRISPR-Cas9 epigenome editing tools (i.e. dead Cas9 linked to transcriptional activators/repressors).

The inspirational success of Luxturna™, an AAV gene replacement therapy for retinal degeneration due to biallelic *RPE65* mutations, has cleared a path for other retinal-targeted gene therapies to follow. Indeed, promising results from clinical trials targeting other IRDs are beginning to emerge. For example, the latest results[43] of the MeiraGTx/Janssen phase 1/2 XLRP trial (NCT03252847), testing an AAV2/5-RPGR gene replacement vector, describe significant improvements in visual function one year after treatment.

However, there is unlikely to be a simple, general model for retinal gene therapy development, given the considerable heterogeneity of retinal degenerations, and much work remains to be done.

With regard to IRDs, the natural history of each genetic subtype requires detailed characterisation. Degenerations that exhibit high preservation of retinal structure relative to function, such as *RPE65*-LCA, are considered to have potential for improvement in visual function by treatment with subretinal gene therapy. For those that do not display this dissociation between structure and function, halting of visual deterioration is a more appropriate objective and requires a longer trial duration for outcome assessment (Garafalo et al., 2020). Clinical outcome measures must also be carefully chosen for each retinal disease. For example, in the case of *RPE65*-LCA gene therapy trials, traditional visual acuity tests, which measure cone function, were not suitable due to the rod-dominated nature of this disease. The full-field stimulus threshold test (Roman et al., 2007), which measures light sensitivity, and the multi-luminance mobility test (Chung et al., 2018), which assesses an individual's navigational capacity over a range of light intensities, were therefore developed in order to assess rod function.

In parallel to developing gene therapies, it is vitally important to increase the accessibility of genetic screening and to molecularly characterise as many IRD cases as possible. Providing genetic diagnoses can empower patients by potentially allowing better

[43] https://www.modernretina.com/view/aao-2020-gene-therapy-for-x-linked-retinitis-pigmentosa-achieves-significant-visual-gains-at-1-year [accessed: 20/11/20]

prediction of their disease's progression (as more natural history studies are carried out) and enabling eligibility for participation in clinical trials. The genetic basis of ~28-50% of IRD cases remain unknown and much of the unresolved cases may be caused by mutations in regulatory or intronic regions, copy number variations or structural variants. Increasing adoption of whole exome and whole genome sequencing strategies (to supplement or replace target capture panel approaches) will likely increase the rate of pathogenic variant detection substantially (Farrar et al., 2017).

It is also worth mentioning that, while retinal gene therapies are envisioned as once-off treatments, this expectation still requires confirmation. So far, the positive effects Luxturna™ in patients have been stable for at least four years (Maguire et al., 2019) and *RPE65*$^{-/-}$ dogs treated with an AAV-RPE65 vector notably displayed preservation of photoreceptors for up to 11 years (Cideciyan et al., 2013). It is encouraging that, should a second treatment be necessary, readministration of Luxturna™ appears well-tolerated in NHPs (Weed et al., 2019).

However, while AAV2/2-RPE65 vectors have displayed generally excellent safety profiles in clinical trial with no deleterious immune responses reported (Pierce and Bennett, 2015, Russell et al., 2017), intraocular inflammation has been observed in some cases (using relatively high doses) (Bainbridge et al., 2015) and a perioperative course of oral corticosteroids is routinely prescribed. In a recent trial of an AAV2/2-REP1 replacement trial for choroideremia, one patient tragically obtained permanent vision loss as a result of inflammation, despite the use of steroids (Dimopoulos et al., 2018). It is therefore necessary to investigate and counteract the origins of AAV immunogenicity in order to increase the safety and efficacy of gene therapies. Further work is required to clarify whether immune response(s) are initiated by the AAV capsid, genome, formation of dsRNA and/or expression of the therapeutic transgene, and which retinal cells initiate this response – in relation to both subretinally and intravitreally delivered vectors. Strategies to evade immune surveillance are currently of high interest in the field. Casey et al. (2020) are working on development of a vector designed to block TLR-9 response to the AAV genome (details undisclosed). In the case of treatments targeted toward photoreceptors, as previously discussed, vectors employing photoreceptor-specific promoters may be inherently less immunogenic than those with ubiquitously active elements (Xiong et al., 2019). Another issue lies in the fact that pre-existing neutralising antibodies (NAbs)

targeting AAV capsids can also limit the efficacy of gene therapy – particularly in the case of intravitreally administered vectors. Generation of NAb-resistant vectors by creation of capsid chimeras (via shuffling of different serotype capsid proteins) and/or directed evolution may circumvent this problem (reviewed by Bucher et al. 2020). As mentioned earlier in this thesis, thorough analysis of the safety profile of each AAV gene therapy vector is warranted in animal models of disease as well as NHPs, using GLP-grade vector.

Subretinal injection also represents an area for improvement – being a highly specialised and relatively invasive procedure with (as previously discussed) potential to cause structural damage to the retina. There is considerable interest in establishing efficient, alternative routes of vector administration to the outer retina. Indeed, Garafalo et al. (2020) predict that subretinal injection will become 'a relic of this early period of human gene therapy trials.' Directed evolution of vectors capable of transducing photoreceptors from an intravitreal starting point (Dalkara et al., 2013), and adoption of sub-ILM (Boye et al., 2016) or transcleral (Yiu et al., 2020) injection techniques are promising avenues under investigation.

As of yet, no gene therapies for glaucoma have reached a clinical trial stage. However, several RGC-targeted AAV therapeutics are currently under assessment in patients. One such strategy is intravitreal injection of AAV vectors expressing channelrhodopsins (microbial light-gated ion channels) to confer light-sensitivity to RGCs in late-stage RP (NCT02556736, NCT03326336, NCT04278131; all Phase 1/2). Trials have also been conducted to test AAV2/2-mediated gene replacement of *ND4* (an mtDNA gene encoding a complex I subunit) directed towards RGCs in LHON patients. There is thus precedent for both transkingdom and mitochondrial gene therapies targeting retinal ganglion cells. So far, the AAV-ND4 vector has been well-tolerated in patients; intraocular inflammation was generally mild and was responsive to treatment (Vignal et al., 2018, Bouquet et al., 2019, Yu-Wai-Man et al., 2020). Viral DNA was also not detectable systemically weeks after intravitreal delivery (Yu-Wai-Man et al., 2020). Recent results from a Phase 3 *ND4* trial included an intriguing finding. Remarkably, almost 80% of the patient cohort displayed visual improvement in *both* AAV-ND4-treated and contralateral 'sham' treated control eyes (Yu-Wai-Man et al., 2020). While spontaneous recovery of vision can occur with LHON, the prevalence of this phenomenon in patients with the mutation in question is estimated to be only ~11% (Newman et al., 2020). Follow-up experiments with NHPs

revealed that rAAV-ND4 genomes were present in retinal and optic nerve tissue of untreated contralateral eyes (Yu-Wai-Man et al., 2020). This apparent transfer of viral DNA from treated to untreated eyes will need to be replicated and the mechanism elucidated. This finding, of course, has important implications for clinical trial design, and raises doubts as to whether contralateral eyes are appropriate negative controls for assessment of intravitreally-delivered gene therapies.

Utilisation of cell-specific promoters may be particularly important for intravitreally-delivered gene therapies, as this route of administration leads to a much higher degree of bio-dissemination that subretinal injection. Intravitreally injected AAV particles can enter the aqueous humour, transduce anterior segment tissues and reach systemic circulation through AH outflow pathways (Bucher et al., 2020). Establishing efficient and AAV-amenable RGC-specific promoters, such as the recently characterised NEFH element (Millington-Ward et al., 2020), will therefore be important in the development of safe and effective gene therapies for glaucoma. As discussed in chapter 4, a combinatorial strategy will likely ultimately prove optimal for treatment of this highly complex optic neuropathy, with RGC protectants used in addition to IOP-lowering agents (with the exception of NTG cases).

To conclude, while a great deal remains to be done, the rate of progress in the field is ever-increasing and the future of retinal gene therapy, for both inherited and acquired diseases, appears bright. The data presented in this thesis represent a relatively small but important contribution to the field and support a sense of optimism.

6 References

AASEN, D. M. & VERGARA, M. N. 2020. New Drug Discovery Paradigms for Retinal Diseases: A Focus on Retinal Organoids. *J Ocul Pharmacol Ther,* 36**,** 18-24. http://dx.doi.org/10.1089/jop.2018.0140.

ABU-AMERO, K., KONDKAR, A. A. & CHALAM, K. V. 2015. An Updated Review on the Genetics of Primary Open Angle Glaucoma. *Int J Mol Sci,* 16**,** 28886-911. http://dx.doi.org/10.3390/ijms161226135.

ABU-AMERO, K. K., MORALES, J. & BOSLEY, T. M. 2006. Mitochondrial abnormalities in patients with primary open-angle glaucoma. *Invest Ophthalmol Vis Sci,* 47**,** 2533-41. http://dx.doi.org/10.1167/iovs.05-1639.

ABUDAYYEH, O. O., GOOTENBERG, J. S., ESSLETZBICHLER, P., HAN, S., JOUNG, J., BELANTO, J. J., . . . ZHANG, F. 2017. RNA targeting with CRISPR–Cas13. *Nature,* 550**,** 280-284. http://dx.doi.org/10.1038/nature24049.

ACAR, İ. E., LORES-MOTTA, L., COLIJN, J. M., MEESTER-SMOOR, M. A., VERZIJDEN, T., COUGNARD-GREGOIRE, A., . . . ZUMBANSEN, M. 2020. Integrating Metabolomics, Genomics, and Disease Pathways in Age-Related Macular Degeneration: The EYE-RISK Consortium. *Ophthalmology,* 127**,** 1693-1709. http://dx.doi.org/https://doi.org/10.1016/j.ophtha.2020.06.020.

ACHBERGER, K., PROBST, C., HADERSPECK, J., BOLZ, S., ROGAL, J., CHUCHUY, J., . . . LOSKILL, P. 2019. Merging organoid and organ-on-a-chip technology to generate complex multi-layer tissue models in a human retina-on-a-chip platform. *Elife,* 8. http://dx.doi.org/10.7554/eLife.46188.

ACLAND, G. M., AGUIRRE, G. D., BENNETT, J., ALEMAN, T. S., CIDECIYAN, A. V., BENNICELLI, J., . . . JACOBSON, S. G. 2005. Long-term restoration of rod and cone vision by single dose rAAV-mediated gene transfer to the retina in a canine model of childhood blindness. *Molecular therapy : the journal of the American Society of Gene Therapy,* 12**,** 1072-1082. http://dx.doi.org/10.1016/j.ymthe.2005.08.008.

ACLAND, G. M., AGUIRRE, G. D., RAY, J., ZHANG, Q., ALEMAN, T. S., CIDECIYAN, A. V., . . . BENNETT, J. 2001. Gene therapy restores vision in a canine model of childhood blindness. *Nat Genet,* 28**,** 92-5. http://dx.doi.org/10.1038/ng0501-92.

ADAV, S. S., PARK, J. E. & SZE, S. K. 2019. Quantitative profiling brain proteomes revealed mitochondrial dysfunction in Alzheimer's disease. *Mol Brain,* 12**,** 8. http://dx.doi.org/10.1186/s13041-019-0430-y.

AGGARWAL, V., TULI, H. S., VAROL, A., THAKRAL, F., YERER, M. B., SAK, K., . . . SETHI, G. 2019. Role of Reactive Oxygen Species in Cancer Progression: Molecular Mechanisms and Recent Advancements. *Biomolecules,* 9**,** 735. http://dx.doi.org/10.3390/biom9110735.

AÏT-ALI, N., FRIDLICH, R., MILLET-PUEL, G., CLÉRIN, E., DELALANDE, F., JAILLARD, C., . . . LÉVEILLARD, T. 2015. Rod-Derived Cone Viability Factor Promotes Cone Survival by Stimulating Aerobic Glycolysis. *Cell,* 161**,** 817-832. http://dx.doi.org/10.1016/j.cell.2015.03.023.

ALEXANDER, I. E. & RUSSELL, D. W. 2015. The Potential of AAV-Mediated Gene Targeting for Gene and Cell Therapy Applications. *Current Stem Cell Reports,* 1**,** 16-22. http://dx.doi.org/10.1007/s40778-014-0001-1.

ALI, S. S., XIONG, C., LUCERO, J., BEHRENS, M. M., DUGAN, L. L. & QUICK, K. L. 2006. Gender differences in free radical homeostasis during aging: shorter-lived female C57BL6 mice have increased oxidative stress. *Aging Cell,* 5**,** 565-74. http://dx.doi.org/10.1111/j.1474-9726.2006.00252.x.

ALKANDERI, S., MOLINARI, E., SHAHEEN, R., ELMAGHLOOB, Y., STEPHEN, L. A., SAMMUT, V., . . . SAYER, J. A. 2018. ARL3 Mutations Cause Joubert Syndrome by Disrupting Ciliary Protein Composition. *Am J Hum Genet,* 103**,** 612-620. http://dx.doi.org/10.1016/j.ajhg.2018.08.015.

ALLOCCA, M., MUSSOLINO, C., GARCIA-HOYOS, M., SANGES, D., IODICE, C., PETRILLO, M., . . . AURICCHIO, A. 2007. Novel adeno-associated virus serotypes efficiently transduce murine photoreceptors. *J Virol,* 81**,** 11372-80. http://dx.doi.org/10.1128/JVI.01327-07.

AMERASINGHE, N. & AUNG, T. 2008. Angle-closure: risk factors, diagnosis and treatment. *Prog Brain Res,* 173**,** 31-45. http://dx.doi.org/10.1016/S0079-6123(08)01104-7.

ANDERSON, A. P., LUO, X., RUSSELL, W. & YIN, Y. W. 2020. Oxidative damage diminishes mitochondrial DNA polymerase replication fidelity. *Nucleic Acids Res,* 48**,** 817-829. http://dx.doi.org/10.1093/nar/gkz1018.

ANDERSON, M. G., LIBBY, R. T., GOULD, D. B., SMITH, R. S. & JOHN, S. W. 2005. High-dose radiation with bone marrow transfer prevents neurodegeneration in an inherited

glaucoma. *Proc Natl Acad Sci U S A,* 102**,** 4566-71. http://dx.doi.org/10.1073/pnas.0407357102.

ANDERSON, M. G., SMITH, R. S., HAWES, N. L., ZABALETA, A., CHANG, B., WIGGS, J. L. & JOHN, S. W. 2002. Mutations in genes encoding melanosomal proteins cause pigmentary glaucoma in DBA/2J mice. *Nat Genet,* 30**,** 81-5. http://dx.doi.org/10.1038/ng794.

ANDZIAK, B., O'CONNOR, T. P., QI, W., DEWAAL, E. M., PIERCE, A., CHAUDHURI, A. R., . . . BUFFENSTEIN, R. 2006. High oxidative damage levels in the longest-living rodent, the naked mole-rat. *Aging Cell,* 5**,** 463-71. http://dx.doi.org/10.1111/j.1474-9726.2006.00237.x.

ANGUELA, X. M. & HIGH, K. A. 2019. Entering the Modern Era of Gene Therapy. *Annu Rev Med,* 70**,** 273-288. http://dx.doi.org/10.1146/annurev-med-012017-043332.

ANSARI, A. M., AHMED, A. K., MATSANGOS, A. E., LAY, F., BORN, L. J., MARTI, G., . . . SUN, Z. 2016. Cellular GFP Toxicity and Immunogenicity: Potential Confounders in in Vivo Cell Tracking Experiments. *Stem Cell Rev Rep,* 12**,** 553-559. http://dx.doi.org/10.1007/s12015-016-9670-8.

ANZALONE, A. V., RANDOLPH, P. B., DAVIS, J. R., SOUSA, A. A., KOBLAN, L. W., LEVY, J. M., . . . LIU, D. R. 2019. Search-and-replace genome editing without double-strand breaks or donor DNA. *Nature,* 576**,** 149-157. http://dx.doi.org/10.1038/s41586-019-1711-4.

ARBEITHUBER, B., HESTER, J., CREMONA, M. A., STOLER, N., ZAIDI, A., HIGGINS, B., . . . MAKOVA, K. D. 2020. Age-related accumulation of de novo mitochondrial mutations in mammalian oocytes and somatic tissues. *PLoS Biol,* 18**,** e3000745. http://dx.doi.org/10.1371/journal.pbio.3000745.

ASHTARI, M., ZHANG, H., COOK, P. A., CYCKOWSKI, L. L., SHINDLER, K. S., MARSHALL, K. A., . . . BENNETT, J. 2015. Plasticity of the human visual system after retinal gene therapy in patients with Leber's congenital amaurosis. *Sci Transl Med,* 7**,** 296ra110. http://dx.doi.org/10.1126/scitranslmed.aaa8791.

ATHANASIOU, D., AGUILA, M., BELLINGHAM, J., LI, W., MCCULLEY, C., REEVES, P. J. & CHEETHAM, M. E. 2018. The molecular and cellular basis of rhodopsin retinitis pigmentosa reveals potential strategies for therapy. *Progress in retinal and eye research,* 62**,** 1-23. http://dx.doi.org/10.1016/j.preteyeres.2017.10.002.

AYUSO, E., BLOUIN, V., LOCK, M., MCGORRAY, S., LEON, X., ALVIRA, M. R., . . . MOULLIER, P. 2014. Manufacturing and characterization of a recombinant adeno-associated virus type 8 reference standard material. *Hum Gene Ther,* 25**,** 977-87. http://dx.doi.org/10.1089/hum.2014.057.

BAE, S., PARK, J. & KIM, J.-S. 2014. Cas-OFFinder: a fast and versatile algorithm that searches for potential off-target sites of Cas9 RNA-guided endonucleases. *Bioinformatics,* 30**,** 1473-1475. http://dx.doi.org/10.1093/bioinformatics/btu048.

BAI, Y., HAJEK, P., CHOMYN, A., CHAN, E., SEO, B. B., MATSUNO-YAGI, A., . . . ATTARDI, G. 2001. Lack of complex I activity in human cells carrying a mutation in MtDNA-encoded ND4 subunit is corrected by the Saccharomyces cerevisiae NADH-quinone oxidoreductase (NDI1) gene. *J Biol Chem,* 276**,** 38808-13. http://dx.doi.org/10.1074/jbc.M106363200.

BAILEY, J. N., LOOMIS, S. J., KANG, J. H., ALLINGHAM, R. R., GHARAHKHANI, P., KHOR, C. C., . . . WIGGS, J. L. 2016. Genome-wide association analysis identifies TXNRD2, ATXN2 and FOXC1 as susceptibility loci for primary open-angle glaucoma. *Nat Genet,* 48**,** 189-94. http://dx.doi.org/10.1038/ng.3482.

BAINBRIDGE, J., SMITH, A., BARKER, S., ROBBIE, S., HENDERSON, R., BALAGGAN, K, VISWANATHAN, A., . . . ALI, R. 2008. Effect of Gene Therapy on Visual Function in Leber's Congenital Amaurosis. *New England Journal of Medicine,* 358**,** 2231-2239.

BAINBRIDGE, J. W. B., MEHAT, M. S., SUNDARAM, V., ROBBIE, S. J., BARKER, S. E., RIPAMONTI, C., . . . ALI, R. R. 2015. Long-Term Effect of Gene Therapy on Leber's Congenital Amaurosis. *New England Journal of Medicine,* 372**,** 1887-1897. http://dx.doi.org/10.1056/NEJMoa1414221.

BAKONDI, B., LV, W., LU, B., JONES, M. K., TSAI, Y., KIM, K. J., . . . WANG, S. 2016. In Vivo CRISPR/Cas9 Gene Editing Corrects Retinal Dystrophy in the S334ter-3 Rat Model of Autosomal Dominant Retinitis Pigmentosa. *Molecular therapy : the journal of the American Society of Gene Therapy,* 24**,** 556-563. http://dx.doi.org/10.1038/mt.2015.220.

BALAKRISHNAN, B. & JAYANDHARAN, G. R. 2014. Basic biology of adeno-associated virus (AAV) vectors used in gene therapy. *Curr Gene Ther,* 14**,** 86-100. http://dx.doi.org/10.2174/1566523214666140302193709.

BALTAN, S., INMAN, D. M., DANILOV, C. A., MORRISON, R. S., CALKINS, D. J. & HORNER, P. J. 2010. Metabolic vulnerability disposes retinal ganglion cell axons to dysfunction

in a model of glaucomatous degeneration. *J Neurosci,* 30**,** 5644-52. http://dx.doi.org/10.1523/jneurosci.5956-09.2010.

BAND, L. R., HALL, C. L., RICHARDSON, G., JENSEN, O. E., SIGGERS, J. H. & FOSS, A. J. 2009. Intracellular flow in optic nerve axons: a mechanism for cell death in glaucoma. *Invest Ophthalmol Vis Sci,* 50**,** 3750-8. http://dx.doi.org/10.1167/iovs.08-2396.

BANEKE, A. J., AUBRY, J., VISWANATHAN, A. C. & PLANT, G. T. 2020. The role of intracranial pressure in glaucoma and therapeutic implications. *Eye (Lond),* 34**,** 178-191. http://dx.doi.org/10.1038/s41433-019-0681-y.

BANERJEE, D., BANERJEE, A., MOOKHERJEE, S., VISHAL, M., MUKHOPADHYAY, A., SEN, A., . . . RAY, K. 2013. Mitochondrial genome analysis of primary open angle glaucoma patients. *PLoS One,* 8**,** e70760. http://dx.doi.org/10.1371/journal.pone.0070760.

BANIN, E., MIZRAHI-MEISSONNIER, L., NEIS, R., SILVERSTEIN, S., MAGYAR, I., ABELIOVICH, D., . . . SHARON, D. 2007. A non-ancestral RPGR missense mutation in families with either recessive or semi-dominant X-linked retinitis pigmentosa. 143A**,** 1150-8. http://dx.doi.org/10.1002/ajmg.a.31642.

BARABAS, P., HUANG, W., CHEN, H., KOEHLER, C. L., HOWELL, G., JOHN, S. W., . . . KRIZAJ, D. 2011. Missing optomotor head-turning reflex in the DBA/2J mouse. *Invest Ophthalmol Vis Sci,* 52**,** 6766-73. http://dx.doi.org/10.1167/iovs.10-7147.

BARJA, G. & HERRERO, A. 2000. Oxidative damage to mitochondrial DNA is inversely related to maximum life span in the heart and brain of mammals. *FASEB J,* 14**,** 312-8. http://dx.doi.org/10.1096/fasebj.14.2.312.

BARREAU, E., BROSSAS, J. Y., COURTOIS, Y. & TRETON, J. A. 1996. Accumulation of mitochondrial DNA deletions in human retina during aging. *Invest Ophthalmol Vis Sci,* 37**,** 384-91.

BARRON, M. J., JOHNSON, M. A., ANDREWS, R. M., CLARKE, M. P., GRIFFITHS, P. G., BRISTOW, E., . . . TURNBULL, D. M. 2001. Mitochondrial abnormalities in ageing macular photoreceptors. *Invest Ophthalmol Vis Sci,* 42**,** 3016-22.

BARTOLINI, F., BHAMIDIPATI, A., THOMAS, S., SCHWAHN, U., LEWIS, S. A. & COWAN, N. J. 2002. Functional overlap between retinitis pigmentosa 2 protein and the tubulin-specific chaperone cofactor C. *J Biol Chem,* 277**,** 14629-34. http://dx.doi.org/10.1074/jbc.M200128200.

BASSETT, E. A. & WALLACE, V. A. 2012. Cell fate determination in the vertebrate retina. *Trends Neurosci,* 35**,** 565-73. http://dx.doi.org/10.1016/j.tins.2012.05.004.

BENNETT, J., WELLMAN, J., MARSHALL, K. A., MCCAGUE, S., ASHTARI, M., DISTEFANO-PAPPAS, J., . . . MAGUIRE, A. M. 2016. Safety and durability of effect of contralateral-eye administration of AAV2 gene therapy in patients with childhood-onset blindness caused by RPE65 mutations: a follow-on phase 1 trial. *Lancet,* 388**,** 661-72. http://dx.doi.org/10.1016/s0140-6736(16)30371-3.

BENNICELLI, J., WRIGHT, J. F., KOMAROMY, A., JACOBS, J. B., HAUCK, B., ZELENAIA, O., . . . BENNETT, J. 2008. Reversal of blindness in animal models of leber congenital amaurosis using optimized AAV2-mediated gene transfer. *Molecular therapy : the journal of the American Society of Gene Therapy,* 16**,** 458-465. http://dx.doi.org/10.1038/sj.mt.6300389.

BERG, J. M., TYMOCZKO, J. L. & STRYER, L. 2002. Chapter 18: Oxidative Phosphorylation. *Biochemistry.* 5th ed. New York: W H Freeman.

BERRY, M. H., HOLT, A., SALARI, A., VEIT, J., VISEL, M., LEVITZ, J., . . . ISACOFF, E. Y. 2019. Restoration of high-sensitivity and adapting vision with a cone opsin. *Nature Communications,* 10**,** 1221. http://dx.doi.org/10.1038/s41467-019-09124-x.

BERTALMÍO, M. 2020. Chapter 2 - The biological basis of vision: the retina. *In:* BERTALMÍO, M. (ed.) *Vision Models for High Dynamic Range and Wide Colour Gamut Imaging.* Academic Press.

BÉTERMIER, M., BERTRAND, P. & LOPEZ, B. S. 2014. Is non-homologous end-joining really an inherently error-prone process? *PLoS genetics,* 10**,** e1004086-e1004086. http://dx.doi.org/10.1371/journal.pgen.1004086.

BHATTACHARYA, S. S., WRIGHT, A. F., CLAYTON, J. F., PRICE, W. H., PHILLIPS, C. I., MCKEOWN, C. M., . . . ET AL. 1984. Close genetic linkage between X-linked retinitis pigmentosa and a restriction fragment length polymorphism identified by recombinant DNA probe L1.28. *Nature,* 309**,** 253-5. http://dx.doi.org/10.1038/309253a0.

BIRTEL, J., GLIEM, M., MANGOLD, E., MULLER, P. L., HOLZ, F. G., NEUHAUS, C., . . . CHARBEL ISSA, P. 2018. Next-generation sequencing identifies unexpected genotype-phenotype correlations in patients with retinitis pigmentosa. *PLoS One,* 13**,** e0207958. http://dx.doi.org/10.1371/journal.pone.0207958.

BLAESE, R. M., CULVER, K. W., MILLER, A. D., CARTER, C. S., FLEISHER, T., CLERICI, M., . . . ANDERSON, W. F. 1995. T lymphocyte-directed gene therapy for ADA- SCID: initial

trial results after 4 years. *Science,* 270**,** 475-80. http://dx.doi.org/10.1126/science.270.5235.475.

BOCK, F. J. & TAIT, S. W. G. 2020. Mitochondria as multifaceted regulators of cell death. *Nat Rev Mol Cell Biol,* 21**,** 85-100. http://dx.doi.org/10.1038/s41580-019-0173-8.

BOGUSZEWSKA, K., SZEWCZUK, M., KAZMIERCZAK-BARANSKA, J. & KARWOWSKI, B. T. 2020. The Similarities between Human Mitochondria and Bacteria in the Context of Structure, Genome, and Base Excision Repair System. *Molecules,* 25. http://dx.doi.org/10.3390/molecules25122857.

BOHRER, L. R., WILEY, L. A., BURNIGHT, E. R., COOKE, J. A., GIACALONE, J. C., ANFINSON, K. R., . . . TUCKER, B. A. 2019. Correction of NR2E3 Associated Enhanced S-cone Syndrome Patient-specific iPSCs using CRISPR-Cas9. *Genes (Basel),* 10. http://dx.doi.org/10.3390/genes10040278.

BORRAS, C., SASTRE, J., GARCIA-SALA, D., LLORET, A., PALLARDO, F. V. & VINA, J. 2003. Mitochondria from females exhibit higher antioxidant gene expression and lower oxidative damage than males. *Free Radic Biol Med,* 34**,** 546-52. http://dx.doi.org/10.1016/s0891-5849(02)01356-4.

BOSLEY, T. M., HELLANI, A., SPAETH, G. L., MYERS, J., KATZ, L. J., MOSTER, M. R., . . . ABU-AMERO, K. K. 2011. Down-regulation of OPA1 in patients with primary open angle glaucoma. *Mol Vis,* 17**,** 1074-9.

BOUQUET, C., VIGNAL CLERMONT, C., GALY, A., FITOUSSI, S., BLOUIN, L., MUNK, M. R., . . . THOMASSON, N. 2019. Immune Response and Intraocular Inflammation in Patients With Leber Hereditary Optic Neuropathy Treated With Intravitreal Injection of Recombinant Adeno-Associated Virus 2 Carrying the ND4 Gene: A Secondary Analysis of a Phase 1/2 Clinical Trial. *JAMA Ophthalmol,* 137**,** 399-406. http://dx.doi.org/10.1001/jamaophthalmol.2018.6902.

BOURNE, R. R. A., FLAXMAN, S. R., BRAITHWAITE, T., CICINELLI, M. V., DAS, A., JONAS, J. B., . . . ZHENG, Y. 2017. Magnitude, temporal trends, and projections of the global prevalence of blindness and distance and near vision impairment: a systematic review and meta-analysis. *The Lancet Global Health,* 5**,** e888-e897. http://dx.doi.org/10.1016/S2214-109X(17)30293-0.

BOYE, S. E., ALEXANDER, J. J., BOYE, S. L., WITHERSPOON, C. D., SANDEFER, K. J., CONLON, T. J., . . . GAMLIN, P. D. 2012. The human rhodopsin kinase promoter in an AAV5

vector confers rod- and cone-specific expression in the primate retina. *Hum Gene Ther,* 23**,** 1101-15. http://dx.doi.org/10.1089/hum.2012.125.

BRANDT, T., MOURIER, A., TAIN, L. S., PARTRIDGE, L., LARSSON, N. G. & KUHLBRANDT, W. 2017. Changes of mitochondrial ultrastructure and function during ageing in mice and Drosophila. *Elife,* 6. http://dx.doi.org/10.7554/eLife.24662.

BRANHAM, K., OTHMAN, M., BRUMM, M., KAROUKIS, A. J., ATMACA-SONMEZ, P., YASHAR, B. M., . . . SWAROOP, A. 2012. Mutations in RPGR and RP2 account for 15% of males with simplex retinal degenerative disease. *Invest Ophthalmol Vis Sci,* 53**,** 8232-7. http://dx.doi.org/10.1167/iovs.12-11025.

BRENNAN, D., CLISSMANN, D., MURPHY, R., WALLACE, D., PASCU, I., HIBBITTS, A., . . . O'BRIEN, C. J. 2019. Biomimetic modelling of the lamina cribrosa region using tissue engineered scaffolds - a novel 3D model for glaucoma research. *Investigative Ophthalmology & Visual Science,* 60**,** 6168-6168.

BREUER, D. K., YASHAR, B. M., FILIPPOVA, E., HIRIYANNA, S., LYONS, R. H., MEARS, A. J., . . . SWAROOP, A. 2002. A comprehensive mutation analysis of RP2 and RPGR in a North American cohort of families with X-linked retinitis pigmentosa. *Am J Hum Genet,* 70**,** 1545-54. http://dx.doi.org/10.1086/340848.

BRINGMANN, A., IANDIEV, I., PANNICKE, T., WURM, A., HOLLBORN, M., WIEDEMANN, P., . . . REICHENBACH, A. 2009. Cellular signaling and factors involved in Muller cell gliosis: neuroprotective and detrimental effects. *Prog Retin Eye Res,* 28**,** 423-51. http://dx.doi.org/10.1016/j.preteyeres.2009.07.001.

BRINKMAN, E. K., CHEN, T., AMENDOLA, M. & VAN STEENSEL, B. 2014. Easy quantitative assessment of genome editing by sequence trace decomposition. *Nucleic Acids Res,* 42**,** e168. http://dx.doi.org/10.1093/nar/gku936.

BRUNNER, S., SKOSYRSKI, S., KIRSCHNER-SCHWABE, R., KNOBELOCH, K. P., NEIDHARDT, J., FEIL, S., . . . BERGER, W. 2010. Cone versus rod disease in a mutant Rpgr mouse caused by different genetic backgrounds. *Invest Ophthalmol Vis Sci,* 51**,** 1106-15. http://dx.doi.org/10.1167/iovs.08-2742.

BUCHER, K., RODRÍGUEZ-BOCANEGRA, E., DAULETBEKOV, D. & FISCHER, M. D. 2020. Immune responses to retinal gene therapy using adeno-associated viral vectors – Implications for treatment success and safety. *Progress in Retinal and Eye Research***,** 100915. http://dx.doi.org/https://doi.org/10.1016/j.preteyeres.2020.100915.

BUCHHOLZ, D. E., HIKITA, S. T., ROWLAND, T. J., FRIEDRICH, A. M., HINMAN, C. R., JOHNSON, L. V. & CLEGG, D. O. 2009. Derivation of functional retinal pigmented epithelium from induced pluripotent stem cells. *Stem Cells,* 27**,** 2427-34. http://dx.doi.org/10.1002/stem.189.

BUCHHOLZ, D. E., PENNINGTON, B. O., CROZE, R. H., HINMAN, C. R., COFFEY, P. J. & CLEGG, D. O. 2013. Rapid and efficient directed differentiation of human pluripotent stem cells into retinal pigmented epithelium. *Stem Cells Transl Med,* 2**,** 384-93. http://dx.doi.org/10.5966/sctm.2012-0163.

BUCK, T. M. & WIJNHOLDS, J. 2020. Recombinant Adeno-Associated Viral Vectors (rAAV)-Vector Elements in Ocular Gene Therapy Clinical Trials and Transgene Expression and Bioactivity Assays. *Int J Mol Sci,* 21. http://dx.doi.org/10.3390/ijms21124197.

BUCKINGHAM, B. P., INMAN, D. M., LAMBERT, W., OGLESBY, E., CALKINS, D. J., STEELE, M. R., . . . HORNER, P. J. 2008. Progressive ganglion cell degeneration precedes neuronal loss in a mouse model of glaucoma. *J Neurosci,* 28**,** 2735-44. http://dx.doi.org/10.1523/JNEUROSCI.4443-07.2008.

BUDENZ, D. L., BARTON, K., WHITESIDE-DE VOS, J., SCHIFFMAN, J., BANDI, J., NOLAN, W., . . . TEMA EYE SURVEY STUDY, G. 2013. Prevalence of glaucoma in an urban West African population: the Tema Eye Survey. *JAMA Ophthalmol,* 131**,** 651-8. http://dx.doi.org/10.1001/jamaophthalmol.2013.1686.

BUIE, L. K., RASMUSSEN, C. A., PORTERFIELD, E. C., RAMGOLAM, V. S., CHOI, V. W., MARKOVIC-PLESE, S., . . . BORRAS, T. 2010. Self-complementary AAV virus (scAAV) safe and long-term gene transfer in the trabecular meshwork of living rats and monkeys. *Invest Ophthalmol Vis Sci,* 51**,** 236-48. http://dx.doi.org/10.1167/iovs.09-3847.

BÜNING, H. & SRIVASTAVA, A. 2019. Capsid Modifications for Targeting and Improving the Efficacy of AAV Vectors. *Molecular therapy. Methods & clinical development,* 12**,** 248-265. http://dx.doi.org/10.1016/j.omtm.2019.01.008.

BURNIGHT, E. R., GUPTA, M., WILEY, L. A., ANFINSON, K. R., TRAN, A., TRIBOULET, R., . . . TUCKER, B. A. 2017. Using CRISPR-Cas9 to Generate Gene-Corrected Autologous iPSCs for the Treatment of Inherited Retinal Degeneration. *Mol Ther,* 25**,** 1999-2013. http://dx.doi.org/10.1016/j.ymthe.2017.05.015.

BUSKIN, A., ZHU, L., CHICHAGOVA, V., BASU, B., MOZAFFARI-JOVIN, S., DOLAN, D., . . . LAKO, M. 2018. Disrupted alternative splicing for genes implicated in splicing and

ciliogenesis causes PRPF31 retinitis pigmentosa. *Nat Commun,* 9**,** 4234. http://dx.doi.org/10.1038/s41467-018-06448-y.

BYRNE, L. C., DALKARA, D., LUNA, G., FISHER, S. K., CLÉRIN, E., SAHEL, J. A., . . . FLANNERY, J. G. 2015. Viral-mediated RdCVF and RdCVFL expression protects cone and rod photoreceptors in retinal degeneration. *J Clin Invest,* 125**,** 105-16. http://dx.doi.org/10.1172/jci65654.

CADENAS, E. & DAVIES, K. J. 2000. Mitochondrial free radical generation, oxidative stress, and aging. *Free Radic Biol Med,* 29**,** 222-30. http://dx.doi.org/10.1016/s0891-5849(00)00317-8.

CAI, Y., CHENG, T., YAO, Y., LI, X., MA, Y., LI, L., . . . XUE, T. 2019. In vivo genome editing rescues photoreceptor degeneration via a Cas9/RecA-mediated homology-directed repair pathway. *Science Advances,* 5**,** eaav3335. http://dx.doi.org/10.1126/sciadv.aav3335.

CALKINS, D. J. 2012. Critical pathogenic events underlying progression of neurodegeneration in glaucoma. *Prog Retin Eye Res,* 31**,** 702-19. http://dx.doi.org/10.1016/j.preteyeres.2012.07.001.

CAO, X., YUNG, J., MAK, H. & LEUNG, C. K. S. 2019. Factors governing the transduction efficiency of adeno-associated virus in the retinal ganglion cells following intravitreal injection. *Gene Ther,* 26**,** 109-120. http://dx.doi.org/10.1038/s41434-019-0060-0.

CAPOWSKI, E. E., SAMIMI, K., MAYERL, S. J., PHILLIPS, M. J., PINILLA, I., HOWDEN, S. E., . . . GAMM, D. M. 2019. Reproducibility and staging of 3D human retinal organoids across multiple pluripotent stem cell lines. *Development,* 146. http://dx.doi.org/10.1242/dev.171686.

CARELLI, V., MARESCA, A., CAPORALI, L., TRIFUNOV, S., ZANNA, C. & RUGOLO, M. 2015. Mitochondria: Biogenesis and mitophagy balance in segregation and clonal expansion of mitochondrial DNA mutations. *Int J Biochem Cell Biol,* 63**,** 21-4. http://dx.doi.org/10.1016/j.biocel.2015.01.023.

CARREL, L. & WILLARD, H. F. 2005. X-inactivation profile reveals extensive variability in X-linked gene expression in females. *Nature,* 434**,** 400-4. http://dx.doi.org/10.1038/nature03479.

CARRIGAN, M. 2014. *Genetic Diagnosis and Treatment of Inherited Retinopathies.* PhD in Genetics, Trinity College Dublin.

CARSS, K. J., ARNO, G., ERWOOD, M., STEPHENS, J., SANCHIS-JUAN, A., HULL, S., . . . RAYMOND, F. L. 2017. Comprehensive Rare Variant Analysis via Whole-Genome Sequencing to Determine the Molecular Pathology of Inherited Retinal Disease. *Am J Hum Genet,* 100**,** 75-90. http://dx.doi.org/10.1016/j.ajhg.2016.12.003.

CARTER-DAWSON, L. D. & LAVAIL, M. M. 1979. Rods and cones in the mouse retina. I. Structural analysis using light and electron microscopy. *J Comp Neurol,* 188**,** 245-62. http://dx.doi.org/10.1002/cne.901880204.

CASEY, G. A., PAPP, K. M. & MACDONALD, I. M. 2020. Ocular Gene Therapy with Adeno-associated Virus Vectors: Current Outlook for Patients and Researchers. *Journal of ophthalmic & vision research,* 15**,** 396-399. http://dx.doi.org/10.18502/jovr.v15i3.7457.

CASSIDY, P. S., KELLY, R. A., REINA-TORRES, E., SHERWOOD, J. M., HUMPHRIES, M. M., KIANG, A.-S., . . . O'CALLAGHAN, J. 2020. Intracameral inoculation of endothelial tight junction siRNA-targeting drug enhances outflow facility and reduces intraocular pressure in a rodent model of steroid-induced ocular hypertension. *Molecular Therapy - Methods & Clinical Development*. http://dx.doi.org/10.1016/j.omtm.2020.10.022.

CASSON, R. J., CHIDLOW, G., WOOD, J. P., CROWSTON, J. G. & GOLDBERG, I. 2012. Definition of glaucoma: clinical and experimental concepts. *Clin Exp Ophthalmol,* 40**,** 341-9. http://dx.doi.org/10.1111/j.1442-9071.2012.02773.x.

CASSON, R. J., CHIDLOW, G. & WOOD, J. P. M. 2019. Estimate of the adenosine triphosphate requirement of human retinal ganglion cells. *Clin Exp Ophthalmol,* 47**,** 683-684. http://dx.doi.org/10.1111/ceo.13476.

CEHAJIC-KAPETANOVIC, J., XUE, K., MARTINEZ-FERNANDEZ DE LA CAMARA, C., NANDA, A., DAVIES, A., WOOD, L. J., . . . MACLAREN, R. E. 2020. Initial results from a first-in-human gene therapy trial on X-linked retinitis pigmentosa caused by mutations in RPGR. *Nat Med,* 26**,** 354-359. http://dx.doi.org/10.1038/s41591-020-0763-1.

CEHAJIC KAPETANOVIC, J., MCCLEMENTS, M. E., MARTINEZ-FERNANDEZ DE LA CAMARA, C. & MACLAREN, R. E. 2019. Molecular Strategies for RPGR Gene Therapy. *Genes (Basel),* 10. http://dx.doi.org/10.3390/genes10090674.

CHADDERTON, N., MILLINGTON-WARD, S., PALFI, A., O'REILLY, M., TUOHY, G., HUMPHRIES, M. M., . . . FARRAR, G. J. 2009. Improved retinal function in a mouse

model of dominant retinitis pigmentosa following AAV-delivered gene therapy. *Mol Ther,* 17**,** 593-9. http://dx.doi.org/10.1038/mt.2008.301.

CHADDERTON, N., PALFI, A., MILLINGTON-WARD, S., GOBBO, O., OVERLACK, N., CARRIGAN, M., . . . FARRAR, G. J. 2013. Intravitreal delivery of AAV-NDI1 provides functional benefit in a murine model of Leber hereditary optic neuropathy. *Eur J Hum Genet,* 21**,** 62-8. http://dx.doi.org/10.1038/ejhg.2012.112.

CHANDRA, S., MUIR, E. R., DEO, K., KIEL, J. W. & DUONG, T. Q. 2016. Effects of Dorzolamide on Retinal and Choroidal Blood Flow in the DBA/2J Mouse Model of Glaucoma. *Invest Ophthalmol Vis Sci,* 57**,** 826-31. http://dx.doi.org/10.1167/iovs.15-18291.

CHAPPLE, J. P., HARDCASTLE, A. J., GRAYSON, C., SPACKMAN, L. A., WILLISON, K. R. & CHEETHAM, M. E. 2000. Mutations in the N-terminus of the X-linked retinitis pigmentosa protein RP2 interfere with the normal targeting of the protein to the plasma membrane. *Hum Mol Genet,* 9**,** 1919-26. http://dx.doi.org/10.1093/hmg/9.13.1919.

CHAPPLE, J. P., HARDCASTLE, A. J., GRAYSON, C., WILLISON, K. R. & CHEETHAM, M. E. 2002. Delineation of the plasma membrane targeting domain of the X-linked retinitis pigmentosa protein RP2. *Invest Ophthalmol Vis Sci,* 43**,** 2015-20.

CHARLESWORTH, C. T., DESHPANDE, P. S., DEVER, D. P., CAMARENA, J., LEMGART, V. T., CROMER, M. K., . . . PORTEUS, M. H. 2019. Identification of preexisting adaptive immunity to Cas9 proteins in humans. *Nature Medicine,* 25**,** 249-254. http://dx.doi.org/10.1038/s41591-018-0326-x.

CHEIGNON, C., TOMAS, M., BONNEFONT-ROUSSELOT, D., FALLER, P., HUREAU, C. & COLLIN, F. 2018. Oxidative stress and the amyloid beta peptide in Alzheimer's disease. *Redox Biol,* 14**,** 450-464. http://dx.doi.org/10.1016/j.redox.2017.10.014.

CHEN, C., TURNBULL, D. M. & REEVE, A. K. 2019a. Mitochondrial Dysfunction in Parkinson's Disease-Cause or Consequence? *Biology (Basel),* 8. http://dx.doi.org/10.3390/biology8020038.

CHEN, G., ABDEEN, A. A., WANG, Y., SHAHI, P. K., ROBERTSON, S., XIE, R., . . . GONG, S. 2019b. A biodegradable nanocapsule delivers a Cas9 ribonucleoprotein complex for in vivo genome editing. *Nature nanotechnology,* 14**,** 974-980. http://dx.doi.org/10.1038/s41565-019-0539-2.

CHEN, H. & WEBER, A. J. 2002. Expression of glial fibrillary acidic protein and glutamine synthetase by Muller cells after optic nerve damage and intravitreal application of brain-derived neurotrophic factor. *Glia,* 38**,** 115-25. http://dx.doi.org/10.1002/glia.10061.

CHEN, J. S., DAGDAS, Y. S., KLEINSTIVER, B. P., WELCH, M. M., SOUSA, A. A., HARRINGTON, L. B., . . . DOUDNA, J. A. 2017. Enhanced proofreading governs CRISPR–Cas9 targeting accuracy. *Nature,* 550**,** 407-410. http://dx.doi.org/10.1038/nature24268.

CHEN, K., GUNTER, K. & MAINES, M. D. 2000. Neurons overexpressing heme oxygenase-1 resist oxidative stress-mediated cell death. *J Neurochem,* 75**,** 304-13. http://dx.doi.org/10.1046/j.1471-4159.2000.0750304.x.

CHEN, L., DENTCHEV, T., WONG, R., HAHN, P., WEN, R., BENNETT, J. & DUNAIEF, J. L. 2003. Increased expression of ceruloplasmin in the retina following photic injury. *Mol Vis,* 9**,** 151-8.

CHIAL, H. & CRAIG, J. 2008. mtDNA and mitochondrial diseases. *Nature Education,* 1.

CHICHAGOVA, V., GEORGIOU, M., DORGAU, B., CARTER, M., CHUNG, G., SERNAGOR, E., . . . LAKO, M. 2020. Enhancing immune function of hiPSC-derived retinal organoids by incorporating microglial cells. *Investigative Ophthalmology & Visual Science,* 61**,** 3797-3797.

CHOI, V. W., MCCARTY, D. M. & SAMULSKI, R. J. 2005. AAV hybrid serotypes: improved vectors for gene delivery. *Current gene therapy,* 5**,** 299-310. http://dx.doi.org/10.2174/1566523054064968.

CHONG, W. C., SHASTRI, M. D. & ERI, R. 2017. Endoplasmic Reticulum Stress and Oxidative Stress: A Vicious Nexus Implicated in Bowel Disease Pathophysiology. *Int J Mol Sci,* 18. http://dx.doi.org/10.3390/ijms18040771.

CHOQUET, H., WIGGS, J. L. & KHAWAJA, A. P. 2020. Clinical implications of recent advances in primary open-angle glaucoma genetics. *Eye (Lond),* 34**,** 29-39. http://dx.doi.org/10.1038/s41433-019-0632-7.

CHOU, S.-J., YANG, P., BAN, Q., YANG, Y.-P., WANG, M.-L., CHIEN, C.-S., . . . CHIOU, S.-H. 2020. Dual Supramolecular Nanoparticle Vectors Enable CRISPR/Cas9-Mediated Knockin of Retinoschisin 1 Gene-A Potential Nonviral Therapeutic Solution for X-Linked Juvenile Retinoschisis. *Advanced science (Weinheim, Baden-Wurttemberg, Germany),* 7**,** 1903432-1903432. http://dx.doi.org/10.1002/advs.201903432.

CHUNG, D. C., MCCAGUE, S., YU, Z. F., THILL, S., DISTEFANO-PAPPAS, J., BENNETT, J., . . . HIGH, K. A. 2018. Novel mobility test to assess functional vision in patients with inherited retinal dystrophies. *Clin Exp Ophthalmol,* 46**,** 247-259. http://dx.doi.org/10.1111/ceo.13022.

CHURCHILL, J. D., BOWNE, S. J., SULLIVAN, L. S., LEWIS, R. A., WHEATON, D. K., BIRCH, D. G., . . . DAIGER, S. P. 2013. Mutations in the X-linked retinitis pigmentosa genes RPGR and RP2 found in 8.5% of families with a provisional diagnosis of autosomal dominant retinitis pigmentosa. *Invest Ophthalmol Vis Sci,* 54**,** 1411-6. http://dx.doi.org/10.1167/iovs.12-11541.

CIDECIYAN, A. V., JACOBSON, S. G., BELTRAN, W. A., SUMAROKA, A., SWIDER, M., IWABE, S., . . . AGUIRRE, G. D. 2013. Human retinal gene therapy for Leber congenital amaurosis shows advancing retinal degeneration despite enduring visual improvement. *Proceedings of the National Academy of Sciences of the United States of America,* 110**,** E517-E525. http://dx.doi.org/10.1073/pnas.1218933110.

CIDECIYAN, A. V., SUDHARSAN, R., DUFOUR, V. L., MASSENGILL, M. T., IWABE, S., SWIDER, M., . . . BELTRAN, W. A. 2018. Mutation-independent rhodopsin gene therapy by knockdown and replacement with a single AAV vector. *Proceedings of the National Academy of Sciences,* 115**,** E8547-E8556. http://dx.doi.org/10.1073/pnas.1805055115.

COLLINS, D. W., GUDISEVA, H. V., CHAVALI, V. R. M., TRACHTMAN, B., RAMAKRISHNAN, M., MERRITT, W. T., III, . . . O'BRIEN, J. M. 2018. The MT-CO1 V83I Polymorphism is a Risk Factor for Primary Open-Angle Glaucoma in African American Men. *Invest Ophthalmol Vis Sci,* 59**,** 1751-1759. http://dx.doi.org/10.1167/iovs.17-23277.

COMANDER, J., WEIGEL-DIFRANCO, C., SANDBERG, M. A. & BERSON, E. L. 2015. Visual Function in Carriers of X-Linked Retinitis Pigmentosa. *Ophthalmology,* 122**,** 1899-906. http://dx.doi.org/10.1016/j.ophtha.2015.05.039.

CORDEIRO, M. F., MIGDAL, C., BLOOM, P., FITZKE, F. W. & MOSS, S. E. 2011. Imaging apoptosis in the eye. *Eye (Lond),* 25**,** 545-53. http://dx.doi.org/10.1038/eye.2011.64.

CORRAL-DEBRINSKI, M., HORTON, T., LOTT, M. T., SHOFFNER, J. M., BEAL, M. F. & WALLACE, D. C. 1992. Mitochondrial DNA deletions in human brain: regional variability and increase with advanced age. *Nat Genet,* 2**,** 324-9. http://dx.doi.org/10.1038/ng1292-324.

CORSO-DÍAZ, X., JAEGER, C., CHAITANKAR, V. & SWAROOP, A. 2018. Epigenetic control of gene regulation during development and disease: A view from the retina. *Prog Retin Eye Res,* 65**,** 1-27. http://dx.doi.org/10.1016/j.preteyeres.2018.03.002.

COUGHLIN, L., MORRISON, R. S., HORNER, P. J. & INMAN, D. M. 2015. Mitochondrial morphology differences and mitophagy deficit in murine glaucomatous optic nerve. *Invest Ophthalmol Vis Sci,* 56**,** 1437-46. http://dx.doi.org/10.1167/iovs.14-16126.

COWAN, C. S., RENNER, M., DE GENNARO, M., GROSS-SCHERF, B., GOLDBLUM, D., HOU, Y., . . . ROSKA, B. 2020. Cell Types of the Human Retina and Its Organoids at Single-Cell Resolution. *Cell,* 182**,** 1623-1640 e34. http://dx.doi.org/10.1016/j.cell.2020.08.013.

CRAIG, J. E., HAN, X., QASSIM, A., HASSALL, M., COOKE BAILEY, J. N., KINZY, T. G., . . . MACGREGOR, S. 2020. Multitrait analysis of glaucoma identifies new risk loci and enables polygenic prediction of disease susceptibility and progression. *Nat Genet,* 52**,** 160-166. http://dx.doi.org/10.1038/s41588-019-0556-y.

CRAVEN, L., ALSTON, C. L., TAYLOR, R. W. & TURNBULL, D. M. 2017. Recent Advances in Mitochondrial Disease. *Annu Rev Genomics Hum Genet,* 18**,** 257-275. http://dx.doi.org/10.1146/annurev-genom-091416-035426.

CREMERS, F. P. M., BOON, C. J. F., BUJAKOWSKA, K. & ZEITZ, C. 2018. Special Issue Introduction: Inherited Retinal Disease: Novel Candidate Genes, Genotype–Phenotype Correlations, and Inheritance Models. *Genes,* 9**,** 215.

CUI, Q. N., RAMAKRISHNAN, M. S., GUDISEVA, H. V., COLLINS, D. W., PISTILLI, M., LEE, R., . . . O'BRIEN, J. M. 2019. Mitochondrial haplogroup L1c2 is associated with increased disease severity in African American patients with primary open-angle glaucoma. *J Clin Exp Ophthalmol,* 10. http://dx.doi.org/10.4172/2155-9570.1000799.

CUI, Y., LIAO, X., PENG, S., TANG, T., HUANG, C. & YANG, C. 2020. OffScan: a universal and fast CRISPR off-target sites detection tool. *BMC genomics,* 21**,** 872-872. http://dx.doi.org/10.1186/s12864-019-6241-9.

CUI, Y., ZHAO, S., WU, Z., DAI, P. & ZHOU, B. 2012. Mitochondrial release of the NADH dehydrogenase Ndi1 induces apoptosis in yeast. *Mol Biol Cell,* 23**,** 4373-82. http://dx.doi.org/10.1091/mbc.E12-04-0281.

CUNHA-VAZ, J. G. 1997. The blood-ocular barriers: past, present, and future. *Doc Ophthalmol,* 93**,** 149-57. http://dx.doi.org/10.1007/bf02569055.

CWERMAN-THIBAULT, H., LECHAUVE, C., AUGUSTIN, S., ROUSSEL, D., REBOUSSIN, E., MOHAMMAD, A., . . . CORRAL-DEBRINSKI, M. 2017. Neuroglobin Can Prevent or Reverse Glaucomatous Progression in DBA/2J Mice. *Mol Ther Methods Clin Dev,* 5**,** 200-220. http://dx.doi.org/10.1016/j.omtm.2017.04.008.

DAER, R., HAMNA, F., BARRETT, C. M. & HAYNES, K. A. 2020. Site-directed targeting of transcriptional activation-associated proteins to repressed chromatin restores CRISPR activity. *APL Bioeng,* 4**,** 016102. http://dx.doi.org/10.1063/1.5127302.

DAER, R. M., CUTTS, J. P., BRAFMAN, D. A. & HAYNES, K. A. 2017. The Impact of Chromatin Dynamics on Cas9-Mediated Genome Editing in Human Cells. *ACS Synth Biol,* 6**,** 428-438. http://dx.doi.org/10.1021/acssynbio.5b00299.

DALY, C., WARD, R., REYNOLDS, A. L., GALVIN, O., COLLERY, R. F. & KENNEDY, B. N. 2018. Brain-Derived Neurotrophic Factor as a Treatment Option for Retinal Degeneration. *Adv Exp Med Biol,* 1074**,** 465-471. http://dx.doi.org/10.1007/978-3-319-75402-4_57.

DAVID, R., ZANGWILL, L., BRISCOE, D., DAGAN, M., YAGEV, R. & YASSUR, Y. 1992. Diurnal intraocular pressure variations: an analysis of 690 diurnal curves. *Br J Ophthalmol,* 76**,** 280-3. http://dx.doi.org/10.1136/bjo.76.5.280.

DAVIDOFF, A. M., GRAY, J. T., NG, C. Y. C., ZHANG, Y., ZHOU, J., SPENCE, Y., . . . NATHWANI, A. C. 2005. Comparison of the ability of adeno-associated viral vectors pseudotyped with serotype 2, 5, and 8 capsid proteins to mediate efficient transduction of the liver in murine and nonhuman primate models. *Molecular Therapy,* 11**,** 875-888. http://dx.doi.org/10.1016/j.ymthe.2004.12.022.

DAVIS, B. M., CRAWLEY, L., PAHLITZSCH, M., JAVAID, F. & CORDEIRO, M. F. 2016. Glaucoma: the retina and beyond. *Acta Neuropathol,* 132**,** 807-826. http://dx.doi.org/10.1007/s00401-016-1609-2.

DE LA ASUNCION, J. G., MILLAN, A., PLA, R., BRUSEGHINI, L., ESTERAS, A., PALLARDO, F. V., . . . VINA, J. 1996. Mitochondrial glutathione oxidation correlates with age-associated oxidative damage to mitochondrial DNA. *FASEB J,* 10**,** 333-8. http://dx.doi.org/10.1096/fasebj.10.2.8641567.

DE SILVA, S. R., ARNO, G., ROBSON, A. G., FAKIN, A., PONTIKOS, N., MOHAMED, M. D., . . . MAHROO, O. A. 2020. The X-linked retinopathies: Physiological insights,

pathogenic mechanisms, phenotypic features and novel therapies. *Prog Retin Eye Res*, 100898. http://dx.doi.org/10.1016/j.preteyeres.2020.100898.

DE SOLIS, C. A., HO, A., HOLEHONNUR, R. & PLOSKI, J. E. 2016. The Development of a Viral Mediated CRISPR/Cas9 System with Doxycycline Dependent gRNA Expression for Inducible In vitro and In vivo Genome Editing. *Frontiers in Molecular Neuroscience,* 9. http://dx.doi.org/10.3389/fnmol.2016.00070.

DENG, W. L., GAO, M. L., LEI, X. L., LV, J. N., ZHAO, H., HE, K. W., . . . JIN, Z. B. 2018. Gene Correction Reverses Ciliopathy and Photoreceptor Loss in iPSC-Derived Retinal Organoids from Retinitis Pigmentosa Patients. *Stem Cell Reports,* 10**,** 2005. http://dx.doi.org/10.1016/j.stemcr.2018.05.012.

DENGLER-CRISH, C. M., SMITH, M. A., INMAN, D. M., WILSON, G. N., YOUNG, J. W. & CRISH, S. D. 2014. Anterograde transport blockade precedes deficits in retrograde transport in the visual projection of the DBA/2J mouse model of glaucoma. *Front Neurosci,* 8**,** 290. http://dx.doi.org/10.3389/fnins.2014.00290.

DEVKOTA, S. 2018. The road less traveled: strategies to enhance the frequency of homology-directed repair (HDR) for increased efficiency of CRISPR/Cas-mediated transgenesis. *BMB Reports,* 51**,** 437-443. http://dx.doi.org/10.5483/BMBRep.2018.51.9.187.

DHUNGEL, B. P., BAILEY, C. G. & RASKO, J. E. J. 2020. Journey to the Center of the Cell: Tracing the Path of AAV Transduction. *Trends in Molecular Medicine*. http://dx.doi.org/10.1016/j.molmed.2020.09.010.

DIAS, V., JUNN, E. & MOURADIAN, M. M. 2013. The role of oxidative stress in Parkinson's disease. *J Parkinsons Dis,* 3**,** 461-91. http://dx.doi.org/10.3233/jpd-130230.

DILAN, T. L., MOYE, A. R., SALIDO, E. M., SARAVANAN, T., KOLANDAIVELU, S., GOLDBERG, A. F. X. & RAMAMURTHY, V. 2019. ARL13B, a Joubert Syndrome-Associated Protein, Is Critical for Retinogenesis and Elaboration of Mouse Photoreceptor Outer Segments. *J Neurosci,* 39**,** 1347-1364. http://dx.doi.org/10.1523/JNEUROSCI.1761-18.2018.

DIMOPOULOS, I. S., HOANG, S. C., RADZIWON, A., BINCZYK, N. M., SEABRA, M. C., MACLAREN, R. E., . . . MACDONALD, I. M. 2018. Two-Year Results After AAV2-Mediated Gene Therapy for Choroideremia: The Alberta Experience. *Am J Ophthalmol,* 193**,** 130-142. http://dx.doi.org/10.1016/j.ajo.2018.06.011.

DING, X., SEEBECK, T., FENG, Y., JIANG, Y., DAVIS, G. D. & CHEN, F. 2019. Improving CRISPR-Cas9 Genome Editing Efficiency by Fusion with Chromatin-Modulating Peptides. *CRISPR J,* 2**,** 51-63. http://dx.doi.org/10.1089/crispr.2018.0036.

DOCKERY, A., STEPHENSON, K., KEEGAN, D., WYNNE, N., SILVESTRI, G., HUMPHRIES, P., . . . FARRAR, G. J. 2017. Target 5000: Target Capture Sequencing for Inherited Retinal Degenerations. *Genes (Basel),* 8. http://dx.doi.org/10.3390/genes8110304.

DOENCH, J. G., FUSI, N., SULLENDER, M., HEGDE, M., VAIMBERG, E. W., DONOVAN, K. F., . . . ROOT, D. E. 2016. Optimized sgRNA design to maximize activity and minimize off-target effects of CRISPR-Cas9. *Nat Biotechnol,* 34**,** 184-191. http://dx.doi.org/10.1038/nbt.3437.

DOENCH, J. G., HARTENIAN, E., GRAHAM, D. B., TOTHOVA, Z., HEGDE, M., SMITH, I., . . . ROOT, D. E. 2014. Rational design of highly active sgRNAs for CRISPR-Cas9-mediated gene inactivation. *Nat Biotechnol,* 32**,** 1262-7. http://dx.doi.org/10.1038/nbt.3026.

DOMENICI, L., ORIGLIA, N., FALSINI, B., CERRI, E., BARLOSCIO, D., FABIANI, C., . . . GIOVANNINI, L. 2014. Rescue of retinal function by BDNF in a mouse model of glaucoma. *PLoS One,* 9**,** e115579. http://dx.doi.org/10.1371/journal.pone.0115579.

DONATIEN, P. & JEFFERY, G. 2002. Correlation between Rod Photoreceptor Numbers and Levels of Ocular Pigmentation. *Investigative Ophthalmology & Visual Science,* 43**,** 1198-1203.

DOWNS, J. C. & GIRKIN, C. A. 2017. Lamina cribrosa in glaucoma. *Current opinion in ophthalmology,* 28**,** 113-119. http://dx.doi.org/10.1097/ICU.0000000000000354.

DRANCE, S., ANDERSON, D. R., SCHULZER, M. & COLLABORATIVE NORMAL-TENSION GLAUCOMA STUDY, G. 2001. Risk factors for progression of visual field abnormalities in normal-tension glaucoma. *Am J Ophthalmol,* 131**,** 699-708. http://dx.doi.org/10.1016/s0002-9394(01)00964-3.

DRYJA, T. P., MCGEE, T. L., REICHEL, E., HAHN, L. B., COWLEY, G. S., YANDELL, D. W., . . . BERSON, E. L. 1990. A point mutation of the rhodopsin gene in one form of retinitis pigmentosa. *Nature,* 343**,** 364-6. http://dx.doi.org/10.1038/343364a0.

DUESTER, G. 2009. Keeping an eye on retinoic acid signaling during eye development. *Chem Biol Interact,* 178**,** 178-81. http://dx.doi.org/10.1016/j.cbi.2008.09.004.

EDGAR, D., SHABALINA, I., CAMARA, Y., WREDENBERG, A., CALVARUSO, M. A., NIJTMANS, L., . . . TRIFUNOVIC, A. 2009. Random point mutations with major effects on protein-coding genes are the driving force behind premature aging in mtDNA mutator mice. *Cell Metab,* 10**,** 131-8. http://dx.doi.org/10.1016/j.cmet.2009.06.010.

EELLS, J. T. 2019. Mitochondrial Dysfunction in the Aging Retina. *Biology (Basel),* 8. http://dx.doi.org/10.3390/biology8020031.

EIRAKU, M., TAKATA, N., ISHIBASHI, H., KAWADA, M., SAKAKURA, E., OKUDA, S., . . . SASAI, Y. 2011. Self-organizing optic-cup morphogenesis in three-dimensional culture. *Nature,* 472**,** 51-6. http://dx.doi.org/10.1038/nature09941.

EIRAKU, M., WATANABE, K., MATSUO-TAKASAKI, M., KAWADA, M., YONEMURA, S., MATSUMURA, M., . . . SASAI, Y. 2008. Self-organized formation of polarized cortical tissues from ESCs and its active manipulation by extrinsic signals. *Cell Stem Cell,* 3**,** 519-32. http://dx.doi.org/10.1016/j.stem.2008.09.002.

ELLIOTT, B., RICHARDSON, C., WINDERBAUM, J., NICKOLOFF, J. A. & JASIN, M. 1998. Gene conversion tracts from double-strand break repair in mammalian cells. *Molecular and cellular biology,* 18**,** 93-101. http://dx.doi.org/10.1128/mcb.18.1.93.

ELLIS, B. L., HIRSCH, M. L., BARKER, J. C., CONNELLY, J. P., STEININGER, R. J., 3RD & PORTEUS, M. H. 2013. A survey of ex vivo/in vitro transduction efficiency of mammalian primary cells and cell lines with Nine natural adeno-associated virus (AAV1-9) and one engineered adeno-associated virus serotype. *Virol J,* 10**,** 74. http://dx.doi.org/10.1186/1743-422X-10-74.

EUROPEAN GLAUCOMA PREVENTION STUDY, G., MIGLIOR, S., PFEIFFER, N., TORRI, V., ZEYEN, T., CUNHA-VAZ, J. & ADAMSONS, I. 2007. Predictive factors for open-angle glaucoma among patients with ocular hypertension in the European Glaucoma Prevention Study. *Ophthalmology,* 114**,** 3-9. http://dx.doi.org/10.1016/j.ophtha.2006.05.075.

EVANGELHO, K., MASTRONARDI, C. A. & DE-LA-TORRE, A. 2019. Experimental Models of Glaucoma: A Powerful Translational Tool for the Future Development of New Therapies for Glaucoma in Humans—A Review of the Literature. *Medicina,* 55**,** 280.

EVANS, R. J., HARDCASTLE, A. J. & CHEETHAM, M. E. 2006. Focus on molecules: X-linked Retinitis Pigmentosa 2 protein, RP2. *Exp Eye Res,* 82**,** 543-4. http://dx.doi.org/10.1016/j.exer.2005.10.023.

EVANS, R. J., SCHWARZ, N., NAGEL-WOLFRUM, K., WOLFRUM, U., HARDCASTLE, A. J. & CHEETHAM, M. E. 2010. The retinitis pigmentosa protein RP2 links pericentriolar vesicle transport between the Golgi and the primary cilium. *Hum Mol Genet,* 19**,** 1358-67. http://dx.doi.org/10.1093/hmg/ddq012.

FAHIM, A. T. & DAIGER, S. P. 2016. The Role of X-Chromosome Inactivation in Retinal Development and Disease. *Adv Exp Med Biol,* 854**,** 325-31. http://dx.doi.org/10.1007/978-3-319-17121-0_43.

FAHIM, A. T., SULLIVAN, L. S., BOWNE, S. J., JONES, K. D., WHEATON, D. K. H., KHAN, N. W., . . . DAIGER, S. P. 2020. X-Chromosome Inactivation Is a Biomarker of Clinical Severity in Female Carriers of RPGR-Associated X-Linked Retinitis Pigmentosa. *Ophthalmol Retina,* 4**,** 510-520. http://dx.doi.org/10.1016/j.oret.2019.11.010.

FAN, B. J., BAILEY, J. C., IGO, R. P., JR., KANG, J. H., BOUMENNA, T., BRILLIANT, M. H., . . . WIGGS, J. L. 2019. Association of a Primary Open-Angle Glaucoma Genetic Risk Score With Earlier Age at Diagnosis. *JAMA Ophthalmol*. http://dx.doi.org/10.1001/jamaophthalmol.2019.3109.

FARINELLI, P., PERERA, A., ARANGO-GONZALEZ, B., TRIFUNOVIC, D., WAGNER, M., CARELL, T., . . . EKSTRÖM, P. A. R. 2014. DNA methylation and differential gene regulation in photoreceptor cell death. *Cell Death & Disease,* 5**,** e1558-e1558. http://dx.doi.org/10.1038/cddis.2014.512.

FARRAR, G. J., CARRIGAN, M., DOCKERY, A., MILLINGTON-WARD, S., PALFI, A., CHADDERTON, N., . . . HUMPHRIES, P. 2017. Toward an elucidation of the molecular genetics of inherited retinal degenerations. *Human molecular genetics,* 26**,** R2-R11. http://dx.doi.org/10.1093/hmg/ddx185.

FARRAR, G. J., KENNA, P. F. & HUMPHRIES, P. 2006. *Genetic suppression and replacement*. US patent application.

FARRAR, G. J., MCWILLIAM, P., BRADLEY, D. G., KENNA, P., LAWLER, M., SHARP, E. M., . . . ET AL. 1990. Autosomal dominant retinitis pigmentosa: linkage to rhodopsin and evidence for genetic heterogeneity. *Genomics,* 8**,** 35-40. http://dx.doi.org/10.1016/0888-7543(90)90223-h.

FARRAR, G. J., MILLINGTON-WARD, S., CHADDERTON, N., CARRIGAN, M. & KENNA, P. 2019. *Variants of yeast NDI1 gene, and uses thereof in the treatment of disease associated with mitochondrial dysfunction*. US patent application. 2019.

FDA 2018. Statement from FDA Commissioner Scott Gottlieb, M.D. on agency's efforts to advance development of gene therapies. https://www.fda.gov/news-events/press-announcements/.

FDA 2019. Statement from FDA Commissioner Scott Gottlieb, M.D. and Peter Marks, M.D., Ph.D., Director of the Center for Biologics Evaluation and Research on new policies to advance development of safe and effective cell and gene therapies. https://www.fda.gov/news-events/press-announcements/.

FERGUSON, L. R., BALAIYA, S., MYNAMPATI, B. K., SAMBHAV, K. & CHALAM, K. V. 2015. Deprivation of bFGF Promotes Spontaneous Differentiation of Human Embryonic Stem Cells into Retinal Pigment Epithelial Cells. *J Stem Cells,* 10**,** 159-70.

FERNANDES, K. A., HARDER, J. M., WILLIAMS, P. A., RAUSCH, R. L., KIERNAN, A. E., NAIR, K. S., . . . LIBBY, R. T. 2015. Using genetic mouse models to gain insight into glaucoma: Past results and future possibilities. *Exp Eye Res,* 141**,** 42-56. http://dx.doi.org/10.1016/j.exer.2015.06.019.

FERNÁNDEZ-SÁNCHEZ, L., DE SEVILLA MÜLLER, L. P., BRECHA, N. C. & CUENCA, N. 2014. Loss of Outer Retinal Neurons and Circuitry Alterations in the DBA/2J Mouse. *Investigative Ophthalmology & Visual Science,* 55**,** 6059-6072. http://dx.doi.org/10.1167/iovs.14-14421.

FERREIRA, S. M., LERNER, S. F., BRUNZINI, R., EVELSON, P. A. & LLESUY, S. F. 2004. Oxidative stress markers in aqueous humor of glaucoma patients. *Am J Ophthalmol,* 137**,** 62-9. http://dx.doi.org/10.1016/s0002-9394(03)00788-8.

FLAXMAN, S. R., BOURNE, R. R. A., RESNIKOFF, S., ACKLAND, P., BRAITHWAITE, T., CICINELLI, M. V., . . . ZHENG, Y. 2017. Global causes of blindness and distance vision impairment 1990–2020: a systematic review and meta-analysis. *The Lancet Global Health,* 5**,** e1221-e1234. http://dx.doi.org/10.1016/S2214-109X(17)30393-5.

FRAENKL, S. A., MUSER, J., GROELL, R., REINHARD, G., ORGUL, S., FLAMMER, J. & GOLDBLUM, D. 2011. Plasma citrate levels as a potential biomarker for glaucoma. *J Ocul Pharmacol Ther,* 27**,** 577-80. http://dx.doi.org/10.1089/jop.2011.0062.

FRANK, S. A. & HURST, L. D. 1996. Mitochondria and male disease. *Nature,* 383**,** 224. http://dx.doi.org/10.1038/383224a0.

FRENZEL, H. & FEIMANN, J. 1984. Age-dependent structural changes in the myocardium of rats. A quantitative light- and electron-microscopic study on the right and left chamber wall. *Mech Ageing Dev,* 27**,** 29-41. http://dx.doi.org/10.1016/0047-6374(84)90080-0.

FRIEDMAN, D. S., JAMPEL, H. D., MUNOZ, B. & WEST, S. K. 2006. The prevalence of open-angle glaucoma among blacks and whites 73 years and older: the Salisbury Eye Evaluation Glaucoma Study. *Arch Ophthalmol,* 124**,** 1625-30. http://dx.doi.org/10.1001/archopht.124.11.1625.

FRISHMAN, L., SUSTAR, M., KREMERS, J., MCANANY, J. J., SAROSSY, M., TZEKOV, R. & VISWANATHAN, S. 2018. ISCEV extended protocol for the photopic negative response (PhNR) of the full-field electroretinogram. *Doc Ophthalmol,* 136**,** 207-211. http://dx.doi.org/10.1007/s10633-018-9638-x.

FRITSCHE, L. G., IGL, W., BAILEY, J. N. C., GRASSMANN, F., SENGUPTA, S., BRAGG-GRESHAM, J. L., . . . HEID, I. M. 2016. A large genome-wide association study of age-related macular degeneration highlights contributions of rare and common variants. *Nature genetics,* 48**,** 134-143. http://dx.doi.org/10.1038/ng.3448.

FRY, L. E., PEDDLE, C. F., BARNARD, A. R., MCCLEMENTS, M. E. & MACLAREN, R. E. 2020. RNA Editing as a Therapeutic Approach for Retinal Gene Therapy Requiring Long Coding Sequences. *International Journal of Molecular Sciences,* 21**,** 777.

FU, Y., SANDER, J. D., REYON, D., CASCIO, V. M. & JOUNG, J. K. 2014. Improving CRISPR-Cas nuclease specificity using truncated guide RNAs. *Nat Biotechnol,* 32**,** 279-284. http://dx.doi.org/10.1038/nbt.2808.

FUCHS, M., SCHOLZ, M., SENDELBECK, A., ATORF, J., SCHLEGEL, C., ENZ, R. & BRANDSTÄTTER, J. H. 2012. Rod photoreceptor ribbon synapses in DBA/2J mice show progressive age-related structural changes. *PLoS One,* 7**,** e44645. http://dx.doi.org/10.1371/journal.pone.0044645.

FUHRMANN, S. 2010. Eye morphogenesis and patterning of the optic vesicle. *Curr Top Dev Biol,* 93**,** 61-84. http://dx.doi.org/10.1016/B978-0-12-385044-7.00003-5.

FUJINAMI, K., LIU, X., UENO, S., MIZOTA, A., SHINODA, K., KUNIYOSHI, K., . . . JAPAN EYE GENETICS CONSORTIUM STUDY, G. 2020. RP2-associated retinal disorder in a Japanese cohort: Report of novel variants and a literature review, identifying a

genotype-phenotype association. *Am J Med Genet C Semin Med Genet,* 184**,** 675-693. http://dx.doi.org/10.1002/ajmg.c.31830.

FUSTER-GARCÍA, C., GARCÍA-GARCÍA, G., GONZÁLEZ-ROMERO, E., JAIJO, T., SEQUEDO, M. D., AYUSO, C., . . . ALLER, E. 2017. USH2A Gene Editing Using the CRISPR System. *Mol Ther Nucleic Acids,* 8**,** 529-541. http://dx.doi.org/10.1016/j.omtn.2017.08.003.

GALVIN, O., CHI, G., BRADY, L., HIPPERT, C., DEL VALLE RUBIDO, M., DALY, A. & MICHAELIDES, M. 2020. The Impact of Inherited Retinal Diseases in the Republic of Ireland (ROI) and the United Kingdom (UK) from a Cost-of-Illness Perspective. *Clinical ophthalmology (Auckland, N.Z.),* 14**,** 707-719. http://dx.doi.org/10.2147/OPTH.S241928.

GAMLIN, P. D., ALEXANDER, J. J., BOYE, S. L., WITHERSPOON, C. D. & BOYE, S. E. 2019. SubILM Injection of AAV for Gene Delivery to the Retina. *Methods in molecular biology (Clifton, N.J.),* 1950**,** 249-262. http://dx.doi.org/10.1007/978-1-4939-9139-6_14.

GARAFALO, A. V., CIDECIYAN, A. V., HÉON, E., SHEPLOCK, R., PEARSON, A., WEIYANG YU, C., . . . JACOBSON, S. G. 2020. Progress in treating inherited retinal diseases: Early subretinal gene therapy clinical trials and candidates for future initiatives. *Prog Retin Eye Res,* 77**,** 100827. http://dx.doi.org/10.1016/j.preteyeres.2019.100827.

GARITA-HERNANDEZ, M., LAMPIČ, M., CHAFFIOL, A., GUIBBAL, L., ROUTET, F., SANTOS-FERREIRA, T., . . . DUEBEL, J. 2019. Restoration of visual function by transplantation of optogenetically engineered photoreceptors. *Nature communications,* 10**,** 4524-4524. http://dx.doi.org/10.1038/s41467-019-12330-2.

GARITA-HERNANDEZ, M., ROUTET, F., GUIBBAL, L., KHABOU, H., TOUALBI, L., RIANCHO, L., . . . DALKARA, D. 2020. AAV-Mediated Gene Delivery to 3D Retinal Organoids Derived from Human Induced Pluripotent Stem Cells. *Int J Mol Sci,* 21. http://dx.doi.org/10.3390/ijms21030994.

GASPARINI, S. J., LLONCH, S., BORSCH, O. & ADER, M. 2019. Transplantation of photoreceptors into the degenerative retina: Current state and future perspectives. *Progress in Retinal and Eye Research,* 69**,** 1-37. http://dx.doi.org/https://doi.org/10.1016/j.preteyeres.2018.11.001.

GAZZARD, G., FOSTER, P. J., DEVEREUX, J. G., OEN, F., CHEW, P., KHAW, P. T. & SEAH, S. 2003. Intraocular pressure and visual field loss in primary angle closure and

primary open angle glaucomas. *Br J Ophthalmol,* 87**,** 720-5. http://dx.doi.org/10.1136/bjo.87.6.720.

GELLER, A. M. & SIEVING, P. A. 1993. Assessment of foveal cone photoreceptors in Stargardt's macular dystrophy using a small dot detection task. *Vision Research,* 33**,** 1509-1524. http://dx.doi.org/https://doi.org/10.1016/0042-6989(93)90144-L.

GELLER, A. M., SIEVING, P. A. & GREEN, D. G. 1992. Effect on grating identification of sampling with degenerate arrays. *Journal of the Optical Society of America A,* 9**,** 472-477. http://dx.doi.org/10.1364/JOSAA.9.000472.

GENOMES PROJECT, C., ABECASIS, G. R., ALTSHULER, D., AUTON, A., BROOKS, L. D., DURBIN, R. M., . . . MCVEAN, G. A. 2010. A map of human genome variation from population-scale sequencing. *Nature,* 467**,** 1061-73. http://dx.doi.org/10.1038/nature09534.

GEOGHEGAN, F., CHADDERTON, N., FARRAR, G. J., ZISTERER, D. M. & PORTER, R. K. 2017. Direct effects of phenformin on metabolism/bioenergetics and viability of SH-SY5Y neuroblastoma cells. *Oncol Lett,* 14**,** 6298-6306. http://dx.doi.org/10.3892/ol.2017.6929.

GHERGHEL, D., GRIFFITHS, H. R., HILTON, E. J., CUNLIFFE, I. A. & HOSKING, S. L. 2005. Systemic reduction in glutathione levels occurs in patients with primary open-angle glaucoma. *Invest Ophthalmol Vis Sci,* 46**,** 877-83. http://dx.doi.org/10.1167/iovs.04-0777.

GIANNELLI, S. G., LUONI, M., CASTOLDI, V., MASSIMINO, L., CABASSI, T., ANGELONI, D., . . . BROCCOLI, V. 2018. Cas9/sgRNA selective targeting of the P23H Rhodopsin mutant allele for treating retinitis pigmentosa by intravitreal AAV9.PHP.B-based delivery. *Hum Mol Genet,* 27**,** 761-779. http://dx.doi.org/10.1093/hmg/ddx438.

GIVENS, B. E., NAGUIB, Y. W., GEARY, S. M., DEVOR, E. J. & SALEM, A. K. 2018. Nanoparticle-Based Delivery of CRISPR/Cas9 Genome-Editing Therapeutics. *The AAPS journal,* 20**,** 108-108. http://dx.doi.org/10.1208/s12248-018-0267-9.

GONZALEZ-CORDERO, A., GOH, D., KRUCZEK, K., NAEEM, A., FERNANDO, M., KLEINE HOLTHAUS, S. M., . . . ALI, R. R. 2018. Assessment of AAV Vector Tropisms for Mouse and Human Pluripotent Stem Cell-Derived RPE and Photoreceptor Cells. *Hum Gene Ther,* 29**,** 1124-1139. http://dx.doi.org/10.1089/hum.2018.027.

GORDOIS, A., CUTLER, H., PEZZULLO, L., GORDON, K., CRUESS, A., WINYARD, S., . . . CHUA, K. 2012. An estimation of the worldwide economic and health burden of visual

impairment. *Glob Public Health,* 7**,** 465-81. http://dx.doi.org/10.1080/17441692.2011.634815.

GOTTHARDT, K., LOKAJ, M., KOERNER, C., FALK, N., GIESSL, A. & WITTINGHOFER, A. 2015. A G-protein activation cascade from Arl13B to Arl3 and implications for ciliary targeting of lipidated proteins. *Elife,* 4. http://dx.doi.org/10.7554/eLife.11859.

GRAYSON, C., BARTOLINI, F., CHAPPLE, J. P., WILLISON, K. R., BHAMIDIPATI, A., LEWIS, S. A., . . . CHEETHAM, M. E. 2002. Localization in the human retina of the X-linked retinitis pigmentosa protein RP2, its homologue cofactor C and the RP2 interacting protein Arl3. *Hum Mol Genet,* 11**,** 3065-74. http://dx.doi.org/10.1093/hmg/11.24.3065.

GREENWALD, S. H., BROWN, E. E., SCANDURA, M. J., HENNESSEY, E., FARMER, R., PAWLYK, B. S., . . . PIERCE, E. A. 2020. Gene Therapy Preserves Retinal Structure and Function in a Mouse Model of NMNAT1-Associated Retinal Degeneration. *Molecular Therapy - Methods & Clinical Development,* 18**,** 582-594. http://dx.doi.org/https://doi.org/10.1016/j.omtm.2020.07.003.

GRESH, J., GOLETZ, P. W., CROUCH, R. K. & ROHRER, B. 2003. Structure-function analysis of rods and cones in juvenile, adult, and aged C57bl/6 and Balb/c mice. *Vis Neurosci,* 20**,** 211-20. http://dx.doi.org/10.1017/s0952523803202108.

GRIEGER, J. C. & SAMULSKI, R. J. 2005. Packaging capacity of adeno-associated virus serotypes: impact of larger genomes on infectivity and postentry steps. *Journal of virology,* 79**,** 9933-9944. http://dx.doi.org/10.1128/JVI.79.15.9933-9944.2005.

GRIENDLING, K. K., TOUYZ, R. M., ZWEIER, J. L., DIKALOV, S., CHILIAN, W., CHEN, Y. R., . . . AMERICAN HEART ASSOCIATION COUNCIL ON BASIC CARDIOVASCULAR, S. 2016. Measurement of Reactive Oxygen Species, Reactive Nitrogen Species, and Redox-Dependent Signaling in the Cardiovascular System: A Scientific Statement From the American Heart Association. *Circ Res,* 119**,** e39-75. http://dx.doi.org/10.1161/RES.0000000000000110.

GRILLO, S. L., MONTGOMERY, C. L., JOHNSON, H. M. & KOULEN, P. 2018. Quantification of Changes in Visual Function During Disease Development in a Mouse Model of Pigmentary Glaucoma. *J Glaucoma,* 27**,** 828-841. http://dx.doi.org/10.1097/IJG.0000000000001024.

GRZYBOWSKI, A., OCH, M., KANCLERZ, P., LEFFLER, C. & MORAES, C. G. 2020. Primary Open Angle Glaucoma and Vascular Risk Factors: A Review of Population Based Studies from 1990 to 2019. *J Clin Med,* 9. http://dx.doi.org/10.3390/jcm9030761.

GUSCHIN, D. Y., WAITE, A. J., KATIBAH, G. E., MILLER, J. C., HOLMES, M. C. & REBAR, E. J. 2010. A rapid and general assay for monitoring endogenous gene modification. *Methods Mol Biol,* 649**,** 247-56. http://dx.doi.org/10.1007/978-1-60761-753-2_15.

HABERMAN, R. P., MCCOWN, T. J. & SAMULSKI, R. J. 2000. Novel transcriptional regulatory signals in the adeno-associated virus terminal repeat A/D junction element. *J Virol,* 74**,** 8732-9. http://dx.doi.org/10.1128/jvi.74.18.8732-8739.2000.

HAFEZI, F., GRIMM, C., SIMMEN, B. C., WENZEL, A. & REMÉ, C. E. 2000. Molecular ophthalmology: an update on animal models for retinal degenerations and dystrophies. *British Journal of Ophthalmology,* 84**,** 922-927. http://dx.doi.org/10.1136/bjo.84.8.922.

HALLAM, D., HILGEN, G., DORGAU, B., ZHU, L., YU, M., BOJIC, S., . . . LAKO, M. 2018. Human-Induced Pluripotent Stem Cells Generate Light Responsive Retinal Organoids with Variable and Nutrient-Dependent Efficiency. *Stem Cells,* 36**,** 1535-1551. http://dx.doi.org/10.1002/stem.2883.

HALLIWELL, B. & ARUOMA, O. I. 1991. DNA damage by oxygen-derived species. Its mechanism and measurement in mammalian systems. *FEBS Lett,* 281**,** 9-19. http://dx.doi.org/10.1016/0014-5793(91)80347-6.

HAMEL, C. 2006. Retinitis pigmentosa. *Orphanet Journal of Rare Diseases,* 1**,** 40. http://dx.doi.org/10.1186/1750-1172-1-40.

HAN, X., GHARAHKHANI, P., MITCHELL, P., LIEW, G., HEWITT, A. W. & MACGREGOR, S. 2020. Genome-wide meta-analysis identifies novel loci associated with age-related macular degeneration. *Journal of Human Genetics,* 65**,** 657-665. http://dx.doi.org/10.1038/s10038-020-0750-x.

HANANY, M., RIVOLTA, C. & SHARON, D. 2020. Worldwide carrier frequency and genetic prevalence of autosomal recessive inherited retinal diseases. *Proceedings of the National Academy of Sciences,* 117**,** 2710-2716. http://dx.doi.org/10.1073/pnas.1913179117.

HANKE-GOGOKHIA, C., WU, Z., GERSTNER, C. D., FREDERICK, J. M., ZHANG, H. & BAEHR, W. 2016. Arf-like Protein 3 (ARL3) Regulates Protein Trafficking and Ciliogenesis in

Mouse Photoreceptors. *J Biol Chem,* 291**,** 7142-55. http://dx.doi.org/10.1074/jbc.M115.710954.

HANLON, K. 2017. *Optimisation of therapies for inherited retinal and mitochondrial diseases.* PhD in Genetics, Trinity College Dublin.

HANLON, K. S., KLEINSTIVER, B. P., GARCIA, S. P., ZABOROWSKI, M. P., VOLAK, A., SPIRIG, S. E., . . . GYÖRGY, B. 2019. High levels of AAV vector integration into CRISPR-induced DNA breaks. *Nature Communications,* 10**,** 4439. http://dx.doi.org/10.1038/s41467-019-12449-2.

HARDCASTLE, A. J., THISELTON, D. L., VAN MALDERGEM, L., SAHA, B. K., JAY, M., PLANT, C., . . . BHATTACHARYA, S. 1999. Mutations in the RP2 gene cause disease in 10% of families with familial X-linked retinitis pigmentosa assessed in this study. *Am J Hum Genet,* 64**,** 1210-5. http://dx.doi.org/10.1086/302325.

HARMAN, D. 1956. Aging: a theory based on free radical and radiation chemistry. *J Gerontol,* 11**,** 298-300. http://dx.doi.org/10.1093/geronj/11.3.298.

HARMAN, D. 1972. The biologic clock: the mitochondria? *J Am Geriatr Soc,* 20**,** 145-7. http://dx.doi.org/10.1111/j.1532-5415.1972.tb00787.x.

HARRISON, P. T., HOPPE, N. & MARTIN, U. 2018. Gene editing & stem cells. *Journal of Cystic Fibrosis,* 17**,** 10-16. http://dx.doi.org/10.1016/j.jcf.2017.11.018.

HARUN-OR-RASHID, M., PAPPENHAGEN, N., PALMER, P. G., SMITH, M. A., GEVORGYAN, V., WILSON, G. N., . . . INMAN, D. M. 2018. Structural and Functional Rescue of Chronic Metabolically Stressed Optic Nerves through Respiration. *J Neurosci,* 38**,** 5122-5139. http://dx.doi.org/10.1523/JNEUROSCI.3652-17.2018.

HARUN-OR-RASHID, M., PAPPENHAGEN, N., ZUBRICKY, R., COUGHLIN, L., JASSIM, A. H. & INMAN, D. M. 2020. MCT2 overexpression rescues metabolic vulnerability and protects retinal ganglion cells in two models of glaucoma. *Neurobiol Dis,* 141**,** 104944. http://dx.doi.org/10.1016/j.nbd.2020.104944.

HASHEMI, H., KASHI, A. H., FOTOUHI, A. & MOHAMMAD, K. 2005. Distribution of intraocular pressure in healthy Iranian individuals: the Tehran Eye Study. *Br J Ophthalmol,* 89**,** 652-7. http://dx.doi.org/10.1136/bjo.2004.058057.

HASS, D. T. & BARNSTABLE, C. J. 2016. Uncoupling protein 2 in the glial response to stress: implications for neuroprotection. *Neural Regen Res,* 11**,** 1197-200. http://dx.doi.org/10.4103/1673-5374.189159.

HAUSWIRTH, W., ALEMAN, T., KAUSHAL, S., CIDECIYAN, A., SCHWARTZ, S., WANG, L., . . . JACOBSON, S. 2008. Treatment of leber congenital amaurosis due to RPE65 mutations by ocular subretinal injection of adeno-associated virus gene vector: short-term results of a phase I trial. *Human Gene Therapy,* 19**,** 979-990.

HAYDINGER, C. D., KITTIPASSORN, T. & PEET, D. J. 2020. Power to see-Drivers of aerobic glycolysis in the mammalian retina: A review. *Clin Exp Ophthalmol*. http://dx.doi.org/10.1111/ceo.13833.

HE, Y., LEUNG, K. W., ZHANG, Y. H., DUAN, S., ZHONG, X. F., JIANG, R. Z., . . . GE, J. 2008. Mitochondrial complex I defect induces ROS release and degeneration in trabecular meshwork cells of POAG patients: protection by antioxidants. *Invest Ophthalmol Vis Sci,* 49**,** 1447-58. http://dx.doi.org/10.1167/iovs.07-1361.

HE, Y., LEUNG, K. W., ZHUO, Y. H. & GE, J. 2009. Pro370Leu mutant myocilin impairs mitochondrial functions in human trabecular meshwork cells. *Mol Vis,* 15**,** 815-25.

HEIDUSCHKA, P., JULIEN, S., SCHUETTAUF, F. & SCHNICHELS, S. 2010. Loss of retinal function in aged DBA/2J mice - New insights into retinal neurodegeneration. *Exp Eye Res,* 91**,** 779-83. http://dx.doi.org/10.1016/j.exer.2010.09.001.

HILDINGER, M., AURICCHIO, A., GAO, G., WANG, L., CHIRMULE, N. & WILSON, J. M. 2001. Hybrid vectors based on adeno-associated virus serotypes 2 and 5 for muscle-directed gene transfer. *J Virol,* 75**,** 6199-203. http://dx.doi.org/10.1128/JVI.75.13.6199-6203.2001.

HIONA, A., SANZ, A., KUJOTH, G. C., PAMPLONA, R., SEO, A. Y., HOFER, T., . . . LEEUWENBURGH, C. 2010. Mitochondrial DNA mutations induce mitochondrial dysfunction, apoptosis and sarcopenia in skeletal muscle of mitochondrial DNA mutator mice. *PLoS One,* 5**,** e11468. http://dx.doi.org/10.1371/journal.pone.0011468.

HIRAMI, Y., OSAKADA, F., TAKAHASHI, K., OKITA, K., YAMANAKA, S., IKEDA, H., . . . TAKAHASHI, M. 2009. Generation of retinal cells from mouse and human induced pluripotent stem cells. *Neurosci Lett,* 458**,** 126-31. http://dx.doi.org/10.1016/j.neulet.2009.04.035.

HIRATA, R., CHAMBERLAIN, J., DONG, R. & RUSSELL, D. W. 2002. Targeted transgene insertion into human chromosomes by adeno-associated virus vectors. *Nature Biotechnology,* 20**,** 735-738. http://dx.doi.org/10.1038/nbt0702-735.

HIRSCH, M. L. 2015. Adeno-associated virus inverted terminal repeats stimulate gene editing. *Gene therapy,* 22**,** 190-195. http://dx.doi.org/10.1038/gt.2014.109.

HODGES, R. S., HEATON, R. J., PARKER, J. M., MOLDAY, L. & MOLDAY, R. S. 1988. Antigen-antibody interaction. Synthetic peptides define linear antigenic determinants recognized by monoclonal antibodies directed to the cytoplasmic carboxyl terminus of rhodopsin. *J Biol Chem,* 263**,** 11768-75.

HOLOPAINEN, J. M., CHENG, C. L., MOLDAY, L. L., JOHAL, G., COLEMAN, J., DYKA, F., . . . MOLDAY, R. S. 2010. Interaction and localization of the retinitis pigmentosa protein RP2 and NSF in retinal photoreceptor cells. *Biochemistry,* 49**,** 7439-47. http://dx.doi.org/10.1021/bi1005249.

HOLPER, L., BEN-SHACHAR, D. & MANN, J. J. 2019. Multivariate meta-analyses of mitochondrial complex I and IV in major depressive disorder, bipolar disorder, schizophrenia, Alzheimer disease, and Parkinson disease. *Neuropsychopharmacology,* 44**,** 837-849. http://dx.doi.org/10.1038/s41386-018-0090-0.

HOLTAN, J. P., TEIGEN, K., AUKRUST, I., BRAGADOTTIR, R. & HOUGE, G. 2019. Dominant ARL3-related retinitis pigmentosa. *Ophthalmic Genet,* 40**,** 124-128. http://dx.doi.org/10.1080/13816810.2019.1586965.

HONG, D. H., PAWLYK, B. S., SHANG, J., SANDBERG, M. A., BERSON, E. L. & LI, T. 2000. A retinitis pigmentosa GTPase regulator (RPGR)-deficient mouse model for X-linked retinitis pigmentosa (RP3). *Proc Natl Acad Sci U S A,* 97**,** 3649-54. http://dx.doi.org/10.1073/pnas.060037497.

HOON, M., OKAWA, H., DELLA SANTINA, L. & WONG, R. O. L. 2014. Functional architecture of the retina: Development and disease. *Progress in Retinal and Eye Research,* 42**,** 44-84. http://dx.doi.org/https://doi.org/10.1016/j.preteyeres.2014.06.003.

HORNER, F., WAWRZYNSKI, J. & MACLAREN, R. E. 2019. Novel non-sense mutation in RP2 (c.843_844insT/p.Arg282fs) is associated with a severe phenotype of retinitis pigmentosa without evidence of primary retinal pigment epithelium involvement. *BMJ Case Rep,* 12. http://dx.doi.org/10.1136/bcr-2018-224451.

HOU, X.-W., WANG, Y. & PAN, C.-W. 2020. Metabolomics in Age-Related Macular Degeneration: A Systematic Review. *Investigative Ophthalmology & Visual Science,* 61**,** 13-13. http://dx.doi.org/10.1167/iovs.61.14.13.

HOWDEN, S. E., MAUFORT, J. P., DUFFIN, B. M., ELEFANTY, A. G., STANLEY, E. G. & THOMSON, J. A. 2015. Simultaneous Reprogramming and Gene Correction of Patient Fibroblasts. *Stem Cell Reports,* 5**,** 1109-1118. http://dx.doi.org/10.1016/j.stemcr.2015.10.009.

HOWELL, G. R., LIBBY, R. T., JAKOBS, T. C., SMITH, R. S., PHALAN, F. C., BARTER, J. W., . . . JOHN, S. W. 2007a. Axons of retinal ganglion cells are insulted in the optic nerve early in DBA/2J glaucoma. *J Cell Biol,* 179**,** 1523-37. http://dx.doi.org/10.1083/jcb.200706181.

HOWELL, G. R., LIBBY, R. T., MARCHANT, J. K., WILSON, L. A., COSMA, I. M., SMITH, R. S., . . . JOHN, S. W. 2007b. Absence of glaucoma in DBA/2J mice homozygous for wild-type versions of Gpnmb and Tyrp1. *BMC Genet,* 8**,** 45. http://dx.doi.org/10.1186/1471-2156-8-45.

HSIAU, T., MAURES, T., WAITE, K., YANG, J., KELSO, R., HOLDEN, K. & STONER, R. 2018. Inference of CRISPR Edits from Sanger Trace Data. *bioRxiv***,** 251082. http://dx.doi.org/10.1101/251082.

HU, S., DU, J., CHEN, N., JIA, R., ZHANG, J., LIU, X. & YANG, L. 2020. In Vivo CRISPR/Cas9-Mediated Genome Editing Mitigates Photoreceptor Degeneration in a Mouse Model of X-Linked Retinitis Pigmentosa. *Investigative Ophthalmology & Visual Science,* 61**,** 31-31. http://dx.doi.org/10.1167/iovs.61.4.31.

HU, X., DAI, Y., ZHANG, R., SHANG, K. & SUN, X. 2018. Overexpression of Optic Atrophy Type 1 Protects Retinal Ganglion Cells and Upregulates Parkin Expression in Experimental Glaucoma. *Front Mol Neurosci,* 11**,** 350. http://dx.doi.org/10.3389/fnmol.2018.00350.

HUANG, K. C., WANG, M. L., CHEN, S. J., KUO, J. C., WANG, W. J., NHI NGUYEN, P. N., . . . CHIOU, S. H. 2019. Morphological and Molecular Defects in Human Three-Dimensional Retinal Organoid Model of X-Linked Juvenile Retinoschisis. *Stem Cell Reports,* 13**,** 906-923. http://dx.doi.org/10.1016/j.stemcr.2019.09.010.

HUFNAGEL, R. B., ZEIN, W. M., HURYN, L. A., TURRIFF, A., BLAIN, D. & BROOKS, B. P. 2018. Multimodal imaging including optical coherence tomography in pediatric RP2 patients. *Journal of American Association for Pediatric Ophthalmology and Strabismus {JAAPOS},* 22**,** e49. http://dx.doi.org/10.1016/j.jaapos.2018.07.177.

HUMPHRIES, M. M., RANCOURT, D., FARRAR, G. J., KENNA, P., HAZEL, M., BUSH, R. A., . . . HUMPHRIES, P. 1997. Retinopathy induced in mice by targeted disruption of the rhodopsin gene. *Nat Genet,* 15**,** 216-9. http://dx.doi.org/10.1038/ng0297-216.

HURD, T., ZHOU, W., JENKINS, P., LIU, C. J., SWAROOP, A., KHANNA, H., . . . MARGOLIS, B. 2010. The retinitis pigmentosa protein RP2 interacts with polycystin 2 and regulates cilia-mediated vertebrate development. *Hum Mol Genet,* 19**,** 4330-44. http://dx.doi.org/10.1093/hmg/ddq355.

HURD, T. W., FAN, S. & MARGOLIS, B. L. 2011. Localization of retinitis pigmentosa 2 to cilia is regulated by Importin beta2. *J Cell Sci,* 124**,** 718-26. http://dx.doi.org/10.1242/jcs.070839.

HURLEY, J. B., LINDSAY, K. J. & DU, J. 2015. Glucose, lactate, and shuttling of metabolites in vertebrate retinas. *J Neurosci Res,* 93**,** 1079-92. http://dx.doi.org/10.1002/jnr.23583.

INMAN, D. M. & HARUN-OR-RASHID, M. 2017. Metabolic Vulnerability in the Neurodegenerative Disease Glaucoma. *Front Neurosci,* 11**,** 146. http://dx.doi.org/10.3389/fnins.2017.00146.

INMAN, D. M., LAMBERT, W. S., CALKINS, D. J. & HORNER, P. J. 2013. alpha-Lipoic acid antioxidant treatment limits glaucoma-related retinal ganglion cell death and dysfunction. *PLoS One,* 8**,** e65389. http://dx.doi.org/10.1371/journal.pone.0065389.

ISHIKAWA, M., YOSHITOMI, T., ZORUMSKI, C. F. & IZUMI, Y. 2015. Experimentally Induced Mammalian Models of Glaucoma. *BioMed Research International,* 2015**,** 281214. http://dx.doi.org/10.1155/2015/281214.

ISMAIL, S. A., CHEN, Y. X., RUSINOVA, A., CHANDRA, A., BIERBAUM, M., GREMER, L., . . . WITTINGHOFER, A. 2011. Arl2-GTP and Arl3-GTP regulate a GDI-like transport system for farnesylated cargo. *Nat Chem Biol,* 7**,** 942-9. http://dx.doi.org/10.1038/nchembio.686.

IWASE, A., SUZUKI, Y., ARAIE, M., YAMAMOTO, T., ABE, H., SHIRATO, S., . . . TAJIMI STUDY GROUP, J. G. S. 2004. The prevalence of primary open-angle glaucoma in Japanese: the Tajimi Study. *Ophthalmology,* 111**,** 1641-8. http://dx.doi.org/10.1016/j.ophtha.2004.03.029.

IWATA, M., LEE, Y., YAMASHITA, T., YAGI, T., IWATA, S., CAMERON, A. D. & MAHER, M. J. 2012. The structure of the yeast NADH dehydrogenase (Ndi1) reveals overlapping

binding sites for water- and lipid-soluble substrates. *Proceedings of the National Academy of Sciences,* 109**,** 15247-15252. http://dx.doi.org/10.1073/pnas.1210059109.

IZZOTTI, A., LONGOBARDI, M., CARTIGLIA, C. & SACCA, S. C. 2011. Mitochondrial damage in the trabecular meshwork occurs only in primary open-angle glaucoma and in pseudoexfoliative glaucoma. *PLoS One,* 6**,** e14567. http://dx.doi.org/10.1371/journal.pone.0014567.

IZZOTTI, A., SACCA, S. C., LONGOBARDI, M. & CARTIGLIA, C. 2009. Sensitivity of ocular anterior chamber tissues to oxidative damage and its relevance to the pathogenesis of glaucoma. *Invest Ophthalmol Vis Sci,* 50**,** 5251-8. http://dx.doi.org/10.1167/iovs.09-3871.

IZZOTTI, A., SACCA, S. C., LONGOBARDI, M. & CARTIGLIA, C. 2010. Mitochondrial damage in the trabecular meshwork of patients with glaucoma. *Arch Ophthalmol,* 128**,** 724-30. http://dx.doi.org/10.1001/archophthalmol.2010.87.

JACOBSON, S., CIDECIYAN, A., RATNAKARAM, R., HEON, E., SCHWART, S., ROMAN, A., . . . AL, E. 2012. Gene therapy for leber congenital amaurosis caused by RPE65 mutations: safety and efficacy in 15 children and adults followed up to 3 years. *Archives of Ophthalmology,* 130**,** 9-24.

JAKOBS, T. C., LIBBY, R. T., BEN, Y., JOHN, S. W. & MASLAND, R. H. 2005. Retinal ganglion cell degeneration is topological but not cell type specific in DBA/2J mice. *J Cell Biol,* 171**,** 313-25. http://dx.doi.org/10.1083/jcb.200506099.

JANES, K. A. 2015. An analysis of critical factors for quantitative immunoblotting. *Science signaling,* 8**,** rs2-rs2. http://dx.doi.org/10.1126/scisignal.2005966.

JANSSEN, S. F., GORGELS, T. G., RAMDAS, W. D., KLAVER, C. C., VAN DUIJN, C. M., JANSONIUS, N. M. & BERGEN, A. A. 2013. The vast complexity of primary open angle glaucoma: disease genes, risks, molecular mechanisms and pathobiology. *Prog Retin Eye Res,* 37**,** 31-67. http://dx.doi.org/10.1016/j.preteyeres.2013.09.001.

JASSIM, A. H., COUGHLIN, L., HARUN-OR-RASHID, M., KANG, P. T., CHEN, Y. R. & INMAN, D. M. 2019. Higher Reliance on Glycolysis Limits Glycolytic Responsiveness in Degenerating Glaucomatous Optic Nerve. *Mol Neurobiol,* 56**,** 7097-7112. http://dx.doi.org/10.1007/s12035-019-1576-4.

JAUREGUI, R., TAKAHASHI, V. K. L., PARK, K. S., CUI, X., TAKIUTI, J. T., LIMA DE CARVALHO, J. R., JR. & TSANG, S. H. 2019. Multimodal structural disease progression of retinitis pigmentosa according to mode of inheritance. *Sci Rep,* 9**,** 10712. http://dx.doi.org/10.1038/s41598-019-47251-z.

JAVITT, J. C., ZHOU, Z. & WILLKE, R. J. 2007. Association between Vision Loss and Higher Medical Care Costs in Medicare Beneficiaries: Costs Are Greater for Those with Progressive Vision Loss. *Ophthalmology,* 114**,** 238-245.e1. http://dx.doi.org/10.1016/j.ophtha.2006.07.054.

JAYASUNDERA, T., BRANHAM, K. E., OTHMAN, M., RHOADES, W. R., KAROUKIS, A. J., KHANNA, H., . . . HECKENLIVELY, J. R. 2010. RP2 phenotype and pathogenetic correlations in X-linked retinitis pigmentosa. *Arch Ophthalmol,* 128**,** 915-23. http://dx.doi.org/10.1001/archophthalmol.2010.122.

JEON, C. J., STRETTOI, E. & MASLAND, R. H. 1998. The major cell populations of the mouse retina. *J Neurosci,* 18**,** 8936-46.

JEOUNG, J. W., SEONG, M. W., PARK, S. S., KIM, D. M., KIM, S. H. & PARK, K. H. 2014. Mitochondrial DNA variant discovery in normal-tension glaucoma patients by next-generation sequencing. *Invest Ophthalmol Vis Sci,* 55**,** 986-92. http://dx.doi.org/10.1167/iovs.13-12968.

JIA, L., CEPURNA, W. O., JOHNSON, E. C. & MORRISON, J. C. 2000. Effect of general anesthetics on IOP in rats with experimental aqueous outflow obstruction. *Invest Ophthalmol Vis Sci,* 41**,** 3415-9.

JIANG, F. & DOUDNA, J. A. 2017. CRISPR–Cas9 Structures and Mechanisms. *Annual Review of Biophysics,* 46**,** 505-529. http://dx.doi.org/10.1146/annurev-biophys-062215-010822.

JINEK, M., CHYLINSKI, K., FONFARA, I., HAUER, M., DOUDNA, J. A. & CHARPENTIER, E. 2012. A Programmable Dual-RNA–Guided DNA Endonuclease in Adaptive Bacterial Immunity. *Science,* 337**,** 816-821. http://dx.doi.org/10.1126/science.1225829.

JINEK, M., EAST, A., CHENG, A., LIN, S., MA, E. & DOUDNA, J. 2013. RNA-programmed genome editing in human cells. *Elife,* 2**,** e00471. http://dx.doi.org/10.7554/eLife.00471.

JING, L. 2012. A General Protocol for GST Pull-down. *Bio-protocol,* 2**,** e177. http://dx.doi.org/10.21769/BioProtoc.177.

JO, D. H., SONG, D. W., CHO, C. S., KIM, U. G., LEE, K. J., LEE, K., . . . LEE, J. M. 2019. CRISPR-Cas9-mediated therapeutic editing of Rpe65 ameliorates the disease phenotypes in a mouse model of Leber congenital amaurosis. *Sci Adv,* 5**,** eaax1210. http://dx.doi.org/10.1126/sciadv.aax1210.

JOE, M. K. & TOMAREV, S. I. 2010. Expression of myocilin mutants sensitizes cells to oxidative stress-induced apoptosis: implication for glaucoma pathogenesis. *Am J Pathol,* 176**,** 2880-90. http://dx.doi.org/10.2353/ajpath.2010.090853.

JOHN, S. W. 2005. Mechanistic insights into glaucoma provided by experimental genetics the cogan lecture. *Invest Ophthalmol Vis Sci,* 46**,** 2649-61. http://dx.doi.org/10.1167/iovs.05-0205.

JOHN, S. W., SMITH, R. S., SAVINOVA, O. V., HAWES, N. L., CHANG, B., TURNBULL, D., . . . HECKENLIVELY, J. R. 1998. Essential iris atrophy, pigment dispersion, and glaucoma in DBA/2J mice. *Invest Ophthalmol Vis Sci,* 39**,** 951-62.

JOHNSON, M., MCLAREN, J. W. & OVERBY, D. R. 2017. Unconventional aqueous humor outflow: A review. *Experimental eye research,* 158**,** 94-111. http://dx.doi.org/10.1016/j.exer.2016.01.017.

JU, W. K., KIM, K. Y., DUONG-POLK, K. X., LINDSEY, J. D., ELLISMAN, M. H. & WEINREB, R. N. 2010. Increased optic atrophy type 1 expression protects retinal ganglion cells in a mouse model of glaucoma. *Mol Vis,* 16**,** 1331-42.

JU, W. K., KIM, K. Y., LINDSEY, J. D., ANGERT, M., DUONG-POLK, K. X., SCOTT, R. T., . . . WEINREB, R. N. 2008. Intraocular pressure elevation induces mitochondrial fission and triggers OPA1 release in glaucomatous optic nerve. *Invest Ophthalmol Vis Sci,* 49**,** 4903-11. http://dx.doi.org/10.1167/iovs.07-1661.

JU, W. K., LIU, Q., KIM, K. Y., CROWSTON, J. G., LINDSEY, J. D., AGARWAL, N., . . . WEINREB, R. N. 2007. Elevated hydrostatic pressure triggers mitochondrial fission and decreases cellular ATP in differentiated RGC-5 cells. *Invest Ophthalmol Vis Sci,* 48**,** 2145-51. http://dx.doi.org/10.1167/iovs.06-0573.

JUTTNER, J., SZABO, A., GROSS-SCHERF, B., MORIKAWA, R. K., ROMPANI, S. B., HANTZ, P., . . . ROSKA, B. 2019. Targeting neuronal and glial cell types with synthetic promoter AAVs in mice, non-human primates and humans. *Nat Neurosci,* 22**,** 1345-1356. http://dx.doi.org/10.1038/s41593-019-0431-2.

KANOW, M. A., GIARMARCO, M. M., JANKOWSKI, C. S., TSANTILAS, K., ENGEL, A. L., DU, J., . . . HURLEY, J. B. 2017. Biochemical adaptations of the retina and retinal pigment

epithelium support a metabolic ecosystem in the vertebrate eye. *Elife,* 6. http://dx.doi.org/10.7554/eLife.28899.

KAPETANAKIS, V. V., CHAN, M. P., FOSTER, P. J., COOK, D. G., OWEN, C. G. & RUDNICKA, A. R. 2016. Global variations and time trends in the prevalence of primary open angle glaucoma (POAG): a systematic review and meta-analysis. *Br J Ophthalmol,* 100**,** 86-93. http://dx.doi.org/10.1136/bjophthalmol-2015-307223.

KARCZEWSKI, K. J., FRANCIOLI, L. C., TIAO, G., CUMMINGS, B. B., ALFOLDI, J., WANG, Q., . . . MACARTHUR, D. G. 2020. The mutational constraint spectrum quantified from variation in 141,456 humans. *Nature,* 581**,** 434-443. http://dx.doi.org/10.1038/s41586-020-2308-7.

KARNKOWSKA, A. & HAMPL, V. 2016. The curious case of vanishing mitochondria. *Microb Cell,* 3**,** 491-494. http://dx.doi.org/10.15698/mic2016.10.531.

KATOH, K., ROZEWICKI, J. & YAMADA, K. D. 2019. MAFFT online service: multiple sequence alignment, interactive sequence choice and visualization. *Brief Bioinform,* 20**,** 1160-1166. http://dx.doi.org/10.1093/bib/bbx108.

KAUPPILA, T. E. S., KAUPPILA, J. H. K. & LARSSON, N. G. 2017. Mammalian Mitochondria and Aging: An Update. *Cell Metab,* 25**,** 57-71. http://dx.doi.org/10.1016/j.cmet.2016.09.017.

KENNEDY, S. R., SALK, J. J., SCHMITT, M. W. & LOEB, L. A. 2013. Ultra-sensitive sequencing reveals an age-related increase in somatic mitochondrial mutations that are inconsistent with oxidative damage. *PLoS Genet,* 9**,** e1003794. http://dx.doi.org/10.1371/journal.pgen.1003794.

KHABOU, H., CORDEAU, C., PACOT, L., FISSON, S. & DALKARA, D. 2018a. Dosage Thresholds and Influence of Transgene Cassette in Adeno-Associated Virus-Related Toxicity. *Hum Gene Ther,* 29**,** 1235-1241. http://dx.doi.org/10.1089/hum.2018.144.

KHABOU, H., GARITA-HERNANDEZ, M., CHAFFIOL, A., REICHMAN, S., JAILLARD, C., BRAZHNIKOVA, E., . . . DALKARA, D. 2018b. Noninvasive gene delivery to foveal cones for vision restoration. *JCI Insight,* 3. http://dx.doi.org/10.1172/jci.insight.96029.

KHACHATRYAN, N., PISTILLI, M., MAGUIRE, M. G., SALOWE, R. J., FERTIG, R. M., MOORE, T., . . . O'BRIEN, J. M. 2019. Primary Open-Angle African American Glaucoma

Genetics (POAAGG) Study: gender and risk of POAG in African Americans. *PLoS One,* 14**,** e0218804. http://dx.doi.org/10.1371/journal.pone.0218804.

KIM, E., KOO, T., PARK, S. W., KIM, D., KIM, K., CHO, H.-Y., . . . KIM, J.-S. 2017. In vivo genome editing with a small Cas9 orthologue derived from Campylobacter jejuni. *Nature Communications,* 8**,** 14500. http://dx.doi.org/10.1038/ncomms14500.

KIM, E. J., GRANT, G. R., BOWMAN, A. S., HAIDER, N., GUDISEVA, H. V. & CHAVALI, V. R. M. 2018. Complete Transcriptome Profiling of Normal and Age-Related Macular Degeneration Eye Tissues Reveals Dysregulation of Anti-Sense Transcription. *Scientific Reports,* 8**,** 3040. http://dx.doi.org/10.1038/s41598-018-21104-7.

KIM, H. & CHOI, B. 2019. Nonlinear Relationship Between Blood Pressure and Glaucoma in US Adults. *Am J Hypertens,* 32**,** 308-316. http://dx.doi.org/10.1093/ajh/hpy186.

KIM, K. Y., PERKINS, G. A., SHIM, M. S., BUSHONG, E., ALCASID, N., JU, S., . . . JU, W. K. 2015. DRP1 inhibition rescues retinal ganglion cells and their axons by preserving mitochondrial integrity in a mouse model of glaucoma. *Cell Death Dis,* 6**,** e1839. http://dx.doi.org/10.1038/cddis.2015.180.

KIMURA, A., NORO, T. & HARADA, T. 2020. Role of animal models in glaucoma research. *Neural regeneration research,* 15**,** 1257-1258. http://dx.doi.org/10.4103/1673-5374.272578.

KINGMAN, S. 2004. Glaucoma is second leading cause of blindness globally. *Bull World Health Organ,* 82**,** 887-8. http://dx.doi.org//S0042-96862004001100019.

KITAJIMA-IHARA, T. & YAGI, T. 1998. Rotenone-insensitive internal NADH-quinone oxidoreductase of Saccharomyces cerevisiae mitochondria: the enzyme expressed in Escherichia coli acts as a member of the respiratory chain in the host cells. *FEBS Lett,* 421**,** 37-40. http://dx.doi.org/10.1016/s0014-5793(97)01533-0.

KONG, F., LI, W., LI, X., ZHENG, Q., DAI, X., ZHOU, X., . . . PANG, J. J. 2010. Self-complementary AAV5 vector facilitates quicker transgene expression in photoreceptor and retinal pigment epithelial cells of normal mouse. *Exp Eye Res,* 90**,** 546-54. http://dx.doi.org/10.1016/j.exer.2010.01.011.

KOSICKI, M., TOMBERG, K. & BRADLEY, A. 2018. Repair of double-strand breaks induced by CRISPR–Cas9 leads to large deletions and complex rearrangements. *Nature Biotechnology,* 36**,** 765-771. http://dx.doi.org/10.1038/nbt.4192.

KOUASSI NZOUGHET, J., CHAO DE LA BARCA, J. M., GUEHLOUZ, K., LERUEZ, S., COULBAULT, L., ALLOUCHE, S., . . . REYNIER, P. 2019. Nicotinamide Deficiency in

Primary Open-Angle Glaucoma. *Invest Ophthalmol Vis Sci,* 60**,** 2509-2514. http://dx.doi.org/10.1167/iovs.19-27099.

KOWLURU, R. A. 2017. Diabetic retinopathy, metabolic memory and epigenetic modifications. *Vision Res,* 139**,** 30-38. http://dx.doi.org/10.1016/j.visres.2017.02.011.

KOWLURU, R. A. & MISHRA, M. 2015. Oxidative stress, mitochondrial damage and diabetic retinopathy. *Biochim Biophys Acta,* 1852**,** 2474-83. http://dx.doi.org/10.1016/j.bbadis.2015.08.001.

KRISHNADAS, R. & RAMAKRISHNAN, R. 2001. Secondary glaucomas: the tasks ahead. *Community Eye Health,* 14**,** 40-2.

KRISHNAMOORTHY, R. R., CLARK, A. F., DAUDT, D., VISHWANATHA, J. K. & YORIO, T. 2013. A forensic path to RGC-5 cell line identification: lessons learned. *Invest Ophthalmol Vis Sci,* 54**,** 5712-9. http://dx.doi.org/10.1167/iovs.13-12085.

KRUCZEK, K. & SWAROOP, A. 2020. Pluripotent stem cell-derived retinal organoids for disease modeling and development of therapies. *Stem Cells*. http://dx.doi.org/10.1002/stem.3239.

KUHNEL, K., VELTEL, S., SCHLICHTING, I. & WITTINGHOFER, A. 2006. Crystal structure of the human retinitis pigmentosa 2 protein and its interaction with Arl3. *Structure,* 14**,** 367-78. http://dx.doi.org/10.1016/j.str.2005.11.008.

KUJOTH, G. C., HIONA, A., PUGH, T. D., SOMEYA, S., PANZER, K., WOHLGEMUTH, S. E., . . . PROLLA, T. A. 2005. Mitochondrial DNA mutations, oxidative stress, and apoptosis in mammalian aging. *Science,* 309**,** 481-4. http://dx.doi.org/10.1126/science.1112125.

KURATA, K., HOSONO, K., HAYASHI, T., MIZOBUCHI, K., KATAGIRI, S., MIYAMICHI, D., . . . HOTTA, Y. 2019. X-linked Retinitis Pigmentosa in Japan: Clinical and Genetic Findings in Male Patients and Female Carriers. *Int J Mol Sci,* 20. http://dx.doi.org/10.3390/ijms20061518.

KWON, Y. H., FINGERT, J. H., KUEHN, M. H. & ALWARD, W. L. 2009. Primary open-angle glaucoma. *N Engl J Med,* 360**,** 1113-24. http://dx.doi.org/10.1056/NEJMra0804630.

LABUN, K., MONTAGUE, T. G., KRAUSE, M., TORRES CLEUREN, Y. N., TJELDNES, H. & VALEN, E. 2019. CHOPCHOP v3: expanding the CRISPR web toolbox beyond

genome editing. *Nucleic Acids Research,* 47**,** W171-W174. http://dx.doi.org/10.1093/nar/gkz365.

LANE, A., JOVANOVIC, K., SHORTALL, C., OTTAVIANI, D., PANES, A. B., SCHWARZ, N., . . . CHEETHAM, M. E. 2020. Modeling and Rescue of RP2 Retinitis Pigmentosa Using iPSC-Derived Retinal Organoids. *Stem Cell Reports,* 15**,** 67-79. http://dx.doi.org/10.1016/j.stemcr.2020.05.007.

LARSSON, N. G. 2010. Somatic mitochondrial DNA mutations in mammalian aging. *Annu Rev Biochem,* 79**,** 683-706. http://dx.doi.org/10.1146/annurev-biochem-060408-093701.

LASCARATOS, G., CHAU, K. Y., ZHU, H., GKOTSI, D., KING, R., GOUT, I., . . . GARWAY-HEATH, D. F. 2015. Resistance to the most common optic neuropathy is associated with systemic mitochondrial efficiency. *Neurobiol Dis,* 82**,** 78-85. http://dx.doi.org/10.1016/j.nbd.2015.05.012.

LATELLA, M. C., DI SALVO, M. T., COCCHIARELLA, F., BENATI, D., GRISENDI, G., COMITATO, A., . . . RECCHIA, A. 2016. In vivo Editing of the Human Mutant Rhodopsin Gene by Electroporation of Plasmid-based CRISPR/Cas9 in the Mouse Retina. *Mol Ther Nucleic Acids,* 5**,** e389. http://dx.doi.org/10.1038/mtna.2016.92.

LE, W. D., XIE, W. J. & APPEL, S. H. 1999. Protective role of heme oxygenase-1 in oxidative stress-induced neuronal injury. *J Neurosci Res,* 56**,** 652-8. http://dx.doi.org/10.1002/(SICI)1097-4547(19990615)56:6<652::AID-JNR11>3.0.CO;2-5.

LEACH, L. L., BUCHHOLZ, D. E., NADAR, V. P., LOWENSTEIN, S. E. & CLEGG, D. O. 2015. Canonical/beta-catenin Wnt pathway activation improves retinal pigmented epithelium derivation from human embryonic stem cells. *Invest Ophthalmol Vis Sci,* 56**,** 1002-13. http://dx.doi.org/10.1167/iovs.14-15835.

LEBHERZ, C., MAGUIRE, A., TANG, W., BENNETT, J. & WILSON, J. M. 2008. Novel AAV serotypes for improved ocular gene transfer. *J Gene Med,* 10**,** 375-82. http://dx.doi.org/10.1002/jgm.1126.

LEE, J. K., JEONG, E., LEE, J., JUNG, M., SHIN, E., KIM, Y.-H., . . . KIM, J.-S. 2018. Directed evolution of CRISPR-Cas9 to increase its specificity. *Nature Communications,* 9**,** 3048. http://dx.doi.org/10.1038/s41467-018-05477-x.

LEE, S., SHECK, L., CROWSTON, J. G., VAN BERGEN, N. J., O'NEILL, E. C., O'HARE, F., . . . TROUNCE, I. A. 2012. Impaired complex-I-linked respiration and ATP synthesis in

primary open-angle glaucoma patient lymphoblasts. *Invest Ophthalmol Vis Sci,* 53**,** 2431-7. http://dx.doi.org/10.1167/iovs.12-9596.

LERUEZ, S., MARILL, A., BRESSON, T., DE SAINT MARTIN, G., BUISSET, A., MULLER, J., . . . CHAO DE LA BARCA, J. M. 2018. A Metabolomics Profiling of Glaucoma Points to Mitochondrial Dysfunction, Senescence, and Polyamines Deficiency. *Invest Ophthalmol Vis Sci,* 59**,** 4355-4361. http://dx.doi.org/10.1167/iovs.18-24938.

LESKE, M. C., CONNELL, A. M., WU, S. Y., HYMAN, L. & SCHACHAT, A. P. 1997. Distribution of intraocular pressure. The Barbados Eye Study. *Arch Ophthalmol,* 115**,** 1051-7. http://dx.doi.org/10.1001/archopht.1997.01100160221012.

LESKE, M. C., WU, S. Y., HONKANEN, R., NEMESURE, B., SCHACHAT, A., HYMAN, L., . . . BARBADOS EYE STUDIES, G. 2007. Nine-year incidence of open-angle glaucoma in the Barbados Eye Studies. *Ophthalmology,* 114**,** 1058-64. http://dx.doi.org/10.1016/j.ophtha.2006.08.051.

LEVEILLARD, T., PHILP, N. J. & SENNLAUB, F. 2019. Is Retinal Metabolic Dysfunction at the Center of the Pathogenesis of Age-related Macular Degeneration? *Int J Mol Sci,* 20. http://dx.doi.org/10.3390/ijms20030762.

LEVITT, N., BRIGGS, D., GIL, A. & PROUDFOOT, N. J. 1989. Definition of an efficient synthetic poly(A) site. *Genes Dev,* 3**,** 1019-25. http://dx.doi.org/10.1101/gad.3.7.1019.

LI, A., TANNER, M. R., LEE, C. M., HURLEY, A. E., DE GIORGI, M., JARRETT, K. E., . . . LAGOR, W. R. 2020. AAV-CRISPR Gene Editing Is Negated by Pre-existing Immunity to Cas9. *Molecular Therapy,* 28**,** 1432-1441. http://dx.doi.org/10.1016/j.ymthe.2020.04.017.

LI, B., CASTANO, A. P., HUDSON, T. E., NOWLIN, B. T., LIN, S. L., BONVENTRE, J. V., . . . DUFFIELD, J. S. 2010. The melanoma-associated transmembrane glycoprotein Gpnmb controls trafficking of cellular debris for degradation and is essential for tissue repair. *FASEB J,* 24**,** 4767-81. http://dx.doi.org/10.1096/fj.10-154757.

LI, F., HUNG, S. S. C., MOHD KHALID, M. K. N., WANG, J. H., CHRYSOSTOMOU, V., WONG, V. H. Y., . . . LIU, G. S. 2019a. Utility of Self-Destructing CRISPR/Cas Constructs for Targeted Gene Editing in the Retina. *Hum Gene Ther,* 30**,** 1349-1360. http://dx.doi.org/10.1089/hum.2019.021.

LI, J., HONG, S., CHEN, W., ZUO, E. & YANG, H. 2019b. Advances in detecting and reducing off-target effects generated by CRISPR-mediated genome editing. *Journal of*

Genetics and Genomics, 46**,** 513-521. http://dx.doi.org/https://doi.org/10.1016/j.jgg.2019.11.002.

LI, K., WANG, G., ANDERSEN, T., ZHOU, P. & PU, W. T. 2014. Optimization of genome engineering approaches with the CRISPR/Cas9 system. *PLoS One,* 9**,** e105779. http://dx.doi.org/10.1371/journal.pone.0105779.

LI, L., KHAN, N., HURD, T., GHOSH, A. K., CHENG, C., MOLDAY, R., . . . KHANNA, H. 2013. Ablation of the X-linked retinitis pigmentosa 2 (Rp2) gene in mice results in opsin mislocalization and photoreceptor degeneration. *Invest Ophthalmol Vis Sci,* 54**,** 4503-11. http://dx.doi.org/10.1167/iovs.13-12140.

LI, L., RAO, K. N. & KHANNA, H. 2019c. Structural but Not Functional Alterations in Cones in the Absence of the Retinal Disease Protein Retinitis Pigmentosa 2 (RP2) in a Cone-Only Retina. *Front Genet,* 10**,** 323. http://dx.doi.org/10.3389/fgene.2019.00323.

LI, L., RAO, K. N., ZHENG-LE, Y., HURD, T. W., LILLO, C. & KHANNA, H. 2015. Loss of retinitis pigmentosa 2 (RP2) protein affects cone photoreceptor sensory cilium elongation in mice. *Cytoskeleton (Hoboken),* 72**,** 447-54. http://dx.doi.org/10.1002/cm.21255.

LI, P., KLEINSTIVER, B. P., LEON, M. Y., PREW, M. S., NAVARRO-GOMEZ, D., GREENWALD, S. H., . . . LIU, Q. 2018. Allele-Specific CRISPR-Cas9 Genome Editing of the Single-Base P23H Mutation for Rhodopsin-Associated Dominant Retinitis Pigmentosa. *CRISPR J,* 1**,** 55-64. http://dx.doi.org/10.1089/crispr.2017.0009.

LI, Q., MILLER, R., HAN, P.-Y., PANG, J., DINCULESCU, A., CHIODO, V. & HAUSWIRTH, W. W. 2008. Intraocular route of AAV2 vector administration defines humoral immune response and therapeutic potential. *Molecular vision,* 14**,** 1760-1769.

LI, T., SNYDER, W. K., OLSSON, J. E. & DRYJA, T. P. 1996. Transgenic mice carrying the dominant rhodopsin mutation P347S: evidence for defective vectorial transport of rhodopsin to the outer segments. *Proc Natl Acad Sci U S A,* 93**,** 14176-81. http://dx.doi.org/10.1073/pnas.93.24.14176.

LIAO, C., ASHLEY, N., DIOT, A., MORTEN, K., PHADWAL, K., WILLIAMS, A., . . . POULTON, J. 2017. Dysregulated mitophagy and mitochondrial organization in optic atrophy due to OPA1 mutations. *Neurology,* 88**,** 131-142. http://dx.doi.org/10.1212/WNL.0000000000003491.

LIBBY, R. T., ANDERSON, M. G., PANG, I. H., ROBINSON, Z. H., SAVINOVA, O. V., COSMA, I. M., . . . JOHN, S. W. 2005a. Inherited glaucoma in DBA/2J mice: pertinent disease

features for studying the neurodegeneration. *Vis Neurosci,* 22**,** 637-48. http://dx.doi.org/10.1017/S0952523805225130.

LIBBY, R. T., LI, Y., SAVINOVA, O. V., BARTER, J., SMITH, R. S., NICKELLS, R. W. & JOHN, S. W. 2005b. Susceptibility to neurodegeneration in a glaucoma is modified by Bax gene dosage. *PLoS Genet,* 1**,** 17-26. http://dx.doi.org/10.1371/journal.pgen.0010004.

LINDE, L., BOELZ, S., NEU-YILIK, G., KULOZIK, A. E. & KEREM, B. 2007a. The efficiency of nonsense-mediated mRNA decay is an inherent character and varies among different cells. *Eur J Hum Genet,* 15**,** 1156-62. http://dx.doi.org/10.1038/sj.ejhg.5201889.

LINDE, L., BOELZ, S., NISSIM-RAFINIA, M., OREN, Y. S., WILSCHANSKI, M., YAACOV, Y., . . . KEREM, B. 2007b. Nonsense-mediated mRNA decay affects nonsense transcript levels and governs response of cystic fibrosis patients to gentamicin. *J Clin Invest,* 117**,** 683-92. http://dx.doi.org/10.1172/JCI28523.

LITTLE, A. 2019. *Functional analysis of RP2 and ARL3 in X-linked retinitis pigmentosa.* University of Edinburgh.

LIU, F., CHEN, J., YU, S., RAGHUPATHY, R. K., LIU, X., QIN, Y., . . . LIU, M. 2015. Knockout of RP2 decreases GRK1 and rod transducin subunits and leads to photoreceptor degeneration in zebrafish. *Hum Mol Genet,* 24**,** 4648-59. http://dx.doi.org/10.1093/hmg/ddv197.

LIU, F., QIN, Y., YU, S., SOARES, D. C., YANG, L., WENG, J., . . . LIU, M. 2017. Pathogenic mutations in retinitis pigmentosa 2 predominantly result in loss of RP2 protein stability in humans and zebrafish. *J Biol Chem,* 292**,** 6225-6239. http://dx.doi.org/10.1074/jbc.M116.760314.

LIU, L., WEI, Y. & CHEN, H. 2001. [Identification of a nonsense mutation causing X-linked RP2 in two Chinese families]. *Zhonghua Yi Xue Za Zhi,* 81**,** 71-2.

LIU, M., REHMAN, S., TANG, X., GU, K., FAN, Q., CHEN, D. & MA, W. 2019. Methodologies for Improving HDR Efficiency. *Frontiers in Genetics,* 9. http://dx.doi.org/10.3389/fgene.2018.00691.

LIU, Y. & ALLINGHAM, R. R. 2017. Major review: Molecular genetics of primary open-angle glaucoma. *Exp Eye Res,* 160**,** 62-84. http://dx.doi.org/10.1016/j.exer.2017.05.002.

LLADO SANTAEULARIA, M., ESPOSITO, F., IODICE, C., MARROCCO, E. & AURICCHIO, A. 2019. Homology-Independent Targeted Integration in Photoreceptors. *Investigative Ophthalmology & Visual Science,* 60**,** 4228-4228.

LOCK, M., MCGORRAY, S., AURICCHIO, A., AYUSO, E., BEECHAM, E. J., BLOUIN-TAVEL, V., . . . SNYDER, R. O. 2010. Characterization of a recombinant adeno-associated virus type 2 Reference Standard Material. *Hum Gene Ther,* 21**,** 1273-85. http://dx.doi.org/10.1089/hum.2009.223.

LOFTUS, S. K., ANTONELLIS, A., MATERA, I., RENAUD, G., BAXTER, L. L., REID, D., . . . PAVAN, W. J. 2009. Gpnmb is a melanoblast-expressed, MITF-dependent gene. *Pigment cell & melanoma research,* 22**,** 99-110. http://dx.doi.org/10.1111/j.1755-148X.2008.00518.x.

LOGAN, A., SHABALINA, I. G., PRIME, T. A., ROGATTI, S., KALINOVICH, A. V., HARTLEY, R. C., . . . MURPHY, M. P. 2014. In vivo levels of mitochondrial hydrogen peroxide increase with age in mtDNA mutator mice. *Aging Cell,* 13**,** 765-8. http://dx.doi.org/10.1111/acel.12212.

LOPEZ-OTIN, C., BLASCO, M. A., PARTRIDGE, L., SERRANO, M. & KROEMER, G. 2013. The hallmarks of aging. *Cell,* 153**,** 1194-217. http://dx.doi.org/10.1016/j.cell.2013.05.039.

LUKOWSKI, S. W., LO, C. Y., SHAROV, A. A., NGUYEN, Q., FANG, L., HUNG, S. S., . . . WONG, R. C. 2019a. A single-cell transcriptome atlas of the adult human retina. *The EMBO Journal,* 38**,** e100811. http://dx.doi.org/https://doi.org/10.15252/embj.2018100811.

LUO, S., VALENCIA, C. A., ZHANG, J., LEE, N. C., SLONE, J., GUI, B., . . . HUANG, T. 2018. Biparental Inheritance of Mitochondrial DNA in Humans. *Proc Natl Acad Sci U S A,* 115**,** 13039-13044. http://dx.doi.org/10.1073/pnas.1810946115.

LUSTHAUS, J. & GOLDBERG, I. 2019. Current management of glaucoma. *Med J Aust,* 210**,** 180-187. http://dx.doi.org/10.5694/mja2.50020.

LYRAKI, R., LOKAJ, M., SOARES, D. C., LITTLE, A., VERMEREN, M., MARSH, J. A., . . . HURD, T. 2018. Characterization of a novel RP2-OSTF1 interaction and its implication for actin remodelling. *J Cell Sci,* 131. http://dx.doi.org/10.1242/jcs.211748.

LYRAKI, R., MEGAW, R. & HURD, T. 2016. Disease mechanisms of X-linked retinitis pigmentosa due to RP2 and RPGR mutations. *Biochem Soc Trans,* 44**,** 1235-1244. http://dx.doi.org/10.1042/BST20160148.

MA, C. C., WANG, Z. L., XU, T., HE, Z. Y. & WEI, Y. Q. 2020. The approved gene therapy drugs worldwide: from 1998 to 2019. *Biotechnol Adv,* 40**,** 107502. http://dx.doi.org/10.1016/j.biotechadv.2019.107502.

MA, Y., KAWASAKI, R., DOBSON, L. P., RUDDLE, J. B., KEARNS, L. S., WONG, T. Y. & MACKEY, D. A. 2012. Quantitative Analysis of Retinal Vessel Attenuation in Eyes with Retinitis Pigmentosa. *Investigative Ophthalmology & Visual Science,* 53**,** 4306-4314. http://dx.doi.org/10.1167/iovs.11-8596.

MACGREGOR, S., ONG, J. S., AN, J., HAN, X., ZHOU, T., SIGGS, O. M., . . . HEWITT, A. W. 2018. Genome-wide association study of intraocular pressure uncovers new pathways to glaucoma. *Nat Genet,* 50**,** 1067-1071. http://dx.doi.org/10.1038/s41588-018-0176-y.

MAEDA, A., TSUJIYA, S., HIGASHIDE, T., TOIDA, K., TODO, T., UEYAMA, T., . . . SUGIYAMA, K. 2006. Circadian intraocular pressure rhythm is generated by clock genes. *Invest Ophthalmol Vis Sci,* 47**,** 4050-2. http://dx.doi.org/10.1167/iovs.06-0183.

MAEDER, M. L., STEFANIDAKIS, M., WILSON, C. J., BARAL, R., BARRERA, L. A., BOUNOUTAS, G. S., . . . JIANG, H. 2019. Development of a gene-editing approach to restore vision loss in Leber congenital amaurosis type 10. *Nature Medicine,* 25**,** 229-233. http://dx.doi.org/10.1038/s41591-018-0327-9.

MAGUIRE, A. M., RUSSELL, S., WELLMAN, J. A., CHUNG, D. C., YU, Z. F., TILLMAN, A., . . . BENNETT, J. 2019. Efficacy, Safety, and Durability of Voretigene Neparvovec-rzyl in RPE65 Mutation-Associated Inherited Retinal Dystrophy: Results of Phase 1 and 3 Trials. *Ophthalmology,* 126**,** 1273-1285. http://dx.doi.org/10.1016/j.ophtha.2019.06.017.

MAGUIRE, A. M., SIMONELLI, F., PIERCE, E. A., PUGH, E. N., JR., MINGOZZI, F., BENNICELLI, J., . . . BENNETT, J. 2008. Safety and efficacy of gene transfer for Leber's congenital amaurosis. *N Engl J Med,* 358**,** 2240-8. http://dx.doi.org/10.1056/NEJMoa0802315.

MALONEY, D. M. 2020. *An Exploration of Mitochondrially Targeted Gene Therapies for Ocular Disorders.* Trinity College Dublin.

MALONEY, D. M., CHADDERTON, N., MILLINGTON-WARD, S., PALFI, A., SHORTALL, C., O'BYRNE, J. J., . . . FARRAR, G. J. 2020. Optimized OPA1 Isoforms 1 and 7 Provide Therapeutic Benefit in Models of Mitochondrial Dysfunction. *Frontiers in Neuroscience,* 14. http://dx.doi.org/10.3389/fnins.2020.571479.

MAO, H., JAMES, T., SCHWEIN, A., SHABASHVILI, A. E., HAUSWIRTH, W. W., GORBATYUK, M. S. & LEWIN, A. S. 2011. AAV Delivery of Wild-Type Rhodopsin Preserves Retinal Function in a Mouse Model of Autosomal Dominant Retinitis Pigmentosa. *Human Gene Therapy,* 22**,** 567-575. http://dx.doi.org/10.1089/hum.2010.140.

MAO, Z., BOZZELLA, M., SELUANOV, A. & GORBUNOVA, V. 2008. Comparison of nonhomologous end joining and homologous recombination in human cells. *DNA Repair,* 7**,** 1765-1771. http://dx.doi.org/https://doi.org/10.1016/j.dnarep.2008.06.018.

MARELLA, M., SEO, B. B., THOMAS, B. B., MATSUNO-YAGI, A. & YAGI, T. 2010. Successful amelioration of mitochondrial optic neuropathy using the yeast NDI1 gene in a rat animal model. *PLoS One,* 5**,** e11472. http://dx.doi.org/10.1371/journal.pone.0011472.

MARESCA, M., LIN, V. G., GUO, N. & YANG, Y. 2013. Obligate ligation-gated recombination (ObLiGaRe): custom-designed nuclease-mediated targeted integration through nonhomologous end joining. *Genome Res,* 23**,** 539-46. http://dx.doi.org/10.1101/gr.145441.112.

MARQUES, A. P., RAMKE, J., CAIRNS, J., BUTT, T., ZHANG, J. H., FAAL, H. B., . . . BURTON, M. J. 2020. Estimating the global cost of vision impairment and its major causes: protocol for a systematic review. *BMJ Open,* 10**,** e036689. http://dx.doi.org/10.1136/bmjopen-2019-036689.

MARTIN, W. & MENTEL, M. 2010. The Origin of Mitochondria. *Nature Education,* 3**,** 58.

MARTÍNEZ-REYES, I. & CHANDEL, N. S. 2020. Mitochondrial TCA cycle metabolites control physiology and disease. *Nature Communications,* 11**,** 102. http://dx.doi.org/10.1038/s41467-019-13668-3.

MASLAND, R. H. 2012. The neuronal organization of the retina. *Neuron,* 76**,** 266-280. http://dx.doi.org/10.1016/j.neuron.2012.10.002.

MASUDA, T., SHIMAZAWA, M. & HARA, H. 2017. Retinal Diseases Associated with Oxidative Stress and the Effects of a Free Radical Scavenger (Edaravone). *Oxid Med Cell Longev,* 2017**,** 9208489. http://dx.doi.org/10.1155/2017/9208489.

MAY-SIMERA, H. L., WAN, Q., JHA, B. S., HARTFORD, J., KHRISTOV, V., DEJENE, R., . . . BHARTI, K. 2018. Primary Cilium-Mediated Retinal Pigment Epithelium Maturation Is Disrupted in Ciliopathy Patient Cells. *Cell Rep,* 22**,** 189-205. http://dx.doi.org/10.1016/j.celrep.2017.12.038.

MCCULLOCH, D. L., MARMOR, M. F., BRIGELL, M. G., HAMILTON, R., HOLDER, G. E., TZEKOV, R. & BACH, M. 2015. ISCEV Standard for full-field clinical electroretinography (2015 update). *Doc Ophthalmol,* 130**,** 1-12. http://dx.doi.org/10.1007/s10633-014-9473-7.

MCCULLOUGH, K. T., BOYE, S. L., FAJARDO, D., CALABRO, K., PETERSON, J. J., STRANG, C. E., . . . BOYE, S. E. 2019. Somatic Gene Editing of GUCY2D by AAV-CRISPR/Cas9 Alters Retinal Structure and Function in Mouse and Macaque. *Hum Gene Ther,* 30**,** 571-589. http://dx.doi.org/10.1089/hum.2018.193.

MCELROY, G. S., RECZEK, C. R., REYFMAN, P. A., MITHAL, D. S., HORBINSKI, C. M. & CHANDEL, N. S. 2020. NAD+ Regeneration Rescues Lifespan, but Not Ataxia, in a Mouse Model of Brain Mitochondrial Complex I Dysfunction. *Cell Metab,* 32**,** 301-308 e6. http://dx.doi.org/10.1016/j.cmet.2020.06.003.

MCWILLIAM, P., FARRAR, G. J., KENNA, P., BRADLEY, D. G., HUMPHRIES, M. M., SHARP, E. M., . . . HUMPHRIES, P. 1989. Autosomal dominant retinitis pigmentosa (ADRP): Localization of an ADRP gene to the long arm of chromosome 3. *Genomics,* 5**,** 619-622. http://dx.doi.org/https://doi.org/10.1016/0888-7543(89)90031-1.

MEARS, A. J., GIESER, L., YAN, D., CHEN, C., FAHRNER, S., HIRIYANNA, S., . . . SWAROOP, A. 1999. Protein-truncation mutations in the RP2 gene in a North American cohort of families with X-linked retinitis pigmentosa. *Am J Hum Genet,* 64**,** 897-900. http://dx.doi.org/10.1086/302298.

MECOCCI, P., MACGARVEY, U., KAUFMAN, A. E., KOONTZ, D., SHOFFNER, J. M., WALLACE, D. C. & BEAL, M. F. 1993. Oxidative damage to mitochondrial DNA shows marked age-dependent increases in human brain. *Ann Neurol,* 34**,** 609-16. http://dx.doi.org/10.1002/ana.410340416.

MEGAW, R., ABU-ARAFEH, H., JUNGNICKEL, M., MELLOUGH, C., GURNIAK, C., WITKE, W., . . . FFRENCH-CONSTANT, C. 2017. Gelsolin dysfunction causes photoreceptor loss in induced pluripotent cell and animal retinitis pigmentosa models. *Nat Commun,* 8**,** 271. http://dx.doi.org/10.1038/s41467-017-00111-8.

MEISSNER, C., BRUSE, P., MOHAMED, S. A., SCHULZ, A., WARNK, H., STORM, T. & OEHMICHEN, M. 2008. The 4977 bp deletion of mitochondrial DNA in human skeletal muscle, heart and different areas of the brain: a useful biomarker or more? *Exp Gerontol,* 43**,** 645-52. http://dx.doi.org/10.1016/j.exger.2008.03.004.

MEISTER, M. & TESSIER-LAVIGNE, M. 2013. Low-Level Visual Processing: The Retina. *In:* KANDEL, E. R., SCHWARTZ, J. H., JESSELL, T. M., SIEGELBAUM, S. A. & HUDSPETH, A. J. (eds.) *Principles of Neural Science.* 5th ed. New York: McGraw-Hill.

MELLOUGH, C. B., COLLIN, J., KHAZIM, M., WHITE, K., SERNAGOR, E., STEEL, D. H. & LAKO, M. 2015. IGF-1 Signaling Plays an Important Role in the Formation of Three-Dimensional Laminated Neural Retina and Other Ocular Structures From Human Embryonic Stem Cells. *Stem Cells,* 33**,** 2416-30. http://dx.doi.org/10.1002/stem.2023.

MELLOUGH, C. B., COLLIN, J., QUEEN, R., HILGEN, G., DORGAU, B., ZERTI, D., . . . LAKO, M. 2019. Systematic Comparison of Retinal Organoid Differentiation from Human Pluripotent Stem Cells Reveals Stage Specific, Cell Line, and Methodological Differences. *Stem Cells Transl Med,* 8**,** 694-706. http://dx.doi.org/10.1002/sctm.18-0267.

MEYER, J. G., GARCIA, T. Y., SCHILLING, B., GIBSON, B. W. & LAMBA, D. A. 2019. Proteome and Secretome Dynamics of Human Retinal Pigment Epithelium in Response to Reactive Oxygen Species. *Scientific Reports,* 9**,** 15440. http://dx.doi.org/10.1038/s41598-019-51777-7.

MEYER, J. S., HOWDEN, S. E., WALLACE, K. A., VERHOEVEN, A. D., WRIGHT, L. S., CAPOWSKI, E. E., . . . GAMM, D. M. 2011. Optic vesicle-like structures derived from human pluripotent stem cells facilitate a customized approach to retinal disease treatment. *Stem Cells,* 29**,** 1206-18. http://dx.doi.org/10.1002/stem.674.

MEYER, J. S., SHEARER, R. L., CAPOWSKI, E. E., WRIGHT, L. S., WALLACE, K. A., MCMILLAN, E. L., . . . GAMM, D. M. 2009. Modeling early retinal development with human embryonic and induced pluripotent stem cells. *Proc Natl Acad Sci U S A,* 106**,** 16698-703. http://dx.doi.org/10.1073/pnas.0905245106.

MILLINGTON-WARD, S., CHADDERTON, N., BERKELEY, M., FINNEGAN, L. K., HANLON, K. S., CARRIGAN, M., . . . FARRAR, G. J. 2020. Novel 199 base pair NEFH promoter drives expression in retinal ganglion cells. *Scientific Reports,* 10**,** 16515. http://dx.doi.org/10.1038/s41598-020-73257-z.

MILLINGTON-WARD, S., CHADDERTON, N., O'REILLY, M., PALFI, A., GOLDMANN, T., KILTY, C., . . . FARRAR, G. J. 2011. Suppression and replacement gene therapy for autosomal dominant disease in a murine model of dominant retinitis pigmentosa. *Mol Ther,* 19**,** 642-9. http://dx.doi.org/10.1038/mt.2010.293.

MILLINGTON-WARD, S., O'NEILL, B., TUOHY, G., AL-JANDAL, N., KIANG, A. S., KENNA, P. F., . . . FARRAR, G. J. 1997. Strategems in vitro for gene therapies directed to dominant mutations. *Hum Mol Genet,* 6**,** 1415-26. http://dx.doi.org/10.1093/hmg/6.9.1415.

MILOT, E., MOREAU, C., GAGNON, A., COHEN, A. A., BRAIS, B. & LABUDA, D. 2017. Mother's curse neutralizes natural selection against a human genetic disease over three centuries. *Nat Ecol Evol,* 1**,** 1400-1406. http://dx.doi.org/10.1038/s41559-017-0276-6.

MIQUEL, J., ECONOMOS, A. C., FLEMING, J. & JOHNSON, J. E., JR. 1980. Mitochondrial role in cell aging. *Exp Gerontol,* 15**,** 575-91. http://dx.doi.org/10.1016/0531-5565(80)90010-8.

MIRZAEI, M., GUPTA, V., CHITRANSHI, N., DENG, L., PUSHPITHA, K., ABBASI, M., . . . GRAHAM, S. L. 2020. Experimental glaucoma retinal proteomics identifies mutually exclusive and overlapping molecular characteristics with human glaucoma. *bioRxiv***,** 2020.05.14.095307. http://dx.doi.org/10.1101/2020.05.14.095307.

MOEY, C., TOPPER, S., KARN, M., JOHNSON, A. K., DAS, S., VIDAURRE, J. & SHOUBRIDGE, C. 2016. Reinitiation of mRNA translation in a patient with X-linked infantile spasms with a protein-truncating variant in ARX. *Eur J Hum Genet,* 24**,** 681-9. http://dx.doi.org/10.1038/ejhg.2015.176.

MOHAMED YUSOFF, A., AHMAD, F., IDRIS, Z. & JAAFAR, H. A., JM. 2015. Understanding Mitochondrial DNA in Brain Tumorigenesis. *In:* LICHTOR, T. (ed.) *Understanding Mitochondrial DNA in Brain Tumorigenesis, Molecular Considerations and Evolving Surgical Management Issues in the Treatment of Patients with a Brain Tumor.* IntechOpen.

MOK, B. Y., DE MORAES, M. H., ZENG, J., BOSCH, D. E., KOTRYS, A. V., RAGURAM, A., . . . LIU, D. R. 2020. A bacterial cytidine deaminase toxin enables CRISPR-free mitochondrial base editing. *Nature,* 583**,** 631-637. http://dx.doi.org/10.1038/s41586-020-2477-4.

MOOKHERJEE, S., HIRIYANNA, S., KANESHIRO, K., LI, L., LI, Y., LI, W., . . . WU, Z. 2015. Long-term rescue of cone photoreceptor degeneration in retinitis pigmentosa 2 (RP2)-knockout mice by gene replacement therapy. *Hum Mol Genet,* 24**,** 6446-58. http://dx.doi.org/10.1093/hmg/ddv354.

MOORE, A. S. & HOLZBAUR, E. L. 2016. Dynamic recruitment and activation of ALS-associated TBK1 with its target optineurin are required for efficient mitophagy. *Proc Natl Acad Sci U S A,* 113**,** E3349-58. http://dx.doi.org/10.1073/pnas.1523810113.

MOOSAJEE, M., TRACEY-WHITE, D., SMART, M., WEETALL, M., TORRIANO, S., KALATZIS, V., . . . WELCH, E. 2016. Functional rescue of REP1 following treatment with PTC124 and novel derivative PTC-414 in human choroideremia fibroblasts and the nonsense-mediated zebrafish model. *Hum Mol Genet,* 25**,** 3416-3431. http://dx.doi.org/10.1093/hmg/ddw184.

MORENO, J. A., STREIFEL, K. M., SULLIVAN, K. A., LEGARE, M. E. & TJALKENS, R. B. 2009. Developmental exposure to manganese increases adult susceptibility to inflammatory activation of glia and neuronal protein nitration. *Toxicol Sci,* 112**,** 405-15. http://dx.doi.org/10.1093/toxsci/kfp221.

MURAKAMI, Y., NAKABEPPU, Y. & SONODA, K. H. 2020. Oxidative Stress and Microglial Response in Retinitis Pigmentosa. *Int J Mol Sci,* 21. http://dx.doi.org/10.3390/ijms21197170.

MUSSOLINO, C., DELLA CORTE, M., ROSSI, S., VIOLA, F., DI VICINO, U., MARROCCO, E., . . . SURACE, E. M. 2011. AAV-mediated photoreceptor transduction of the pig cone-enriched retina. *Gene Ther,* 18**,** 637-45. http://dx.doi.org/10.1038/gt.2011.3.

NADAL-NICOLÁS, F. M., JIMÉNEZ-LÓPEZ, M., SALINAS-NAVARRO, M., SOBRADO-CALVO, P., ALBURQUERQUE-BÉJAR, J. J., VIDAL-SANZ, M. & AGUDO-BARRIUSO, M. 2012. Whole number, distribution and co-expression of brn3 transcription factors in retinal ganglion cells of adult albino and pigmented rats. *PloS one,* 7**,** e49830-e49830. http://dx.doi.org/10.1371/journal.pone.0049830.

NADAL-NICOLÁS, F. M., KUNZE, V. P., BALL, J. M., PENG, B. T., KRISHNAN, A., ZHOU, G., . . . LI, W. 2020. True S-cones are concentrated in the ventral mouse retina and wired for color detection in the upper visual field. *eLife,* 9**,** e56840. http://dx.doi.org/10.7554/eLife.56840.

NAGY, E. & MAQUAT, L. E. 1998. A rule for termination-codon position within intron-containing genes: when nonsense affects RNA abundance. *Trends Biochem Sci,* 23**,** 198-9. http://dx.doi.org/10.1016/s0968-0004(98)01208-0.

NAKANO, T., ANDO, S., TAKATA, N., KAWADA, M., MUGURUMA, K., SEKIGUCHI, K., . . . SASAI, Y. 2012. Self-formation of optic cups and storable stratified neural retina

from human ESCs. *Cell Stem Cell,* 10**,** 771-785. http://dx.doi.org/10.1016/j.stem.2012.05.009.

NAKATA, A., AMEMURA, M. & MAKINO, K. 1989. Unusual nucleotide arrangement with repeated sequences in the Escherichia coli K-12 chromosome. *J Bacteriol,* 171**,** 3553-6. http://dx.doi.org/10.1128/jb.171.6.3553-3556.1989.

NARAYAN, D. S., CHIDLOW, G., WOOD, J. P. M. & CASSON, R. J. 2019. Investigations Into Bioenergetic Neuroprotection of Cone Photoreceptors: Relevance to Retinitis Pigmentosa. *Frontiers in Neuroscience,* 13. http://dx.doi.org/10.3389/fnins.2019.01234.

NATKUNARAJAH, M., TRITTIBACH, P., MCINTOSH, J., DURAN, Y., BARKER, S. E., SMITH, A. J., . . . ALI, R. R. 2008. Assessment of ocular transduction using single-stranded and self-complementary recombinant adeno-associated virus serotype 2/8. *Gene Ther,* 15**,** 463-7. http://dx.doi.org/10.1038/sj.gt.3303074.

NEIDHARDT, J., GLAUS, E., LORENZ, B., NETZER, C., LI, Y., SCHAMBECK, M., . . . BERGER, W. 2008. Identification of novel mutations in X-linked retinitis pigmentosa families and implications for diagnostic testing. *Mol Vis,* 14**,** 1081-93.

NEMESURE, B., LESKE, M. C., HE, Q. & MENDELL, N. 1996. Analyses of reported family history of glaucoma: a preliminary investigation. The Barbados Eye Study Group. *Ophthalmic Epidemiol,* 3**,** 135-41. http://dx.doi.org/10.3109/09286589609080119.

NEU-YILIK, G., AMTHOR, B., GEHRING, N. H., BAHRI, S., PAIDASSI, H., HENTZE, M. W. & KULOZIK, A. E. 2011. Mechanism of escape from nonsense-mediated mRNA decay of human beta-globin transcripts with nonsense mutations in the first exon. *RNA,* 17**,** 843-54. http://dx.doi.org/10.1261/rna.2401811.

NEWMAN, N. J. & BIOUSSE, V. 2004. Hereditary optic neuropathies. *Eye,* 18**,** 1144-1160. http://dx.doi.org/10.1038/sj.eye.6701591.

NEWMAN, N. J., CARELLI, V., TAIEL, M. & YU-WAI-MAN, P. 2020. Visual Outcomes in Leber Hereditary Optic Neuropathy Patients With the m.11778G>A (MTND4) Mitochondrial DNA Mutation. *J Neuroophthalmol,* 40**,** 547-557. http://dx.doi.org/10.1097/wno.0000000000001045.

NGUYEN, L. S., WILKINSON, M. F. & GECZ, J. 2014. Nonsense-mediated mRNA decay: inter-individual variability and human disease. *Neurosci Biobehav Rev,* 46 Pt 2**,** 175-86. http://dx.doi.org/10.1016/j.neubiorev.2013.10.016.

NISHIGUCHI, K. M., FUJITA, K., MIYA, F., KATAYAMA, S. & NAKAZAWA, T. 2020. Single AAV-mediated mutation replacement genome editing in limited number of photoreceptors restores vision in mice. *Nat Commun,* 11**,** 482. http://dx.doi.org/10.1038/s41467-019-14181-3.

NISHIYAMA, J., MIKUNI, T. & YASUDA, R. 2017. Virus-Mediated Genome Editing via Homology-Directed Repair in Mitotic and Postmitotic Cells in Mammalian Brain. *Neuron,* 96**,** 755-768.e5. http://dx.doi.org/10.1016/j.neuron.2017.10.004.

NIWA, H., YAMAMURA, K. & MIYAZAKI, J. 1991. Efficient selection for high-expression transfectants with a novel eukaryotic vector. *Gene,* 108**,** 193-9. http://dx.doi.org/10.1016/0378-1119(91)90434-d.

NOMURA-KOMOIKE, K., SAITOH, F. & FUJIEDA, H. 2020. Phosphatidylserine recognition and Rac1 activation are required for Muller glia proliferation, gliosis and phagocytosis after retinal injury. *Sci Rep,* 10**,** 1488. http://dx.doi.org/10.1038/s41598-020-58424-6.

NOUWS, J., NIJTMANS, L. G., SMEITINK, J. A. & VOGEL, R. O. 2012. Assembly factors as a new class of disease genes for mitochondrial complex I deficiency: cause, pathology and treatment options. *Brain,* 135**,** 12-22. http://dx.doi.org/10.1093/brain/awr261.

NUNNARI, J. & SUOMALAINEN, A. 2012. Mitochondria: in sickness and in health. *Cell,* 148**,** 1145-59. http://dx.doi.org/10.1016/j.cell.2012.02.035.

O'CALLAGHAN, J. 2018. *A novel gene-based therapy for glaucoma:from discovery to preclinical development.* PhD, Trinity College Dublin.

O'CALLAGHAN, J., CROSBIE, D. E., CASSIDY, P. S., SHERWOOD, J. M., FLUGEL-KOCH, C., LUTJEN-DRECOLL, E., . . . HUMPHRIES, P. 2017. Therapeutic potential of AAV-mediated MMP-3 secretion from corneal endothelium in treating glaucoma. *Hum Mol Genet,* 26**,** 1230-1246. http://dx.doi.org/10.1093/hmg/ddx028.

O'HARE DOIG, R. L., BARTLETT, C. A., MAGHZAL, G. J., LAM, M., ARCHER, M., STOCKER, R. & FITZGERALD, M. 2014. Reactive species and oxidative stress in optic nerve vulnerable to secondary degeneration. *Exp Neurol,* 261**,** 136-46. http://dx.doi.org/10.1016/j.expneurol.2014.06.007.

OJAIMI, J., MASTERS, C. L., OPESKIN, K., MCKELVIE, P. & BYRNE, E. 1999. Mitochondrial respiratory chain activity in the human brain as a function of age. *Mech Ageing Dev,* 111**,** 39-47. http://dx.doi.org/10.1016/s0047-6374(99)00071-8.

OKITA, K., MATSUMURA, Y., SATO, Y., OKADA, A., MORIZANE, A., OKAMOTO, S., . . . YAMANAKA, S. 2011. A more efficient method to generate integration-free human iPS cells. *Nat Methods,* 8**,** 409-12. http://dx.doi.org/10.1038/nmeth.1591.

OLSSON, J. E., GORDON, J. W., PAWLYK, B. S., ROOF, D., HAYES, A., MOLDAY, R. S., . . . DRYJA, T. P. 1992. Transgenic mice with a rhodopsin mutation (Pro23His): a mouse model of autosomal dominant retinitis pigmentosa. *Neuron,* 9**,** 815-30. http://dx.doi.org/10.1016/0896-6273(92)90236-7.

OMRI, S., OMRI, B., SAVOLDELLI, M., JONET, L., THILLAYE-GOLDENBERG, B., THURET, G., . . . BEHAR-COHEN, F. 2010. The outer limiting membrane (OLM) revisited: clinical implications. *Clin Ophthalmol,* 4**,** 183-95. http://dx.doi.org/10.2147/opth.s5901.

OSAKADA, F., IKEDA, H., MANDAI, M., WATAYA, T., WATANABE, K., YOSHIMURA, N., . . . TAKAHASHI, M. 2008. Toward the generation of rod and cone photoreceptors from mouse, monkey and human embryonic stem cells. *Nat Biotechnol,* 26**,** 215-24. http://dx.doi.org/10.1038/nbt1384.

OSBORNE, N. N. & DEL OLMO-AGUADO, S. 2013. Maintenance of retinal ganglion cell mitochondrial functions as a neuroprotective strategy in glaucoma. *Curr Opin Pharmacol,* 13**,** 16-22. http://dx.doi.org/10.1016/j.coph.2012.09.002.

OSBORNE, N. N., NUNEZ-ALVAREZ, C., JOGLAR, B. & DEL OLMO-AGUADO, S. 2016. Glaucoma: Focus on mitochondria in relation to pathogenesis and neuroprotection. *Eur J Pharmacol,* 787**,** 127-33. http://dx.doi.org/10.1016/j.ejphar.2016.04.032.

OZAKI, E., GIBBONS, L., NETO, N. G., KENNA, P., CARTY, M., HUMPHRIES, M., . . . DOYLE, S. L. 2020. SARM1 deficiency promotes rod and cone photoreceptor cell survival in a model of retinal degeneration. *Life Science Alliance,* 3**,** e201900618. http://dx.doi.org/10.26508/lsa.201900618.

PALFI, A., CHADDERTON, N., MCKEE, A. G., BLANCO FERNANDEZ, A., HUMPHRIES, P., KENNA, P. F. & FARRAR, G. J. 2012. Efficacy of codelivery of dual AAV2/5 vectors in the murine retina and hippocampus. *Hum Gene Ther,* 23**,** 847-58. http://dx.doi.org/10.1089/hum.2011.142.

PALFI, A., MILLINGTON-WARD, S., CHADDERTON, N., O'REILLY, M., GOLDMANN, T., HUMPHRIES, M. M., . . . FARRAR, G. J. 2010. Adeno-associated virus-mediated rhodopsin replacement provides therapeutic benefit in mice with a targeted

disruption of the rhodopsin gene. *Hum Gene Ther,* 21**,** 311-23. http://dx.doi.org/10.1089/hum.2009.119.

PALFI, A., YESMAMBETOV, A., HUMPHRIES, P., HOKAMP, K. & FARRAR, G. J. 2020a. Non-photoreceptor Expression of Tulp1 May Contribute to Extensive Retinal Degeneration in Tulp1-/- Mice. *Front Neurosci,* 14**,** 656. http://dx.doi.org/10.3389/fnins.2020.00656.

PALFI, A., YESMAMBETOV, A., MILLINGTON-WARD, S., SHORTALL, C., HUMPHRIES, P., KENNA, P. F., . . . FARRAR, G. J. 2020b. AAV-Delivered Tulp1 Supplementation Therapy Targeting Photoreceptors Provides Minimal Benefit in Tulp1−/− Retinas. *Frontiers in Neuroscience,* 14. http://dx.doi.org/10.3389/fnins.2020.00891.

PANAGIOTOPOULOS, A. L., KARGUTH, N., PAVLOU, M., BÖHM, S., GASPARONI, G., WALTER, J., . . . BECIROVIC, E. 2020. Antisense Oligonucleotide- and CRISPR-Cas9-Mediated Rescue of mRNA Splicing for a Deep Intronic CLRN1 Mutation. *Mol Ther Nucleic Acids,* 21**,** 1050-1061. http://dx.doi.org/10.1016/j.omtn.2020.07.036.

PANG, J.-J., DAI, X., BOYE, S. E., BARONE, I., BOYE, S. L., MAO, S., . . . HAUSWIRTH, W. W. 2011. Long-term Retinal Function and Structure Rescue Using Capsid Mutant AAV8 Vector in the rd10 Mouse, a Model of Recessive Retinitis Pigmentosa. *Molecular Therapy,* 19**,** 234-242.

PARFITT, D. A., LANE, A., RAMSDEN, C. M., CARR, A. J., MUNRO, P. M., JOVANOVIC, K., . . . CHEETHAM, M. E. 2016. Identification and Correction of Mechanisms Underlying Inherited Blindness in Human iPSC-Derived Optic Cups. *Cell Stem Cell,* 18**,** 769-81. http://dx.doi.org/10.1016/j.stem.2016.03.021.

PARK, J. S., LI, Y. F. & BAI, Y. 2007. Yeast NDI1 improves oxidative phosphorylation capacity and increases protection against oxidative stress and cell death in cells carrying a Leber's hereditary optic neuropathy mutation. *Biochim Biophys Acta,* 1772**,** 533-42. http://dx.doi.org/10.1016/j.bbadis.2007.01.009.

PATEL, A. & SOWDEN, J. C. 2019. Genes and pathways in optic fissure closure. *Semin Cell Dev Biol,* 91**,** 55-65. http://dx.doi.org/10.1016/j.semcdb.2017.10.010.

PATIL, S. B., HURD, T. W., GHOSH, A. K., MURGA-ZAMALLOA, C. A. & KHANNA, H. 2011. Functional analysis of retinitis pigmentosa 2 (RP2) protein reveals variable pathogenic potential of disease-associated missense variants. *PLoS One,* 6**,** e21379. http://dx.doi.org/10.1371/journal.pone.0021379.

PAUSCH, P., AL-SHAYEB, B., BISOM-RAPP, E., TSUCHIDA, C. A., LI, Z., CRESS, B. F., . . . DOUDNA, J. A. 2020. CRISPR-CasΦ from huge phages is a hypercompact genome editor. *Science,* 369**,** 333-337. http://dx.doi.org/10.1126/science.abb1400.

PEARRING, J. N., SALINAS, R. Y., BAKER, S. A. & ARSHAVSKY, V. Y. 2013. Protein sorting, targeting and trafficking in photoreceptor cells. *Progress in retinal and eye research,* 36**,** 24-51. http://dx.doi.org/10.1016/j.preteyeres.2013.03.002.

PEI, W.-D., ZHANG, Y., YIN, T.-L. & YU, Y. 2019. Epigenome editing by CRISPR/Cas9 in clinical settings: possibilities and challenges. *Briefings in Functional Genomics,* 19**,** 215-228. http://dx.doi.org/10.1093/bfgp/elz035.

PENDSE, N., LAMAS, V., MAEDER, M., PAWLYK, B., GLOSKOWSKI, S., PIERCE, E. A., . . . LIU, Q. 2020. Exon 13-skipped USH2A protein retains functional integrity in mice, suggesting an exo-skipping therapeutic approach to treat USH2A-associated disease. *bioRxiv***,** 2020.02.04.934240. http://dx.doi.org/10.1101/2020.02.04.934240.

PEREZ DE LARA, M. J., GUZMAN-ARANGUEZ, A., DE LA VILLA, P., DIAZ-HERNANDEZ, J. I., MIRAS-PORTUGAL, M. T. & PINTOR, J. 2015. Increased levels of extracellular ATP in glaucomatous retinas: Possible role of the vesicular nucleotide transporter during the development of the pathology. *Mol Vis,* 21**,** 1060-70.

PEREZ DE LARA, M. J., SANTANO, C., GUZMAN-ARANGUEZ, A., VALIENTE-SORIANO, F. J., AVILES-TRIGUEROS, M., VIDAL-SANZ, M., . . . PINTOR, J. 2014. Assessment of inner retina dysfunction and progressive ganglion cell loss in a mouse model of glaucoma. *Exp Eye Res,* 122**,** 40-9. http://dx.doi.org/10.1016/j.exer.2014.02.022.

PEREZ, V. I., BOKOV, A., VAN REMMEN, H., MELE, J., RAN, Q., IKENO, Y. & RICHARDSON, A. 2009. Is the oxidative stress theory of aging dead? *Biochim Biophys Acta,* 1790**,** 1005-14. http://dx.doi.org/10.1016/j.bbagen.2009.06.003.

PERGE, J. A., KOCH, K., MILLER, R., STERLING, P. & BALASUBRAMANIAN, V. 2009. How the optic nerve allocates space, energy capacity, and information. *J Neurosci,* 29**,** 7917-28. http://dx.doi.org/10.1523/JNEUROSCI.5200-08.2009.

PETIT, L., MA, S., CHENG, S. Y., GAO, G. & PUNZO, C. 2017. Rod Outer Segment Development Influences AAV-Mediated Photoreceptor Transduction After Subretinal Injection. *Hum Gene Ther,* 28**,** 464-481. http://dx.doi.org/10.1089/hum.2017.020.

PETRITI, B., CHAU, D., LASCARATOS, G., CAMPBELL, P., LAZARIDIS, G. & GARWAY-HEATH, D. F. 2020. Normal Tension Glaucoma patients have reduced systemic mitochondrial function compared to High Tension Glaucoma patients. *Investigative Ophthalmology & Visual Science,* 61**,** 1009-1009.

PETROSILLO, G., MATERA, M., MORO, N., RUGGIERO, F. M. & PARADIES, G. 2009. Mitochondrial complex I dysfunction in rat heart with aging: critical role of reactive oxygen species and cardiolipin. *Free Radic Biol Med,* 46**,** 88-94. http://dx.doi.org/10.1016/j.freeradbiomed.2008.09.031.

PHILLIPS, M. J., PEREZ, E. T., MARTIN, J. M., RESHEL, S. T., WALLACE, K. A., CAPOWSKI, E. E., . . . GAMM, D. M. 2014. Modeling human retinal development with patient-specific induced pluripotent stem cells reveals multiple roles for visual system homeobox 2. *Stem Cells,* 32**,** 1480-92. http://dx.doi.org/10.1002/stem.1667.

PIERCE, E. A. & BENNETT, J. 2015. The Status of RPE65 Gene Therapy Trials: Safety and Efficacy. *Cold Spring Harb Perspect Med,* 5**,** a017285. http://dx.doi.org/10.1101/cshperspect.a017285.

POLLARD, A. K., CRAIG, E. L. & CHAKRABARTI, L. 2016. Mitochondrial Complex 1 Activity Measured by Spectrophotometry Is Reduced across All Brain Regions in Ageing and More Specifically in Neurodegeneration. *PLoS One,* 11**,** e0157405. http://dx.doi.org/10.1371/journal.pone.0157405.

POMARES, E., RIERA, M., CASTRO-NAVARRO, J., ANDRES-GUTIERREZ, A., GONZALEZ-DUARTE, R. & MARFANY, G. 2009. Identification of an intronic single-point mutation in RP2 as the cause of semidominant X-linked retinitis pigmentosa. *Invest Ophthalmol Vis Sci,* 50**,** 5107-14. http://dx.doi.org/10.1167/iovs.08-3208.

PORCIATTI, V. 2015. Electrophysiological assessment of retinal ganglion cell function. *Exp Eye Res,* 141**,** 164-70. http://dx.doi.org/10.1016/j.exer.2015.05.008.

PORTER, L. F., SAPTARSHI, N., FANG, Y., RATHI, S., DEN HOLLANDER, A. I., DE JONG, E. K., . . . PARAOAN, L. 2019. Whole-genome methylation profiling of the retinal pigment epithelium of individuals with age-related macular degeneration reveals differential methylation of the SKI, GTF2H4, and TNXB genes. *Clinical Epigenetics,* 11**,** 6. http://dx.doi.org/10.1186/s13148-019-0608-2.

PORTEUS, M. H., CATHOMEN, T., WEITZMAN, M. D. & BALTIMORE, D. 2003. Efficient gene targeting mediated by adeno-associated virus and DNA double-strand breaks.

Molecular and cellular biology, 23**,** 3558-3565. http://dx.doi.org/10.1128/mcb.23.10.3558-3565.2003.

PORTO, E. M., KOMOR, A. C., SLAYMAKER, I. M. & YEO, G. W. 2020. Base editing: advances and therapeutic opportunities. *Nature Reviews Drug Discovery*. http://dx.doi.org/10.1038/s41573-020-0084-6.

PROKISCH, H., HARTIG, M., HELLINGER, R., MEITINGER, T. & ROSENBERG, T. 2007. A population-based epidemiological and genetic study of X-linked retinitis pigmentosa. *Invest Ophthalmol Vis Sci,* 48**,** 4012-8. http://dx.doi.org/10.1167/iovs.07-0071.

PUK, O., DALKE, C., HRABE DE ANGELIS, M. & GRAW, J. 2008. Variation of the response to the optokinetic drum among various strains of mice. *Front Biosci,* 13**,** 6269-75. http://dx.doi.org/10.2741/3153.

QASIM, W., ZHAN, H., SAMARASINGHE, S., ADAMS, S., AMROLIA, P., STAFFORD, S., . . . VEYS, P. 2017. Molecular remission of infant B-ALL after infusion of universal TALEN gene-edited CAR T cells. *Sci Transl Med,* 9. http://dx.doi.org/10.1126/scitranslmed.aaj2013.

QUIGLEY, H. A. 1996. Number of people with glaucoma worldwide. *Br J Ophthalmol,* 80**,** 389-93. http://dx.doi.org/10.1136/bjo.80.5.389.

QUIGLEY, H. A. 2019. 21st century glaucoma care. *Eye (Lond),* 33**,** 254-260. http://dx.doi.org/10.1038/s41433-018-0227-8.

QUIGLEY, H. A. & BROMAN, A. T. 2006. The number of people with glaucoma worldwide in 2010 and 2020. *Br J Ophthalmol,* 90**,** 262-7. http://dx.doi.org/10.1136/bjo.2005.081224.

QUINN, J., MUSA, A., KANTOR, A., MCCLEMENTS, M., CEHAJIC-KAPETANOVIC, J., MACLAREN, R. E. & XUE, K. 2020. Genome editing strategies for treating human retinal degenerations. *Hum Gene Ther*. http://dx.doi.org/10.1089/hum.2020.231.

QUINN, P. M., BUCK, T. M., MULDER, A. A., OHONIN, C., ALVES, C. H., VOS, R. M., . . . WIJNHOLDS, J. 2019. Human iPSC-Derived Retinas Recapitulate the Fetal CRB1 CRB2 Complex Formation and Demonstrate that Photoreceptors and Muller Glia Are Targets of AAV5. *Stem Cell Reports,* 12**,** 906-919. http://dx.doi.org/10.1016/j.stemcr.2019.03.002.

QUINN, P. M. J. & WIJNHOLDS, J. 2019. Retinogenesis of the Human Fetal Retina: An Apical Polarity Perspective. *Genes (Basel),* 10. http://dx.doi.org/10.3390/genes10120987.

RAJALA, R. V. S. 2020. Aerobic Glycolysis in the Retina: Functional Roles of Pyruvate Kinase Isoforms. *Front Cell Dev Biol,* 8**,** 266. http://dx.doi.org/10.3389/fcell.2020.00266.

RAN, F. A., CONG, L., YAN, W. X., SCOTT, D. A., GOOTENBERG, J. S., KRIZ, A. J., . . . ZHANG, F. 2015. In vivo genome editing using Staphylococcus aureus Cas9. *Nature,* 520**,** 186-91. http://dx.doi.org/10.1038/nature14299.

RATHOD, R., GAJERA, B., NAZIR, K., WALLENIUS, J. & VELAGAPUDI, V. 2020. Simultaneous Measurement of Tricarboxylic Acid Cycle Intermediates in Different Biological Matrices Using Liquid Chromatography-Tandem Mass Spectrometry; Quantitation and Comparison of TCA Cycle Intermediates in Human Serum, Plasma, Kasumi-1 Cell and Murine Liver Tissue. *Metabolites,* 10**,** 103. http://dx.doi.org/10.3390/metabo10030103.

RATNAPRIYA, R., ACAR, İ. E., GEERLINGS, M. J., BRANHAM, K., KWONG, A., SAKSENS, N. T. M., . . . DEN HOLLANDER, A. I. 2020. Family-based exome sequencing identifies rare coding variants in age-related macular degeneration. *Human Molecular Genetics,* 29**,** 2022-2034. http://dx.doi.org/10.1093/hmg/ddaa057.

RE, S., DOGAN, A. A., BEN-SHACHAR, D., BERGER, G., WERLING, A. M., WALITZA, S. & GRÜNBLATT, E. 2018. Improved Generation of Induced Pluripotent Stem Cells From Hair Derived Keratinocytes – A Tool to Study Neurodevelopmental Disorders as ADHD. *Frontiers in Cellular Neuroscience,* 12. http://dx.doi.org/10.3389/fncel.2018.00321.

REICHENBACH, A. & BRINGMANN, A. 2013. New functions of Müller cells. *Glia,* 61**,** 651-678. http://dx.doi.org/https://doi.org/10.1002/glia.22477.

REICHENBACH, A. & BRINGMANN, A. 2020. Glia of the human retina. *Glia,* 68**,** 768-796. http://dx.doi.org/10.1002/glia.23727.

REICHMAN, S., SLEMBROUCK, A., GAGLIARDI, G., CHAFFIOL, A., TERRAY, A., NANTEAU, C., . . . GOUREAU, O. 2017. Generation of Storable Retinal Organoids and Retinal Pigmented Epithelium from Adherent Human iPS Cells in Xeno-Free and Feeder-Free Conditions. *Stem Cells,* 35**,** 1176-1188. http://dx.doi.org/10.1002/stem.2586.

REICHMAN, S., TERRAY, A., SLEMBROUCK, A., NANTEAU, C., ORIEUX, G., HABELER, W., . . . GOUREAU, O. 2014. From confluent human iPS cells to self-forming neural retina and retinal pigmented epithelium. *Proc Natl Acad Sci U S A,* 111**,** 8518-23. http://dx.doi.org/10.1073/pnas.1324212111.

REYNOLDS, A. L., DANCIGER, M., FARRAR, G. J., HUMPHRIES, P. & KENNA, P. F. 2008a. Influence of a quantitative trait locus on mouse chromosome 19 to the light-adapted electroretinogram. *Invest Ophthalmol Vis Sci,* 49**,** 4058-63. http://dx.doi.org/10.1167/iovs.07-1620.

REYNOLDS, A. L., FARRAR, G. J., HUMPHRIES, P. & KENNA, P. F. 2008b. Variation in the electroretinogram of C57BL/6 substrains of mouse. *Adv Exp Med Biol,* 613**,** 383-91. http://dx.doi.org/10.1007/978-0-387-74904-4_45.

RICHARDS, S., AZIZ, N., BALE, S., BICK, D., DAS, S., GASTIER-FOSTER, J., . . . COMMITTEE, A. L. Q. A. 2015. Standards and guidelines for the interpretation of sequence variants: a joint consensus recommendation of the American College of Medical Genetics and Genomics and the Association for Molecular Pathology. *Genet Med,* 17**,** 405-24. http://dx.doi.org/10.1038/gim.2015.30.

RICHARDSON, C. D., KAZANE, K. R., FENG, S. J., ZELIN, E., BRAY, N. L., SCHÄFER, A. J., . . . CORN, J. E. 2018. CRISPR–Cas9 genome editing in human cells occurs via the Fanconi anemia pathway. *Nature Genetics,* 50**,** 1132-1139. http://dx.doi.org/10.1038/s41588-018-0174-0.

RIERA, M., NAVARRO, R., RUIZ-NOGALES, S., MENDEZ, P., BURES-JELSTRUP, A., CORCOSTEGUI, B. & POMARES, E. 2017. Whole exome sequencing using Ion Proton system enables reliable genetic diagnosis of inherited retinal dystrophies. *Sci Rep,* 7**,** 42078. http://dx.doi.org/10.1038/srep42078.

RODENBURG, R. J. 2016. Mitochondrial complex I-linked disease. *Biochim Biophys Acta,* 1857**,** 938-45. http://dx.doi.org/10.1016/j.bbabio.2016.02.012.

RODRIGUEZ, A. R., DE SEVILLA MULLER, L. P. & BRECHA, N. C. 2014. The RNA binding protein RBPMS is a selective marker of ganglion cells in the mammalian retina. *J Comp Neurol,* 522**,** 1411-43. http://dx.doi.org/10.1002/cne.23521.

ROMAN, A. J., CIDECIYAN, A. V., ALEMAN, T. S. & JACOBSON, S. G. 2007. Full-field stimulus testing (FST) to quantify visual perception in severely blind candidates for treatment trials. *Physiol Meas,* 28**,** N51-6. http://dx.doi.org/10.1088/0967-3334/28/8/n02.

ROSSMILLER, B., MAO, H. & LEWIN, A. S. 2012. Gene therapy in animal models of autosomal dominant retinitis pigmentosa. *Molecular vision,* 18**,** 2479-2496.

ROUET, P., SMIH, F. & JASIN, M. 1994. Introduction of double-strand breaks into the genome of mouse cells by expression of a rare-cutting endonuclease. *Molecular and cellular biology,* 14**,** 8096-8106. http://dx.doi.org/10.1128/mcb.14.12.8096.

RUAN, G. X., BARRY, E., YU, D., LUKASON, M., CHENG, S. H. & SCARIA, A. 2017. CRISPR/Cas9-Mediated Genome Editing as a Therapeutic Approach for Leber Congenital Amaurosis 10. *Mol Ther,* 25**,** 331-341. http://dx.doi.org/10.1016/j.ymthe.2016.12.006.

RUDNICKA, A. R., MT-ISA, S., OWEN, C. G., COOK, D. G. & ASHBY, D. 2006. Variations in primary open-angle glaucoma prevalence by age, gender, and race: a Bayesian meta-analysis. *Invest Ophthalmol Vis Sci,* 47**,** 4254-61. http://dx.doi.org/10.1167/iovs.06-0299.

RUSSELL, D. W. & HIRATA, R. K. 1998. Human gene targeting by viral vectors. *Nature genetics,* 18**,** 325-330. http://dx.doi.org/10.1038/ng0498-325.

RUSSELL, S., BENNETT, J., WELLMAN, J. A., CHUNG, D. C., YU, Z. F., TILLMAN, A., . . . MAGUIRE, A. M. 2017. Efficacy and safety of voretigene neparvovec (AAV2-hRPE65v2) in patients with RPE65-mediated inherited retinal dystrophy: a randomised, controlled, open-label, phase 3 trial. *Lancet,* 390**,** 849-860. http://dx.doi.org/10.1016/S0140-6736(17)31868-8.

SACCÀ, S. C., CARTIGLIA, C. & IZZOTTI, A. 2014. Chapter 4 - Glaucoma: An Overview. *In:* PREEDY, V. R. (ed.) *Handbook of Nutrition, Diet and the Eye.* San Diego: Academic Press.

SACCÀ, S. C., CUTOLO, C. A., GANDOLFI, S., MARCHINI, G., QUARANTA, L., TOMMASO, R., . . . TRAVERSO, C. E. 2019. The Prevalence of Loss-of-Function Polymorphism of Genes Encoding for Glutathione Transferase in an Italian Population Affected by Primary Open-Angle Glaucoma. *J Biomed Res Rev,* 2**,** 21-26.

SACCA, S. C., IZZOTTI, A., ROSSI, P. & TRAVERSO, C. 2007. Glaucomatous outflow pathway and oxidative stress. *Exp Eye Res,* 84**,** 389-99. http://dx.doi.org/10.1016/j.exer.2006.10.008.

SACCA, S. C., PASCOTTO, A., CAMICIONE, P., CAPRIS, P. & IZZOTTI, A. 2005. Oxidative DNA damage in the human trabecular meshwork: clinical correlation in patients with

primary open-angle glaucoma. *Arch Ophthalmol,* 123**,** 458-63. http://dx.doi.org/10.1001/archopht.123.4.458.

SAFARI, F., ZARE, K., NEGAHDARIPOUR, M., BAREKATI-MOWAHED, M. & GHASEMI, Y. 2019. CRISPR Cpf1 proteins: structure, function and implications for genome editing. *Cell & Bioscience,* 9**,** 36. http://dx.doi.org/10.1186/s13578-019-0298-7.

SAKAI, H., SHEN, X., KOGA, T., PARK, B. C., NOSKINA, Y., TIBUDAN, M. & YUE, B. Y. 2007. Mitochondrial association of myocilin, product of a glaucoma gene, in human trabecular meshwork cells. *J Cell Physiol,* 213**,** 775-84. http://dx.doi.org/10.1002/jcp.21147.

SAKAMI, S., IMANISHI, Y. & PALCZEWSKI, K. 2019. Muller glia phagocytose dead photoreceptor cells in a mouse model of retinal degenerative disease. *FASEB J,* 33**,** 3680-3692. http://dx.doi.org/10.1096/fj.201801662R.

SALEH, M., NAGARAJU, M. & PORCIATTI, V. 2007. Longitudinal evaluation of retinal ganglion cell function and IOP in the DBA/2J mouse model of glaucoma. *Invest Ophthalmol Vis Sci,* 48**,** 4564-72. http://dx.doi.org/10.1167/iovs.07-0483.

SALOWE, R., SALINAS, J., FARBMAN, N. H., MOHAMMED, A., WARREN, J. Z., RHODES, A., . . . O'BRIEN, J. M. 2015. Primary Open-Angle Glaucoma in Individuals of African Descent: A Review of Risk Factors. *J Clin Exp Ophthalmol,* 6. http://dx.doi.org/10.4172/2155-9570.1000450.

SALVETTI, A. P., NANDA, A. & MACLAREN, R. E. 2020. RPGR-Related X-Linked Retinitis Pigmentosa Carriers with a Severe "Male Pattern". *Ophthalmologica***,** 1-8. http://dx.doi.org/10.1159/000503687.

SAMULSKI, R. J. & MUZYCZKA, N. 2014. AAV-Mediated Gene Therapy for Research and Therapeutic Purposes. *Annual Review of Virology,* 1**,** 427-451. http://dx.doi.org/10.1146/annurev-virology-031413-085355.

SANJURJO-SORIANO, C., ERKILIC, N., BAUX, D., MAMAEVA, D., HAMEL, C. P., MEUNIER, I., . . . KALATZIS, V. 2020. Genome Editing in Patient iPSCs Corrects the Most Prevalent USH2A Mutations and Reveals Intriguing Mutant mRNA Expression Profiles. *Mol Ther Methods Clin Dev,* 17**,** 156-173. http://dx.doi.org/10.1016/j.omtm.2019.11.016.

SANTOS-FERREIRA, T., VOLKNER, M., BORSCH, O., HAAS, J., CIMALLA, P., VASUDEVAN, P., . . . ADER, M. 2016. Stem Cell-Derived Photoreceptor Transplants Differentially

Integrate Into Mouse Models of Cone-Rod Dystrophy. *Invest Ophthalmol Vis Sci,* 57**,** 3509-20. http://dx.doi.org/10.1167/iovs.16-19087.

SCHENE, I. F., JOORE, I. P., OKA, R., MOKRY, M., VAN VUGT, A. H. M., VAN BOXTEL, R., . . . FUCHS, S. A. 2020. Prime editing for functional repair in patient-derived disease models. *Nature Communications,* 11**,** 5352. http://dx.doi.org/10.1038/s41467-020-19136-7.

SCHLAMP, C. L., LI, Y., DIETZ, J. A., JANSSEN, K. T. & NICKELLS, R. W. 2006. Progressive ganglion cell loss and optic nerve degeneration in DBA/2J mice is variable and asymmetric. *BMC Neurosci,* 7**,** 66. http://dx.doi.org/10.1186/1471-2202-7-66.

SCHLAMP, C. L., MONTGOMERY, A. D., MAC NAIR, C. E., SCHUART, C., WILLMER, D. J. & NICKELLS, R. W. 2013. Evaluation of the percentage of ganglion cells in the ganglion cell layer of the rodent retina. *Molecular vision,* 19**,** 1387-1396.

SCHLEE, M. & HARTMANN, G. 2016. Discriminating self from non-self in nucleic acid sensing. *Nat Rev Immunol,* 16**,** 566-80. http://dx.doi.org/10.1038/nri.2016.78.

SCHOLZ, M., BUDER, T., SEEBER, S., ADAMEK, E., BECKER, C.-M. & LÜTJEN-DRECOLL, E. 2008. Dependency of Intraocular Pressure Elevation and Glaucomatous Changes in DBA/2J and DBA/2J-Rj Mice. *Investigative Ophthalmology & Visual Science,* 49**,** 613-621. http://dx.doi.org/10.1167/iovs.07-0745.

SCHRICK, J. J., VOGEL, P., ABUIN, A., HAMPTON, B. & RICE, D. S. 2006. ADP-ribosylation factor-like 3 is involved in kidney and photoreceptor development. *Am J Pathol,* 168**,** 1288-98. http://dx.doi.org/10.2353/ajpath.2006.050941.

SCHUETTAUF, F., REJDAK, R., WALSKI, M., FRONTCZAK-BANIEWICZ, M., VOELKER, M., BLATSIOS, G., . . . GRIEB, P. 2004. Retinal neurodegeneration in the DBA/2J mouse-a model for ocular hypertension. *Acta Neuropathol,* 107**,** 352-8. http://dx.doi.org/10.1007/s00401-003-0816-9.

SCHWAHN, U., LENZNER, S., DONG, J., FEIL, S., HINZMANN, B., VAN DUIJNHOVEN, G., . . . BERGER, W. 1998. Positional cloning of the gene for X-linked retinitis pigmentosa 2. *Nat Genet,* 19**,** 327-32. http://dx.doi.org/10.1038/1214.

SCHWARZ, N., CARR, A. J., LANE, A., MOELLER, F., CHEN, L. L., AGUILA, M., . . . HARDCASTLE, A. J. 2015. Translational read-through of the RP2 Arg120stop mutation in patient iPSC-derived retinal pigment epithelium cells. *Hum Mol Genet,* 24**,** 972-86. http://dx.doi.org/10.1093/hmg/ddu509.

SCHWARZ, N., HARDCASTLE, A. J. & CHEETHAM, M. E. 2012a. Arl3 and RP2 mediated assembly and traffic of membrane associated cilia proteins. *Vision Res,* 75**,** 2-4. http://dx.doi.org/10.1016/j.visres.2012.07.016.

SCHWARZ, N., LANE, A., JOVANOVIC, K., PARFITT, D. A., AGUILA, M., THOMPSON, C. L., . . . CHEETHAM, M. E. 2017. Arl3 and RP2 regulate the trafficking of ciliary tip kinesins. *Hum Mol Genet,* 26**,** 3451. http://dx.doi.org/10.1093/hmg/ddx245.

SCHWARZ, N., NOVOSELOVA, T. V., WAIT, R., HARDCASTLE, A. J. & CHEETHAM, M. E. 2012b. The X-linked retinitis pigmentosa protein RP2 facilitates G protein traffic. *Hum Mol Genet,* 21**,** 863-73. http://dx.doi.org/10.1093/hmg/ddr520.

SCOTT, A. W., BRESSLER, N. M., FFOLKES, S., WITTENBORN, J. S. & JORKASKY, J. 2016. Public Attitudes About Eye and Vision Health. *JAMA Ophthalmol,* 134**,** 1111-1118. http://dx.doi.org/10.1001/jamaophthalmol.2016.2627.

SEARS, N. C., BOESE, E. A., MILLER, M. A. & FINGERT, J. H. 2019. Mendelian genes in primary open angle glaucoma. *Exp Eye Res,* 186**,** 107702. http://dx.doi.org/10.1016/j.exer.2019.107702.

SEITZ, I. P., MICHALAKIS, S., WILHELM, B., REICHEL, F. F., OCHAKOVSKI, G. A., ZRENNER, E., . . . CONSORTIUM, F. T. R.-C. 2017. Superior Retinal Gene Transfer and Biodistribution Profile of Subretinal Versus Intravitreal Delivery of AAV8 in Nonhuman Primates. *Investigative Ophthalmology & Visual Science,* 58**,** 5792-5801. http://dx.doi.org/10.1167/iovs.17-22473.

SENIOR, M. 2017. After Glybera's withdrawal, what's next for gene therapy? *Nature Biotechnology,* 35**,** 491-492. http://dx.doi.org/10.1038/nbt0617-491.

SENONER, T. & DICHTL, W. 2019. Oxidative Stress in Cardiovascular Diseases: Still a Therapeutic Target? *Nutrients,* 11**,** 2090. http://dx.doi.org/10.3390/nu11092090.

SEO, B. B., KITAJIMA-IHARA, T., CHAN, E. K., SCHEFFLER, I. E., MATSUNO-YAGI, A. & YAGI, T. 1998. Molecular remedy of complex I defects: rotenone-insensitive internal NADH-quinone oxidoreductase of Saccharomyces cerevisiae mitochondria restores the NADH oxidase activity of complex I-deficient mammalian cells. *Proc Natl Acad Sci U S A,* 95**,** 9167-71. http://dx.doi.org/10.1073/pnas.95.16.9167.

SEO, B. B., NAKAMARU-OGISO, E., FLOTTE, T. R., MATSUNO-YAGI, A. & YAGI, T. 2006. In vivo complementation of complex I by the yeast Ndi1 enzyme. Possible application for treatment of Parkinson disease. *J Biol Chem,* 281**,** 14250-5. http://dx.doi.org/10.1074/jbc.M600922200.

SEO, B. B., WANG, J., FLOTTE, T. R., YAGI, T. & MATSUNO-YAGI, A. 2000. Use of the NADH-quinone oxidoreductase (NDI1) gene of Saccharomyces cerevisiae as a possible cure for complex I defects in human cells. *J Biol Chem,* 275**,** 37774-8. http://dx.doi.org/10.1074/jbc.M007033200.

SEOL, J.-H., SHIM, E. Y. & LEE, S. E. 2018. Microhomology-mediated end joining: Good, bad and ugly. *Mutation research,* 809**,** 81-87. http://dx.doi.org/10.1016/j.mrfmmm.2017.07.002.

SHAO, W., EARLEY, L. F., CHAI, Z., CHEN, X., SUN, J., HE, T., . . . LI, C. 2018. Double-stranded RNA innate immune response activation from long-term adeno-associated virus vector transduction. *JCI Insight,* 3. http://dx.doi.org/10.1172/jci.insight.120474.

SHARMA, L. K., LU, J. & BAI, Y. 2009. Mitochondrial respiratory complex I: structure, function and implication in human diseases. *Curr Med Chem,* 16**,** 1266-77. http://dx.doi.org/10.2174/092986709787846578.

SHARON, D., SANDBERG, M. A., RABE, V. W., STILLBERGER, M., DRYJA, T. P. & BERSON, E. L. 2003. RP2 and RPGR mutations and clinical correlations in patients with X-linked retinitis pigmentosa. *Am J Hum Genet,* 73**,** 1131-46. http://dx.doi.org/10.1086/379379.

SHERIDAN, C. 2018. Sangamo's landmark genome editing trial gets mixed reception. *Nature Biotechnology,* 36**,** 907-908. http://dx.doi.org/10.1038/nbt1018-907.

SHERRY, S. T., WARD, M. H., KHOLODOV, M., BAKER, J., PHAN, L., SMIGIELSKI, E. M. & SIROTKIN, K. 2001. dbSNP: the NCBI database of genetic variation. *Nucleic Acids Res,* 29**,** 308-11. http://dx.doi.org/10.1093/nar/29.1.308.

SHIGENAGA, M. K., HAGEN, T. M. & AMES, B. N. 1994. Oxidative damage and mitochondrial decay in aging. *Proc Natl Acad Sci U S A,* 91**,** 10771-8. http://dx.doi.org/10.1073/pnas.91.23.10771.

SHIM, M. S., TAKIHARA, Y., KIM, K. Y., IWATA, T., YUE, B. Y., INATANI, M., . . . JU, W. K. 2016. Mitochondrial pathogenic mechanism and degradation in optineurin E50K mutation-mediated retinal ganglion cell degeneration. *Sci Rep,* 6**,** 33830. http://dx.doi.org/10.1038/srep33830.

SHIMADA, H., LU, Q., INSINNA-KETTENHOFEN, C., NAGASHIMA, K., ENGLISH, M. A., SEMLER, E. M., . . . SWAROOP, A. 2017. In Vitro Modeling Using Ciliopathy-Patient-

Derived Cells Reveals Distinct Cilia Dysfunctions Caused by CEP290 Mutations. *Cell Rep,* 20**,** 384-396. http://dx.doi.org/10.1016/j.celrep.2017.06.045.

SHIN, D. H., BECKER, B. & KOLKER, A. E. 1977. Family History in Primary Open-Angle Glaucoma. *Archives of Ophthalmology,* 95**,** 598-600. http://dx.doi.org/10.1001/archopht.1977.04450040064007.

SHU, X., BLACK, G. C., RICE, J. M., HART-HOLDEN, N., JONES, A., O'GRADY, A., . . . WRIGHT, A. F. 2007. RPGR mutation analysis and disease: an update. *Hum Mutat,* 28**,** 322-8. http://dx.doi.org/10.1002/humu.20461.

SHUI, B., HERNANDEZ MATIAS, L., GUO, Y. & PENG, Y. 2016. The Rise of CRISPR/Cas for Genome Editing in Stem Cells. *Stem Cells International,* 2016**,** 8140168. http://dx.doi.org/10.1155/2016/8140168.

SIMHADRI, V. L., MCGILL, J., MCMAHON, S., WANG, J., JIANG, H. & SAUNA, Z. E. 2018. Prevalence of Pre-existing Antibodies to CRISPR-Associated Nuclease Cas9 in the USA Population. *Mol Ther Methods Clin Dev,* 10**,** 105-112. http://dx.doi.org/10.1016/j.omtm.2018.06.006.

SINHA, D., STEYER, B., SHAHI, P. K., MUELLER, K. P., VALIAUGA, R., EDWARDS, K. L., . . . GAMM, D. M. 2020. Human iPSC Modeling Reveals Mutation-Specific Responses to Gene Therapy in a Genotypically Diverse Dominant Maculopathy. *The American Journal of Human Genetics,* 107**,** 278-292. http://dx.doi.org/https://doi.org/10.1016/j.ajhg.2020.06.011.

SINN, R. & WITTBRODT, J. 2013. An eye on eye development. *Mech Dev,* 130**,** 347-58. http://dx.doi.org/10.1016/j.mod.2013.05.001.

SMITH, B. J., WANG, X., CHAUHAN, B. C., COTE, P. D. & TREMBLAY, F. 2014. Contribution of retinal ganglion cells to the mouse electroretinogram. *Doc Ophthalmol,* 128**,** 155-68. http://dx.doi.org/10.1007/s10633-014-9433-2.

SMITH, J. N., WALKER, H. M., THOMPSON, H., COLLINSON, J. M., VARGESSON, N. & ERSKINE, L. 2018. Lens-regulated retinoic acid signalling controls expansion of the developing eye. *Development,* 145. http://dx.doi.org/10.1242/dev.167171.

SNELL, R. S. & LEMP, L. A. 1998. The Eyeball. *Clinical Anatomy of the Eye.* 2nd ed.

SONG, J., YANG, D., XU, J., ZHU, T., CHEN, Y. E. & ZHANG, J. 2016. RS-1 enhances CRISPR/Cas9- and TALEN-mediated knock-in efficiency. *Nature Communications,* 7**,** 10548. http://dx.doi.org/10.1038/ncomms10548.

SONG, P., WANG, J., BUCAN, K., THEODORATOU, E., RUDAN, I. & CHAN, K. Y. 2017. National and subnational prevalence and burden of glaucoma in China: A systematic analysis. *J Glob Health,* 7**,** 020705. http://dx.doi.org/10.7189/jogh.07.020705.

SORKHABI, R., GHORBANIHAGHJO, A., JAVADZADEH, A., RASHTCHIZADEH, N. & MOHARRERY, M. 2011. Oxidative DNA damage and total antioxidant status in glaucoma patients. *Mol Vis,* 17**,** 41-6.

SOTO, I., OGLESBY, E., BUCKINGHAM, B. P., SON, J. L., ROBERSON, E. D., STEELE, M. R., . . . MARSH-ARMSTRONG, N. 2008. Retinal ganglion cells downregulate gene expression and lose their axons within the optic nerve head in a mouse glaucoma model. *J Neurosci,* 28**,** 548-61. http://dx.doi.org/10.1523/JNEUROSCI.3714-07.2008.

SPINAZZI, M., CASARIN, A., PERTEGATO, V., SALVIATI, L. & ANGELINI, C. 2012. Assessment of mitochondrial respiratory chain enzymatic activities on tissues and cultured cells. *Nat Protoc,* 7**,** 1235-46. http://dx.doi.org/10.1038/nprot.2012.058.

SRIDHAR, A., HOSHINO, A., FINKBEINER, C. R., CHITSAZAN, A., DAI, L., HAUGAN, A. K., . . . REH, T. A. 2020. Single-Cell Transcriptomic Comparison of Human Fetal Retina, hPSC-Derived Retinal Organoids, and Long-Term Retinal Cultures. *Cell Rep,* 30**,** 1644-1659 e4. http://dx.doi.org/10.1016/j.celrep.2020.01.007.

STAERK, J., DAWLATY, M. M., GAO, Q., MAETZEL, D., HANNA, J., SOMMER, C. A., . . . JAENISCH, R. 2010. Reprogramming of human peripheral blood cells to induced pluripotent stem cells. *Cell Stem Cell,* 7**,** 20-4. http://dx.doi.org/10.1016/j.stem.2010.06.002.

STAMER, W. D. & CLARK, A. F. 2017. The many faces of the trabecular meshwork cell. *Exp Eye Res,* 158**,** 112-123. http://dx.doi.org/10.1016/j.exer.2016.07.009.

STEVENS, C. B., CAMERON, D. A. & STENKAMP, D. L. 2011. Plasticity of photoreceptor-generating retinal progenitors revealed by prolonged retinoic acid exposure. *BMC Dev Biol,* 11**,** 51. http://dx.doi.org/10.1186/1471-213X-11-51.

STIEGER, K., COLLE, M. A., DUBREIL, L., MENDES-MADEIRA, A., WEBER, M., LE MEUR, G., . . . ROLLING, F. 2008. Subretinal delivery of recombinant AAV serotype 8 vector in dogs results in gene transfer to neurons in the brain. *Mol Ther,* 16**,** 916-23. http://dx.doi.org/10.1038/mt.2008.41.

STOTHERT, A. R., FONTAINE, S. N., SABBAGH, J. J. & DICKEY, C. A. 2016. Targeting the ER-autophagy system in the trabecular meshwork to treat glaucoma. *Exp Eye Res,* 144**,** 38-45. http://dx.doi.org/10.1016/j.exer.2015.08.017.

STRAUSS, O. 2005. The Retinal Pigment Epithelium in Visual Function. *Physiological Reviews,* 85**,** 845-881. http://dx.doi.org/10.1152/physrev.00021.2004.

STREILEIN, J. W. 2003. Ocular immune privilege: the eye takes a dim but practical view of immunity and inflammation. *Journal of Leukocyte Biology,* 74**,** 179-185. http://dx.doi.org/https://doi.org/10.1189/jlb.1102574.

SUGIMOTO, E., AIHARA, M., OTA, T. & ARAIE, M. 2006. Effect of light cycle on 24-hour pattern of mouse intraocular pressure. *J Glaucoma,* 15**,** 505-11. http://dx.doi.org/10.1097/01.ijg.0000212275.57853.c2.

SUH, S., CHOI, E. H., LEINONEN, H., FOIK, A. T., NEWBY, G. A., YEH, W.-H., . . . PALCZEWSKI, K. 2020. Restoration of visual function in adult mice with an inherited retinal disease via adenine base editing. *Nature Biomedical Engineering*. http://dx.doi.org/10.1038/s41551-020-00632-6.

SUN, X., DAI, Y., CHEN, Y., YU, D. Y., CRINGLE, S. J., CHEN, J., . . . JIANG, C. 2017. Primary angle closure glaucoma: What we know and what we don't know. *Prog Retin Eye Res,* 57**,** 26-45. http://dx.doi.org/10.1016/j.preteyeres.2016.12.003.

SUNDARESAN, P., SIMPSON, D. A., SAMBARE, C., DUFFY, S., LECHNER, J., DASTANE, A., . . . WILLOUGHBY, C. E. 2015. Whole-mitochondrial genome sequencing in primary open-angle glaucoma using massively parallel sequencing identifies novel and known pathogenic variants. *Genet Med,* 17**,** 279-84. http://dx.doi.org/10.1038/gim.2014.121.

SUNG, C. H., MAKINO, C., BAYLOR, D. & NATHANS, J. 1994. A rhodopsin gene mutation responsible for autosomal dominant retinitis pigmentosa results in a protein that is defective in localization to the photoreceptor outer segment. *J Neurosci,* 14**,** 5818-33.

SURACEA, E. & AURICCHIO, A. 2008. Versatility of AAV vectors for retinal gene transfer. *Vision Research,* 48**,** 353-359.

SÜRÜN, D., SCHNEIDER, A., MIRCETIC, J., NEUMANN, K., LANSING, F., PASZKOWSKI-ROGACZ, M., . . . BUCHHOLZ, F. 2020. Efficient Generation and Correction of Mutations in Human iPS Cells Utilizing mRNAs of CRISPR Base Editors and Prime Editors. *Genes (Basel),* 11. http://dx.doi.org/10.3390/genes11050511.

SUZUKI, K. & IZPISUA BELMONTE, J. C. 2018. In vivo genome editing via the HITI method as a tool for gene therapy. *J Hum Genet,* 63**,** 157-164. http://dx.doi.org/10.1038/s10038-017-0352-4.

SUZUKI, K., TSUNEKAWA, Y., HERNANDEZ-BENITEZ, R., WU, J., ZHU, J., KIM, E. J., . . . BELMONTE, J. C. 2016. In vivo genome editing via CRISPR/Cas9 mediated homology-independent targeted integration. *Nature,* 540**,** 144-149. http://dx.doi.org/10.1038/nature20565.

SUZUKI, Y., IWASE, A., ARAIE, M., YAMAMOTO, T., ABE, H., SHIRATO, S., . . . TAJIMI STUDY, G. 2006. Risk factors for open-angle glaucoma in a Japanese population: the Tajimi Study. *Ophthalmology,* 113**,** 1613-7. http://dx.doi.org/10.1016/j.ophtha.2006.03.059.

TAKAHASHI, K. & YAMANAKA, S. 2006. Induction of pluripotent stem cells from mouse embryonic and adult fibroblast cultures by defined factors. *Cell,* 126**,** 663-76. http://dx.doi.org/10.1016/j.cell.2006.07.024.

TAKAHASHI, V. K. L., TAKIUTI, J. T., JAUREGUI, R., MAHAJAN, V. B. & TSANG, S. H. 2018. Rates of Bone Spicule Pigment Appearance in Patients With Retinitis Pigmentosa Sine Pigmento. *Am J Ophthalmol,* 195**,** 176-180. http://dx.doi.org/10.1016/j.ajo.2018.07.036.

TAKAHASHI, V. K. L., XU, C. L., TAKIUTI, J. T., APATOFF, M. B. L., DUONG, J. K., MAHAJAN, V. B. & TSANG, S. H. 2019. Comparison of structural progression between ciliopathy and non-ciliopathy associated with autosomal recessive retinitis pigmentosa. *Orphanet J Rare Dis,* 14**,** 187. http://dx.doi.org/10.1186/s13023-019-1163-9.

TALIB, M., VAN SCHOONEVELD, M. J., VAN CAUWENBERGH, C., WIJNHOLDS, J., TEN BRINK, J. B., FLORIJN, R. J., . . . BOON, C. J. F. 2018. The Spectrum of Structural and Functional Abnormalities in Female Carriers of Pathogenic Variants in the RPGR Gene. *Invest Ophthalmol Vis Sci,* 59**,** 4123-4133. http://dx.doi.org/10.1167/iovs.17-23453.

TALLA, V., KOILKONDA, R. & GUY, J. 2020. Gene Therapy with Single-Subunit Yeast NADH-Ubiquinone Oxidoreductase (NDI1) Improves the Visual Function in Experimental Autoimmune Encephalomyelitis (EAE) Mice Model of Multiple Sclerosis (MS). *Mol Neurobiol,* 57**,** 1952-1965. http://dx.doi.org/10.1007/s12035-019-01857-6.

TALLA, V., YU, H., CHOU, T. H., PORCIATTI, V., CHIODO, V., BOYE, S. L., . . . GUY, J. 2013. NADH-dehydrogenase type-2 suppresses irreversible visual loss and neurodegeneration in the EAE animal model of MS. *Mol Ther,* 21**,** 1876-88. http://dx.doi.org/10.1038/mt.2013.104.

TAN, E., WANG, Q., QUIAMBAO, A. B., XU, X., QTAISHAT, N. M., PEACHEY, N. S., . . . AL-UBAIDI, M. R. 2001. The relationship between opsin overexpression and photoreceptor degeneration. *Invest Ophthalmol Vis Sci,* 42**,** 589-600.

TAN, N. Y., KOH, V., GIRARD, M. J. & CHENG, C.-Y. 2018. Imaging of the lamina cribrosa and its role in glaucoma: a review. *Clinical & Experimental Ophthalmology,* 46**,** 177-188. http://dx.doi.org/https://doi.org/10.1111/ceo.13126.

TAN, Y., CHU, A. H. Y., BAO, S., HOANG, D. A., KEBEDE, F. T., XIONG, W., . . . ZHENG, Z. 2019. Rationally engineered Staphylococcus aureus Cas9 nucleases with high genome-wide specificity. *Proceedings of the National Academy of Sciences,* 116**,** 20969-20976. http://dx.doi.org/10.1073/pnas.1906843116.

TATUM, E. L. 1966. Molecular biology, nucleic acids, and the future of medicine. *Perspect Biol Med,* 10**,** 19-32. http://dx.doi.org/10.1353/pbm.1966.0027.

THAM, Y. C., LI, X., WONG, T. Y., QUIGLEY, H. A., AUNG, T. & CHENG, C. Y. 2014. Global prevalence of glaucoma and projections of glaucoma burden through 2040: a systematic review and meta-analysis. *Ophthalmology,* 121**,** 2081-90. http://dx.doi.org/10.1016/j.ophtha.2014.05.013.

TIAN, G. & COWAN, N. J. 2013. Tubulin-specific chaperones: components of a molecular machine that assembles the alpha/beta heterodimer. *Methods Cell Biol,* 115**,** 155-71. http://dx.doi.org/10.1016/B978-0-12-407757-7.00011-6.

TIELSCH, J. M., KATZ, J., SOMMER, A., QUIGLEY, H. A. & JAVITT, J. C. 1994. Family history and risk of primary open angle glaucoma. The Baltimore Eye Survey. *Arch Ophthalmol,* 112**,** 69-73. http://dx.doi.org/10.1001/archopht.1994.01090130079022.

TIELSCH, J. M., SOMMER, A., KATZ, J., ROYALL, R. M., QUIGLEY, H. A. & JAVITT, J. 1991. Racial variations in the prevalence of primary open-angle glaucoma. The Baltimore Eye Survey. *JAMA,* 266**,** 369-74.

TOGI, S., MUROMOTO, R., HIRASHIMA, K., KITAI, Y., OKAYAMA, T., IKEDA, O., . . . MATSUDA, T. 2016. A New STAT3-binding Partner, ARL3, Enhances the

Phosphorylation and Nuclear Accumulation of STAT3. *J Biol Chem,* 291**,** 11161-71. http://dx.doi.org/10.1074/jbc.M116.724849.

TORNABENE, P., TRAPANI, I., MINOPOLI, R., CENTRULO, M., LUPO, M., DE SIMONE, S., . . . AURICCHIO, A. 2019. Intein-mediated protein trans-splicing expands adeno-associated virus transfer capacity in the retina. *Sci Transl Med,* 11. http://dx.doi.org/10.1126/scitranslmed.aav4523.

TORNABENE, P. T., I. 2020. Can Adeno-Associated Viral Vectors Deliver Effectively Large Genes? *Human Gene Therapy,* 31**,** 47-56. http://dx.doi.org/10.1089/hum.2019.220.

TREVINO, A. E. & ZHANG, F. 2014. Genome editing using Cas9 nickases. *Methods Enzymol,* 546**,** 161-74. http://dx.doi.org/10.1016/b978-0-12-801185-0.00008-8.

TRIFUNOVIC, A., HANSSON, A., WREDENBERG, A., ROVIO, A. T., DUFOUR, E., KHVOROSTOV, I., . . . LARSSON, N. G. 2005. Somatic mtDNA mutations cause aging phenotypes without affecting reactive oxygen species production. *Proc Natl Acad Sci U S A,* 102**,** 17993-8. http://dx.doi.org/10.1073/pnas.0508886102.

TRIFUNOVIC, A., WREDENBERG, A., FALKENBERG, M., SPELBRINK, J. N., ROVIO, A. T., BRUDER, C. E., . . . LARSSON, N. G. 2004. Premature ageing in mice expressing defective mitochondrial DNA polymerase. *Nature,* 429**,** 417-23. http://dx.doi.org/10.1038/nature02517.

TSAI, S. Q., ZHENG, Z., NGUYEN, N. T., LIEBERS, M., TOPKAR, V. V., THAPAR, V., . . . JOUNG, J. K. 2015. GUIDE-seq enables genome-wide profiling of off-target cleavage by CRISPR-Cas nucleases. *Nat Biotechnol,* 33**,** 187-197. http://dx.doi.org/10.1038/nbt.3117.

TSAI, Y.-T., WU, W.-H., LEE, T.-T., WU, W.-P., XU, C. L., PARK, K. S., . . . TSANG, S. H. 2018. Clustered Regularly Interspaced Short Palindromic Repeats-Based Genome Surgery for the Treatment of Autosomal Dominant Retinitis Pigmentosa. *Ophthalmology,* 125**,** 1421-1430. http://dx.doi.org/10.1016/j.ophtha.2018.04.001.

TSIN, A., BETTS-OBREGON, B. & GRIGSBY, J. 2018. Visual cycle proteins: Structure, function, and roles in human retinal disease. *The Journal of biological chemistry,* 293**,** 13016-13021. http://dx.doi.org/10.1074/jbc.AW118.003228.

TURNER, A. J., VANDER WALL, R., GUPTA, V., KLISTORNER, A. & GRAHAM, S. L. 2017. DBA/2J mouse model for experimental glaucoma: pitfalls and problems. *Clin Exp Ophthalmol,* 45**,** 911-922. http://dx.doi.org/10.1111/ceo.12992.

URNOV, F. D. 2018. Genome Editing B.C. (Before CRISPR): Lasting Lessons from the "Old Testament". *Crispr j,* 1**,** 34-46. http://dx.doi.org/10.1089/crispr.2018.29007.fyu.

VAGNI, P., PERLINI, L. E., CHENAIS, N. A. L., MARCHETTI, T., PARRINI, M., CONTESTABILE, A., . . . GHEZZI, D. 2019. Gene Editing Preserves Visual Functions in a Mouse Model of Retinal Degeneration. *Front Neurosci,* 13**,** 945. http://dx.doi.org/10.3389/fnins.2019.00945.

VAN BERGEN, N. J., CROWSTON, J. G., CRAIG, J. E., BURDON, K. P., KEARNS, L. S., SHARMA, S., . . . TROUNCE, I. A. 2015. Measurement of Systemic Mitochondrial Function in Advanced Primary Open-Angle Glaucoma and Leber Hereditary Optic Neuropathy. *PLoS One,* 10**,** e0140919. http://dx.doi.org/10.1371/journal.pone.0140919.

VANDENBERGHE, L. H. & AURICCHIO, A. 2012. Novel adeno-associated viral vectors for retinal gene therapy. *Gene Ther,* 19**,** 162-8. http://dx.doi.org/10.1038/gt.2011.151.

VANDENBERGHE, L. H., BELL, P., MAGUIRE, A. M., XIAO, R., HOPKINS, T. B., GRANT, R., . . . WILSON, J. M. 2013. AAV9 targets cone photoreceptors in the nonhuman primate retina. *PloS one,* 8**,** e53463-e53463. http://dx.doi.org/10.1371/journal.pone.0053463.

VANDERWALL, K. B., HUANG, K.-C., PAN, Y., LAVEKAR, S. S., FLIGOR, C. M., ALLSOP, A. R., . . . MEYER, J. S. 2020. Retinal Ganglion Cells With a Glaucoma OPTN(E50K) Mutation Exhibit Neurodegenerative Phenotypes when Derived from Three-Dimensional Retinal Organoids. *Stem Cell Reports,* 15**,** 52-66. http://dx.doi.org/https://doi.org/10.1016/j.stemcr.2020.05.009.

VASIREDDY, V., MILLS, J. A., GADDAMEEDI, R., BASNER-TSCHAKARJAN, E., KOHNKE, M., BLACK, A. D., . . . BENNETT, J. 2013. AAV-mediated gene therapy for choroideremia: preclinical studies in personalized models. *PLoS One,* 8**,** e61396. http://dx.doi.org/10.1371/journal.pone.0061396.

VECINO, E., RODRIGUEZ, F. D., RUZAFA, N., PEREIRO, X. & SHARMA, S. C. 2016. Glia-neuron interactions in the mammalian retina. *Prog Retin Eye Res,* 51**,** 1-40. http://dx.doi.org/10.1016/j.preteyeres.2015.06.003.

VELEZ, G., MACHLAB, D. A., TANG, P. H., SUN, Y., TSANG, S. H., BASSUK, A. G. & MAHAJAN, V. B. 2018. Proteomic analysis of the human retina reveals region-specific susceptibilities to metabolic- and oxidative stress-related diseases. *PLOS ONE,* 13**,** e0193250. http://dx.doi.org/10.1371/journal.pone.0193250.

VELTEL, S., GASPER, R., EISENACHER, E. & WITTINGHOFER, A. 2008. The retinitis pigmentosa 2 gene product is a GTPase-activating protein for Arf-like 3. *Nat Struct Mol Biol,* 15**,** 373-80. http://dx.doi.org/10.1038/nsmb.1396.

VERBAKEL, S. K., VAN HUET, R. A. C., BOON, C. J. F., DEN HOLLANDER, A. I., COLLIN, R. W. J., KLAVER, C. C. W., . . . KLEVERING, B. J. 2018. Non-syndromic retinitis pigmentosa. *Progress in Retinal and Eye Research,* 66**,** 157-186. http://dx.doi.org/https://doi.org/10.1016/j.preteyeres.2018.03.005.

VIGNAL, C., URETSKY, S., FITOUSSI, S., GALY, A., BLOUIN, L., GIRMENS, J. F., . . . SAHEL, J. A. 2018. Safety of rAAV2/2-ND4 Gene Therapy for Leber Hereditary Optic Neuropathy. *Ophthalmology,* 125**,** 945-947. http://dx.doi.org/10.1016/j.ophtha.2017.12.036.

VINA, J., BORRAS, C. & MIQUEL, J. 2007. Theories of ageing. *IUBMB Life,* 59**,** 249-54. http://dx.doi.org/10.1080/15216540601178067.

VOIGT, A. P., MULFAUL, K., MULLIN, N. K., FLAMME-WIESE, M. J., GIACALONE, J. C., STONE, E. M., . . . MULLINS, R. F. 2019. Single-cell transcriptomics of the human retinal pigment epithelium and choroid in health and macular degeneration. *Proceedings of the National Academy of Sciences,* 116**,** 24100-24107. http://dx.doi.org/10.1073/pnas.1914143116.

VOLLAND, S., ESTEVE-RUDD, J., HOO, J., YEE, C. & WILLIAMS, D. S. 2015. A comparison of some organizational characteristics of the mouse central retina and the human macula. *PLoS One,* 10**,** e0125631. http://dx.doi.org/10.1371/journal.pone.0125631.

VORSTER, A. A., REBELLO, M. T., COUTTS, N., EHRENREICH, L., GAMA, A. D., ROBERTS, L. J., . . . GREENBERG, L. J. 2004. Arg120stop nonsense mutation in the RP2 gene: mutational hotspot and germ line mosaicism? *Clin Genet,* 65**,** 7-10. http://dx.doi.org/10.1111/j..2004.00163.x.

VOUILLOT, L., THELIE, A. & POLLET, N. 2015. Comparison of T7E1 and surveyor mismatch cleavage assays to detect mutations triggered by engineered nucleases. *G3 (Bethesda),* 5**,** 407-15. http://dx.doi.org/10.1534/g3.114.015834.

VROEMEN, P. A. M. M., GORGELS, T. G. M. F., WEBERS, C. A. B. & DE BOER, J. 2019. Modeling the Mechanical Parameters of Glaucoma. *Tissue Engineering Part B: Reviews,* 25**,** 412-428. http://dx.doi.org/10.1089/ten.teb.2019.0044.

WAGNER, D. L., AMINI, L., WENDERING, D. J., BURKHARDT, L.-M., AKYÜZ, L., REINKE, P., . . . SCHMUECK-HENNERESSE, M. 2019. High prevalence of Streptococcus pyogenes Cas9-reactive T cells within the adult human population. *Nature Medicine,* 25**,** 242-248. http://dx.doi.org/10.1038/s41591-018-0204-6.

WAHLIN, K. J., MARUOTTI, J. A., SRIPATHI, S. R., BALL, J., ANGUEYRA, J. M., KIM, C., . . . ZACK, D. J. 2017. Photoreceptor Outer Segment-like Structures in Long-Term 3D Retinas from Human Pluripotent Stem Cells. *Sci Rep,* 7**,** 766. http://dx.doi.org/10.1038/s41598-017-00774-9.

WALTON, R. T., CHRISTIE, K. A., WHITTAKER, M. N. & KLEINSTIVER, B. P. 2020. Unconstrained genome targeting with near-PAMless engineered CRISPR-Cas9 variants. *Science,* 368**,** 290-296. http://dx.doi.org/10.1126/science.aba8853.

WANG, A. L., LUKAS, T. J., YUAN, M. & NEUFELD, A. H. 2010a. Age-related increase in mitochondrial DNA damage and loss of DNA repair capacity in the neural retina. *Neurobiol Aging,* 31**,** 2002-10. http://dx.doi.org/10.1016/j.neurobiolaging.2008.10.019.

WANG, D., TAI, P. W. L. & GAO, G. 2019a. Adeno-associated virus vector as a platform for gene therapy delivery. *Nature Reviews Drug Discovery,* 18**,** 358-378. http://dx.doi.org/10.1038/s41573-019-0012-9.

WANG, D., ZHANG, F. & GAO, G. 2020. CRISPR-Based Therapeutic Genome Editing: Strategies and In Vivo Delivery by AAV Vectors. *Cell,* 181**,** 136-150. http://dx.doi.org/https://doi.org/10.1016/j.cell.2020.03.023.

WANG, J. & DONG, Y. 2016. Characterization of intraocular pressure pattern and changes of retinal ganglion cells in DBA2J glaucoma mice. *Int J Ophthalmol,* 9**,** 211-7. http://dx.doi.org/10.18240/ijo.2016.02.05.

WANG, J., YUSUFU, M., KHOR, C. C., AUNG, T. & WANG, N. 2019b. The genetics of angle closure glaucoma. *Exp Eye Res,* 189**,** 107835. http://dx.doi.org/10.1016/j.exer.2019.107835.

WANG, S. K., XUE, Y., RANA, P., HONG, C. M. & CEPKO, C. L. 2019c. Soluble CX3CL1 gene therapy improves cone survival and function in mouse models of retinitis pigmentosa. *Proceedings of the National Academy of Sciences,* 116**,** 10140-10149. http://dx.doi.org/10.1073/pnas.1901787116.

WANG, X., HARMON, J., ZABRIESKIE, N., CHEN, Y., GROB, S., WILLIAMS, B., . . . ZHANG, K. 2010b. Using the Utah Population Database to assess familial risk of primary open

angle glaucoma. *Vision Res,* 50**,** 2391-5. http://dx.doi.org/10.1016/j.visres.2010.09.018.

WANG, Y. X., XU, L., WEI, W. B. & JONAS, J. B. 2018. Intraocular pressure and its normal range adjusted for ocular and systemic parameters. The Beijing Eye Study 2011. *PLoS One,* 13**,** e0196926. http://dx.doi.org/10.1371/journal.pone.0196926.

WATAKABE, A., OHTSUKA, M., KINOSHITA, M., TAKAJI, M., ISA, K., MIZUKAMI, H., . . . YAMAMORI, T. 2015. Comparative analyses of adeno-associated viral vector serotypes 1, 2, 5, 8 and 9 in marmoset, mouse and macaque cerebral cortex. *Neurosci Res,* 93**,** 144-57. http://dx.doi.org/10.1016/j.neures.2014.09.002.

WATANABE, S., SANUKI, R., UENO, S., KOYASU, T., HASEGAWA, T. & FURUKAWA, T. 2013. Tropisms of AAV for subretinal delivery to the neonatal mouse retina and its application for in vivo rescue of developmental photoreceptor disorders. *PloS one,* 8**,** e54146-e54146. http://dx.doi.org/10.1371/journal.pone.0054146.

WEBB, T. R., PARFITT, D. A., GARDNER, J. C., MARTINEZ, A., BEVILACQUA, D., DAVIDSON, A. E., . . . HARDCASTLE, A. J. 2012. Deep intronic mutation in OFD1, identified by targeted genomic next-generation sequencing, causes a severe form of X-linked retinitis pigmentosa (RP23). *Hum Mol Genet,* 21**,** 3647-54. http://dx.doi.org/10.1093/hmg/dds194.

WEED, L., AMMAR, M. J., ZHOU, S., WEI, Z., SERRANO, L. W., SUN, J., . . . ALEMAN, T. S. 2019. Safety of Same-Eye Subretinal Sequential Readministration of AAV2-hRPE65v2 in Non-human Primates. *Mol Ther Methods Clin Dev,* 15**,** 133-148. http://dx.doi.org/10.1016/j.omtm.2019.08.011.

WEI, W., PAGNAMENTA, A. T., GLEADALL, N., SANCHIS-JUAN, A., STEPHENS, J., BROXHOLME, J., . . . CHINNERY, P. F. 2020. Nuclear-mitochondrial DNA segments resemble paternally inherited mitochondrial DNA in humans. *Nat Commun,* 11**,** 1740. http://dx.doi.org/10.1038/s41467-020-15336-3.

WEI, Z., LI, X., LI, X., LIU, Q. & CHENG, Y. 2018. Oxidative Stress in Parkinson's Disease: A Systematic Review and Meta-Analysis. *Frontiers in Molecular Neuroscience,* 11. http://dx.doi.org/10.3389/fnmol.2018.00236.

WEINREB, R. N., AUNG, T. & MEDEIROS, F. A. 2014. The pathophysiology and treatment of glaucoma: a review. *JAMA,* 311**,** 1901-11. http://dx.doi.org/10.1001/jama.2014.3192.

WEISHEIT, I., KROEGER, J. A., MALIK, R., KLIMMT, J., CRUSIUS, D., DANNERT, A., . . . PAQUET, D. 2020. Detection of Deleterious On-Target Effects after HDR-Mediated CRISPR Editing. *Cell Reports,* 31. http://dx.doi.org/10.1016/j.celrep.2020.107689.

WELBY, E., LAKOWSKI, J., DI FOGGIA, V., BUDINGER, D., GONZALEZ-CORDERO, A., LUN, A. T. L., . . . SOWDEN, J. C. 2017. Isolation and Comparative Transcriptome Analysis of Human Fetal and iPSC-Derived Cone Photoreceptor Cells. *Stem Cell Reports,* 9**,** 1898-1915. http://dx.doi.org/10.1016/j.stemcr.2017.10.018.

WERT, K. J., SKEIE, J. M., DAVIS, R. J., TSANG, S. H. & MAHAJAN, V. B. 2012. Subretinal injection of gene therapy vectors and stem cells in the perinatal mouse eye. *Journal of visualized experiments : JoVE***,** 4286. http://dx.doi.org/10.3791/4286.

WHELAN, L., DOCKERY, A., WYNNE, N., ZHU, J., STEPHENSON, K., SILVESTRI, G., . . . FARRAR, G. J. 2020. Findings from a Genotyping Study of over 1000 People with Inherited Retinal Disorders in Ireland. *Genes,* 11**,** 105.

WIGNAKUMAR, T. & FAIRCHILD, P. J. 2019. Evasion of Pre-Existing Immunity to Cas9: a Prerequisite for Successful Genome Editing In Vivo? *Current Transplantation Reports,* 6**,** 127-133. http://dx.doi.org/10.1007/s40472-019-00237-2.

WILEY, L. A., BURNIGHT, E. R., KAALBERG, E. E., JIAO, C., RIKER, M. J., HALDER, J. A., . . . MULLINS, R. F. 2018. Assessment of Adeno-Associated Virus Serotype Tropism in Human Retinal Explants. *Hum Gene Ther,* 29**,** 424-436. http://dx.doi.org/10.1089/hum.2017.179.

WILLIAMS, D. A. & THRASHER, A. J. 2014. Concise review: lessons learned from clinical trials of gene therapy in monogenic immunodeficiency diseases. *Stem cells translational medicine,* 3**,** 636-642. http://dx.doi.org/10.5966/sctm.2013-0206.

WILLIAMS, D. S. 2008. Usher syndrome: animal models, retinal function of Usher proteins, and prospects for gene therapy. *Vision research,* 48**,** 433-441. http://dx.doi.org/10.1016/j.visres.2007.08.015.

WILLIAMS, P. A., HARDER, J. M., FOXWORTH, N. E., COCHRAN, K. E., PHILIP, V. M., PORCIATTI, V., . . . JOHN, S. W. 2017. Vitamin B3 modulates mitochondrial vulnerability and prevents glaucoma in aged mice. *Science,* 355**,** 756-760. http://dx.doi.org/10.1126/science.aal0092.

WILSON, J. M. 2009. Lessons learned from the gene therapy trial for ornithine transcarbamylase deficiency. *Molecular Genetics and Metabolism,* 96**,** 151-157. http://dx.doi.org/https://doi.org/10.1016/j.ymgme.2008.12.016.

WILSON, P. D. & FRANKS, L. M. 1975. The effect of age on mitochondrial ultrastructure and enzyme cytochemistry. *Biochem Soc Trans,* 3**,** 126-8. http://dx.doi.org/10.1042/bst0030126.

WOJNO, A. P., PIERCE, E. A. & BENNETT, J. 2013. Seeing the light. *Sci Transl Med,* 5**,** 175fs8. http://dx.doi.org/10.1126/scitranslmed.3005798.

WOLFS, R. C., KLAVER, C. C., RAMRATTAN, R. S., VAN DUIJN, C. M., HOFMAN, A. & DE JONG, P. T. 1998. Genetic risk of primary open-angle glaucoma. Population-based familial aggregation study. *Arch Ophthalmol,* 116**,** 1640-5. http://dx.doi.org/10.1001/archopht.116.12.1640.

WRIGHT, A. F., CHAKAROVA, C. F., ABD EL-AZIZ, M. M. & BHATTACHARYA, S. S. 2010. Photoreceptor degeneration: genetic and mechanistic dissection of a complex trait. *Nature Reviews Genetics,* 11**,** 273-284. http://dx.doi.org/10.1038/nrg2717.

WRIGHT, C. B., BECKER, S. M., LOW, L. A., TAGLE, D. A. & SIEVING, P. A. 2020. Improved Ocular Tissue Models and Eye-On-A-Chip Technologies Will Facilitate Ophthalmic Drug Development. *J Ocul Pharmacol Ther,* 36**,** 25-29. http://dx.doi.org/10.1089/jop.2018.0139.

WRIGHT, K. J., BAYE, L. M., OLIVIER-MASON, A., MUKHOPADHYAY, S., SANG, L., KWONG, M., . . . JACKSON, P. K. 2011. An ARL3-UNC119-RP2 GTPase cycle targets myristoylated NPHP3 to the primary cilium. *Genes Dev,* 25**,** 2347-60. http://dx.doi.org/10.1101/gad.173443.111.

WRIGHT, Z. C., SINGH, R. K., ALPINO, R., GOLDBERG, A. F., SOKOLOV, M. & RAMAMURTHY, V. 2016. ARL3 regulates trafficking of prenylated phototransduction proteins to the rod outer segment. *Hum Mol Genet,* 25**,** 2031-2044. http://dx.doi.org/10.1093/hmg/ddw077.

WU, X., SCOTT, D. A., KRIZ, A. J., CHIU, A. C., HSU, P. D., DADON, D. B., . . . SHARP, P. A. 2014. Genome-wide binding of the CRISPR endonuclease Cas9 in mammalian cells. *Nat Biotechnol,* 32**,** 670-6. http://dx.doi.org/10.1038/nbt.2889.

WU, Z., YANG, H. & COLOSI, P. 2010. Effect of genome size on AAV vector packaging. *Mol Ther,* 18**,** 80-6. http://dx.doi.org/10.1038/mt.2009.255.

XIONG, W., WU, D. M., XUE, Y., WANG, S. K., CHUNG, M. J., JI, X., . . . CEPKO, C. L. 2019. AAV cis-regulatory sequences are correlated with ocular toxicity. *Proc Natl Acad Sci U S A,* 116**,** 5785-5794. http://dx.doi.org/10.1073/pnas.1821000116.

YAMAMOTO, Y., BLISS, J. & GERBI, S. A. 2015. Whole Organism Genome Editing: Targeted Large DNA Insertion via ObLiGaRe Nonhomologous End-Joining in Vivo Capture. *G3 (Bethesda),* 5**,** 1843-7. http://dx.doi.org/10.1534/g3.115.019901.

YAMAMOTO, Y. & GERBI, S. A. 2018. Making ends meet: targeted integration of DNA fragments by genome editing. *Chromosoma,* 127**,** 405-420. http://dx.doi.org/10.1007/s00412-018-0677-6.

YANG, N. C., HO, W. M., CHEN, Y. H. & HU, M. L. 2002. A convenient one-step extraction of cellular ATP using boiling water for the luciferin-luciferase assay of ATP. *Anal Biochem,* 306**,** 323-7. http://dx.doi.org/10.1006/abio.2002.5698.

YANG, X. L., VAN DER MERWE, Y., SIMS, J., PARRA, C., HO, L. C., SCHUMAN, J. S., . . . CHAN, K. C. 2018. Age-related Changes in Eye, Brain and Visuomotor Behavior in the DBA/2J Mouse Model of Chronic Glaucoma. *Sci Rep,* 8**,** 4643. http://dx.doi.org/10.1038/s41598-018-22850-4.

YIU, G., CHUNG, S. H., MOLLHOFF, I. N., NGUYEN, U. T., THOMASY, S. M., YOO, J., . . . NORONHA, G. 2020. Suprachoroidal and Subretinal Injections of AAV Using Transscleral Microneedles for Retinal Gene Delivery in Nonhuman Primates. *Molecular Therapy - Methods & Clinical Development,* 16**,** 179-191. http://dx.doi.org/10.1016/j.omtm.2020.01.002.

YOULE, R. J. & VAN DER BLIEK, A. M. 2012. Mitochondrial fission, fusion, and stress. *Science,* 337**,** 1062-5. http://dx.doi.org/10.1126/science.1219855.

YOUNGBLOOD, H., HAUSER, M. A. & LIU, Y. 2019. Update on the genetics of primary open-angle glaucoma. *Exp Eye Res,* 188**,** 107795. http://dx.doi.org/10.1016/j.exer.2019.107795.

YOUSEFI, S., SAKAI, H., MURATA, H., FUJINO, Y., GARWAY-HEATH, D., WEINREB, R. & ASAOKA, R. 2018. Asymmetric Patterns of Visual Field Defect in Primary Open-Angle and Primary Angle-Closure Glaucoma. *Investigative Ophthalmology & Visual Science,* 59**,** 1279-1287. http://dx.doi.org/10.1167/iovs.17-22980.

YU-WAI-MAN, P. 2012. Mitochondrial dysfunction in glaucoma: closing the loop. *Invest Ophthalmol Vis Sci,* 53**,** 2438. http://dx.doi.org/10.1167/iovs.12-9815.

YU-WAI-MAN, P., NEWMAN, N. J., CARELLI, V., MOSTER, M. L., BIOUSSE, V., SADUN, A. A., . . . SAHEL, J.-A. 2020. Bilateral visual improvement with unilateral gene therapy injection for Leber hereditary optic neuropathy. *Science Translational Medicine,* 12**,** eaaz7423. http://dx.doi.org/10.1126/scitranslmed.aaz7423.

YU-WAI-MAN, P., STEWART, J. D., HUDSON, G., ANDREWS, R. M., GRIFFITHS, P. G., BIRCH, M. K. & CHINNERY, P. F. 2010. OPA1 increases the risk of normal but not high tension glaucoma. *J Med Genet,* 47**,** 120-5. http://dx.doi.org/10.1136/jmg.2009.067512.

YU-WAI-MAN, P., TURNBULL, D. M. & CHINNERY, P. F. 2002. Leber hereditary optic neuropathy. *J Med Genet,* 39**,** 162-9. http://dx.doi.org/10.1136/jmg.39.3.162.

YUAN, R., TSAIH, S. W., PETKOVA, S. B., MARIN DE EVSIKOVA, C., XING, S., MARION, M. A., . . . PAIGEN, B. 2009. Aging in inbred strains of mice: study design and interim report on median lifespans and circulating IGF1 levels. *Aging Cell,* 8**,** 277-87. http://dx.doi.org/10.1111/j.1474-9726.2009.00478.x.

YUSOFF, A. A. M., ABDULLAH, W. S. W., KHAIR, S. & RADZAK, S. M. A. 2019. A comprehensive overview of mitochondrial DNA 4977-bp deletion in cancer studies. *Oncol Rev,* 13**,** 409. http://dx.doi.org/10.4081/oncol.2019.409.

ZETTERBERG, M. 2016. Age-related eye disease and gender. *Maturitas,* 83**,** 19-26. http://dx.doi.org/10.1016/j.maturitas.2015.10.005.

ZHANG, H., CONSTANTINE, R., VOROBIEV, S., CHEN, Y., SEETHARAMAN, J., HUANG, Y. J., . . . BAEHR, W. 2011. UNC119 is required for G protein trafficking in sensory neurons. *Nat Neurosci,* 14**,** 874-80. http://dx.doi.org/10.1038/nn.2835.

ZHANG, H., HANKE-GOGOKHIA, C., JIANG, L., LI, X., WANG, P., GERSTNER, C. D., . . . BAEHR, W. 2015a. Mistrafficking of prenylated proteins causes retinitis pigmentosa 2. *FASEB J,* 29**,** 932-42. http://dx.doi.org/10.1096/fj.14-257915.

ZHANG, Y., MA, Y., BU, D., LIU, H., XIA, C., ZHANG, Y., . . . QI, Y. 2015b. Deletion of a 4977-bp Fragment in the Mitochondrial Genome Is Associated with Mitochondrial Disease Severity. *PLoS One,* 10**,** e0128624. http://dx.doi.org/10.1371/journal.pone.0128624.

ZHAO, R. Z., JIANG, S., ZHANG, L. & YU, Z. B. 2019. Mitochondrial electron transport chain, ROS generation and uncoupling (Review). *Int J Mol Med,* 44**,** 3-15. http://dx.doi.org/10.3892/ijmm.2019.4188.

ZHAO, X., WEI, C., LI, J., XING, P., LI, J., ZHENG, S. & CHEN, X. 2017. Cell cycle-dependent control of homologous recombination. *Acta Biochimica et Biophysica Sinica,* 49**,** 655-668. http://dx.doi.org/10.1093/abbs/gmx055.

ZHENG, S., XIAO, L., LIU, Y., WANG, Y., CHENG, L., ZHANG, J., . . . CHEN, D. 2018. DZNep inhibits H3K27me3 deposition and delays retinal degeneration in the rd1 mice. *Cell Death Dis,* 9**,** 310. http://dx.doi.org/10.1038/s41419-018-0349-8.

ZHENG, T., HOU, Y., ZHANG, P., ZHANG, Z., XU, Y., ZHANG, L., . . . DU, Q. 2017. Profiling single-guide RNA specificity reveals a mismatch sensitive core sequence. *Sci Rep,* 7**,** 40638. http://dx.doi.org/10.1038/srep40638.

ZHONG, L., BRADLEY, J., SCHUBERT, W., AHMED, E., ADAMIS, A. P., SHIMA, D. T., . . . NG, Y. S. 2007. Erythropoietin promotes survival of retinal ganglion cells in DBA/2J glaucoma mice. *Invest Ophthalmol Vis Sci,* 48**,** 1212-8. http://dx.doi.org/10.1167/iovs.06-0757.

ZHONG, X., GUTIERREZ, C., XUE, T., HAMPTON, C., VERGARA, M. N., CAO, L. H., . . . CANTO-SOLER, M. V. 2014. Generation of three-dimensional retinal tissue with functional photoreceptors from human iPSCs. *Nat Commun,* 5**,** 4047. http://dx.doi.org/10.1038/ncomms5047.

ZHOU, L., LI, Y. & YUE, B. Y. 1999. Oxidative stress affects cytoskeletal structure and cell-matrix interactions in cells from an ocular tissue: the trabecular meshwork. *J Cell Physiol,* 180**,** 182-9. http://dx.doi.org/10.1002/(SICI)1097-4652(199908)180:2<182::AID-JCP6>3.0.CO;2-X.

ZHOU, T., BENDA, C., DUNZINGER, S., HUANG, Y., HO, J. C., YANG, J., . . . ESTEBAN, M. A. 2012. Generation of human induced pluripotent stem cells from urine samples. *Nature Protocols,* 7**,** 2080-2089. http://dx.doi.org/10.1038/nprot.2012.115.

ZODE, G. S., KUEHN, M. H., NISHIMURA, D. Y., SEARBY, C. C., MOHAN, K., GROZDANIC, S. D., . . . SHEFFIELD, V. C. 2011. Reduction of ER stress via a chemical chaperone prevents disease phenotypes in a mouse model of primary open angle glaucoma. *J Clin Invest,* 121**,** 3542-53. http://dx.doi.org/10.1172/JCI58183.

7 Appendices

7.1 Appendix 1 – Publication associated with Chapter 2

Please cite this article in press as: Lane et al., Modeling and Rescue of RP2 Retinitis Pigmentosa Using iPSC-Derived Retinal Organoids, Stem Cell Reports (2020), https://doi.org/10.1016/j.stemcr.2020.05.007

Stem Cell Reports
Article

ISSCR

OPEN ACCESS

Modeling and Rescue of RP2 Retinitis Pigmentosa Using iPSC-Derived Retinal Organoids

Amelia Lane,[1,3] Katarina Jovanovic,[1,3] Ciara Shortall,[2] Daniele Ottaviani,[1] Anna Brugulat Panes,[1] Nele Schwarz,[1] Rosellina Guarascio,[1] Matthew J. Hayes,[1] Arpad Palfi,[2] Naomi Chadderton,[2] G. Jane Farrar,[2,*] Alison J. Hardcastle,[1,*] and Michael E. Cheetham[1,*]

[1]UCL Institute of Ophthalmology, London, UK
[2]Smurfit Institute of Genetics, Trinity College Dublin, Dublin 2, Ireland
[3]Co-first author
*Correspondence: jane.farrar@tcd.ie (G.J.F.), a.hardcastle@ucl.ac.uk (A.J.H.), michael.cheetham@ucl.ac.uk (M.E.C.)
https://doi.org/10.1016/j.stemcr.2020.05.007

SUMMARY

RP2 mutations cause a severe form of X-linked retinitis pigmentosa (XLRP). The mechanism of *RP2*-associated retinal degeneration in humans is unclear, and animal models of *RP2* XLRP do not recapitulate this severe phenotype. Here, we developed gene-edited isogenic *RP2* knockout (RP2 KO) induced pluripotent stem cells (iPSCs) and *RP2* patient-derived iPSC to produce 3D retinal organoids as a human retinal disease model. Strikingly, the RP2 KO and *RP2* patient-derived organoids showed a peak in rod photoreceptor cell death at day 150 (D150) with subsequent thinning of the organoid outer nuclear layer (ONL) by D180 of culture. Adeno-associated virus-mediated gene augmentation with human RP2 rescued the degeneration phenotype of the RP2 KO organoids, to prevent ONL thinning and restore rhodopsin expression. Notably, these data show that 3D retinal organoids can be used to model photoreceptor degeneration and test potential therapies to prevent photoreceptor cell death.

INTRODUCTION

The reprogramming of patient-derived cells into induced pluripotent stem cells (iPSCs) has enabled the derivation and differentiation of a range of somatic cell types and has revolutionized our ability to study inherited disease (Takahashi et al., 2007). The differentiation of iPSCs toward retinal lineages has seen huge advances in recent years with the refinement of protocols for the generation of 3D retinal organoids (ROs) (Gagliardi et al., 2019; Nakano et al., 2012). Unlike previous models in 2D, these 3D structures contain photoreceptors with morphologically identifiable features; including, inner segments rich in mitochondria, rudimentary outer segments with connecting cilia, and synaptic pedicles, in addition to bipolar, Müller glia, ganglion and amacrine cells, synaptic layers, and an outer limiting membrane (OLM), arranged in retinal layers (reviewed in Capowski et al., 2019). These advanced models have proven to have many translational research applications, including transplantation studies (Gonzalez-Cordero et al., 2017; Shirai et al., 2016), retinal disease modeling, and testing the efficacy of potential therapies in human photoreceptor cells (Deng et al., 2018; Parfitt et al., 2016; Schwarz et al., 2017; Sharma et al., 2017). To date, however, they have not been used to model and rescue photoreceptor cell death.

Mutations in *RP2* account for approximately 15% of all cases of X-linked retinitis pigmentosa (XLRP) (Breuer et al., 2002; Hardcastle et al., 1999). RP2 is a GTPase-activating protein (GAP) for the small GTPase ARL3 (Veltel et al., 2008), which is also regulated by its guanine nucleotide exchange factor (GEF) ARL13B (Gotthardt et al., 2015). ARL13B is localized to the ciliary axoneme, whereas a pool of RP2 and ARL3 localize at the basal body and associated centriole at the base of photoreceptors (Evans et al., 2010; Grayson et al., 2002). ARL3, with its effectors (UNC119 and PDEdelta [PDED]) and GAP RP2, are thought to be important in the retina to traffic lipidated proteins, such as transducin, GRK1, and PDE6, to the photoreceptor outer segment (Ismail et al., 2011; Schwarz et al., 2012; Wright et al., 2011; Zhang et al., 2011; Zhang et al., 2015). *Rp2* knockout mice have a relatively mild phenotype compared with human disease. In one model mis-localization/absence of GRK1 and cone PDE6a was evident at 14 months (Zhang et al., 2015), whereas another model was reported to have rhodopsin and M opsin mis-localization at 2 months and outer nuclear layer (ONL) thinning at 5 months (Li et al., 2013). In contrast, the human phenotype is relatively severe with some patients experiencing macular atrophy in childhood (Jayasundera et al., 2010), highlighting the necessity for human retinal models of disease.

Currently there are no treatments for this condition, so there is a need to develop potential therapies. Characterization of iPSC-derived RPE and early-stage ROs from an individual carrying a nonsense mutation in *RP2* (c.358C > T, p.R120X) showed changes in Golgi cohesion, Gbeta trafficking in RPE, and ciliary trafficking of KIF7 in ROs (Schwarz et al., 2015, 2017). Furthermore, treatment with the readthrough drugs, G418 and/or Ataluren (PTC124),

Please cite this article in press as: Lane et al., Modeling and Rescue of RP2 Retinitis Pigmentosa Using iPSC-Derived Retinal Organoids, Stem Cell Reports (2020), https://doi.org/10.1016/j.stemcr.2020.05.007

could restore detectable full-length RP2 protein and rescue the Golgi cohesion and Gbeta mis-localization in iPSC-RPE and kinesin traffic in ROs. Gene therapy for other inherited retinal diseases using adeno-associated viruses (AAVs) has been shown to efficiently transduce photoreceptors and RPE following subretinal injection (Sarra et al., 2002) in animal models. There is a Food and Drug Administration- and European Medicines Agency-approved AAV-mediated ocular gene therapy (Russell et al., 2017), and a number of AAV-mediated ocular gene therapies are currently in phase I/II and III clinical trials (clinicaltrials.gov). AAV delivery of human RP2 to a mouse knockout model of RP2-XLRP preserved cone function, but had no effect on rod cell function and toxicity was observed at a higher viral dose (Mookherjee et al., 2015).

Here, we describe the temporal maturation of CRISPR gene-edited *RP2* knockout ROs relative to their isogenic control, in addition to ROs derived from two unrelated individuals with the same R120X nonsense mutation. These studies reveal that the loss of RP2 leads to rod photoreceptor degeneration that can be rescued by AAV delivery of RP2.

RESULTS

RP2 Knockout and *RP2* Patient iPSCs Develop Mature ROs

Fibroblasts from two unrelated individuals (R120X-A and R120X-B) carrying the nonsense mutation c.358C > T; p.R120X were reprogrammed into iPSCs by nucleofection (Okita et al., 2011; Schwarz et al., 2015). CRISPR/Cas9 with guides designed to target exon 2 of *RP2* were used to generate RP2 knockout iPSCs using a simultaneous reprogramming and gene-editing protocol (Howden et al., 2015). The location of the gRNA on exon 2 was selected due to its proximity to the c.358C > T p.R120X site, thus any knockout lines generated would closely mimic the consequences of this nonsense mutation. RP2 KO iPSC clones were identified through non-homologous end-joining-mediated creation of indels; one clone with an 8-bp deletion in exon 2 of *RP2* (RP2 c.371_378delAAGCTGGA; p.Lys124SerfsTer11) was selected for further study as it had the shortest frameshift extension before a premature stop codon. Western blotting of iPSCs showed efficient knockout, as no RP2 protein was detectable (Figures 1A and 1B).

The RP2 KO line, the non-edited isogenic control, and two R120X patient iPSC lines were differentiated into ROs over a period of 4–10 months using methods described previously (Nakano et al., 2012; Zhong et al., 2014) with slight modifications. Both methods produced biologically similar organoids that were developmentally and structurally comparable at the time points tested. By day 180 (D180) a transparent ONL with a brush-like border was visible by light microscopy (Figure 1C). Scattered rhodopsin-positive cells were first detectable in control organoids in the recoverin-positive ONL from D150 then increased in number over time as the ROs matured up to D180 (Figure S1A). By D180 all cell lines were able to generate ROs consisting of a laminated structure with a compacted ONL containing recoverin and cone arrestin-positive photoreceptors (Figure 1D), above an inner nuclear layer (INL) containing protein kinase C alpha (PKCα)-positive bipolar cells and CRALBP/Nestin-positive Müller glia (Figure S1B). In all ROs, the ONL terminated at the apical edge, with an OLM that was strongly immunoreactive for F actin (Figure 1D). Above the OLM, mitochondria (immunoreactive for TOM20) were enriched in globular inner segments. Immunostaining for the ciliary marker ARL13B and polyglutamylated tubulin (GT335) revealed the bulging shape at the tip of the photoreceptor connecting cilia, as they matured to form outer segment (OS) like structures from D150 onward (Figure S1C). RP2 could be detected in control ROs at the plasma membrane in all cells in the INL and ONL. In RP2 KO and R120X cell lines, RP2 immunoreactivity was absent by immunocytochemistry (ICC), although some background fluorescence was observed at the edges of the presumptive OS. qPCR was used to measure relative *RP2* mRNA expression in ROs at D180. The RP2 KO clone had only 20% *RP2* mRNA relative to its isogenic control, similar to the R120X patient ROs (n = 3) (Figure 1E), suggesting that the mutant allele transcript is subject to nonsense-mediated decay in all these ROs. Electron microscopy confirmed the presence of membranous-rich structures at the apical ciliary tip, reminiscent of early OS formation, in both controland RP2 KO ROs (Figure 1F). These rudimentary OS were often found detached from the body of the RO indicating the flexibility, or fragility, of these structures in the absence of RPE. Collectively, these results show that RP2 ablation does not prevent the differentiation of iPSC into photoreceptors bearing OS-like structures in 3D RO culture.

Loss of RP2 Leads to Photoreceptor Cell Death and ONL Thinning

Similar to the neural retina *in vivo*, the outermost cell layer of the ROs consists of a uniform compacted ONL, which terminates with photoreceptor synaptic pedicles that are separated from the inner retinal cells by a layer immunoreactive for synaptic structural protein Bassoon in the outer plexiform layer (Figure 2A). A reduction in the number of photoreceptor nuclei in the ONL, and thereby thickness, *in vivo* is a marker of photoreceptor cell degeneration. Therefore, ONL thickness was measured in isogenic controls and RP2 KO at D120, D150, and D180 (Figure 2B).

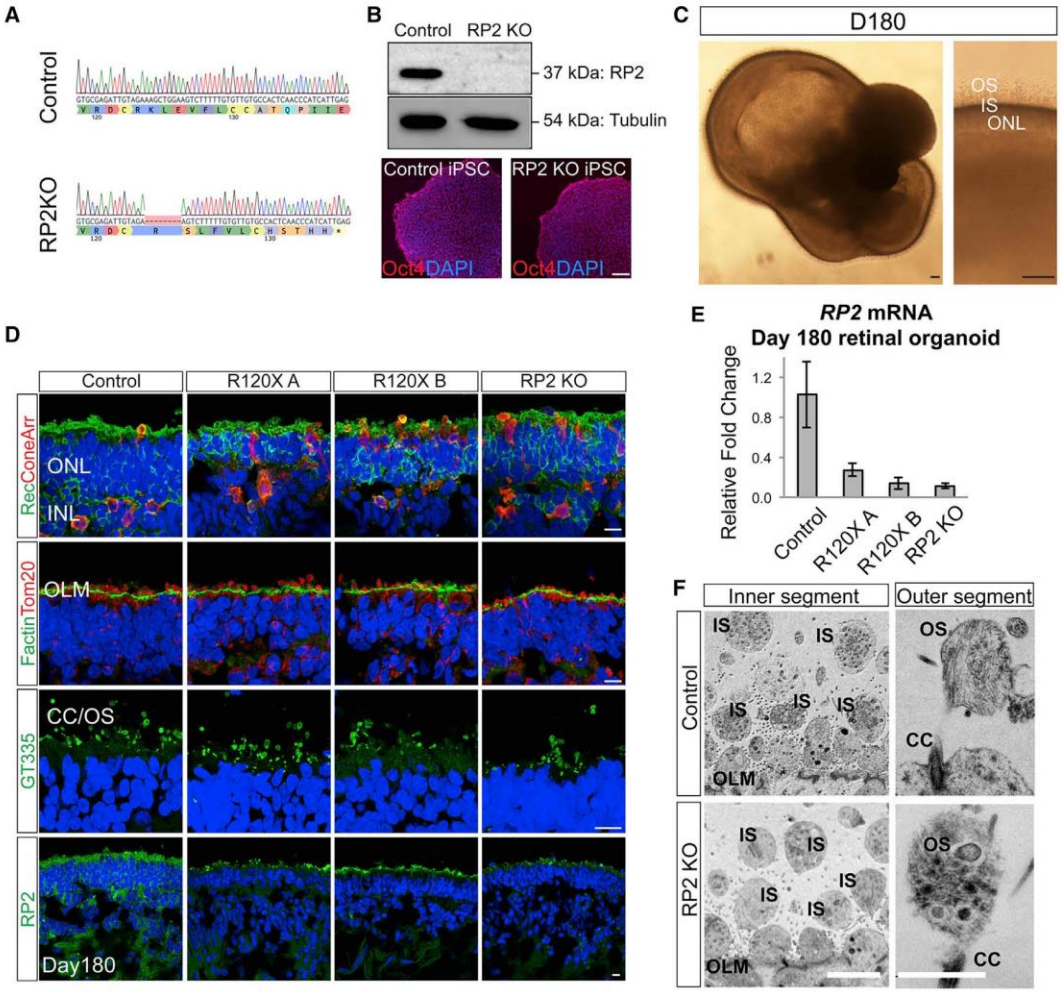

Figure 1. Retinal Organoids from R120X, RP2 KO, and Isogenic Control iPSCs

(A) Sanger sequence trace of edited RP2 KO iPSCs. CRISPR/Cas9 gene editing was used to create an 8-bp deletion in exon 2 of *RP2* by NHEJ.

(B) Western blot and immunocytochemistry (ICC) of control and RP2 KO iPSC. Scale bar, 50 μm.

(C) Retinal organoid morphology at D180, a layer of IS/OS is visible by differential interference contrast above the transparent ONL. Scale bar, 50 μm.

(D) ICC of retinal organoids at D180. Photoreceptors (recoverin and cone arrestin [coneArr]), outer limiting membrane (OLM, F actin) mitochondria (Tom20), and connecting cilia/OS (GT335) expression in the ONL of control and RP2 null iPSC retinal organoids. RP2 is expressed at the plasma membrane of cells in the ONL and inner nuclear layer (INL) in control organoids. Scale bar, 10 μm.

(E) qPCR of *RP2* mRNA in whole retinal organoids at D180 (n = 3 independent organoids). Mean ± standard error of the mean (SEM).

(F) Electron micrographs of control and RP2 KO retinal organoids at D180. Scale bars, 5 μm (left), 1 μm (right).

In control ROs, the average ONL thickness increased between D120 and D150 from 20 to 25 μm, then did not change significantly between D150 and D180. In contrast, in RP2 KO ROs the average ONL thickness decreased significantly between D150 and D180 ($p = 0.02$). Similarly, R120X ROs from both patients had significantly thinner ONLs at D180 compared with the control cell line ($p \leq 0.01$; Figures 2 and S2). This suggested that photoreceptor cell death might be occurring between D150 and D180 in the RP2 null cell lines.

To test this hypothesis further, we measured TUNEL reactivity across the ONL in RP2 KO and control ROs at D120, D150, and D180 (Figures 2C and 2D). A small percentage of TUNEL-positive nuclei were detectable in the photoreceptor ONL at all time points. In control ROs, TUNEL reactivity was not significantly different at D120, D150, or

Please cite this article in press as: Lane et al., Modeling and Rescue of RP2 Retinitis Pigmentosa Using iPSC-Derived Retinal Organoids, Stem Cell Reports (2020), https://doi.org/10.1016/j.stemcr.2020.05.007

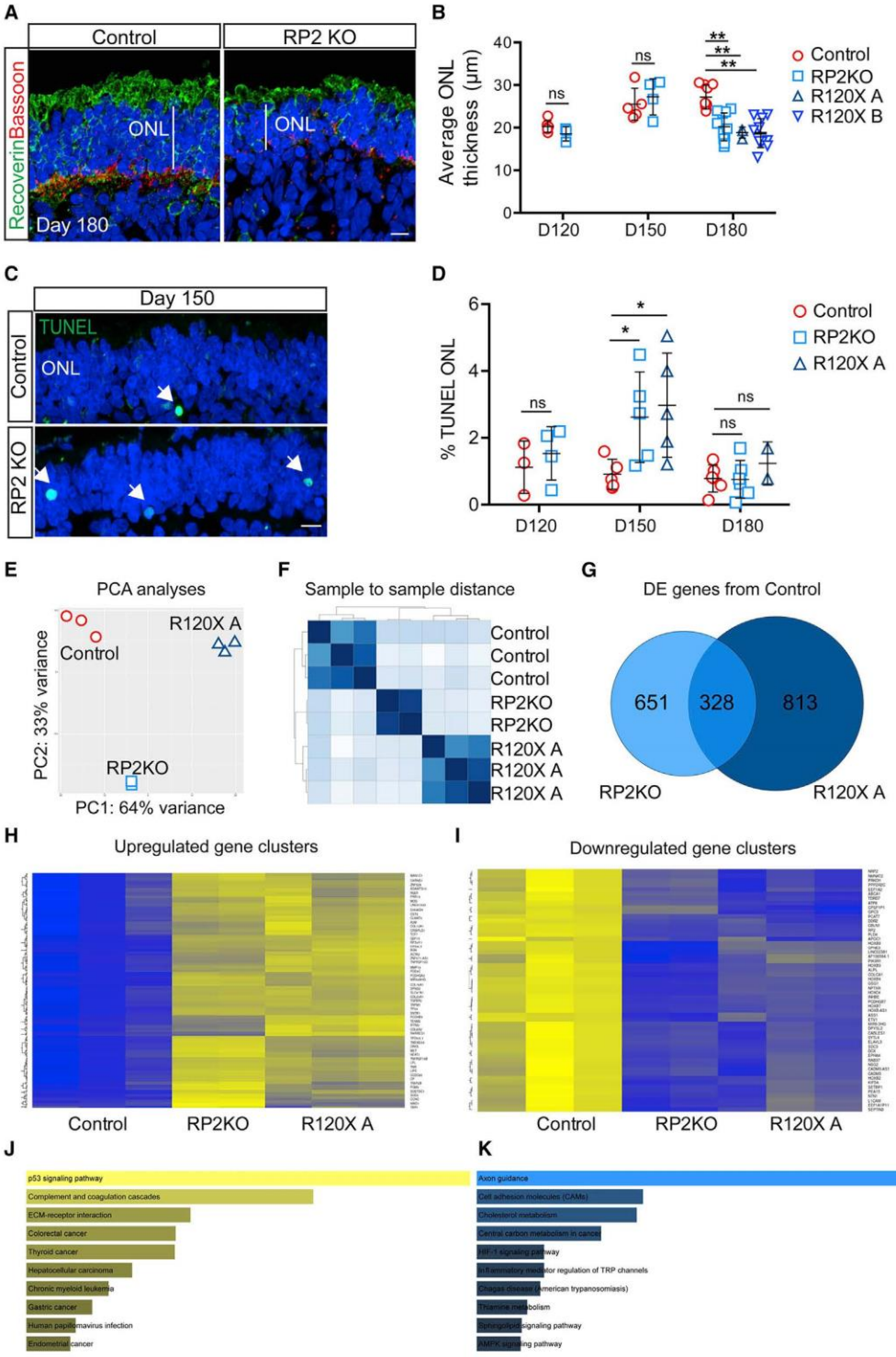

(legend on next page)

D180. Whereas, the RP2 KO ROs had a significantly higher percentage of TUNEL-positive cells in the ONL at D150. There was no significant difference between RP2 KO and controls at D120 or D180, suggesting a peak of cell death during photoreceptor differentiation and maturation around D150 in RP2-deficient cell lines. This was confirmed in R120X-A ROs, with an increase in TUNEL reactivity at D150, which had resolved by D180 (Figure 2D). These data show that there is a peak in photoreceptor cell death that correlates with their maturation and the time course of increased rhodopsin expression.

Gene Expression Changes Associated with Loss of RP2

To investigate gene expression changes that might be associated with the death of photoreceptors in the RP2 null organoids, RNA sequencing (RNA-seq) was performed on D150 controls, RP2 KO, and R120X-A ROs. Principal-component analyses and sample to sample distance shows that the gene expression profiles of the RP2 KO ROs were between the R120X-A patient line and the parental isogenic control (Figures 2E and 2F). There were 328 shared differentially expressed (DE) genes between the RP2 KO and R120X ROs compared with control (Figures 2G–2I). By contrast there were 651 and 813 DE genes between control and RP2 KO and R120X-A ROs, respectively, that were not shared. Kyoto Encyclopedia of Genes and Genomes (KEGG) pathway analyses of the shared DE genes revealed that the "p53 signaling pathway" was the major upregulated pathway, whereas the major downregulated pathway was "axon guidance" (Figures 2J and 2K). KEGG pathway analyses of the axon guidance-related changes showed that expression of genes in pathways that stimulate axon outgrowth, attraction, and repulsion were reduced (Figure S3). Whereas further investigation of the KEGG apoptosis and p53 signaling pathways showed that a number of pro-apoptotic genes, such as p21, BAX, and PUMA, were upregulated in both RP2 null ROs (Figure S3), supporting the observation that loss of RP2 induces cell death in ROs.

Rod Photoreceptor Differentiation and Survival Is Compromised in RP2 KO and R120X ROs

To identify which types of photoreceptor cells were most affected by the loss of RP2, rods and cones were stained with rhodopsin and cone arrestin at D180 (Figure 3A). Strikingly, in the RP2 KO ROs, there was reduced immunoreactivity for rhodopsin compared with isogenic controls. Unlike recoverin expression, which was widespread in the RP2 KO ROs, rhodopsin was restricted to patches of the ONL. To assess photoreceptor gene expression, we quantified rhodopsin (*RHO*) and rod transducin (*GNAT1*) expression by qPCR. In the controls both *RHO* and *GNAT1* showed an age-dependent increase, with a major increase between D150 and D180. In contrast, the RP2 KO ROs had reduced expression of *RHO* and *GNAT1* mRNA at D180, but not D120 or D150, confirming that this difference manifested from D150 onward. The percentage of photoreceptors that were immunoreactive for rhodopsin was quantified as a percentage of DAPI-positive nuclei across the full length of the ONL in sections from all ROs (Figure 3C). The controls showed an increase in rhodopsin-positive cells as the ROs matured. Despite variation between individual ROs, there was a significant difference in the percentage of rhodopsin-expressing cells in mature ROs (D180) between the isogenic control and RP2 KO cell lines (Figures 3A and 3C). Furthermore, the two R120X lines also showed very few rhodopsin-positive photoreceptors at D180, similar to the RP2 KO ROs (Figure 3C). By contrast, the percentage of cone arrestin-positive cells was significantly increased in the RP2 KO and R120X ROs compared with controls at D180, and the mRNA (*ARR3*) was also increased in the RP2 KO ROs at D150 and D180

Figure 2. Photoreceptor Differentiation-Associated Cell Death in RP2 KO Organoids

(A) ICC of control and RP2 KO retinal organoids showing reduced ONL thickness in RP2 KO. Recoverin staining demarcates the ONL terminating in the synaptic layer stained with Bassoon. Scale bar, 10 μm.

(B) Mean ONL thickness per organoid was measured from tilescans of cryosections of a whole organoid at D120, D150 (n = 5 control; n = 4 RP2 KO at both time points), and D180. Significant ONL thinning was recorded at D180 in RP2 KO (n = 9 independent organoids) and R120X lines (n = 3 R120X A organoids, n = 9 R120X B organoids), but not in controls (n = 10 independent organoids; $p \leq 0.01$; mean ± SD).

(C) TUNEL reactive nuclei (arrows) in the ONL of RP2 KO and isogenic control organoids at D150. Scale bar, 10 μm.

(D) Quantification of TUNEL reactivity. RP2 KO organoids had a significantly higher proportion of TUNEL-positive cells at D150 (n = 5 independent organoids $p \leq 0.05$, mean ± SD) but not at D120 (n = 3 control; n = 4 RP2 KO) or D180 (n = 5 control; n = 6 RP2 KO). R120X organoids also had increased TUNEL reactivity at D150 (n = 5 at D150 n = 2 at D180 independent organoids).

(E) Principal-component analyses of RNA-seq data from ROs (n = 3 control and R120X A, n = 2 RP2 KO independent organoids).

(F) Sample to sample distance between samples.

(G) Venn diagram showing differentially expressed genes between RP2 KO and control and R120X and control and common genes.

(H) Heatmap showing upregulated clusters of differentially expressed genes (blue, lower expression; yellow, higher expression).

(I) Heatmap of downregulated clusters of differentially expressed genes.

(J) KEGG pathway analyses of upregulated genes.

(K) KEGG pathway analyses of downregulated genes.

Please cite this article in press as: Lane et al., Modeling and Rescue of RP2 Retinitis Pigmentosa Using iPSC-Derived Retinal Organoids, Stem Cell Reports (2020), https://doi.org/10.1016/j.stemcr.2020.05.007

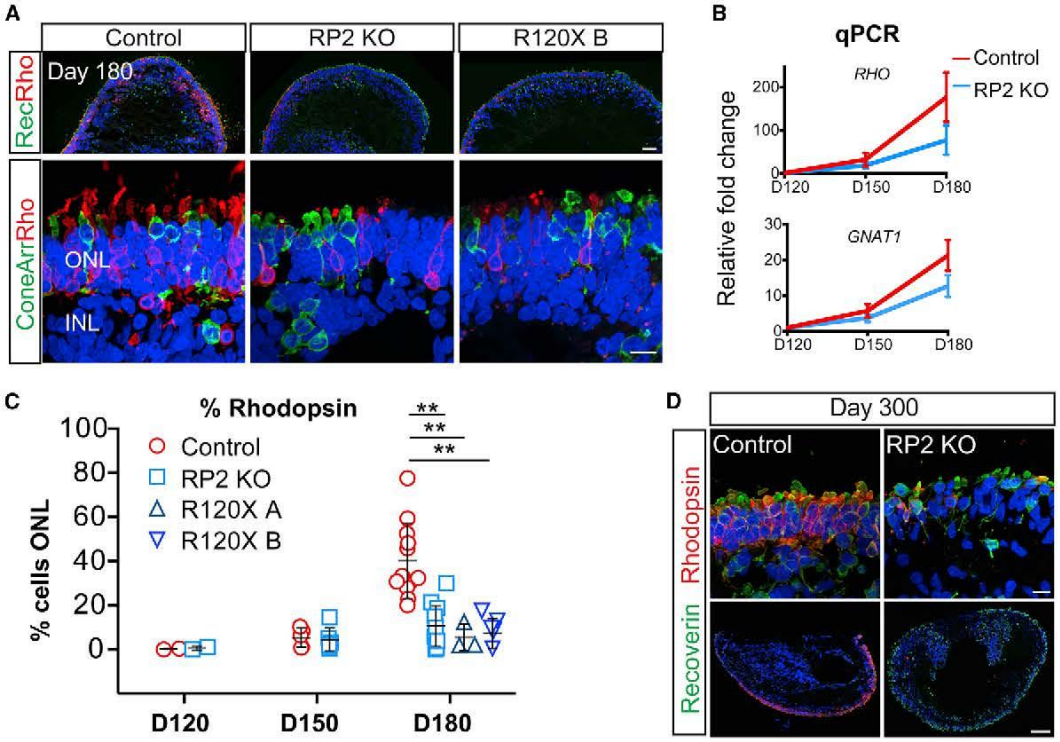

Figure 3. Reduced Number of Rod Cells in RP2 KO and R120X Patient Retinal Organoids

(A) ICC of retinal organoids. Low (upper panel) and high (lower panel) power magnification of recoverin, rhodopsin, and cone arrestin immunoreactivity in the ONL at D180 in control, RP2 KO, and R120X RP2 retinal organoids. Scale bars, 50 μm and 10 μm.

(B) *RHO* and *GNAT1* levels in retinal organoids. qPCR showing relative fold change in mRNA in control and RP2 KO retinal organoids at D120, D150, and D180 (n = 3, 3, 4 independent organoids). Mean ± SEM.

(C) Quantification of rhodopsin-positive cells as a percentage of ONL in control, RP2 KO and R120X patient cell lines from D120 to D180 of differentiation. Each data point represents the mean of 1 independent organoid, counts are from tilescans of whole organoid cross-sections (D120 n = 2 control, n = 2 RP2 KO; D150 n = 5 control, n = 6 RP2 KO; D180 n = 12 control, n = 11 RP2 KO, n = 3 R120X A, n = 5 R120X B; $^{**}p \leq 0.01$; mean ± SD).

(D) High and low magnification of control and RP2 KO organoids at D300 of differentiation stained with recoverin and rhodopsin. Scale bars, 10 μm (upper panel) and 100 μm (lower panel).

(Figure S4), suggesting that the defect primarily affects rods and not cones. There was no significant difference in bipolar cell numbers (Chx10/PKCα) between control and RP2 KO ROs (Figure S4). To exclude that these differences might be attributed to simply a delay in the rate of maturation between the cell lines, control and RP2 KO ROs were maintained in culture for a further 120 days to D300. The RP2 KO had fewer rhodopsin-positive cells relative to the control ROs at D300, whereas recoverin-positive photoreceptors were maintained (Figure 3E).

AAV2/5 Efficiently Transduces ROs to Augment RP2 Expression in RP2 Null Photoreceptors

AAVs are able to transduce post-mitotic rods and cones in mice following subretinal injection (Sarra et al., 2002) and in iPSC-derived rod and cone photoreceptors in ROs with varying efficiency (Gonzalez-Cordero et al., 2018). To assess the ability of AAVs to deliver RP2 to deficient photoreceptors, RP2 KO ROs were transduced with AAV2/5.CAGp.RP2 (Figure 4A) at D140, before the observed onset of ONL thinning, and harvested at D180. At D180, RP2 protein could be detected by ICC throughout the ONL (Figure 4B). At higher magnification, the RP2 signal was detected on the plasma membrane of photoreceptors (Figure 4C). The percentage of RP2-positive cells was determined by scoring nuclei with closely adjacent RP2 signal on the plasma membrane that matched that cell morphology. The transduction efficiency was 90% ± 7% in the ONL (Figure 4D). This included both rhodopsin-positive rod cells

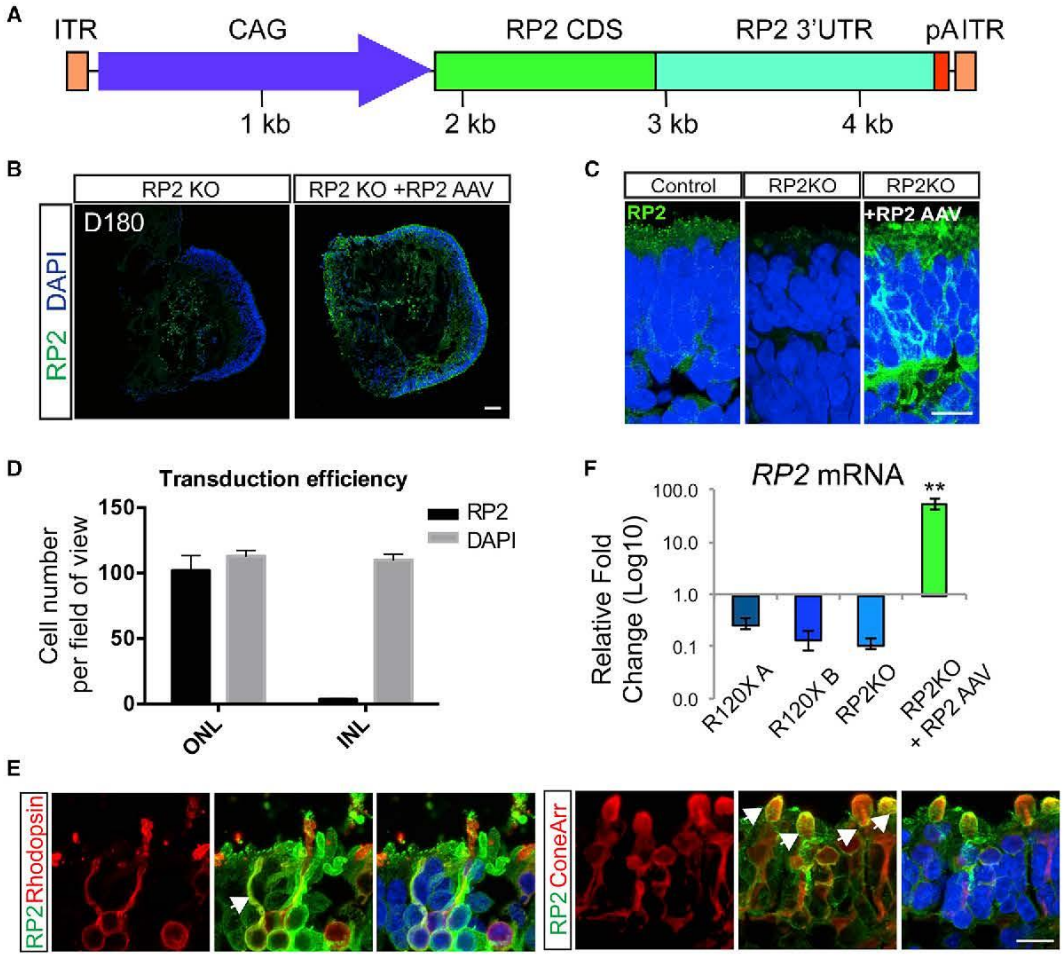

Figure 4. AAV2/5 RP2 Efficiently Transduces Rod and Cone Photoreceptors

(A) Schematic of AAV construction. CAG promoter (blue); RP2 CDS (green); RP2 3′ UTR (teal); pA (red, minimal rabbit b globin poly A); ITR (orange).

(B) RP2 expression in RP2 KO retinal organoids after transduction. ICC on RP2 KO retinal organoid cryosections 6 weeks after transduction with AAV2/5 CAG RP2 showing RP2 expression across the photoreceptor layer (ONL). Scale bar, 50 μm.

(C) High-power magnification of RP2 immunoreactivity. Scale bar, 10 μm.

(D) Cells with RP2 immunoreactivity in the ONL and INL scored against DAPI (mean = 90% ± 7% ONL versus 3% ± 0.4% INL, n = 3 independent organoids; mean ± SD).

(E) ICC co-staining RP2 with cone arrestin or rhodopsin showing AAV-driven RP2 expression in both rod and cone photoreceptors. Scale bar, 10 μm.

(F) qPCR of RP2 mRNA transcript levels in AAV-transduced RP2 KO organoids relative to endogenous expression in control organoids (n = 3 independent organoids; mean = 55-fold ±7.7 SEM).

(Figure 4E) and cone arrestin-positive cone cells (Figure 4E). Sporadic RP2 staining in the inner retinal layers was also visible, suggesting that a small proportion of the AAV is able to penetrate the RO and transduce inner retinal cells (Figure S5). Analysis of mRNA levels by qPCR revealed an average 55-fold increase in RP2 transcript relative to control organoids (Figure 4F).

AAV2/5-Driven RP2 Gene Augmentation Improves Photoreceptor Survival

To investigate if the increase in RP2 levels was altering the degenerative phenotype of the ROs, ONL thickness and rhodopsin immunoreactivity were compared in RP2 AAV-transduced versus untransduced RP2 KO ROs at D180 (Figures 5A and 5C). The ONL was stained with

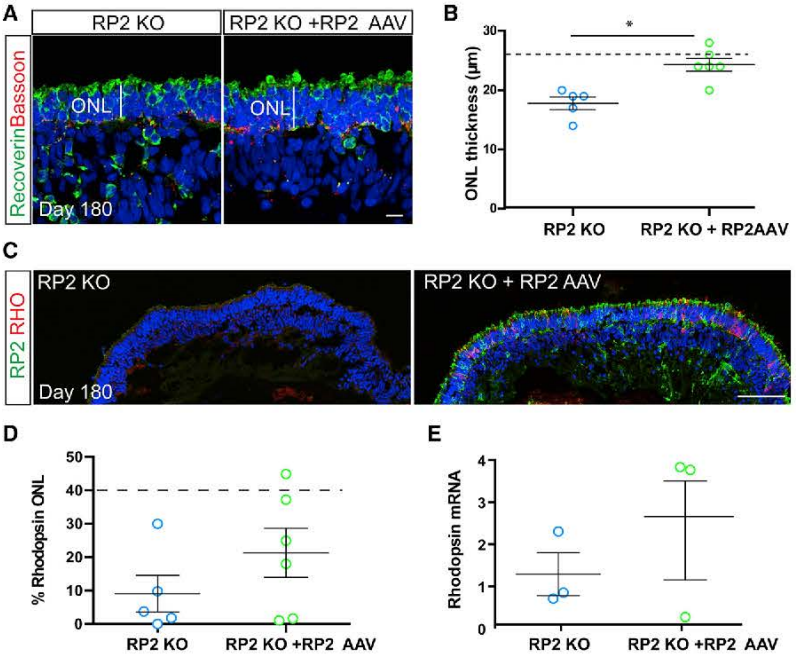

Figure 5. AAV2/5-Driven RP2 Overexpression Rescues Photoreceptor Survival

(A) ICC of retinal organoid ONL with recoverin (green) and Bassoon (red) in RP2 KO control and AAV RP2-treated retinal organoids showing improved ONL thickness in the AAV-treated group. Scale bar, 10 µm.

(B) Quantification of ONL thickness in control and AAV transduced retinal organoids (n = 5 RP2-KO, 6 RP2 KO + AAV independent organoids, *p = 0.016, mean ± SEM). Dotted line represents mean thickness in isogenic control parent cell line.

(C) ICC showing RP2 (green) and rhodopsin (red) expression after transduction. Scale bar, 50 µm.

(D) Quantification of ICC to assess rhodopsin-positive cells in control and RP2 AAV-transduced RP2 KO retinal organoids. Dotted line represents average control values (n = 5 RP2 KO, n = 6 RP2 KO + RP2 AAV independent organoids, p = 0.23; mean ± SEM).

(E) qPCR for *RHO* mRNA levels in control and RP2 AAV-treated RP2 KO retinal organoids (n = 3 independent organoids). Mean ± SEM.

recoverin and Bassoon (Figure 5A). Measurement of the ONL revealed that AAV-RP2-transduced RP2 KO organoids had a significantly thicker ONL than non-transduced controls at D180 ($p \leq 0.01$, Figure 5B) with increased numbers of photoreceptors (Figure S5). The ONL thickness post-transduction was similar to that observed for the isogenic control cells at D180, suggesting near complete rescue. In most, but not all, transduced organoids the percentage of rhodopsin-positive cells was above the average for non-transduced RP2 KOs suggesting that AAV RP2 expression could restore rhodopsin immunoreactivity (Figure 5D). This was also observed at the mRNA level, with up to a 3-fold increase in *RHO* level in transduced ROs; however, one transduced RO showed no response at the level of rhodopsin expression (Figure 5E). The percentage of cone arrestin-positive cells was also reduced following AAV transduction, but *ARR3* mRNA was unchanged (Figure S5).

DISCUSSION

Here, we describe an *in vitro* model of RP2 XLRP and show that AAV gene augmentation of RP2 can successfully reverse measurable and clinically relevant disease phenotypes. The combination of iPSC reprogramming, CRISPR gene-editing technology, and AAV gene delivery has enabled a side by side comparison of RP2 KO, isogenic controls, and XLRP patient ROs, to obviate some of the inherent variation in iPSC-derived organoid models.

Differentiation of iPSCs presents an opportunity to probe genetic disease mechanisms in the cells and tissues that are affected by specific genetic changes. This is particularly useful in the case of ubiquitously expressed genes, such as *RP2*, that have disease pathology restricted to a specific tissue, such as the retina. Here, we used iPSC reprogramming technology in combination with CRISPR/Cas9 gene editing to probe disease mechanisms in *RP2* XLRP.

All of the RP2-deficient cell lines used in this study successfully developed 3D ROs with advanced morphological features, including lamination and formation of rod and cone photoreceptors. Strikingly, we observed a significant decline in photoreceptor cell numbers, specifically rhodopsin-positive rods, and significantly thinner ONL after 150 days of differentiation in all RP2-deficient lines. Widespread rhodopsin expression is one of the later events in RO development, in keeping with the developmental time line *in vivo*; however, the presence of other late-emerging cell markers in the RP2 KO and patient cell lines, such as cone arrestin-positive cone photoreceptors, PKCα-positive bipolar cells, and OS structures, together with the persistence of this rhodopsin-deficient phenotype up to 300 days of differentiation suggests that this is not merely a case of developmental delay.

This phenotype has not been reported in any existing animal models of RP2 XLRP (Li et al., 2013; Zhang et al., 2015),

suggesting that this is either specific to human retina, or to the *in vitro* organoid system. Despite the relative stability of ROs in comparison with *ex vivo* retinal explant culture, which can be maintained for around 14 days (Johnson and Martin, 2008), it is likely that the conditions for retinal cell maintenance in culture are suboptimal. The absence of an opposing RPE monolayer, nutrient and oxygen deprivation through the lack of vascular blood supply, or the lack of connectivity for the inner retinal neurons, for example, may be sources of stress that accelerate the onset of disease phenotypes. This may go some way to explain the early "age" of detectable changes relative to mouse and human RP2 XLRP *in vivo*. In RP2 KO mice, ONL thinning is detectable only at 5 months of age in one model (Li et al., 2013), whereas almost no ONL thinning was observed at 12 months of age in another model (Zhang et al., 2015). Here, we detected measurable differences in photoreceptor survival at the onset of rod differentiation and rhodopsin expression. Cell death is an important, non-pathological process during retinal development (Vecino et al., 2004), but is increased during differentiation in the photoreceptor cell layer of RP2-deficient ROs, linking rod maturation temporally with rod cell death in this model. Interestingly, ROs from an individual with a mutation in *RPGR*, the other major form of XLRP, also showed signs of photoreceptor cell death at around 150 days of RO differentiation, which was rescued by CRISPR-mediated repair of the RPGR mutation in the iPSC (Deng et al., 2018). The induction of p53 pathways was also observed in the RPGR retinal organoid model (Deng et al., 2018), suggesting that this could be a common pathway in both forms of XLRP in human ROs. Therefore, photoreceptor cell death appears to be a feature in ROs for some forms of inherited retinal disease, but the precise mechanisms and whether there is an opportunity to inhibit the cell death process will require further investigation.

AAV is a highly efficient method of delivering therapeutic genes to photoreceptor cells and AAV2/5 has been shown to effectively transduce photoreceptors in a variety of species *inter alia* mice (Palfi et al., 2012), non-human primates (Boye et al., 2012), and human retinal explants (Wiley et al., 2018). The use of AAV in human ROs is currently limited, but studies have reported varying efficiency of transduction, which could be attributed to age of treatment, time of harvesting, vector tropisms, viral titer, the promotor used, and the sensitivity of detection of the transgene, e.g., antibody versus intrinsic fluorescence of a reporter (Garita-Hernandez et al., 2020; Gonzalez-Cordero et al., 2018; Quinn et al., 2019). Here, we demonstrate highly efficient transduction using an AAV2/5 vector with RP2 under the control of a CAG promoter. The AAV appears to deliver RP2 more or less exclusively to the photoreceptor cells despite the use of a ubiquitous promotor. This may be due to a combination of vector tropisms and the organization of the organoid, where the photoreceptor layer is outermost and, therefore, in contact the viral particles in solution. In addition, the OLM may prevent diffusion of AAV into the inner retinal layers. The interaction of AAV and photoreceptors in this system is analogous to the situation following subretinal delivery. Indeed, in a human treatment context, the optimal route of administration for this vector would be subretinal injection. Although intravitreal injection is less invasive, most AAV serotypes cannot transduce photoreceptors efficiently when administered intravitreally.

AAV RP2 was delivered at D140, before the onset of the increase in photoreceptor TUNEL reactivity and ONL thinning, but late enough to ensure efficient uptake, following reports of inefficient transduction at earlier time points (Gonzalez-Cordero et al., 2018). Not only was RP2 efficiently expressed at the mRNA and protein level, but it was also able to rescue the ONL-thinning phenotype in RP2 KO ROs implying a protective effect of RP2 overexpression in photoreceptor cells. Interestingly, although RP2 was expressed at over 55-fold the endogenous level, we did not observe any overt deleterious effects. In a previous study, some toxicity was observed with RP2 overexpression in mice 3 months after administration of the highest dose of AAV-RP2 vector (1×10^9 viral genomes [vg]/eye), although the level of RP2 overexpression in transduced mouse eyes was not defined (Mookherjee et al., 2015). As RP2 is a GAP for ARL3, it is possible that increasing RP2 to a high level would inhibit the production of ARL3-GTP and mimic the effect of loss of the ARL3 GEF, ARL13b, which causes Joubert syndrome; however, this might not occur in the cellular context because of the spatial separation of the proteins, with RP2 predominantly at the base of the cilium and ARL13b in the axoneme, which leads to a gradient of ARL3-GTP in the cilium. Despite very high levels of RP2, once ARL3 is trafficked into the cilium it can be converted to ARL3-GTP by ARL13b; however, this would not exclude other activities of overexpressed RP2 from disrupting homeostasis. Therefore, additional studies evaluating the therapeutic index for AAV-RP2 therapies in ROs, and/or the primate eye, would be of value, before translation to the clinic.

Although RP2 is expressed in multiple retinal cell types, it remains to be established whether optimal rescue of the RP2 disease phenotype may require expression of a replacement *RP2* gene in other retinal cell types, such as the RPE. The use of a ubiquitous promoter in the current study should, in principle, enable expression of the therapeutic gene in multiple cell types. Additional studies will be required to fully elucidate the requirement, or otherwise, for RP2 in the RPE, to develop optimal RP2 gene therapies. In contrast to the current study, Mookherjee et al. (2015) used the photoreceptor-specific rhodopsin kinase

promoter to drive expression of the RP2 gene and achieved a partial rescue of the cone phenotype in a null RP2 mouse model but had no beneficial effect on the rod phenotype.

This study provides insights into the use of ROs for retinal disease modeling, with a phenotype related to loss of RP2 that is unique to the human retina cell culture model. Importantly, the photoreceptor cell death in the RP2-deficient organoids correlates with the timing of rod cell maturation and rhodopsin expression. Furthermore, we highlight how the use of AAV for the restoration of RP2 expression can reverse this phenotype, and as such could be further investigated as a potential therapeutic avenue for the treatment of XLRP.

EXPERIMENTAL PROCEDURES

Reprogramming and Gene Editing

Following informed consent, a skin biopsy was obtained from study participants to obtain dermal fibroblasts. The study followed the tenets of the Declaration of Helsinki and was approved by the Moorfields Eye Hospital and Royal Victoria Eye and Ear Hospital Dublin Research Ethics Committees. iPSCs were generated from two unrelated R120X individuals and control fibroblasts (BJ fibroblast ATCC CRL-2522) as described previously (Schwarz et al., 2015). RP2 KO iPSCs were produced by simultaneous reprogramming and gene editing using a method described previously (Howden et al., 2015). Guide RNAs were designed to target exon 2 of *RP2* (see Table S1 for sequences), and were cloned into the pSpCas9(BB)-2A-Puro (PX459) V2.0 plasmid (Addgene plasmid no. 62,988) according to a previously described protocol (Ran et al., 2013). iPSC clones were manually isolated, genomic DNA extracted (Promega), and PCR amplified with primers designed around the target site (Table S1). iPSC clones were analyzed by Sanger sequencing to confirm *RP2* gene disruption. Off-Spotter (https://cm.jefferson.edu/Off-Spotter/) was used to predict off-targets for the selected gRNA and the top 10 off-targets were assessed with Sanger sequencing, which detected no changes (Figure S1D; Table S1). In addition, all DE genes from the RNA-seq analysis were cross-referenced with off-target predictions and a further eight potential off-target sites with four or five mismatches were analyzed (Figure S1E; Table S1). These showed no sequence changes.

Differentiation of iPSCs to ROs

RO differentiation was carried out as described previously (Nakano et al., 2012; Zhong et al., 2014). In brief, iPSCs were grown to near confluence in E8 medium before detaching colonies in gentle dissociation buffer (STEMCELL Technologies) to form embryoid bodies (EBs). EBs were transitioned to neural induction medium in the presence of blebbistatin, before plating down at a density of approximately 20 EBs per cm^2. Emerging transparent pouches of neuroepithelium were isolated using a needle and cultured in suspension in retinal maturation media +0.5 μm retinoic acid up to D140, after which retinoic acid was removed. Alternatively EBs were generated by single-cell dissociation and forced aggregation in 96-well V-bottomed plates and cultured in suspension thereafter (Nakano et al., 2012). Days of culture are ±3days.

AAV Production

The RP2 replacement vector comprising a CAG promoter, human RP2 CDS, RP2 3′ UTR, including an RP2 poly(A) sequence, and a minimal rabbit β-globin poly(A), was synthesized by GeneArt (Life Technologies) and cloned into pAAV-MCS using flanking NotI sites. More detail of sequences is in the Supplemental Information. Recombinant AAV2/5 viruses were generated by helper virus-free, triple transfection (Xiao et al., 1998). Human embryonic kidney cells (accession number CRL-1573; ATCC, USA) were transfected with pAAV-RP2, pRep/Cap5 (Hildinger et al., 2001) and pHelper (Agilent Technologies, USA) at a ratio of 1:1:2, as described previously (O'reilly et al., 2007). Seventy-two hours after transfection, AAV particles were purified from the clarified lysate by differential precipitation with polyethylene glycol followed by cesium gradient centrifugation (Ayuso et al., 2010). AAV-containing fractions were dialyzed against PBS supplemented with Pluronic F68 (0.001%; Bennicelli et al., 2008). Genomic titers (vg/mL) were determined by quantitative real-time PCR (qPCR; Rohr et al., 2002).

AAV Treatment

RP2 AAV was prepared to a final titer 4.73×10^{12} vg/mL. At 140 days, organoids with brush borders visible by light microscopy, which show inner segment and OS development, were transferred to the well of 96-well plate and incubated with 1E11 viral genomes in 75 μL media for 8 h before topping the media up to 200 μL. Followed by 50/50 medium changes every 2 days until day 180.

RNA Extraction and qPCR

ROs or half ROs were subjected to RNA extraction using an RNeasy MicroKit (QIAGEN) and cDNA synthesis was performed using a Tetro cDNA synthesis kit (Bioline). qPCR was carried out on an Applied Biosystems 7900HT Fast Real-Time PCR system using the SYBR Green method using 1 μL cDNA per triplicate. Data from the qPCR were normalized to the geometric mean of the expression of two internal reference genes in each sample. *POLR2A* and *MAN1B1* were chosen due to their consistency across the sample groups, which was determined using the GeNorm algorithm (Vandesompele et al., 2002). Primers were designed to cross exon boundaries (see Table S2).

RNA-Seq

Three ROs from BJ controls and R120X cell lines and two ROs from the RP2 KO cell line were harvested at D150. The RNA was extracted with the RNeasy micro kit (QIAGEN) following the manufacturer's instructions, followed by paired-end sequencing at 100 million read depth for each sample (Illumina, Otogenetics, Atlanta, GA, USA). Raw.fastq sequences were cleaned from any residual sequencing adapter using cutadapt with parameters -m 20 and -e 0.1. Fragments were then aligned to the human genome

(build 38, Ensembl version 92) using STAR and genes counted using featurecounts.

Differential expression analysis was then performed using the DESeq2 pipeline. Initial inspection of the dataset showed biases, which were blind estimated and corrected using the sva package (DESeq2 manual). The differential expression analysis showed that 1,141 genes were differentially expressed between the R120X ROs and the control, whereas 979 genes were differentially expressed between the RP2 KO ROs and the isogenic control and 328 genes were common to the 2 RP2-depleted backgrounds. Of these, 232 genes were consistently upregulated and 56 were downregulated. The list of DE genes is shown in Table S3. Finally, we used the web platform Enricher to source any significant pathway (https://amp.pharm.mssm.edu/Enrichr/). According to the KEGG there was a significant upregulation of the "p53 signaling pathway" in the RP2 KO and RP2-R120X retina (Figure S3).

Immunofluorescence

ROs were either fixed whole or bisected under a dissecting microscope using micro scissors (Fine Science Tools) with the other half processed for RNA extraction. ROs or half ROs were fixed in 4% paraformaldehyde at 4°C for 20–30 min before cryoprotection by immersion overnight in 30% sucrose/PBS. Following orientation under a dissecting microscope in OCT they were frozen and cryosectioned into 6-μm sections. For ICC, slides were blocked in 10% donkey serum, 0.1% Triton X for 1 h before incubation with primary antibodies for 2 h (see Table S4 for primary antibodies) and donkey anti-rabbit or mouse Alexa Flour 488 or 555 secondary antibodies for 1 h (Thermo Fisher). Nuclei were visualized using DAPI (2 μg/mL) staining for all images.

Imaging

All images were obtained using a Carl Zeiss LSM700 or LSM 710 laser scanning confocal microscope. Images were exported from Zen imaging software and prepared using Adobe Photoshop and Illustrator CS4. All measurements were performed in Fiji (Schindelin et al., 2012). For quantification of TUNEL, rod and cone cell numbers, and ONL thickness measurements, the tilescan function was used to obtain images of whole organoid sections at 40× magnification (more detail in Supplemental Information). Individual rod-, cone-, and TUNEL-positive cell numbers in the ONL were manually counted across the whole section. ONL thickness was calculated by measuring the length and area of the whole recoverin-positive ONL in the DAPI channel using Fiji.

Electron Microscopy

ROs were fixed overnight in 3% glutaraldehyde and 1% paraformaldehyde buffered to pH 7.4 with 0.08 M sodium cacodylate-HCl buffer. After rinsing in 0.1 M sodium cacodylate-HCl buffer (pH 7.4) twice for 5 min, the ROs were post-fixed in 1% aqueous osmium tetroxide for 2 h, dehydrated by passage through ascending alcohols (10-min steps, 1× 50%–90% and 3% × 100%) and two changes of propylene oxide, and infiltrated overnight with a 1:1 mixture of propylene oxide:araldite on a rotator. Finally, ROs were infiltrated with araldite resin over 4–6 h and embedded in fresh resin, which was then cured by overnight incubation at 60°C. Semithin sections (0.75 μm) were stained with a 1% mixture of toluidine blue-borax in 50% ethanol, and ultrathin sections were contrasted with Reynolds lead citrate for imaging in a JEOL 1010 TEM operating at 80 kV. Images were captured using a Gatan Orius CCD camera using Digital Micrograph software.

Statistical Analysis

Statistical analysis was carried out on GraphPad Prism. Data were subjected to two-way ANOVA and/or by multiple t tests using the Holm-Sidak method, with $\alpha = 5.00\%$. Each time point was analyzed individually, without assuming a consistent standard deviation (SD). Significance was determined at a p value of < 0.05.

Data and Code Availability

The RNA-seq data are available at GEO: GSE148300.

SUPPLEMENTAL INFORMATION

Supplemental Information can be found online at https://doi.org/10.1016/j.stemcr.2020.05.007.

AUTHOR CONTRIBUTIONS

A.L., K.J., C.S., D.O., A.B.P., N.S., R.G., M.J.H., N.E.S., A.P., and N.C. performed the experiments and/or analyzed the data. A.L., K.J., C.S., D.O., N.E.S., G.J.F., A.J.H., and M.E.C. conceived the hypothesis and designed the experiments. A.L., K.J., C.S., G.J.F., A.J.H., and M.E.C. drafted the manuscript. All authors edited the draft manuscript.

ACKNOWLEDGMENTS

We are grateful to Robert Molday (UBC), Cheryl Craft (USC), Peter MacLeish (Morehouse School of Medicine), and Wolfgang Baehr (University of Utah) for providing antibodies. This work was funded by Moorfields Eye Charity through a generous donation (to A.J.H. and M.E.C.), Fight for Sight (to M.E.C. and A.J.H.), the NC3Rs (to M.E.C.), and the Wellcome Trust (to M.E.C.). It was also supported by the NIH Research Biomedical Research Centre at Moorfields Eye Hospital NHS Foundation Trust and UCL Institute of Ophthalmology (A.J.H. is NIHR BRC Faculty). Support was also provided by the Health Research Board of Ireland (HRB), Fighting Blindness Ireland (FBI), the Medical Research Charities Group (MRCG), and Science Foundation Ireland (to G.J.F.).

Received: February 7, 2020
Revised: May 13, 2020
Accepted: May 13, 2020
Published: June 11, 2020

REFERENCES

Ayuso, E., Mingozzi, F., Montane, J., Leon, X., Anguela, X.M., Haurigot, V., Edmonson, S.A., Africa, L., Zhou, S., High, K.A., et al. (2010). High AAV vector purity results in serotype- and tissue-independent enhancement of transduction efficiency. Gene Ther. *17*, 503–510.

Bennicelli, J., Wright, J.F., Komaromy, A., Jacobs, J.B., Hauck, B., Zelenaia, O., Mingozzi, F., Hui, D., Chung, D., Rex, T.S., et al. (2008). Reversal of blindness in animal models of leber congenital amaurosis using optimized AAV2-mediated gene transfer. Mol. Ther. *16*, 458–465.

Boye, S.E., Alexander, J.J., Boye, S.L., Witherspoon, C.D., Sandefer, K.J., Conlon, T.J., Erger, K., Sun, J., Ryals, R., Chiodo, V.A., et al. (2012). The human rhodopsin kinase promoter in an AAV5 vector confers rod- and cone-specific expression in the primate retina. Hum. Gene Ther. *23*, 1101–1115.

Breuer, D.K., Yashar, B.M., Filippova, E., Hiriyanna, S., Lyons, R.H., Mears, A.J., Asaye, B., Acar, C., Vervoort, R., Wright, A.F., et al. (2002). A comprehensive mutation analysis of RP2 and RPGR in a North American cohort of families with X-linked retinitis pigmentosa. Am. J. Hum. Genet. *70*, 1545–1554.

Capowski, E.E., Samimi, K., Mayerl, S.J., Phillips, M.J., Pinilla, I., Howden, S.E., Saha, J., Jansen, A.D., Edwards, K.L., Jager, L.D., et al. (2019). Reproducibility and staging of 3D human retinal organoids across multiple pluripotent stem cell lines. Development *146*.

Deng, W.L., Gao, M.L., Lei, X.L., Lv, J.N., Zhao, H., He, K.W., Xia, X.X., Li, L.Y., Chen, Y.C., Li, Y.P., et al. (2018). Gene correction reverses ciliopathy and photoreceptor loss in iPSC-derived retinal organoids from retinitis pigmentosa patients. Stem Cell Reports *10*, 1267–1281.

Evans, R.J., Schwarz, N., Nagel-Wolfrum, K., Wolfrum, U., Hardcastle, A.J., and Cheetham, M.E. (2010). The retinitis pigmentosa protein RP2 links pericentriolar vesicle transport between the Golgi and the primary cilium. Hum. Mol. Genet. *19*, 1358–1367.

Gagliardi, G., Ben M'barek, K., and Goureau, O. (2019). Photoreceptor cell replacement in macular degeneration and retinitis pigmentosa: a pluripotent stem cell-based approach. Prog. Retin. Eye Res. *71*, 1–25.

Garita-Hernandez, M., Routet, F., Guibbal, L., Khabou, H., Toualbi, L., Riancho, L., Reichman, S., Duebel, J., Sahel, J.A., Goureau, O., and Dalkara, D. (2020). AAV-mediated gene delivery to 3D retinal organoids derived from human induced pluripotent stem cells. Int. J. Mol. Sci. *21*.

Gonzalez-Cordero, A., Goh, D., Kruczek, K., Naeem, A., Fernando, M., Kleine Holthaus, S.M., Takaaki, M., Blackford, S.J.I., Kloc, M., Agundez, L., et al. (2018). Assessment of AAV vector tropisms for mouse and human pluripotent stem cell-derived RPE and photoreceptor cells. Hum. Gene Ther. *29*, 1124–1139.

Gonzalez-Cordero, A., Kruczek, K., Naeem, A., Fernando, M., Kloc, M., Ribeiro, J., Goh, D., Duran, Y., Blackford, S.J.I., Abelleira-Hervas, L., et al. (2017). Recapitulation of human retinal development from human pluripotent stem cells generates transplantable populations of cone photoreceptors. Stem Cell Reports *9*, 820–837.

Gotthardt, K., Lokaj, M., Koerner, C., Falk, N., Giessl, A., and Wittinghofer, A. (2015). A G-protein activation cascade from Arl13B to Arl3 and implications for ciliary targeting of lipidated proteins. eLife *4*.

Grayson, C., Bartolini, F., Chapple, J.P., Willison, K.R., Bhamidipati, A., Lewis, S.A., Luthert, P.J., Hardcastle, A.J., Cowan, N.J., and Cheetham, M.E. (2002). Localization in the human retina of the X-linked retinitis pigmentosa protein RP2, its homologue cofactor C and the RP2 interacting protein Arl3. Hum. Mol. Genet. *11*, 3065–3074.

Hardcastle, A.J., Thiselton, D.L., Van Maldergem, L., Saha, B.K., Jay, M., Plant, C., Taylor, R., Bird, A.C., and Bhattacharya, S. (1999). Mutations in the RP2 gene cause disease in 10% of families with familial X-linked retinitis pigmentosa assessed in this study. Am. J. Hum. Genet. *64*, 1210–1215.

Hildinger, M., Auricchio, A., Gao, G., Wang, L., Chirmule, N., and Wilson, J.M. (2001). Hybrid vectors based on adeno-associated virus serotypes 2 and 5 for muscle-directed gene transfer. J. Virol. *75*, 6199–6203.

Howden, S.E., Maufort, J.P., Duffin, B.M., Elefanty, A.G., Stanley, E.G., and Thomson, J.A. (2015). Simultaneous reprogramming and gene correction of patient fibroblasts. Stem Cell Reports *5*, 1109–1118.

Ismail, S.A., Chen, Y.X., Rusinova, A., Chandra, A., Bierbaum, M., Gremer, L., Triola, G., Waldmann, H., Bastiaens, P.I., and Wittinghofer, A. (2011). Arl2-GTP and Arl3-GTP regulate a GDI-like transport system for farnesylated cargo. Nat. Chem. Biol. *7*, 942–949.

Jayasundera, T., Branham, K.E., Othman, M., Rhoades, W.R., Karoukis, A.J., Khanna, H., Swaroop, A., and Heckenlively, J.R. (2010). RP2 phenotype and pathogenetic correlations in X-linked retinitis pigmentosa. Arch. Ophthalmol. *128*, 915–923.

Johnson, T.V., and Martin, K.R. (2008). Development and characterization of an adult retinal explant organotypic tissue culture system as an in vitro intraocular stem cell transplantation model. Invest. Ophthalmol. Vis. Sci. *49*, 3503–3512.

Li, L., Khan, N., Hurd, T., Ghosh, A.K., Cheng, C., Molday, R., Heckenlively, J.R., Swaroop, A., and Khanna, H. (2013). Ablation of the X-linked retinitis pigmentosa 2 (Rp2) gene in mice results in opsin mislocalization and photoreceptor degeneration. Invest. Ophthalmol. Vis. Sci. *54*, 4503–4511.

Mookherjee, S., Hiriyanna, S., Kaneshiro, K., Li, L., Li, Y., Li, W., Qian, H., Li, T., Khanna, H., Colosi, P., et al. (2015). Long-term rescue of cone photoreceptor degeneration in retinitis pigmentosa 2 (RP2)-knockout mice by gene replacement therapy. Hum. Mol. Genet. *24*, 6446–6458.

Nakano, T., Ando, S., Takata, N., Kawada, M., Muguruma, K., Sekiguchi, K., Saito, K., Yonemura, S., Eiraku, M., and Sasai, Y. (2012). Self-formation of optic cups and storable stratified neural retina from human ESCs. Cell Stem Cell *10*, 771–785.

O'reilly, M., Palfi, A., Chadderton, N., Millington-Ward, S., Ader, M., Cronin, T., Tuohy, T., Auricchio, A., Hildinger, M., Tivnan, A., et al. (2007). RNA interference-mediated suppression and replacement of human rhodopsin in vivo. Am. J. Hum. Genet. *81*, 127–135.

Okita, K., Matsumura, Y., Sato, Y., Okada, A., Morizane, A., Okamoto, S., Hong, H., Nakagawa, M., Tanabe, K., Tezuka, K., et al. (2011). A more efficient method to generate integration-free human iPS cells. Nat. Methods *8*, 409–412.

Palfi, A., Chadderton, N., Mckee, A.G., Blanco Fernandez, A., Humphries, P., Kenna, P.F., and Farrar, G.J. (2012). Efficacy of

codelivery of dual AAV2/5 vectors in the murine retina and hippocampus. Hum. Gene Ther. *23*, 847–858.

Parfitt, D.A., Lane, A., Ramsden, C.M., Carr, A.J., Munro, P.M., Jovanovic, K., Schwarz, N., Kanuga, N., Muthiah, M.N., Hull, S., et al. (2016). Identification and correction of mechanisms underlying inherited blindness in human iPSC-derived optic cups. Cell Stem Cell *18*, 769–781.

Quinn, P.M., Buck, T.M., Mulder, A.A., Ohonin, C., Alves, C.H., Vos, R.M., Bialecka, M., Van Herwaarden, T., Van Dijk, E.H.C., Talib, M., et al. (2019). Human iPSC-derived retinas recapitulate the fetal CRB1 CRB2 complex formation and demonstrate that photoreceptors and muller glia are targets of AAV5. Stem Cell Reports *12*, 906–919.

Ran, F.A., Hsu, P.D., Wright, J., Agarwala, V., Scott, D.A., and Zhang, F. (2013). Genome engineering using the CRISPR-Cas9 system. Nat. Protoc. *8*, 2281–2308.

Rohr, U.P., Wulf, M.A., Stahn, S., Steidl, U., Haas, R., and Kronenwett, R. (2002). Fast and reliable titration of recombinant adeno-associated virus type-2 using quantitative real-time PCR. J. Virol. Methods *106*, 81–88.

Russell, S., Bennett, J., Wellman, J.A., Chung, D.C., Yu, Z.F., Tillman, A., Wittes, J., Pappas, J., Elci, O., Mccague, S., et al. (2017). Efficacy and safety of voretigene neparvovec (AAV2-hRPE65v2) in patients with RPE65-mediated inherited retinal dystrophy: a randomised, controlled, open-label, phase 3 trial. Lancet *390*, 849–860.

Sarra, G.M., Stephens, C., Schlichtenbrede, F.C., Bainbridge, J.W., Thrasher, A.J., Luthert, P.J., and Ali, R.R. (2002). Kinetics of transgene expression in mouse retina following sub-retinal injection of recombinant adeno-associated virus. Vis. Res *42*, 541–549.

Schwarz, N., Carr, A.J., Lane, A., Moeller, F., Chen, L.L., Aguila, M., Nommiste, B., Muthiah, M.N., Kanuga, N., Wolfrum, U., et al. (2015). Translational read-through of the RP2 Arg120stop mutation in patient iPSC-derived retinal pigment epithelium cells. Hum. Mol. Genet. *24*, 972–986.

Schwarz, N., Hardcastle, A.J., and Cheetham, M.E. (2012). The role of the X-linked retinitis pigmentosa protein RP2 in vesicle traffic and cilia function. Adv. Exp. Med. Biol. *723*, 527–532.

Schwarz, N., Lane, A., Jovanovic, K., Parfitt, D.A., Aguila, M., Thompson, C.L., da Cruz, L., Coffey, P.J., Chapple, J.P., Hardcastle, A.J., and Cheetham, M.E. (2017). Arl3 and RP2 regulate the trafficking of ciliary tip kinesins. Hum. Mol. Genet. *26*, 2480–2492.

Sharma, T.P., Wiley, L.A., Whitmore, S.S., Anfinson, K.R., Cranston, C.M., Oppedal, D.J., Daggett, H.T., Mullins, R.F., Tucker, B.A., and Stone, E.M. (2017). Patient-specific induced pluripotent stem cells to evaluate the pathophysiology of TRNT1-associated retinitis pigmentosa. Stem Cell Res. *21*, 58–70.

Schindelin, J., Arganda-Carreras, I., Frise, E., Kaynig, V., Longair, M., Pietzsch, T., Preibisch, S., Rueden, C., Saalfeld, S., Schmid, B., et al. (2012). Fiji: an open-source platform for biological-image analysis. Nat. Methods *9*, 676–682.

Shirai, H., Mandai, M., Matsushita, K., Kuwahara, A., Yonemura, S., Nakano, T., Assawachananont, J., Kimura, T., Saito, K., Terasaki, H., et al. (2016). Transplantation of human embryonic stem cell-derived retinal tissue in two primate models of retinal degeneration. Proc. Natl. Acad. Sci. U S A *113*, E81–E90.

Takahashi, K., Tanabe, K., Ohnuki, M., Narita, M., Ichisaka, T., Tomoda, K., and Yamanaka, S. (2007). Induction of pluripotent stem cells from adult human fibroblasts by defined factors. Cell *131*, 861–872.

Vandesompele, J., De Preter, K., Pattyn, F., Poppe, B., Van Roy, N., De Paepe, A., and Speleman, F. (2002). Accurate normalization of real-time quantitative RT-PCR data by geometric averaging of multiple internal control genes. Genome Biol. *3*, research0034.1.

Vecino, E., Hernandez, M., and Garcia, M. (2004). Cell death in the developing vertebrate retina. Int. J. Dev. Biol. *48*, 965–974.

Veltel, S., Gasper, R., Eisenacher, E., and Wittinghofer, A. (2008). The retinitis pigmentosa 2 gene product is a GTPase-activating protein for Arf-like 3. Nat. Struct. Mol. Biol. *15*, 373–380.

Wiley, L.A., Burnight, E.R., Kaalberg, E.E., Jiao, C., Riker, M.J., Halder, J.A., Luse, M.A., Han, I.C., Russell, S.R., Sohn, E.H., et al. (2018). Assessment of adeno-associated virus serotype tropism in human retinal explants. Hum. Gene Ther. *29*, 424–436.

Wright, K.J., Baye, L.M., Olivier-Mason, A., Mukhopadhyay, S., Sang, L., Kwong, M., Wang, W., Pretorius, P.R., Sheffield, V.C., Sengupta, P., et al. (2011). An ARL3-UNC119-RP2 GTPase cycle targets myristoylated NPHP3 to the primary cilium. Genes Dev. *25*, 2347–2360.

Xiao, X., Li, J., and Samulski, R.J. (1998). Production of high-titer recombinant adeno-associated virus vectors in the absence of helper adenovirus. J. Virol. *72*, 2224–2232.

Zhang, H., Constantine, R., Vorobiev, S., Chen, Y., Seetharaman, J., Huang, Y.J., Xiao, R., Montelione, G.T., Gerstner, C.D., Davis, M.W., et al. (2011). UNC119 is required for G protein trafficking in sensory neurons. Nat. Neurosci. *14*, 874–880.

Zhang, H., Hanke-Gogokhia, C., Jiang, L., Li, X., Wang, P., Gerstner, C.D., Frederick, J.M., Yang, Z., and Baehr, W. (2015). Mistrafficking of prenylated proteins causes retinitis pigmentosa 2. FASEB J. *29*, 932–942.

Zhong, X., Gutierrez, C., Xue, T., Hampton, C., Vergara, M.N., Cao, L.H., Peters, A., Park, T.S., Zambidis, E.T., Meyer, J.S., et al. (2014). Generation of three-dimensional retinal tissue with functional photoreceptors from human iPSCs. Nat. Commun. *5*, 4047.

Stem Cell Reports, Volume *15*

Supplemental Information

Modeling and Rescue of RP2 Retinitis Pigmentosa Using iPSC-Derived Retinal Organoids

Amelia Lane, Katarina Jovanovic, Ciara Shortall, Daniele Ottaviani, Anna Brugulat Panes, Nele Schwarz, Rosellina Guarascio, Matthew J. Hayes, Arpad Palfi, Naomi Chadderton, G. Jane Farrar, Alison J. Hardcastle, and Michael E. Cheetham

Supplemental Information

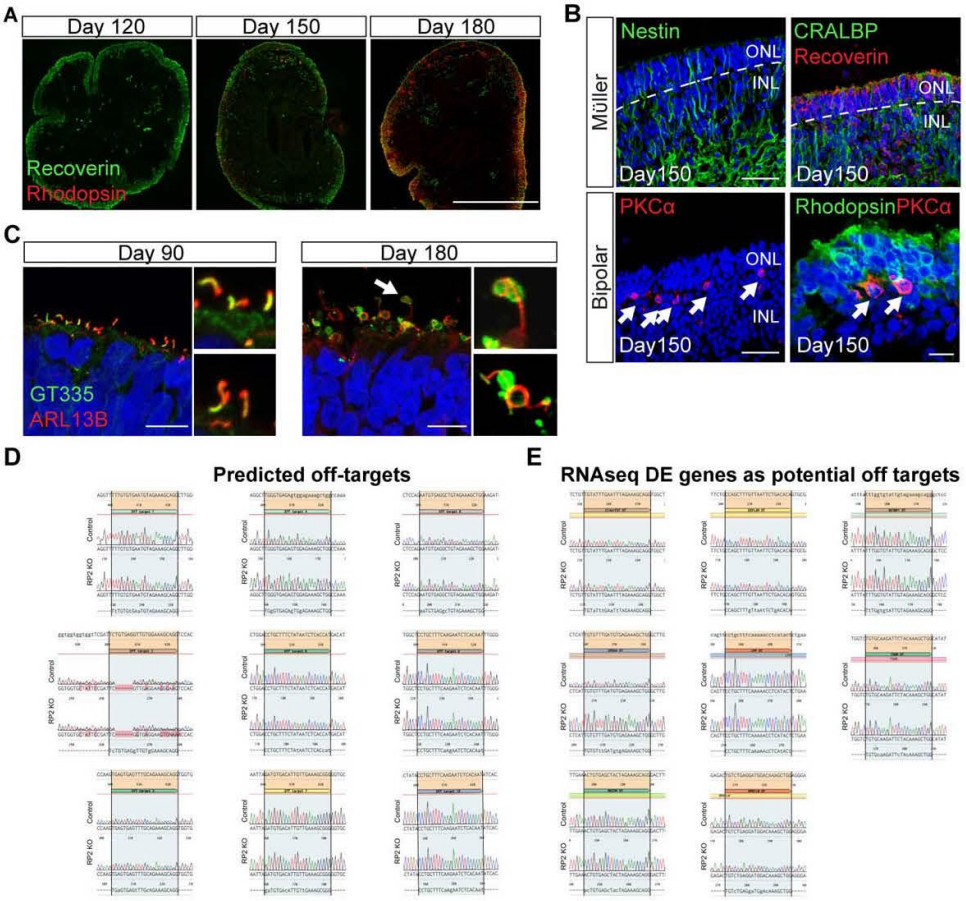

Figure S1. ***Control retinal organoid differentiation and lack of off-target editing in the RP2 KO.*** Related to Figure 1 and experimental methods.

A. ROs show increased rhodopsin expression between D150 and D180 Scale bar =500 µm.

B. ROs contain Muller glia, stained with nestin (green) and CRALBP (green) and bipolar cells, stained with PKCα Scale bars left = 50 µm; lower right = 10 µm.

C. Apical cilia in ROs stained with ARL13b (red) and GT335 (green) Scale bars = 10 µm.

D. Sanger sequencing results of Top 10 predicted off-targets for RP2 gRNA2. No mutations were observed in any of the predicted off-target sites. Off target 2 happens to occur in a region where the control line has a naturally occurring variation. Lower case letters in the off-target sequences below the traces indicate the sites at which the off-targets vary from RP2 gRNA2.

E. Sequencing results of RNAseq DE genes with possible similarity to the gRNA sequence. Sanger sequencing revealed that none of these sites showed any editing by off-target Cas9 activity.

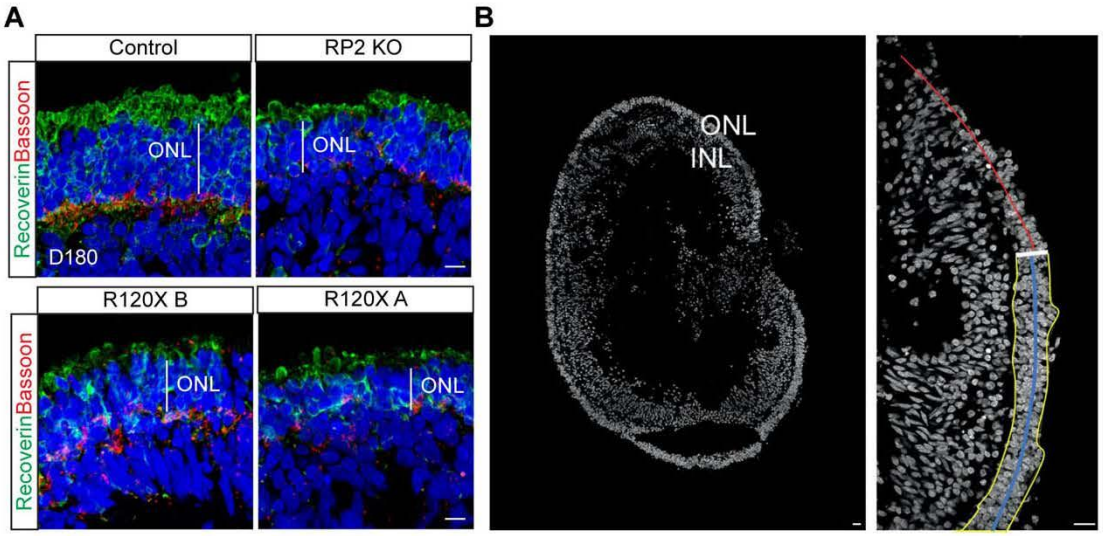

Figure S2. ***Thinning of the ONL in RP2 null cells.*** Related to Figure 2.

A. Representative images showing reduced ONL thickness in RP2 KO, R120X A and R120X B ROs. The Control and RP2 KO images are also shown in Figure 2. Scale bar = 10 µm.

B. Tilescans of retinal organoid to illustrate the method of ONL measurement. Whole organoid (left panel) close up of ONL (right panel). The area of the ONL is enclosed within the yellow marked area and the length of ONL indicated by the blue line. The red line indicates an area of non-photoreceptors that were not included. Scale = 20µm

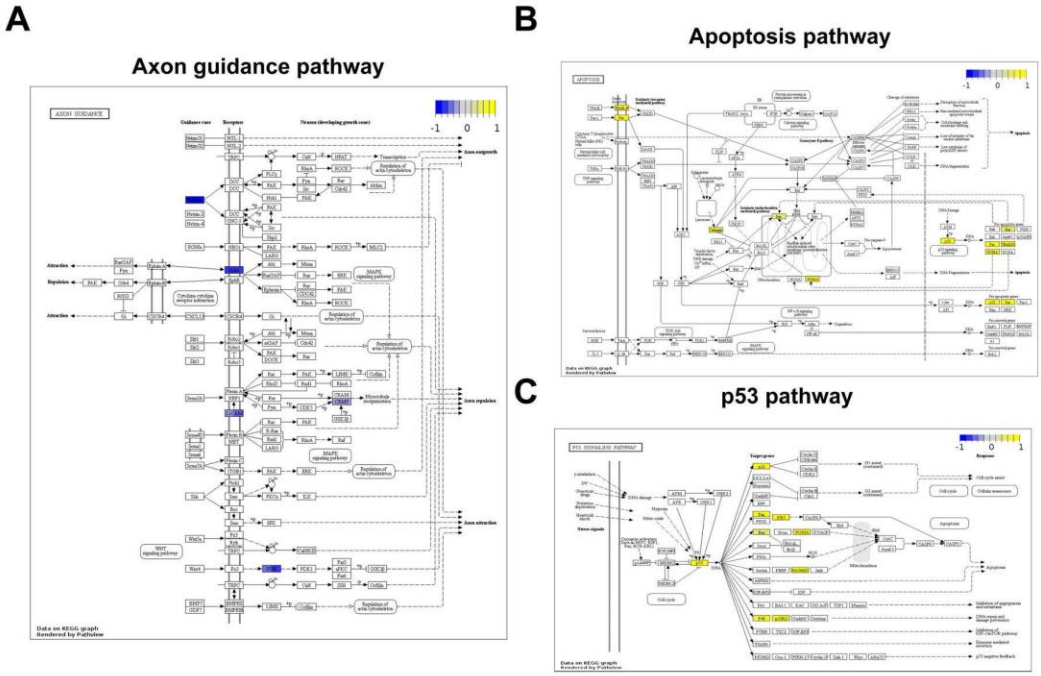

Figure S3. ***KEGG analyses of shared DE genes between RP2 nulls and control.*** Related to Figure 2.

A. KEGG analyses of RP2 KO and RP2 R120X common downregulated DE genes compared to control ROs at D150 in 'axon guidance' pathways.

B. KEGG analyses of RP2 KO and RP2 R120X common DE genes that are upregulated compared to control ROs at D150 in the 'apoptosis' pathway.

C. KEGG analyses of RP2 KO and RP2 R120X common DE genes that are upregulated compared to control ROs at D150 in the 'p53' pathway

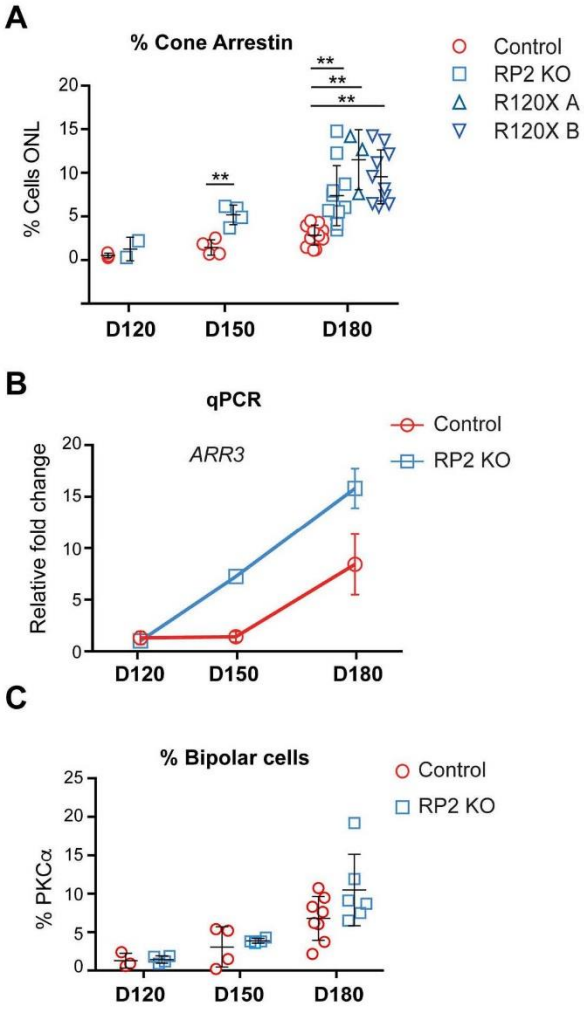

Figure S4. ***Cone photoreceptor and bipolar cells in RP2 null organoids.*** Related to Figure 3.

A. Percent of cells in ONL positive for cone arrestin immunostaining, Control (red circle; n=3, D120; n=4 D150 n=10 D180); RP2 KO (blue square; n=2, D120; n=4 D150 n=10 D180) R120X A (blue triangle; n=3 D180), R120X B (blue inverted triangle; n=10 D180); ** $p<0.01$ each n represents the mean from a full tilescan of an independent organoid. Mean ±SD

B. *ARR3* levels in retinal organoids. qPCR showing relative fold change in mRNA in control and RP2 KO retinal organoids at D120, D150 and D180 (n=3,3,4 independent organoids respectively; mean ±SEM).

C. Cell counts of bipolar cells (positive for PKCα) in control and RP2 KO ROs showed no significant differences in bipolar cell numbers at D120, D150 or D180 (controls n=3, 4 and 8 RP2 KO n=4, 4, 6, mean of tilescan of full independent organoids; mean ±SEM).

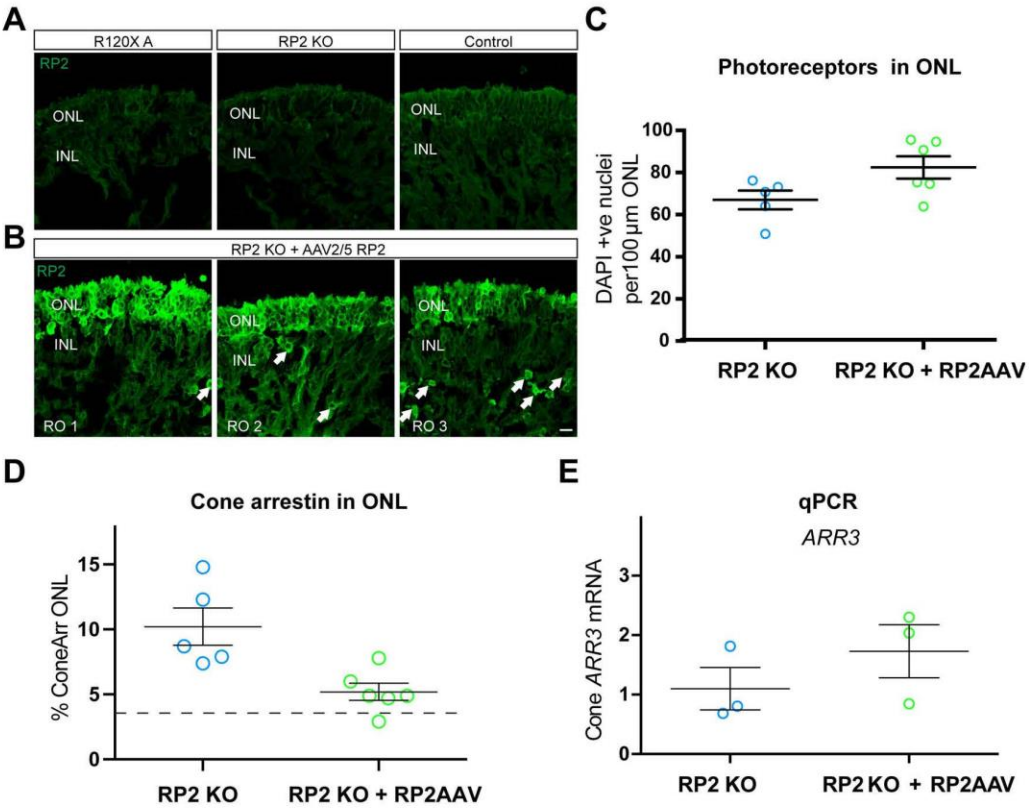

Figure S5. ***Transduction of RP2 KO organoids with RP2-AAV.*** Related to Figure 5.

A. ICC for RP2 in untreated D180 RP2 R120X A and RP2 KO and control ROs.

B. RP2 immunostaining after RP2-AAV transduction in 3 different organoids (RO1, RO2 and RO3). The few strongly positive cells for RP2 outside of the ONL are indicated with arrows. Scale bar = 10 µm.

C. The number of photoreceptors in the ONL. Mean of nuclei in the ONL per 100 µm (n=5 RP2 KO and n=6 RP2 KO + RP2AAV independent organoids for each condition; p=0.058; mean ±SEM).

D. Percentage of cells in the ONL that were positive for cone arrestin staining in untreated and after RP2-AAV transduction at D180, the dotted line indicates the mean percent in controls (RP2 KO n=5, RP2+RP2AAV n=6 independent organoids; p=0.055; mean ±SD).

E. *ARR3* levels in retinal organoids following RP2-AAV transduction. qPCR showing relative fold change in mRNA at D180 (n=3 independent organoids for both conditions; mean ±SEM).

Table S1. gRNA, Primer and Off-target sequences. Related to Figures 1, 4, and S1

Table S1. gRNA, Primer and Off-target sequences. Related to Figures 1, 4, and S1

Target	Forward	Reverse
gRNA sequence for RP2 exon 2 CRISPR		
RP2 gRNA2	TGTGTGAGATTGTAGAAAGC**TGG**	
PCR primer sequences		
RP2 exon2	CCAAAAGACTACATGTTCAGTGGA	GCATGATTCATCGCTGCTCT
Off-target PCR Primer sequences		
OT1 – Chr13 + 99786425 - 99786447	GGTCAGGGCCAGCACATAAT	TAGCTAATGTGCCCTCAGCG
OT2 - Chr 6 + 38143360 – 38143382 (BTBD9 pre-mRNA)	ACCACGAGGGAGTTAGAGGA	AGCCACATGAGGTTGAAGTCC
OT3 - Chr 9 + 91974085 – 91974107 (SECISBP2 pre- mRNA)	AGTTCTTGCCTGTGTGTCTGT	TAGCAGAACCCCCACTACGC
OT4 - Chr 7 + 157998199 – 157998221 (PTPRN2 pre-mRNA)	TAGCCAAAGCTCTTGCTTCAGT	GTGCCCTATCCTACTTGGCTG
OT5 - Chr 3 – 132906887 -132906909 (TMEM108 pre-mRNA)	CTGTCAAGGAAGGAAGGGAGG	GGAGAAAGGGCCCCCTATAA
OT6 - Chr 5 – 116400519 - 116400541	AACTGTGTCCCACAATAAGGGG	TGCTGGGACCTCCTCAAATTC
OT7 - Chr X + 119452379 - 119452401	AAGCCCACAGGAACTGGGTT	AAACCAAAGTAGGTGGGTCCT
OT8 - Chr 10 + 22037281 - 22037303	ATTCTGCCGGGGTTTAGAGC	AGCAAGGTGAACTGACACTGG
OT9 - Chr 1 – 23887266 - 23887288	AGTAGCTCCAGCTCCATCTGA	ATCTTTCTTGGGCCACAGAGC
OT10 - Chr 11 – 109695393 - 109695415	AAAATGGCTATGCAGCACAAGTT	TTAGCTTCTCCCTTACACCTGAAC
RNAseq DE gene potential off-target PCR Primer sequences		
C14orf37	ACTGGGCTTTGAAAGATGGAGA	AGGCACTCAAATGGTGGAGC
EGFLAM	TAGGGCTTTGCACATCGCA	CGGGTTTAGTGGGAAGGCAG
EPHA4	CCTTGTCGATCTTCCACTCCC	ATGACGTGTGGAGCACTGAC
LPP	TCCGACTTTGCCTTCCTTCT	CTCTGTGGCACCTATCACAACT
MECOM	AGCTGCCATTGCTTTTTCTCA	TGCTTAGGAAACACACGCCT
OPN1LW	TGGGTAGTGGTCTTCCCCTC	AGCCCATTTGTGAAGACGGA
SETBP1	TTTCATGCCAGTGACCTTCG	TTGCTCATTGACTTTTGACATGGG
TSHR	AGCCACAACCACTCTTGACT	TGACTGGTTTTCAGGTGCTAGAT

Table S2. Primer sequences for qPCR. Related to Figures 3, 4, 5 and S4, and S5

qPCR primer sequences		
Target	**Forward**	**Reverse**
RHO	GGTGGTGTGTAAGCCCATGA	CCTCGGGGATGTACCTGGAC
GNAT1	CTGCTCACTCTGTCCCTTCG	TTGACGATGGTGCTCTTCCC
RP2 EX1-2	GACCATGGGCTGCTTCTTCT	ACTGTTGTCCTGCTACCGTC
ARR3	CATGTGCCTTTCGCTATGGC	TCAATCCCACAGGGCTTTCC
MAN1B1	ACCGTGGAGAGCCTGTTCTA	GTTTGGGTCATCGGAGAAGA
GAPDH	CCCCACCACACTGAATCTCC	GGTACTTTATTGATGGTAC
POLR2A	GCGGGGTGAAGTGATGAAC	ATCATCGGGATGGGTGCTGT

Table S3. List of DE genes from D150 RNAseq analyses. Related to Figure 2.
See excel file Supplementary Table S3.xls.

Table S4. List of antibodies used. Related to all figures.

Marker	Species	Dilution	Supplier	Catalog number
Oct4	Rabbit	1:1000	Abcam	ab19857
Nanog	Mouse	1:1000	Thermo Invitrogen	MA-1-017
RP2 (western blot)	Sheep	1:2500	Sheep serum	References 1, 2
RP2 (ICC)	Rabbit	1:200	ProteinTech	14151-1-AP
Recoverin	Rabbit	1:500	Millipore	AB5585
Cone Arrestin (7G6)	Mouse	1:100	Gift from Wolfgang Baehr	
Rhodopsin (4D2)	Mouse	1:500	Millipore	MABN15
F-actin	AlexaFluor 488 Phalloidin		Thermo Invitrogen	A12379
TOM20	Mouse	1:150	Santa Cruz	SC17764
GT335	Mouse	1:800	Adipogen Life Sciences	AG-20B-0020
Arl13B	Mouse	1:1000	Abcam	ab136648
Bassoon	Mouse	1:500	Enzo	SAP7F407
Nestin	Mouse	1:200	Abcam	ab22035
CRALBP	Mouse	1:300	Thermo Invitrogen	MA1-813
PKCα	Rabbit	1:200	Abcam	ab32376

2. Grayson C, Bartolini F, Chapple JP, Willison KR, Bhamidipati A, Lewis SA, Luthert PJ, Hardcastle AJ, Cowan NJ, Cheetham ME (2002) Localization in the human retina of the X-linked retinitis pigmentosa protein RP2, its homologue cofactor C and the RP2 interacting protein Arl3. Hum Mol Genet 11: 3065-74
3. Levitt, N., Briggs, D., Gil, A. & Proudfoot, N. J. (1989). Definition of an efficient synthetic poly(A) site. *Genes Dev,* **3,** 1019-25.

7.2 Appendix 2 - RP2 mutation survey

RP2 variants that were likely or possibly pathogenic were compiled by searching PubMed for relevant literature and cross-checking with the HGMD and ClinVar databases.

Total no. RP2 mutations:	Total no. RP2 probands
108	170

Table 7.1 Summary of *RP2* XLRP mutations. Presumed pathogenic mutations and the number of times they have been reported in the literature are listed.

Region	Percentage of RP2 mutations	Percentage of RP2 probands
Exon 1 (102bp)	12.03703704	13.52941176
Exon 2 (666bp)	60.18518519	64.11764706
Exon 3 (115bp)	8.333333333	6.470588235
Exon 4 (86bp)	5.555555556	3.529411765
Exon 5 (84bp)	0	0
Intronic	10.18518519	10
Gross deletions (>1 exon)	3.703703704	2.352941176

Table 7.2. Summary of *RP2* XLRP mutation locations. The percentage of total *RP2* mutations located in different regions of the gene are listed alongside the proportion of total probands affected. Note: deletions that span multiple exons are listed separately under 'gross deletions.'

Mutation class	Percentage of RP2 mutations	Percentage of RP2 probands
Deletion	12.03703704	14.11764706
Frameshift	36.11111111	28.23529412
Insertion	0.925925926	0.588235294
Missense	28.7037037	31.76470588
Nonsense	12.96296296	15.88235294
Slice site change	9.259259259	9.411764706

Table 7.3. Summary of *RP2* XLRP mutation classes. The proportion of total RP2 variants belonging to different mutation classes are listed, alongside the percentage of reported probands affected.

Genomic/CDS location	Exon/ Intron	Mutation consequence	Mutation Class	Total no. cases reported	Percentage of total reported RP2 cases affected by variant
c.353G>A	Exon 2	p.Arg118His. Reduces affinity for ARL3.	Missense	16	11.27
c.358C>T	Exon 2	p.Arg120X. Nonsense-mediated decay.	Nonsense	9	6.34
c.409_411del	Exon 2	p.Ile137del. Destabilises protein.	Deletion	7	4.93
c.16_18del	Exon 1	p.Ser6del. Disrupts targeting RP2 to the plasma membrane.	Deletion	6	4.23
c.688_692del	Exon 2	p.Lys230fs	Frameshift	5	3.52

Table 7.4. Most frequently reported *RP2* XLRP mutations in the literature.

The following table describes, to my knowledge, all *RP2* XLRP mutations reported in the literature (as of August 2020).

Genomic/CDS location	Exon/Intron	Mutation consequence	Mutation Class	Incidence and cohort information	Total no. cases reported	Percentage of reported RP2 cases affected by variant
c.(?_-46)_(*62_?)	5'UTR/Exon 1	Deletion of CDS start	Deletion	1/88 XLRP families in French cohort (Pelletier et al., 2007)	1	0.70
DelExon1	Exon 1	Deletion of exon 1	Deletion	1/58 XLRP probands (Bader et al., 2003)	1	0.70
g.45,222,470-46,491,666del (UCSC Genome Browser, build 35)	Exon 1 - 3	1.27Mb deletion that includes the 5' end of RP2 and ends within intron 3.	Deletion	1 family (Zhang et al., 2006)	1	0.70
c.5G>T	Exon 1	p.Gly2Val. Disrupts motif for N-terminal myristoylation (Chapple et al., 2002)	Missense	1/88 (1.1%) XLRP families in French cohort (Pelletier et al., 2007)	1	0.70
c.8G>C	Exon 1	p.Cys3Ser. Predicted to disrupt targeting to plasma membrane.	Missense	1/13 RP2 families or 1/326 XLRP probands (Jayasundera et al. 2010). 1/185 male simplex RP patients (suspected XLRP) (Branham et al. 2012).	2	1.41
c.9_11del	Exon 1	p.Phe4del	Deletion	1/59 families initially classified as adRP (Spain) (Fernandez-San Jose et al., 2015)	1	0.70
c.13_15del	Exon 1	p.Phe5del	Deletion	1/90 XLRP probands (Central European and Danish) (Neidhardt et al., 2008)	1	0.70
c.16_18del	Exon 1	p.Ser6del. Disrupts targeting of RP2 to the plasma membrane (Chapple et al., 2000).	Deletion	1/14 XLRP Danish families (Rosenberg et al., 1999); 4/33 XLRP families in Danish cohort (Prokisch et al., 2007). 1/26 XLRP probands (central Europe) (Schwahn et al., 1998).	6	4.23
c.17C>T	Exon 1	p.Ser6Phe	Missense	1 Japanese proband (Fujinami et al., 2020)	1	0.70
c.52G>T	Exon 1	p.Glu18X	Nonsense	1/30 Spanish XLRP probands (Garcia-Hoyos et al., 2006)	1	0.70
c.61G>T	Exon 1	p.Glu20X	Nonsense	1 family (cohort of Swiss/Algerian/Tunisian descent) (Schorderet et al., 2013)	1	0.70
c.76C>T	Exon 1	p.Gln26X	Nonsense	1/26 XLRP probands (central Europe and Denmark) (Schwahn et al., 1998). 1/14 XLRP Danish families (Rosenberg et al., 1999); 2/33 XLRP Danish cohort (Prokisch et al., 2007)	4	2.82

Genomic/CDS location	Exon/Intron	Mutation consequence	Mutation Class	Incidence and cohort information	Total no. cases reported	Percentage of reported RP2 cases affected by variant
c.77insCA	Exon 1	p.Gln26fs	Frameshift	1/51 North American XLRP probands (Mears et al., 1999). 1/13 RP2 families or 1/326 XLRP probands (Jayasundera et al., 2010)	2	1.41
c.82C>G	Exon 1	p.Tyr27X	Nonsense	1/171 X-linked probands (N. American) (Breuer et al., 2002).	1	0.70
Line1ins	Intron 1	Line 1 retrotransposition, may lead to abherrant splicing. No RP2 mRNA expression detected.	Insertion	1/26 XLRP probands (central Europe) (Schwahn et al., 1998)	1	0.70
c.102+1G>A	Intron 1		Splice site change	1/13 RP2 families or 1/326 XLRP probands (Jayasundera et al., 2010). 1/537 IRD probands (Ellingford et al., 2016). 1 proband in Japanese cohort (Kurata et al., 2019)	3	2.11
c.102+3A>G	Intron 1		Splice site change	1/171 X-linked probands (N. American) (Breuer et al., 2002). 1/13 RP2 families or 1/326 XLRP probands (Jayasundera et al., 2010)	2	1.41
c.102+3A>T	Intron 1		Splice site change	1/85 XLRP probands (Sharon et al., 2000). 1/135 XLRP male probands (Sharon et al., 2003)	2	1.41
c.103_1053del	Exon 2 - 5	p.Val35_Ile350del	Deletion	1/10 Chinese XLRP families (Ji et al., 2010)	1	0.70
c.111insC	Exon 2	p.Pro37fs	Frameshift	1 Han Taiwanese family (De Lin et al., 2014)	1	0.70
c.193C>T	Exon 2	p.Gln65X	Nonsense	1 Chinese family (Pan et al., 2014)	1	0.70
c.200G>A	Exon 2	p.Cys67Tyr. Destabilises protein (Liu et al., 2017).	Missense	1/171 X-linked probands (N. American) (Breuer et al., 2002).	1	0.70
c.217del	Exon 2	p.Tyr73Ifs	Frameshift	1 proband in Japanese cohort (Kurata et al., 2019).	1	0.70
c.226G>T	Exon 2	p.Asp76Tyr	Missense	1 proband (Eisenberger et al., 2013)	1	0.70
c.257G>A	Exon 2	p.Cys86Tyr. Destabilises protein (Liu et al., 2017)	Missense	1/85 XLRP probands (USA/Canada) (Sharon et al., 2000). 1/135 XLRP male probands (Sharon et al., 2003). 1 proband (Consugar et al., 2015).	3	2.11

Genomic/CDS location	Exon/Intron	Mutation consequence	Mutation Class	Incidence and cohort information	Total no. cases reported	Percentage of reported RP2 cases affected by variant
c.260_268del	Exon 2	p.Thr87_Cys89del	Deletion	1/537 IRD probands (Ellingford et al., 2016).	1	0.70
c.260C>T	Exon 2	p.Thr87Ile. Predicted to disrupt interaction with proteins other than ARL3 and transducin β (Liu et al., 2017).	Missense	1/13 RP2 families or 1/326 XLRP probands (Jayasundera et al., 2010). **Note:** Branham et al. (2012) re-classified this as a variant of unknown significance.	1	0.70
c.284C>T	Exon 2	p.Pro95Leu. Destabilises protein (Liu et al., 2017).	Missense	1/85 XLRP probands (Sharon et al., 2000). 1 out of 135 XLRP male probands (Sharon et al., 2003).	2	1.41
c.292insA	Exon 2	p.Gly98fs	Frameshift	1/88 XLRP families in French cohort (Pelletier et al., 2007)	1	0.70
c.293_297dup	Exon 2	p.Val300delinsAlaAlafs	Frameshift	1/88 XLRP families in French cohort (Pelletier et al., 2007)	1	0.70
c.299insT	Exon 2	p.Val100fs	Frameshift	1/30 Spanish XLRP probands (Garcia-Hoyos et al., 2006)	1	0.70
c.299T>A	Exon 2	p.Val100Glu	Missense	1 family (Misky et al., 2016)	1	0.70
c.303insT	Exon 2	p.Phe102fs	Frameshift	1/50 XLRP probands previously screened for RPGR mutations (Spain) (Miano et al., 2001)	1	0.70
c.305delT	Exon 2	p.Phe102fs	Frameshift	1/88 XLRP families in French cohort (Pelletier et al., 2007)	1	0.70
c.315C>G	Exon 2	p.Cys105Trp. Destabilises protein (Liu et al., 2017).	Missense	1/88 XLRP families in French cohort (Pelletier et al., 2007)	1	0.70
c.318_319del	Exon 2	p.Asp107fs.	Frameshift	1/134 probands in RP cohort (Neveling et al., 2012)	1	0.70
c.322T>G	Exon 2	p.Cys108Gly. Destabilises protein (Liu et al., 2017).	Missense	1/51 North American XLRP probands (Mears et al., 1999).	1	0.70
c.330_342del	Exon 2	p.Cys110fs	Frameshift	1/51 North American XLRP probands (Mears et al., 1999).	1	0.70
c.337G>A	Exon 2	p.Arg113Thr	Missense	1 proband (Consugar et al., 2015)	1	0.70
c.350_351del	Exon 2	p.Phe117fs	Frameshift	1 North American patient out of 171 XLRP probands (Breuer et al., 2002).	1	0.70
c.352C>G	Exon 2	p.Arg118Gly. Likely disrupts interaction with ARL3.	Missense	1/33 XLRP families in Danish cohort (Prokisch et al., 2007)	1	0.70
c.352C>T	Exon 2	p.Arg118Cys. Likely disrupts interaction with ARL3.	Missense	1/135 XLRP male probands (Sharon et al., 2003). 1/58 XLRP probands (Bader et al., 2003). 1/13 RP2 families or 1/326 XLRP probands (Jayasundera et al., 2010)	3	2.11

Genomic/CDS location	Exon/Intron	Mutation consequence	Mutation Class	Incidence and cohort information	Total no. cases reported	Percentage of reported RP2 cases affected by variant
c.352del	Exon 2	p.Arg118fs	Frameshift	At least 1 proband (ClinVar)	1	0.70
c.353G>A	Exon 2	p.Arg118His. Reduces affinity for ARL3 (Kuhnel et al.,, 2006).	Missense	1/88 XLRP families in French cohort (Pelletier et al., 2007). 2 North American patients out of 171 X-linked probands (Breuer et al., 2002). 1/85 XLRP probands (N. American) (Sharon et al., 2000). 1/135 XLRP male probands (Sharon et al., 2003). 1/58 XLRP probands (Bader et al., 2003). 1/26 XLRP probands (central Europe)(Schwahn et al., 1998). 2/326 XLRP probands (Jayasundera et al., 2010). 3/59 XLRP families or 3/33 XLRP families already screened for RPGR (Hardcastle et al., 1999). 1/33 XLRP families in Danish cohort (Prokisch et al., 2007). 1/14 XLRP Danish families (Rosenberg et al., 1999). 1/10 Chinese XLRP families (Ji et al., 2010). 1/537 IRD probands (Ellingford et al., 2016)	16	11.27
c.354G>T	Exon 2	p. Arg118Leu. Likely disrupts interaction with ARL3.	Missense	1/50 XLRP probands previously screened for RPGR mutations (Miano et al., 2001)	1	0.70
c.358C>T	Exon 2	p.Arg120X. Nonsense-mediated decay.	Nonsense	1 family in South Africa (Vorster et al., 2003). 1/51 XLRP probands (N. America) (Mears et al., 1999). 3/59 XLRP families or 3/33 XLRP families already screened for RPGR (Hardcastle et al., 1999). 1/90 XLRP probands (Central Europe and Denmark) (Neidhardt et al., 2008). 1/26 XLRP pedigrees (Ireland) (Whelan et al., 2020). 1/26 RP probands (Riera et al., 2017). 1 Japanese proband (Fujinami 2020).	9	6.34
c.382_383del	Exon 2	p.Phe128fs	Frameshift	1/88 IRD probands (Bernadis et al., 2016).	1	0.70
c.386dupT	Exon 2	p.Leu129fs	Frameshift	1/33 XLRP families in Danish cohort (Prokisch et al., 2007)	1	0.70
c.395_419del	Exon 2	p.Thr133fs	Frameshift	1/20 non-syndromic RP probands (Thailand) (Jinda et al., 2014)	1	0.70
c.400C>T	Exon 2	p.Gln134X	Nonsense	1/30 Spanish XLRP probands (Garcia-Hoyos et al., 2006)	1	0.70

Genomic/CDS location	Exon/Intron	Mutation consequence	Mutation Class	Incidence and cohort information	Total no. cases reported	Percentage of reported RP2 cases affected by variant
c.409_411del	Exon 2	p.Ile137del. Destabilises protein (Liu et al., 2017).	Deletion	1/85 XLRP probands (Sharon et al., 2000). 1 North American patient out of 171 X-linked probands (Breuer et al., 2002). 1/135 male XLRP probands (Sharon et al., 2003). 1/185 male simplex RP cases (suspected XLRP) (Branham et al., 2012). 1/85 XLRP probands (Sharon et al., 2000). 1/326 XLRP probands (Jayasundera et al., 2010). 1 Chinese family (Pan et al., 2014)	7	4.93
c.414A>G or c.413A>G	Exon 2	p.Glu138Gly. Reduces affinity for ARL3 (Kuhnel et al., 2006).	Missense	1/50 XLRP probands previously screened for RPGR mutations (Italian patient) (Miano et al., 2001); 1/3 XLRP families (Parmeggiani et al., 2017). 1 proband in Japanese cohort (Kurata et al., 2019).	3	2.11
c.419_426del	Exon 2	p.Ser140_Asn142delinsTyrfs	Frameshift	1/88 XLRP families in French cohort (Pelletier et al., 2007)	1	0.70
c.419C>T	Exon 2	p.Ser140Phe. Destabilises protein (Liu et al., 2017).	Missense	1/30 Spanish XLRP probands (Garcia-Hoyos et al., 2006)	1	0.70
c.425delA	Exon 2	p.Asn142fs	Frameshift	1 out of 26 XLRP pedigrees (Ireland) (Dockery et al., 2017, Whelan et al., 2020)	1	0.70
c.428T>C	Exon 2	p.Ile143Thr	Missense	1 proband in Chinese cohort (Xu et al., 2014).	1	0.70
c.449G>A	Exon 2	p.Trp150X.	Nonsense	1/88 XLRP families in French cohort (Pelletier et al., 2007). 1/7 RP2 XLRP Italian families (De Luca et al., 2001). 1/326 XLRP probands (Jayasundera et al., 2010).	3	2.11
c.453C>G	Exon 2	p.Tyr151X. NMD (Schwahn et al., 2001).	Nonsense	1/26 XLRP probands (central Europe) (Schwahn et al., 1998)	1	0.70
c.453delC	Exon 2	p.Tyr151fs	Frameshift	1/26 XLRP probands (central Europe) (Schwahn et al., 1998)	1	0.70
c.473A>C	Exon 2	p.Gln158Pro. Destablises protein.	Missense	1 Chinese proband (Zhang et al., 2019)	1	0.70
c.481G>T	Exon 2	p.Asp161Tyr	Missense	1 family (cohort of Swiss/Algerian/Tunisian descent) (Schorderet et al., 2013)	1	0.70
c.483insGGGCTAA	Exon 2	p.Asp161fs	Frameshift	1/51 North American XLRP probands (Mears et al., 1999).	1	0.70

Genomic/CDS location	Exon/Intron	Mutation consequence	Mutation Class	Incidence and cohort information	Total no. cases reported	Percentage of reported RP2 cases affected by variant
c.507delT	Exon 2	p.Asn161fs	Frameshift	1/537 IRD probands (Ellingford et al., 2016).	1	0.70
c.515insG	Exon 2	p.Ser172fs	Frameshift	1 North American patient out of 171 XLRP probands (Breuer et al., 2002). 1/13 RP2 families or 1/326 XLRP probands (Jayasundera et al., 2010).	2	1.41
c.540_541del	Exon 2	p.Ser181fs	Frameshift	1/88 XLRP families in French cohort (Pelletier et al., 2007)	1	0.70
c.547G>T	Exon 2	p.Glu183X	Nonsense	1/7 Italian RP2 XLRP families (De Luca et al., 2001)	1	0.70
c.557G>T	Exon 2	p.Trp186X	Nonsense	1/88 XLRP families in French cohort (Pelletier et al., 2007)	1	0.70
c.560_561	Exon 2	p.Ser187fs	Frameshift	1 proband in Korean cohort (Yu et al., 2015)	1	0.70
c.565T>C	Exon 2	p.Leu188Pro. Destabilises protein (Liu et al., 2017).	Missense	1/171 X-linked probands (N. American) (Breuer et al., 2002).	1	0.70
c.566T>C	Exon 2	p.Leu189Pro	Missense	1 Japanese proband (Fujinami et al., 2020)	1	0.70
c.591_597del	Exon 2	p.Tyr198LeucinefsTer38	Frameshift	1 proband in Chinese cohort (Xu et al., 2014).	1	0.70
c.632G>A	Exon 2	p.Arg211His. Predicted to disrupt interaction with proteins other than ARL3 and transducin β (Liu et al., 2017). Probably disrupts interaction with OSTF1 (Lyraki et al. 2018).	Missense	1/25 sporadic male RP2 cases in French cohort (Pelletier et al., 2007)	1	0.70
c.632G>C	Exon 2	p.Arg211Leu. Abolishes interaction with OSTF1 (Lyraki et al. 2018).	Missense	Villaverde-Montero et al., 2007	1	0.70
c.665delC	Exon 2	p.Pro222fs	Nonsense	1 proband (Lim et al., 2016)	1	0.70
c.670insC or c.673insC	Exon 2	p.Arg225fs	Frameshift	1 North American patient out of 171 X-linked probands (Breuer et al., 2002). 1/13 RP2 families or 1 out of 326 XLRP probands (Jayasundera et al., 2010).	2	1.41
c.685C>T	Exon 2	p.Gln229X	Nonsense	1 proband in Japanese cohort (Kurata et al., 2019).	1	0.70
c.688_692del	Exon 2	p.Lys230fs	Frameshift	1 out of 258 "adRP" pedigrees lacking male-to-male transmission (Churchill et al., 2013). 1 out of 85 XLRP probands (Sharon et al., 2000). 3 out of 59 XLRP families or 3 out of 33 XLRP families with linkage to RP2 (Hardcastle et al., 1999)	5	3.52
c.700G>T	Exon 2	p.Glu234X	Nonsense	1/26 XLRP pedigrees (Ireland) (Whelan et al., 2020)	1	0.70

Genomic/CDS location	Exon/Intron	Mutation consequence	Mutation Class	Incidence and cohort information	Total no. cases reported	Percentage of reported RP2 cases affected by variant
c.708C>G	Exon 2	p.Cys236Trp	Missense	1/47 Spanish arRP/simplex RP probands (Perez-Carro et al., 2016)	1	0.70
c.718delT	Exon 2	p.Leu240fs	Frameshift	1/105 RP probands (Ge et al., 2015)	1	0.70
c.723del	Exon 2	p.Ala242fs	Frameshift	1/21 XLRP probands (British) (Thiselton et al., 2000)	1	0.70
c.751A>G	Exon 2	p.Arg251Gly	Missense	1 proband in Chinese cohort (Wang et al., 2015).	1	0.70
c.758T>C	Exon 2	p.Leu253Pro. Destabilises protein (Liu et al., 2017).	Missense	1/13 RP2 families or 1/326 XLRP probands (Jayasundera et al., 2010)	1	0.70
c.758T>G	Exon 2	p.Leu253Arg. Destabilises protein (Liu et al., 2017).	Missense	1/25 Japanese XLRP probands (Wada et al., 2000)	1	0.70
c.769-1G>A	Intron 2		Splice site change	1/88 XLRP families in French cohort (Pelletier et al., 2007)	1	0.70
c.769-2A>G	Intron 2		Splice site change	1/50 XLRP probands previously screened for RPGR mutations (Italy) (Miano et al., 2001)	1	0.70
c.769-3C>A	Intron 2		Splice site change	1/90 XLRP probands (central Europe and Denmark) (Neidhardt et al., 2008)	1	0.70
c.797A>C	Exon 3	p.Gln266Pro	Missense	1 proband (Consugar et al. 2015)	1	0.70
c.798_801del	Exon 3	p.Gln266fs	Frameshift	1/21 XLRP probands (British) (Thiselton et al. 2000). 1/135 XLRP male probands (Sharon et al. 2003).	2	1.41
c.801_804del	Exon 3	p.Glu269fs	Frameshift	1/88 XLRP families in French cohort (Pelletier et al. 2007). 1 Japanese proband (Fujinami et al. 2020).	2	1.41
c.803delA	Exon 3	p. Lys268fs	Frameshift	1/185 male simplex RP cases (suspected XLRP) (Branham et al., 2012)	1	0.70
c.829dupG	Exon 3	p.Ala277fs	Frameshift	1 proband in German cohort (Birtel et al., 2018)	1	0.70
c.832insTC	Exon 3	p.Gln278fs	Frameshift	1 Japanese family (Mashima et al., 2000)	1	0.70
c.843_844insT	Exon 3	p.Arg282fs	Frameshift	1 proband (Horner et al., 2019)	1	0.70
c.846C>T	Exon 3	p.Arg282Try	Missense	1/50 XLRP probands previously screened for RPGR mutations (Yugoslavian patient) (Miano et al., 2001). **Note:** Thiselton et al. (2000) called this variant as a non-pathogenic SNP.	1	0.70
c.853insG	Exon 3	p.Ala285fs	Frameshift	1/7 Italian XLRP families in linkage with RP2 locus (De Luca et al., 2001)	1	0.70

Genomic/CDS location	Exon/Intron	Mutation consequence	Mutation Class	Incidence and cohort information	Total no. cases reported	Percentage of reported RP2 cases affected by variant
c.884-1G>C	Intron 3		Splice site change	1/90 XLRP probands (central Europe and Denmark) (Neidhardt et al., 2008)	1	0.70
c.884-1G>T	Intron 3		Splicing site change	1/20 retinal dystrophy families (Watson et al., 2014)	1	0.70
c.925insAG	Exon 4	p.Glu309fs	Frameshift	1/51 North American XLRP probands (Mears et al., 1999).	1	0.70
c.929insT	Exon 4	pVal310fs	Frameshift	1/33 non-RPGR XLRP families (Hardcastle et a. 1999)	1	0.70
c.968delAinsTCC	Exon 4	p.Lys323fs	Frameshift	1/90 XLRP probands (central Europe and Denmark) (Neidhardt et al., 2008)	1	0.70
Del15.2 kb including exon 4	Exon 4	Deletion of exon 4; truncation of protein	Deletion	1/33 XLRP probands in Danish cohort (Prokisch et al., 2007)	1	0.70
DelExon4	Exon 4	Exon 3 and 5 spliced together. Frameshift results in termination codon at 295.	Frameshift	1/26 XLRP probands (central Europe) (Schwahn et al., 1998)	1	0.70
DelExon4 (approx. 46,725,365 to 46,737,820bp (hg19))	Exon 4	12.5 Kb deletion of exon 4 and flanking regions	Deletion	1/258 families originally classed as adRP (Churchill et al., 2013)	1	0.70
DelExon4and5 (3,562 bp before exon 4 until 10790 bp after exon 5)	Exons 4 and 5	Truncated mutant protein of 294 amino acids predicted to escape NMD (Jiang et al., 2017)	Deletion	1/5 Han Chinese families (Jiang et al., 2017)	1	0.70
c.969+3A>C	Intron 4		Splice site change	1/135 XLRP male probands (Sharon et al., 2003).	1	0.70
c.969+3A>G	Intron 4	Exon 4 skipped, followed by frameshift.	Splice site change	1/135 XLRP male probands (Sharon et al., 2003). 1/33 XLRP families in Danish cohort (Prokisch et al., 2007). 1/537 IRD probands (Ellingford et al., 2016).	3	2.11
g.(?_168546)_(155233731_?)del (assembly GRCh37)	Whole gene.		Deletion/CNV	At least 1 proband (ClinVar)	1	0.70

References for Appendix 2

BADER, I., BRANDAU, O., ACHATZ, H., APFELSTEDT-SYLLA, E., HERGERSBERG, M., LORENZ, B., . . . MEITINGER, T. 2003. X-linked retinitis pigmentosa: RPGR mutations in most families with definite X linkage and clustering of mutations in a short sequence stretch of exon ORF15. *Invest Ophthalmol Vis Sci,* 44**,** 1458-63. http://dx.doi.org/10.1167/iovs.02-0605.

BERNARDIS, I., CHIESI, L., TENEDINI, E., ARTUSO, L., PERCESEPE, A., ARTUSI, V., . . . TAGLIAFICO, E. 2016. Unravelling the Complexity of Inherited Retinal Dystrophies Molecular Testing: Added Value of Targeted Next-Generation Sequencing. *BioMed Research International,* 2016**,** 6341870. http://dx.doi.org/10.1155/2016/6341870.

BIRTEL, J., GLIEM, M., MANGOLD, E., MÜLLER, P. L., HOLZ, F. G., NEUHAUS, C., . . . CHARBEL ISSA, P. 2018. Next-generation sequencing identifies unexpected genotype-phenotype correlations in patients with retinitis pigmentosa. *PLoS One,* 13**,** e0207958. http://dx.doi.org/10.1371/journal.pone.0207958.

BRANHAM, K., OTHMAN, M., BRUMM, M., KAROUKIS, A. J., ATMACA-SONMEZ, P., YASHAR, B. M., . . . SWAROOP, A. 2012. Mutations in RPGR and RP2 account for 15% of males with simplex retinal degenerative disease. *Invest Ophthalmol Vis Sci,* 53**,** 8232-7. http://dx.doi.org/10.1167/iovs.12-11025.

BREUER, D. K., YASHAR, B. M., FILIPPOVA, E., HIRIYANNA, S., LYONS, R. H., MEARS, A. J., . . . SWAROOP, A. 2002. A comprehensive mutation analysis of RP2 and RPGR in a North American cohort of families with X-linked retinitis pigmentosa. *Am J Hum Genet,* 70**,** 1545-54. http://dx.doi.org/10.1086/340848.

CHAPPLE, J. P., HARDCASTLE, A. J., GRAYSON, C., SPACKMAN, L. A., WILLISON, K. R. & CHEETHAM, M. E. 2000. Mutations in the N-terminus of the X-linked retinitis pigmentosa protein RP2 interfere with the normal targeting of the protein to the plasma membrane. *Hum Mol Genet,* 9**,** 1919-26. http://dx.doi.org/10.1093/hmg/9.13.1919.

CHAPPLE, J. P., HARDCASTLE, A. J., GRAYSON, C., WILLISON, K. R. & CHEETHAM, M. E. 2002. Delineation of the plasma membrane targeting domain of the X-linked retinitis pigmentosa protein RP2. *Invest Ophthalmol Vis Sci,* 43**,** 2015-20.

CHURCHILL, J. D., BOWNE, S. J., SULLIVAN, L. S., LEWIS, R. A., WHEATON, D. K., BIRCH, D. G., . . . DAIGER, S. P. 2013. Mutations in the X-linked retinitis pigmentosa genes

RPGR and RP2 found in 8.5% of families with a provisional diagnosis of autosomal dominant retinitis pigmentosa. *Invest Ophthalmol Vis Sci,* 54**,** 1411-6. http://dx.doi.org/10.1167/iovs.12-11541.

CONSUGAR, M. B., NAVARRO-GOMEZ, D., PLACE, E. M., BUJAKOWSKA, K. M., SOUSA, M. E., FONSECA-KELLY, Z. D., . . . PIERCE, E. A. 2015. Panel-based genetic diagnostic testing for inherited eye diseases is highly accurate and reproducible, and more sensitive for variant detection, than exome sequencing. *Genet Med,* 17**,** 253-261. http://dx.doi.org/10.1038/gim.2014.172.

DE LIN, W.-., WANG, C.-H., CHOU, I.-C. & TSAI, F.-J. 2014. A novel one-base insertion mutation in the retinitis pigmentosa 2 gene in a large X-linked Taiwanese family. *Acta Ophthalmologica,* 92**,** e161-e162. http://dx.doi.org/https://doi.org/10.1111/aos.12226.

DE LUCA, A., TORRENTE, I., MANGINO, M., DANESI, R., DALLAPICCOLA, B. & NOVELLI, G. 2001. Three novel mutations causing a truncated protein within the RP2 gene in Italian families with X-linked retinitis pigmentosa. *Mutat Res,* 432**,** 79-82. http://dx.doi.org/10.1016/s1383-5726(00)00007-8.

DOCKERY, A., STEPHENSON, K., KEEGAN, D., WYNNE, N., SILVESTRI, G., HUMPHRIES, P., . . . FARRAR, G. J. 2017. Target 5000: Target Capture Sequencing for Inherited Retinal Degenerations. *Genes (Basel),* 8. http://dx.doi.org/10.3390/genes8110304.

EISENBERGER, T., NEUHAUS, C., KHAN, A. O., DECKER, C., PREISING, M. N., FRIEDBURG, C., . . . BOLZ, H. J. 2013. Increasing the yield in targeted next-generation sequencing by implicating CNV analysis, non-coding exons and the overall variant load: the example of retinal dystrophies. *PloS one,* 8**,** e78496-e78496. http://dx.doi.org/10.1371/journal.pone.0078496.

ELLINGFORD, J. M., BARTON, S., BHASKAR, S., O'SULLIVAN, J., WILLIAMS, S. G., LAMB, J. A., . . . BLACK, G. C. M. 2016. Molecular findings from 537 individuals with inherited retinal disease. *J Med Genet,* 53**,** 761-767. http://dx.doi.org/10.1136/jmedgenet-2016-103837.

FERNANDEZ-SAN JOSE, P., CORTON, M., BLANCO-KELLY, F., AVILA-FERNANDEZ, A., LOPEZ-MARTINEZ, M. A., SANCHEZ-NAVARRO, I., . . . AYUSO, C. 2015. Targeted Next-Generation Sequencing Improves the Diagnosis of Autosomal Dominant Retinitis Pigmentosa in Spanish Patients. *Investigative Ophthalmology & Visual Science,* 56**,** 2173-2182. http://dx.doi.org/10.1167/iovs.14-16178.

FUJINAMI, K., LIU, X., UENO, S., MIZOTA, A., SHINODA, K., KUNIYOSHI, K., . . . JAPAN EYE GENETICS CONSORTIUM STUDY, G. 2020. RP2-associated retinal disorder in a Japanese cohort: Report of novel variants and a literature review, identifying a genotype-phenotype association. *Am J Med Genet C Semin Med Genet,* 184**,** 675-693. http://dx.doi.org/10.1002/ajmg.c.31830.

GARCÍA-HOYOS, M., GARCIA-SANDOVAL, B., CANTALAPIEDRA, D., RIVEIRO, R., LORDA-SÁNCHEZ, I., TRUJILLO-TIEBAS, M. J., . . . AYUSO, C. 2006. Mutational Screening of the RP2 and RPGR Genes in Spanish Families with X-Linked Retinitis Pigmentosa. *Investigative Ophthalmology & Visual Science,* 47**,** 3777-3782. http://dx.doi.org/10.1167/iovs.06-0323.

GE, Z., BOWLES, K., GOETZ, K., SCHOLL, H. P. N., WANG, F., WANG, X., . . . CHEN, R. 2015. NGS-based Molecular diagnosis of 105 eyeGENE® probands with Retinitis Pigmentosa. *Scientific Reports,* 5**,** 18287. http://dx.doi.org/10.1038/srep18287.

HARDCASTLE, A. J., THISELTON, D. L., VAN MALDERGEM, L., SAHA, B. K., JAY, M., PLANT, C., . . . BHATTACHARYA, S. 1999. Mutations in the RP2 gene cause disease in 10% of families with familial X-linked retinitis pigmentosa assessed in this study. *Am J Hum Genet,* 64**,** 1210-5. http://dx.doi.org/10.1086/302325.

HORNER, F., WAWRZYNSKI, J. & MACLAREN, R. E. 2019. Novel non-sense mutation in RP2 (c.843_844insT/p.Arg282fs) is associated with a severe phenotype of retinitis pigmentosa without evidence of primary retinal pigment epithelium involvement. *BMJ Case Rep,* 12. http://dx.doi.org/10.1136/bcr-2018-224451.

JAYASUNDERA, T., BRANHAM, K. E., OTHMAN, M., RHOADES, W. R., KAROUKIS, A. J., KHANNA, H., . . . HECKENLIVELY, J. R. 2010. RP2 phenotype and pathogenetic correlations in X-linked retinitis pigmentosa. *Arch Ophthalmol,* 128**,** 915-23. http://dx.doi.org/10.1001/archophthalmol.2010.122.

JI, Y., WANG, J., XIAO, X., LI, S., GUO, X. & ZHANG, Q. 2010. Mutations in RPGR and RP2 of Chinese patients with X-linked retinitis pigmentosa. *Curr Eye Res,* 35**,** 73-9. http://dx.doi.org/10.3109/02713680903395299.

JIANG, J., WU, X., SHEN, D., DONG, L., JIAO, X., HEJTMANCIK, J. F. & LI, N. 2017. Analysis of RP2 and RPGR Mutations in Five X-Linked Chinese Families with Retinitis Pigmentosa. *Scientific Reports,* 7**,** 44465. http://dx.doi.org/10.1038/srep44465.

JINDA, W., TAYLOR, T. D., SUZUKI, Y., THONGNOPPAKHUN, W., LIMWONGSE, C., LERTRIT, P., . . . ATCHANEEYASAKUL, L. O. 2014. Whole exome sequencing in Thai patients

with retinitis pigmentosa reveals novel mutations in six genes. *Invest Ophthalmol Vis Sci,* 55**,** 2259-68. http://dx.doi.org/10.1167/iovs.13-13567.

KUHNEL, K., VELTEL, S., SCHLICHTING, I. & WITTINGHOFER, A. 2006. Crystal structure of the human retinitis pigmentosa 2 protein and its interaction with Arl3. *Structure,* 14**,** 367-78. http://dx.doi.org/10.1016/j.str.2005.11.008.

KURATA, K., HOSONO, K., HAYASHI, T., MIZOBUCHI, K., KATAGIRI, S., MIYAMICHI, D., . . . HOTTA, Y. 2019. X-linked Retinitis Pigmentosa in Japan: Clinical and Genetic Findings in Male Patients and Female Carriers. *Int J Mol Sci,* 20. http://dx.doi.org/10.3390/ijms20061518.

LIM, H., PARK, Y. M., LEE, J. K. & TAEK LIM, H. 2016. Single-Exome sequencing identified a novel RP2 mutation in a child with X-linked retinitis pigmentosa. *Can J Ophthalmol,* 51**,** 326-330. http://dx.doi.org/10.1016/j.jcjo.2016.03.017.

LIU, F., QIN, Y., YU, S., SOARES, D. C., YANG, L., WENG, J., . . . LIU, M. 2017. Pathogenic mutations in retinitis pigmentosa 2 predominantly result in loss of RP2 protein stability in humans and zebrafish. *J Biol Chem,* 292**,** 6225-6239. http://dx.doi.org/10.1074/jbc.M116.760314.

LYRAKI, R., LOKAJ, M., SOARES, D. C., LITTLE, A., VERMEREN, M., MARSH, J. A., . . . HURD, T. 2018. Characterization of a novel RP2-OSTF1 interaction and its implication for actin remodelling. *J Cell Sci,* 131. http://dx.doi.org/10.1242/jcs.211748.

MASHIMA, Y., SAGA, M., HIIDA, Y., IMAMURA, Y., KUDOH, J. & SHIMIZU, N. 2000. Novel mutation in RP2 gene in two brothers with X-linked retinitis pigmentosa and mtDNA mutation of leber hereditary optic neuropathy who showed marked differences in clinical severity. *Am J Ophthalmol,* 130**,** 357-9. http://dx.doi.org/10.1016/s0002-9394(00)00553-5.

MEARS, A. J., GIESER, L., YAN, D., CHEN, C., FAHRNER, S., HIRIYANNA, S., . . . SWAROOP, A. 1999. Protein-truncation mutations in the RP2 gene in a North American cohort of families with X-linked retinitis pigmentosa. *Am J Hum Genet,* 64**,** 897-900. http://dx.doi.org/10.1086/302298.

MIANO, M. G., TESTA, F., FILIPPINI, F., TRUJILLO, M., CONTE, I., LANZARA, C., . . . CICCODICOLA, A. 2001. Identification of novel RP2 mutations in a subset of X-linked retinitis pigmentosa families and prediction of new domains. *Hum Mutat,* 18**,** 109-19. http://dx.doi.org/10.1002/humu.1160.

MISKY, D., GUILLAUMIE, T., BAUDOIN, C., BOCQUET, B., BELTRAN, M., KAPLAN, J., . . . HAMEL, C. P. 2016. Pattern dystrophy in a female carrier of RP2 mutation. *Ophthalmic Genet,* 37**,** 453-455. http://dx.doi.org/10.3109/13816810.2015.1081253.

NEIDHARDT, J., GLAUS, E., LORENZ, B., NETZER, C., LI, Y., SCHAMBECK, M., . . . BERGER, W. 2008. Identification of novel mutations in X-linked retinitis pigmentosa families and implications for diagnostic testing. *Mol Vis,* 14**,** 1081-93.

NEVELING, K., COLLIN, R. W. J., GILISSEN, C., VAN HUET, R. A. C., VISSER, L., KWINT, M. P., . . . SCHEFFER, H. 2012. Next-generation genetic testing for retinitis pigmentosa. *Human Mutation,* 33**,** 963-972. http://dx.doi.org/https://doi.org/10.1002/humu.22045.

PAN, X., CHEN, X., LIU, X., GAO, X., KANG, X., XU, Q., . . . ZHAO, C. 2014. Mutation analysis of pre-mRNA splicing genes in Chinese families with retinitis pigmentosa. *Mol Vis,* 20**,** 770-9.

PARMEGGIANI, F., BARBARO, V., MIGLIORATI, A., RAFFA, P., NESPECA, P., DE NADAI, K., . . . DI IORIO, E. 2017. Novel variants of RPGR in X-linked retinitis pigmentosa families and genotype-phenotype correlation. *Eur J Ophthalmol,* 27**,** 240-248. http://dx.doi.org/10.5301/ejo.5000879.

PELLETIER, V., JAMBOU, M., DELPHIN, N., ZINOVIEVA, E., STUM, M., GIGAREL, N., . . . ROZET, J. M. 2007. Comprehensive survey of mutations in RP2 and RPGR in patients affected with distinct retinal dystrophies: genotype-phenotype correlations and impact on genetic counseling. *Hum Mutat,* 28**,** 81-91. http://dx.doi.org/10.1002/humu.20417.

PEREZ-CARRO, R., CORTON, M., SÁNCHEZ-NAVARRO, I., ZURITA, O., SANCHEZ-BOLIVAR, N., SÁNCHEZ-ALCUDIA, R., . . . AYUSO, C. 2016. Panel-based NGS Reveals Novel Pathogenic Mutations in Autosomal Recessive Retinitis Pigmentosa. *Scientific reports,* 6**,** 19531-19531. http://dx.doi.org/10.1038/srep19531.

PROKISCH, H., HARTIG, M., HELLINGER, R., MEITINGER, T. & ROSENBERG, T. 2007. A population-based epidemiological and genetic study of X-linked retinitis pigmentosa. *Invest Ophthalmol Vis Sci,* 48**,** 4012-8. http://dx.doi.org/10.1167/iovs.07-0071.

RIERA, M., NAVARRO, R., RUIZ-NOGALES, S., MÉNDEZ, P., BURÉS-JELSTRUP, A., CORCÓSTEGUI, B. & POMARES, E. 2017. Whole exome sequencing using Ion

Proton system enables reliable genetic diagnosis of inherited retinal dystrophies. *Sci Rep,* 7**,** 42078. http://dx.doi.org/10.1038/srep42078.

ROSENBERG, T., SCHWAHN, U., FEIL, S. & BERGER, W. 1999. Genotype-phenotype correlation in X-linked retinitis pigmentosa 2 (RP2). *Ophthalmic Genet,* 20**,** 161-72. http://dx.doi.org/10.1076/opge.20.3.161.2278.

SCHORDERET, D. F., IOURANOVA, A., FAVEZ, T., TIAB, L. & ESCHER, P. 2013. IROme, a new high-throughput molecular tool for the diagnosis of inherited retinal dystrophies. *Biomed Res Int,* 2013**,** 198089. http://dx.doi.org/10.1155/2013/198089.

SCHWAHN, U., LENZNER, S., DONG, J., FEIL, S., HINZMANN, B., VAN DUIJNHOVEN, G., . . . BERGER, W. 1998. Positional cloning of the gene for X-linked retinitis pigmentosa 2. *Nat Genet,* 19**,** 327-32. http://dx.doi.org/10.1038/1214.

SCHWAHN, U., PALAND, N., TECHRITZ, S., LENZNER, S. & BERGER, W. 2001. Mutations in the X-linked RP2 gene cause intracellular misrouting and loss of the protein. *Hum Mol Genet,* 10**,** 1177-83. http://dx.doi.org/10.1093/hmg/10.11.1177.

SHARON, D., BRUNS, G. A. P., MCGEE, T. L., SANDBERG, M. A., BERSON, E. L. & DRYJA, T. P. 2000. X-Linked Retinitis Pigmentosa: Mutation Spectrum of the RPGR and RP2 Genes and Correlation with Visual Function. *Investigative Ophthalmology & Visual Science,* 41**,** 2712-2721.

SHARON, D., SANDBERG, M. A., RABE, V. W., STILLBERGER, M., DRYJA, T. P. & BERSON, E. L. 2003. RP2 and RPGR mutations and clinical correlations in patients with X-linked retinitis pigmentosa. *Am J Hum Genet,* 73**,** 1131-46. http://dx.doi.org/10.1086/379379.

THISELTON, D. L., ZITO, I., PLANT, C., JAY, M., HODGSON, S. V., BIRD, A. C., . . . HARDCASTLE, A. J. 2000. Novel frameshift mutations in the RP2 gene and polymorphic variants. *Human Mutation,* 15**,** 580-580. http://dx.doi.org/https://doi.org/10.1002/1098-1004(200006)15:6<580::AID-HUMU15>3.0.CO;2-3.

VILLAVERDE-MONTERO, C., GARCÍA-HOYOS, M., GIMÉNEZ-PARDO, A., TRUJILLO-TIEBAS, M. J., BAIGET, M. & AYUSO, C. 2007. Gene symbol: RP2. *Hum Genet,* 121**,** 289.

VORSTER, A. A., REBELLO, M. T., COUTTS, N., EHRENREICH, L., GAMA, A. D., ROBERTS, L. J., . . . GREENBERG, L. J. 2004. Arg120stop nonsense mutation in the RP2 gene: mutational hotspot and germ line mosaicism? *Clin Genet,* 65**,** 7-10. http://dx.doi.org/10.1111/j..2004.00163.x.

WADA, Y., NAKAZAWA, M., ABE, T. & TAMAI, M. 2000. A New Leu253Arg Mutation in the RP2 Gene in a Japanese Family with X-Linked Retinitis Pigmentosa. *Investigative Ophthalmology & Visual Science,* 41**,** 290-293.

WANG, H., WANG, X., ZOU, X., XU, S., LI, H., SOENS, Z. T., . . . SUI, R. 2015. Comprehensive Molecular Diagnosis of a Large Chinese Leber Congenital Amaurosis Cohort. *Investigative Ophthalmology & Visual Science,* 56**,** 3642-3655. http://dx.doi.org/10.1167/iovs.14-15972.

WATSON, C. M., EL-ASRAG, M., PARRY, D. A., MORGAN, J. E., LOGAN, C. V., CARR, I. M., . . . ALI, M. 2014. Mutation Screening of Retinal Dystrophy Patients by Targeted Capture from Tagged Pooled DNAs and Next Generation Sequencing. *PLOS ONE,* 9**,** e104281. http://dx.doi.org/10.1371/journal.pone.0104281.

WHELAN, L., DOCKERY, A., WYNNE, N., ZHU, J., STEPHENSON, K., SILVESTRI, G., . . . FARRAR, G. J. 2020. Findings from a Genotyping Study of over 1000 People with Inherited Retinal Disorders in Ireland. *Genes,* 11**,** 105.

XU, Y., GUAN, L., SHEN, T., ZHANG, J., XIAO, X., JIANG, H., . . . ZHANG, Q. 2014. Mutations of 60 known causative genes in 157 families with retinitis pigmentosa based on exome sequencing. *Hum Genet,* 133**,** 1255-71. http://dx.doi.org/10.1007/s00439-014-1460-2.

YU H.G., PARK U.C. & C.K., Y. 2017. Retinitis Pigmentosa in Korean Patients. *In:* PRAKASH G. & T., I. (eds.) *Advances in Vision Research, Volume I. Essentials in Ophthalmology.* Tokyo: Springer.

ZHANG, J., GAO, F., DU, C., WANG, J., PI, X., GUO, W., . . . CUI, X. 2019. A novel RP2 missense mutation Q158P identified in an X-linked retinitis pigmentosa family impaired RP2 protein stability. *Gene,* 707**,** 86-92. http://dx.doi.org/10.1016/j.gene.2019.05.006.

ZHANG, L., WANG, T., WRIGHT, A. F., SURI, M., SCHWARTZ, C. E., STEVENSON, R. E. & VALLE, D. 2006. A microdeletion in Xp11.3 accounts for co-segregation of retinitis pigmentosa and mental retardation in a large kindred. *Am J Med Genet A,* 140**,** 349-57. http://dx.doi.org/10.1002/ajmg.a.31080.

7.3 Appendix 3 – Sequence analysis of the *RHO* 5'UTR region

The human rhodopsin 5'UTR and flanking regions were Sanger sequenced in *RHO* P347 mice and HEK 293 cells. The resulting sequences were aligned and compared to the *RHO* reference gene (RefSeq: NG_009115.1). The 5'UTR is highlighted by an overlying purple line. No deviations from the *RHO* reference sequence were evident in this region. Alignments were carried out using MAFFT[44].

[44] https://mafft.cbrc.jp/alignment/server/

7.4 Appendix 4 – HuNdi1 construct sequence

Features included in the AAV-CMV-huNdi1 construct and their sequences are given (ITRs not shown).

Features

CMV promoter (sequence highlighted in yellow)

HuNdi1 coding sequence (blue)

Minimal polyadenylation signal (red)

Sequence

GCGGCCCGGATCCTAGTGGATGCGGCCAAACTTAAAAACGCGTGGAGCTAGTTATTAATAGTAAT
CAATTACGGGGTCATTAGTTCATAGCCCATATATGGAGTTCCGCGTTACATAACTTACGGTAAATG
GCCCGCCTGGCTGACCGCCCAACGACCCCCGCCCATTGACGTCAATAATGACGTATGTTCCCATA
GTAACGCCAATAGGGACTTTCCATTGACGTCAATGGGTGGAGTATTTACGGTAAACTGCCCACTT
GGCAGTACATCAAGTGTATCATATGCCAAGTACGCCCCCTATTGACGTCAATGACGGTAAATGGC
CCGCCTGGCATTATGCCCAGTACATGACCTTATGGGACTTTCCTACTTGGCAGTACATCTACGTAT
TAGTCATCGCTATTACCATGGTGATGCGGTTTTGGCAGTACATCAATGGGCGTGGATAGCGGTTT
GACTCACGGGGATTTCCAAGTCTCCACCCCATTGACGTCAATGGGAGTTTGTTTTGGCACCAAAAT
CAACGGGACTTTCCAAAATGTCGTAACAACTCCGCCCCATTGACGCAAATGGGCGGTAGGCGTGT
ACGGTGGGAGGTCTATATAAGCAGAGCTCGTTTAGTGAACCGTCAGATCGCCTGGAGACGCCAT
CCACGCTGTTTTGACCTCCATAGAAGACACCGGGACCGATCCAGCCTCCGCGGATTCAAACGGGC
CCTCTAGAGGTGTCAGTTTCATCACATCATCGAATTACACGTTTACCCAAGAGAAGAAACTAAAAA
CCACTATGCTGAGCAAGAACCTGTACAGCAACAAGCGGCTGCTGACCAGCACCAACACCCTCGTG
CGCTTCGCCAGCACCAGATCCACCGGCGTCGAAAACAGCGGGGCTGGCCCCACCAGCTTCAAGA
CCATGAAGGTCATCGACCCCCAGCACAGCGACAAGCCCAACGTGCTGATCCTGGGCTCTGGCTGG
GGCGCCATCAGCTTTCTGAAGCACATCGACACCAAGAAGTACAACGTCAGCATCATCAGCCCCAG
AAGCTACTTCCTGTTCACCCCCCTGCTGCCCAGCGCCCCTGTGGGAACCGTGGACGAGAAGTCCA
TCATCGAGCCCATCGTGAACTTCGCCCTGAAGAAAAAGGGCAACGTCACCTACTACGAGGCCGA
GGCCACCAGCATCAACCCCGACCGGAACACCGTGACCATCAAGAGCCTGAGCGCCGTGTCCCAG
CTGTACCAGCCCGAGAACCACCTGGGCCTGCACCAGGCCGAGCCCGCCGAGATTAAGTACGACT
ACCTGATCAGCGCCGTGGGCGCCGAGCCCAACACCTTTGGAATCCCCGGCGTGACCGACTACGG
CCACTTCCTGAAAGAGATCCCCAACAGCCTGGAAATCCGGCGGACCTTCGCCGCCAACCTGGAAA
AGGCCAACCTGCTGCCTAAGGGCGACCCCGAGCGGAGAAGGCTGCTGAGCATCGTGGTCGTGG
GCGGAGGCCCCACAGGCGTGGAAGCTGCTGGCGAGCTGCAGGACTACGTGCACCAGGACCTGC
GGAAGTTCCTGCCCGCCCTGGCCGAGGAAGTGCAGATTCACCTGGTGGAAGCCCTGCCCATCGT
GCTGAACATGTTCGAGAAGAAGCTGAGCAGCTACGCCCAGAGCCACCTGGAAAACACCTCCATC
AAGGTGCACCTGAGAACCGCCGTGGCCAAGGTGGAAGAGAAGCAGCTGCTGGCCAAGACCAAG
CACGAGGACGGCAAGATTACCGAGGAAACCATCCCCTACGGCACCCTGATTTGGGCCACCGGCA
ACAAGGCCAGACCCGTGATCACCGACCTGTTCAAGAAGATCCCCGAGCAGAACAGCAGCAAGCG
GGGCCTGGCCGTGAACGACTTCCTGCAGGTCAAAGGCAGCAACAACATCTTCGCCATCGGCGAC
AACGCCTTTGCCGGCCTGCCTCCTACAGCCCAGGTGGCCCACCAGGAAGCCGAGTACCTGGCCAA
GAACTTCGACAAGATGGCCCAGATCCCCAATTTCCAGAAGAACCTGTCCTCCCGGAAGGATAAGA
TCGACCTGCTGTTCGAGGAAAACAACTTCAAGCCCTTCAAGTACAACGACCTGGGCGCCCTGGCC
TACCTGGGCAGCGAAAGAGCCATTGCCACCATCAGAAGCGGCAAGCGGACCTTCTACACCGGCG
GAGGCCTGATGACCTTCTACCTGTGGCGGATCCTGTACCTGAGCATGATCCTGAGCGCCCGCAGC
AGACTGAAGGTGTTCTTCGACTGGATCAAGCTGGCCTTCTTCAAGAGGGACTTCTTCAAGGGCCT
GTGAATGAAATTAACATGCCCTTTTCTGGAAAAAGGAAAAAAGGTGGTAGGCACCGTTTTTTCCT

GAGTTTGCATCCTTTTTTTTCTAAAACCCTCTAAACAAAACCTAACACACACACACACGCACAAAAA
AATGCACATGATGTTTTATTATTTATATATTCCCACTTTTTTCGAAATGATGCTTGACTAATGCACA
AGCAAAAAACCCCGACAAGATTGGTTGATCACTGCGGCCGCAATAAAGGAAATTTATTTTCATTG
CAATAGTGTGTTGGTTTTTTGTGTGGATATCCAGGGCCCGTTTGG